Environmental γ-Ray Spectrometry:
Simulation of Absolute Calibration of In-Situ and Airborne Spectrometers for Natural and Anthropogenic Sources

by

J.D. Allyson

Submitted to

The University of Glasgow

(Faculty of Science)

for the degree of

Doctor of Philosophy

September 1994

This research was conducted at the Scottish Universities Research and Reactor Centre, East Kilbride.

Environmental γ-Ray Spectrometry: Simulation of Absolute Calibration of In-Situ and Airborne Spectrometers for Natural and Anthropogenic Sources

Abstract

The purpose of this work is to investigate experimentally and theoretically a range of problems encountered in calibration of γ-ray spectrometers (converting count rates to radioelement ground concentrations), for the natural and manmade radionuclides. For in-situ and aerial survey measurements, the form of radionuclide deposition with soil depth, aerial survey altitude, and detector spectral responses are important considerations when calibrating detector systems. A modification of spectral shape is apparent, owing to scattering and attenuation in the soil and air path between source and detector. A variety of depth profiles and detector configurations have therefore been considered, which are usually encountered in practice.

It has been shown for the first time, that it is possible to reconstruct the full spectral response of a detector to calibrate a spectrometer from absolutely theoretical first principles. In doing so, one can avoid some of the problems inherent in experimental approaches. After overcoming technical and methodological problems, the work has been successful in all of its objectives.

Experimental investigations of in-situ and aerial survey detectors serve as useful validation studies for theoretical models of the same detector types. The research therefore began with laboratory based measurements using point sources of radionuclides of interest. The acquisition of doped concrete calibration pads has enabled comparisons to be made with other facilities and spectrometers found world-wide. Small scale experimental simulations of detector responses at different altitudes have been made using the calibration pads and perspex absorbers. This extends and improves upon previous work done elsewhere, and uses more suitable absorber types.

For the consideration of full energy responses only, analytical methods can be conveniently to applied. The sensitivity to short lived radionuclides, detector fields of view under different environmental conditions and geometrical effects due to variations

in topographic relief can be investigated by these methods in a rapid manner. In this study, standard expressions were extended to describe radionuclide distributions (which is usually assumed to be homogeneous) and detector angular responses (usually assumed to be symmetrical).

For the full simulation of γ-ray transport and the response of detector systems, Monte Carlo techniques provide complete solutions by consideration of full and partial energy interactions. Any form of deposition can be introduced quite easily. In addition, it has been possible to simulate detector angular response of large aerial survey systems, including detector housings and photomultiplier tubes. The inclusion of scattering in the environment, and within the source itself, is essential for the authentic simulation of spectral data. The low energy, Compton scatter continuum and back scatter peak carry potentially useful information and may ultimately enable the description of radionuclide depth profiles from in-situ measurements.

The effects of air path scattering increase with altitude. To account for this behaviour, Monte Carlo methods offer significant advantages over large scale experimental approaches where source homogeneity is uncertain and cannot be practically assessed over such large fields of view, and where small scale experiments only consider (by their very nature) limited geometries. Differences between simulation and experimental methods can be attributed to both approaches and underlying assumptions.

The results from this research have been applied to a number of studies conducted on behalf of BNF plc and The Scottish Office (HMIPI). The spectral separation of ^{234m}Pa and ^{228}Ac, found in the Ribble Estuary, near the Springfields fuel fabrication facility of BNF plc was achieved for the first time, using an extension of the usual data processing methodology. More recently these spectral processing tools have been applied to the search of depleted uranium military projectiles near a gunnery range in SW Scotland.

The combination of experimental, analytical, and Monte Carlo simulation of the response of aerial survey detectors has provided an important contribution to putting radiometric measurements on an absolute basis, thus assisting to establish these techniques for environmental measurements.

Acknowledgements

I would like to thank a number of people who have helped and encouraged during my period of research at the Scottish Universities Research and Reactor Centre, East Kilbride, Scotland. My supervisor, Dr. David Sanderson, provided the opportunities to enable personal experience of aerial surveys within the UK and abroad. Without this it would have been very difficult to appreciate the practical difficulties involved in collecting significant quantities of data, the detailed processing and mapping in a highly interesting way. I would also like to thank Prof. Roger Scott for additional support and critical assessments.

I would like to thank all friends and colleagues within SURRC, and especially Andrew Tyler, Lorna Carmichael, Christine Slater, Peter Clark and Marian Scott for their cheerfulness, encouragement, assistance, trust and humour.

I would also like to thank Mum, Dad and Jayne for their belief that one day I might achieve an ambition to provide some contribution to the field of science.

Contents

List of Tables

List of Figures

"Science teaches those who immerse themselves in it to know the workings of God in Nature, but the practice of science does more than this. As the depth of their understanding grows, its students cannot fail to learn the interdependence of all creation. This is even more than the brotherhood of man, this is the harmony of all nature. Furthermore, those who devote themselves to science, thereby learn humility",

Magnus Pike, *The Guardian* (1974).

1. Introduction to In-situ and Aerial Gamma-ray Spectrometry

1.1 Introduction

In-situ environmental gamma-ray spectrometry has long been recognised as a method of estimating radionuclide concentration. Aerial γ-ray spectrometry is a special case of in-situ spectrometry. A major advantage of this technique, over analysis of samples in the laboratory, is that a large and representative sample volume is analysed. Minor inhomogeneities are averaged out. It is quick and easy to perform and is suitable for assessments of environmental and radiological impacts in emergency situations. However, there are several criteria that have to be met to ensure reliable results and some prior knowledge of source characteristics may be necessary. By contrast laboratory based analysis of environmental samples is time consuming in collection, preparation and counting. Individual samples can be accurately assayed but owing to the sample size collected, the spread of results between samples may be large. It is often more productive to target potential ground sampling regions by using in-situ techniques.

While laboratory based counting and calibration procedures use a standardised sample geometry, in-situ measurements use a geometry approaching 2π (*half-space*) and require some understanding of the radionuclide distribution, attenuating properties of a soil matrix and detector responses. Individual radionuclides are identified by means of their characteristic γ-rays. Identification and correct interpretation of spectral analysis depends upon the underlying physical processes that influence the behaviour of γ-rays between emission and detection. Superficially dispersed activity (eg. fallout) is only partially attenuated within surface layers of ground matrices, whereas for buried sources (eg. natural radionuclides), γ-rays barely penetrate more than 50cm of dry, loosely consolidated overburden. Additional information about the bedrock beneath residual soil cover is possible if the soil has not undergone excessive leaching (this increases in hot and humid tropical climates). Ninety percent of the γ-ray radiation is emitted from the top 15-25cm of surface rock of density 2.7 g cm^{-3} (Grasty, 1976a). In areas of little outcrop, the surface material then must be reasonably representative (locally derived)

of the underlying bedrock for geological interpretation purposes.

Detection of γ-ray fluence rates from surface or relatively shallow subsurface layers at ground level by in-situ spectrometry (by stationary or vehicular based instrumentation) and at elevated heights (by fixed or rotary wing aircraft based systems) enable radionuclide inventories to be estimated if suitable calibrations are applied. For interrogations deep below the surface in-situ bore hole measurements are necessary.

Gamma-ray spectrometry or *radiometrics* is of considerable value to mineral and geological mapping, where the natural radioelements show correlations and are potential indicators of natural resources. The mapping of different soil types is possible. Natural radiation also represents the minimum level of potential exposure to man and can be used in relating the significance of man-made sources.

The uses of nuclear energy have led to pollution of the environment from man-made or *anthropogenic* radionuclides. Environmental monitoring of these nuclear species has become increasingly important for radiological and epidemiological studies. Accidental releases of radioactive materials and their proliferation in general must be guarded against. The most serious accidents have occurred in industrialised, developed nations (Windscale, Three Mile Island & Chernobyl): the prospects for those developing countries which are not yet recognised as being responsible members of the international community are of fundamental concern. Whilst every effort must be made to encourage those countries to achieve economic and political stability through technological exchanges and trade, proper inspection and enforcement of safety principles must also be exercised. Whatever the future, the monitoring of environmental damage from man-made radioactive materials will remain a continuous and necessary obligation.

1.2 Ground Based In-situ Measurements

Geiger-Müller tubes are very sensitive to ß-radiation and have been used extensively in uranium ore prospecting. They are cheap, compact and are able to sustain rough handling. However only crude energy discrimination is possible and they are not suitable for multi-component γ-ray spectroscopy. The advent of scintillation detectors and modern nucleonics provided the means for efficient γ-ray spectrometry.

Scintillation NaI(Tl) detectors continue to be used in many environmental investigations, due to their inherent efficiency, cost and ruggedness, despite often complex data processing techniques that are used to analyse multi γ-ray energy fields. Portable semi-conductor detectors of relatively lower efficiency offer unequivocal advantages due to their high resolving powers. The use of these in aerial survey applications remains a developing area. The largest germanium detectors offer efficiencies comparable with small NaI(Tl) detectors. Lightweight dewar designs with holding times of at least 24 hours, enable a semiconductor based spectrometer to be carried into the field.

Field based detectors are usually placed at 1m height on even, open terrain, thus avoiding nearby rock outcrops, trees and potentially attenuating structures. For other than fresh radionuclide deposition, where the activity may be regarded as a planar source, some knowledge of source depth profile must be procured. A uniform distribution is usually assumed for the natural decay series radionuclides and exponential for aged fallout. Where activity is brought by complex hydrodynamic processes, activity profiles may create subsurface maxima (Sanderson *et al*, 1993a).

Jones *et al* (1984) have extended stationary in-situ spectrometry to a moving platform. To study exposed intertidal sediments of the Solway Firth, a 7.62x7.62 cm NaI(Tl) spectrometer was employed, carried by hovercraft. This offers the advantages of mobility, little additional expense and reasonable area coverage within a given time. If the detector could be raised to increase the field of view, then the advantages of low-level airborne surveys are reproduced.

1.3 Aerial Measurements

The variations of radionuclide distribution over a wide area, may be mapped and assessed very quickly and relatively inexpensively by raising a detector to heights that can be flown by rotary or fixed wing aircraft. As the detector is raised, the proportion of land area interrogated rapidly increases. The influences of ground roughness and small topographic features are diminished.

Gamma-ray emissions of sufficient energy can penetrate several hundred metres in air. At 300m however, interaction in air results in a much degraded energy spectrum. The half-depth of ^{137}Cs (662keV) is 72m; ^{208}Tl (2615keV) is 158m. Other half depths are listed in table 1.1. Therefore the measurement of even the most energetic γ-rays must be made within a few hundred metres of the ground and only those originating within a few centimetres below the ground surface are detectable.

Most terrestrial materials (rocks, air, water) encountered in γ-ray surveys have low atomic number and because energies are less than 3 MeV, Compton scattering is the predominant process occurring between ground and detector. Air scattering of γ-rays into windows of lower energy (like source scattering), increases with altitude and must be accounted for during deconvolution. Aerial surveys are usually performed at constant height h. Owing to aircraft flying restrictions and topography, variations in survey altitude (often $\pm 20\%$) are corrected for by using an exponential function ,$e^{-\mu.h}$, valid for heights >50m. The height attenuation coefficients (μ), which are energy dependent, can be determined experimentally over a calibration range if available. A radar altimeter is the preferred method of recording height above ground.

The development of portable multi-channel spectrometers and advances in producing large single crystal scintillants of high resolution, have provided incentives to complement ground based measurements with high quality aerial spectral data.

Table 1.1 A comparison of half depths.

Energy / keV	Half Thickness /m			
	Air	**Water**	**Soil**	**Concrete**
100	37.5	0.042	0.025	0.018
500	65.2	0.072	0.049	0.035
1000	89.1	0.098	0.068	0.047
2000	127.1	0.141	0.097	0.068
3000	158.5	0.175	0.119	0.083
Density / g cm^{-3}	1.225×10^{-3}	1.0	1.6	2.3

In recent years, the use of rectangular shaped (prismatic) NaI(Tl) detectors has been favoured, since they allow compact packaging. Volumes of up to 50 litres have been regularly utilised for geological research and uranium exploration programmes (Bristow, 1979, 1983), (Aviv & Vulkan, 1983).

The use of scintillation detectors was first applied to environmental and radiological concerns following the Windscale fire in 1957 (Williams *et al*, 1957), (Williams & Cambray, 1960), but was of limited extent. Lister (1963) later recognised the greater potential of mapping fallout from low flying helicopters.

The potential of monitoring radioactive fallout at national scale was shown to be of great importance following the Chernobyl nuclear reactor accident in 1986 (Mellander, 1989). The planning of emergency responses following accidents is essential to limit external radiation doses in the immediate vicinity and restrict the sale of agricultural produce, which may be transported far away. The speed with which aerial surveys can cover vast areas of contaminated ground, is the most important advantage.

The monitoring of nuclear establishments has since become a regular occurrence in

many countries (Feimster, 1979), (Hilton, 1979), (Rangelov *et al*, 1990). In the United Kingdom, The Scottish Universities Research and Reactor Centre (SURRC) and British Nuclear Fuels plc (BNF), have brought together their respective expertise for the regular measurement and practice of airborne surveys near nuclear power and reprocessing plants: Sellafield (Sanderson *et al*, 1990c); Chapelcross (Sanderson *et al*, 1992) and Springfields (Sanderson *et al*, 1993a).

Environmental measurements of existing pre- and post-Chernobyl fallout patterns, can establish background levels against which future deposition measurements can be compared (Sanderson *et al*, 1989, 1990a, 1993c). Baseline maps quantifying levels of natural radioactivity are also of benefit to epidemiological studies concerning incidence of leukaemia (Sanderson *et al*, 1993e). Several important and quite unprecedented surveys (within the UK) have been completed by SURRC jointly with externally funded bodies (Sanderson *et al*, 1988a), (Sanderson & Scott, 1988c), (Sanderson *et al*, 1990b), (Sanderson *et al*, 1993b).

The search for and recovery of lost sources of intense radioactivity have been quite successful. Deal *et al* (1972) reported the finding of an errant Athena missile and distributed remains of its two ^{57}Co sources, by the Aerial Radiological Measuring System (ARMS). In early 1978, the radioactive debris from the Russian satellite Cosmos 954 was found across the Northwest Territories of Canada using airborne detectors and coordinated effort between teams of Canadians and Americans (Bristow, 1978), (Grasty, 1980a). The SURRC has conducted two search surveys. The first in 1988, to find the remains of an industrial level gauge containing 6.22 GBq of ^{137}Cs, following an accident at BP Grangemouth oil refinery (Sanderson *et al*, 1988b). The second in the Niger Delta of Nigeria, where a 74 GBq (2 Ci) ^{137}Cs had been stolen by local bandits (Sanderson, Allyson, 1991).

1.4 Data Processing Procedure

In estimating radionuclide inventory, it is necessary to determine without ambiguity, the full energy deposition signified by the characteristic peaks of a spectrum. These are

then converted to radionuclide concentrations via a suitable calibration. Photopeaks are spread due to finite detector resolution. Generally, γ-rays from uranium, potassium and thorium, together with any others of interest (eg. ^{137}Cs), are counted within energy windows defined essentially by the resolution of the detector. Each window records primarily the counts from each radionuclide, plus a detector background. However there are interferences and some γ-rays originating from thorium are also recorded in the uranium and potassium windows. The interferences are due to nearby or overlapping peaks, or due to Compton scatter. The problem of eliminating interferences by *stripping*, is to assign true window counts to their proper source radionuclide. Full spectral unfolding is possible although not often necessary and has been accomplished by comparing measured spectra with those in a library, determined under the same operating conditions. This has included *interpolated* spectra (for those radionuclides for which it is difficult to obtain standard measured spectra) and completely calculated spectra (Heath, 1966).

Stripping ratios are applied in order to reduce net window count-rates to a simple set of linear equations, and produce true count-rates by solving an inverse matrix transformation. A stripping ratio is defined to be the fractional contribution, from Compton scatter or photopeak interference, from one gamma ray energy window into another. Unfolding of spectra is based upon the superposition principle: the response function of one radioisotope is unaffected by the presence of others. A method of estimating the fractional interferences, between energy windows, in relation to a full energy peak is by using small, individual, pure sources and assuming that these are representative of much larger sources. This may not necessarily be valid however. The stripping ratios measured from pure point sources are different from those found for sources having attenuating properties. The scattered γ-rays occurring in the sub-surface layers (if not accounted for by calibration methods) can lead to misleading concentration estimates.

1.5 Aerial Survey Operational and Data Processing Procedure

Nowadays, full spectral and window counts are recorded simultaneously, together with navigational co-ordinates and flight altitude. Dead time corrections are automatically made by a multi-channel analyser. A background subtraction is made, interferences removed and through calibration, estimates of radioelement concentrations listed. While real time data processing is possible, usually analyses and corrections are applied after the survey.

The following considerations are relevant to background subtraction. Although few primary cosmic-rays (mainly protons, alpha's and heavy nuclei) reach sea-level, showers of secondary particles (electrons, positrons, muons and γ-ray photons) can affect measurements and must be considered. The intensity of cosmic rays increases exponentially with increasing altitude. The usual method of measuring cosmic-ray count-rates in the spectral windows is to record all particles above 3 MeV in a cosmic-ray window. The fraction occurring in the other spectral windows can then be determined. Usually, a series of flights at different altitudes, well above terrestrial sources of activity and radon decay products in the atmosphere is necessary (say, 1500 to 3000m at 300m intervals). Linear regression of counts within each window against the cosmic window also provides the aircraft contribution at the intercept.

Atmospheric radon is usually determined by flying at survey altitude (around 100m) over water. For areas with few lakes, upward looking auxiliary detectors shielded by lead sheet or by the main, downward facing detectors have been used. A ^{214}Bi window is used from the upward looking detector to predict the component in the ^{214}Bi window of the downward facing detector. This can then be used to remove the components occurring in the other windows of the downward facing detector.

Spectral deconvolution of background corrected data is made to determine true counts from net counts of the radionuclide of interest. Grasty (1976b) notes that since calibration sources of infinite size, containing pure radioelements of interest (and in sufficient concentrations) are unavailable, it is practically impossible to determine

stripping ratio altitude dependence in a realistic experiment. The Geological Survey of Canada has compromised and determined the value of the stripping ratio of ^{208}Tl into ^{214}Bi window (α) at ground level, and applied an analytical solution to find the increase of α with altitude, over an infinite homogeneous source. It was assumed that other stripping ratios were invariant with altitude. This has since been amended by the IAEA (IAEA, 1979). In aerial survey, the effects of air scattering must however be taken into account for proper spectral deconvolution. The primary (full energy deposition) and secondary (scattered) components vary somewhat independently of each other. Both are attenuated with increasing height (depth of media): multiple Compton scattering of the primary component increases with height. The overall effect is that peak-to-scatter ratio decreases with height.

A calibration is usually made by a linear regression between true counts and radionuclide concentrations from ground based measurements (Killeen and Carmichael, 1970). The latter is done either by sampling or alternatively, by using large concrete calibration pads that have been constructed elsewhere for this purpose. Burson (1974) reports that calibration experiments have been performed using hundreds of ^{60}Co and ^{137}Cs sources scattered over a 610m side square. IAEA (1991) report that ground concentrations of uranium over an airborne calibration range should be measured with a calibrated portable spectrometer because of changes in radon emission in later laboratory analyses.

1.6 Calibration

Published results from early radiometric surveys show only relative count rates and restrict cross comparisons between different equipment and environmental forms of radioactivity. To provide continuity between surveys, the preferred reporting units are in terms of radioelement concentrations which requires a calibration. The correct calibration of field γ-ray spectrometers is essential if radionuclide inventories are estimated in-situ. Reporting of results using uncalibrated equipment may sometimes be unavoidable if no calibration exists. In these circumstances it is better simply to correct gross count rates for background, interferences (via stripping) and altitude.

Laboratory measurements of detector responses can form a crude basis of calibration, but are limited to estimates of photopeak count rates only. Characterisation of Compton scattering depends upon the matrix within which the source is found: there may be an underestimate of the scattering component from point sources. The IAEA (IAEA, 1976) recommends the use of doped concrete calibration pads for the determination of stripping ratios and spectrometric sensitivities of the natural radionuclides. They consist as a set of at least four large and well separated sources of potassium, uranium and thorium. The fourth pad is blank and defines the background count rate. The potassium and blank pad are made of K-feldspar and quartz sand respectively. The uranium pad contains pitchblende of low radon emanation. The thorium pad usually contains thorite or monazite. For airborne γ-ray spectrometers concrete calibration pads of quite large surface area have been manufactured (Grasty, 1987). The pads are sometimes sealed with plastic films to reduce radon loss. The accuracies of instrumental sensitivities (cps per radioelement concentration) have been determined by combining measurements on pads at six world wide facilities (Løvborg, 1982). This is calculated by the combination of counting statistics and estimated calibration error. For the former, instrumental drifts may introduce systematic errors: Løvborg *et al* (1971) reports that for a 7.62x7.62cm NaI(Tl) detector, a 1% gain shift results in a 6% error in measured uranium content. Estimates of pad concentrations are usually based upon sampling during manufacture and laboratory analysis. Actual pad concentrations may differ owing to pore size, moisture content and system disequilibrium. Corrections are also necessary to account for rather less than 2π geometry on small pads. Løvborg (1982) concludes that instrumental sensitivities of potassium and thorium can be derived to $\pm$2% for 7.62x7.62cm NaI(Tl) detectors. Uranium calibrations are accurate to $\pm$4-6%.

The advantages of theoretically based calibration are attractive since control of all parameters is in principle possible. Radionuclides uncommonly found in the environment, with any distribution and source energies can be modelled as appropriate. The scattering contributions from surrounding media and detector responses can be accurately predicted. Table 1.2 lists the calibration methods available to in-situ and aerial survey methodologies.

Table 1.2 Calibration techniques.

Calibration Method	Advantages	Disadvantages
1. Empirical.		
Calibration pads.	Direct (some corrections may be necessary). IAEA recommended.	May not represent full matrix characteristics. Do not allow different vertical distributions. Radon problems.
Cross calibration between in-situ & core sampling.	Direct. Learn about vertical profile.	Slow. Only for radionuclides in the environment. Core sampling errors. Radon problems.
2. Semi empirical.		
Laboratory measurements of detector response.	Established.	Limited calculation of full energy peak count rate.
3. Theoretical.		
Analytical or numerical methods.	Easily performed. Not detector specific. Not radionuclide specific.	Only non-scattered component realistically dealt with. Requires validation. Limited range of spatially deposited sources.
Monte Carlo techniques.	Full spectral and detector simulation. Determination of altitude dependence of stripping ratios possible. Not detector or radionuclide specific. Spatially complex deposited sources.	Slow. Requires validation (may be prone to inaccuracies).

1.7 Objectives

A theoretical approach to the many in-situ calibration problems may supplement current operating procedures. For example, in order to estimate equivalent ground concentrations from raw data it is necessary to know stripping ratios, height attenuation coefficients (if applicable) and detector sensitivities (cps per unit radioelement concentration). Theoretical estimation of primary and secondary fluence rates and their variation with altitude have been investigated for the natural decay series and 7.62x7.62cm NaI(Tl) detectors (Kirkegaard and Løvborg, 1974), (Løvborg and Kirkegaard, 1974), (Løvborg and Kirkegaard, 1975), (Kirkegaard and Løvborg, 1980). Computation is based upon solution of the one-dimensional Boltzmann equation (a photon conservation equation). Only limited work has been published concerning anthropogenic measurements (Saito and Moriuchi, 1985) or large airborne detector responses at survey heights. Grasty (1980b) and Dickson *et al* (1981) used plywood sheets interposed between source and detector to simulate air path scattering. However, the geometry and scale of this experiment is unlike the one found in practice and it remains to be seen if these results can be corroborated by alternative means.

The purpose of this thesis is to investigate experimentally and theoretically a wide range of associated problems that lead to corrections of detector responses and calibrations, for the natural and anthropogenic radionuclides. In addition to developing experimental and theoretical solutions to these problems, a series of rigorous comparisons with experimental and published results for simplified geometries was conducted to validate the new methods. The development of specific purpose Monte Carlo codes was thought to be essential for this, since general purpose programs cover too wide a range of applications to be efficient or easy to use (Verghese and Gardner, 1990). It will primarily discuss results from commonly used 7.62x7.62cm NaI(Tl) right cylindrical scintillation detectors and 10x40x40cm prismatic NaI(Tl) detector arrays (16 litres).

An important objective of this research is to show that detector calibration can be achieved using absolute, fundamental, methods rather than by air-ground comparisons as currently used. This would provide an independent means of testing the validity of

current calibration data, and also provides the only means of estimating sensitivity for short lived nuclides which are not normally available in the environment, but which would be present after an accidental release of fission products. In addition, the theoretical tools can be used to investigate environmental factors influencing spectral characteristics eg. source distribution deviations from uniform plane or volume geometry. Sources of short lifetimes are well suited to be investigated by numerical methods and where pre-calibrations are desirable.

With respect to aerial survey detectors, this thesis has looked at a number of aspects of operation and calibration methodology:

1. Operational characteristics (gain, windows, resolution), and their influences.

2. Laboratory experimental simulations of altitude dependency, using materials that closely resemble air.

3. Detector sensitivities to a range of radionuclides by numerical methods, by consideration of fields of view and detector angular characteristics.

4. These sensitivities relate to the primary information carried by gamma-ray emissions, but the full spectral response has been additionally modelled by Monte Carlo methods. The full simulation of dispersed activity, gamma transport and detection mechanisms, can be used as either supplementary or complementary means of performing calibrations. In this way activity distributions and spatial variability can be represented in a clearly defined manner. Certainty in uniformity is assured over extended regions. Further to this, the geometrical scale of simulated gamma transport can be defined to match proper aerial survey conditions. In addition, understanding detector response from an unlimited number of source configurations is of considerable advantage.

The simulation models have been validated with known and measurable data. It has been possible to define pure spectral shape, for stripping ratio determination, investigate altitude dependency of stripping ratios and possible application to studying depth profile

characteristics.

The methodologies for the extraction of the anthropogenic nuclides (^{137}Cs, ^{134}Cs, ^{131}I), naturals (^{40}K), equilibrated naturals (^{214}Bi and ^{208}Tl) and technically enhanced naturals (^{234m}Pa, ^{228}Ac) have been included. This extends and expands on current IAEA international standard calibration methods.

2. Principles of Gamma-Ray Interactions and Detection

In 1895, Roentgen discovered x-rays: a year later Becquerel observed the radioactive nature of uranium compounds that blackened a photographic plate. The chemists Marie and Pierre Curie later succeeded in isolating polonium and radium from uranium ore, which led to the further isolation and identification of other naturally occurring radionuclides. These events heralded the start of investigations that would have pronounced effects in the fields of science.

A radioactive material contains unstable species of atoms each capable of transformation and which are accompanied by the detectable emission of radiation. The decay processes may lead to the emission of radiation in the form of α and ß particles, or electromagnetic waves such as γ-rays and x-rays. Some decay promptly, others only rarely, but all are governed by the laws of chance: every nucleus has an equal probability of decaying within a given period and each is an independent event. Any atomic or nuclear configuration is stable if it is unable to transform to another configuration, without the addition of energy from outside the system. Radioactivity is then the transformation of nuclei to a structural state of much lower energy. For radiations whose energies are emitted as a result of transitions between excited energy levels of a nucleus, a unique identification signal is produced. When a transition occurs from a higher (excited) to a lower energy (though not necessarily ground) state, the difference in energy is equal (approximately, owing to recoil effects) to the γ-ray energy emitted. Excited states occur as a result of α or ß decay processes, nuclear reactions, direct excitation from a ground state and γ-ray transitions from higher levels.

The energies of γ-ray line emissions offer characteristic signatures which can be used for unequivocal identification of the emitting radionuclides. Their measured intensities are complicated by the detection processes however. Line emission spectra are transformed by the various absorption processes that occur in the detector, and scattering processes in the radionuclide's environment. An appreciation of the fundamental events involved in γ-ray transport and detection is needed to understand why measured spectral shape differs from line emission. This will now follow.

2.1 Gamma-Ray Interactions

The form of nuclear radiation and characteristics of media through which emissions traverse, condition the resulting atomic and nuclear interactions. Energy may be transferred to and absorbed in the media in a concentrated form or distributed over a long track length. Since we are principally interested only in detection of γ-rays, a description of their interactions will facilitate their mathematical simulation in later chapters. At the γ-ray energies of concern here, only Rayleigh scattering, photoelectric absorption, Compton scattering and pair production will be of interest. Each single interaction results in full or partial transfer of energy to the media in which they occur.

2.1.1 Coherent Elastic Gamma-ray Scattering

Scattering of γ-rays by atomic electrons and nuclei may be elastic or inelastic. The laws of energy and momentum conservation hold for elastic scattering. The probability of nuclear elastic scattering is generally small compared to the probability of scattering by the atomic electrons. The contribution to the total attenuation coefficient (μ_{tot})is negligible: less than 0.1% in the 15-20 MeV range for the heavy elements (Grodstein, 1957).

2.1.2 Rayleigh Scattering

In Rayleigh scattering, the momentum transfer is from the incident photon to the atom as a whole, resulting in a strongly forward peaked angular distribution of scattered photons with effectively no energy loss. It occurs due to the cooperative effect of all electrons in an atom. The atomic system recoils as a whole under the impact just enough to conserve momentum. The probability of this process is large for photons of low energy (less than 100 keV), in the region where photoelectric absorption gives the main contribution to μ_{tot}. Sometimes, the coherent scattering cross-section is omitted from μ_{tot}, particularly in broad-beam geometries (Hubbell, 1977). The Rayleigh scattering cross section varies as a function of Z^2 (Z, atomic number).

2.1.3 Photoelectric Absorption

Photoelectric absorption occurs with atoms as a whole: owing to the conservation of momentum, it cannot occur with free electrons. It results in the incident γ-ray interacting in such a way that a photoelectron is ejected from an atomic bound shell, usually the inner most or K shell, if the γ-ray energy is greater than the binding energy of that shell. The γ-ray ceases to exist after this interaction. The photoelectron carries away the γ-ray energy, less the binding energy of the shell from which it originated and therefore will include some kinetic energy. The vacancy that the photoelectron has created is quickly filled by an electron from an outer shell or free electron of the medium. In doing so, a x-ray is released often being re-absorbed close to the original interaction site, although migration can occur (fluorescent radiation). The emission of an Auger electron is an alternative form of releasing excitation energy. If characteristic x-rays are produced near the surface of a NaI(Tl) detector, then they may escape producing an iodine escape peak about 28 keV below the photopeak in a γ-ray spectrum. This is likely to happen in dimensionally small detectors and at low γ-ray energies because the interactions occur near the surface.

Photoelectric absorption (τ) becomes more probable with increasing atomic number (Z) and decreasing energy (E). An approximation takes the form

$$\tau = Constant.\frac{Z^n}{E^q} \qquad (2.1)$$

where, n=varies between 4 and 5

q=varies between 1 and 3

Sharp discontinuities occur in photoelectric interaction probabilities at energies equal to the binding energies of the K, L and M electron shells. The interactions mostly occur with the K-shell, less so with the L shell since the probability of occurrence increases with binding energy, if energetically possible.

2.1.4 Compton (Incoherent) Scattering

In Compton scattering, only a portion of the incident γ-ray energy is transferred to the kinetic energy of an electron. A new photon is created of lower energy and its direction will not in general be in the same direction as the original. The new photon is generally considered to be the original photon, but scattered by the electron interaction. Compton scattering takes place with free or effectively free, loosely bound orbital electrons of absorber atoms and therefore does not generate a significant amount of K or L x-rays. At γ-ray energies that greatly exceed the binding energy of the bound electrons, the γ-rays are scattered as if the electrons were free and at rest.

For conservation of energy and momentum, it can be shown that

$$h\nu' = \frac{h\nu}{1 + \frac{h\nu}{m_0 c^2}(1 - \cos\theta)} \tag{2.2}$$

where, $h\nu$=energy of incident γ-ray

$h\nu'$=energy of scattered γ-ray

m_0=rest mass of electron

Θ=angle of γ-ray scattering

Note. $\alpha = h\nu / m_0 c^2$

The recoil electron takes a proportion of the γ-ray energy ranging from zero to a large fraction and is equal to $h\nu$-$h\nu'$.

The fraction of energy absorbed in any interaction is a function of incident γ-ray energy and scattering angle. Low energy photons lose only a small fraction of their original energy; high energy photons suffer a much greater loss in scattering through the same angle. For glancing angles, little transference of energy occurs. When $\Theta = \pi$ radians, the maximum energy is transferred, which corresponds to the feature known in a spectral measurement as the *Compton edge*.

The energy of backscattered photons is given by

$$h\nu_{bs} = \frac{h\nu}{1+2\alpha} \tag{2.3}$$

For energies greater than m_0c^2, the energy of backscattered γ-rays approaches 250 keV.

The Compton mass attenuation coefficient is

$$\frac{\sigma_{Comp}}{\rho} = N_A \left(\frac{Z}{A}\right) {}_e\sigma \tag{2.4}$$

where, N_A=Avogadro's number

A=Atomic weight

ρ=density of absorber ($g.cm^{-3}$)

$\sigma_{Comp}/\rho = 0.45 \pm 0.05$ for almost all elements

Compton interactions can occur many times during the lifetime of a γ-ray and may ultimately result in a photoelectric absorption. Hence, full energy deposition may occur despite only partial energy transfer at each Compton process. If this occurs within a detector, especially scintillation detector, the light generated at each interaction is summed as though it is coincident and collectively produces a single pulse.

2.1.5 Pair Production

Pair production must take place in the Coulomb field of a charged particle (or nucleus): triplet production occurs near the electric field of an electron and will be disregarded here (threshold $4m_0c^2$). It is energetically possible at γ-ray energies of at least 1022 keV (twice the rest mass of an electron), but remains low in intensity until higher energies are available. The incident γ-ray disappears and an electron-positron pair is created, with total kinetic energy equal to the γ-ray energy less rest mass energy of the two particles (511 keV). The positron annihilates with a free electron and two 511 keV annihilation γ-rays are emitted at a random orientation with respect to the original photon direction (with approximately 180° separation since the linear momentum of the system is nearly zero). Annihilation of an electron-positron pair generally does not

occur until almost all of the kinetic energy of the positron has been lost through ionization or radiative processes. If pair production occurs inside a detector, the 511 keV photons may be both absorbed or one or both escape. The *escape peaks* therefore are formed at photopeak energies less 511 keV and 1022 keV. The likelihood of this is a function of original photon energy and size of detector.

The pair production cross section given by Bethe is

$$\chi = {}_e\sigma_0 Z^2 \left[\frac{28}{9} \ln 2\alpha - \frac{218}{27} \right] \tag{2.5}$$

This is valid for absorbers such as lead from threshold to 15 MeV and living tissue from threshold to 30 MeV. The probability of pair production increases slowly with increasing energy, but above 4 MeV becomes approximately proportional to $\log(h\nu)$.

2.2 Electron Interactions

Electrons lose energy by Coulomb interactions with the absorbing medium, creating ionisation and excitation. The path length is much more devious than that of a γ-ray, because their masses are equal to those of the orbital electrons they are interacting with. Electrons also lose energy by radiative processes, such as bremsstrahlung. Radiative losses can become important at high electron energies and in materials of high atomic number. Often x-ray bremsstrahlung are absorbed close to the point of origin.
Positrons undergo the same form of interactions as electrons, their charge resulting in attractive rather than repulsive forces between orbital electrons.

2.3 Radiation Detection

Charged particles cause ionisation of atomic electrons in the surrounding matter: the detection of nuclear particles and radiation is based upon this. If a particle is electrically neutral, and therefore does not cause direct ionisation, then an intermediate process is required to produce an energetic charged particle that can be detected.

2.3.1 Scintillation Detectors

Some materials emit light when irradiated with ionising radiation; they scintillate. Roentgen discovered x-rays by observing the visible light produced by irradiation of ZnS. Rutherford's measurements of α-particles were made using a ZnS screen. Each flash was viewed tediously by microscope.

We shall concern ourselves only with response of those materials having an ionic crystal structure, like the alkali halides. Scintillators of all types are commonly called *phosphors*. There are two classes of light emission following radiation absorption in these materials. Fluorescence is emitted within 10^{-8} seconds and is in the visible and ultra violet regions; phosphorescence is delayed light emitted somewhat later following irradiation. The energy trapped and released promptly is of most use in recording individual pulses of radiation. Phosphorescent devices are useful however for measuring intensities integrated over an extended period. Pure samples of NaI and CsI scintillate because their ions are in excess and occupy interstitial positions in the lattice. The significance of this will be seen shortly, but it follows that their light is enhanced by the addition of impurities like thallium (called activators). Most of the absorption in NaI occurs due to iodine since the atomic number is 53 compared with 11 of sodium.

Band theory of crystalline solids is the most useful model in describing scintillation processes. In ionic crystals, the lowest energy bands are completely filled with electrons and separated by forbidden bands. The top, valence band is also completely occupied. Above another forbidden band lies the empty conduction band and therefore these materials are insulators: motions of electrons in filled bands do not constitute

conduction. For this to occur, electrons must be excited from the valence to conduction bands, leaving behind holes in the valence band. Conduction can occur if a photon (of ultra-violet wavelength) interacts with the crystal in an applied electric field and has energy sufficiently greater than the forbidden gap energy. This is called photoconduction. If an excited electron falls back to the valence band, an ultra-violet photon is emitted. It is postulated that if an electron excited into the conduction band can be captured by a hole in the valence band to produce a short-lived bound electron-hole pair called an *exciton*, it may move through the crystal rather like a free electron. If the binding energy of the exciton is given up to crystal phonons (energy packets analogous to photons), exciton bands are created at energy levels within the forbidden region just beneath the conduction band. From these, the electron of the exciton can decay to the valence band with the accompanying emission of ultra-violet photons.

In an imperfect or doped (activated with thallium) crystal, luminescence and trapping centres are formed in the forbidden band. The former consists of both excited and ground states owing to impurities and interstitial ions (Tl^+, Na^+) or defects, the latter of single levels owing to oxygen impurities and negative ion vacancies. The trapping centres are much longer lived electron levels. The excitation of luminescence centres is done by capturing an exciton, via a radiation-less phonon transition (energy is given directly to lattice bonds in the form of phonons). This can decay to the ground state by fluorescent emission (if such a transition is allowed) or by *quenching*, involving phonon transitions between overlapping excited and ground sub-states. The scintillation rise and decay times of NaI(Tl) depend upon activator concentration, specific energy loss and temperature. The rise time of the main emission at 420nm is 60ns. The pulse remains approximately constant for a period of 150ns, but depends upon specific ionisation. The decay time constant is 230nsec and accounts for 60% of the total light output. A second decay, called delayed fluorescence (1.5μs time constant), makes up the remainder.

When scintillation photons strike a photosensitive material (forming a thin coating on a plane glass window, called a photocathode), low energy electrons are emitted (by the photoelectric effect) and are accelerated towards an electrode (dynode) held at positive potential with respect to the photocathode. The electrons are sufficiently energetic to

cause secondary electron emission and these are accelerated towards a second dynode. where a similar process occurs. This may be repeated many times eventually producing a large pulse of charge.

The resolution of scintillation detectors is relatively worse than semiconductor detectors owing to the combined effects of scintillation efficiency, light loss, and quantum efficiency of the photocathode resulting in a statistical spread in the number of photoelectrons produced at the photocathode. A MgO or alumina reflector improves light collection efficiency (high coefficient of reflectivity), and maximises the number of photons falling on the entrance window of the photomultiplier. Uniformity of light collected over the active detector volume (by grading the reflector) may be more important than maximum light intensity, especially for large scintillators and certain photomultiplier tube combinations where the position of the original ionising event may become significant (Salomon, 1978). Of the fraction that reach the photocathode, only a proportion result in the emission of photoelectrons (photoelectric quantum efficiency), which are accelerated then to the first dynode. At room temperature, there may be appreciable emission of thermionic electrons to produce an undesirable *dark current or noise*. Thus, for a NaI(Tl) having say 7-8% overall resolution, about 4% is due to variation in photoproduction efficiency, phototransmission efficiency and photocollection. The remainder is due to a combination of photocathode efficiency, multiplication factors for the dynode stage and mean number of photons produced per scintillation. The charge collected at the end of the many dynode stages is proportional to the number of fluorescent photons created, but is usually a non-linear function of original energy of charged particle. However, it is linearly proportional at energies greater than 100keV.

NaI(Tl) is hygroscopic and therefore has to be encapsulated inside a hermetically sealed can, usually of aluminium, with thin rubber inserts to reduce mechanical shock. Other physical properties are listed in table 2.1.

Table 2.1 Physical Properties of NaI(Tl).

Atomic Number of I:	53
Wavelength of max. emission:	420 nm
Main decay time constant:	230 ns
½ Thickness for ^{137}Cs:	2.5 cm
Refractive Index:	1.85
Density:	3.67 g cm^{-3}
Melting Point:	924 °K
$I_{Binding\ energy}$:	33.2 keV
Temperature Coefficient:	-0.1% /°C

The fabrication of extremely large single crystals of scintillation detectors is possible, enabling much better detection efficiencies than that currently possible with the largest semiconductor detectors.

From the foregoing discussion it will have become apparent that γ-rays must first interact within a detector and transfer energy to secondary radiations before detection can occur. Further more, γ-rays may travel relatively large distances before interactions occur at all. The detection *efficiency* is the parameter that describes this conversion process: the higher the efficiency, the greater the number of incident γ-rays are detected. Owing to the nature of the interactions, detection efficiency is related to energy of incident γ-rays and atomic number of detector materials. The terminology describing detector efficiencies is often confused and so a summary of the definitions is presented in Appendix A.

2.4 Chapter Summary

The measured spectrum of pure γ-ray line emissions from radionuclides is downgraded by interactions with the environment of the source and detector and by the detection processes themselves. Interferences from external and internal sources have to be accounted for in order that radionuclide concentrations can be estimated. Detector resolution is a factor that limits the unambiguous observation of γ-ray lines of interest. Detector efficiency is a factor that limits the statistical precision that can be applied to

radionuclide estimates. The interactions involved in detection processes result in complete and partial energy depositions. This introduces a Compton continuum background level upon which peaks may occur. The magnitude of this continuum level further limits statistical estimates.

3. Instrumentation and Associated Equipment

3.1 Introduction

A γ-ray energy spectroscopy system comprises the following items.

1. A detector.

2. Low noise charge sensitive pre-amplifier of little or no gain.

3. High and low-voltage, filtered, stable power supplies.

4. Main, linear spectroscopy amplifier enabling further pulse processing.

5. Single channel (SCA) and multichannel (MCA) acquisition systems.

A charge sensitive pre-amp integrates the current pulse and provides pulse shaping to give an output signal across relatively low impedance. This feeds into a main amplifier from which at low count-rates a unipolar output is taken and corrected by pole-zero cancellation and baseline restoration circuits. Shaping time constants are chosen as a compromise between minimising noise and pulse pile-up effects (mutually conflicting). Pulses are then sorted and stored according to their individual pulse heights. A multichannel analyser will record (depending upon configured selection) a well resolved γ-ray spectrum: the number of counts per channel as a function of channel number (pulse height or energy).

All of the above components must be interconnected with proper terminations to avoid signal reflections and furnished with the same a.c. supply to prevent ground loops. The complete system is d.c. coupled from the pre-amplifier to the MCA.

The most serious form of instability of a scintillation spectroscopy system is gain shift of the photomultiplier tubes, which degrades resolution. Some tubes tend to exhibit a tendency to drift through increasing count-rate (phototube current); the time required for stabilization can vary from minutes to several hours. Gain shifts of $<0.5\%$ from a change in counting rate from 100-10,000 cps can be achieved however (Heath, 1966). Since gain is also proportional to the applied dynode voltage, precision voltage supplies and regulators are required to ensure minimisation of any gain drift. A 0.1% change

in voltage can produce a 1% change in gain (Heath, 1966). However, temperature variations account for most of the instabilities of an output signal. For detectors that are taken into the field and have no additional thermal insulation, the operator must monitor the relative peak positions of the recorded spectra in order to be aware of gain changes. This is especially so during periods of high thermal gradients, usually occurring during the early morning or late evening.

The equipment used by SURRC during the course of this research will now be described to clarify the results that follow in subsequent chapters. Some of the equipment has been custom made to be application specific and developed over extended periods, with much practical experience.

3.2 Measurement of Radionuclide Inventories by In-situ Ground Based Instrumentation: SURRC Procedures

Lightweight portable equipment is essential, particularly where regions to be investigated can only be reached by foot. A 7.62x7.62cm NaI(Tl) scintillation detector, Canberra Series 10 multichannel analyser and strong tripod offer this advantage, and are acceptably robust for rough handling (figure 3.1). This equipment has been successfully used by SURRC over many years. Up to eight spectra may be stored using RAM memory of the MCA. A small tape recorder provides a useful additional storage facility and back-up. One full day of measurements is usually possible under power of the MCA internal rechargeable battery.

The acquisition of 6 N-type portable HP-Ge Canberra semiconductor detectors (2 LO-AX & 4 GMX) has extended the potential of inventory assessments, particularly to low energy Americium and Neptunium series. These detectors are able to operate continuously for 2-4 days, before requiring a resupply of coolant. Smaller dewars are available and are even more convenient to handle, but operation time is reduced.

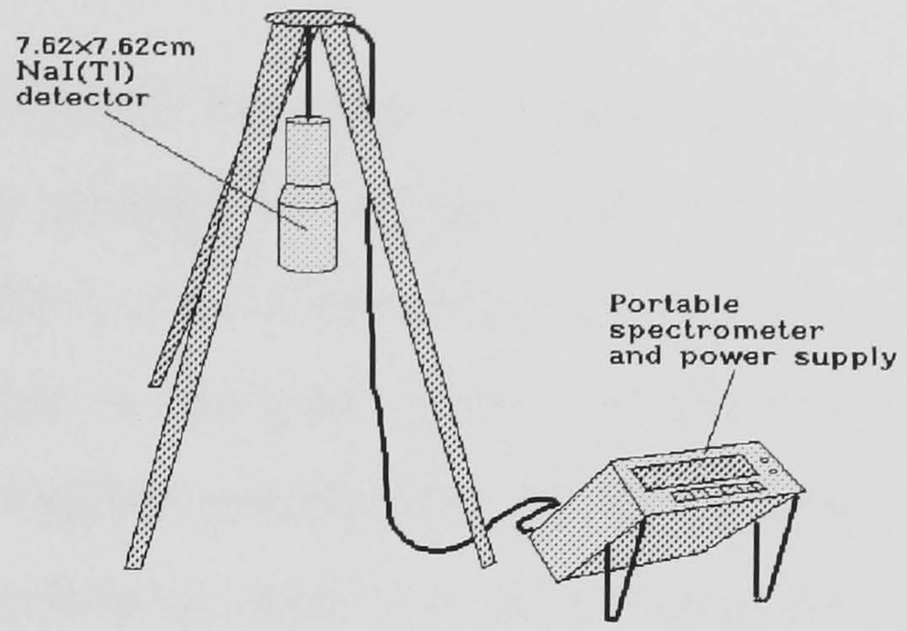

Figure 3.1 Ground based in-situ spectrometer.

Complementing and comparing field spectral measurements are soil sampling methods and laboratory based high resolution gamma-ray spectrometry. It is essential that a representative sample of soil is taken from the area being investigated, ie. beneath and around the in-situ spectrometer. It has been shown by Tyler (1994) that gross error may occur if an insufficient sample is taken, sampling area is limited and poor sampling scheme is selected.

For the first part, a Harwell standard coring system was originally used. This consisted of 38mm diameter coring tool, that can be driven to depths of 30 and 45cm, in steps of 15cm. A newly adopted coring tool (modified golf hole cutter) of 105mm diameter, which can be taken to similar depths, offers the sectioning of the sample in a much more convenient way. It also reduces the possibility of smearing activity through a core (particularly in high water content cores), which is important if vertical profile is to be accurately assayed. In the second part, if activity is deposited in a very irregular way, or because of its particulate nature or chemical absorptive properties, then a large number of sampling points must be considered to ensure good representative collection. Finally, cross comparison must be made in such a way that a weighting scheme is employed similar in manner to that inherent in ground based (and aerial) spectroscopy (the detector has a weighted *field of view*). A hexagonal sampling strategy has been adopted that offers this advantage in addition to being extendable to aerial survey heights and is relatively easy to perform in the field with marked lengths of rope and

compass.

Soil samples returned to SURRC are dried in a large capacity oven and homogenized in a mixer-mill to reduce particle size to approximately 50 microns. These are then normally dispensed into 150 cm^3 containers and stored for 2-3 weeks to allow for radon equilibration. Each sample is analysed under consistent conditions, and traceable records prepared of the logging and labelling of each sample, the bulk weight, wet weight, sample geometry, detector employed, date of measurement and analytical data. Reference standards and background matrices, contained in identical geometries, are interleaved with field samples and used to tabulate calibrated results, with density corrections if required. Programmes have been written to enable the rapid analysis of large numbers of field samples (Sanderson *et al*, 1993b).

In late 1991, four concrete calibration pads were obtained from The Geological Survey of Canada. These are constructed with elementally known amounts of material. They define a calibrated source of principally potassium, uranium and thorium series. A fourth pad defines a reference or blank. Concrete provides a convenient medium in terms of chemical stability and approximate attenuating properties similar to that of most soil types, although of greater density. The count-rate from a detector placed on the surface of each pad may be related to concentration (%K, ppm eU & ppm eTh). Factors exist to correct field of view of a $1m^2$ pad to the infinite source yield of 2π geometry. Each pad is 30cm thick and represents effectively infinite depth. The calibration of detectors under conditions where uniform activity with depth is present is therefore valid.

3.3 Measurement of Radionuclide Inventories by Aerial Survey Instrumentation: SURRC Procedures

Over the last few years the Scottish Universities Research & Reactor Centre has conducted developmental and baseline radiometric studies to record and quantify existing levels of man-made and natural activity in the environment (Sanderson *et al*, 1993c). Feasibility studies were carried out at SURRC during 1987, using a health

physics 29.21 x 10.16cm (7 litre) NaI(Tl) scintillation detector (resolution 13-15% at 662 keV), Canberra Series 10 portable multichannel analyser and laptop computer. Integration times of 30 seconds were used. Checks on detector drifts were made by manually observing the ^{40}K peak. Full spectra, radioaltimetry and position (NavStar radio-beacon navigation system) were recorded concurrently. These trials were sufficiently successful that in 1988 two packages of four 10.16x10.16x40.64cm (16.7 litres volume each, figure 3.2) and one package of two 10.16x10.16x40.64cm (volume 8.3 litres) prismatic Harshaw NaI(Tl) scintillation crystals were acquired from a Canadian geophysical survey company.

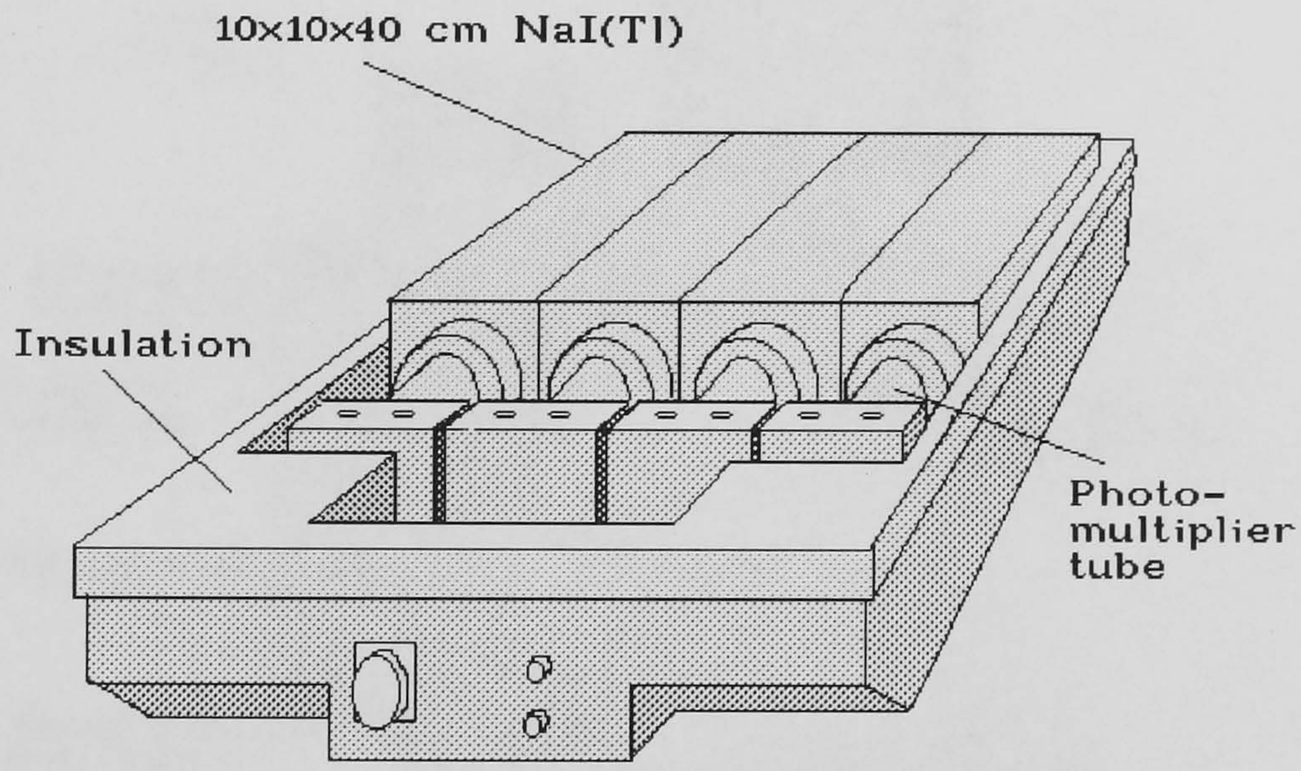

Figure 3.2 Box of four 10x10x40cm NaI(Tl) detectors (total 16 litres).

It is commonly believed that a 10.16cm thick crystal and diameter of at least 15.24cm is the most suitable for airborne geological purposes (Løvborg *et al*, 1976). Each individual crystal has an energy resolution of around 8%. The detector packages are encased within a tough plastic box, electrically screened and thermally insulated. A box of two crystals weighs approximately 48kg; a box of four crystals weighs about 94kg. In 1989, a standard Locland 286AT PC (20 Megabyte Winchester hard disc) replaced the portable computer for data logging purposes and the system was designed such that two parallel detector arrays could be operated simultaneously. Automatic background subtraction and ^{40}K gain monitor were further developments at this stage.

Since 1991, a satellite based navigation system (GPS: Global Positioning System) has been successfully in use. Also at this time, all instrumentation (except detectors) has been self contained within a 19" purpose built rack, including battery power supplies, power inverters and built in redundancy (figure 3.3). This can be mounted to a base plate and secured to the floor pan of a Squirrel type helicopter by quick release pins. The complete system satisfied CAA requirements. A Phillips LCD flat screen replaced an earlier monitor and reduced weight. The use of physically smaller batteries reduced weight further, at the expense of endurance: self contained powered operation is about 30 minutes.

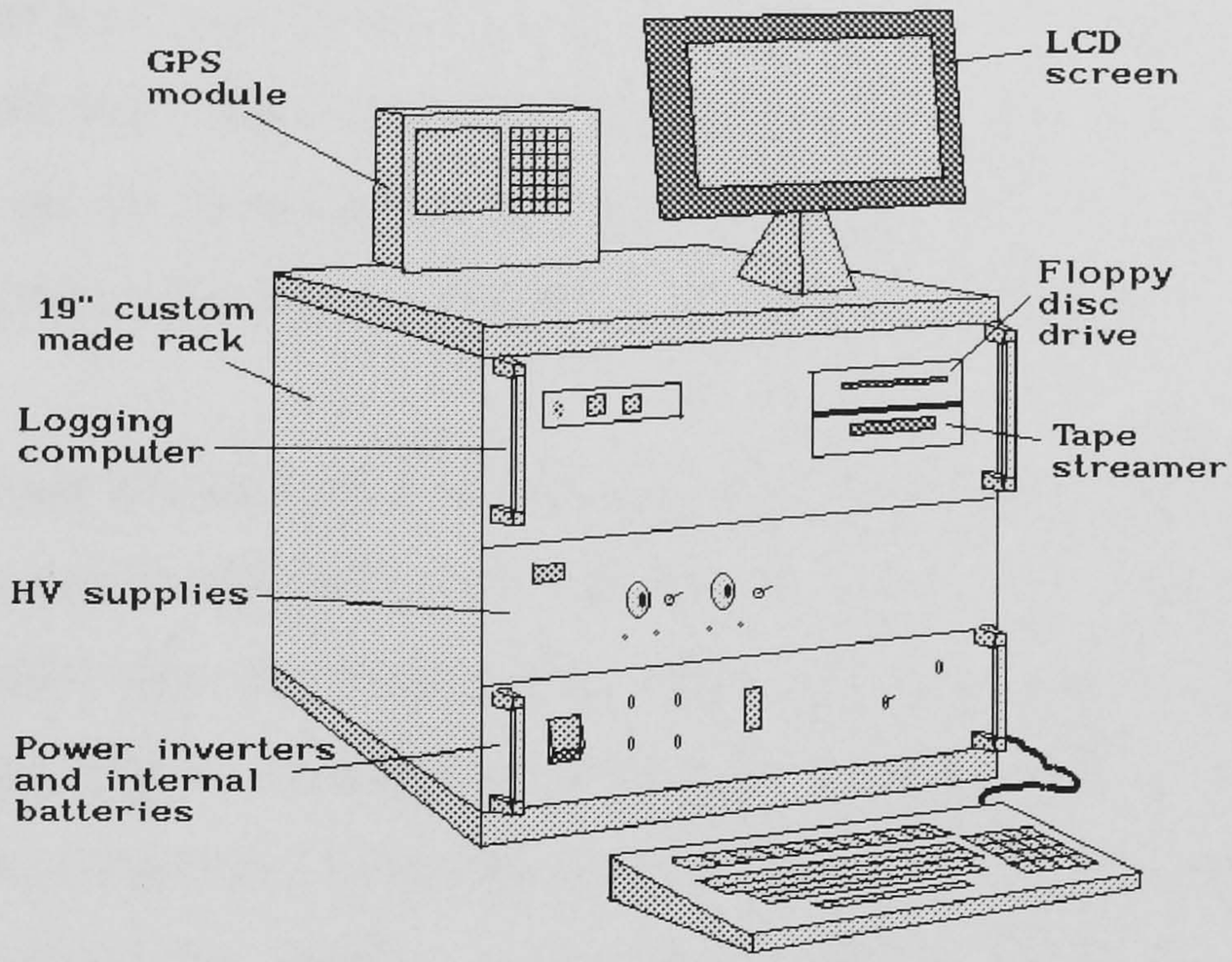

Figure 3.3 Custom made aerial survey spectrometer.

An auxiliary radioaltimeter signal feeds via a ADC/DAC interface card mounted in the PC, to record aircraft altitude after each measurement period. A protected (with breakers and fuses) 6A, 28V dc aircraft power supply is usually taken through to sealed rechargeable batteries, and to an 240v 50Hz ac power inverter and distribution unit. These provide the computer power and low noise supplies to the detectors.

A preamplification stage (with pulse shaping and line driver) and summing amplifier combines linear detector output signals from each PMT to form a single output. This is subsequently processed by EG&G Ortec 916 multi-channel buffer (MCB) cards (2Kb), *ACE* MCA emulation and SURRC developed software. The combination of signal outputs degrades resolution by approximately 0.5-3% subject to manual

adjustment by a skilled operator. The gain and focus of each PMT can be individually adjusted to ensure, at the start of the survey period, that the combined signal output resolution is around 9-10%. Variations throughout the day may occur and regular checks are essential. Integration times of 5-15 seconds have been used with the increase in detector sensitivity. The installation of Jumbo QIC40 tape streamers enables the rapid down loading of ten's of megabytes of recorded data, into a small media format. All data is backed-up at least twice and summarised before any deletion from the data logging computer. No complete hard disc failure has ever occurred during many hundreds of hours of exhausting aerial surveys, sometimes at high g-loads and climatically hostile environments. Data is subsequently processed using SURRC *AERO* programs which have been developed to give easily understood calibrated colour contour maps of the radionuclides of interest, using 486 PC type machines. All programs have been extensively validated with known sets of data.

Use has been made of video cameras to record surveys either continuously or at regular time intervals (every 5 seconds). A camera mounted in the front window of a helicopter can archive flight lines for navigational cross reference purposes and as an aid to operator training. The use of such data is thought invaluable, visibility permitting, to record emergency response flight paths around nuclear facilities. Local features can be readily distinguished and recalled, useful in the case of navigational system failure during such an emergency. Timing fidicials enable correlations with spectrometric recorded data.

The potential use of semiconductor detectors in aerial survey is undergoing trials. Vibration to the sensitive cryostat system and induced electronic noise are the most serious limitations: the efficiency of these modern detectors is approaching that (greater than 50%, relative) of sodium iodide detectors. A parallel bank of at least four semiconductor detectors, preferably externally mounted is envisaged for future operation.

The use of aerial survey equipment as a land based spectrometer has also been investigated. A broad area of land can be systematically swept, provided the conditions

are suitable, preferably by four wheel drive vehicle. For local and economical surveys, this method offers great potential to find isolated radioactivity.

4. Experimental Investigations Relating to Spectral Deconvolution

4.1 General

A single set of stripping ratios has been used in the deconvolution procedure of SURRC and other aerial surveys, for a given survey altitude, irrespective of changes in detector resolution or detector gain. An investigation of the dependence of stripping ratios for these operational parameters was undertaken since **little** information in the literature appears to address this problem in the calibration methodology. For an aerial survey multi-detector array, variations in resolution may occur due to gain drifts in individual detectors owing to temperature, photomultiplier tube (PMT) anode voltage or count-rate related effects. Such changes have been artificially investigated by adjusting the gain potentiometer of each PMT preamplifier of a four crystal package. In addition, collective variation in gain (of all detectors) has also been investigated (defined *gain shift*) and stripping ratios determined over a practical range. Emphasis is given towards multi-array detectors because of their inherent operational problems.

Stripping ratios also vary with detector altitude, since the scatter component relative to the full energy component, of a recorded spectrum increases with air pathlength. Similarly, this is observed for buried nuclides too. Small scale laboratory simulations of this phenomena will be shown for an aerial survey 16 litre detector, and present useful data for cross comparisons between full scale field experiments and Monte Carlo calculated stripping ratios.

4.2 Spectral Deconvolution

A spectrum taken using a 7.62x7.62cm NaI(Tl) scintillation detector is shown in figure 4.1, as way of example, containing , lines from both natural and manmade nuclides. The principal gamma-rays of interest to the geologist are: 2615 keV, ^{208}Tl (channel 429); 1764 keV, ^{214}Bi (ch. 290) and 1462 keV, ^{40}K (ch. 243). Following the Chernobyl accident in 1986 however, environmental interest has included: ^{137}Cs, 662 keV (ch. 114) and ^{134}Cs, principally 605 & 796 keV (ch. 105 & ch. 135).

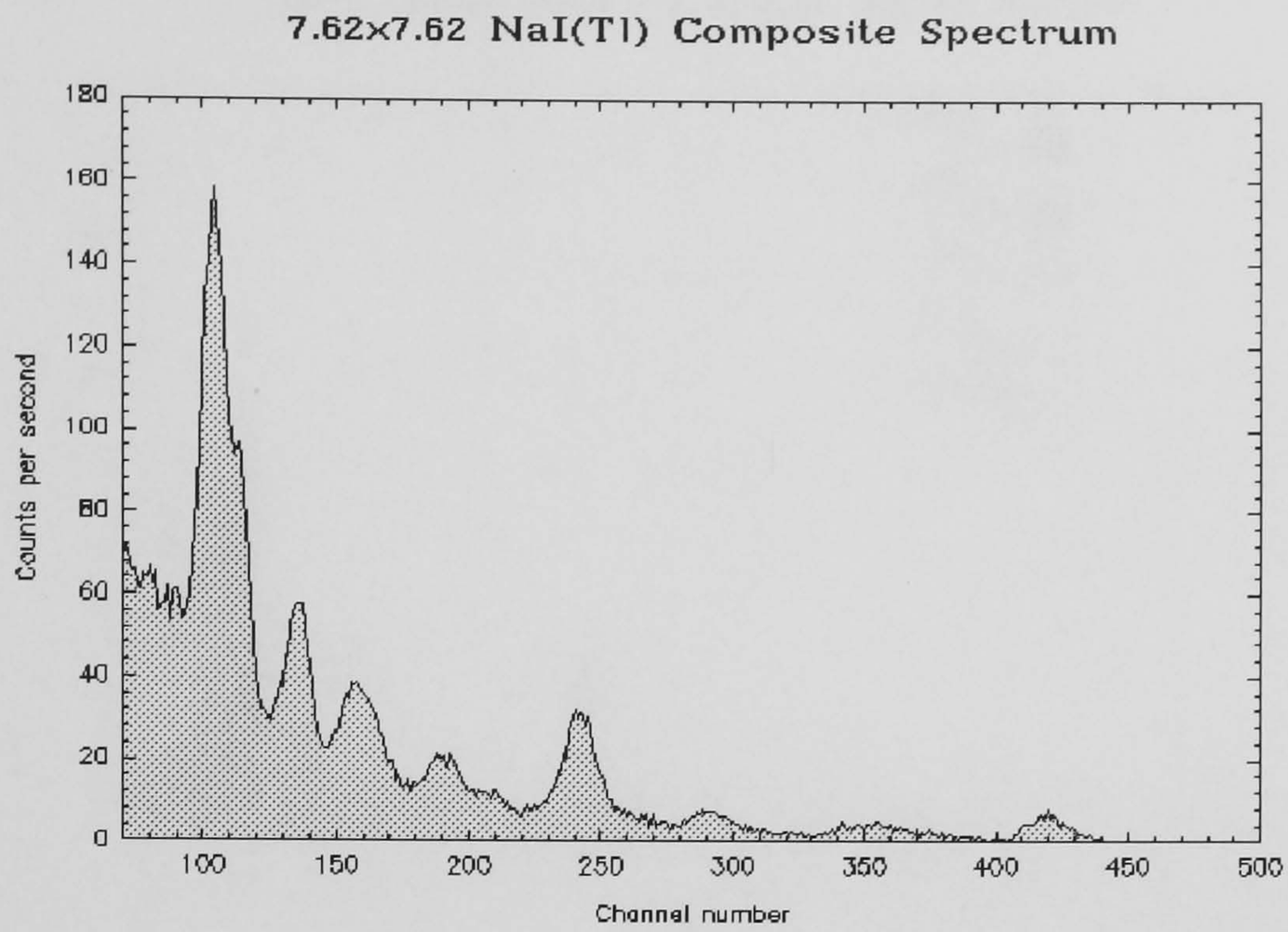

Figure 4.1 Composite spectrum from many radionuclides.

The relative proportions of full and partial energy deposition in the spectrum (at the energies considered here) depend on the relative interaction probabilities of photoelectric absorption, incoherent Compton scattering and pair production, and are also a function of the atomic number of the interacting medium and the gamma-ray energy. Compton scattering produces a broad continuum of energies upon which full energy peaks can occur. The normal practice in determination of gamma-ray emission rate and therefore estimating radionuclide concentration is by recording full energy peak count rate in spectral windows preset around these regions of interest. Clearly then, within these windows, interferences can occur from gamma-rays other than those of importance. The determination of ^{137}Cs, from measurements around the 662 keV peak will include contributions from lines from ^{134}Cs and ^{214}Bi as seen in figure 4.2. The contributions to this figure are exaggerated for clarity. The fractional interferences between the recorded peaks can be expressed as stripping ratios, and compiled into a matrix used to solve a series of linear equations. This is the basis of deconvolution using the window method most readily appropriate in a rapid context.

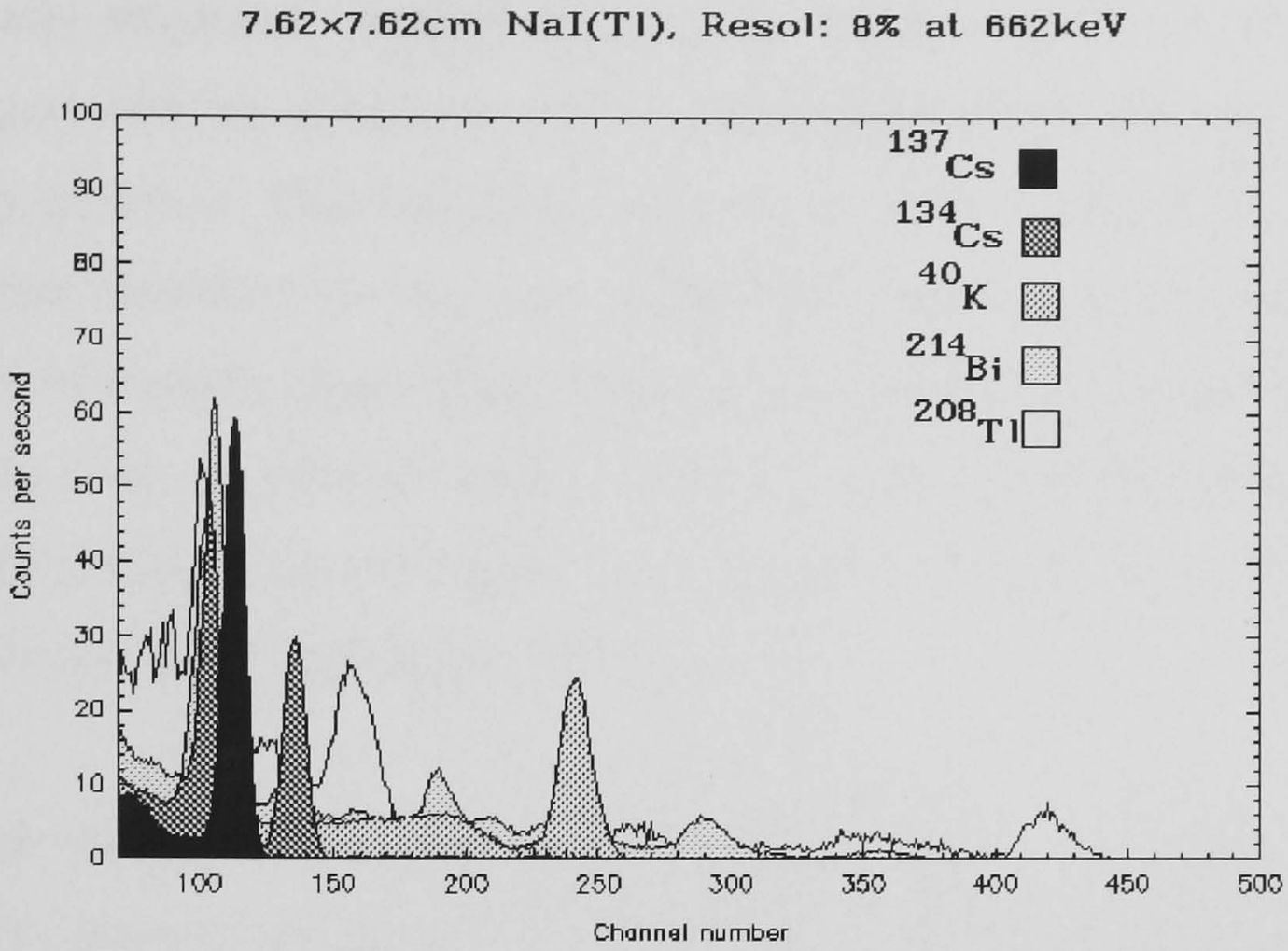

Figure 4.2 Separated spectra.

The evaluation of the separate components of a composite spectrum measured by a scintillation detector is complicated owing to the inherently poor energy resolution. However, spectral deconvolution or stripping techniques have been developed to enable this to be achieved. Most of these methods assume that the response function of one radioisotope is unaffected by the presence of others. This is true only when pulse pile-up, amplifier saturation and random coincidences are minimised. Deconvolution must be made by comparison with individual pure spectra, comprising each of the components of the composite spectrum. These components may be experimentally measured or based on analytical functions (and interpolations) fitted to experimental data or completely derived by mathematical methods. Whichever is chosen, the components must be comparable with the composite in terms of energy, geometry, gain and threshold. Also, it is desirable that there is much smaller uncertainty associated with these than the composite. The generation of response functions from monoenergetic radionuclide sources is limited by availability and intensity. Non-linearities of the detection system may introduce errors into interpolated response functions.

Full spectral deconvolution is relatively more time consuming to perform, especially in

complex radiation fields. Historically, a manual and visual method of full deconvolution was originally employed, depending upon the subjective skill of the scientist. This process began with the subtraction of the radioisotope giving the most energetic peak of the γ-ray spectrum. This was then worked progressively towards the low energy end (a region that becomes less precisely known with each successive subtraction). The introduction of computer processing and statistical analysis has removed operator errors from a very time consuming method. By the method of least squares, libraries of expected spectra are compared and the system of linear equations formed are reduced by matrix inversion procedures (Salmon, 1961).

For all these methods some form of gain monitoring prior to processing is essential. Monte Carlo calculations can be used to derive expected response functions from a knowledge of the physical processes and their respective interaction cross-sections. However, these often only assume a point source, an idealized detector and no account of scattering from the source or surroundings is made.

4.2.1 Deconvolution by Solving Linear Equations

Systems of linear equations of the form $Ax=b$ may be solved by Gaussian elimination. As a matrix this may be shown as

$$\begin{bmatrix} a_{11} & a_{12} & a_{13} & a_{1n} \\ a_{21} & a_{22} & a_{23} & a_{2n} \\ a_{31} & a_{32} & a_{33} & a_{3n} \\ a_{n1} & a_{n2} & a_{n3} & a_{nn} \end{bmatrix} \begin{bmatrix} x_1 \\ x_2 \\ x_3 \\ x_n \end{bmatrix} = \begin{bmatrix} b_1 \\ b_2 \\ b_3 \\ b_n \end{bmatrix} \qquad (4.1)$$

where, A = coefficient matrix (containing stripping ratios)

x = solution vector (true, interference free, count rates)

b = vector containing the equations constants (net count rates)

The equations of $Ax=b$, constituting an (n x n) matrix, may be solved by computing the matrix inversion of A (as A^{-1}) and its product with b.

Thus,

$$x = A^{-1}b \tag{4.2}$$

This is a form of *direct* matrix inversion of linear simultaneous equations, but the use of least squares matrix inversion is commonly applied (Salmon, 1961), (Heath, 1966), (Crossley and Reid, 1982). Desbarats and Killeen (1990), have noted that the use of ordinary linear least squares techniques tends to produce negative stripped counts especially where count rates are low or counting periods are short. They have suggested the use of a constrained, non-linear least squares inversion that yields positive stripped counts in these instances.

4.3 Choice of Energy Windows

The IAEA (IAEA, 1979) has recommended energy windows for γ-ray radiation surveys for geological purposes (table 4.1) and these have been adopted by survey teams: no recommendations have been made by IAEA with regard to the caesium radionuclides. Up to 1989, SURRC had been using independently defined spectral windows shown in table 4.2, and based upon operation of a health physics detector of inferior resolution ($>12\%$). The windows for the natural radionuclides are broader than those suggested by the IAEA.

Table 4.1 IAEA recommended energy windows.

Element	**Radionuclide**	**Energy / keV**	**IAEA Window Energy / keV**
Potassium	^{40}K	1461	1370 - 1570
Uranium	^{214}Bi	1764	1660 - 1860
Thorium	^{208}Tl	2615	2410 - 2810
Total			410 - 2810

The choice is conditional upon detector resolution and susceptibility to gain shifts. It is important that all full energy peak deposition is properly recorded within designated windows. For ^{137}Cs and ^{134}Cs, a broad overlapping window was chosen despite being some what undesirable in terms of spectral deconvolution.

Table 4.2 SURRC energy and equivalent channel windows (c.1989).

Radionuclide	**SURRC Windows / channels**	**SURRC Windows / keV**
^{137}Cs	95 - 128	544 - 749
^{134}Cs	118 - 143	687 - 842
^{40}K	220 - 270	1319 - 1629
^{214}Bi	270 - 318	1629 - 1927
^{208}Tl	390 - 480	2374 - 2932

It became clear, that improvements could be made in choosing peak window regions than those presented in table 4.2. This is something of a compromise. To minimise effects of variations in resolution and gain shift, a wide window can be considered. However, to minimise spectral interferences and improve precision, a narrow window is required. If the window is too narrow, precision also suffers. This is shown in table 4.3: the caesium radionuclide windows have been chosen as far as practical to minimise interferences without undue loss of full peak counts. A small overlap still exists between ^{137}Cs and ^{134}Cs, but it does ensure that all peak counts are collected. For very closely overlapping peaks, the problem may be too difficult to resolve satisfactorily using scintillation detectors.

4.4 Stripping Ratios of Ground Survey Detectors: 7.62x7.62 cm NaI(Tl)

In order to deconvolute a complex multi γ-ray spectrum, prior knowledge of the likely radionuclide composition is necessary. Spectral measurements are made of radionuclides in the absence of any other isotopic interferences. This provides the basis upon which

Table 4.3 SURRC energy and equivalent channel windows (proposed).

Radionuclide	SURRC Windows / channels	SURRC Windows / keV
^{137}Cs	95 - 130	544 - 761
^{134}Cs	125 - 150	730 - 885
^{40}K	220 - 270	1319 - 1629
^{214}Bi	270 - 318	1629 - 1927
^{208}Tl	390 - 480	2374 - 2932

stripping ratios are calculated. Such sources may be difficult if not impossible to obtain and ideally must be presented to the detector in the same geometric conditions.

Figures 4.3 to 4.7, show spectra recorded using a Bicron 7.62x7.62 cm NaI(Tl) detector in close (0.3m) proximity to essentially small, discrete sources of radioactivity. For ^{137}Cs, a standard 370kBq (10μCi) reference source was used (500s live time); ^{134}Cs activity, in the form of a solution contained within a small bottle (600s); ^{40}K made available through using about 5 kg of potassium chloride (600s); a ^{214}Bi source by using a ^{226}Ra health physics standard (600s) and ^{208}Tl source using an aged thorium ore (600s). None of these necessarily fulfils the geometric situation in which a detector is used. Note the strong backscatter peak around channel 35 (about 180 keV), as a result of γ-ray scatter around the nearby environment.

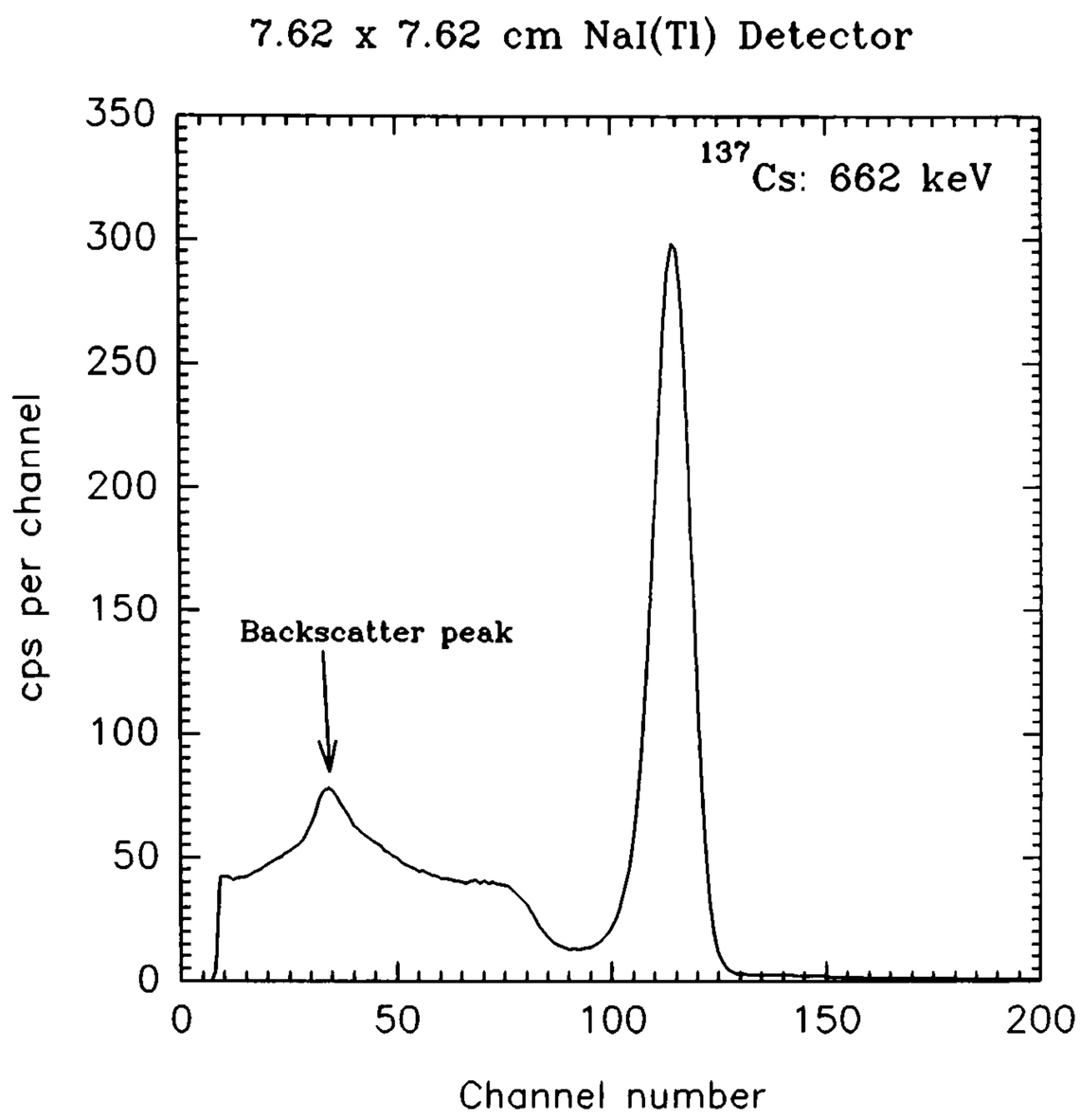

Figure 4.3 Net spectrum from a point source of ^{137}Cs at 0.3m from a 7.62 x 7.62cm NaI(Tl) detector.

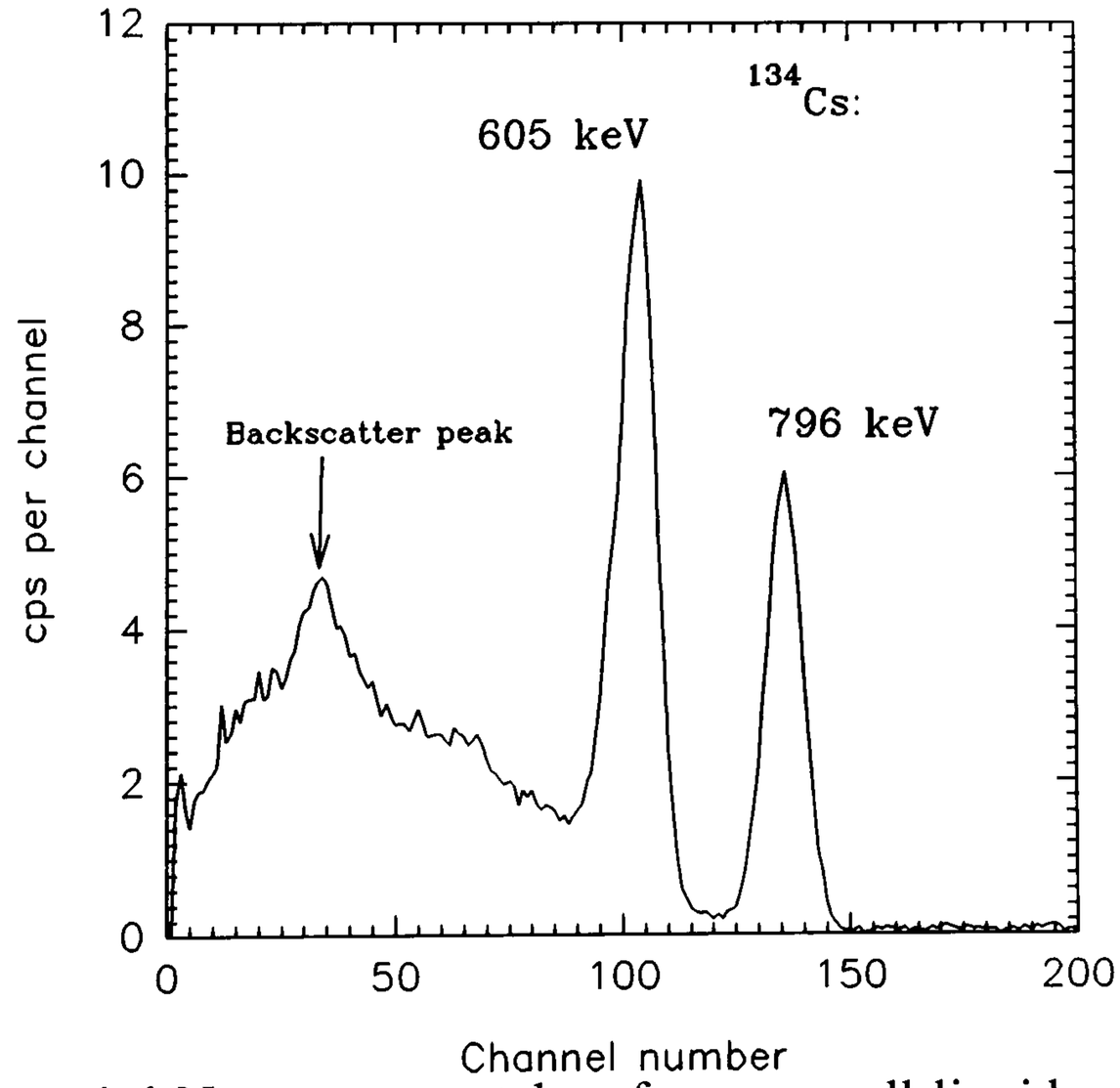

Figure 4.4 Net spectrum taken from a small liquid source of ^{134}Cs, 0.3m from a 7.62 x 7.62cm NaI(Tl) detector.

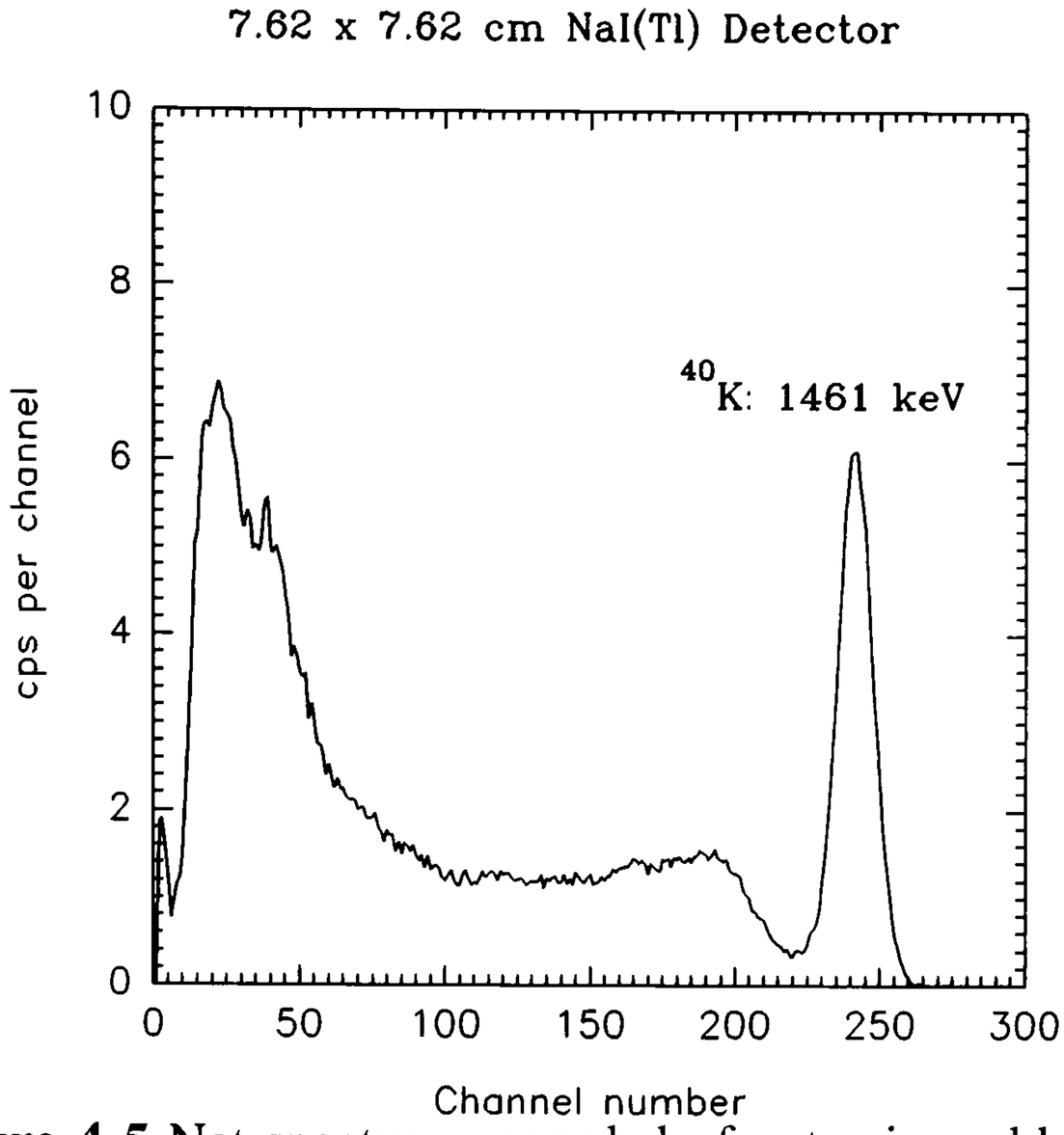

Figure 4.5 Net spectrum recorded of potassium chloride (5kg), using a 7.62 x 7.62cm NaI(Tl).

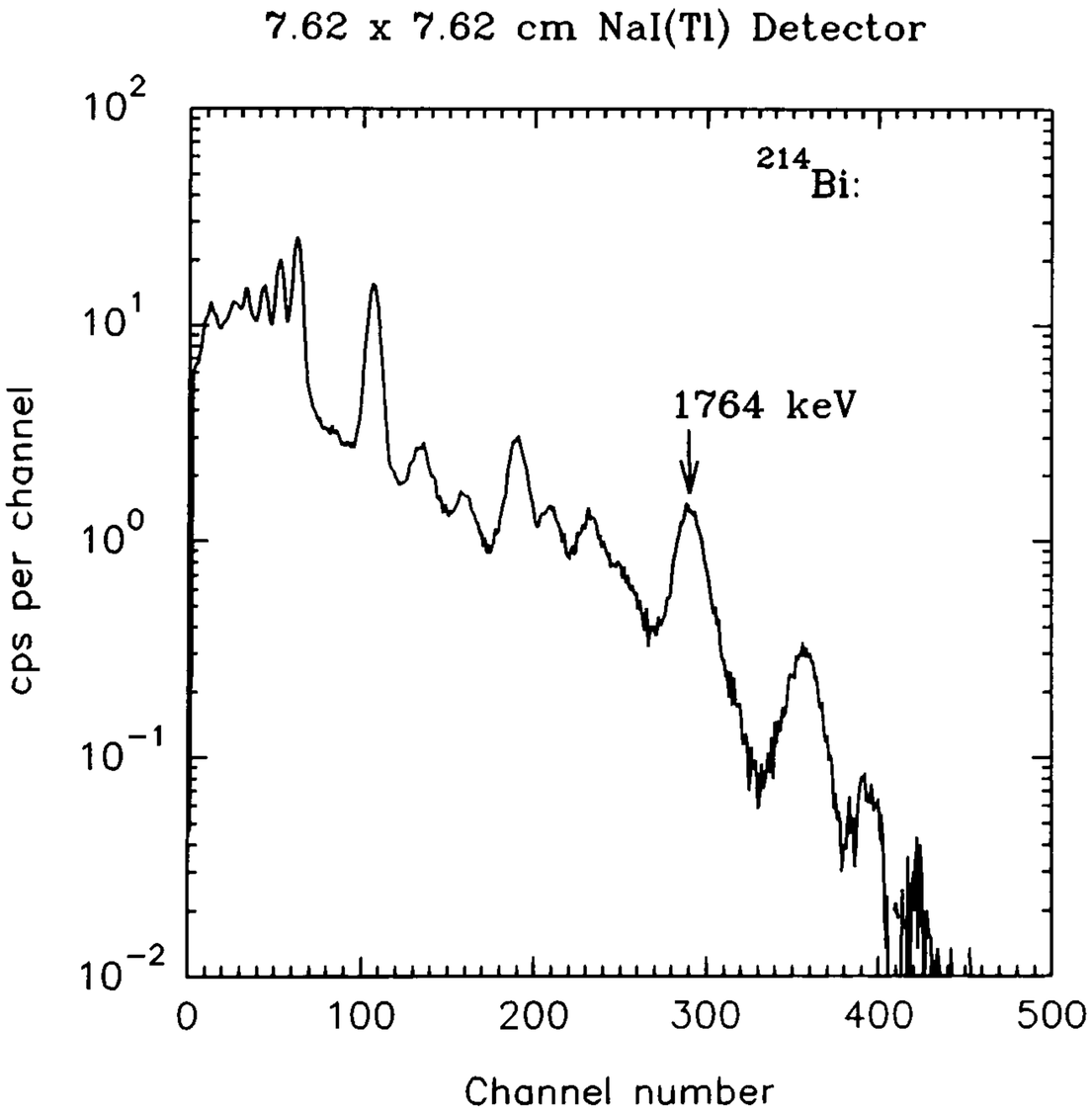

Figure 4.6 Net spectrum of a ^{226}Ra reference source, 0.3m from a 7.62 x 7.62cm NaI(Tl) detector.

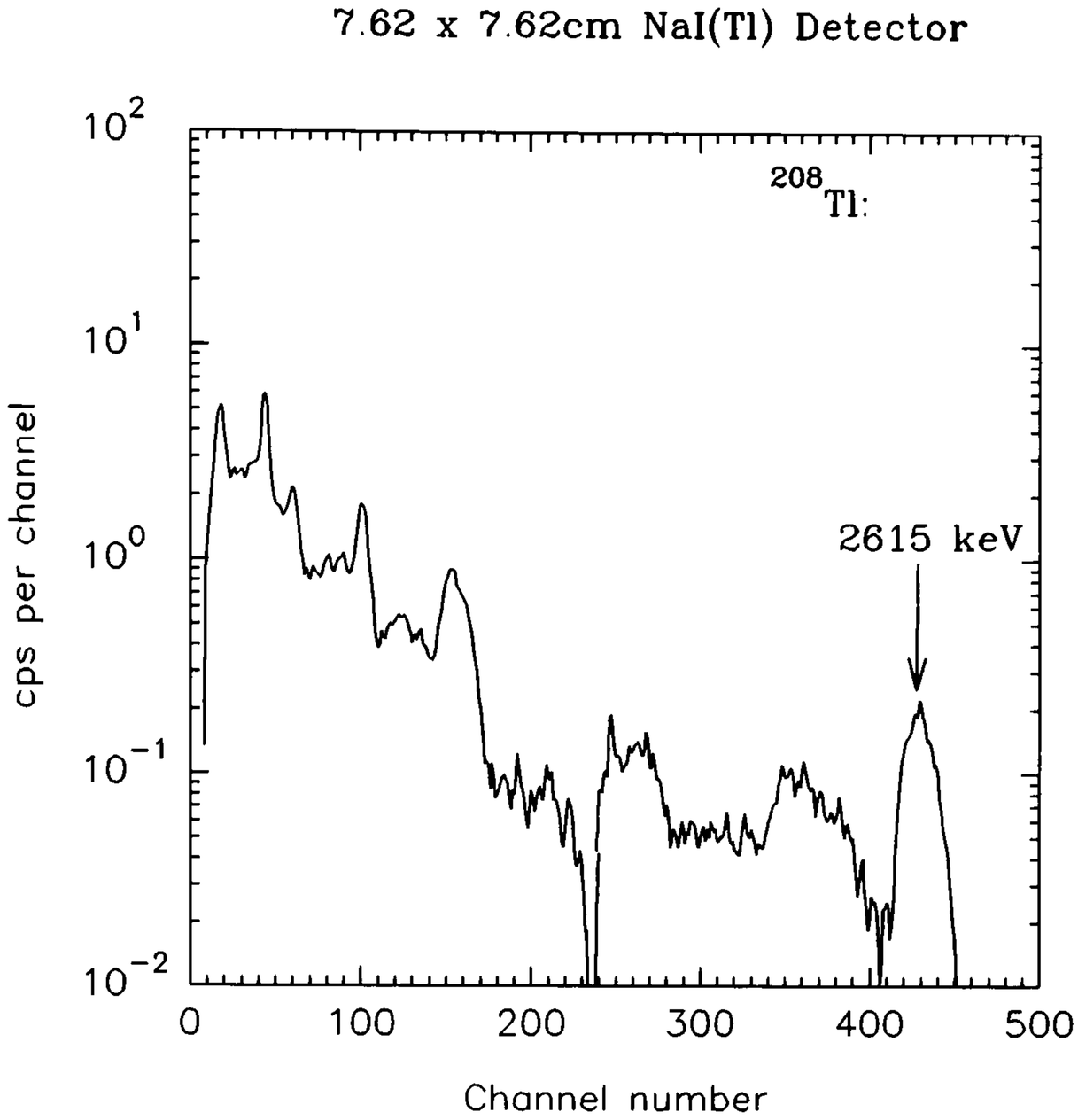

Figure 4.7 Net spectrum of a small mass of aged thorium ore, 0.3m from a 7.62 x 7.62cm NaI(Tl) detector.

The stripping ratios calculated from these measurements are shown in table 4.4. The uncertainties quoted are due to counting (poisson) statistics and a combination of errors from the adjacent windows. Reproducibilty for single crystal systems is far easier to achieve than multi-detector arrays.

Table 4.4 Stripping ratios of 7.62 x 7.62cm Bicron NaI(Tl), determined with discrete sources. Resolution: 8%.

	Spectral Windows				
	^{137}Cs	**^{134}Cs**	**^{40}K**	**^{214}Bi**	**^{208}Tl**
	95-130 ch.	**125-150 ch.**	**220-270 ch.**	**270-318 ch.**	**390-480 ch.**
^{137}Cs	1	0.0219 ±0.0001	0.00336 ±0.00007	0.0	0.0
^{134}Cs	1.87 ±0.02	1	0.026 ±0.003	0.002 ±0.002	0.0
^{40}K	0.462 ±0.004	0.324 ±0.003	1	0.0	0.0
^{214}Bi	5.67 ±0.05	1.57 ±0.02	1.21 ±0.01	1	0.045 ±0.002
^{208}Tl	5.81 ±0.08	2.56 ±0.05	0.94 ±0.03	0.64 ±0.02	1

During 1991, four concrete calibration pads were acquired from the Geological Survey of Canada. Each is approximately 1m square, 0.3m thick, of mass 700kg and density 2.3 g cm^{-3}. The pads are doped with known concentrations of potassium, uranium and thorium and are intended for calibrating γ-ray spectrometers. The pad compositions are shown in table 4.5.

Table 4.5 Transportable calibration pad composition (Grasty *et al*, 1991).

	K (%)	**U (ppm)**	**Th (ppm)**
Blank	1.43±0.01	0.94±0.02	2.32±0.06
K-Pad	7.57±0.05	1.22±0.09	1.40±0.12
U-Pad	1.07±0.01	46.93±0.32	2.75±0.22
Th-Pad	1.43±0.02	1.74±0.16	121.6±1.66

Concrete provides a useful, practical and stable matrix for this purpose. The fourth pad enables background radiation from the surroundings and equipment to be accounted for. Radon emanation is low owing to construction materials, provided that the pads are kept in a controlled environment. Løvborg *et al* (1978) have shown a $\pm 20\%$ variation in radiation output from an outdoor uranium pad owing to seasonal conditions. The mass attenuation coefficients of concrete also bear a very good comparison to that of most soils. For very large (20m diameter) concrete calibration pads, a 2π geometry is attained for a detector placed at their centre. For small transportable pads, corrections are necessary for relative calibrations to be geometrically valid (15% correction).

The volume of source presented to a detector by using calibration pads provides a realistic scattering medium through which γ-rays traverse. Spectral measurements made on calibration pads therefore include an intense scatter component and is always present in field observations. This is seen in figures 4.8 to 4.10, where a Bicron 3x3" NaI(Tl) detector has been placed on each pad for a live time of 3600s. The stripping ratios shown in table 4.6, have been calculated using the calibration pad standards with the exception of the caesium radionuclides.

Comparison of tables 4.4 & 4.6 indicates some important differences. Compton scatter from ^{40}K within the calibration pad results in an enhanced contribution into the ^{137}Cs window (a 67% increase). This is similarly seen in the ^{134}Cs window (50% increase). For the uranium pad, the ^{214}Bi contribution into the ^{137}Cs window is 9.6% less, owing to attenuation of the 609 keV ^{214}Bi full energy peak. However, the scatter component of ^{214}Bi into ^{134}Cs window is greater by 13%. The ^{208}Tl contributions into the ^{137}Cs and ^{134}Cs windows are less by about 10% (583 keV, ^{208}Tl interference) & 8% (795 keV & 836 keV, ^{228}Ac interference) respectively, again owing to attenuation within the concrete matrix. Greater scatter contributions occur in the ^{40}K and ^{214}Bi windows from ^{208}Tl by about 9 & 24% respectively.

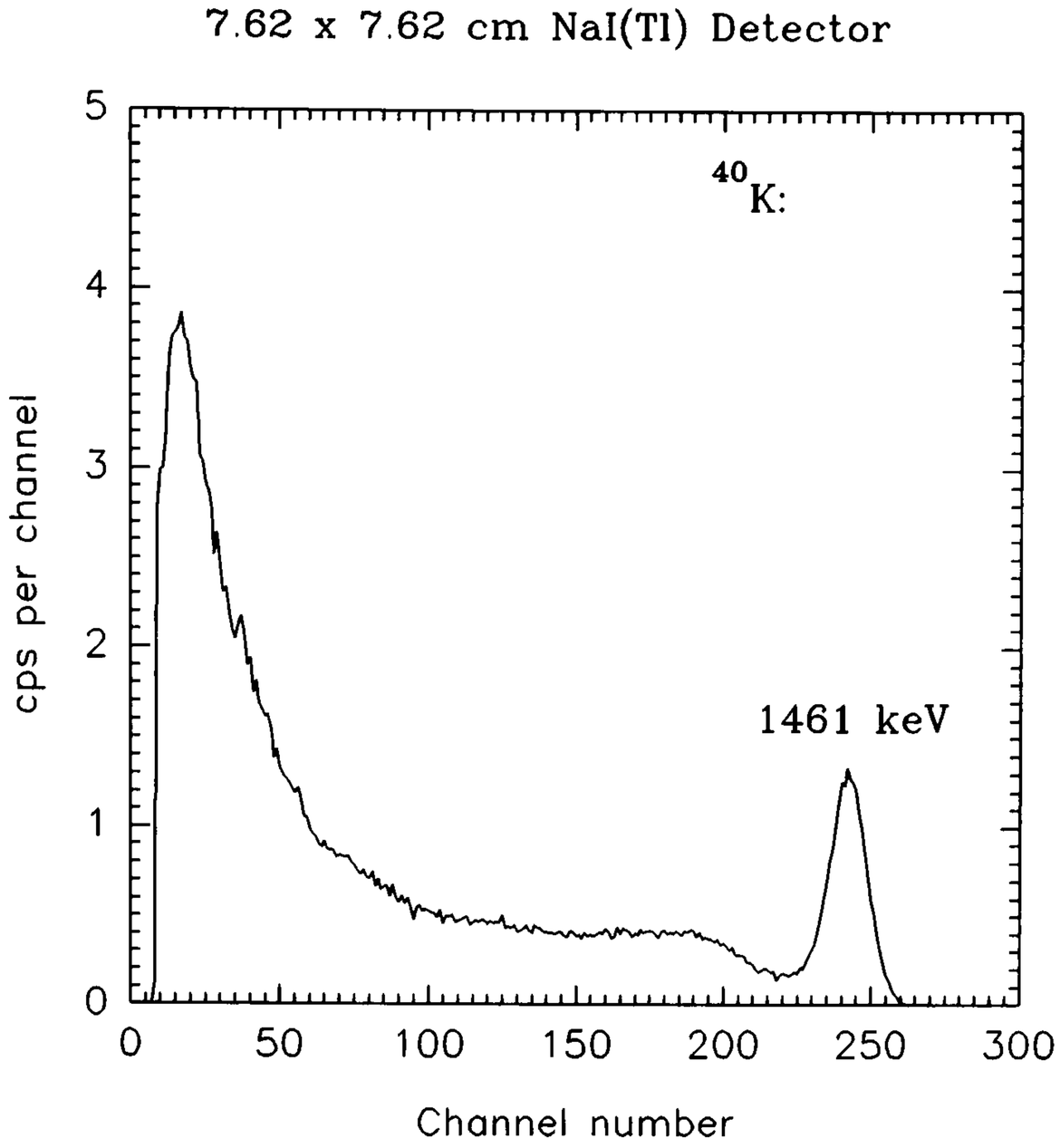

Figure 4.8 Net spectrum taken from a potassium rich concrete calibration pad, recorded using a 7.62 x 7.62cm NaI(Tl) detector.

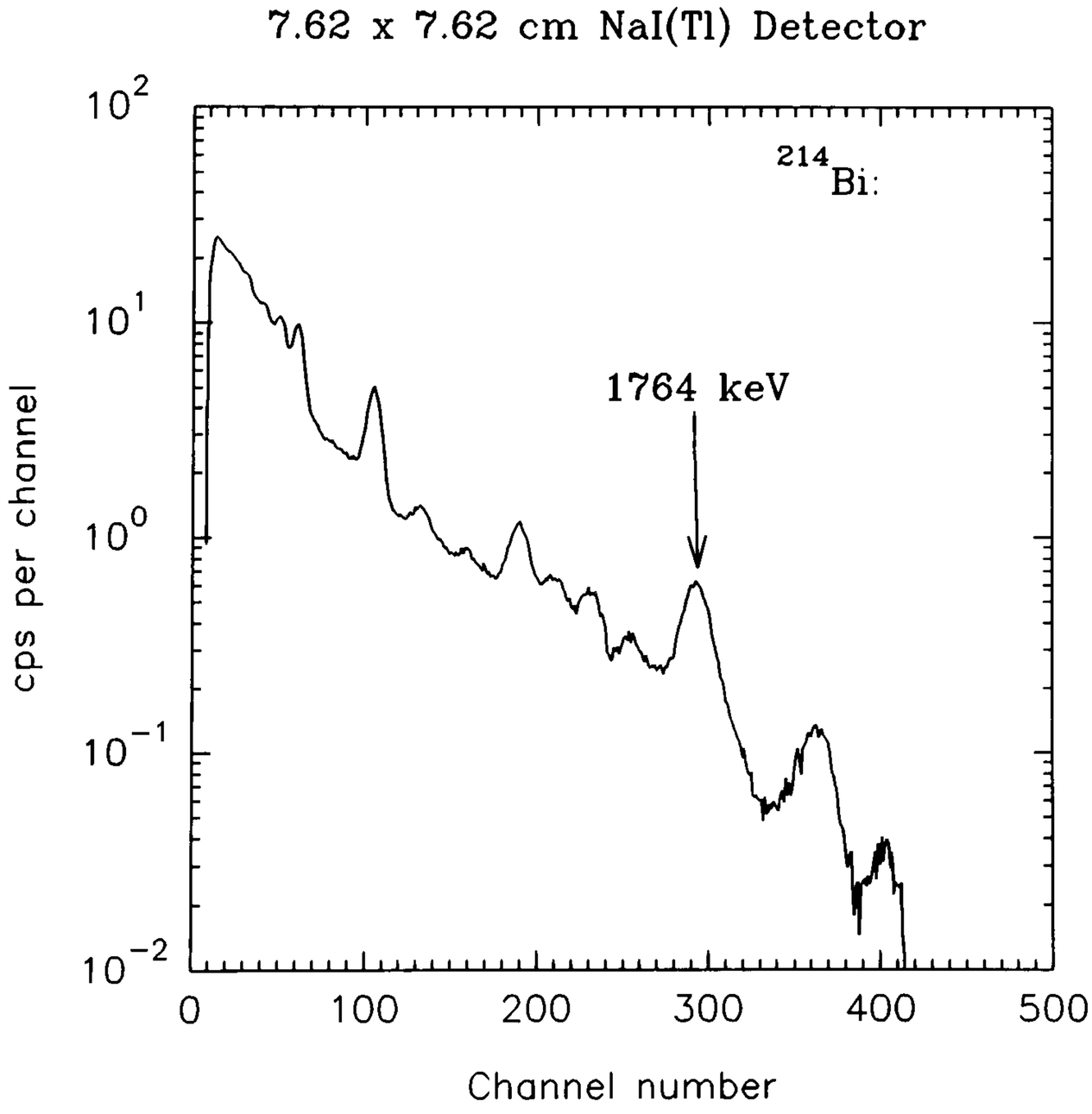

Figure 4.9 Net spectrum of a uranium rich concrete calibration pad, recorded using a 7.62 x 7.62cm NaI(Tl) detector.

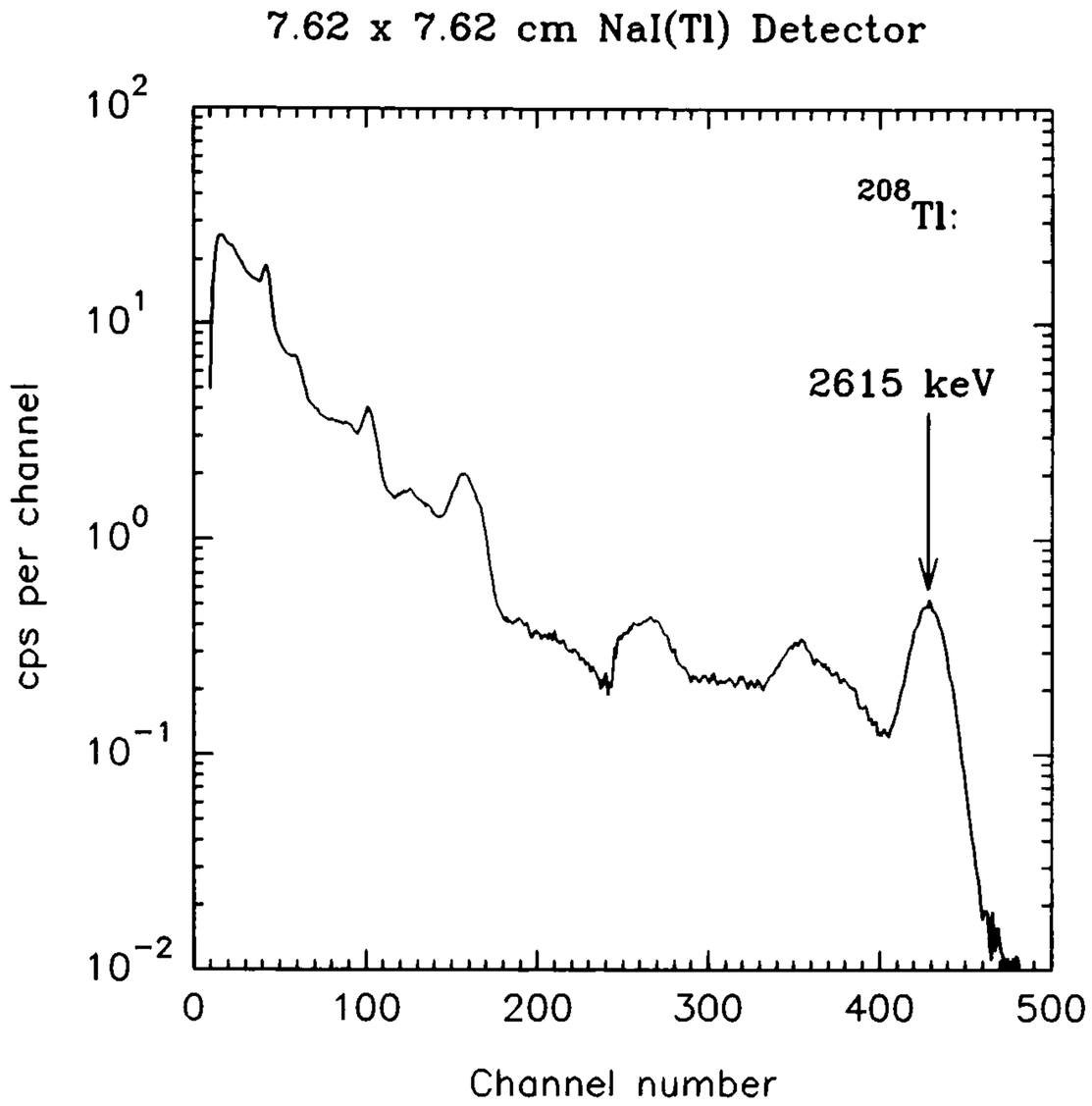

Figure 4.10 Net spectrum of a thorium rich concrete calibration pad, recorded using a 7.62 x 7.62cm NaI(Tl) detector.

Table 4.6 Stripping ratios of 7.62 x 7.62cm NaI(Tl), determined with discrete sources (Cs radionuclides) and calibration pads (natural sources).

	Spectral Windows				
	^{137}Cs	**^{134}Cs**	**^{40}K**	**^{214}Bi**	**^{208}Tl**
	95-130 ch.	**125-150 ch.**	**220-270 ch.**	**270-318 ch.**	**390-480 ch.**
^{137}Cs	1	0.0219 ±0.0001	0.00336 ±0.00007	0.0	0.0
^{134}Cs	1.87 ±0.02	1	0.026 ±0.003	0.002 ±0.002	0.0
^{40}K	0.774 ±0.007	0.487 ±0.005	1	0.0	0.0
^{214}Bi	5.13 ±0.03	1.77 ±0.01	1.151 ±0.008	1	0.050 ±0.002
^{208}Tl	5.23 ±0.03	2.35 ±0.02	1.021 ±0.008	0.789 ±0.006	1

4.5 Stripping Ratios of Aerial Survey Detectors

Stripping ratios of the 16 litre NaI(Tl) array (comprising of 4 crystals) were calculated using discrete sources in the same manner as the 7.62x7.62 cm NaI(Tl) detector and are shown in tables 4.7 and 4.8. The sources used were placed 1m from the underside of the detector (with the exception of the potassium chloride) to ensure that dead time was less than 20% and each crystal viewed the source in an approximately equal manner. Five kilograms of KCL were placed on the top surface of the outer detector casing to increase counting statistics. A counting time of 60s was used throughout. The data in tables 4.7 and 4.8 show mean values, calculated from five separate measurements (n=5) and the errors are single standard deviations.

The choice of caesium windows in tables 4.7 (previous set) and 4.8 (new set) is well demonstrated by comparing stripping ratios. Primarily, the full energy peak encroachment of ^{137}Cs into the ^{134}Cs window is reduced by 80%.

Table 4.7 Mean stripping ratios of 16 litre NaI(Tl), determined with discrete sources. Resolution=11.0-11.5%.

	Spectral Windows				
	^{137}Cs	**^{134}Cs**	**^{40}K**	**^{214}Bi**	**^{208}Tl**
	95-128 ch.	**118-143 ch.**	**220-270 ch.**	**270-318 ch.**	**390-480 ch.**
^{137}Cs	1	0.28 ±0.02	0.0026 ±0.0009	0.0013 ±0.0017	0.0011 ±0.0024
^{134}Cs	1.73 ±0.02	1	0.0289 ±0.0081	0.0062 ±0.0081	-0.0009 ±0.0040
^{40}K	0.21 ±0.02	0.15 ±0.01	1	0.017 ±0.003	0.0066 ±0.0035
^{214}Bi	3.41 ±0.14	1.012 ±0.08	0.98 ±0.03	1	0.067 ±0.017
^{208}Tl	2.56 ±0.13	1.34 ±0.12	0.54 ±0.08	0.33 ±0.04	1

Other contributions from scatter or full energy deposition or both, vary ±6% between

the tables and are within experimental errors. The exception to this is a 13.8% increase of contribution from ^{208}Tl into ^{134}Cs window (increased 836 keV, ^{228}Ac interference). For this to be valid, reliable control, and adjustment of detector gain and resolution must be achievable.

Table 4.8 Mean stripping ratios of 16 litre NaI(Tl), determined with discrete sources. Resolution=11.0-11.5%.

	Spectral Windows				
	^{137}Cs	**^{134}Cs**	**^{40}K**	**^{214}Bi**	**^{208}Tl**
	95-130 ch.	**125-150 ch.**	**220-270 ch.**	**270-318 ch.**	**390-480 ch.**
^{137}Cs	1	0.056 ±0.005	0.0025 ±0.0009	0.0013 ±0.0017	0.0001 ±0.0024
^{134}Cs	1.77 ±0.01	1	0.028 ±0.008	0.0061 ±0.0059	-0.0008 ±0.0039
^{40}K	0.22 ±0.02	0.161 ±0.007	1	0.017 ±0.003	0.0066 ±0.0035
^{214}Bi	3.51 ±0.15	0.99 ±0.07	0.98 ±0.03	1	0.067 ±0.017
^{208}Tl	2.67 ±0.17	1.53 ±0.14	0.54 ±0.07	0.33 ±0.04	1

The stripping ratios of an 8 litre NaI(Tl) detector array (2 crystals) are listed in table 4.9. The table shows the improved windows. The problems associated with gain drift between each individual crystal are less severe with a 2 crystal detector. This was confirmed through practical experience, during aerial surveys in tropical, humid climates (Sanderson & Allyson, 1991).

Table 4.10 shows stripping ratios of a 16 litre detector array, determined over a 1m^2 plane ^{137}Cs SURRC calibration source (500s live time), a discrete ^{134}Cs source (60s) and concrete calibration pads (K, 100s; U, 500s; Th, 300s). The detector was placed on a wooden frame 29cm directly above the plane source and calibration pads. The ^{134}Cs source was placed 1m beneath the detector, as before. For the pads, an intense scatter component and self absorption into the lower energy windows makes a systematic

difference to stripping ratios: some increase, others decrease.

Table 4.9 Mean stripping ratios of 8 litre NaI(Tl), determined with discrete sources. Resolution = 8.8%.

	Spectral Windows				
	^{137}Cs	^{134}Cs	^{40}K	^{214}Bi	^{208}Tl
	95-130 ch.	125-150 ch.	220-270 ch.	270-318 ch.	390-480 ch.
^{137}Cs	1	0.033 ±0.005	0.0 ±0.008	0.002 ±0.002	0.0 ±0.002
^{134}Cs	1.74 ±0.05	1	0.038 ±0.019	0.002 ±0.034	0.0 ±0.004
^{40}K	0.251 ±0.007	0.18 ±0.02	1	0.009 ±0.004	0.0 ±0.003
^{214}Bi	4.14 ±0.20	1.09 ±0.13	0.91 ±0.07	1	0.057 ±0.029
^{208}Tl	2.91 ±0.57	1.49 ±0.06	0.59 ±0.30	0.37 ±0.11	1

Table 4.10 Stripping ratios of 16 litre NaI(Tl), determined with a plane ^{137}Cs source, a ^{134}Cs discrete source & calibration pads (natural sources).

	Spectral Windows				
	^{137}Cs	^{134}Cs	^{40}K	^{214}Bi	^{208}Tl
	95-130 ch.	125-150 ch.	220-270 ch.	270-318 ch.	390-480 ch.
^{137}Cs	1	0.054 ±0.002	0.0015 ±0.0020	0.0029 ±0.0009	-0.0007 ±0.0009
^{134}Cs	1.77 ±0.01	1	0.028 ±0.008	0.0061 ±0.0006	-0.00008 ±0.0039
^{40}K	0.459 ±0.008	0.278 ±0.006	1	0.027 ±0.003	-0.0036 ±0.0022
^{214}Bi	3.49 ±0.02	1.269 ±0.006	0.903 ±0.006	1	0.142 ±0.002
^{208}Tl	2.82 ±0.01	1.574 ±0.008	0.601 ±0.006	0.439 ±0.003	1

4.6 Operational Investigations of Aerial Survey 16 litre Detector: Results & Discussion

4.6.1 Stripping Ratios and Resolution

Energy resolution is an important spectrometric parameter. Its relative value is a measure of how well defined a given full energy peak will be, particularly when close to neighbouring peaks. The most common method of calculating and reporting resolution is by using a ^{137}Cs source of 662 keV γ-rays and determining the full width at half peak maximum as a percentage of the peak channel position (or energy). Thus,

$$Resolution = \frac{Channels\ of\ FWHM}{Peak\ Channel}\ 100\% \qquad (4.3)$$

The variation of stripping ratio (SURRC windows) as function of resolution is seen graphically below. Figure 4.11 shows the interference photopeak component of ^{137}Cs occurring in the ^{134}Cs window. The fraction increases, as expected, but only slowly with increasing (worsening) resolution: the ^{137}Cs peak progressively broadens with increasing resolution, and more of the full energy peak overlaps into the ^{134}Cs window.

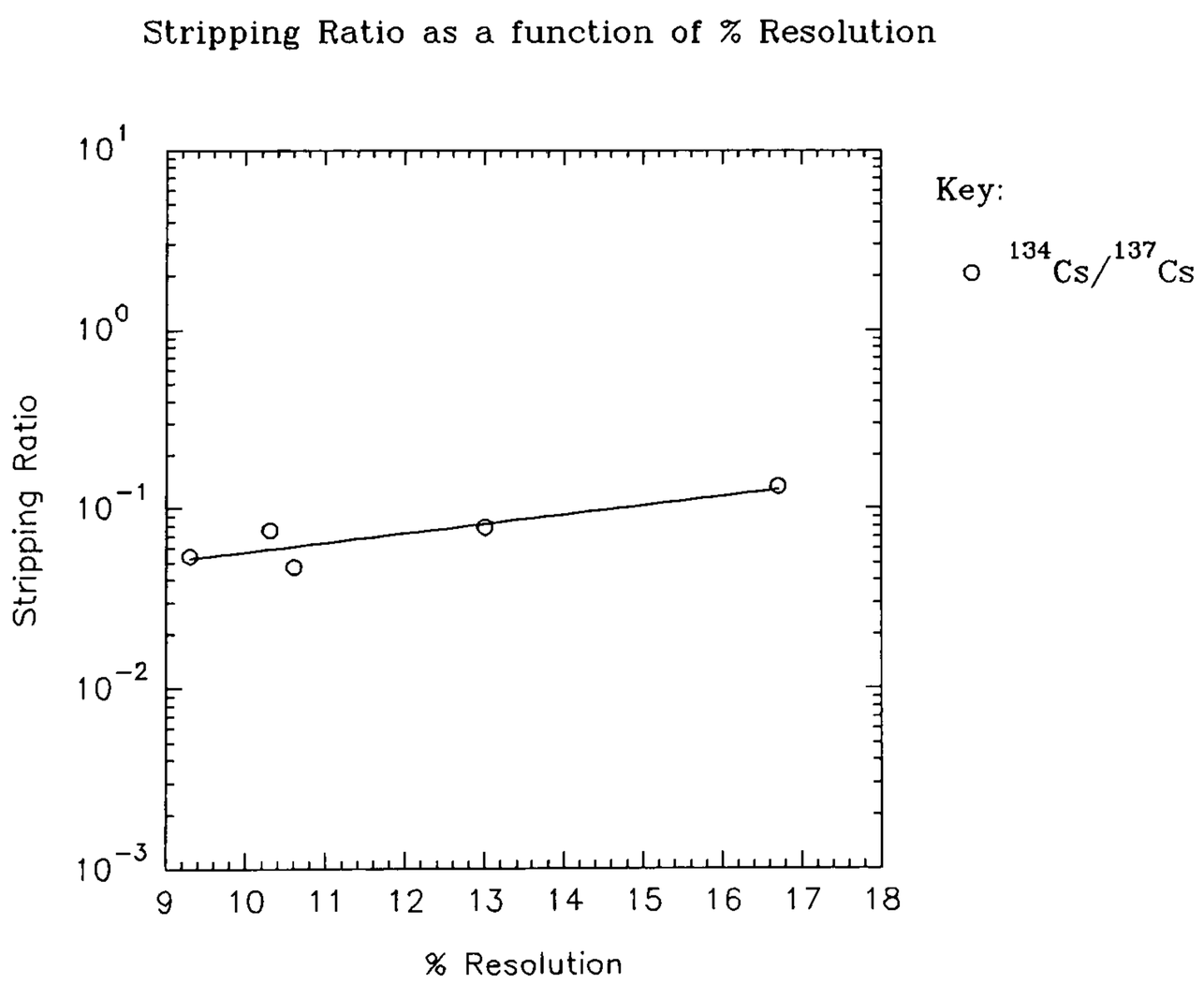

Figure 4.11 The variation of $^{134}Cs/^{137}Cs$ stripping ratio as a function of resolution.

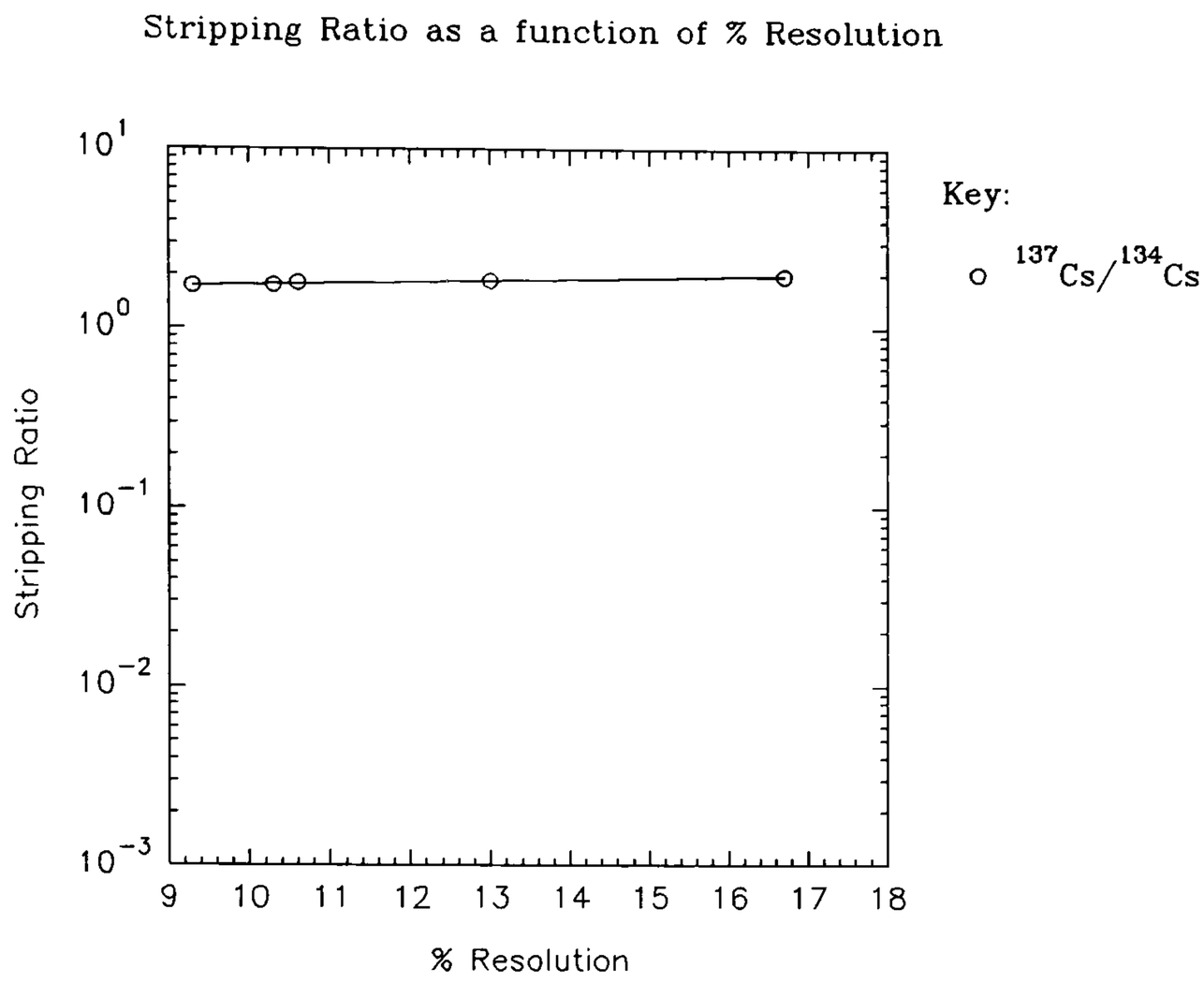

Figure 4.12 The variation of $^{137}Cs/^{134}Cs$ stripping ratio as a function of resolution.

Figures 4.13 to 4.15 show the variations of stripping ratios of ^{40}K, ^{214}Bi and ^{208}Tl. A near constant stripping ratio variation with change in resolution is observed for most: the proportion of interference from one window into another remains the same. The $^{214}Bi/^{40}K$ stripping ratio shows a gradual increase with resolution. All data points have relative errors of less than $\pm 5\%$.

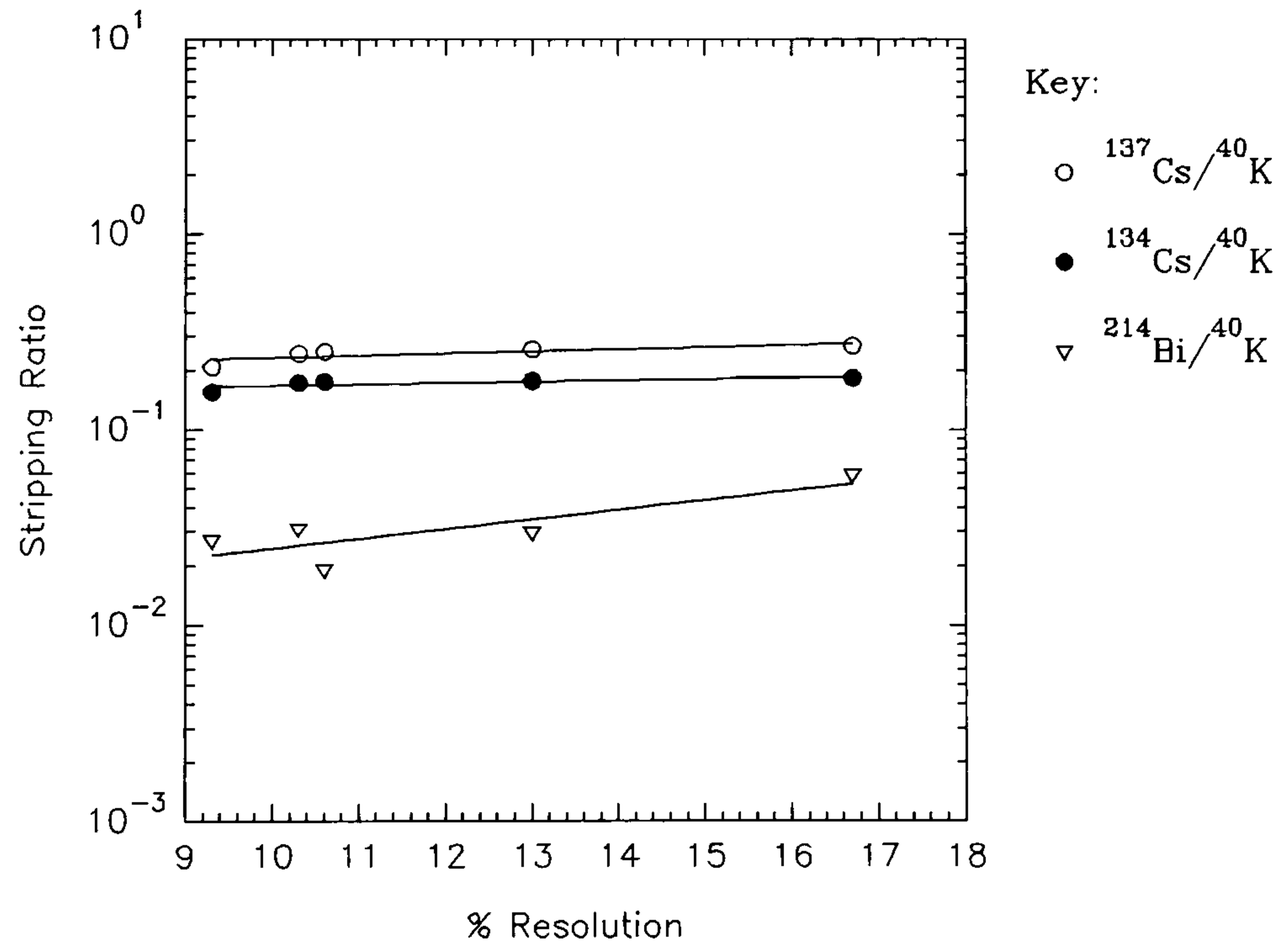

Figure 4.13 The variation of $^{137}Cs/^{40}K$, $^{134}Cs/^{40}K$ & $^{214}Bi/^{40}K$ stripping ratios as a function of resolution.

The resolution of a 16 litre, 4 crystal array package often varies over a range from a minimum of about 8.5% to 12%. It is usually advisable to make gain adjustments when the collective detector resolution is worse than 13%.

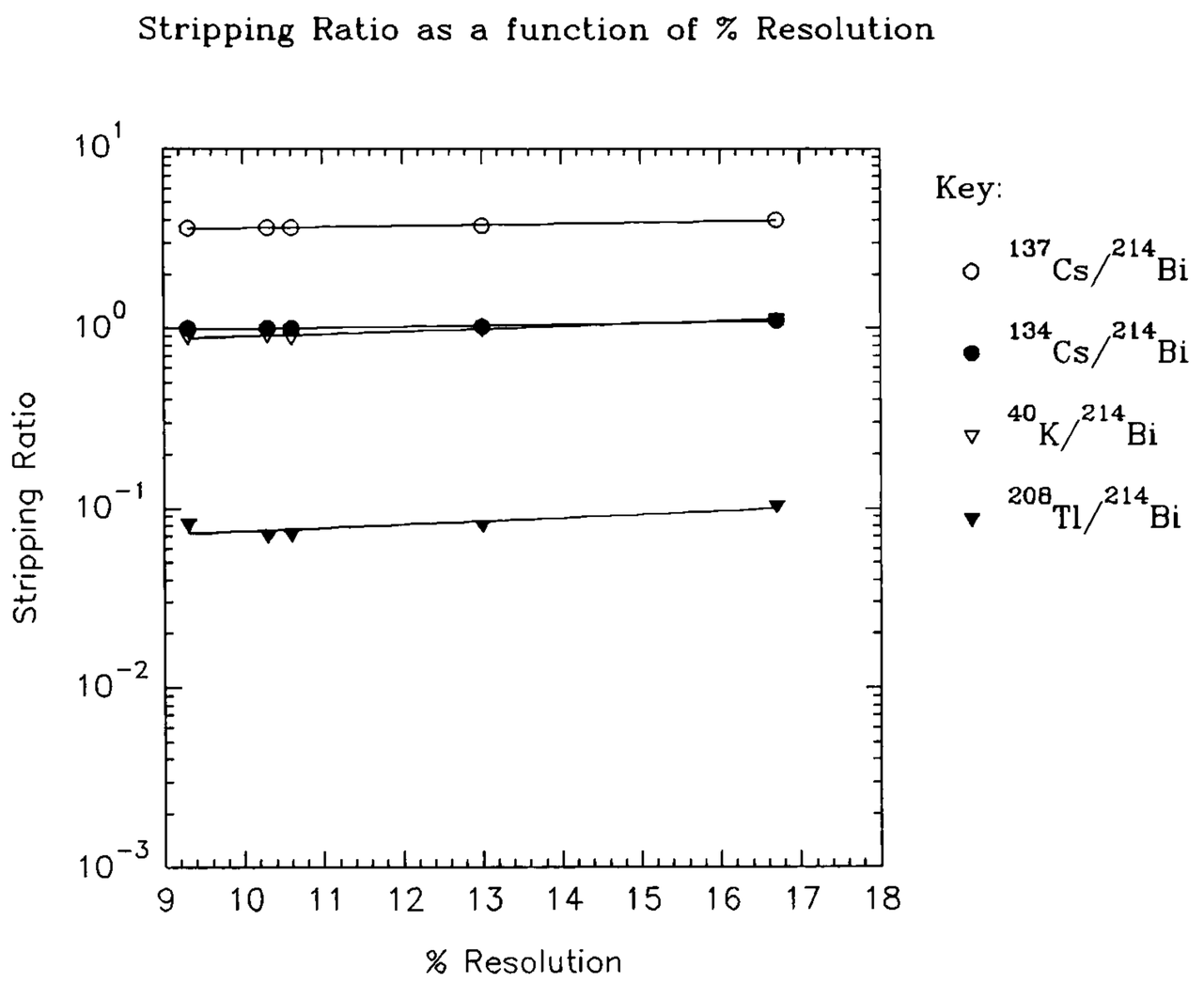

Figure 4.14 The variation of $^{137}Cs/^{214}Bi$, $^{134}Cs/^{214}Bi$, $^{40}K/^{214}Bi$ & $^{208}Tl/^{214}Bi$ stripping ratios as a function of resolution.

A detector beyond 13% resolution yields relatively poor spectrometric detail. We may conclude that for a 8.5-13% resolution, variations of stripping ratios for the chosen windows, are small and well within statistical errors of field measurements. A single stripping ratio matrix can be reasonably applied to aerial survey data within the resolution 8.5-13%.

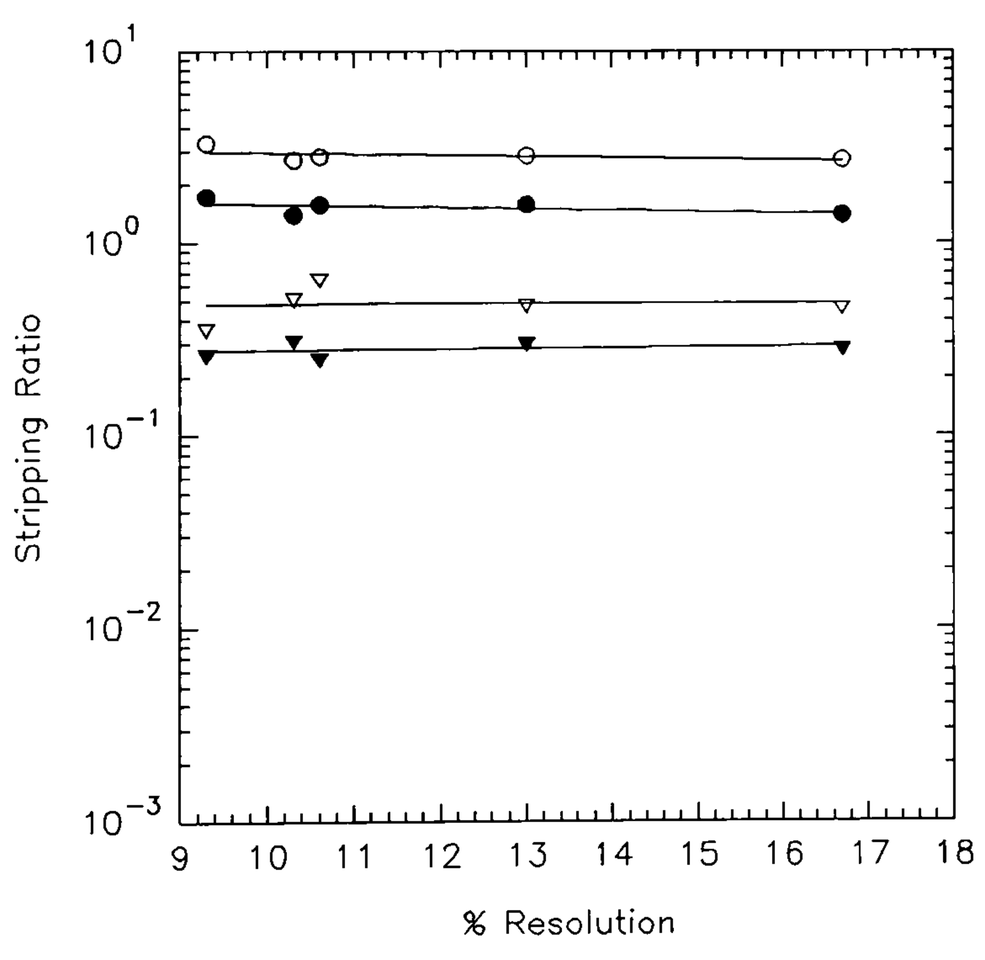

Figure 4.15 The variation of $^{137}Cs/^{208}Tl$, $^{134}Cs/^{208}Tl$, $^{40}K/^{208}Tl$ & $^{214}Bi/^{208}Tl$ stripping ratios as a function of resolution.

Table 4.11 summarises the findings from this section, for a 16 litre aerial survey detector array and SURRC windows. The rate of change of stripping ratio per % resolution, from a resolution of 9.3 to 16.7% is shown to be relatively small.

Table 4.11 Increase in stripping ratio per %, from 9.3% to 16.7% resolution for aerial survey detector (16 litre).

Stripping Ratio:	**Stripping ratio @9.3% resolution**	**Stripping ratio increase per % from 9.3-16.7% resolution**
$^{134}Cs/^{137}Cs$	0.050	0.010
$^{137}Cs/^{134}Cs$	1.73	0.035
$^{137}Cs/^{40}K$	0.230	0.0061
$^{134}Cs/^{40}K$	0.166	0.0027
$^{214}Bi/^{40}K$	0.021	0.0044
$^{137}Cs/^{214}Bi$	3.59	0.053
$^{134}Cs/^{214}Bi$	0.986	0.015
$^{40}K/^{214}Bi$	0.873	0.034
$^{208}Tl/^{214}Bi$	0.072	0.0038
$^{137}Cs/^{208}Tl$	3.00	-0.044
$^{134}Cs/^{208}Tl$	1.61	-0.028
$^{40}K/^{208}Tl$	0.500	-0.002
$^{214}Bi/^{208}Tl$	0.278	0.0018

4.6.2 Stripping Ratios and % Gain Shift

The variation of stripping ratios with % gain shift (collective gain drift of the detector package) has been investigated. This variation is usually as a result of temperature effects on associated counting electronics or voltage level irregularities of power supplies. SURRC aerial survey logging software incorporates a gain shift monitor. This is called the *k1/k2 ratio* and utilises the normally present ^{40}K peak. This peak is divided into two halves at its peak position. The ratio of the respective counts recorded within these adjacent windows (k1 & k2) is measure of gain shift. Figure 4.16 shows k1/k2 ratio as a function of percentage gain shift. A value of 1 is normal (dotted line). The relative error of all data is less than $\pm 0.5\%$. Corrections are manually applied to the collective high voltage power supply to return any unacceptable variation to a reference channel position (channel 243, 1462 keV). k1 is integrated within a window of 1400-1461 keV (233-243 ch.) & k2 within 1462-1524 keV (243-253 ch.).

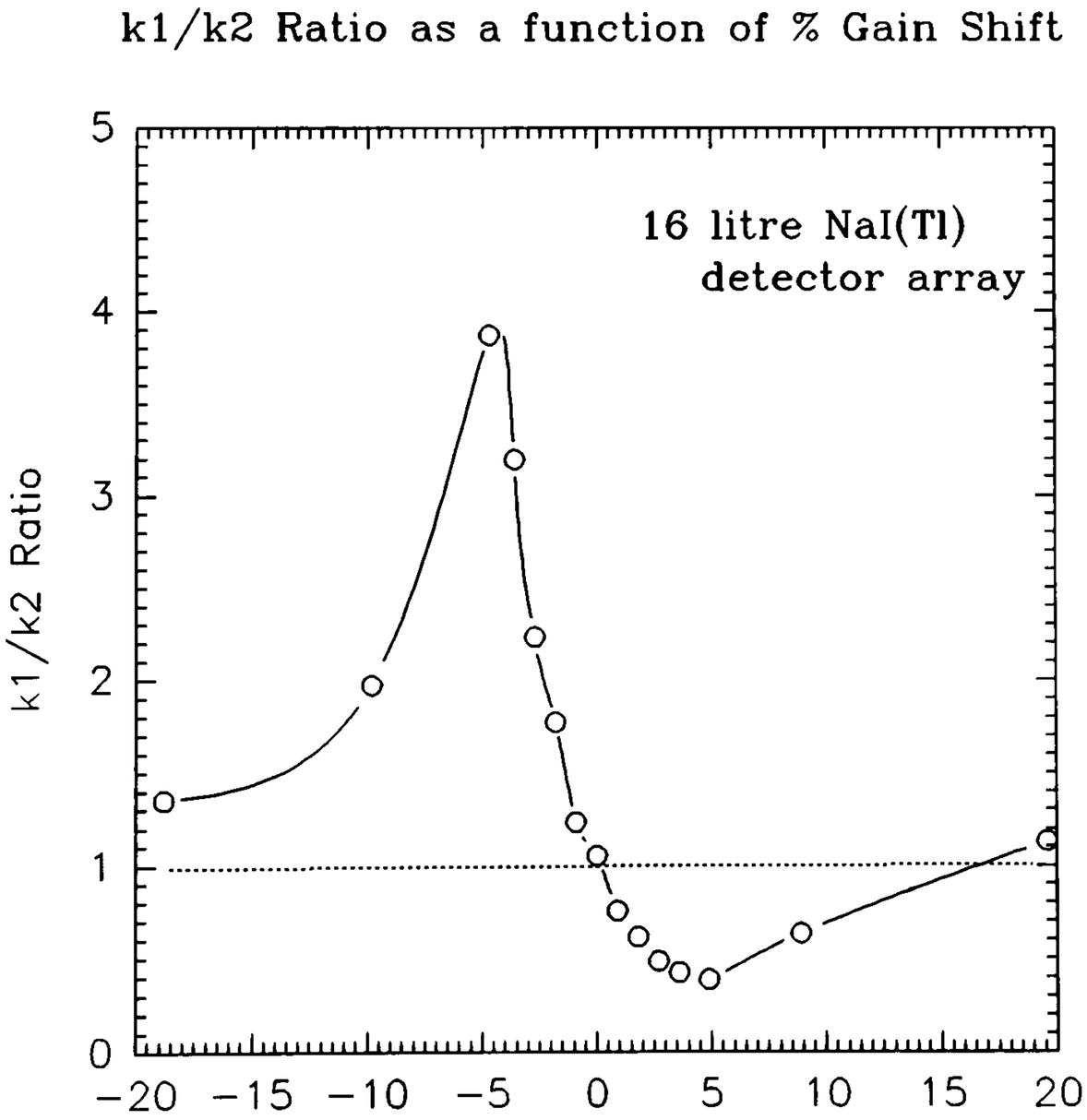

Figure 4.16 k1/k2 ratio of an aerial survey detector, as a function of % gain shift.

Variation of stripping ratios for ^{137}Cs and ^{134}Cs are shown in figures 4.17 and 4.18 respectively. The stripping ratio of ^{137}Cs into ^{134}Cs gradually increases with increasing % gain shift, owing to the two caesium windows being adjacent.

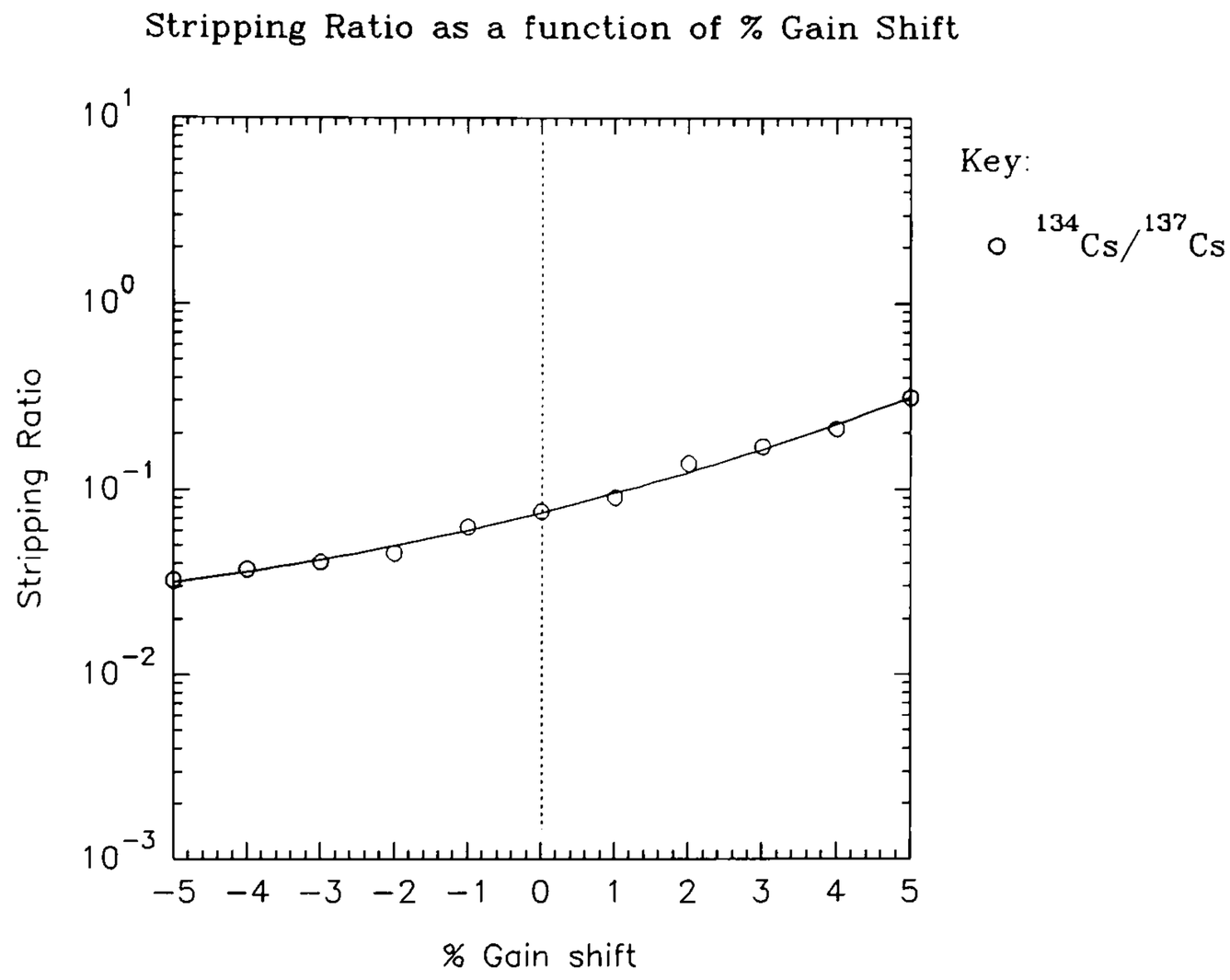

Figure 4.17 The variation of $^{134}Cs/^{137}Cs$ stripping ratio as a function of % gain shift.

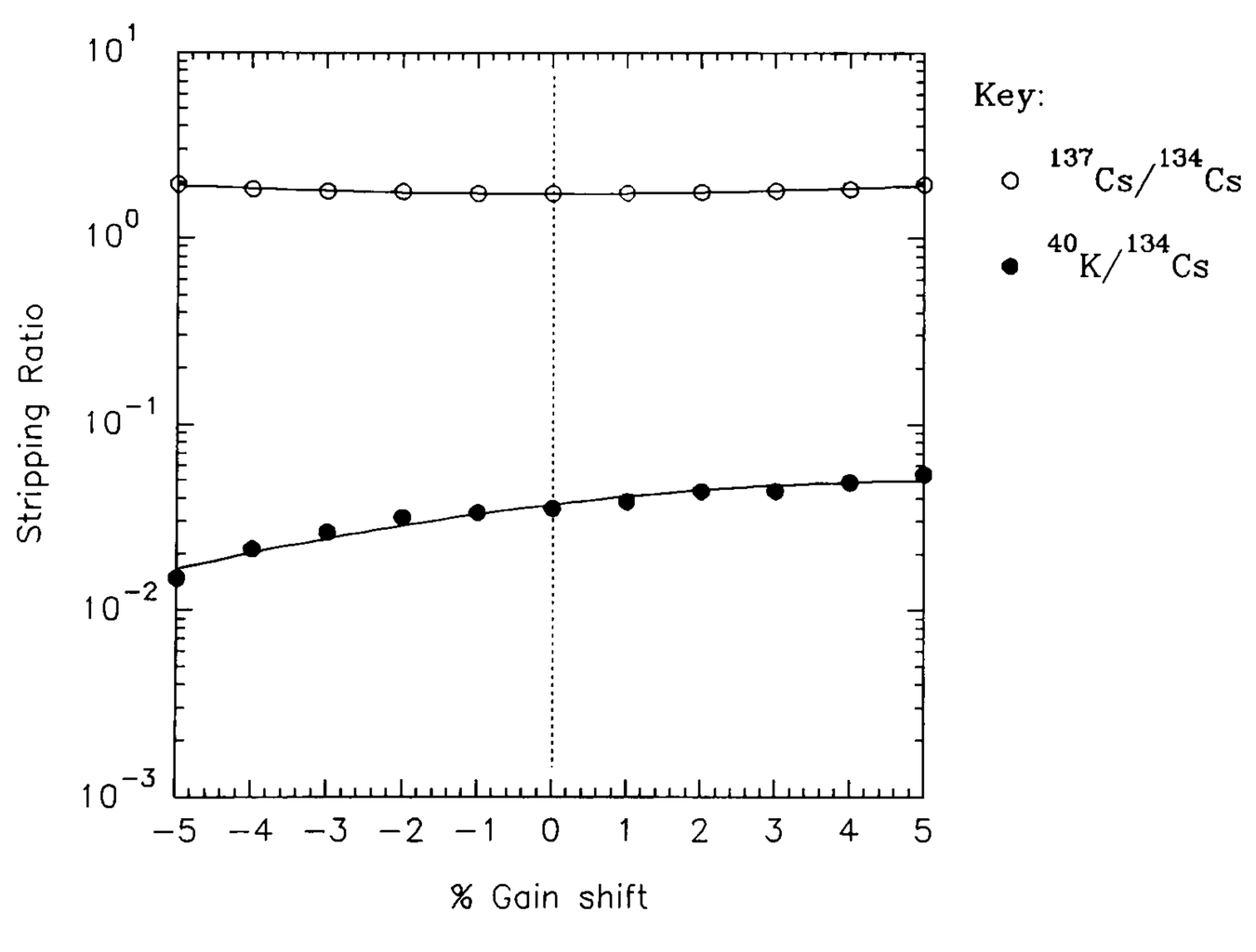

Figure 4.18 The variation of $^{137}Cs/^{134}Cs$ & $^{40}K/^{134}Cs$ stripping ratios as a function of % gain shift.

The stripping ratios of of the other radionuclides also show some variations. From figure 4.16, it may be seen that for a 30% increase in k1/k2 ratio, a decrease in gain of 1% occurs. For a 25% decrease in k1/k2 ratio, a 1% gain increase occurs. A ±1% gain shift is clearly observable in field operations. Surveys conducted in low potassium environments may require alternative gain monitoring arrangements.

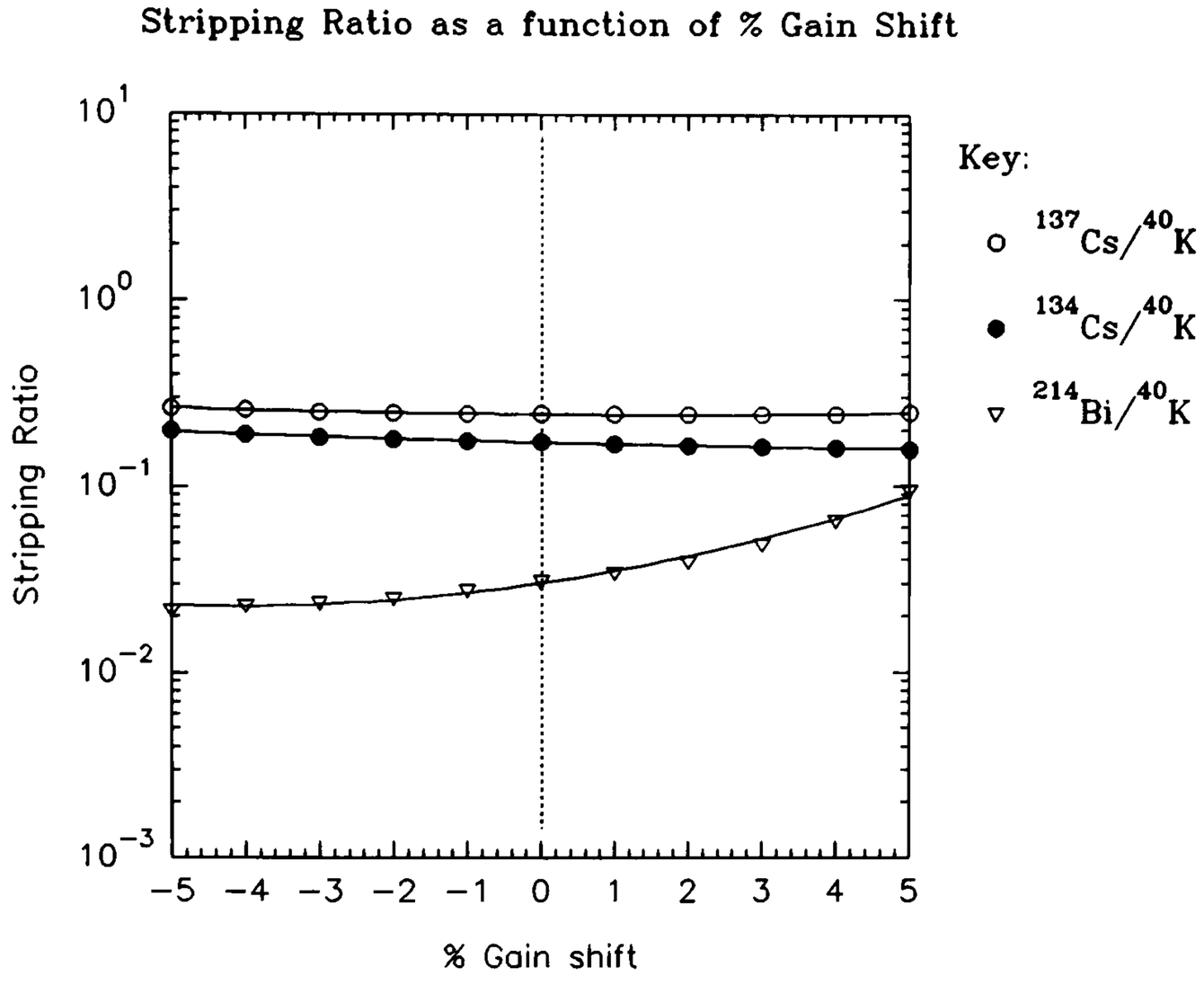

Figure 4.19 The variation of $^{137}Cs/^{40}K$, $^{134}Cs/^{40}K$ & $^{214}Bi/^{40}K$ stripping ratios as function of % gain shift.

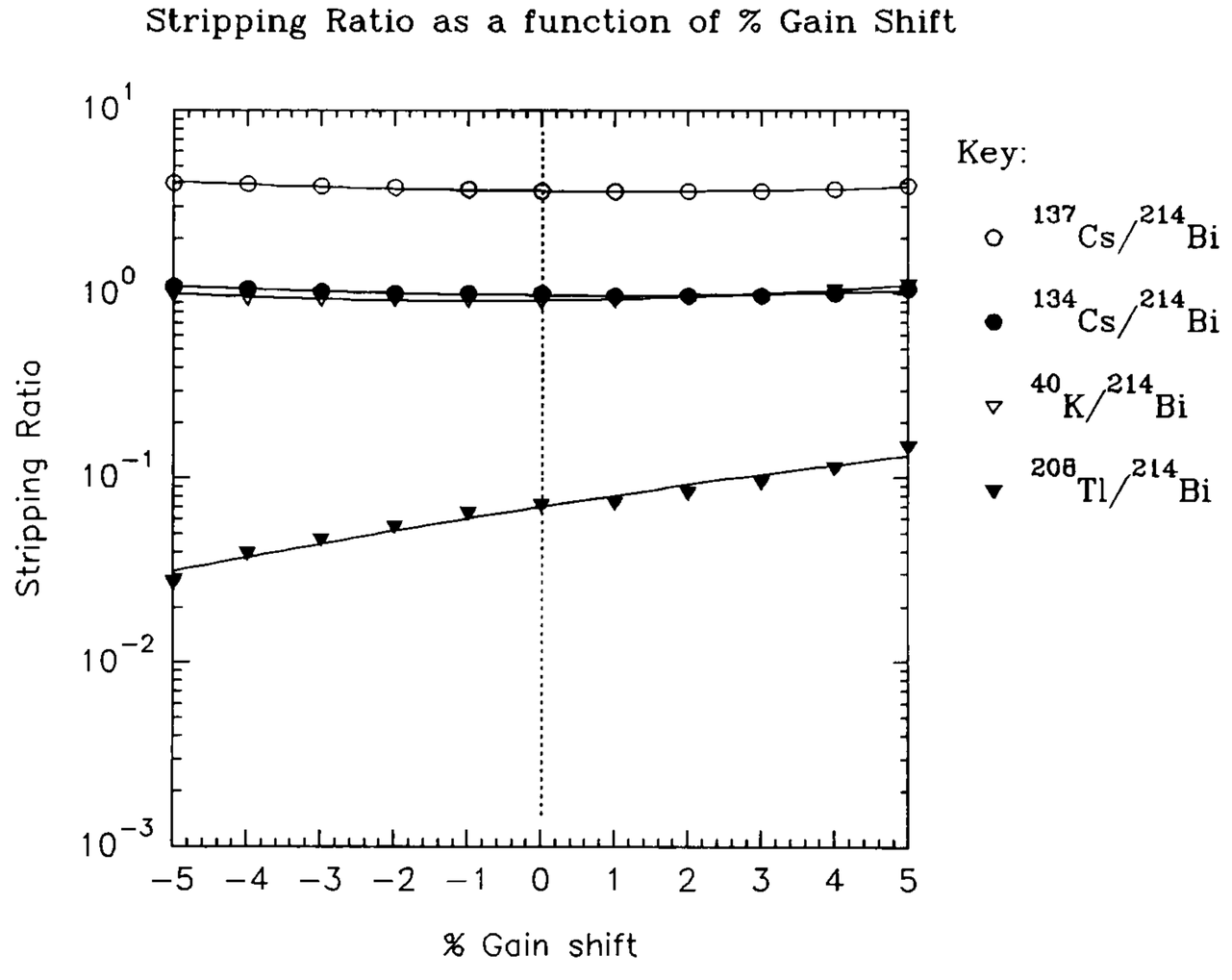

Figure 4.20 The variation of $^{137}Cs/^{214}Bi$, $^{134}Cs/^{214}Bi$, $^{40}K/^{214}Bi$ & $^{208}Tl/^{214}Bi$ stripping ratios as a function of % gain shift.

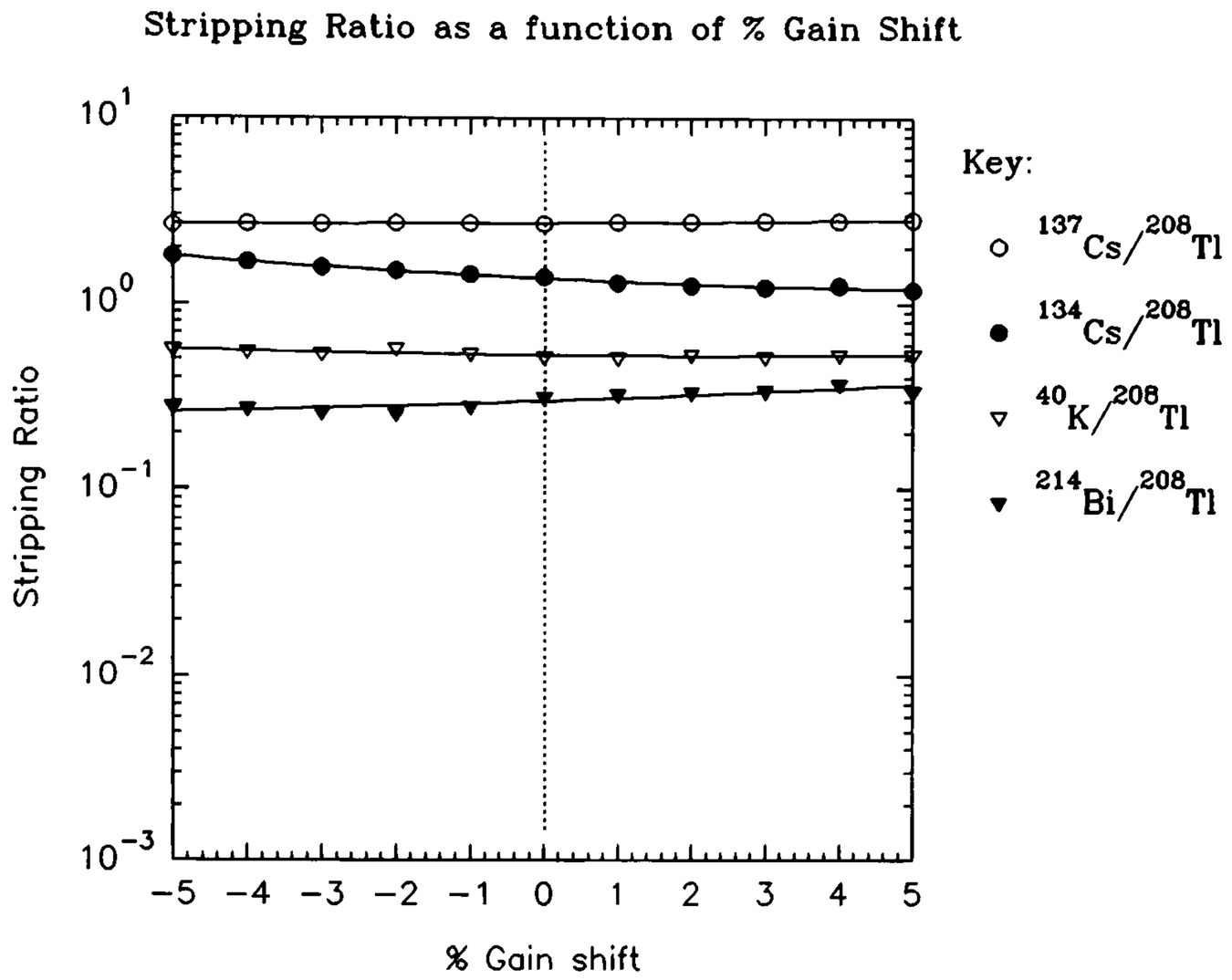

Figure 4.21 The variation of $^{137}Cs/^{208}Tl$, $^{134}Cs/^{208}Tl$, $^{40}K/^{208}Tl$ & $^{214}Bi/^{208}Tl$ stripping ratios as a function of % gain shift.

We can conclude that for survey data stripped using a single set of stripping ratios, a variation of $\pm 1\%$ in collective gain is tolerable. Software at SURRC has been developed to post-correct survey data if these specifications are exceeded (Sanderson *et al*, 1993a). SURRC data logging software labels each spectral measurement with a k1/k2 ratio. A correction was conceived by means of averaging two successive pairs of k1/k2 ratio in order to reduce statistical fluctuation. By using figure 4.16 to determine the % gain shift, these averages are applied to linearly compensate each spectral window and a complete reintegration of spectral data is made. Paatero (1964) offers more sophistication by a subroutine to compensate for gain shifting of entire spectral data by a method of *shifts* and *stretches*.

Table 4.12 shows a summary of the findings for the gain range over ±1% and for a 10.3% resolution at 662 keV.

Table 4.12 Increase in stripping ratio per %, from -1% to +1% gain for aerial survey detector at 10.3% resolution (16 litre).

Stripping Ratio:	**Stripping ratio @ -1% gain**	**Stripping ratio @ +1% gain**	**Stripping ratio increase per %, from -1 to +1% gain**
$^{134}Cs/^{137}Cs$	0.063	0.090	0.0138
$^{137}Cs/^{134}Cs$	1.74	1.75	0.006
$^{40}K/^{134}Cs$	0.0334	0.0382	0.0024
$^{137}Cs/^{40}K$	0.245	0.244	-0.0006
$^{134}Cs/^{40}K$	0.176	0.170	-0.003
$^{214}Bi/^{40}K$	0.028	0.034	0.003
$^{137}Cs/^{214}Bi$	3.70	3.60	-0.050
$^{134}Cs/^{214}Bi$	1.01	0.98	-0.017
$^{40}K/^{214}Bi$	0.928	0.925	-0.002
$^{208}Tl/^{214}Bi$	0.065	0.074	0.004
$^{137}Cs/^{208}Tl$	2.71	2.74	0.016
$^{134}Cs/^{208}Tl$	1.45	1.31	-0.073
$^{40}K/^{208}Tl$	0.535	0.507	-0.014
$^{214}Bi/^{208}Tl$	0.283	0.327	0.022

4.6.3 Experimental Measurements of Altitude Dependency of Stripping Ratios

Generally, stripping ratios of ^{40}K, ^{214}Bi & ^{208}Tl increase with altitude because a greater fraction of air scattered γ-rays is detected in the lower energy windows. In theory, the variation in spectral shape may be studied by flying a detector at different altitudes over suitable test sites. In practice, this is difficult to achieve owing to inhomogeneity and large ground area required (see chapter 5).

The IAEA (1991) has listed experimentally measured, ground level, stripping ratios α, ß and γ and calculated their change at greater detector altitudes. α represents the ratio of counts detected in the ^{214}Bi window to those detected in the ^{208}Tl, from a pure thorium source. ß is the ratio of counts in the ^{40}K window to ^{208}Tl window, from a pure thorium source and γ is the ^{40}K to ^{214}Bi ratio from a pure uranium source. The increments of α, ß and γ are almost independent of detector dimensions (IAEA, 1979). These data, and others, are shown in table 4.14. IAEA (1991) state that depending upon quality of spectrometer α varies 0.25-0.38; ß, 0.40-0.43 and γ, 0.81-0.92. No data are currently available as to the variation of other stripping ratios with altitude, particularly of ^{137}Cs, ^{134}Cs and ^{131}I. Therefore an experimental investigation was carried out to simulate the air path scattering by the use of a suitable medium. Grasty (1975) used point sources of ThO_2 near the base of a water filled tank to investigate the variation of α for small detectors. Later, Grasty (1980b) and Dickson *et al* (1981) used plywood sheets to represent air in a similar trial with a standard 16 litre aerial survey package. However, water can be an inconvenient medium to use and the composition of plywood may not be accurately known. Perspex is an alternative that closely resembles the mass attenuation coefficients and average atomic number of air (Z=7.4) over a wide range of energies (Figure 4.22) and has been used here. Perspex consists of $C_4H_6O_2$ (C: 55.8%; H: 7.03%; O: 37.17%), average Z=6.4 and a density of 1.176 g cm^{-3}. It is available in sheets of approximately 1.05 x 1.05 x 0.01m which conveniently fit across the transportable calibration pads. For air of density $1.225x10^{-3}$ g cm^{-3} (15°C, 1 atm.), a single perspex sheet is equivalent to 9.6m of air. Ten sheets approximates to 100m standard survey altitude. It is noted that while such an experiment may simulate attenuation and forward scatter through a relatively narrow angle, little account of

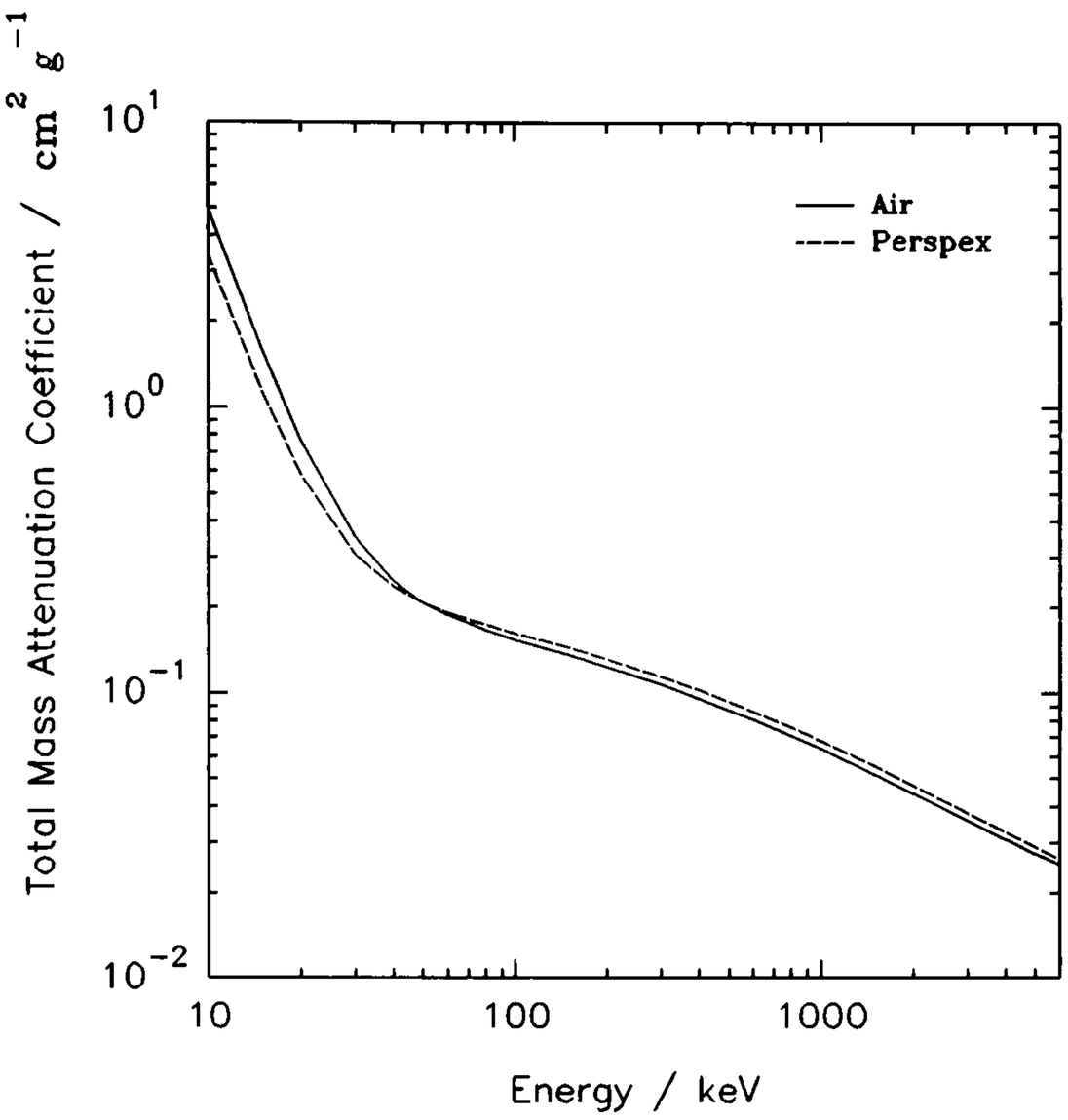

Figure 4.22 Comparison of mass attenuation coefficients of air and perspex.

sideways scatter and no account of backscatter (*skyshine*) is made. Skyshine may be simulated by placing perspex sheeting above the detector, but was not done here. The calibration pads were carefully placed within a cell, bounded on three sides by adjoining thick concrete blocks. Although the open fourth side potentially allowed *cross-talk* interference, in order to permit ease of access, this opening was considered to have minimal practical effect. A background measurement within each cell was made prior to lowering the calibration pads inside to ensure that similar readings were obtained, since the whole facility was within a decommissioned accelerator building and residual activity in certain areas was high. In light of some findings this method could be reviewed. The height of the surrounding concrete blocks was only just above that of the calibration pads themselves. These also served as a convenient and stable foundation to mount the aerial survey detector supporting frame. The concrete blocks also provided some side ways scatter mechanism (90° to the normal), but little $>45°$ forward scatter (in addition to the contribution the perspex sheets provide) towards the detector.

Experiments were performed on the potassium, uranium, thorium and blank calibration pads using the 16 litre NaI(Tl) detector array, for an air equivalent thickness from 0 to

200m. As noted previously, a $1m^2$ ^{137}Cs plane calibration source (total surface activity 40 kBq m^{-2}) was manufactured at SURRC (by A.N. Tyler) and enabled the variation of 662 keV γ-rays through equivalent air to be studied, in a more realistic manner than using a point source. This source was placed upon the blank calibration pad upon which the perspex sheets were stacked. The aerial survey detector was placed on the wooden supporting frame, 29cm above each pad surface. A net spectral response was determined by subtracting a blank calibration pad measurement where equal number of perspex sheets had been used. Figures 4.23-4.26 show the gross spectral measurements taken from each pad. The ^{137}Cs source was counted for 500s, potassium pad 100s, uranium pad 500s, thorium pad 300s and blank 500s. The data processing was done using standard aerial survey logging software to record full spectral data and window responses. Figures 4.27-4.33 and Appendix B show the calculated stripping ratios (for SURRC & IAEA windows), including ^{137}Cs plane source. Experimental errors are within the symbol size plotted (mostly better than 8%) and have been derived from counting statistics and a combination of errors between spectral windows. Since the whole experiment took several hours to complete, some gain drift appears to have occurred and contributed to small systematic variations observed around perspex sheet number 15.

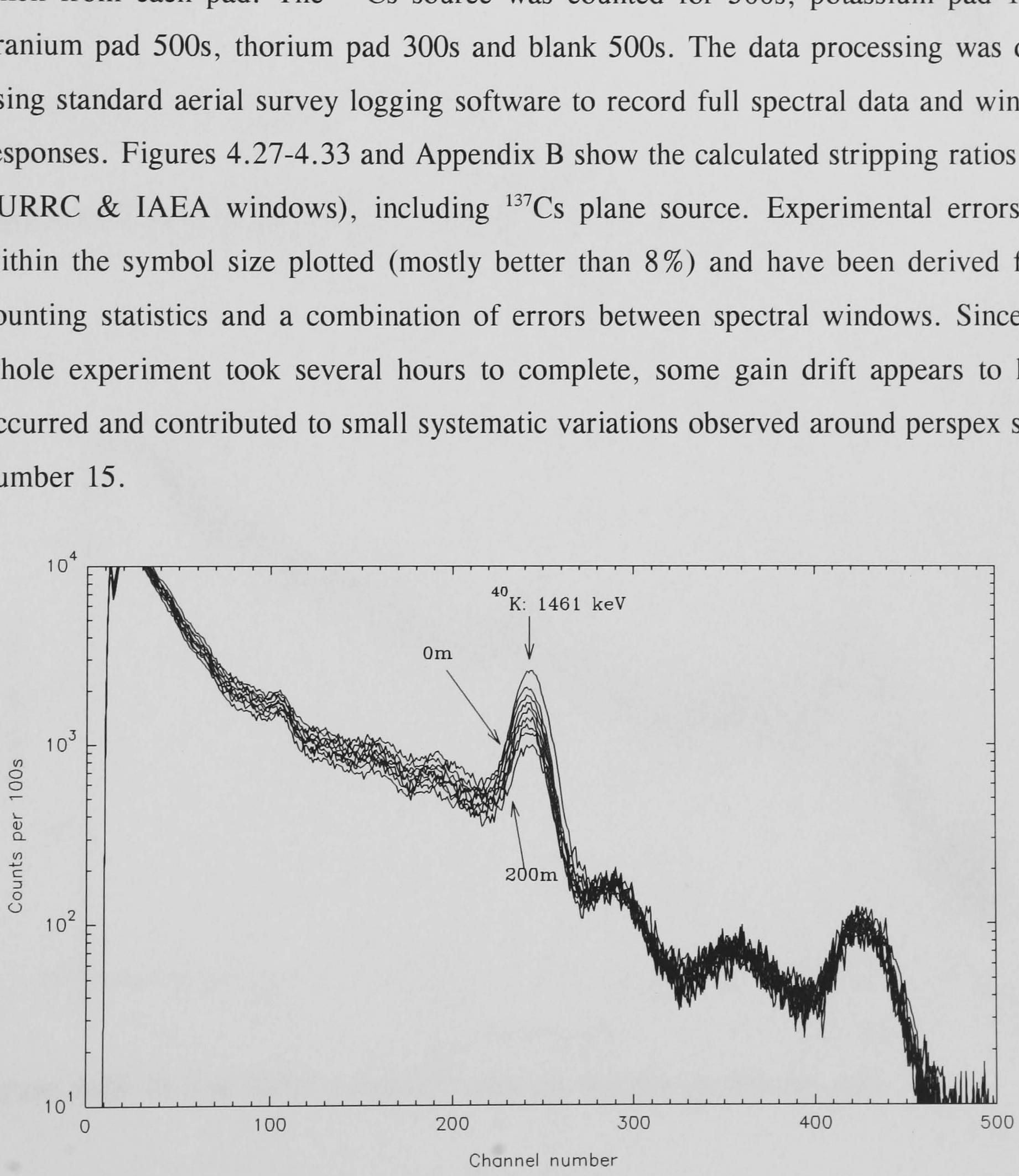

Figure 4.23 16 litre NaI(Tl) detector array on potassium calibration pad.

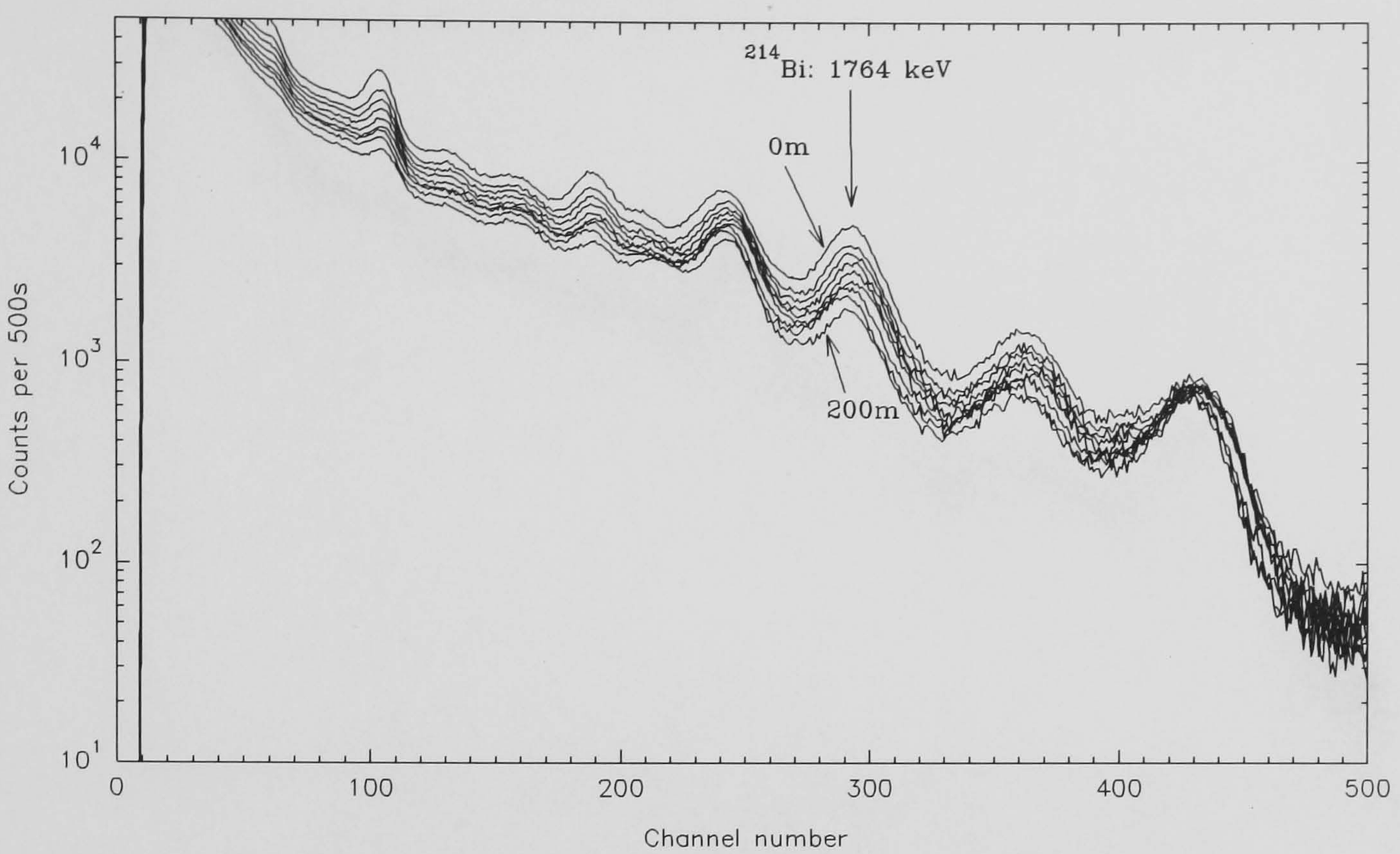

Figure 4.24 16 litre NaI(Tl) detector array on uranium calibration pad.

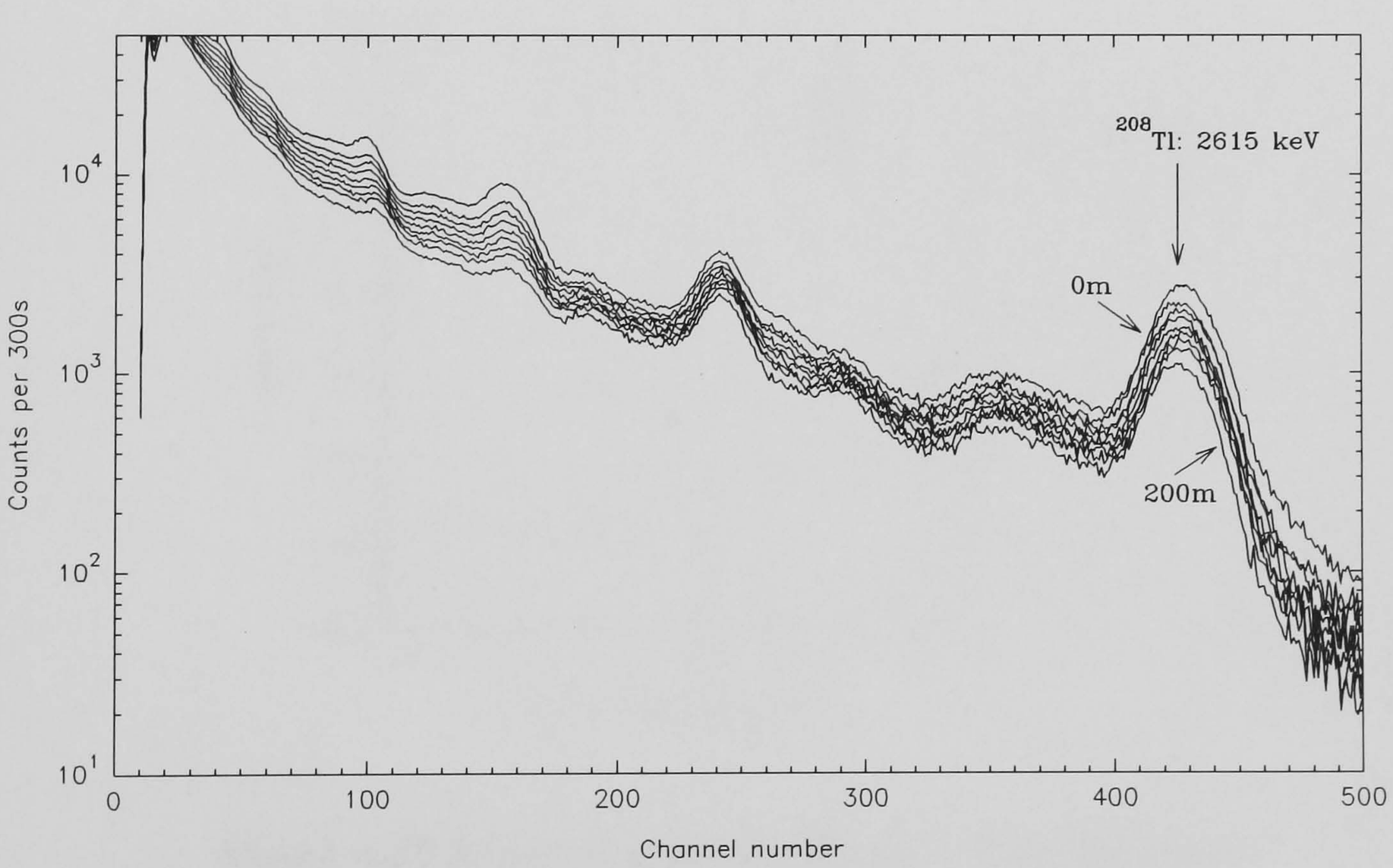

Figure 4.25 16 litre NaI(Tl) detector array on thorium calibration pad.

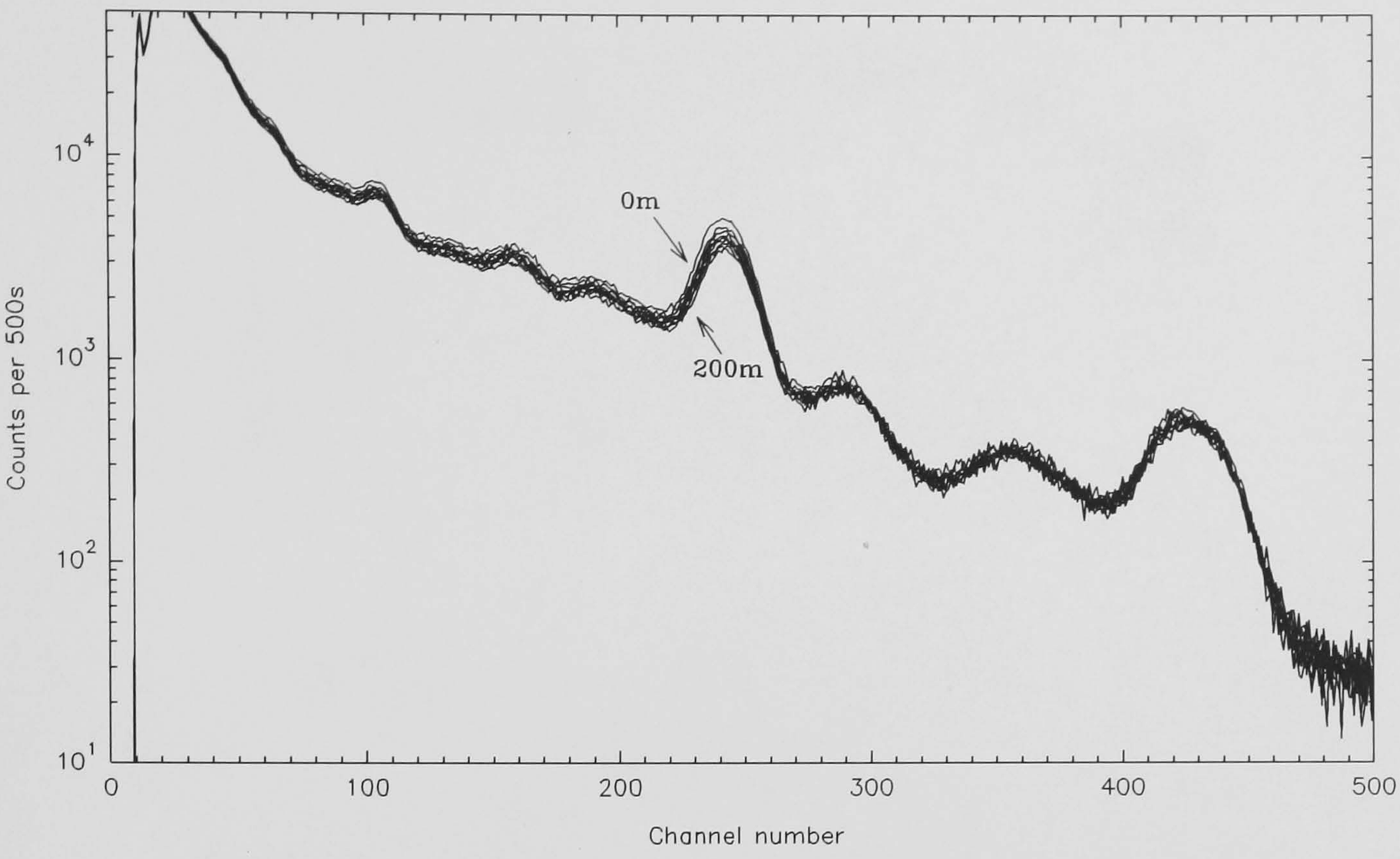

Figure 4.26 16 litre NaI(Tl) detector array on blank calibration pad.

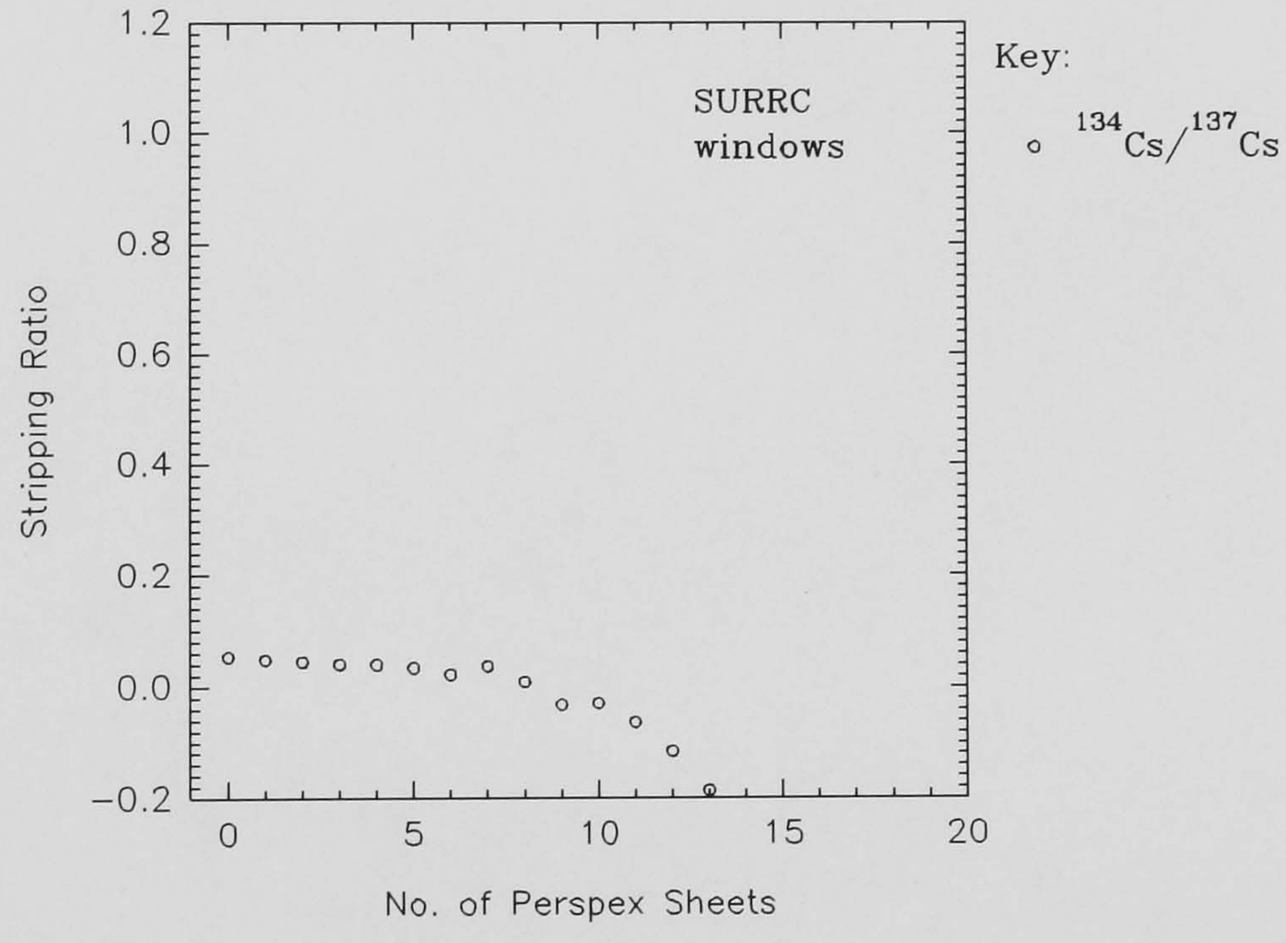

Figure 4.27 Stripping ratios of ^{137}Cs into ^{134}Cs from a pure source of ^{137}Cs, for SURRC windows.

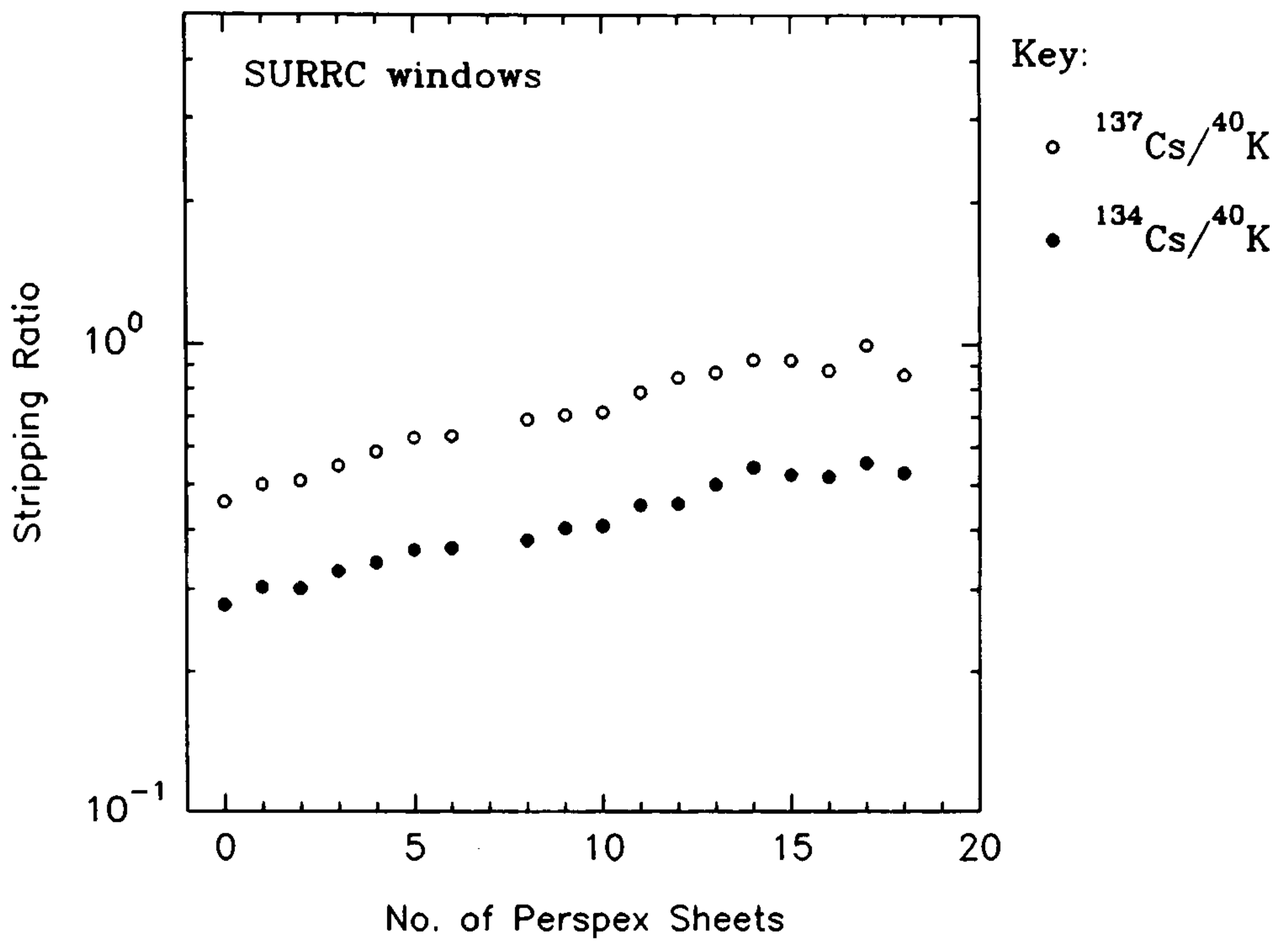

Figure 4.28 Stripping ratios of ^{40}K into ^{137}Cs and ^{134}Cs, from a ^{40}K calibration pad, for SURRC windows.

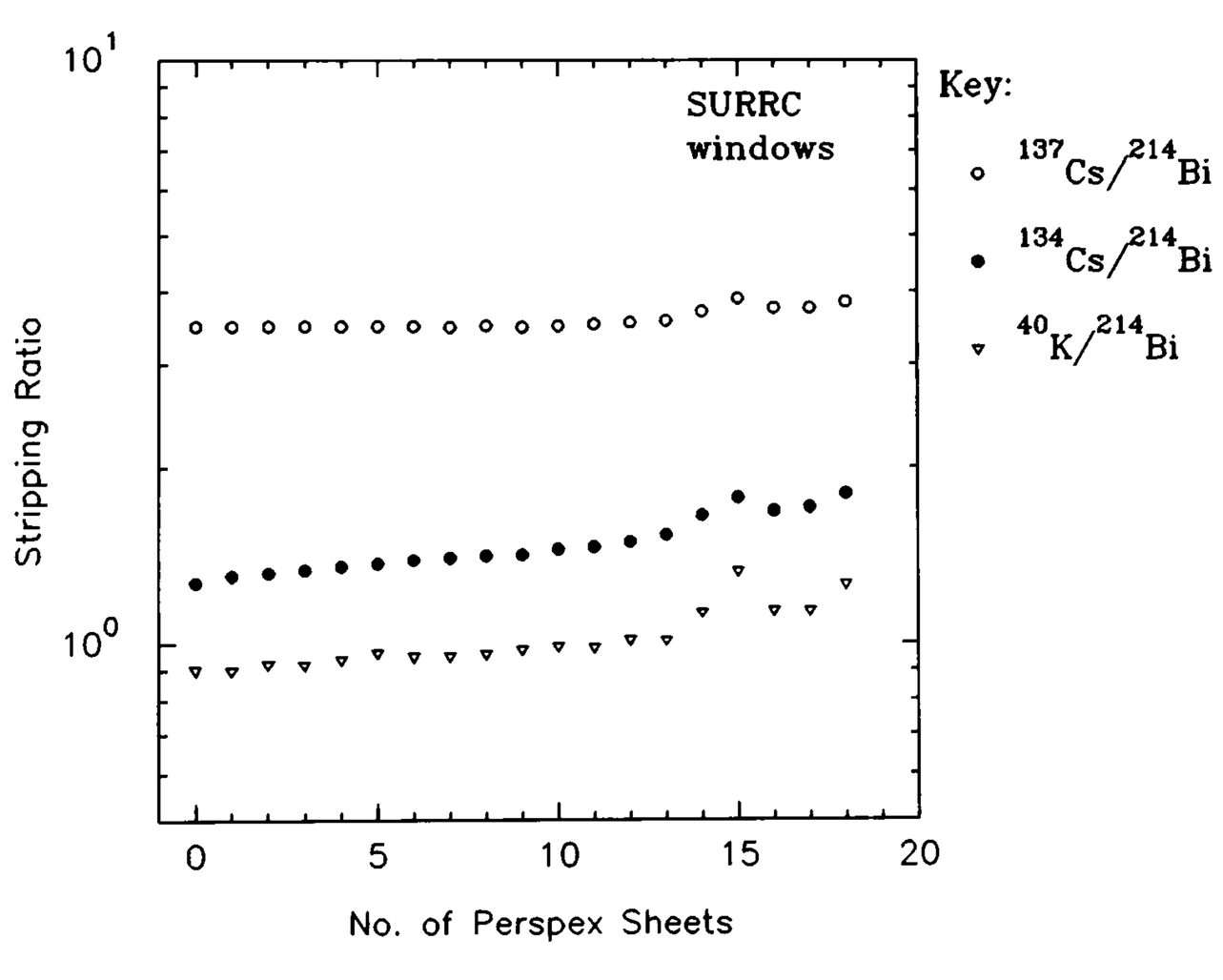

Figure 4.29 Stripping ratios of ^{214}Bi into ^{137}Cs, ^{134}Cs and ^{40}K from a ^{214}Bi calibration pad, for SURRC windows.

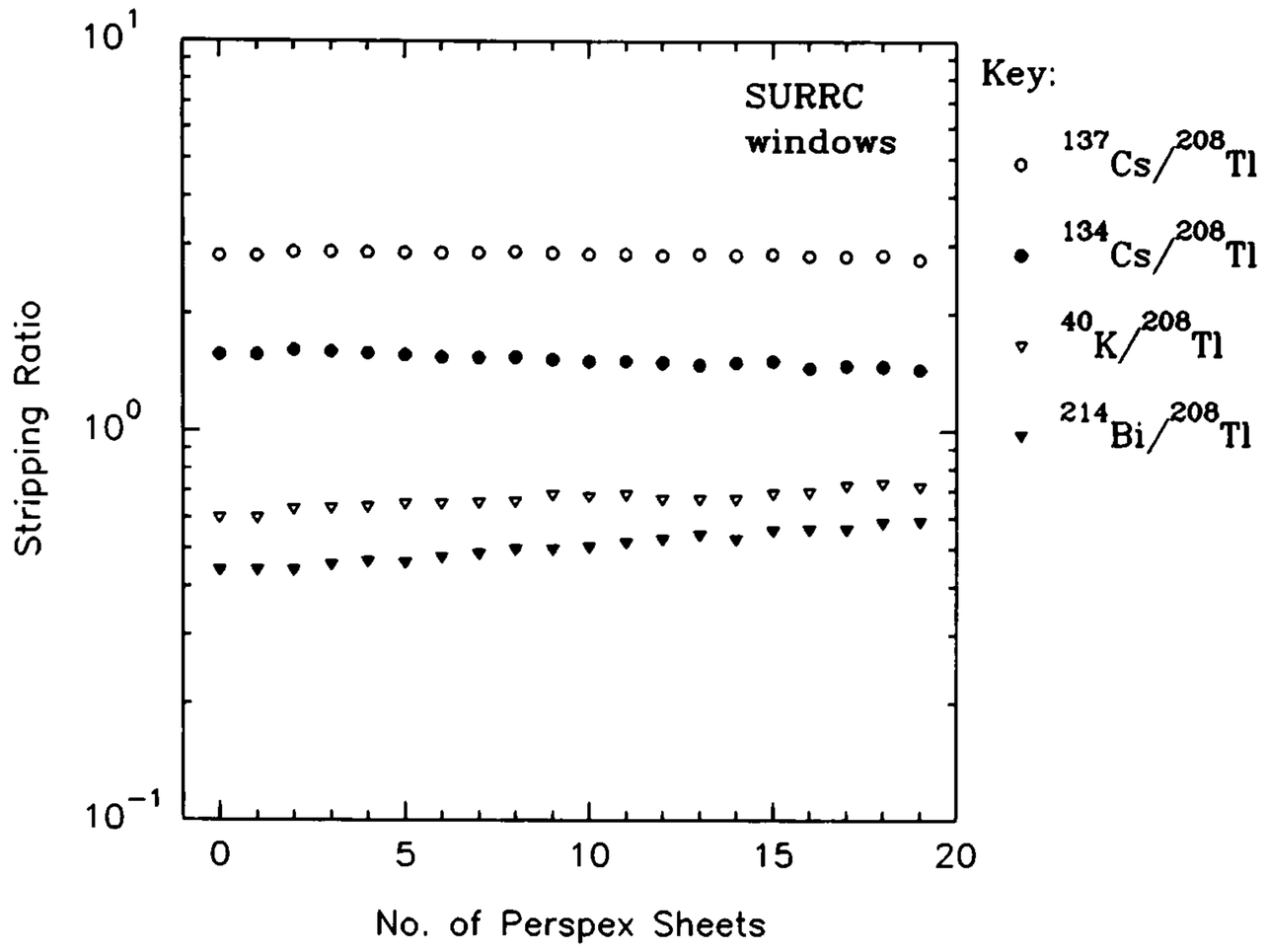

Figure 4.30 Stripping ratios of ^{208}Tl into ^{137}Cs, ^{134}Cs, ^{40}K and ^{214}Bi from a ^{208}Tl calibration pad, for SURRC windows.

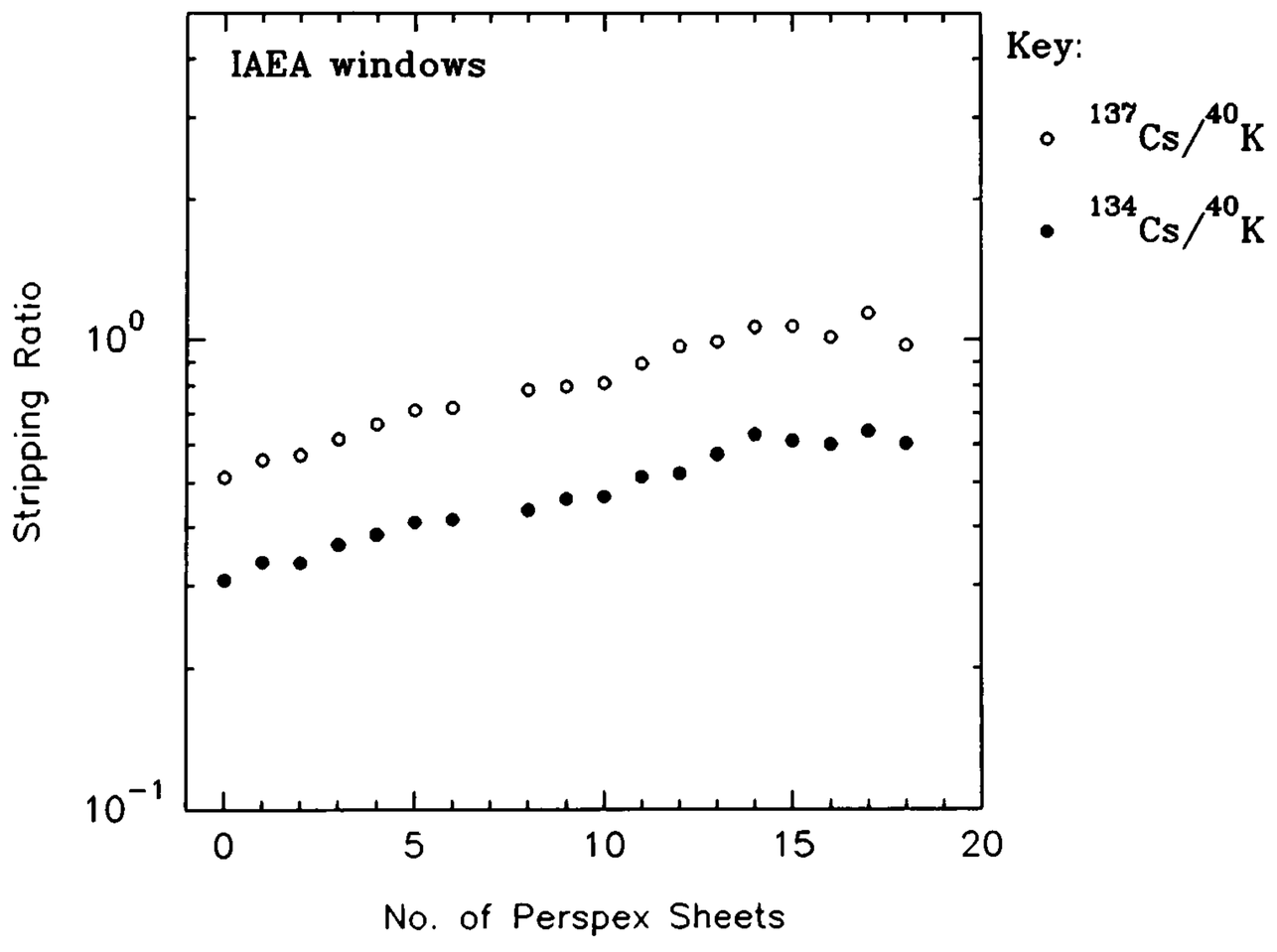

Figure 4.31 Stripping ratios of ^{40}K into ^{137}Cs and ^{134}Cs, from a ^{40}K calibration pad, for IAEA windows.

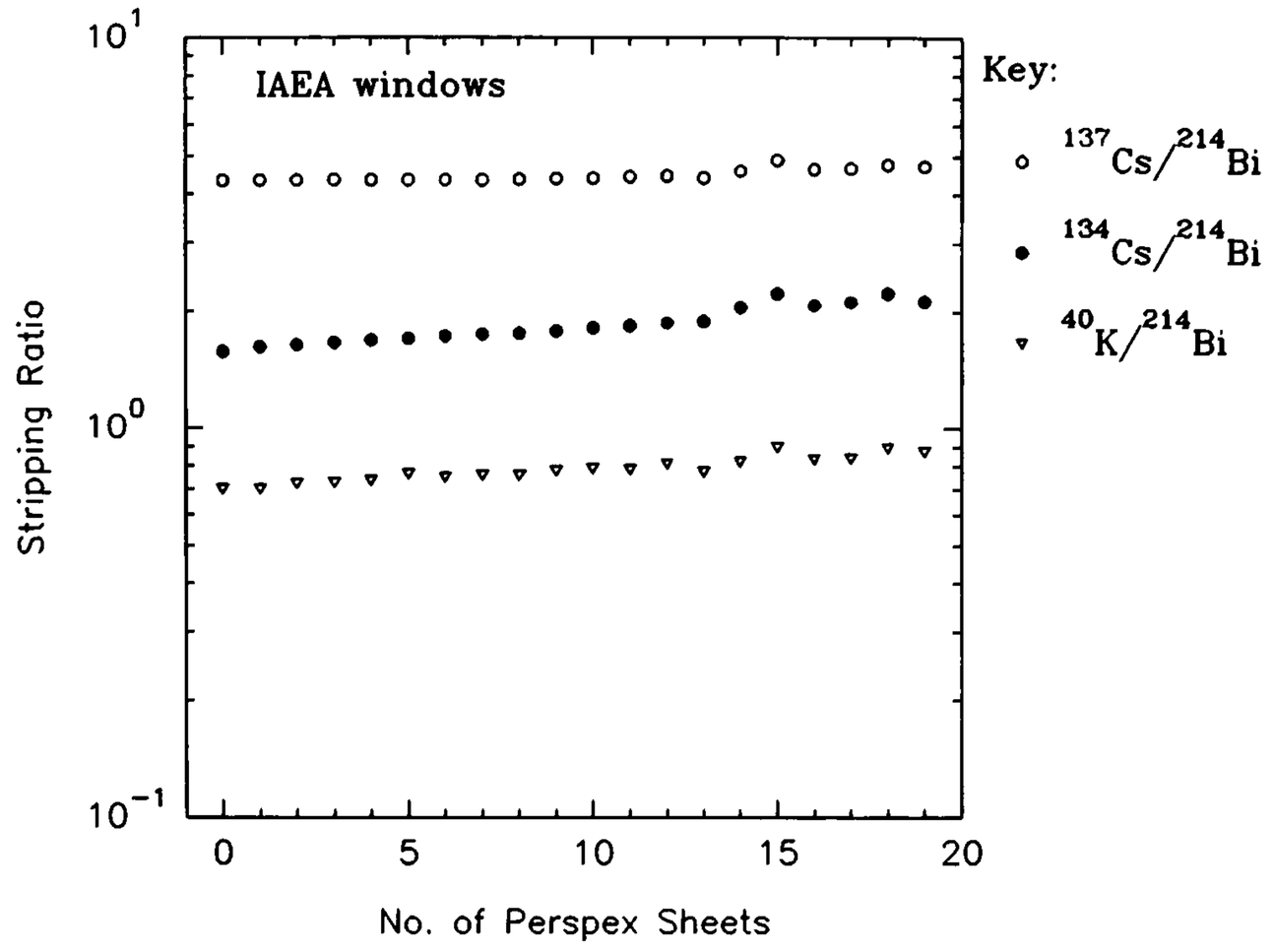

Figure 4.32 Stripping ratios of ^{214}Bi into ^{137}Cs, ^{134}Cs and ^{40}K from a ^{214}Bi calibration pad, for IAEA windows.

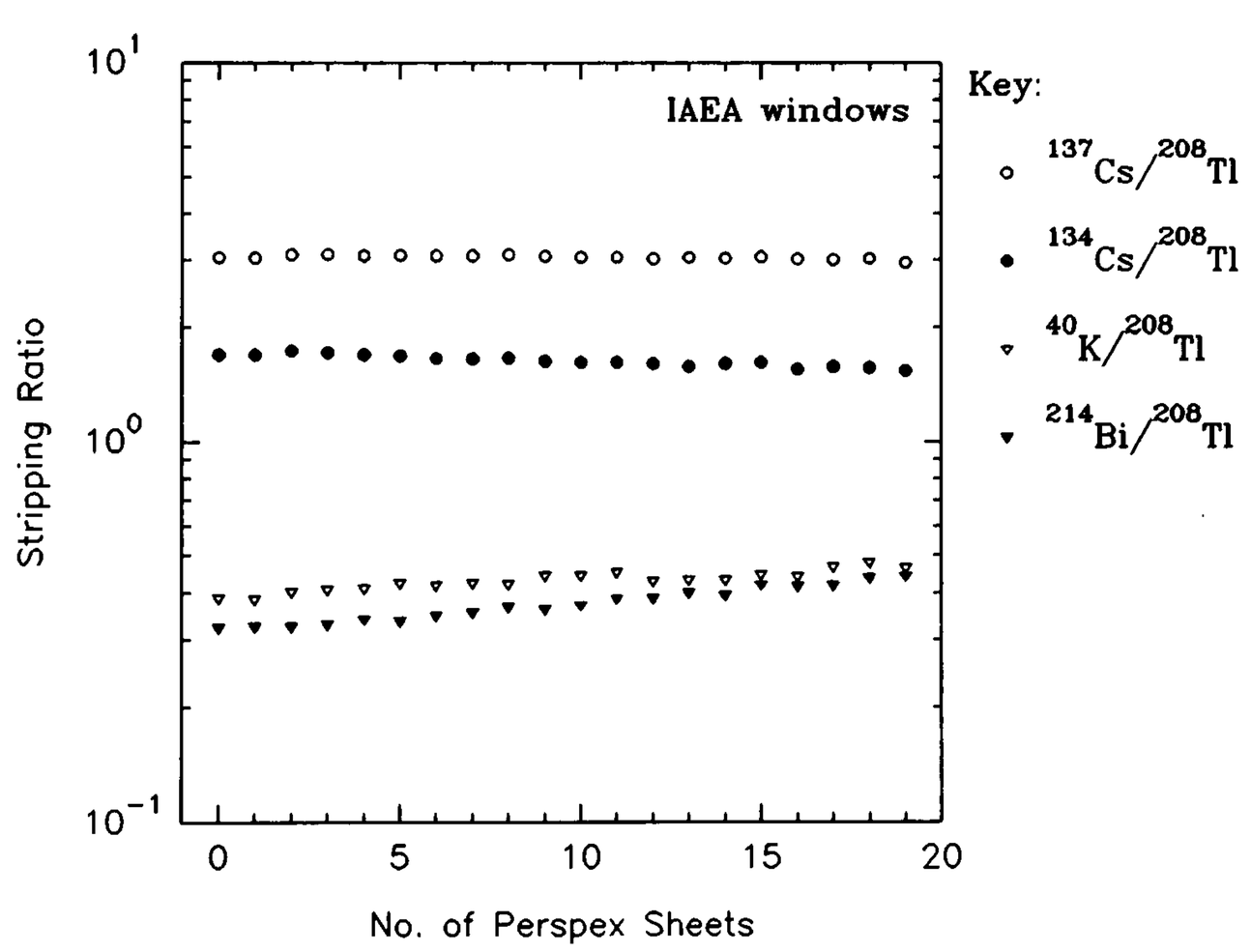

Figure 4.33 Stripping ratios of ^{208}Tl into ^{137}Cs, ^{134}Cs, ^{40}K and ^{214}Bi from a ^{208}Tl calibration pad, for IAEA windows.

Table 4.13 IAEA equivalent channel windows.

Radionuclide	IAEA Windows / channels
^{40}K	228 - 260
^{214}Bi	275 - 307
^{208}Tl	396 - 460

From Appendix B, tables B.5-B.8 (IAEA windows, table 4.13), α, ß and γ have been calculated for comparative purposes. A linear regression of stripping ratio as a function of air equivalent height z was performed on α, ß and γ. This gave

$$\alpha = 0.000596z + 0.3172 \tag{4.4}$$

$$\beta = 0.000427z + 0.3921 \tag{4.5}$$

$$\gamma = 0.000787z + 0.7110 \tag{4.6}$$

The stripping ratios given by IAEA windows are less for the natural radionuclides, but greater for the caesium radionuclides than those of SURRC, since the former sharply define the ^{40}K, ^{214}Bi and ^{208}Tl peaks. It is felt that careful monitoring of detector gain and resolution must accompany use of the IAEA windows to ensure that no counts fall outside the extremities.

From a pure source of ^{137}Cs, the stripping ratio of $^{134}Cs/^{137}Cs$ shows a gradual decrease with increasing altitude. This is expected since 662 keV γ-rays are attenuated with altitude and the mean path length through a medium is a function of γ-ray energy. From a source of ^{40}K, the stripping ratios of $^{137}Cs/^{40}K$ and $^{134}Cs/^{40}K$ show gradual increases with altitude, as the proportion of scattered γ-rays from ^{40}K correspondingly increases. There is little contribution to ^{214}Bi and ^{208}Tl windows and stripping ratios $^{214}Bi/^{40}K$ & $^{208}Tl/^{40}K$ remain constant. From a source of ^{214}Bi, the $^{137}Cs/^{214}Bi$ stripping ratio remains constant up to around 150m (equivalent) and then a perturbation occurs, which may be due to a some detector gain variations. This is also seen in the $^{134}Cs/^{214}Bi$ stripping

ratio. The constant nature of the $^{137}Cs/^{214}Bi$ is interesting because it shows that the attenuation of the full energy line at 609 keV from ^{214}Bi is compensating for the relative increase in the magnitude of scatter from higher energy lines. If one compares the $^{134}Cs/^{214}Bi$ stripping ratio a modest increase is observed owing to an increasing scatter only component.

From a source of ^{208}Tl, the contribution into the ^{137}Cs window shows little change with altitude. Again this suggests a compensating effect of 583 keV attenuation from ^{208}Tl relative to its scattered component. $^{134}Cs/^{208}Tl$ shows a modest decrease with altitude, while $^{40}K/^{208}Tl$ and $^{214}Bi/^{208}Tl$ show an expected, but only slight increase.

Table 4.14 Comparison of $\Delta\alpha$, Δß and $\Delta\gamma$.

$\Delta\alpha$	Δß	$\Delta\gamma$	Reference
0.00053 per m	0.00074 per m	0.00066 per m	Løvborg, Kirkegaard, Christiansen, 1976 (calculated)
0.00049 per m	0.00065 per m	0.00069 per m	IAEA, 1991 (calculated)
0.00112 per m	0.00205 per m	0.00184 per m	Raghuwanshi & Bhaumik, 1989 (test range)
0.00060 $\pm$0.0004 per m	0.00042 $\pm$0.00006 per m	0.00079 $\pm$0.00009 per m	Allyson IAEA windows. (pads and absorbers)

Raghuwanshi and Bhaumik (1989) have experimentally estimated the stripping ratios α, ß and γ as a function of height by a linear least squares method over a suitable test site in India and are shown in table 4.14. They used a twelve 10x10x40cm NaI(Tl) detector

array. Løvborg *et al* (1976) determined stripping ratios over a range of altitudes. A linear expression has been fitted to their results and is approximately correct over a range of 50-200m, for a 15.24x10.16cm NaI(Tl) detector. Comparisons are made with Allyson (IAEA windows). Table 4.15 shows a further comparison between experimental methods at approximately equivalent heights. Grasty (1980b) determined α, ß and γ using a box of four NaI(Tl) crystals (16 litres). The stripping ratios of Løvborg *et al* (1977) are for a 29.2x10.2cm NaI(Tl) detector, but report that the values vary little with other crystal diameters and the same thickness.

At survey altitudes of 50-250m, count rates tend to fall exponentially with increasing height. The softer, low energy incident γ-ray fluence is nearly isotropic but the angular distribution of the high energy, direct radiation becomes more forward peaked with height.

Table 4.15 Comparison of stripping ratios at approximately equal heights.

Stripping Ratio	Grasty, 1980b	Raguwanshi & Bhaumi, 1989		Løvborg, Grasty & Kirkegaard, 1977		Allyson (IAEA windows)	
	At ground level	At ground level	At 122m	At ground level	At 125m	At ground level	At 125m
α	0.26	0.34	0.47	0.37	0.43	0.32	0.39
ß	0.365	0.38	0.63	0.50	0.56	0.39	0.44
γ	0.815	0.83	1.05	0.88	0.95	0.71	0.81
	pads	test range		pads	calculated	pads	absorbers

It is noted that the results of Allyson, yield significantly smaller values of α, ß and γ for an extended height above ground level. It would seem on the basis of this, given that the detector packages are apparently comparable, the use of calibration pads and artificial air equivalent media may result in an underestimate of the scattering influences on stripping ratios.

Grasty (1980b) realised that virtually no downward scatter originating from the calibration pads was incorporated into stripping ratio estimates. This is because skyshine is a function of surface extension of the radioactive body. However, using plywood sheets as an air equivalent medium above a 16 litre (4 crystal) detector array centrally placed upon a calibration pad (of size 12.2 x 12.2 x 0.5m), he was able to show that the resulting simulated skyshine increased α, ß and γ by only 5%, 12% and 4% respectively at ground level. The lack of skyshine on calibration pads does not necessarily invalidate the calibration procedure except in areas where unusually high Th/U and U/K ratios are found (Grasty, 1980b). As the detector height is increased, skyshine as a proportion of total fluence rate tends to decrease owing to attenuation of the ground based activity. The skyshine contribution to the total count rate of a 30.38x10.16cm NaI(Tl) detector at 150m height is about 25% for a discriminator setting of 100 keV: at a threshold of 400 keV it is only 4% (Løvborg *et al*, 1976).

Dickson *et al* (1981) and Grasty (1982, 1985) were able to analyse experimentally derived height equivalent spectra (between 0-112m), using *principal component analysis*. This is a mathematical method of reducing a spectral measurement into independent components of which the first two (primary and secondary) are the most important. The proportions of each component are given by an amplitude that varies exponentially with height. By this means a complete spectrum can be reproduced at any intermediate height.

We may conclude that significant variation can occur between stripping ratios measured at ground level and those at standard survey height (100m), particularly due to ^{40}K scattering into ^{137}Cs and ^{134}Cs windows. Only small variations are seen into these windows from ^{214}Bi and ^{208}Tl. We shall see later, given real aerial survey data, it is advisable that stripping ratios for a given survey height are employed.

4.7 Chapter Summary

We have seen how ground based 7.62x7.62 cm NaI(Tl) and 16 litre aerial survey detectors behave when their respective stripping ratios are determined from different types of sources. All volume sources produce considerably more scattering with respect to their full energy peaks than small or point sources. For aerial survey detectors, there is a variation with altitude which for some radionuclides and energy windows can be significant, having both positive and negative dependency. This may not have been realised previously. This work has also shown for the first time that stripping ratios of airborne detectors to be quite robust for variations in resolution and gain shifts, over a workable range of 8.5-13% and $\pm$1% respectively.

5. Detector Sensitivities and Calibrations using Numerical Methods

This chapter will extend existing work and present **new** findings by incorporating detector angular responses, calculated by the Monte Carlo methods found in chapter 6. The effects on fields of view and terrain geometry will be described. The conversion of fluence rates to count rates (per unit radionuclide deposition) by the calibration factors shown, are of particular use in the planning of aerial surveys, interpretation of results and ground to air comparisons. Calibrations derived wholly theoretically are compared with those measured from field sampling and laboratory anaylsis.

5.1 Introduction

Remote sensing of terrestrial radioactivity and correct interpretation of the measurement is dependent upon a certain amount of prior knowledge being available or assumptions being taken. A ground sampling survey, although limited in time and resources, remains essential in this to minimise ambiguity that may result as follows:

a). lateral extent of activity deposition (non-uniformity);

b). vertical depth profile of activity;

c). prevalent air and ground conditions (soil density, snow cover, flooding).

Even so, a representative sample may be very difficult to acquire. In-situ gamma-ray spectroscopy has the advantage of interrogating a large volume of dispersed activity. However, anomalously high levels and discrete zones of activity within the field of view may not contribute significantly to the total signal if these are far from the detector. The collimation of ground based detectors can force the field of view to be limited to that directly beneath the detector (high sampling resolution), at the cost of good representative sample size.

Gamma-ray attenuation is almost entirely due to interactions with atomic electrons, hence is dependent upon atomic number or average atomic number of the constituent materials acting as a shielding medium and gamma-ray energy. It has become accepted

practice to use a standard soil composition, introduced by Beck (Beck *et al*, 1972). For energies greater than 100 keV, there is little change in mass attenuation coefficients for a wide range of soil types and the Beck standard is adequate for many applications (see section 5.3.5.4). Recently however, there has been interest in developing direct methods of estimating vertical profile characteristics of deposited activity. Some of these use x-ray lines and therefore knowledge of soil composition is necessary because of enhanced attenuation at energies less than 100 keV.

Scintillation NaI(Tl) detectors continue to be used in many environmental investigations, due to inherent efficiency, cost and ruggedness, despite often complex deconvolution techniques that are used to analyse multi gamma-ray energy fields. Portable semi-conductor detectors of relatively high efficiency (eg. 50%) offer unequivocal advantages due to their high resolving powers. The use of these in aerial survey applications remains a developing area.

In order to convert calculable fluence rates to counting rates, it is necessary to know the detection cross-section at a given energy and the detector angular response. These requirements are particulary important for detectors having asymmetrical geometries.

The field of view or *circle of investigation* is a circular area centred at the point directly beneath the detector from within which a specified fraction of the total gamma-ray intensity originates.

In sampling an increasingly large concentric area surrounding the detector, a radius is reached where no further practical increase in intensity is achieved. It is only in the special case of a flat, homogeneous infinite source that the field of view concept has a precise meaning.Increasing the height of the detector above ground level will

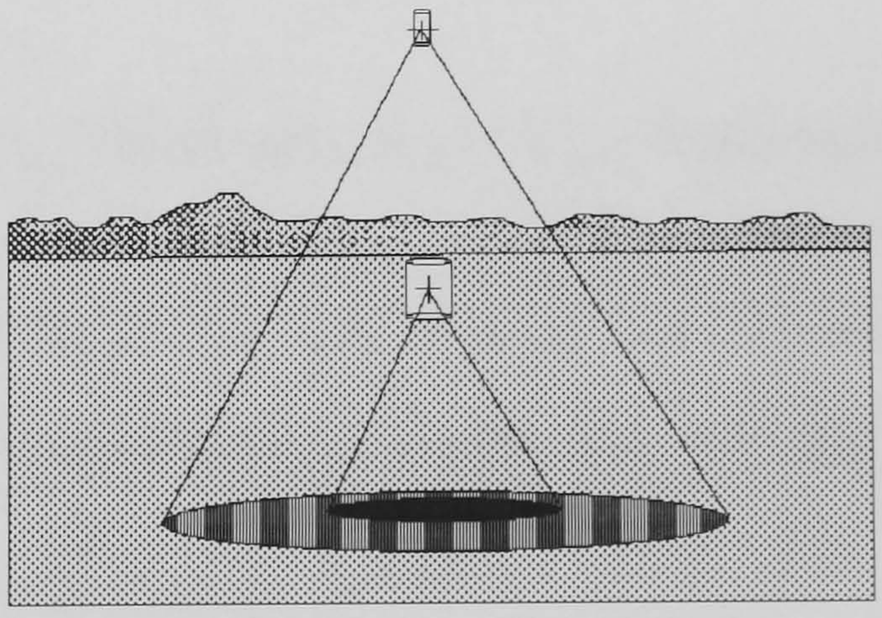

Figure 5.1 Field of View at different altitudes.

correspondingly increase the radius of the field of view, at the expense of signal intensity (figure 5.1).

The theoretical treatment of the photopeak detection takes account of ground activity and distribution throughout a soil matrix of known composition, decay branching ratio, soil and air densities, angular detector full photopeak counting cross-section, height of detector and any topographical effects.

5.2 Theory

The fraction of the unscattered photon yield is the ratio of fluence-rate F ($\gamma\ s^{-1}\ m^{-2}$) measured at a point in space, emanating from within a circular area of radius R (centred at that point) to the maximum fluence-rate attainable. For surface activity, the maximum fluence-rate is governed by the attenuating properties of the air path at very large radii or pathlengths. For activity beneath the surface, attenuation within the ground layers is additionally considered. The field of view is by definition then

$$COI = \frac{F_R}{F_\infty} \tag{5.1}$$

An equation to calculate F is given by (Beck *et al*, 1972):

$$F = \int_0^{2\pi} \int_0^{\frac{\pi}{2}} \int_{\frac{h}{\cos\theta}}^{\infty} \frac{A_v e^{-\alpha z} De_{100}}{4\pi P_{tot}^2} P_{tot}^2 \sin\theta\ e^{-\mu_{l\,air} P_{air}} e^{-\mu_{l\,soil} P_{soil}} dP\, d\theta\, d\phi \tag{5.2}$$

where, P_{tot}=Total gamma-ray pathlength; P_{air}=Pathlength in air; P_{soil}=Pathlength in soil; $\mu_{l\ air}$=linear attenuation coefficient in air; $\mu_{l\ soil}$=linear attenuation coefficient in soil; z=vertical depth from surface; A_v=Activity per unit volume; α=exponential source distribution constant; De_{100}=no. of gamma-rays emitted per 100 decays; h=detector height above ground.

Equation 5.2 is in spherical coordinates and may be solved by using analytical and numerical methods. The coordinate system is shown in figure 5.2.

There are three forms of this general equation.

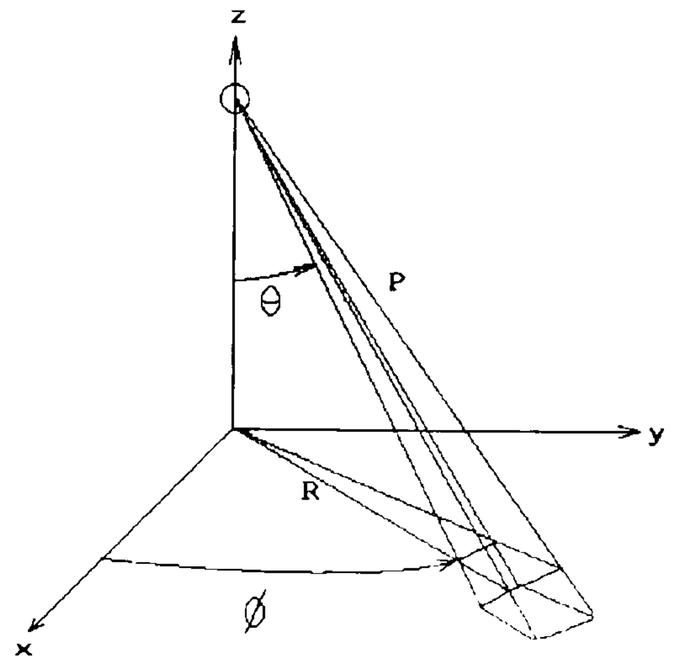

Figure 5.2 Co-ordinates of field of view calculations.

a). For activity that is distributed homogeneously across a plane surface (other geometries are considered in section 5.3.6), equation 5.2 can be re-written:

$$F = \int_0^{\frac{\pi}{2}} \frac{A_a De_{100}}{2\cos\theta} e^{-\mu_{1\ air}\frac{h}{\cos\theta}} \sin\theta\ d\theta \qquad (5.3)$$

where, A_a=unit Bq m^{-2}.

b). For activity that is uniformly dispersed laterally and with depth (as is the usual case for the natural radionuclides), equation 5.2 becomes (and A_m=unit Bq kg^{-1}):

$$F = \int_0^{\frac{\pi}{2}} \frac{A_m \rho_{soil} De_{100}}{2\mu_{l\ soil}} e^{-\mu_{1\ air}\frac{h}{\cos\theta}} \sin\theta\ d\theta \qquad (5.4)$$

c). For activity that is uniformly dispersed laterally, but is vertically distributed (usually assumed exponentially) into a depth dimension between z and z+dz, equation 5.2 becomes:

$$F = \int_0^{\frac{\pi}{2}} \frac{A_a De_{100}\alpha}{2\rho_{soil}} \left[\frac{1}{\left(\frac{\alpha}{\rho_{soil}}\right)\cos\theta + \left(\frac{\mu_{l\ soil}}{\rho_{soil}}\right)}\right] e^{-\mu_{1\ air}\frac{h}{\cos\theta}} \sin\theta\ d\theta \qquad (5.5)$$

This may be represented by a superposition of plane sources.

The count rate expected from a detector is the integration of the detection cross section, $\sigma_{det,\theta,\phi}$, with equations 5.2-5.5, over the polar θ and azimuthal ϕ angles. The angular response of a detector must also be considered and is discussed in section 5.3.1.

5.3 Results and Discussion

Six radionuclides have been considered here and are listed in table 5.1. The composition of Beck soil is shown in table 5.2. The total mass attenuation coefficients (without Rayleigh scattering) are shown in table 5.3. Air density is taken to be at U.S. Standard Atmosphere (1976) conditions at sea level (pressure: 1.01325×10^5 Pa; density: 1.225 kg m^{-3}; temperature: 288.15 °K).

Note. The ICAO standard (1964), *International Civil Aviation Organization*, is identical with the U.S. Standard Atmosphere (1976) from the surface to 32 km altitude.

Table 5.1 Radionuclides of interest: Browne & Firestone (1986).

Radionuclide	**Energy / keV**	**Half-life**	**No. of γ-rays emitted per 100 decays**
^{131}I	364.483	8.04d	81.2
^{137}Cs	661.66	30.2a	85.21
^{134}Cs	795.9	2.062a	85.4
^{40}K	1460.83	1.227×10^9a	10.67
^{214}Bi	1764.49	19.94m	15.9
^{208}Tl	2614.35	3.053m	99.79

An exact knowledge of soil composition is generally not critical in the evaluation of fluence rates, since mass attenuation coefficients of typical soils remain relatively constant for energies above 100 keV. For detailed analysis below 100 keV, soils

Table 5.2 Beck soil composition: Beck *et al* (1972).

Composition	% by weight
Al_2O_3	13.5
Fe_2O_3	4.5
SiO_2	67.5
CO_2	4.5
H_2O	10.0

containing uranium and thorium may be in sufficient concentrations that enhanced attenuation occurs, owing to the photoelectric effect (the presence of absorption edges). This is described in more detail in chapter 6.

Table 5.3 Mass attenuation coefficients: calculated from Storm & Israel (1970).

Energy / keV	$\mu_{\text{Beck soil}}$ / $cm^2\ g^{-1}$	μ_{air} / $cm^2\ g^{-1}$
364.483	0.10101	0.09975
661.66	0.07759	0.07695
795.9	0.07105	0.07049
1460.83	0.05224	0.05173
1764.49	0.04755	0.04693
2614.35	0.03925	0.03837

5.3.1 Detector Cross-section and Angular Response

Duval *et al* (1971) considered the field of view of a spherical airborne γ-ray spectrometer but for detectors other than spherical in geometry, the angular detection response must be accounted for. Right cylindrical detectors of equal height and diameter are approximately spherical. In practice, there are often additional geometrical complexities owing to the presence of photo-multiplier tubes and pre-amplifiers. However, since detectors normally used in environmental counting are with the front face pointing downwards, the attenuating properties of peripheral instrumentation is

regarded as unimportant to the evaluation of the primary unscattered component. Scattering effects from the rear of the crystal may generate back-scattered peaks in the secondary component.

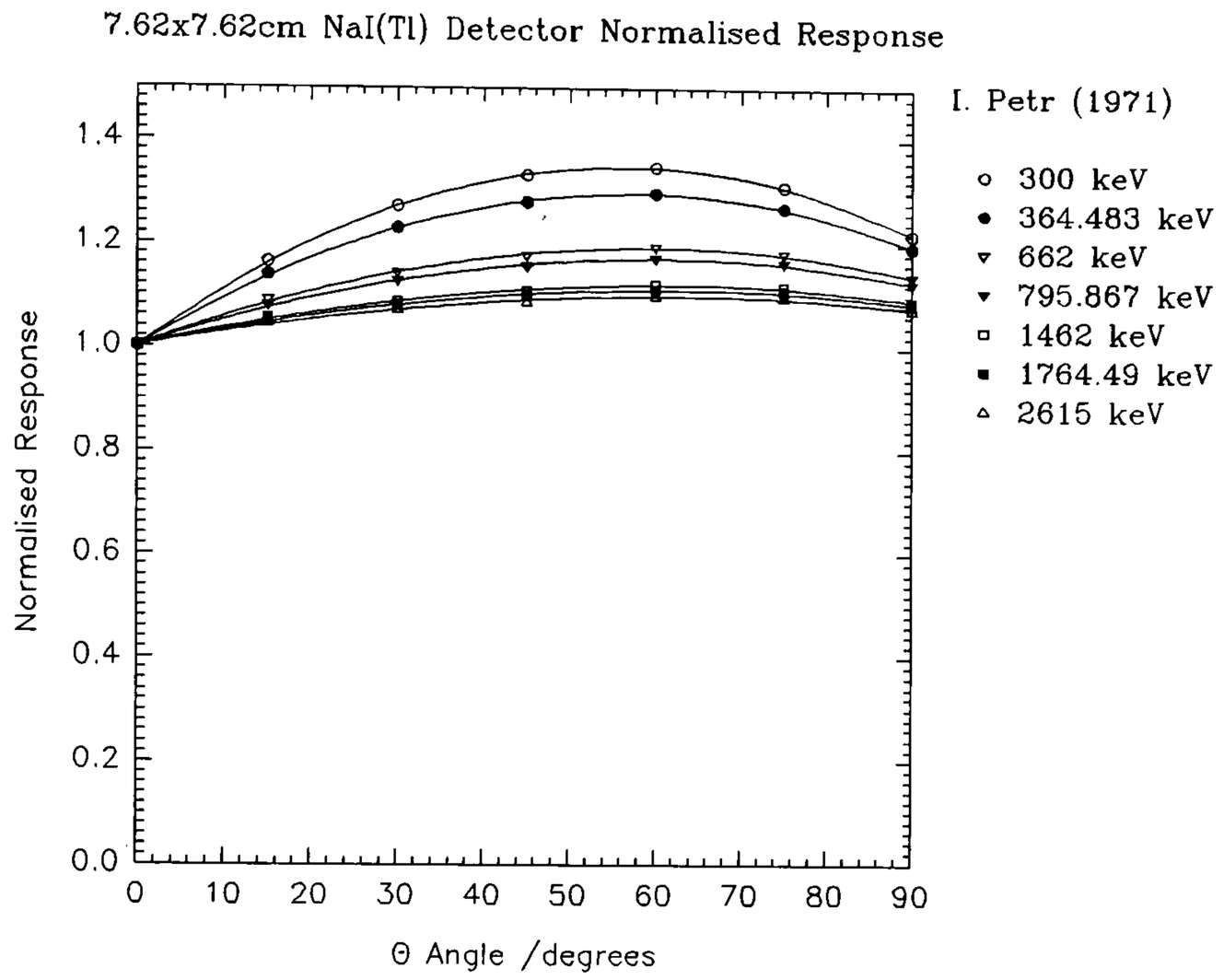

Figure 5.3

The mathematical treatment of angular response of right cylindrical detectors has been carried out analytically by Petr *et al* (1971). Their algorithm has been implemented for a 7.62x7.62 cm NaI(Tl) scintillation detector and some γ-ray energies of primary interest (figure 5.3). A comparison with Monte Carlo based estimates of angular response is made in chapter 6. Here the response has been normalised to $\theta=0°$: θ is the angle of incidence of parallel gamma-rays to the front face of the crystal.

For more complex shapes, Monte Carlo techniques offer many advantages and have been used to determine the angular response of rectangular (prismatic) scintillation detectors to parallel beams of gamma-rays (figure 5.4). θ is the polar angle and angle of incidence to the underside of the rectangular detector. ϕ is the azimuthal angle with respect to one side. The response varies only slightly with ϕ from 0-90° (see 6.5.1.3) and a mean response for all these angles is demonstrated.

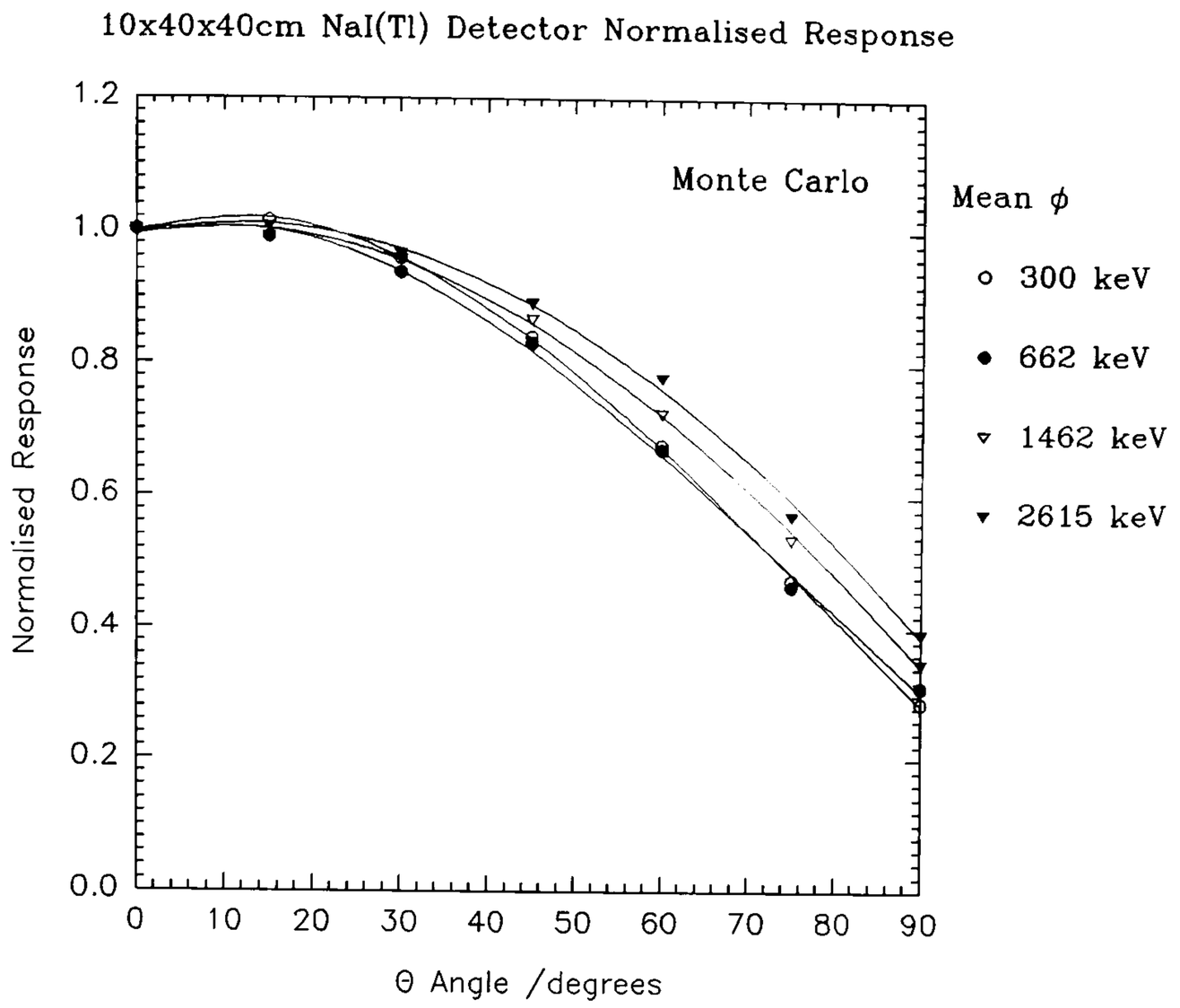

Figure 5.4

The detection cross section ($\sigma_{det,\theta,\phi}$) is the product of the normalised angular response and the detection cross section at $\theta=0°$ ($\sigma_{det,0,\phi}$). $\sigma_{det,0,\phi}$ is thus equal to the geometrical cross section multiplied by ($1-e^{-\mu x}$), which is the total intrinsic efficiency ($\varepsilon_{int,tot}$) for a parallel beam of γ-rays (see chapter 2.8.1). In order to convert the total energy deposition to photopeak or full energy deposition, then values of photofraction (R) for the detector in question need to be evaluated. Again, Monte Carlo methods have been used for this (table 5.4). Arrays built up from adjacent blocks of individual detectors were assumed to behave in the same way as a single detector. However, there is some evidence that an overestimate of photofraction occurs due to the neglect of losses in the canning materials between modular detector systems. For a 10x40x40cm detector array, the calculated values are also somewhat higher then measured since this was performed on a *bare* detector and enclosing packages come in a variety of different types and materials. The difference between measured and calculated photofractions is approximately 12%. Photofraction shows some angular independence (chapter 6). Grasty *et al* (1979) used an angular sensitivity factor of the form

$$S = K\,(1 + a\cos\theta) \tag{5.6}$$

The constants a & K are detector dependent, and valid for right cylindrical detectors.

Table 5.4 Detection cross sections at $\theta=0°$.

Energy / keV	$\sigma_{det,0,\phi}$ / m^2	Photofraction R (Allyson, Monte Carlo)
7.62 x 7.62cm NaI(Tl) Scintillation Detector:		
364.48	0.004446	0.765
661.66	0.004035	0.549
795.9	0.003879	0.481
1460.83	0.003335	0.324
1764.49	0.003199	0.310
2614.35	0.003000	0.219
10.16 x 40.64 x 40.64cm NaI(Tl) Array:		
364.48	0.1639	0.893
661.66	0.1558	0.789
795.9	0.1520	0.752
1460.83	0.1365	0.619
1764.49	0.1322	0.578
2614.35	0.1256	0.449

Results shown for the 7.62x7.62 cm NaI(Tl) detector shown in table 5.4 bear good agreement with Schaarschimidt and Keller (1969).

5.3.2 Field of View and Detector Angular Response

The field of view of a spherical detector is shown in figure 5.5, at 100m height and uniform activity with depth through a soil of density 1.6g cm^{-3}. Higher energy gamma-rays penetrate further and therefore the field of view is correspondingly greater. At 100m height the field of view is a circular diameter that varies between 460-520m, for the natural emitters. This is narrowed to 390-440m for a NaI(Tl) array (figure 5.6) owing to the detector being more *downward looking*. Figure 5.7 indicates a field of view of diameter 25m, for a 7.62x7.62 cm NaI(Tl) at 1m height, for the natural

radionuclides. For anthropogenic radionuclides deposited as a surface layer (as would occur after a recent release, for example), the fields of view for ^{131}I, ^{137}Cs and ^{134}Cs at aerial survey heights are shown in figures 5.8, 5.9 and 5.10 respectively.

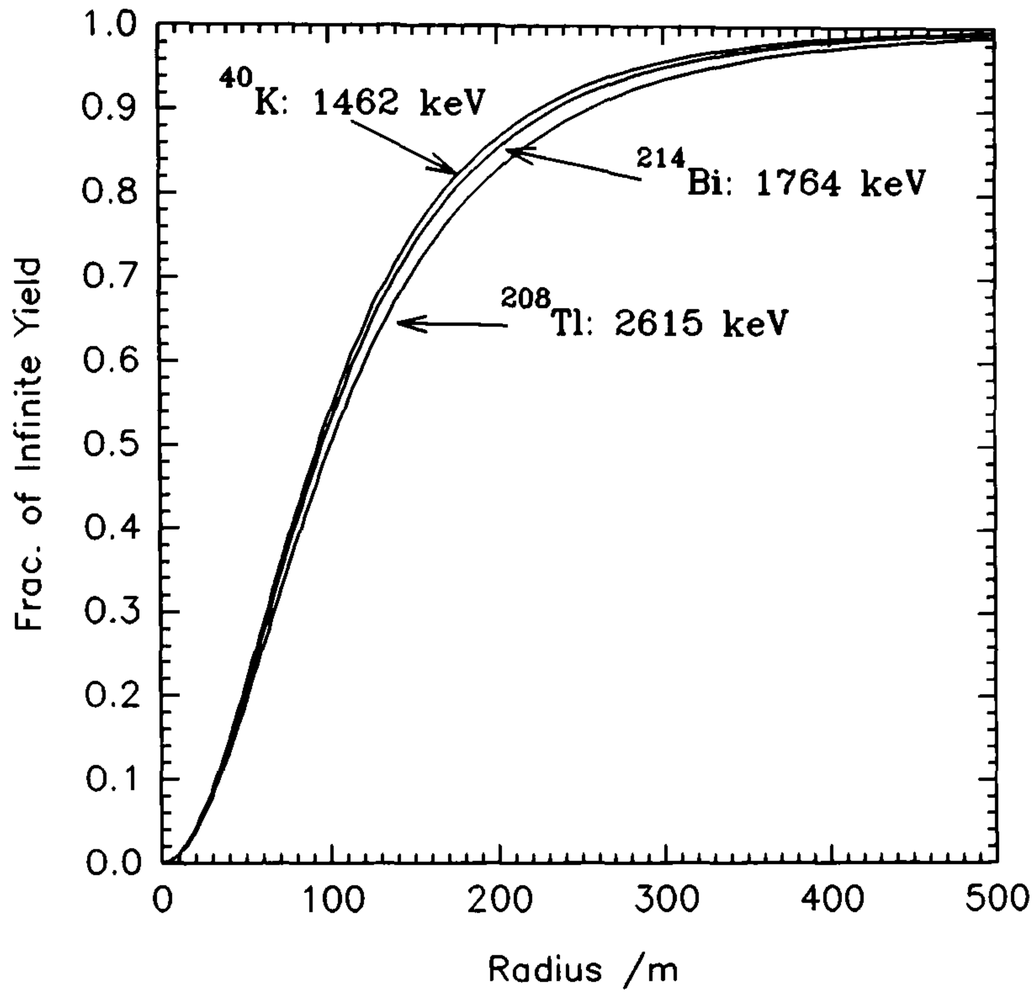

Figure 5.5

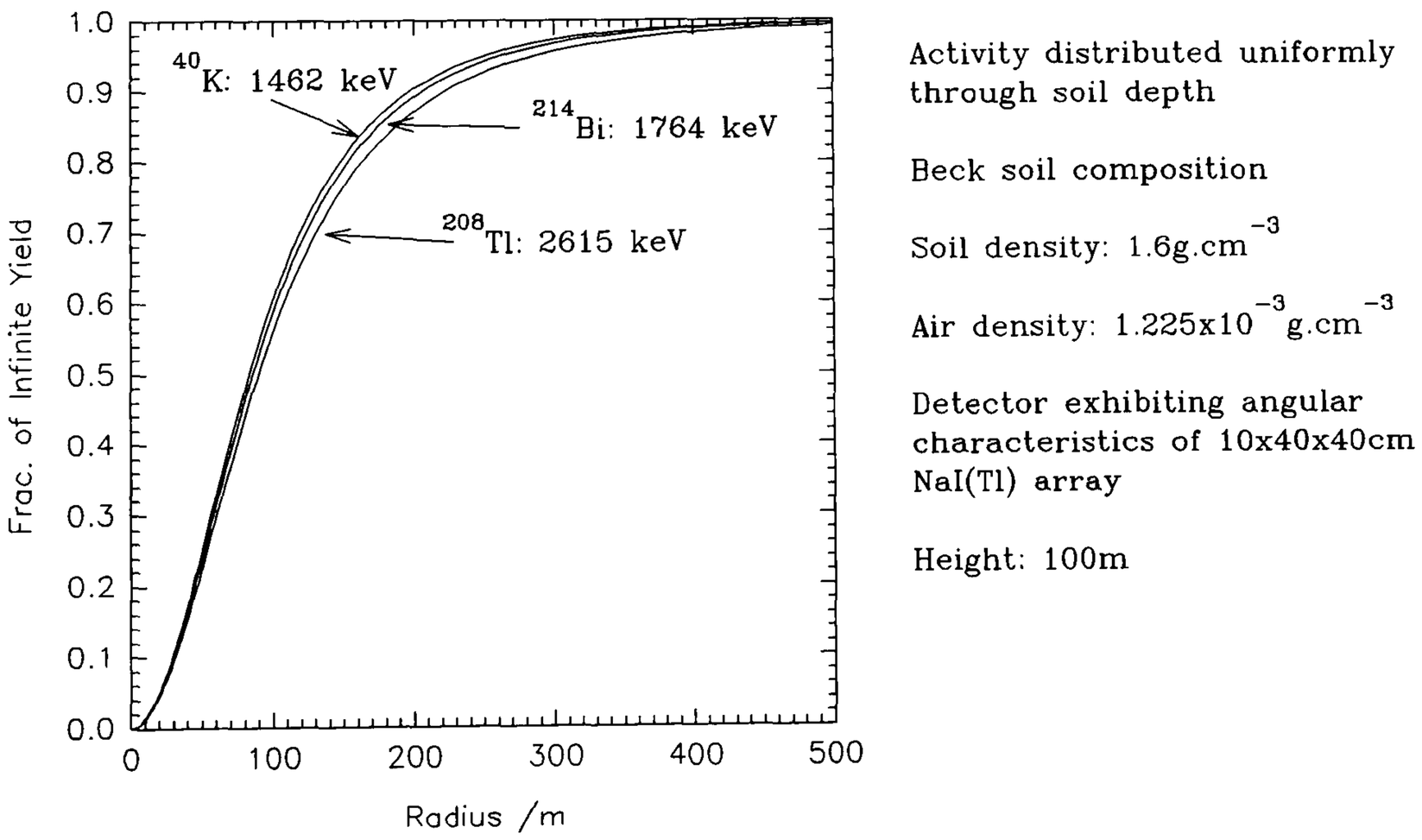

Figure 5.6

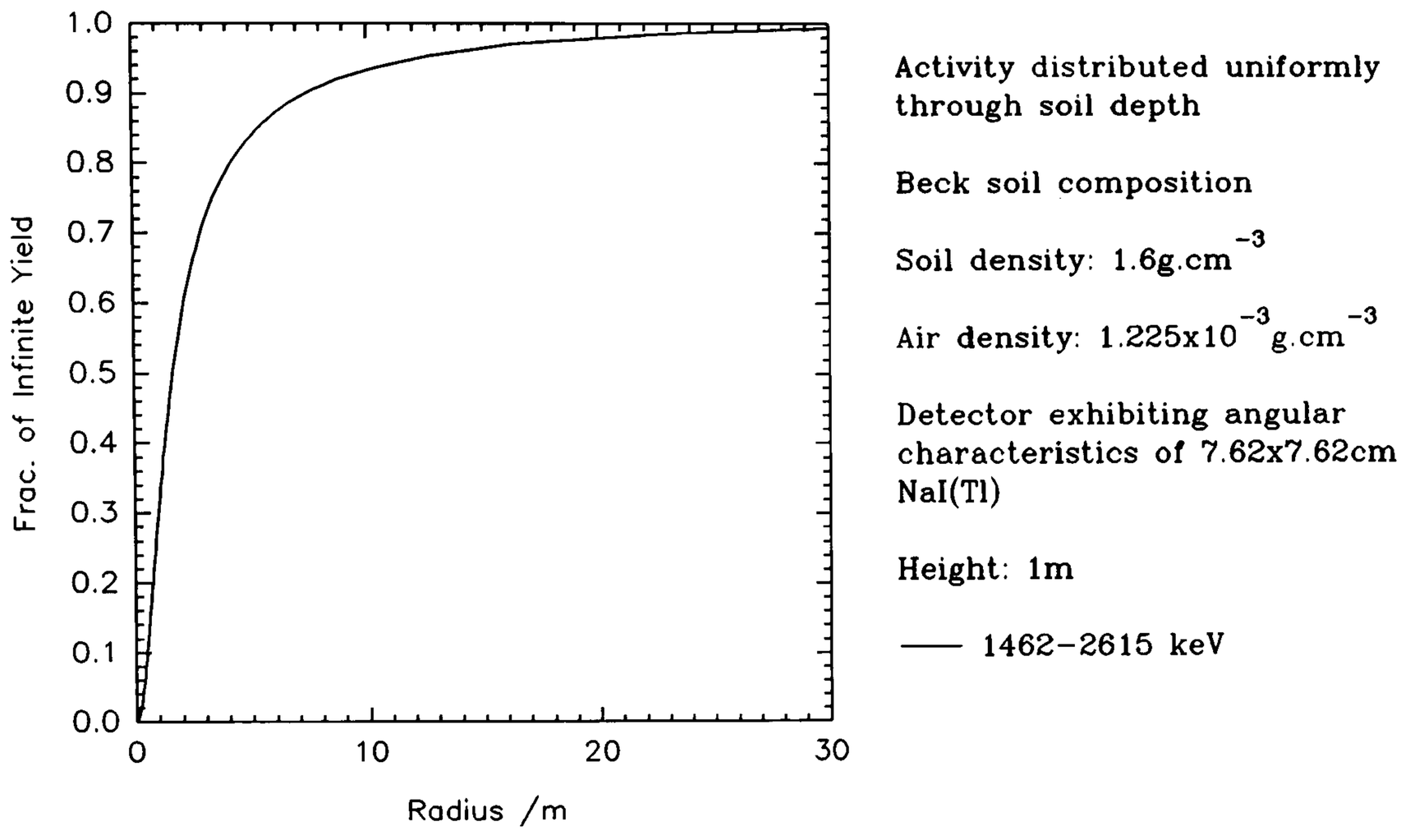

Figure 5.7

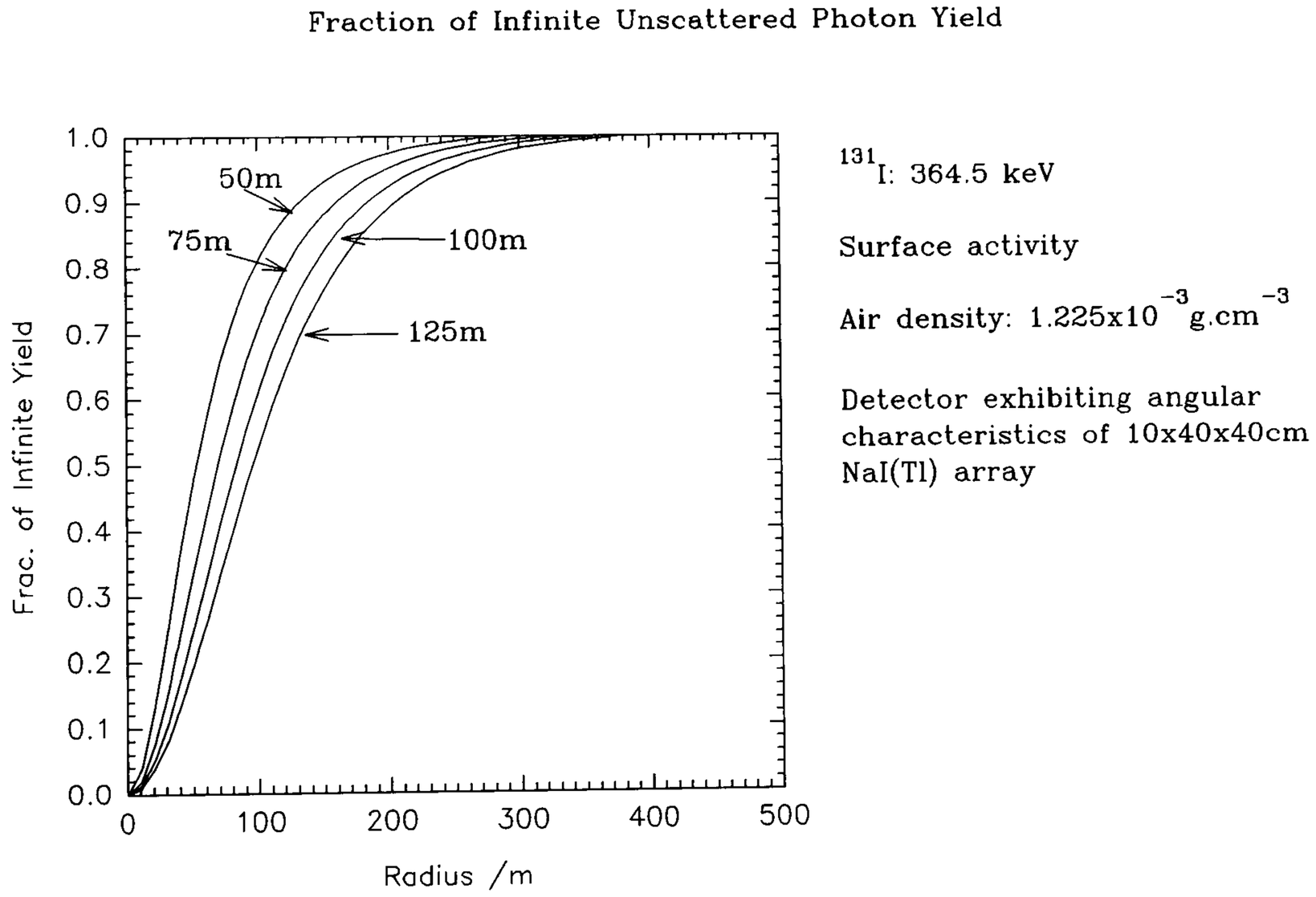

Figure 5.8

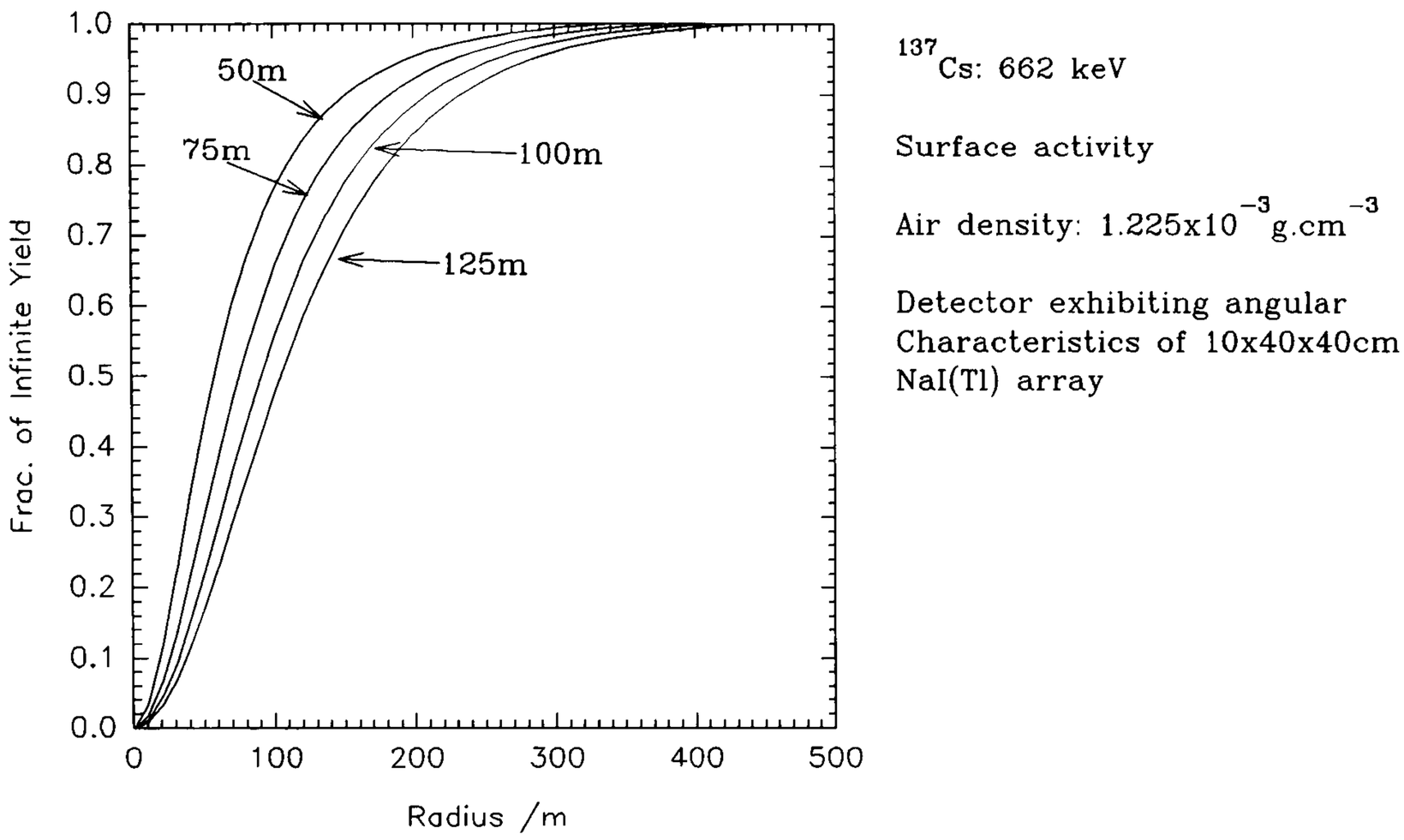

^{137}Cs: 662 keV

Surface activity

Air density: 1.225×10^{-3} g.cm^{-3}

Detector exhibiting angular Characteristics of 10x40x40cm NaI(Tl) array

Figure 5.9

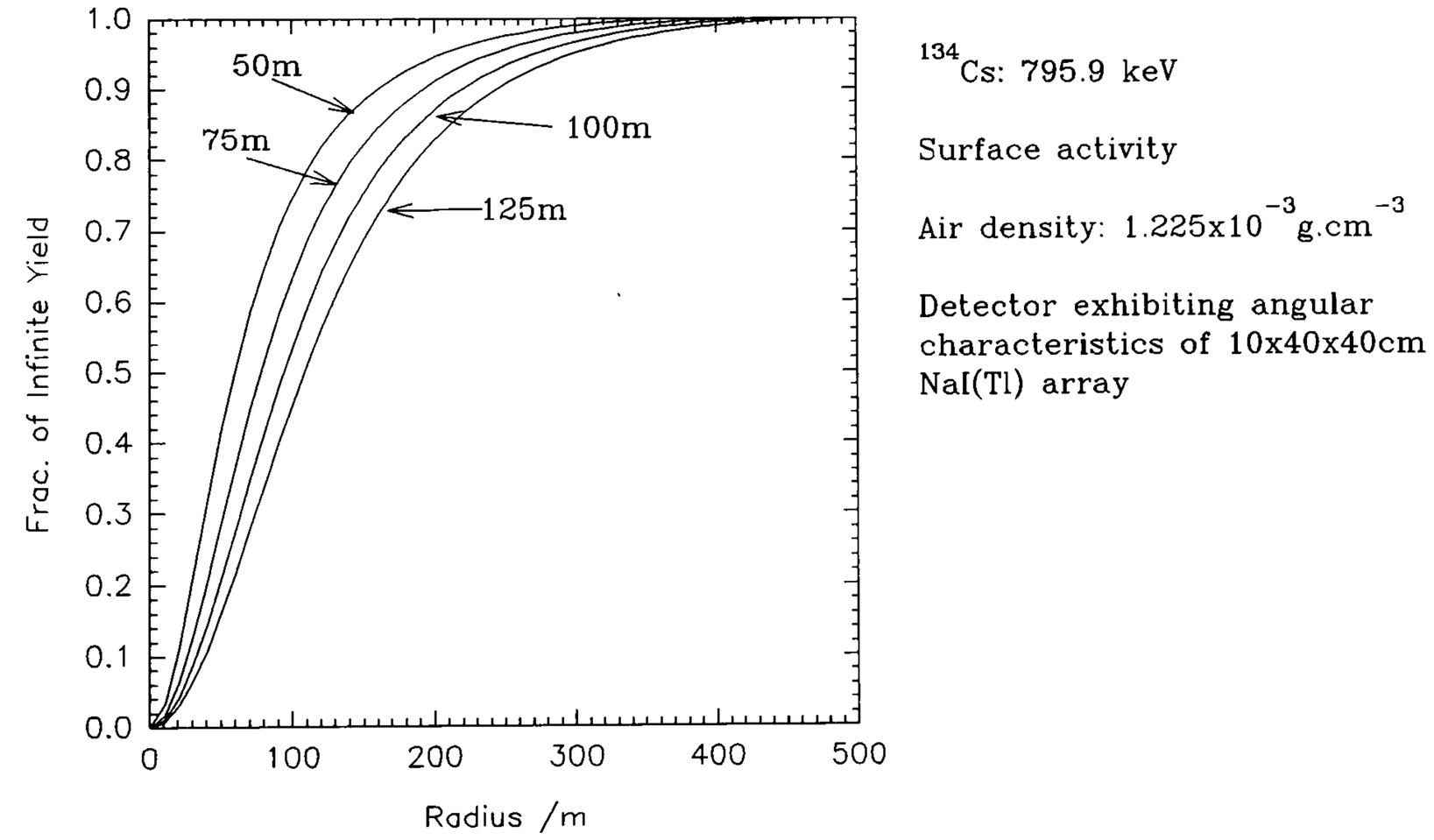

^{134}Cs: 795.9 keV

Surface activity

Air density: 1.225×10^{-3} g.cm^{-3}

Detector exhibiting angular characteristics of 10x40x40cm NaI(Tl) array

Figure 5.10

5.3.3 Radionuclide Vertical Depth Distribution Profile

External irradiation to man from deposited radionuclides as a result of nuclear processing or reactor accidents can be a significant contributor to total exposure. The deposition does not necessarily remain static in the environment and may be transported within its physical half-life. The migration of activity is a complex subject involving the radionuclide chemistry, soil characteristics, time and weathering. Dry deposition may result in most of the activity being deposited on vegetation. Wet deposition may migrate quickly through subsurface layers with attenuation of its emitted radiation. Deeper penetration into the soil column will decrease the resuspension of radioactive material in air, and potentially increase availabilities for plant root uptake.

The relaxation mass per unit area, ß, (g cm^{-2}) is commonly used as a parameter to describe the properties of radionuclide distribution with depth, assuming the profile has an exponential nature.

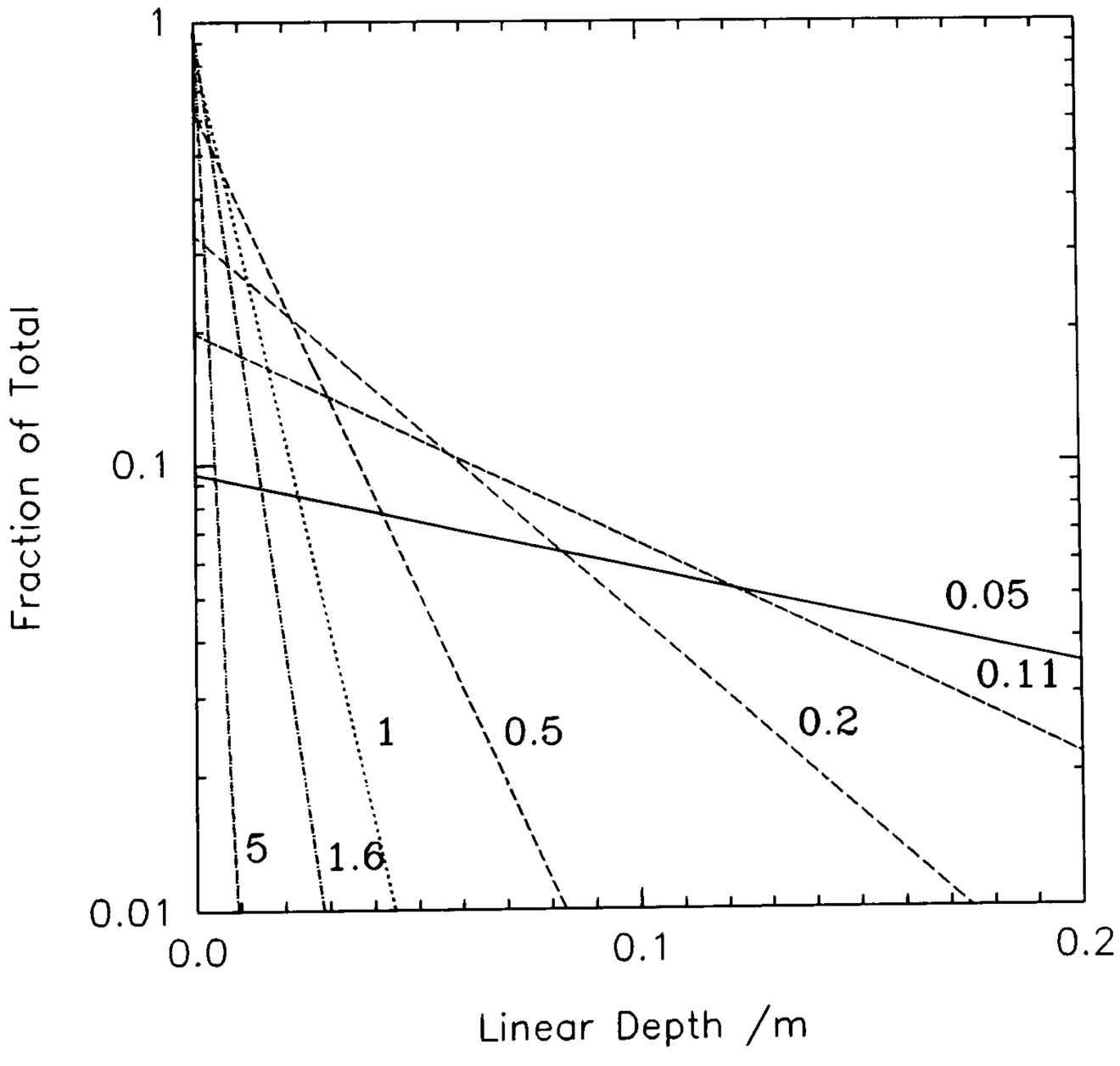

Figure 5.11 Exponential activity profiles as a function of depth, for different values of depth distribution constant, α (per cm).

There is some evidence, particularly in active inter-tidal zones, that a modification, for example to a double-exponential form may be more appropriate to describe a subsurface maximum distribution. Even in landward soils, fissures allow contaminated rainfall to reach deeper levels and distort the profile assumption. Only simple single exponential forms will be considered here. This is discussed further in section 5.3.5.4.

Beck describes the inverse of relaxation mass per unit area as being the parameter α/ρ, where α is a depth distribution constant and is applied to soils of different densities. α is the reciprocal of the relaxation length (mean length), of activity exponentially distributed with depth (figure 5.11).

For radionuclides that exhibit a vertical profile, the field of view is modified: the largest field of view is seen for activity deposited at the surface; the least for that activity driven deeper into the soil matrix (figure 5.12).

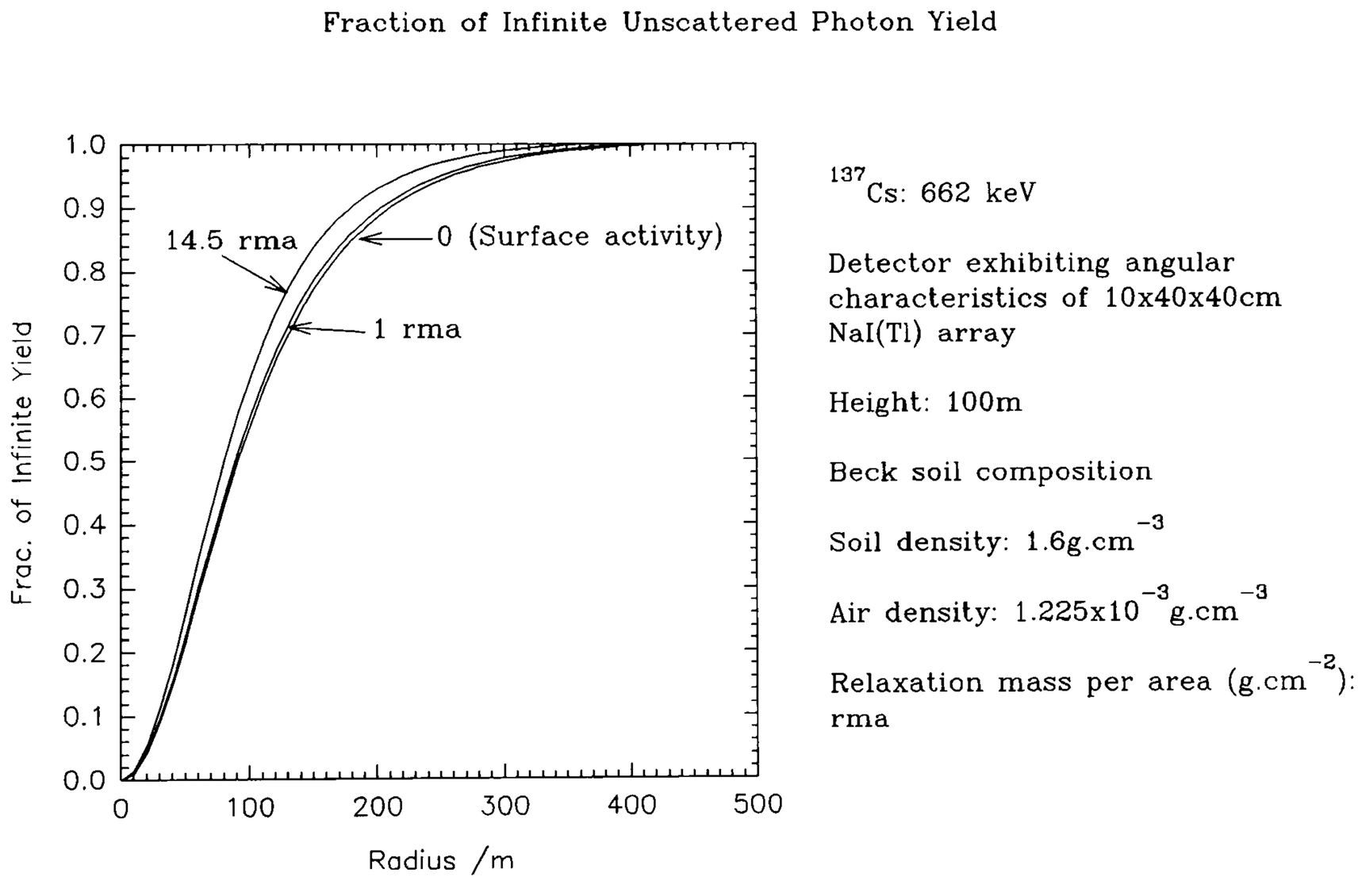

Figure 5.12

The effects of vertical distribution profile on spectral shape are further discussed in section 6.8.4.

5.3.4 Estimates of Fluence and Count Rates

Estimated fluence rates and count-rates at *infinite source yield* (a source emanating up to 2π geometry) for natural and anthropogenic radionuclides are shown in table 5.5 and figures 5.13-5.24 respectively. Detector response (cps) is independent of soil density for the naturals with a uniform depth distribution.

Ground level in-situ measurements are normally taken at 1m height, with the detector face pointing downwards. Variation of fluence rates with height is relatively small close to the ground, therefore estimates at 1m (a nominal height) are generally adequate for heights 0.5-1.5m. For the detectors described here, the field of view is not strongly dependent upon angular response at energies above 500 keV. At high angles of incidence, sensitivity is low and significant air path attenuation occurs.

Fluence rates are strongly dependent upon activity depth distribution. One possible method of inferring the depth profile in-situ is to determine spectral measurements at two different energies from the same source (or assume the same depth profile for different sources). The ratio of the respective fluence rates gives some indication, although sensitivity is low and assumptions of form of profile are necessary (see section 5.3.5.4). It has been found that the angular distributions of total and fluence rate greater than 500 keV, are insensitive to source depth profile or type of soil (Beck ,1977). As altitude increases angular distributions become much more forward peaked owing to the attenuation from the outer regions of the field of view.

For anthropogenic radionuclides and 1m detector height, soil density plays a less important role the deeper the activity is driven: the overriding consideration is the depth distribution profile. This proposition is somewhat different at 100m altitude, where variation of soil density has as much an effect as depth distribution.

The relative contributions of the annular areas of ground sources surrounding a detector, to the total fluence rate, depends upon their lateral distribution. A source at peripheral regions may still be detected if sufficiently intense.

Table 5.5 Calculated fluence and count rates per activity concentration for the natural radionuclides, assuming a homogeneous distribution with depth.

Radionuclide	Fluence Rate / Bq kg^{-1}	cps / Bq kg^{-1}
7.62x7.62cm NaI(Tl) at 1m height		
^{40}K	9.785	0.01171
^{214}Bi	16.056	0.01749
^{208}Tl	122.578	0.08755
10.16x40.64x40.64cm NaI(Tl) at 50m		
^{40}K	4.639	0.3181
^{214}Bi	8.037	0.5066
^{208}Tl	67.849	3.1701
10.16x40.64x40.64cm NaI(Tl) at 75m		
^{40}K	3.481	0.2447
^{214}Bi	6.157	0.3973
^{208}Tl	53.992	2.5765
10.16x40.64x40.64cm NaI(Tl) at 100m		
^{40}K	2.669	0.1912
^{214}Bi	4.813	0.3161
^{208}Tl	43.728	2.1205
10.16x40.64x40.64cm NaI(Tl) at 125m		
^{40}K	2.076	0.1509
^{214}Bi	3.814	0.2539
^{208}Tl	35.838	1.7605

a). Fluence Rates and Count Rates at 1m: Anthropogenic Radionuclides

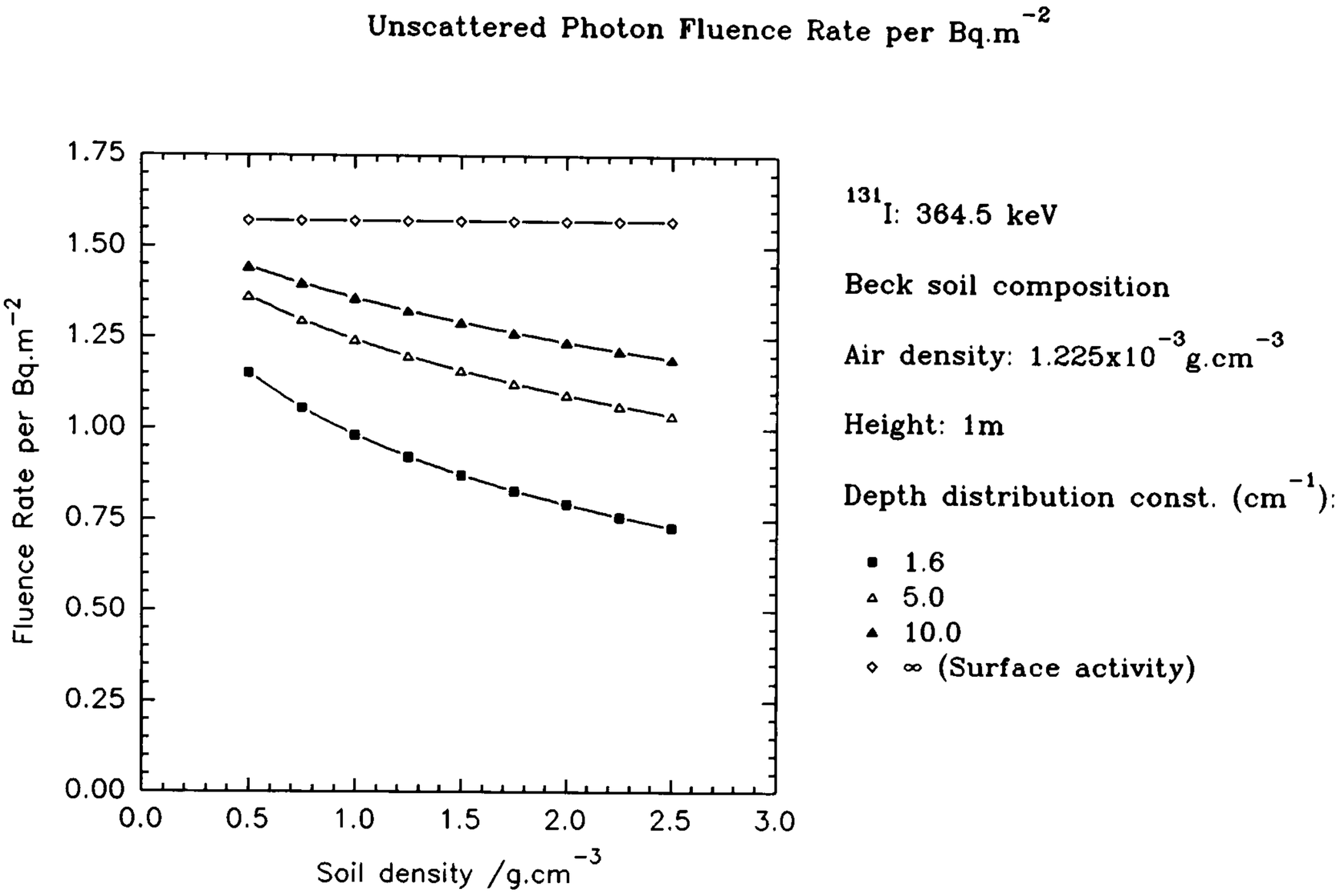

Figure 5.13

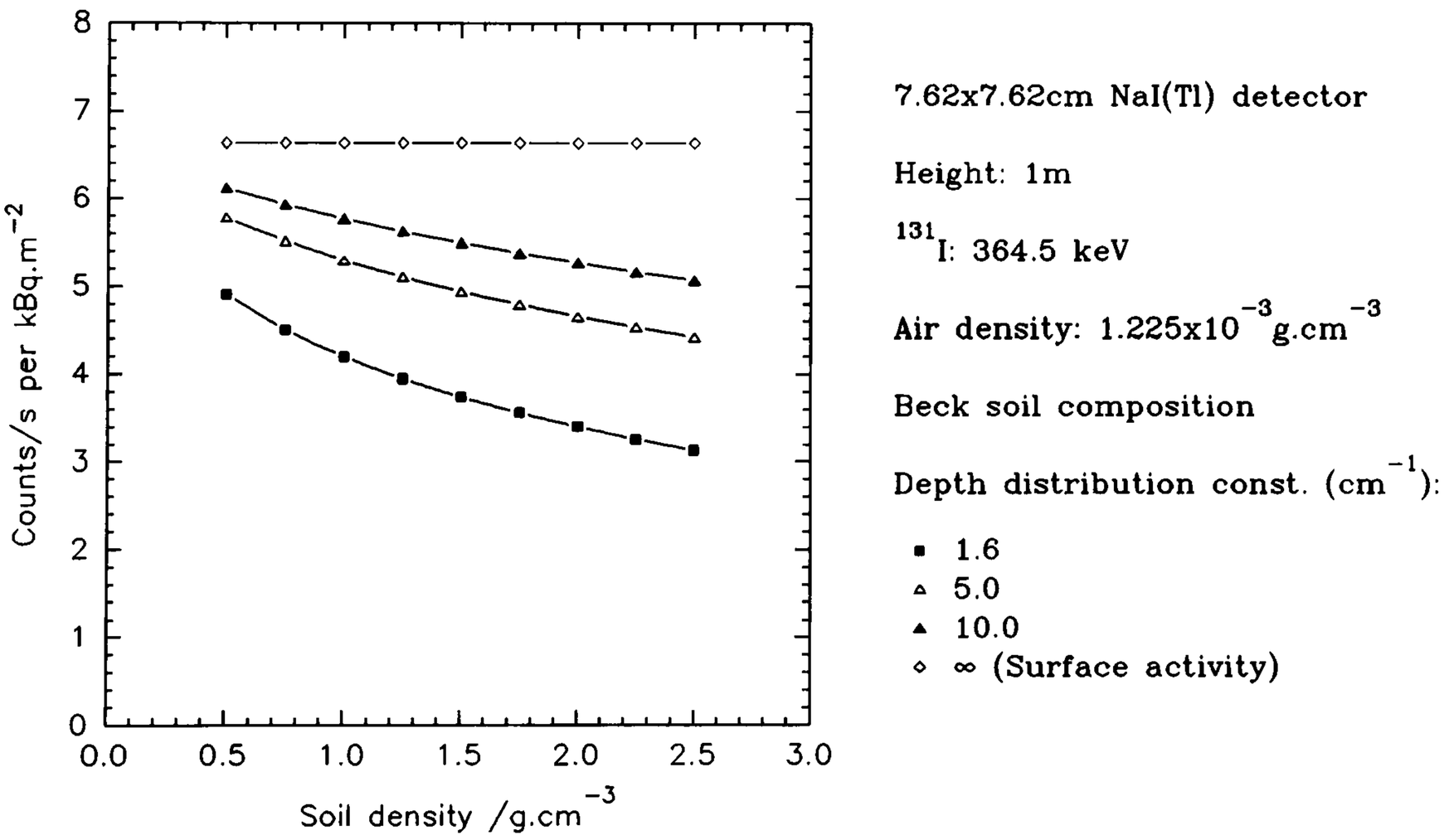

Figure 5.14

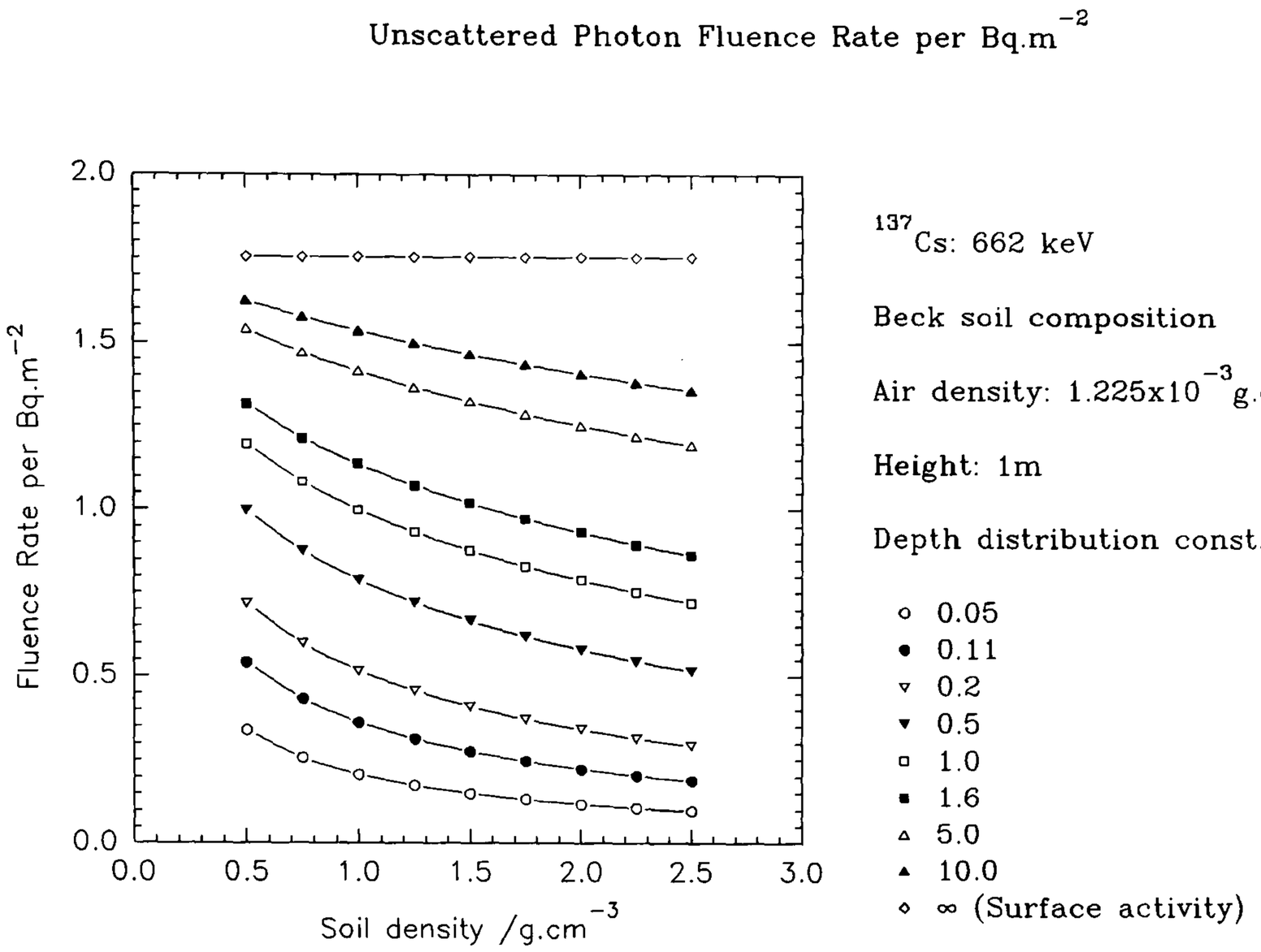

Figure 5.15

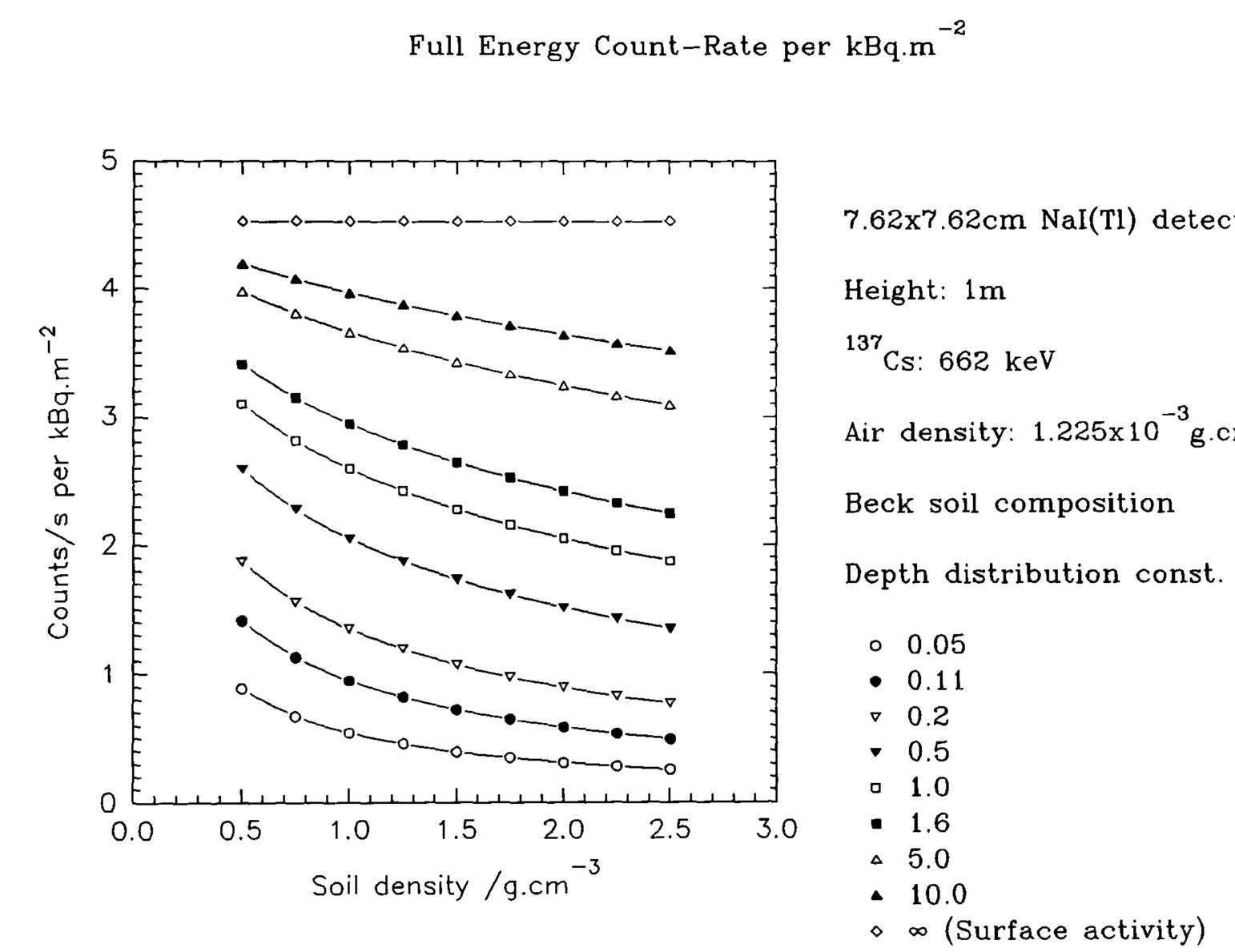

Figure 5.16

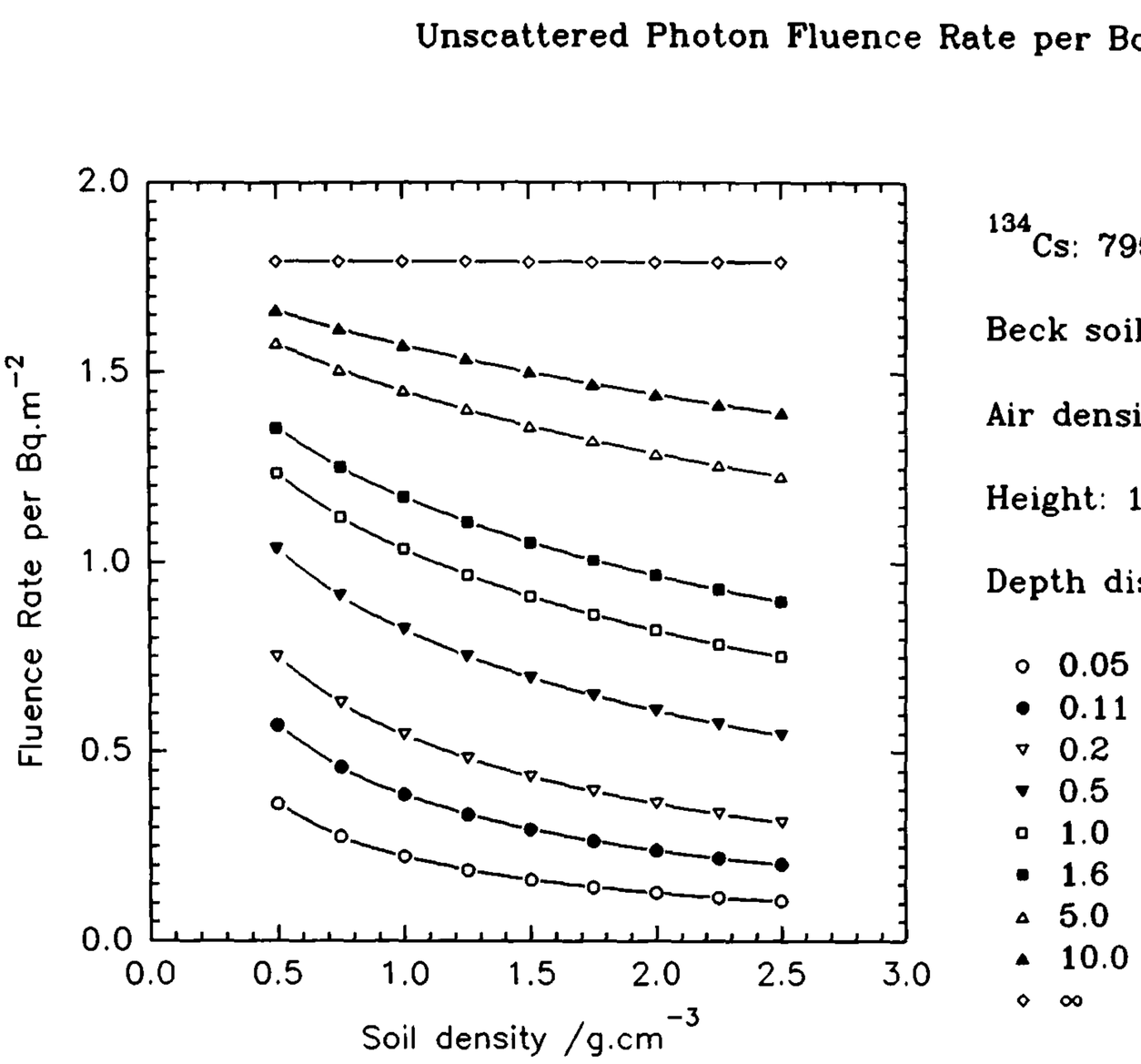

Figure 5.17

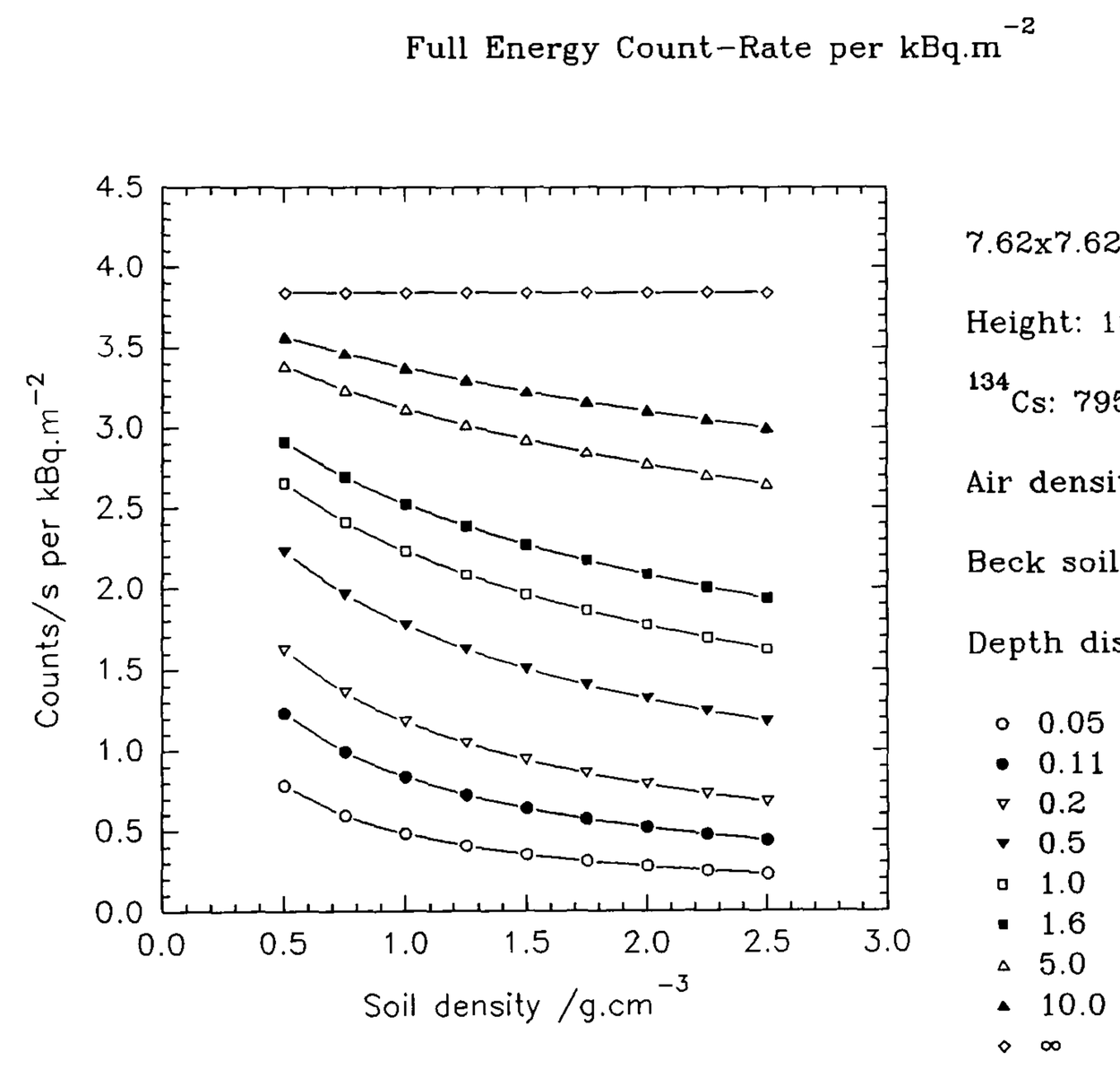

Figure 5.18

b). Fluence Rates and Count Rates at >1m: Anthropogenic Radionuclides

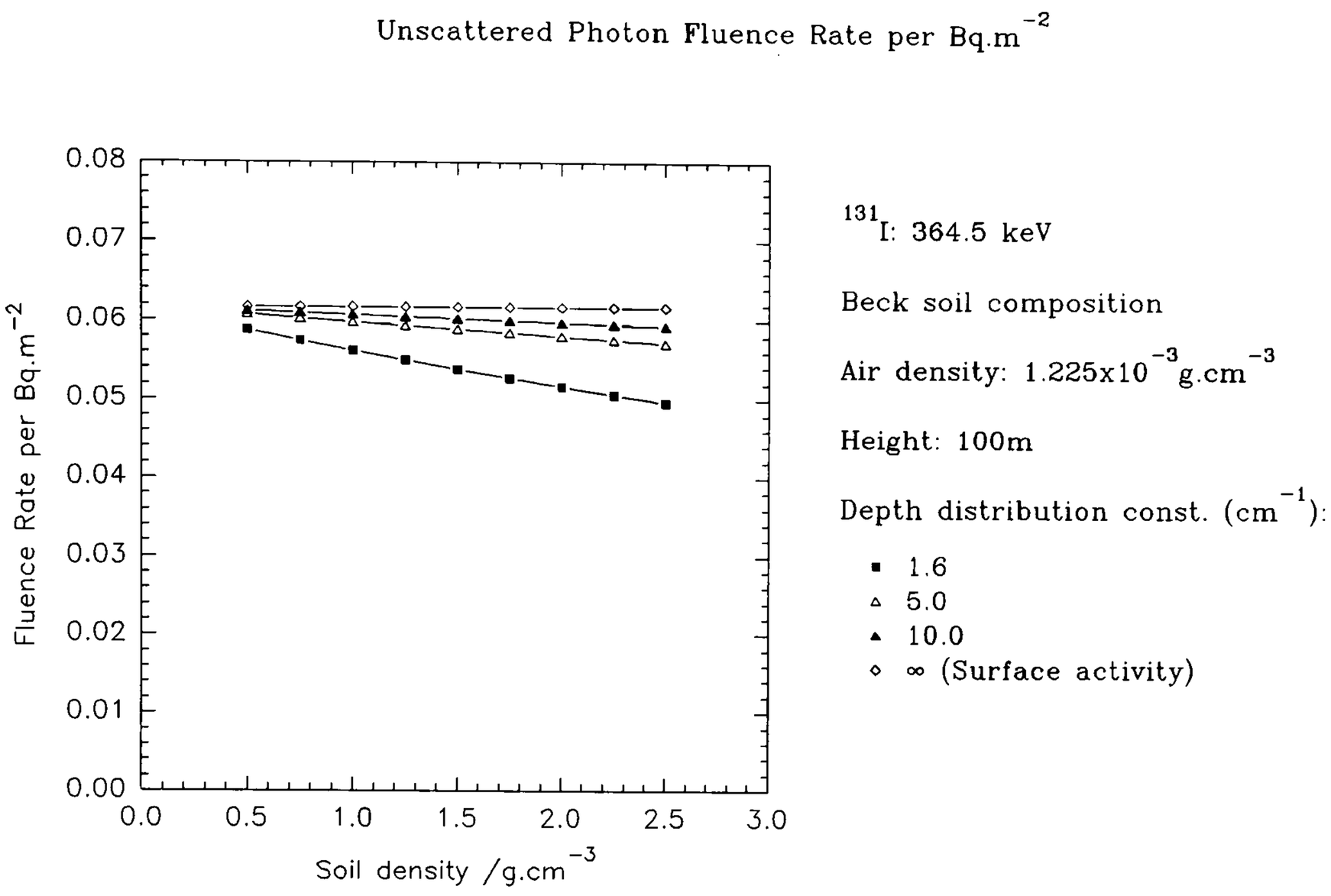

Figure 5.19

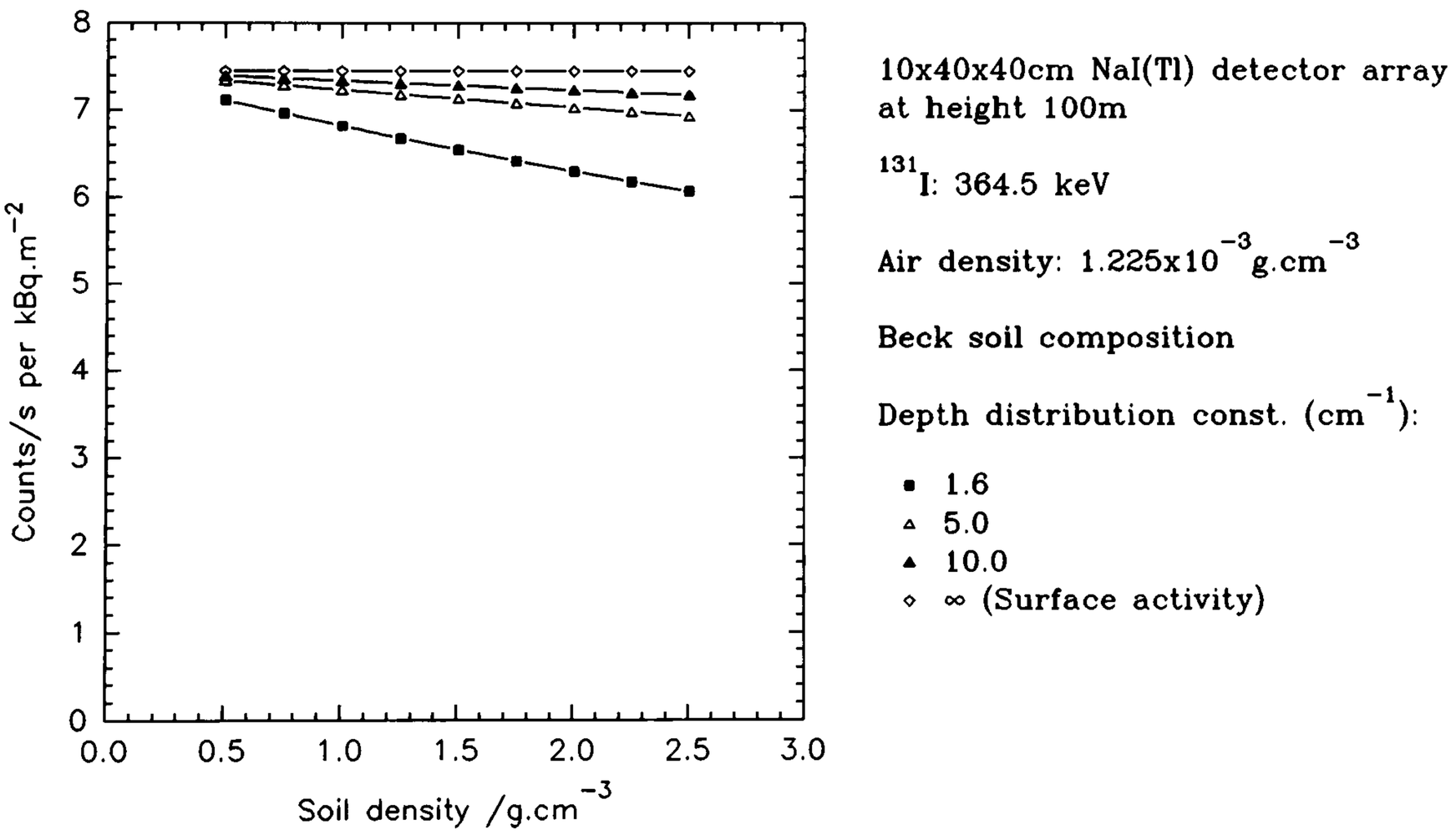

Figure 5.20

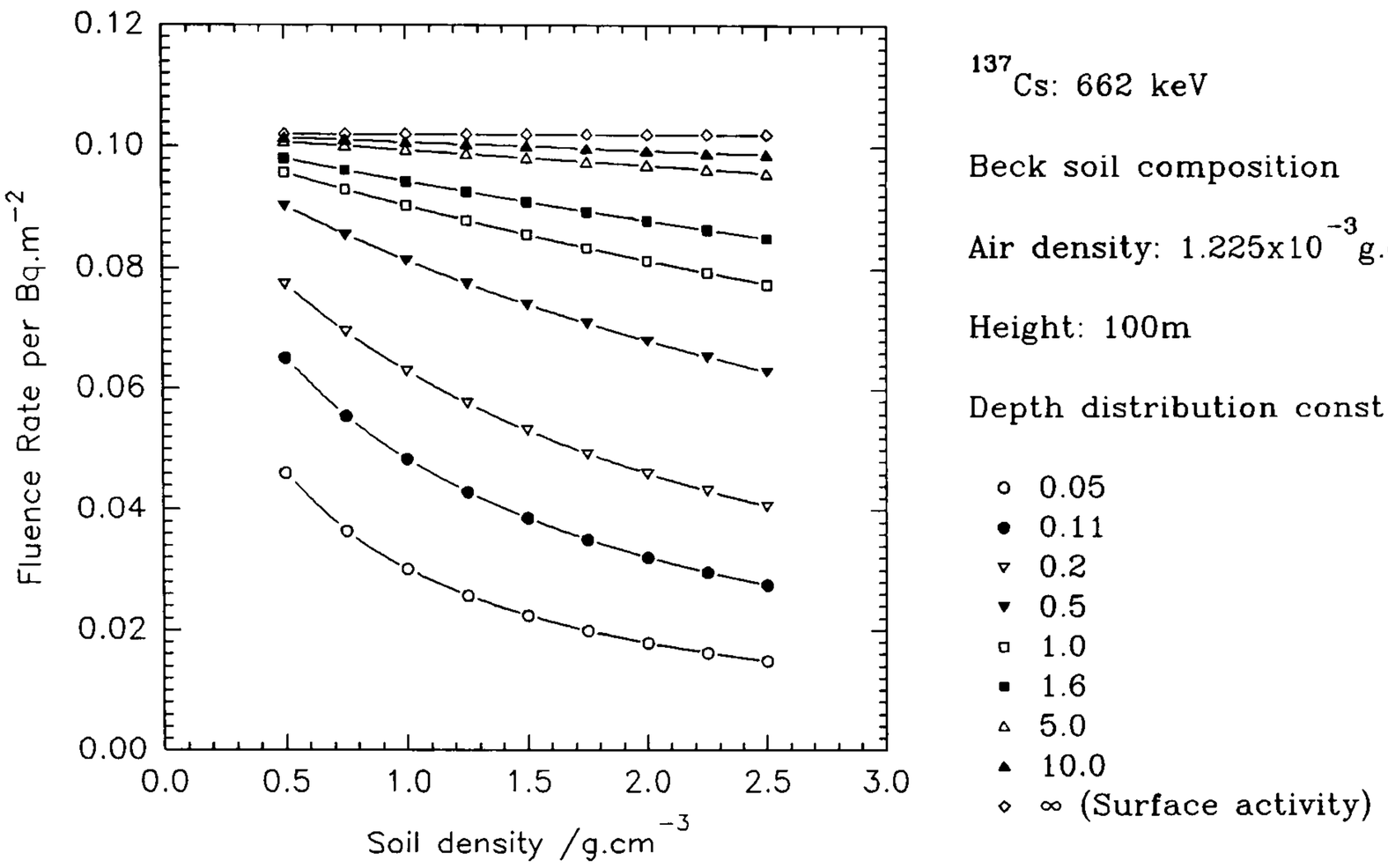

Figure 5.21

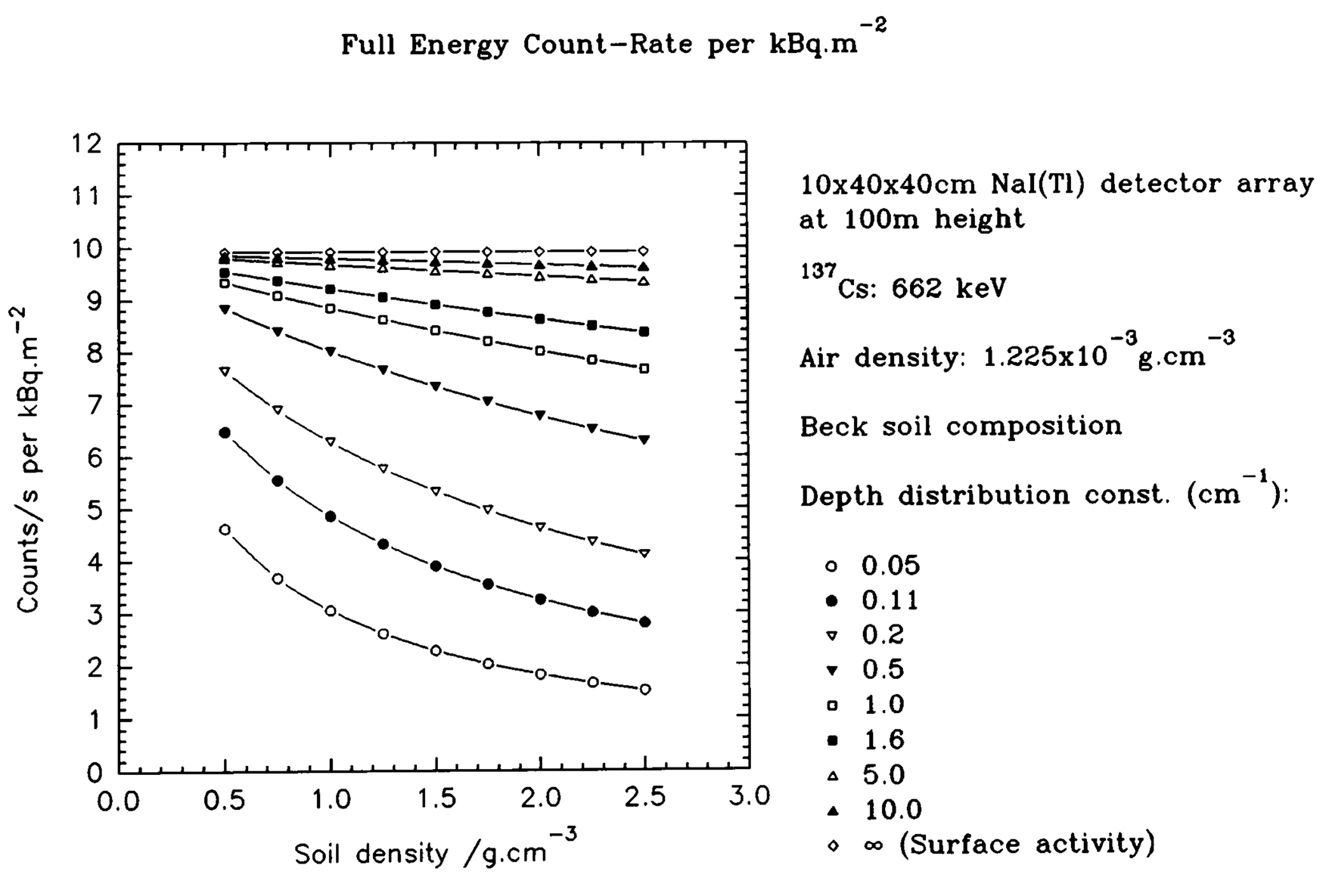

Figure 5.22

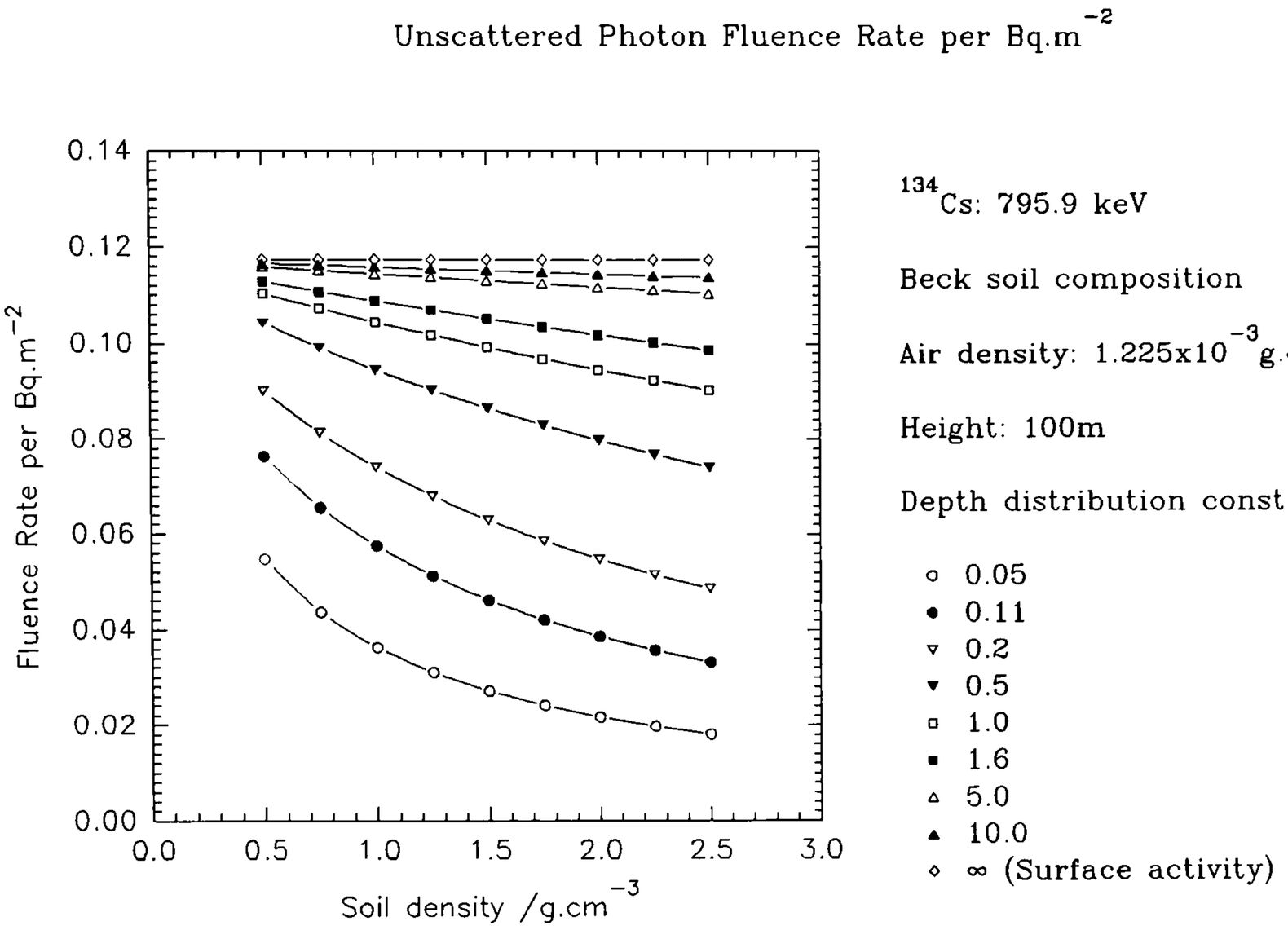

Figure 5.23

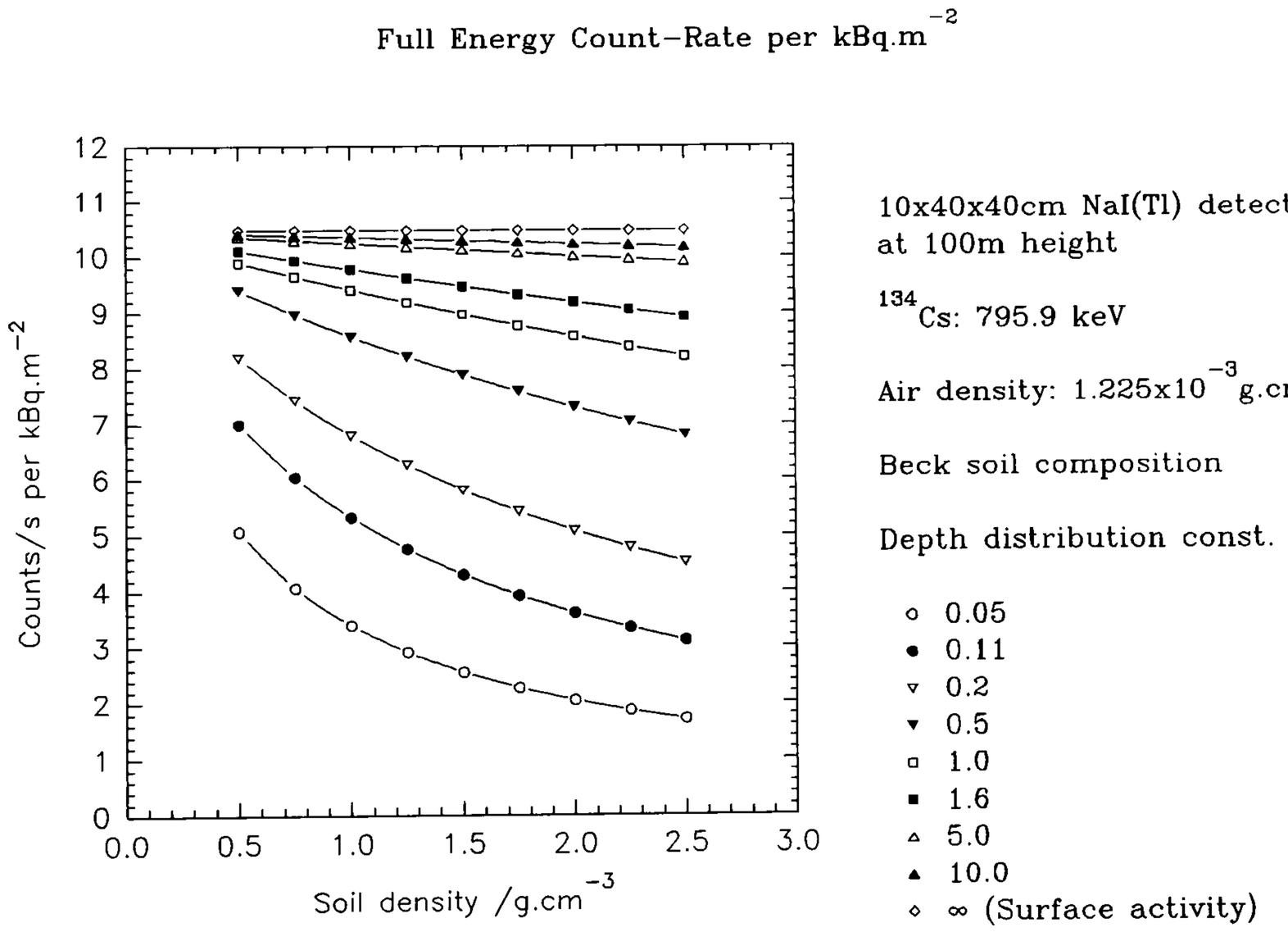

Figure 5.24

5.3.5 Environmental Radionuclides

All common rocks and soils contain natural (primordial) radioactive elements. Of these, the most significant relating to γ-ray spectrometry are potassium, uranium and thorium. Potassium undergoes a simple radioactive decay process; uranium and thorium decays are complex and proceed along a sequential chain, creating daughter products with γ-ray emissions of varying intensity. Only one of several potassium isotopes is found radioactive in the natural environment; ^{40}K. Uranium has principally two isotopes; ^{238}U and ^{235}U. The former is the most abundant (99.27%). For natural thorium, ^{232}Th is the principal isotope. Appendix C lists the ^{238}U, ^{232}Th and ^{235}U series in order of decay.

5.3.5.1 Concentrations of Potassium, Uranium & Thorium

Bedrock is usually covered with soil, and the radioactive mineral content of soil depends upon that of the original parent rock. These minerals may be homogeneously spread throughout the soil or concentrated. Uranium and thorium minerals are small and fragile, and can concentrate in fine grained fractions like clay. Soil concentrations of potassium, uranium and thorium are typically 1-2%, 1-2ppm and 6 ppm respectively, and somewhat less than found in common rocks. In crustal rocks, the average concentrations are 2.1%, 3ppm and 12ppm respectively, but are dependent upon rock type eg. igneous, sediments and metamorphics (IAEA, 1979). Table 5.6 shows averages and ranges for common rock types.

A state of equilibrium is reached within the radioactive decay of uranium and thorium if a chemically closed system is sustained. In this, daughter products are produced at the same rate as their decay. Approximately 10^6 years are required for ^{238}U to reach equilibrium; 40 years for ^{232}Th.

Table 5.6 Common rock composition (IAEA, 1990).

Rock Type	%K		ppm U		ppm Th	
	Average	Range	Average	Range	Average	Range
Basaltic	0.7	0.2-1.6	1.0	0.2-4.0	4.0	0.5-10.0
Granitic	2.5	1.6-4.8	3.0	1.0-7.0	12.0	1.0-25.0
Shales	2.2	1.3-3.5	3.7	1.5-5.5	12.0	8.0-18.0
Sand-stones	1.0	0.6-3.2	0.5	0.2-0.6	1.7	0.7-2.0
Carbon-ates	0.25	0-1.6	2.2	0.1-9.0	1.7	0.1-7.0
Lime-stones		< 1		1.0-2.0		1.0-2.0

For a decay system in equilibrium, a measure of the abundance of any daughter product can provide an estimate of the abundance of the parent element. For measurement purposes, the most commonly used γ-ray emission lines associated with uranium are from ^{214}Bi and ^{214}Pb. A precursor to both daughter radionuclides is ^{222}Rn. It is an inert gas with short half-life, dissolves readily in water and may escape to the atmosphere through permeable rock. Also, radium (another U-series daughter) is mobile in sulphate free, neutral or acid solutions. It can be precipitated by gypsum, anhydrite, barite and hydroxides of iron, manganese and aluminium. Estimation of uranium concentrations conventionally assumes that no disequilibrium occurs. However, near surface processes such as weathering (climate, surface hydrology), erosion and transportation may cause introduction and removal of material to or from the ground matrix. Chemical and physical dispersal of the parent and daughter products may result. Under these conditions, the abundance of a decay product will not provide a accurate estimate of parent element concentration. For the thorium decay series, radon appears as ^{220}Rn which has a very short half-life in comparison with ^{222}Rn and loss by emanation is considered less likely. The concentration of radon and its daughter products in outdoor air varies with place, time, altitude and prevailing weather conditions. Under an inversion air layer, concentrations can markedly increase. *Disequilibrium* in the uranium and thorium series may be investigated readily by using high resolution spectrometry

(including alpha and mass spectrometry). For example, by measuring the relative γ-ray fluence rates within each series with respect to the radon radionuclides, one can deduce the emanation fraction.

To express that secular equilibrium is assumed for a given estimate the term *equivalent* is applied to such determinations (eU, eTh). This doesn't apply to potassium. However, it is assumed that when γ-ray measurements of potassium are done in the presence of uranium and thorium, that these are in secular equilibrium. The use of *apparent radioelement concentration* is sometimes applied to spectrometric surveys where survey conditions are likely to diverge from standard calibration conditions. These conditions include geometry effects, thick and dense overburden, and moisture.

An important characteristic of the geologic radioactive elements are their strong correlations over a wide range of rock types. The Th/K and U/K ratios tend to show larger variations than the U/Th ratio.

It is assumed that natural radioactivity is distributed uniformly throughout soil matrix. Table 5.7 shows the unscattered gamma ray component for typical concentration values, using the transformation parameters listed in Appendix D and table 5.5.

5.3.5.2 Anthropogenic Radionuclides in the Environment

As a result of nuclear weapons testing, nuclear power fuel reprocessing, loss of medical and industrial equipment utilizing radioactive sources and accidental releases, the presence of man-made radionuclides in the environment has progressively increased since 1945. One of the most important artificial γ-ray emitting radionuclides for consideration to external exposure is ^{137}Cs. The world wide distribution of ^{137}Cs is such that it is more prevalent in the northern than southern hemispheres by approximately 2-3 times. The average deposition at latitudes 40-50°N is 2.9 kBq m^{-2} (IAEA, 1990).

Table 5.7 Uncollided γ-ray component of potassium, uranium & thorium.

	Uncollided γ-ray Component / γ cm^{-2} s^{-1}
Soil Concentration:	
K: 1%	0.08199
eU: 1 - 2 ppm	0.00592 - 0.01184
eTh: 6 ppm	0.03896
Crustal Rock Concentration (mean):	
K: 2.1%	0.1722
eU: 3 ppm	0.0178
eTh: 12 ppm	0.0779

Air density: 1.225×10^{-3} g cm^{-3}; altitude: 100m.

For fresh deposition, sources can be assumed to be distributed as a thin surface layer on the air-ground interface. Beck *et al* (1972) reported that for ^{137}Cs weapons fallout, α/ρ_{soil} varies between 0.05 and 0.5 cm^2 g^{-1}. For a soil density of 1.6 g cm^{-3}, this gives a relaxation length of 12.5 and 1.25 cm respectively. The former clearly relates to activity that has been deposited earlier.

The attenuation of ^{134}Cs owing to surface roughness and migration through the soil column in Southern Bavaria has been observed to be 0.5-0.7 about 0.1 years after deposition; 0.35-0.60 after 1 year and 0.15-0.35 after 5 years (ICRU, 1993). This is for decay corrected data (half-life: 2.062a).

In the United Kingdom, the passage of the Chernobyl plume during late April and early May 1986, led to deposition of fission products by wet and dry mechanisms. Clark and Smith (1988) have analysed meteorological data and correlated rainfall patterns with deposition. The particulate matter containing ^{137}Cs was predominantly deposited by

interception with rainfall and ground concentrations have been estimated from weather station recordings. Not surprisingly, large errors arise especially in remote upland areas and due to the vagaries of the weather. ^{131}I existed both in the particulate and vapour phases, which led to both wet and dry deposition. It is estimated that less than 1% of the total Chernobyl releases were deposited within the UK. In-situ spectrometry is the favoured method by which recent radionuclide depositions can be estimated reliably. Aerial survey is the most practical and economical method of nationwide coverage, even in the most isolated regions.

5.3.5.3 Comparisons with other Estimates

A few comparisons with other similar work are now presented in order to validate and highlight discrepancies. Uncollided fluence rates for the natural radionuclides are given in table 5.8 at 1m and 100m heights, again using the transformation parameters listed in Appendix D and table 5.5. Comparison is made with data from IAEA (1979), showing good agreement. Minor differences between these data are probably due to cross sectional data, soil composition and densities used. Equivalent uranium is calculated to be 7-9% greater than the IAEA data and may be attributed to the chosen decay scheme branching ratio.

Table 5.8 Uncollided γ-ray component of potassium, uranium & thorium.

	Uncollided γ-ray Component / γ cm^{-2} s^{-1}	
Composition	**Allyson**	**IAEA (1979)**
Altitude: 1m		
K: 1%	0.300	0.30
eU: 10 ppm	0.197	0.18
eTh: 10 ppm	0.182	0.18
Altitude: 100m		
K: 1%	0.082	0.083
eU: 10 ppm	0.059	0.055
eTh: 10ppm	0.065	0.066
	$\rho_{air}=1.225\text{x}10^{-3}$ g cm^{-3}	$\rho_{air}=1.204\text{x}10^{-3}$ g cm^{-3}

Table 5.9 shows fluence rates per Bq kg^{-1} in comparison with work done by Beck *et al* (1972). This reference is also used to compare ^{137}Cs in terms of fluence rate per Bq m^{-2} in table 5.10. Again, good agreement is observed.

Table 5.9 Uncollided γ-ray component at 1m height

	Fluence rate per Bq kg^{-1}	
	Allyson	**Beck *et al* (1972)**
^{40}K (1462 keV)	9.785	9.759 (9.147 flux per γ s^{-1} g^{-1})
^{214}Bi (1764 keV)	16.056	16.045 (10.091 flux per γ s^{-1} g^{-1})

Table 5.10 Uncollided γ-ray component of ^{137}Cs at 1m height. ρ_{soil}=1.6 g cm^{-3}

Linear depth distribution constant α / cm^{-1}	**α/ρ_{soil} / cm^{-2} g^{-1}**	**Relaxation mass per area / g cm^{-2}**	**Flux per γ s^{-1} cm^{-2}**	**Fluence rate per Bq m^{-2}**	
			Beck *et al* (1972)*	**Allyson**	
0.1	0.0625	16.0	0.2788	0.238	0.25
0.329	0.206	4.854	0.6041	0.515	0.50
0.5	0.312	3.206	0.7412	0.6325	0.64
1.0	0.625	1.6	0.9889	0.843	0.85
10.0	6.25	0.16	1.7190	1.465	1.46
∞ (plane)	∞ (plane)	0	2.0540	1.750	1.75

* calculations are estimated to be within error of $\pm$5%.

Xiangbao & Yangzhong (1992) have calculated the total fluence rates of ^{131}I per activity deposition by Monte Carlo methods. Radioiodine has important radiological implications to people and livestock. It is released as a gaseous and particulate fission product following a nuclear accident. Since the physical half-life is relatively short (8.04 days), the dispersion of activity through the subsurface layers of soil is low: consequently ^{131}I activity is usually regarded as a planar source. The susceptibility of the thyroid gland to absorb large quantities of radioactive iodine, and to receive a significant radiation dose is of concern. The ability to take prompt action following such a release must be based upon monitoring procedures: aerial survey is ideally suited to provide fast and extensive coverage of radioactive contamination. The conversion of count rates to recognized contamination levels therefore is of prime requisite. Table 5.11 shows a comparison of fluence rates at 364 keV determined by Xiangbao & Yangzhong with those of this chapter.

Table 5.11 A comparison of fluence rates at 364 keV determined by Monte Carlo (Xiangbao and Yangzhong) and numerical methods (Allyson).

Height /m	**Fluence Rate (γ m^{-2} s^{-1} per Bq m^{-2})**	
	Xiangbao & Yangzhong (1992)	**Allyson**
1	1.265	1.570
100	0.064	0.062

Comparison of estimated count rate of 7.62x7.62 cm NaI(Tl) at 1m height and an equivalent volume of aerial survey detector at 100m is presented in table 5.12. For the latter, Pitkin & Duval (1980) have listed expected full energy count rates per volume of NaI(Tl) scintillant at various altitudes. The comparison at 100m is therefore made with an equivalent volume of 10.16x40.64x40.64cm detector array and does not include factors such as differences in resolution or geometry of detector. IAEA (1990) data are taken as one third of the sensitivity from a 12 crystal detector package (50 litre), taken flying over a calibration range at 122m. As will be shown in chapter 6, the convolution of full energy detector response and especially of large aerial survey spectrometers

introduces departures in calculating peak count rate from those obtained by experimental means. Cross sectional data are of the order $\pm 5\%$ true, but the inclusion of Monte Carlo derived estimates of angular and full energy absorption will increase this uncertainty up to approximately $\pm 12\%$. Direct cross comparison between data must be carefully considered because of the before mentioned geometrical effects and specifically the assumptions of how to treat detector arrays of prismatic crystals as either separate detectors (contributing to a single output) or single large crystal detector (of the same total volume), in order to simplify mathematical description. This will be addressed later in chapter 6.

Table 5.12 Count rate sensitivities of 7.62x7.62cm NaI(Tl) detector at 1m and 10.16x40.64x40.64cm NaI(Tl) at 100m height.

	Full Energy Peak Count Rate / cps		
7.62x7.62cm NaI(Tl) detector at 1m			
Composition	Allyson (Numerical)	IAEA (1979) (Experimental)	Løvborg (1982) (Experimental)[#]
K: 1%	3.59	3.0	3.391 ± 0.068
eU: 1ppm	0.22	0.25	0.314 ± 0.019
eTh: 1ppm	0.13	0.12	0.1275 ± 0.0026

	Full Energy Peak Count Rate / cps		
10.16x40.64x40.64cm NaI(Tl) array at 100m			
Composition	Allyson (Numerical)	Pitkin & Duvall (1980) (Numerical)[*]	IAEA (1990) (Experimental, test range)[+]
K: 1%	58.74	36.99	35.35
eU: 1ppm	3.89	6.85	3.43
eTh: 1ppm	3.15	2.12	2.28

[*]an equivalent volume of NaI(Tl)

[+] 1/3 of 50 litre sensitivity

[#]Geometrics GR-410

5.3.5.4 Comparisons with Experimental Evidence and Other Influencing Factors

Calibration of in-situ γ-ray spectrometry, at ground level or aerial survey altitudes, frequently relies on ground sampling schemes in order to convert true spectral count rates to radionuclide concentrations. An extensive study of radionuclides in the environment to direct relevance to ground and aerial survey work has been made by Tyler (1994). Ground coring in many different geographical regions, encompassing variable inland soil, intertidal marsh (merse), sea shore, geochemical and geological conditions produces a data base of information to calibrate detectors. A table of practical sampling data is provided below in table 5.13. Soil density lies in the range 1.0-2.0 g cm^{-3}, but is typically 1.1-1.8 g cm^{-3} (Beck, 1968).

Table 5.13 Field sampling information: A.N. Tyler (1994)

Typical Soil Conditions:	**Soil Density / g cm^{-3}**
Peat:	0.8 - 1.0
Merse (salt marsh):	1.2 - 1.5
Average:	1.6
Soil Coring information:	
Coring Depth:	0.3m
Core Diameter:	0.0378m, 0.105m
Average Wet Core Mass:	3.4kg

The significance of differences in soil type compared to the Beck standard has been investigated by SURRC (1992). Twenty three standard soils have been identified from Govindaraju (1989), with additional types from Mudahar and Sahota (1988) and dry/wet (80% water content) peats analysed by Tyler (1994). Their major composition as defined by up to 36 elements, has been used to calculate their respective mass attenuation coefficients (30 keV-6 MeV) from data presented by Storm and Israel

(1970). Elements exhibiting high atomic numbers ($Z > 50$) and concentrations (> 1 ppm) have been included, and shown to have importance for energies of less than 100 keV especially near absorption edges. The conclusions drawn show that the total mass attenuation coefficients of standard soils are greater by 20-150% for energies below 100 keV, compared with Beck soil; for energies greater than 100 keV, the coefficients are less by about 5%. The total mass attenuation coefficients of organic soils are less by up to 70% below 100 keV, compared with Beck soil, and greater by about 10% above 100 keV. It is clear that for energies greater than 100 keV and for a relative error of $\pm$10-20%, soil composition is not critical: for energies of less than 100 keV, individual soil type must be considered and accounted for in calibration methods. Coppola and Reiniger (1974), have studied five different types of soil and conclude that below 50 keV appreciable variation in mass attenuation coefficient occurs; above 300 keV the differences are negligible. Mudahar *et al* (1991) have shown that variations in mass attenuation coefficients occur for chemically different soils at energies below 300 keV.

Field sampling methods are prone to errors owing to inadequate cross correlation, poor sampling methodology and spatial sampling. A weighted sampling method (Tyler, 1994) applies field of view characteristics to a sampling strategy and therefore is more likely to succeed in good calibrations.

Unless the physical nature of an area can be analysed and extensively sampled, the various and different soil characteristics cannot be completely accounted for. This is particularly difficult at aerial survey heights where the volume required for interrogation is high indeed. Nevertheless, if calibration sites are chosen with care and with geochemical experience, a reasonably good experimental calibration can be achieved. This has been the case at SURRC for a number of years now. In so doing, the resulting linear calibration, in terms of kBq m^{-2} per stripped cps, has led to non zero intercepts (possibly due to background errors) as seen in table 5.14. These calibrations have been made across many different sites and it is likely that differences in soil geochemistry and radionuclide dispersion are reflected in these calibrations. A non-uniform vertical distribution of the natural radionuclides has been observed, in areas of salt marsh and intertidal regions (Sanderson *et al* 1993a).

Table 5.14 Comparison of field calibration constants using a 7.62x7.62cm NaI(Tl) detector at 1m height (Tyler, 1994) and calculated constants (Allyson).

Radio-nuclide	Soil Type	Experimental Calibration Factors	Calculated Calibration Factors (Allyson)	
^{40}K	High ρ	kBq m^{-2}=37.818 x cps - 4.907	kBq m^{-2}=25.62 x cps	ρ=1 gcm^{-3}
	All soils	kBq m^{-2}=38.998 x cps + 4.565	kBq m^{-2}=40.99 x cps	ρ=1.6 gcm^{-3}
^{214}Bi	High ρ	kBq m^{-2}=15.183 x cps - 0.955	kBq m^{-2}=17.15 x cps	ρ=1 gcm^{-3}
			kBq m^{-2}=27.44 x cps	ρ=1.6 gcm^{-3}
^{208}Tl	All soils	kBq m^{-2}=3.536 x cps - 0.283	kBq m^{-2}=3.43 x cps	ρ=1 gcm^{-3}
			kBq m^{-2}=5.48 x cps	ρ=1.6 gcm^{-3}
^{137}Cs	Organic soils	kBq m^{-2}=0.360 x cps + 0.831	kBq m^{-2}=0.3846 x cps	rma= 1 gcm^{-2}
	Clay soils	kBq m^{-2}=0.967 x cps + 0.318	kBq m^{-2}=0.5882 x cps	rma=3 gcm^{-2}
			kBq m^{-2}=1.4286 x cps	rma=10 gcm^{-2}
			ρ_{soil}=1.6 gcm^{-3}	
^{134}Cs	Organic soils	kBq m^{-2}=0.365 x cps + 0.0197	kBq m^{-2}=0.4545 x cps	rma=1 gcm^{-2}
	Clay soils	kBq m^{-2}=0.648 x cps - 0.044	kBq m^{-2}=0.6897 x cps	rma=3 gcm^{-2}
			kBq m^{-2}=1.667 x cps	rma=10 gcm^{-2}
			ρ_{soil}=1.6 gcm^{-3}	

Table 5.15 shows the corresponding calibration factors determined by field work and calculation, for a 16 litre aerial survey detector.

Table 5.15 Uncollided γ-ray component calibration factors for potassium, uranium & thorium at 100m altitude.

	Uncollided γ-ray Component Calibration Factors	
Radionuclide	**Allyson**	**SURRC Fieldwork**
^{40}K	kBq m^{-2}=2.51 x cps	kBq m^{-2}=2.79 x cps
^{214}Bi	kBq m^{-2}=1.519 x cps	kBq m^{-2}=0.606 x cps - 0.67
^{208}Tl	kBq m^{-2}=0.226 x cps	kBq m^{-2}=0.245 x cps - 0.20
	ρ_{soil}=1.6 g cm^{-3}	ρ_{soil}=variable
	ρ_{air}=1.225x10^{-3} g cm^{-3}	ρ_{air}=variable
	Soil core depth=0.3m	Nominal depth=0.3m
	Altitude=100m	Altitude=100m

An exponential distribution has often been assumed since interest has been in terms of fresh or relatively recent deposition or even simplification. However, in regions where the conditions of deposition are dynamically changing over periods short compared with the half-life of the activity, subsurface maxima can be established. In stable environments a chronological record of deposition may be observed, which can be correlated to discharge inventories. In more active areas, this record is unlikely to be so preserved. In order to parameterize the activity vertical distribution, the relaxation mass depth no longer can be satisfactorily applied. A mean relaxation mass depth can be constructed from the activity $A(m)$ found at mass depth m, for intervals between a and b:

$$\textit{Mean Relaxation Depth } \overline{m} = \frac{\int_a^b m.A(m)\ dm}{\int_a^b A(m)\ dm} \qquad (5.7)$$

The use of mass depth corrects for any ground density variations found with linear depth. The usefulness of this as a parameter to describe conveniently a given vertical distribution is limited and may even be misleading. A better description may be achieved through using a cumulative frequency distribution and identifying the first and third quartiles, in addition to the mass depth at which half the activity is situated.
Table 5.16 shows a comparison of sensitivity estimates by calculation (assuming a single exponential profile) and those determined by SURRC staff over many field trips.

Table 5.16 Uncollided γ-ray component calibration factors for ^{137}Cs & ^{134}Cs at 100m altitude.

		Uncollided γ-ray Component Calibration Factors / kBq m^{-2} per cps	
Element	**Dispersion Type**	**Allyson**	**SURRC Fieldwork**
^{137}Cs:	Surface	0.1	
	Chernobyl	0.125 - 0.135	0.198
	Merse, shallow	0.156 - 0.182	
	Merse, deep	0.204 - 0.250	0.533*
			0.348+
^{134}Cs:	Surface	0.097	
	Chernobyl	0.117 - 0.125	0.131
	Merse, shallow		
	Merse, deep	0.147 - 0.167	
	ρ_{soil} / g cm^{-3}	1.6	variable
	ρ_{air} / g cm^{-3}	1.225x10^{-3}	variable
	Soil core depth / m	0.3	0.3
	Altitude / m	100	100

* Subsurface maxima, peak activity occurring 5-8cm below surface (Warton Bank, Ribble Estuary).
+ SW Scotland Survey (Sanderson *et al*, 1993b).

The determination of radionuclide profiles by in-situ spectrometry is of key advantage. The ratio of scattered to unscattered radiation increases with mass of material between source and detector. Zambori *et al* (to be published) uses only the region immediately below a full energy peak (predominantly forward Compton scattering) to calculate this *peak to valley* ratio. The presence of interferences from other radionuclides and of higher γ-ray energies into the scattered part of a spectrum may limit this technique.

The relative intensity of a pair of γ-ray lines of quite separate energy emitted from the same buried radionuclide has been investigated by Rybacek *et al* (1991). The use of the 32 keV x-ray and 662 keV γ-ray of ^{137}Cs can yield profile parameters, but is restricted to depths of only a few centimetres owing to the strong attenuation of the x-ray line. This technique also relies on the application of high resolution semiconductor detectors.

Increasing soil density effectively buries a source more deeply. This is because the linear attenuation coefficient is proportional to density of material: as density increases, μ_{tot} increases and therefore the mean free path decreases, reducing the fluence rate at the detector in the air half-space.

An increase in soil moisture will suppress fluence and measured count rate. A 10% water content is considered typical of temperate regions (Beck, 1972). A soil moisture increase of 10-20% will decrease count rates by approximately 10% (IAEA, 1976). The average Z/A of a soil increases with water content and this is proportional to the Compton mass absorption coefficient: $(Z/A)_{0\%}$: 0.497; $(Z/A)_{10\%}$: 0.503; $(Z/A)_{20\%}$: 0.508). The average atomic numbers for Beck soil with 0, 10 and 20% moisture content are: $Z_{0\%}$, 11.102; $Z_{10\%}$, 10.714; $Z_{20\%}$, 10.325. Since the photoelectric mass absorption coefficient increases with average Z^3 (see chapter 2), relatively more Compton scattering is expected with rising moisture content. Increased soil moisture also increases soil density, which for uniformly distributed radionuclides reduces the source activity per mass and hence measured fluence rates. For exponentially distributed radionuclides, the sources are effectively buried deeper.

Increased soil moisture also retards radon emanation but little build-up of fluence rate

occurs owing to the correspondingly higher attenuation.

Attenuation by snow cover can be significant. Indeed, water equivalent snow measurements have been made to forecast the snow-melt available for water storage requirements, by comparison between pre-snow conditions and the winter season. Frozen ground reduces radon mobility and may increase surface γ-activity, but depends upon the attenuating soil properties in such instances (moisture content, see above). The field of view of a detector above snow covered ground can also be smaller due to the attenuation at the more extreme angles of incidence. Saito (1991) estimates that 45% of air kerma, at 1m height, is from a source of radius 1m with a snow covering of 30cm (snow density 1 gcm^{-3}). This is compared with 25% at the same radius without snow. IAEA (1990) reports that 10cm of fresh snow is equivalent to 10m of air, and that surveys should be discontinued if there is more than 1-2cm of snow on the ground.

Finally, concentrated forestation has a shielding and collimating effect. In Canada, the exposure rate has been seen to have an attenuation of about 15%. In addition, Richardson (1981) reports failure of radioaltimetry to penetrate dense forest foliage and the introduction of systematic errors into data collection.

5.3.6 Effects of Topographic Relief

The location of a detector with respect to nearby topographic features (placing the detector in a steep sided valley or on the brow of a hill/ridge) can lead to erroneous measurements. In order to quantify this, an investigation was made using the preceding numerical formulations and the most commonly found geometries, shown in figure 5.25. The degree of the effect is a function of the steepness of angle ϕ: the change in fluence-rate of ^{137}Cs is shown in figures 5.26 and 5.27.

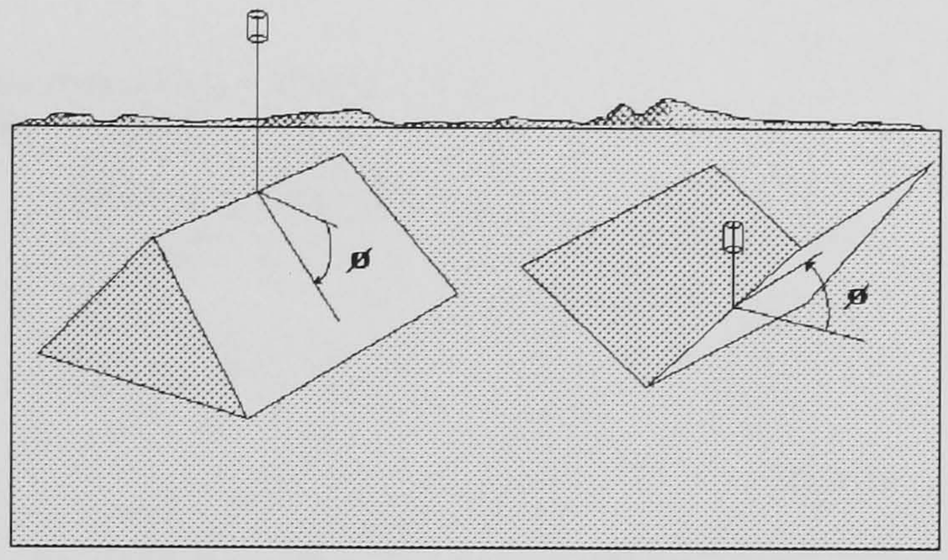

Figure 5.25 Effects of topography on measured fluence rate.

Interpreting the results it would appear that a ridge geometry has a less significant effect than a valley. At ground level, measurements taken within a valley (eg. stream sediments at the valley bottom) may lead to over-estimation of the inventory unless relatively simple precautions are taken. A restriction of the field of view is recommended by reducing the detector height or by collimation. An additional cross-calibration for this would be necessary.

For aerial survey detectors used in highly mountainous regions, it would be possible in principle to correct for count-rate changes owing to geometrical variations if topographical information is available and accurate positional data is recorded using GPS. A flight path reconstruction made at the data processing stage, would enable count-rates from an equivalent plane surface to be estimated.

Maximum Unscattered Photon Fluence–Rate per Bq.m^{-2}

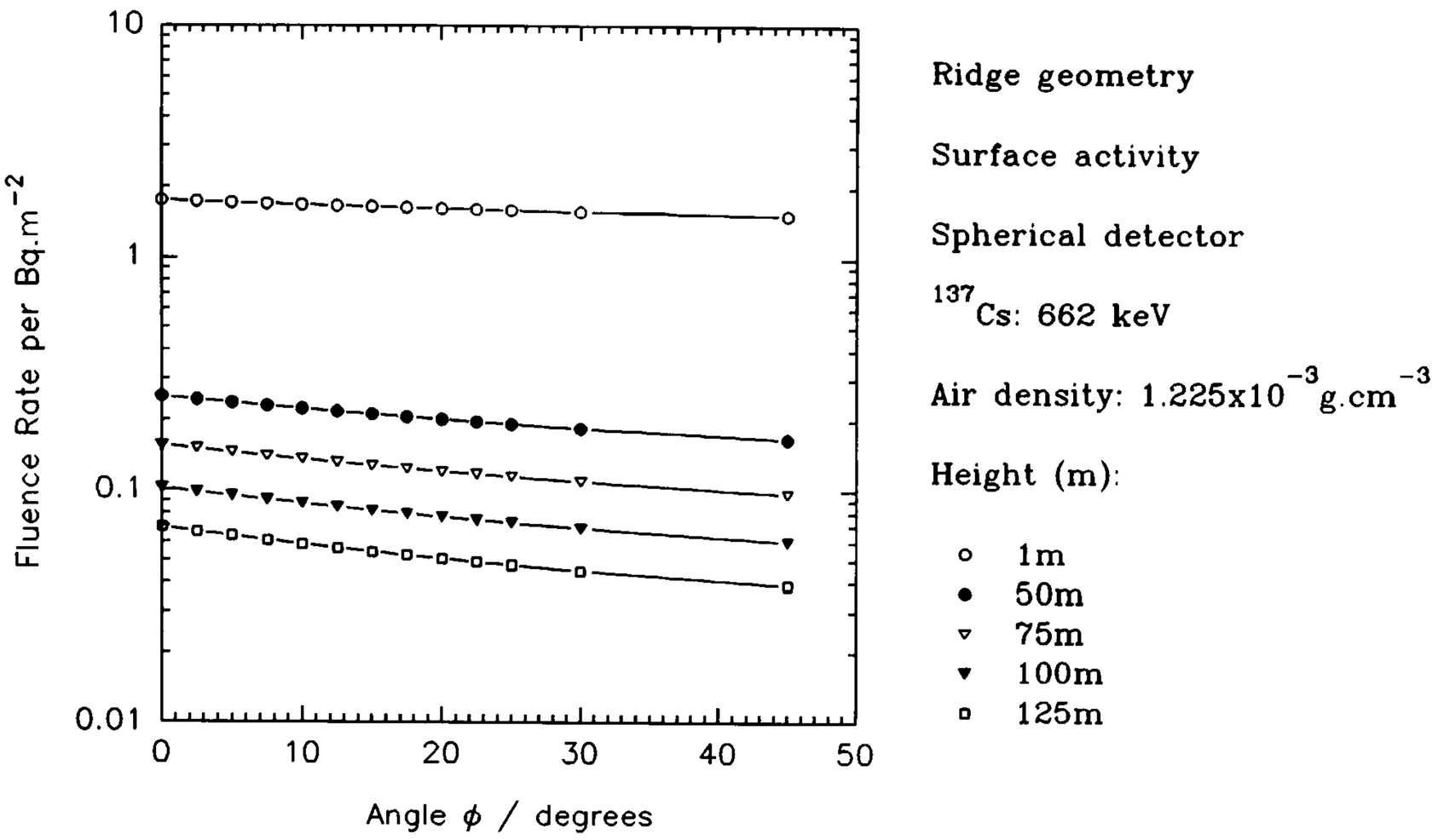

Figure 5.26

Maximum Unscattered Photon Fluence–Rate per Bq.m^{-2}

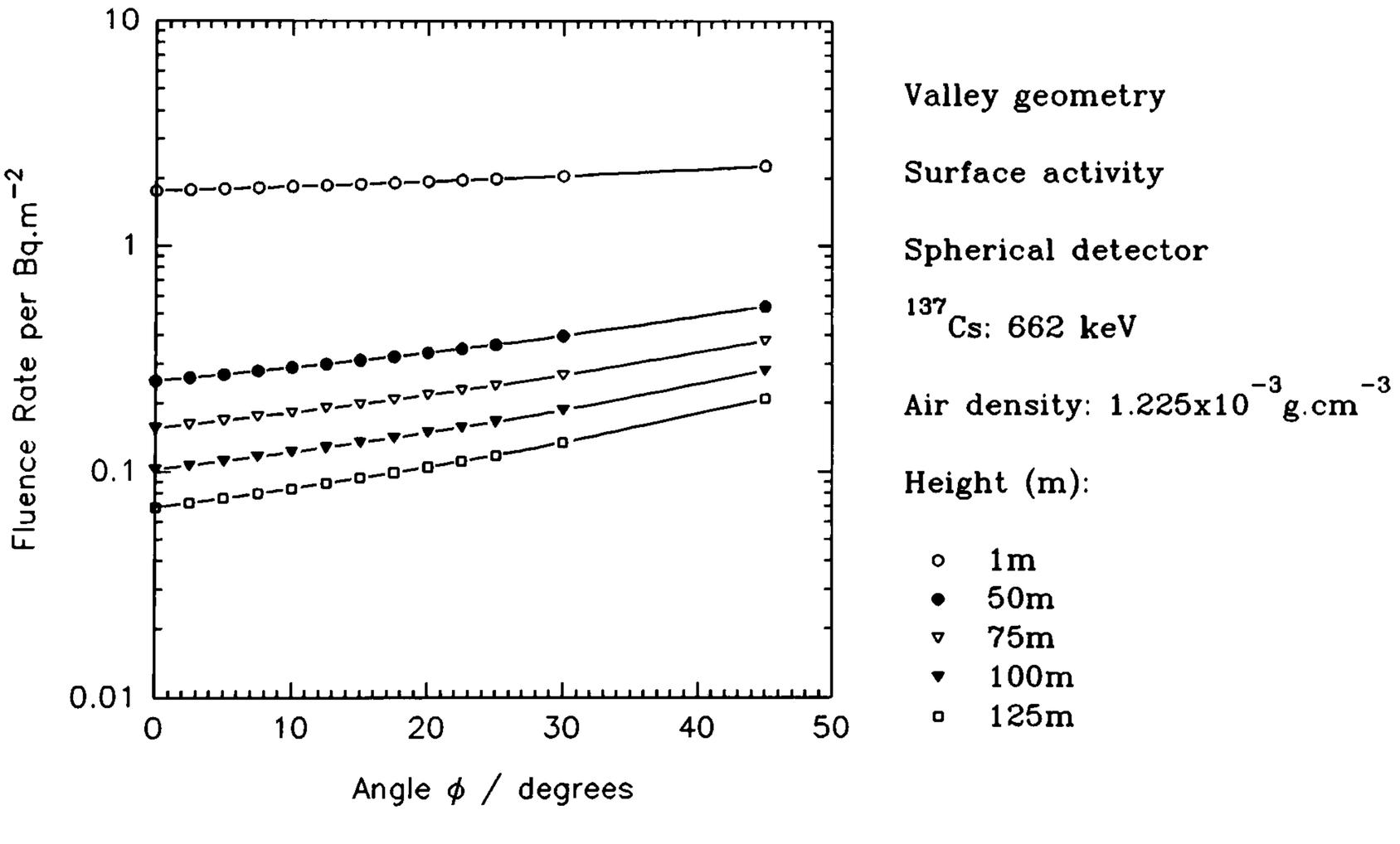

Figure 5.27

Ground roughness effects have been investigated by numerous authors. This will appear to bury a surface source deeper into the subsurface. The stimulus behind the investigation of ground roughness has been from the need to quantify shielding effects from nuclear fallout. There are four models upon which these effects have been investigated (French, 1968). The most popular is the *buried source model*. It corresponds to fallout that is covered by a uniform layer of soil, of thickness depending upon the degree of roughness. Alternatively, an air equivalent distance can be attributed to ground roughness. The findings have been compared with experimental measurements in different types of terrain: dry lake bed, ploughed field and wild desert (Huddleston *et al*, 1965). For the first, an air equivalent distance of 6.1m has been calculated (compared with an actual height of 1m). This is surprising since it would seem that even slight irregularities of an apparently smooth surface results in significant attenuation (a dose-rate reduction factor of 0.67 was found for the dry lake bed). For the wild Nevada desert, an air equivalent distance of 12.2m was derived. The ploughed field cannot be accounted for by such a simple model. The assumption is then that a plane, infinite source commonly credited to fallout can lead to overestimates of radiation intensity, especially near the air-ground interface. At greater altitudes, the effects of ground roughness become less important.

Uncollided components of fluence are usually dealt with numerically, but the use of Monte Carlo methods is appropriate for multi-scattered γ-rays. If the degree of roughness is large, the total energy spectrum can change considerably by increasing the scattered-uncollided ratio. Radionuclide source concentration estimates can thus be affected.

5.3.7 Minimum Levels of Detection

The *detection limit* or *minimum detectable activity* has several interpretations and mathematical descriptions. The detection limit of a radioelement is the minimum concentration with a net count rate that can be statistically significant from a net count rate of zero. Window sensitivities convert net count rates to the appropriate radioelement concentration. The more common definitions are shown below.

a). The simplest definition consists of taking 1/10 of the background count-rate (Crouthamel, 1970):

$$\textit{Minimum Detection Limit} = 0.1(\textit{count rate})_{bgd} \qquad (5.8)$$

b). The minimum detectable activity is defined (ICRU, 1972):

$$\textit{Minimum Detectable Activity} = \frac{3\sigma_{cps,bgd}}{\textit{Sensitivity}} \qquad (5.9)$$

where, $\sigma_{cps,bgd}=1$ standard deviation of background count rate

Sensitivity=count rate per Bq m^{-2} or cps per Bq kg^{-1}

c). Finally, a common expression for the detection limit at the 95% confidence level is (Currie, 1968), (Løvborg, 1987):

$$L_D = 2.71 + 3.29\sqrt{2\ \textit{Background Counts}} \qquad (5.10)$$

Typical background count rates for an aerial survey NaI(Tl) array (16 litres) are shown in table 5.17. From this and the sensitivities at 100m height and a soil density of 1.6 g cm^{-3}, estimates of minimum detection levels from the above formulas are compared in table 5.18.

Table 5.17 Background count rates from a NaI(Tl) aerial survey detector.

Count rate / cps				
^{137}Cs	^{134}Cs	^{40}K	^{214}Bi	^{208}Tl
43.4	20.9	19.1	9.6	8.4

Table 5.18 A comparison of minimum detection levels from a 16 litre aerial survey detector at 100m.

	Minimum Detectable Activity				
Live Time / s	**^{137}Cs / kBq m^{-2}**	**^{134}Cs / kBq m^{-2}**	**^{40}K / Bq kg^{-1}**	**^{214}Bi / Bq kg^{-1}**	**^{208}Tl / Bq kg^{-1}**
Formula: 5.8					
Independent	0.438	0.200	9.99	3.04	0.39
Formula: 5.9					
1	2.000	1.327	68.57	29.41	4.10
5	0.890	0.598	30.66	13.15	1.83
10	0.630	0.404	21.68	9.29	1.29
15	0.530	0.346	17.71	7.59	1.06
20	0.450	0.288	15.22	6.58	0.92
Formula: 5.10					
1	3.367	2.295	120.53	54.23	7.52
5	1.438	0.962	50.39	22.13	3.05
10	1.006	0.669	35.05	15.29	2.11
15	0.817	0.543	28.41	12.36	1.70
20	0.705	0.468	24.49	10.64	1.46
	Surface Activity		Uniform activity		

5.4 Effects of Motion

Until now all the detectors have been assumed to be stationary. For an infinite source of activity, there is no effect of observed count rate with velocity. The response to a finite local source depends upon its position relative to the flight line. Maximum peak counts vary only slowly with velocity; integrated peak counts (area beneath recorded peak) decrease with increasing velocity. Kosanke and Koch (1978) have developed a modelling program to overlay a moving two dimensional detector sensitivity array with

a fixed two dimensional ground concentration array. A profile of count rate can then be determined across a simulated flight line. Clark *et al* (1972) have similarly modelled an aerial survey detector and shown results for simulated flights over circular and linear sources.

5.5 Terminology Applied to Aerial Surveys Deduced from Fields of View

Estimated ground resolution is a parameter frequently chosen to describe spatial resolution. It is the ability to differentiate ground sources of finite extent that have different radionuclide concentrations:

$$\textit{Estimated ground resolution} = \pi\,(\textit{Field of View Radius})^2 \qquad km^2 \quad (5.11)$$

Ignoring motion is not thought to alter this significantly (Pitkin and Duval, 1980). The ideal flying pattern for most environmental and geological surveys is parallel and closely spaced flight lines intersected by several tie lines. The tie lines act as calibration markers outside the survey area to link together potential future areas of investigation. The survey must be approached in a thoroughly systematic manner in order to control as many variables as closely as practicable. Quality assurance is essential. Contour flying may be used in valleys or across ridges, where a straight line is not possible. The percentage ground coverage is an additional parameter to describe aerial surveys. For a given fraction of the infinite yield for a field of view, and flight line spacing (between adjacent flight lines), then

$$\textit{\% Ground Coverage} = \frac{\textit{Field of View Strip Width}}{\textit{Flight Line Spacing}} 100 \qquad (5.12)$$

Percentage ground coverage increases with increasing altitude. However, ground spatial resolution decreases with increasing height. It must be borne in mind that especially for fixed wing aircraft, there exists a minimum safe operating altitude depending upon topography. Generally, coarse ($>$3km) line spacing is adequate to discover broad, regional anomalies. Line spacing of less than 3km is required to detect localised features and detailed mapping. Large variations of concentration or dimension of localised sources are required, within a given field of view, before a significant change

in yield occurs. The smaller the source to be resolved, the lower and slower the aircraft should fly.

5.6 Chapter Summary

We have seen that detector field of view is an important concept in order to understand and interpret recorded spectral data from ground based or airborne detectors. The overall spectral measurement is a function of many different factors concerning a particular radionuclide found in the environment and the detectors inherent characteristics.

The calculated estimates of infinite source yield from level terrains, in terms of fluence and count rates, show compatibility with other like results and with experimental sensitivity determinations. Some differences with the former may be attributed to choice of decay scheme data, interaction cross sections, geometrical considerations, angular responses and absorption qualities. Differences with experimental measurements may be attributed to field sampling errors. These should be borne in mind when making direct cross comparisons. However, the data presented here can be used as a complementary platform upon which a calibration can be provided in a wide variety of conditions. For sources of size much less than the detector field of view, this work has much less meaning and significant errors may occur in attributing ground concentrations to detector responses, whose sensitivities have been derived on the basis of an infinite source.

This new work has extended existing calibration factors used for the natural radionuclides to include anthropogenic sources of activity, distributed in an assumed manner, and in addition incorporating detector angular responses (for the first time for large aerial survey detectors) to form a set of useful data from which interpretations and planning of surveys can be readily performed.

6. Simulation of Radiation Transport by Monte Carlo

In this chapter, Monte Carlo codes are described that have been written from first principles to account for and investigate a wide range of problems encountered in making γ-ray measurements. The simulations are complete in concept and allow more advanced interpretations to be made than can be achieved with any other numerical methods. They combine both γ-ray transportation processes and detector characteristics within a single simulation package. Monte Carlo code MCI and MCII will investigate: the variation of stripping ratios with scattering media (within source and air volumes) and their respective mass thicknesses; the calculation of stripping ratios from radionuclides not commonly met in the environment; the simulation of energy deposition within different NaI(Tl) detector sizes, geometries (cylindrical and rectangular) and housing; the determination of the detector angular characteristics; the potential use of spectral shape as a method of estimating radionuclide depth distributions. Finally, examples are given of how the application of Monte Carlo methods and formation of simulated spectra can reveal **new** spectral detail contained within real field measurements.

6.1 Introduction

Monte Carlo methods derive from the mathematical methods used by the scientists working on the nuclear weapons of the 1940s' at Los Alamos and make extensive use of numbers that might arise in gambling with a roulette wheel: they are concerned with experiments on random numbers. Here a random number is understood to be a random variable uniformly distributed between 0 and 1. Monte Carlo methods are the application of the random sampling concept to the problem of obtaining random samples from general probability distributions. Monte Carlo methods are frequently used in the evaluation of definite integrals. Actually, for integrals over only one variable, then one would rarely use the Monte Carlo technique. However, for multi-dimensional problems, the evaluation of the integrand may be too difficult to perform by conventional numerical methods. In addition, by the use of random numbers, Monte Carlo methods are able to simulate the component form of complex physical processes. The solution

of the integro-differential Boltzmann equation for example, which describes mathematically the transport of radiation, may be solved by standard numerical techniques (Bennett and Beck, 1967) or by Monte Carlo methods.

The emission of radiation from atoms and its interaction with matter is an example of a natural stochastic process since each individual event is to some degree un-predictable. The Boltzmann equation can be effectively solved by a rather straight forward simulation of the stochastic physical processes involved, the events and outcomes of which are followed and recorded over many thousands of event histories. There are several characteristics that are necessary to fulfil simulations of this kind. A clear statement of the system to be simulated is needed. The probability distribution functions that will be involved must be identified, defined and sampled. Monte Carlo sampling can be used to generate the random distances that monoenergetic photons travel between interactions in a medium. The law governing this is the exponential probability law. The inclusion of charged particles leads to a complex and time consuming simulation, since the radiation no longer travels in straight lines between well separated collisions or interactions. Kahn (1950), Raeside (1974), Carter & Cashwell (1975) and Turner *et al* (1985) have produced introductory texts on Monte Carlo methods applied to neutron and photon transport problems.

Background effects owing to source scattering are unique to experimental arrangement in the real world. The absence of this gives the true detector response and many Monte Carlo calculations are performed by only considering point monoenergetic sources (coaxially with detectors) and bare right cylindrical detectors within infinite vacuum: Berger and Doggett (1956), collimated source; Berger and Seltzer (1972); Beattie and Bryne (1974); Beam *et al* (1978), arbitrarily located point sources. The difference between such calculations and experiments can be significant especially in regions of low pulse height and low response (the valley between full energy peak and Compton edge). However, Belluscio *et al* (1974) conducted Monte Carlo simulations of NaI(Tl) detectors and thick disc sources at close separations, thus accounting for source self absorption and scattering effects. Capponi *et al* (1983) have developed a Monte Carlo code to deal with extended γ-ray sources and cylindrical detectors, however only the

front face of the crystal contributes to the scoring method and analytic expressions for absorption coefficients have been used in only four crude energy intervals from 0-20 MeV.

6.2 Summary of Monte Carlo Code I (MCI)

6.2.1 Geometrical Coordinate System

A γ-ray is traced in a fixed 3-dimensional rectangular Cartesian reference frame (z, x & y), inside which ground, air and detector elements are defined. The vertical height is taken from the ground surface (at z=0) to the centre of the detector. The detector is positioned in air directly over the x, y origin. Right circular cylindrical and rectangular detector dimensions may be freely chosen as can length, width and depth of ground.

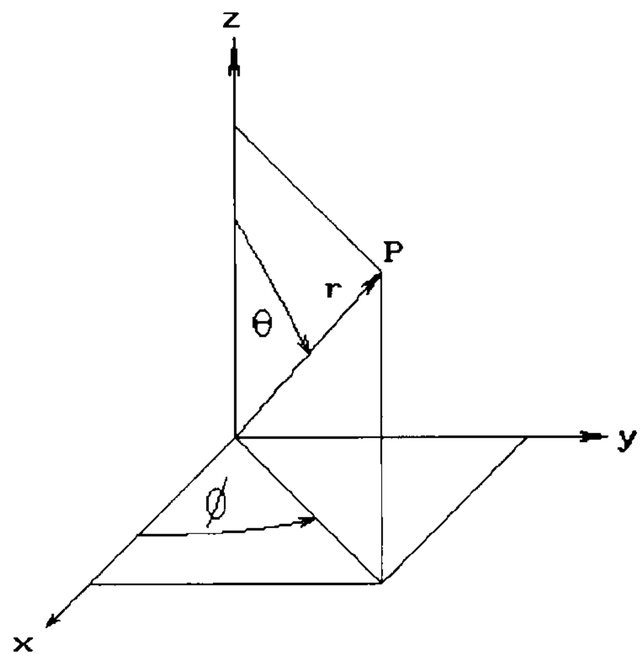

Figure 6.1 Spherical polar co-ordinates.

For a point P in the coordinate system shown in figure 6.1, the following equations may be written:

$$P_x = r \sin\theta \cos\phi \tag{6.1}$$

$$P_y = r \sin\theta \sin\phi \tag{6.2}$$

$$P_z = r \cos\theta \tag{6.3}$$

6.2.2 Source Characterisation

Initial γ-ray emission is assumed to be isotropic and singular in energy. Random sampling of the polar angle Θ $[0,\pi]$ and azimuthal angle ϕ $[0,2\pi]$ from uniform distributions provides the initial directional parameters of the source γ-ray.

A random variable z is obtained from the cumulative probability distribution of the function to be sampled $f(z)$ by solving for z:

$$R = \frac{\int_{zmin}^{z} f(z)\ dz}{\int_{zmin}^{zmax} f(z)\ dz} \tag{6.4}$$

where pseudo-random number R is chosen from a uniform distribution $[0,1]$. It follows that

$$\theta = \cos^{-1}(1-2R) \tag{6.5}$$

$$\phi = 2\pi R \tag{6.6}$$

where R is a pseudo-random number uniformly distributed between 0 and 1, generated by PC internal routines and all angles are in radians. Energy of the source γ-ray is characteristic of the nuclear decay of the radionuclide.

6.2.3 Path Tracing

6.2.3.1 Direction Cosines

The description of the directional sense of the γ-ray is made by using *directional cosines* within a local frame of reference (fig. 6.2).

Thus,

$$\cos\alpha = \sin\theta \cos\phi \qquad (6.7)$$

$$\cos\beta = \sin\theta \sin\phi \qquad (6.8)$$

$$\cos\gamma = \cos\theta \qquad (6.9)$$

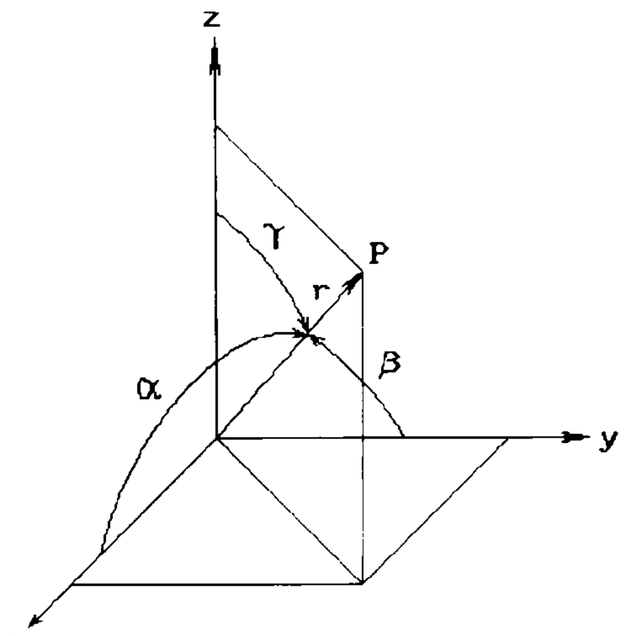

Figure 6.2 Direction cosines α, ß and γ.

This local frame moves within the main reference frame, attached to the γ-ray and along its straight line path. New direction cosines ($\cos\alpha'$, etc) of an emergent γ-ray following an interaction (with polar Θ' and azimuthal angles ϕ'), can be related to the direction cosines of the original ($\cos\alpha$, etc) by rotation of coordinates (Zerby, 1963).

For $\cos\gamma \neq 1$ then,

$$\cos\alpha' = \cos\theta' \cos\alpha + \left[\frac{(1-\cos^2\theta')}{(1-\cos^2\gamma)}\right]^{\frac{1}{2}} [\cos\alpha \cos\gamma \cos\phi' - \cos\beta \sin\phi'] \qquad (6.10)$$

$$\cos\beta' = \cos\theta' \cos\beta + \left[\frac{(1-\cos^2\theta')}{(1-\cos^2\gamma)}\right]^{\frac{1}{2}} [\cos\beta \cos\gamma \cos\phi' + \cos\alpha \sin\phi'] \qquad (6.11)$$

$$\cos\gamma' = \cos\theta' \cos\gamma - \left[\frac{(1-\cos^2\theta')}{(1-\cos^2\gamma)}\right]^{\frac{1}{2}} [1-\cos^2\gamma] \cos\phi' \qquad (6.12)$$

For $\cos\gamma = +1$ or -1 then,

$$\cos\alpha' = (1 - \cos^2\theta')^{\frac{1}{2}} \cos\phi' \qquad (6.13)$$

$$\cos\beta' = (1 - \cos^2\theta')^{\frac{1}{2}} \sin\phi' \qquad (6.14)$$

$$\cos\gamma' = \frac{\cos\gamma}{|\cos\gamma|} \cos\theta' \qquad (6.15)$$

6.2.3.2 Pathlength

Pathlength is a distance a γ-ray traverses through a medium or several composite media before an interaction takes place. This is obtained by random sampling an exponential probability distribution defined by the total attenuation coefficients of the medium through which the γ-ray is traversing.

From equation 6.4 therefore

$$R = \frac{\int_0^x I_0 e^{-\mu x}\, dx}{\int_0^\infty I_0 e^{-\mu x}\, dx} \tag{6.16}$$

This may be solved by analytical integration and rearranged for the mean pathlength x,

$$x = -\frac{1}{\mu}\ln(1-R) \tag{6.17}$$

where, μ is the total linear attenuation coefficient. This is valid for a single medium. For heterogeneous media however the following expression may be used (Shreider, 1966):

$$x = \sum_{j=1}^{j=l-1} x_j - \frac{\left[\sum_{j=1}^{j=l-1} \mu_j x_j + \ln R\right]}{\mu_l} \tag{6.18}$$

where, l is the total number of media through which a γ-ray passes and x_j represents the individual pathlength in each medium.

Since the direction cosines of a γ-ray are known, together with the source position (or position of last interaction), by using the simple rules of analytical geometry it is possible to both identify the media through which a traverse is made together with the

respective distances between media interfaces and the point at which an interaction takes place. In terms of applying this technique to numerical computing, the most difficult task is to ensure that rounding errors do not malfunction the code, by incorrectly calculating distances between the boundary regions.

6.2.4 Selection of Interaction

The interactions that are possible at energies up to 3 MeV consist of the following:

a). Rayleigh scattering (σ_{Ray});
b). Photoelectric absorption (τ);
c). Compton scattering (σ_{Comp});
d). Pair production (χ).

The probability that one of these interactions occurs is a function of atomic number and γ-ray energy. The magnitudes of each attenuation coefficient relative to the total (μ) can provide the weighting factors by which one is chosen as the most likely to occur (Zerby, 1963).

If R is a uniformly distributed pseudo-random number,

$$R = \frac{\sigma_{Ray}}{\mu} + \frac{\tau}{\mu} + \frac{\sigma_{Comp}}{\mu} + \frac{\chi}{\mu} \qquad (6.19)$$

the interaction may be chosen such that if $R < \sigma_{Ray}/\mu$ then Raleigh scattering occurs; if $\sigma_{Ray}/\mu \leq R < \sigma_{Ray}/\mu+\tau/\mu$ a photoelectric absorption occurs; if $\sigma_{Ray}/\mu+\tau/\mu \leq R < \sigma_{Ray}/\mu+\tau/\mu+\sigma_{Comp}/\mu$ a Compton scattering event occurs and if $\sigma_{Ray}/\mu+\tau/\mu+\sigma_{Comp}/\mu \leq R < \sigma_{Ray}/\mu+\tau/\mu+\sigma_{Comp}/\mu+\chi/\mu$ pair production occurs.

6.2.5 Consequence of Interaction

6.2.5.1 Rayleigh Scattering

The primary γ-ray is scattered without energy loss. It is assumed that this scattering is predominantly in the forward direction. Effectively no change to the incident γ-ray occurs. It is often convenient to ignore Rayleigh scattering by making the cross-section zero.

6.2.5.2 Photoelectric Absorption

In this interaction an incident γ-ray is absorbed and a photoelectron ejected (K or L-shell most likely) from an atom. The photoelectron has energy equal to the γ-ray energy minus binding energy. The binding energy appears as an x-ray or Auger electron, that is assumed to be deposited close to the first interaction centre. The incident γ-ray thus transfers all its energy to the medium.

The angular distribution of photoelectrons is sampled from which the direction cosines are determined. Potential escape of photoelectrons from within a detector and hence only partial energy deposition can then be evaluated. Random sampling to obtain the polar angle of the photoelectron Θ is achieved by numerical integration of equation 6.20 (Compton and Allison, 1935), (Lal and Iyengar, 1970), and the use of general expression 6.4:

$$\frac{dn}{d\Omega} = A\sin^2\theta\left[1+2\beta\left(1+\frac{E_{be}}{E_e}\right)\cos\theta\right] \qquad (6.20)$$

where, A is a constant

E_e is the photoelectron energy and E_{be} is the binding energy of the K-shell (33.2 keV)

dn = number of photoelectrons ejected into a small solid angle $d\Omega$ making an angle Θ with the photon

$\beta = v/c$, v being the velocity of the ejected photoelectron and $c = 3\times10^8$ ms^{-1}

Lapp & Andrews (1972) provide an alternative formula.

At low photon energies a $\sin^2\theta$ angular distribution is formed with a maximum at right angles to the photon direction (figure 6.3). At higher photon energies, the distribution leans towards a forward direction (figure 6.4).

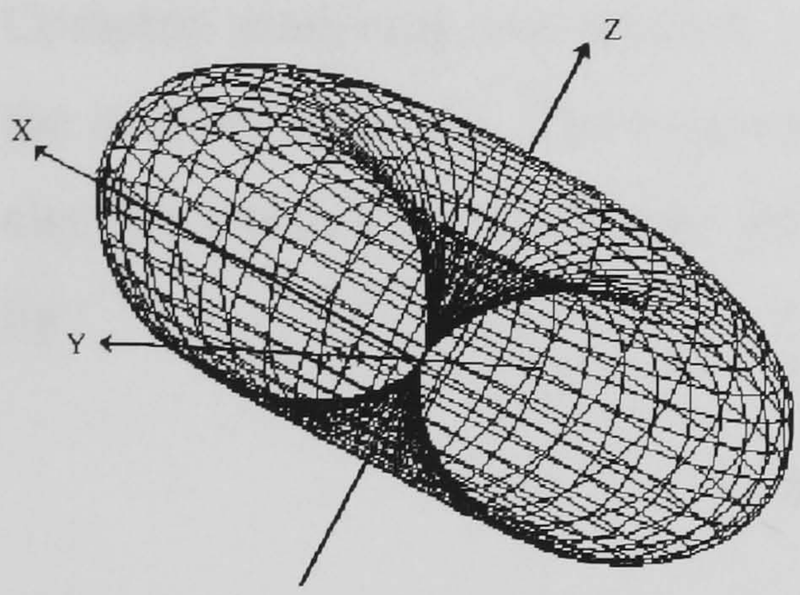

Figure 6.3 Angular distribution of photoelectrons at low energy ($\approx$50 keV).

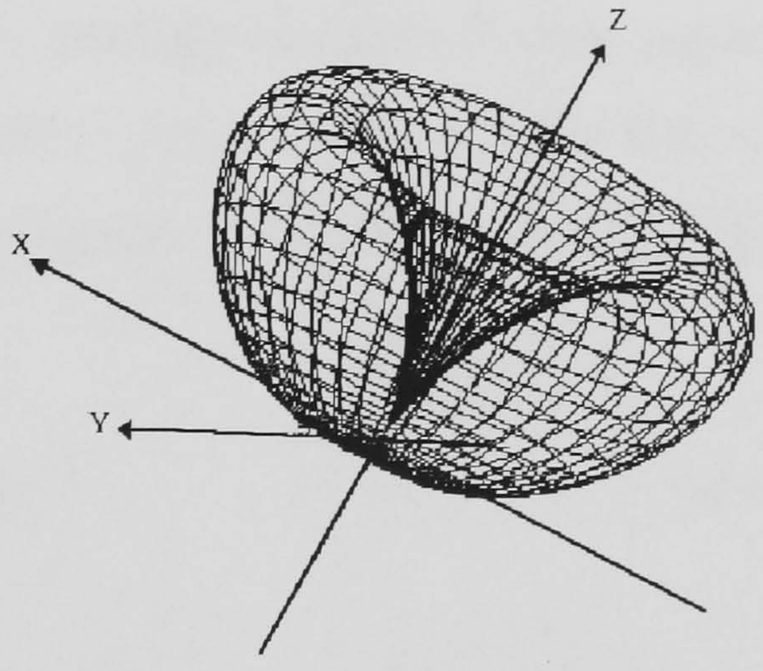

Figure 6.4 Angular distribution of photoelectrons at high energy ($\approx$500 keV).

Sampling was done in small increments (of 1°) and normalised to a pseudo-random number R until the right hand side of equation 6.21 is $\geq R$.

$$R = \frac{\int_0^{\theta} \left(\frac{dn}{d\Omega}\right) d\Omega}{\int_0^{\pi} \left(\frac{dn}{d\Omega}\right) d\Omega} \qquad (6.21)$$

where $d\Omega = 2\pi \sin\theta \, d\theta \, d\phi$. The azimuthal angle ϕ is obtained by equation 6.6. Θ and ϕ are with respect to the direction of the primary γ-ray.

The photoelectron energy is,

$$E_e = E_\gamma - E_{be} \qquad (6.22)$$

where E_γ is the γ-ray energy.

Fluorescent radiation and Auger electrons following photoelectric absorption are assumed to be totally absorbed.

6.2.5.3 Compton Scattering

A γ-ray may partially transfer energy to a free or loosely bound orbital electron through Compton scattering. An incident γ-ray will scatter through an angle Θ with respect to the original direction. The trajectories of the incident γ-ray, scattered γ-ray and recoil electron are in the same plane. Therefore Θ is correlated to the recoil electron angle ϕ by

$$\cot\theta = (1+\alpha)\tan\frac{\phi}{2} \qquad (6.23)$$

The probability of Compton scattering is a function of electron density and therefore increases linearly with atomic number. It is a function of energy, gradually falling with increasing energy. The three Klein-Nishina equations give the total probability of photon removal from the primary beam (attenuation) as a function of scattering angle, the probability of photon scattering from the beam as a function of scattering angle, and the probability of true absorption of the beam of photons as a function of scattering angle. The total differential Klein-Nishina cross-section per electron for scattering a photon in the direction Θ per unit solid angle shows the angular distribution of scattered γ-rays and is given by

$$\frac{d_e\sigma}{d\Omega} = r_0^2\left[\frac{1}{1+\alpha(1-\cos\theta)}\right]^2\left[\frac{1+\cos^2\theta}{2}\right]\left[1+\frac{\alpha^2(1-\cos\theta)^2}{(1+\cos^2\theta)[1+\alpha(1-(\cos\theta)]}\right]$$

(6.24)

where, $r_0=2.818\text{x}10^{-13}$ cm

The distribution becomes more peaked in the forward direction as the incident γ-ray energy increases (figure 6.5 to figure 6.6).

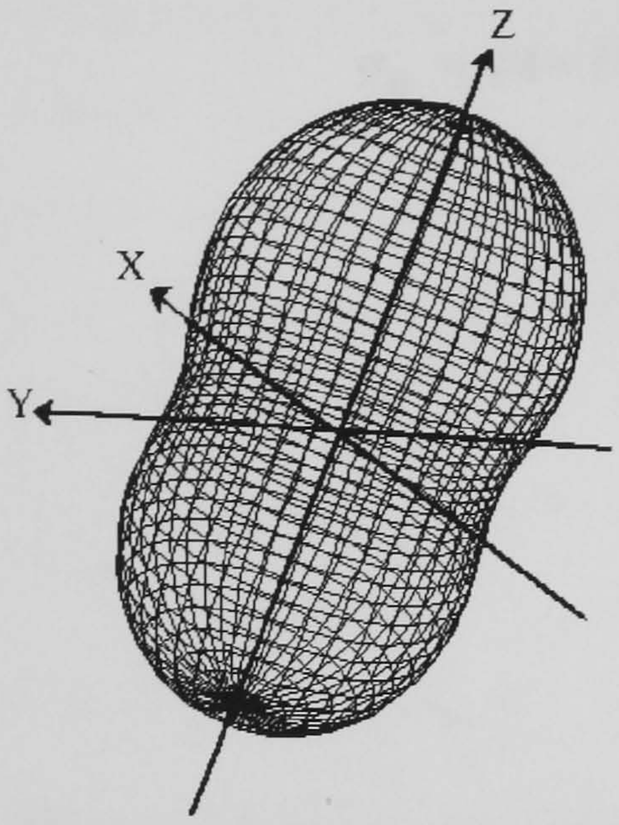

Figure 6.5 Angular distribution of scattered γ-rays at low incident energies ($\approx$50 keV).

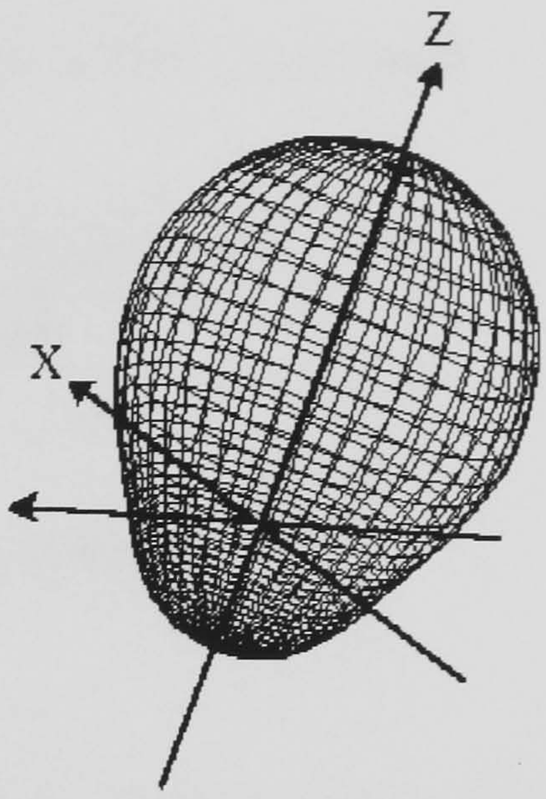

Figure 6.6 Angular distribution of scattered γ-rays at high incident energies ($\approx$500 keV).

The total Compton cross section (cm^2) per electron is obtained by integrating expression 6.24 over the polar angle Θ and azimuthal angle ϕ (0 to 2π).

$$ {}_e\sigma = 2\pi r_0^2 \left[\frac{1+\alpha}{\alpha^3} \left[\frac{2\alpha(1+\alpha)}{1+2\alpha} - \ln(1+2\alpha) \right] + \frac{\ln(1+2\alpha)}{2\alpha} - \frac{1+3\alpha}{(1+2\alpha)^2} \right] $$

(6.25)

The Klein-Nishina formula for unpolarized primary radiation is randomly sampled to obtain the polar angle Θ, through which the γ-ray is scattered using the general expression 6.4. However, integration of equation 6.24 over the solid angle dΩ for ϕ [0,2π] and θ [0,θ] can be approximated by the expression (Grosswendt and Waibel, 1975);

$$\sigma_\theta = (4+10\alpha+8\alpha^2+\alpha^3)-(4+16+\alpha+16\alpha^2+2\alpha^3)\cos\theta$$

$$\frac{+(6\alpha+10\alpha^2+\alpha^3)\cos^2\theta-2\alpha^2\cos^3\theta}{2\alpha^2(1+\alpha-\alpha\cos\theta)^2}$$

$$+\frac{(\alpha^2-2\alpha-2)}{\alpha^3}\ln(1+\alpha-\alpha\cos\theta) \qquad (6.26)$$

where $\alpha = h\nu/mc^2$. The energy of the scattered γ-ray E_γ' is then given by equation 2.2.

The recoil electron energy is,

$$E_e = E_\gamma - E_\gamma' \qquad (6.27)$$

The recoil electron polar angle θ_e is given by

$$\theta_e = \tan^{-1}\left[\frac{E_\gamma'\sin\theta}{E_\gamma - E_\gamma'\cos\theta}\right] \qquad (6.28)$$

The azimuthal angle of the scattered γ-ray ϕ is given by equation 6.6 from which the recoil electron polar angle may be calculated;

$$\phi_e = \phi + \pi \qquad (6.29)$$

Compton scattering occurs in a plane, the azimuthal angle specifies the tilt of this plane. Therefore the azimuthal angle ϕ is uniformly distributed between 0 and 2π radians. Having obtained Θ, the energy loss of the γ-ray and kinetic energy of the recoil electron can be calculated.

Multiple compton scattering may result in total energy transfer.

6.2.5.4 Pair Production

At energies in excess of twice the rest mass of an electron, pair production becomes

energetically possible. However, it remains low in probability for energies of less than 2 MeV. An electron-positron pair is produced with kinetic energies equal and in any proportion, to the incident γ-ray less 1022 keV (2 times electron rest mass energy). The directions of each particle are determined and their path traced.

Total kinetic energy available to an electron-positron pair is,

$$E_{Tot} = E_{\gamma} - 2m_0c^2 \tag{6.30}$$

The total kinetic energy is divided such that,

$$E_{\beta^-} = E_{Tot}R \tag{6.31}$$

and

$$E_{\beta^+} = E_{Tot}(1-R) \tag{6.32}$$

where R is a uniformly distributed pseudo-random number.

The angular distribution of the created electrons and positrons is a complicated function of photon energy. At just above threshold, they tend to favour the forward direction which becomes more pronounced at higher energies. For γ-ray energies near the pair production threshold, the polar and azimuthal angles of the electron-positron pair are given by (Belluscio *et al*, 1974):

$$\theta_{\beta^{\mp}} = \tan^{-1}\left(\frac{m_0c^2}{E_{\beta^{\mp}}}\right) \tag{6.33}$$

$$\phi_{\beta^-} = 2\pi R \tag{6.34}$$

$$\phi_{\beta^+} = \phi_{\beta^-} + \pi \tag{6.35}$$

Although it is assumed that a positron deposits all its kinetic energy before annihilating with an electron, *annihilation-in-flight* is possible but unlikely at the energies of less than 3 MeV.

6.2.5.5 Electron Interactions

The treatment of electron interactions has been made by a simple rather than rigorously exact approach. Energy degradation is by inelastic collisions with bound atomic electrons (mostly at low electron energies) and radiative collisions with nuclei and electrons (at higher energies). These losses are equal in NaI(Tl) at a critical energy $E_c = 16.75$ MeV (Mukoyama, 1976). The particles follow a very tortuous path, but migrate a shorter radial distance on average from the point of origin. It is assumed therefore that electrons travel in effectively straight lines and empirical formulae exist to calculate their pathlength for a given initial energy.

Electron interactions in the detector are of the prime importance in this application, rather than in the other media. Ranges in NaI are approximately 1mm per MeV. Electron leakage losses from the detector crystal become significant at high energies and within detector dimensions that are small in comparison with their ranges (Snyder, 1967). Energy deposition is calculated by using equation 6.36, solving for E_e and comparing particle range with distance to the crystal boundary. For detectors with dimensions that are large in comparison with the electron ranges encountered, it is often assumed that electrons deposit their energy at their point of formation.

Electron range in NaI(Tl) is given by Mukoyama (1976), Knasel (1970) and corrected from Wilson (1951):

$$Range = F \ln 2 \ln\left[1 + \frac{E_e}{E_c \ln 2}\right] 9.71 \qquad gcm^{-2} \tag{6.36}$$

where E_e is electron energy. The correction factor F is:

$$F = 1.5 - 1.3e^{-2E_e}$$

This expression gives good approximate values in the energy range 70 keV to 100 MeV. Positrons are treated in the same manner. However, at the end of their range, annihilation will occur producing two 511 keV γ-rays (travelling in opposite directions).

If pair production occurs inside the detector, subsequent annihilation may result in the loss of one or both of the annihilation photons and *first and second escape peaks* are produced. Isotropic emission is assumed: polar and azimuthal angles of annihilation quanta for a pseudo-random number R [0,1], are given by,

$$\theta_{\gamma_1} = \cos^{-1}(1-2R) \tag{6.37}$$

$$\theta_{\gamma_2} = \pi - \theta_{\gamma_1} \tag{6.38}$$

$$\phi_{\gamma_1} = 2\pi R \tag{6.39}$$

$$\phi_{\gamma_2} = \phi_{\gamma_1} + \pi \tag{6.40}$$

6.2.5.6 Bremsstrahlung

Bremsstrahlung losses become significant at high γ-ray energies and within dimensionally small detectors. At the electron energies considered here, merely a small fraction of electron kinetic energy is transformed into Bremsstrahlung radiation. However an algorithm has been included to treat such losses at a very simple level and only a single x-ray photon is created of mean energy E_{brem}. The fraction, ϵ_{brem}, of monoenergetic electron energy E_e transferred to bremsstrahlung is given by (Compton and Allison, 1935):

$$\epsilon_{brem} = E_e Z k \tag{6.41}$$

where $k \approx (0.7 \pm 0.2)\text{x}10^{-3}$ MeV^{-1}, Z=45.78 for NaI(Tl).

Emission direction is assumed isotropic and the x-ray is tested to see if it escapes the detector crystal. If this occurs then the original energy deposition in the detector is reduced by E_{brem}. No further path tracing is made and therefore no secondary bremsstrahlung is considered. If the x-ray does not escape the crystal, then it is assumed that energy E_{brem} is transferred completely via photoelectric absorption.

Isotropic angular distribution of bremsstrahlung photons is assumed since multiple scattering of electrons renders their direction very devious (individual bremsstrahlung photons are emitted in a forward direction).

Energy loss of electrons by inelastic collisions (causing ionization and excitation via Coulomb interactions with bound electrons) and radiative collisions (interactions with the electric field of nuclei), with the accompaniment of bremsstrahlung emission are dealt with by Giannini *et al* (1970), and Berger & Seltzer (1972) in a much more sophisticated manner for energies up to at least 6 MeV. A simplified approach given here is appropriate for the energy range considered.

6.2.6 Termination

All γ-rays are sequentially followed until their energy reduces below an arbitrary cut-off (10 keV) or they escape from the field of interest completely. If this occurs whilst inside the detector, all remaining energy is absorbed at that point. Many source γ-rays have to be followed until a sufficient number of events have been detected, since Monte Carlo simulation is bound by the same statistical laws as a real experiment. The preceding text describes an example of an analogue Monte Carlo code (Zerby, 1963), (Snyder & Knoll, 1966) A schematic diagram of the summary is shown in figure 6.7. MCI has been written in a high level, compiled basic language (Power/Turbo Basic) and can run on 33Mhz 486 processor or faster PC machines. A decade ago this was the sole province of main-frame or powerful minicomputers. Execution times are critically dependent upon geometry, source energy, energy cut-off and treatment of secondary radiations. Gorrod *et al* (1989) report the use of transputer arrays for parallel processing of efficient Monte Carlo codes. Thses are seen to have a promising future.

MCI has also been written in modular form: each module contains various subroutines and algorithms, that have been thoroughly tested and output compared with known data. The entire code has then been thoroughly tested to ensure no conflicts between modules exist. In this way, the program has been progressively developed in a manner that is consistent, easily documented, lends itself to improved sophistication and updates.

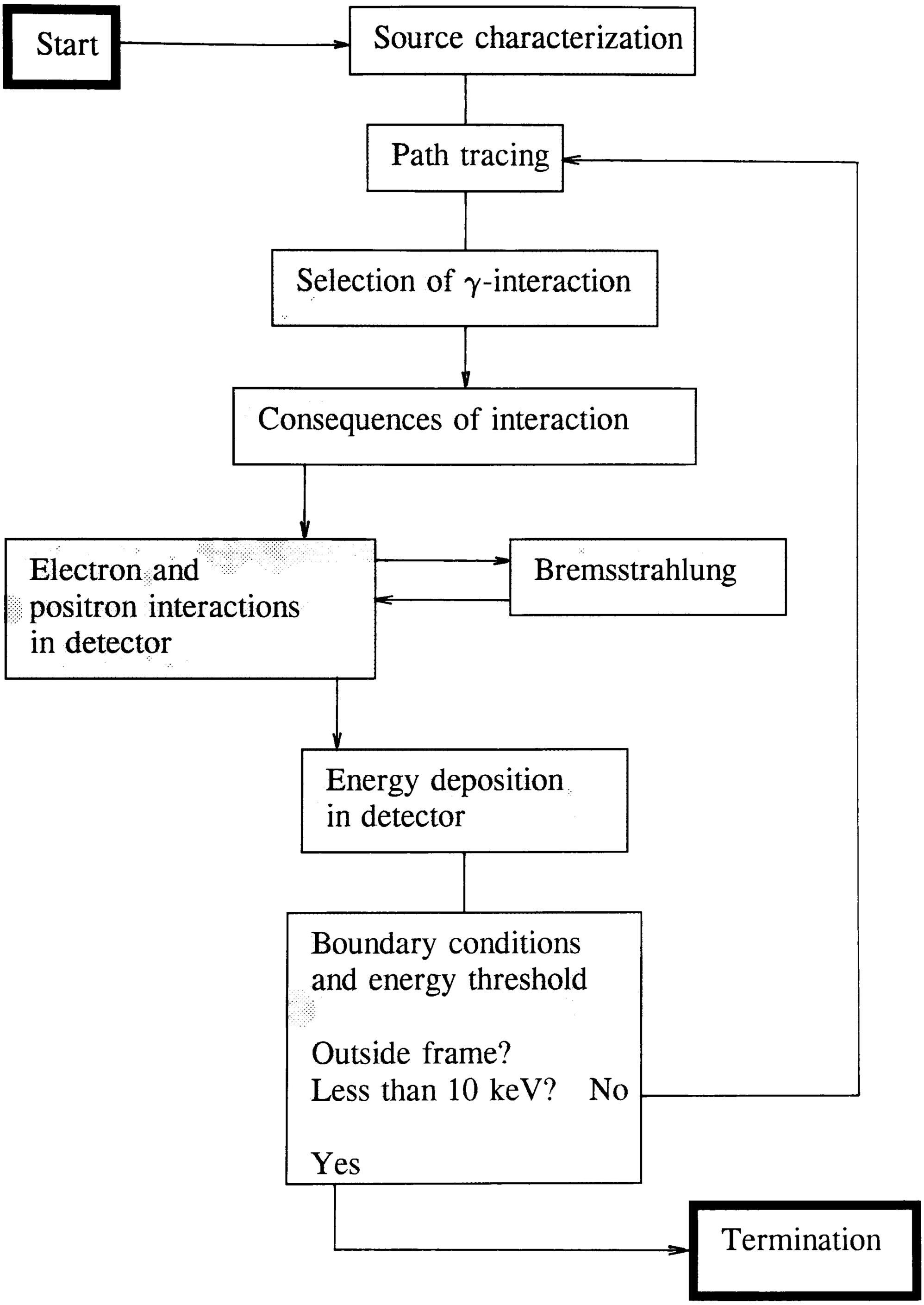

Figure 6.7 Analogue Monte Carlo code flow chart.

6.3 Interaction Cross Sections

Gamma-ray interaction cross sections have been taken from Storm and Israel (1970), and Hubbell (1977, 1982). In primary form, these are converted from units of barns per atom to linear attenuation and absorption coefficients for NaI(Tl) and mass attenuation and absorption coefficients for air, Beck soil, concrete and aluminium. The densities of these materials are: NaI(Tl), 3.67 g cm^{-3}; air $1.225x10^{-3}$ g cm^{-3} (U.S. Standard Atmosphere, 1976); Beck soil, 1.6 g cm^{-3}; concrete (K-1 calibration pad), 2.23 g cm^{-3} and aluminium 2.7 g cm^{-3}. Figure 6.8 below, shows the linear attenuation and absorption coefficients of NaI(Tl).

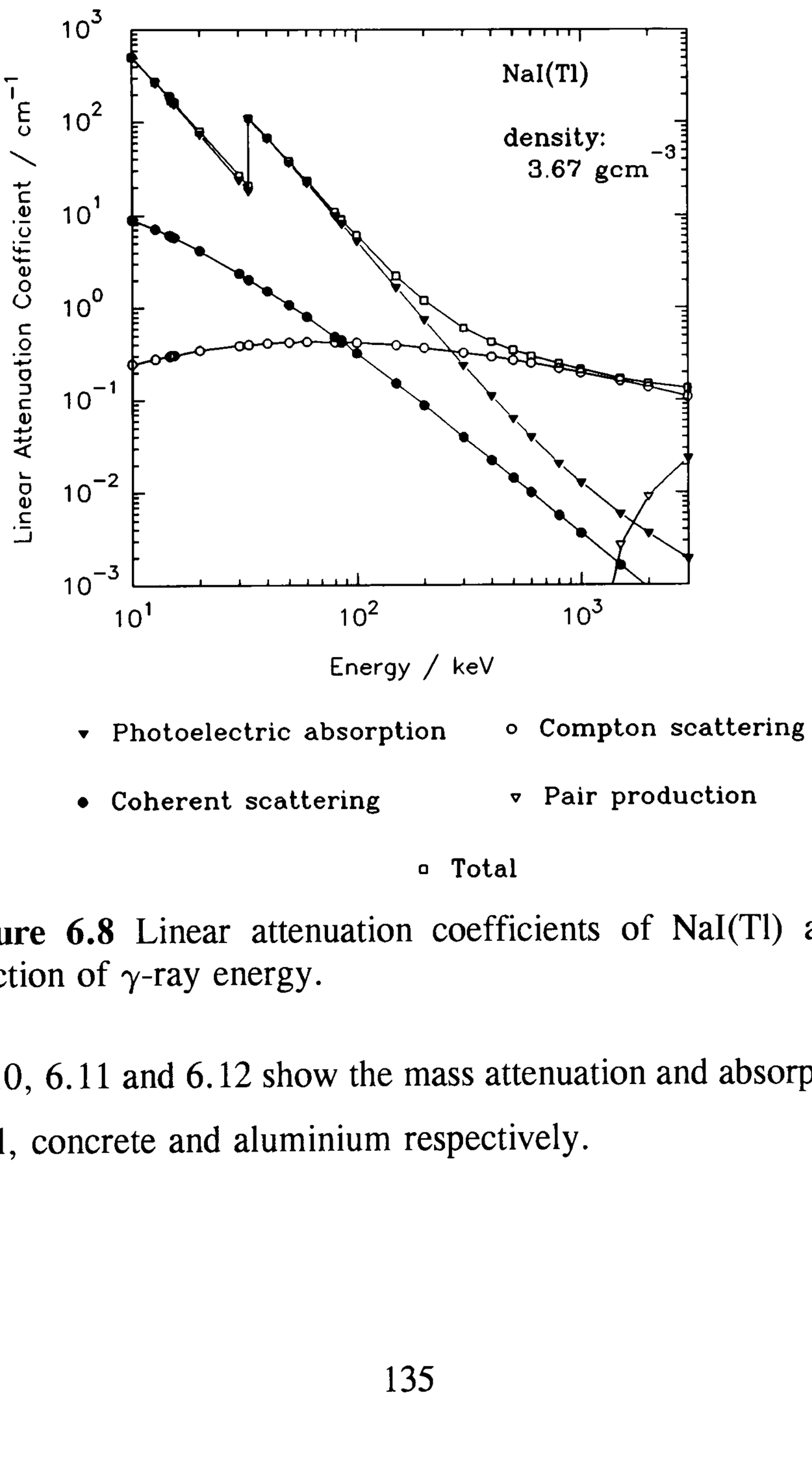

Figure 6.8 Linear attenuation coefficients of NaI(Tl) as a function of γ-ray energy.

Figures 6.9, 6.10, 6.11 and 6.12 show the mass attenuation and absorption coefficients of air, Beck soil, concrete and aluminium respectively.

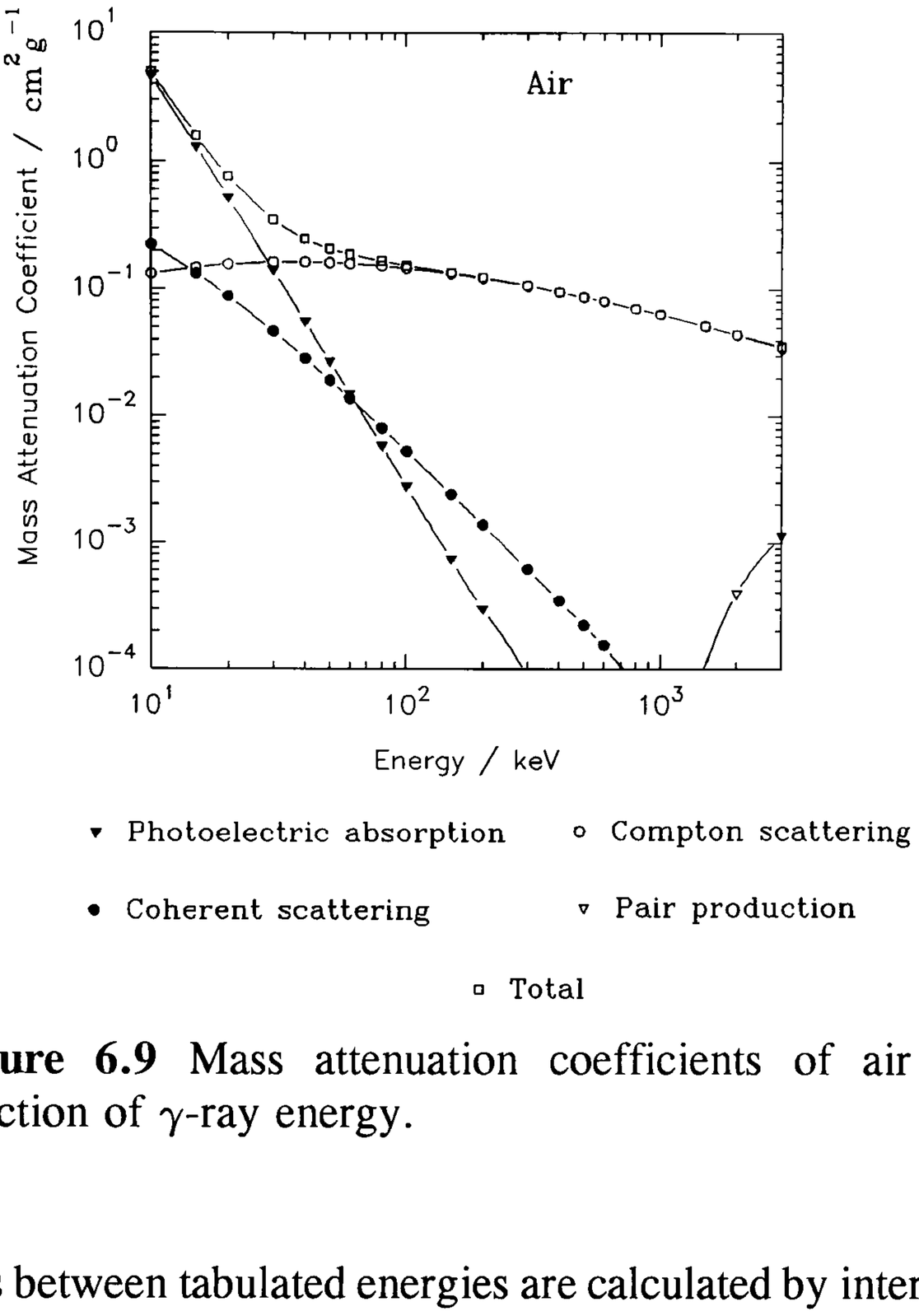

Figure 6.9 Mass attenuation coefficients of air as function of γ-ray energy.

Intermediate values between tabulated energies are calculated by interpolation from least squares fitting of second and third degree polynomials to the natural log of attenuation and absorption coefficients as a function of energy. This is also described by Avignone and Jeffreys (1981). Where absorption edges become significant factors of the photoelectric absorption cross section, the function is divided into several components to ensure the fit is good at these sudden inflexions. Tabulated data are quoted to be accurate within $\pm 5\%$ error and better for widely used elements. Accuracy of polynomial fitting is estimated to be within $\pm 4\%$.

The composition of air has been taken to be O: 23.2%; N: 75.5% and Ar: 1.3% by weight (20.95%; 78.09%; 0.93% by volume, respectively). The composition of Beck soil is listed in table 5.2.

The concrete composition used has been listed by Grasty *et al* (1991). It is described as being pad K-1 (the blank calibration pad). Samples of concrete were taken from

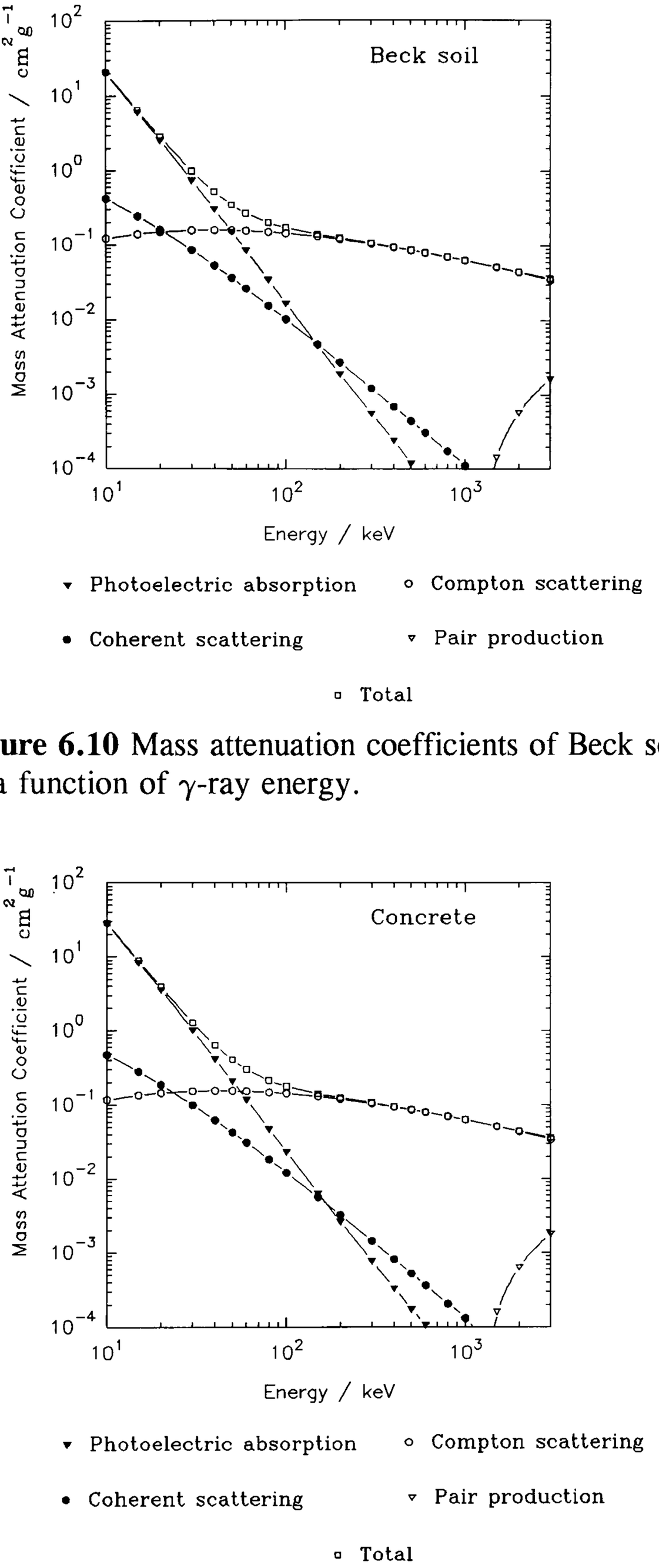

Figure 6.10 Mass attenuation coefficients of Beck soil as a function of γ-ray energy.

Figure 6.11 Mass attenuation coefficients of concrete as a function of γ-ray energy.

each of the cast pads during manufacture and show an accuracy in concentration of potassium, uranium and thorium of less than $\pm 1.5\%$.

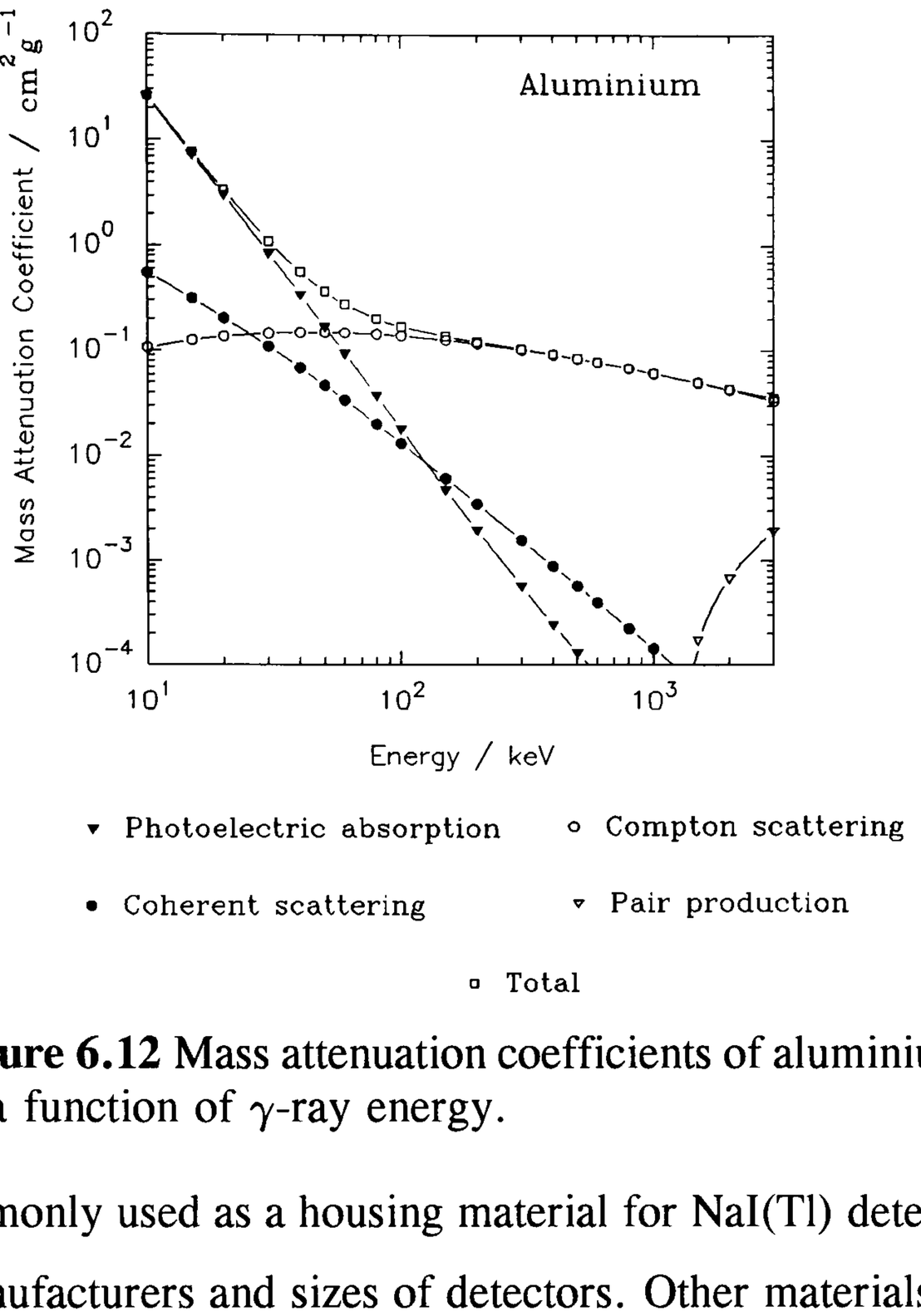

Figure 6.12 Mass attenuation coefficients of aluminium as a function of γ-ray energy.

Aluminium is commonly used as a housing material for NaI(Tl) detectors. Its thickness varies between manufacturers and sizes of detectors. Other materials used are stainless steel and some shock absorbing plastics and rubbers. A reflector is usually made of Al_2O_3 or MgO. These composite housing materials modify a γ-ray measurement most significantly at low energies. In order to keep the Monte Carlo code to manageable proportions these composites are replaced by a single layer of aluminium of thickness 0.0008m for 7.62x7.62 cm NaI(Tl) detectors. This was calculated on the basis of information from the manufacturer Bicron whose detector consisted of: aluminium window 0.000508m and Al_2O_3 reflector 0.00159m. The thickness of reflector has been replaced by an equivalent thickness of aluminium, 0.0003m. Chinaglia and Malvano (1966) conducted experimental measurements on 7.62x7.62 cm NaI(Tl) detectors, to determine the aluminium equivalent thickness (0.00114m for a Harshaw detector). Nardi (1970) found a satisfactory agreement with his experimental spectra if a thickness of aluminium 0.0024m was used: Saito and Moriuchi (1981) found 0.0023m and 0.0033m for the front face and side respectively. Rogers (1982) provides further reference data to produce more realistic calculated detector responses.

6.4 Detector Energy Resolution

The simulated spectrum is treated before final analysis in order to display the energy resolution characteristics of the detector employed.

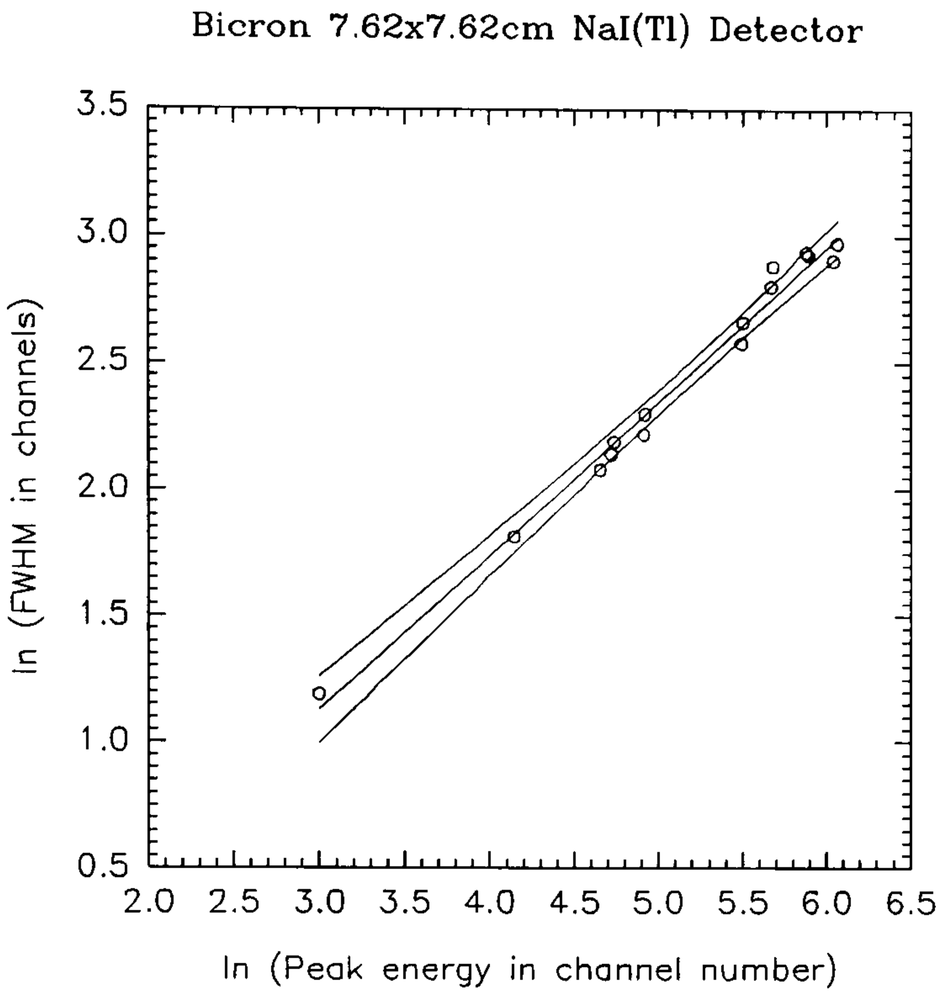

Figure 6.13 Energy resolution of 7.62x7.62cm NaI(Tl) detector, in terms of $\log_e$(FWHM channels) and $\log_e$(Peak energy in channels).

The line width is broadened with an experimentally measured resolution function. Figure 6.13 shows the natural log of FWHM (in channels) as a function of the natural log of peak channel position for a Bicron 7.62x7.62 cm NaI(Tl) detector. Ninety-nine percent confidence limits are indicated.

Figure 6.14 shows a resolution function of a 10.16x40.64x40.64cm NaI(Tl) aerial survey detector array. With careful trimming, the combined resolution of such a unit has a lower limit of typically about 9.5%. A lower limit discriminator is set higher in the aerial survey detector in order to lessen dead-time (there is a large low energy "tail") and hence the range of the resolution function is not quite as wide.

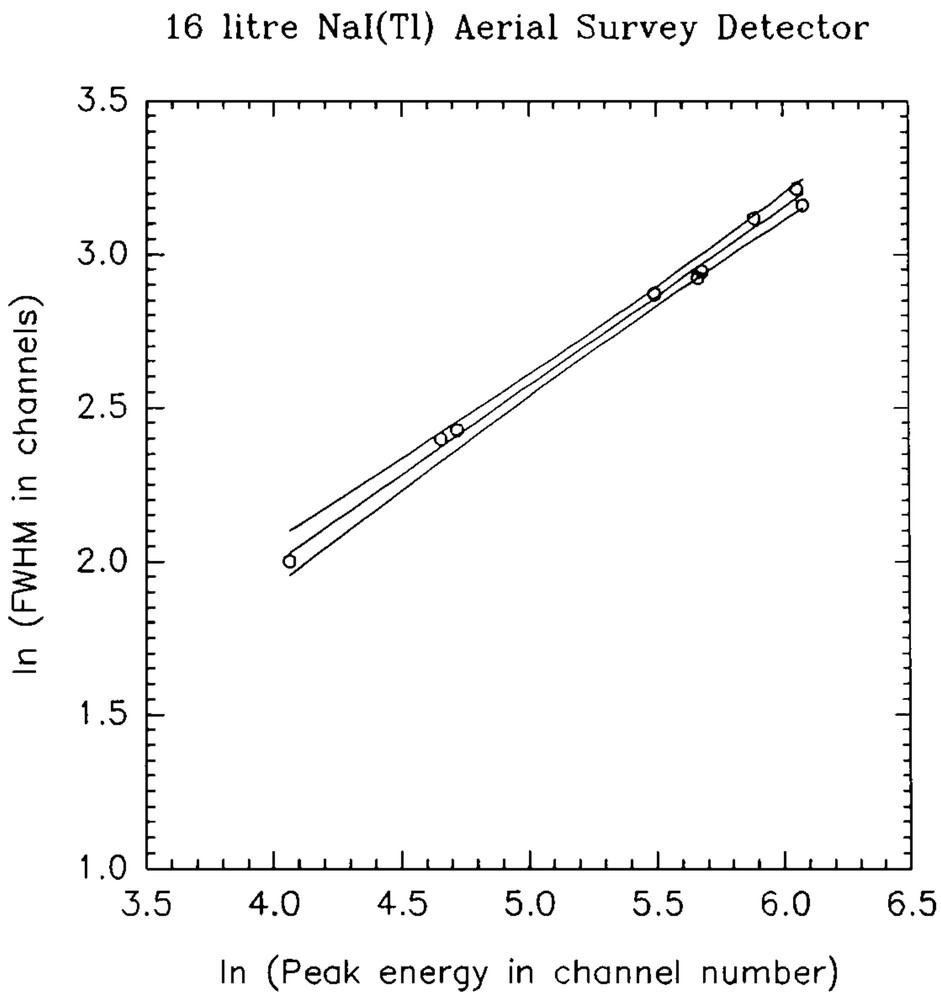

Figure 6.14 Aerial survey detector resolution function.

Markevich and Gertner (1989) provide a comparison of different methods of calculating FWHM and the relative errors associated with each. Here, two methods have been used: a simple estimation of the difference between left and right channels with respect to the peak channel, at which half the peak maximum occurs and a least squares Gaussian fit to channel data. Both gave comparable results.

The broadening procedure is applied after the main Monte Carlo computation and approximated by a Gaussian distribution: such a distribution is expected from the statistical nature of the production of photocathode electrons. The response of the detector at a particular pulse height is spread out over a range of adjacent pulse heights and then summed over the whole spectrum. Formally;

$$g(ch') = \sum_{ch=0}^{511} \frac{g(ch)}{\sqrt{2\pi}\,\sigma(ch)} .e^{-\frac{(ch'-ch)^2}{2\sigma(ch)^2}} \qquad (6.42)$$

where, $g(ch')$ is the channel contribution into channel ch' from $g(ch)$ owing to a Gaussian distribution with parameter $\sigma(ch)$=FWHM(ch)/2.3548.

A measured energy calibration of

$$\gamma\text{-}ray\ energy\ (keV) = 6.20155\ channel\ number - 44.9767 \qquad (6.43)$$

has been used throughout.

Non-proportionality of detector responses has been neglected and does not lead to significant error. Saito and Moriuchi (1981) investigated this by Monte Carlo methods and discovered that the effect on response function at energies of approximately less than 1 MeV is to improve the fit along the energy (channel) axis. The differences are very small however. At higher energies the effect becomes even less.

6.5 Results and Discussion I

A picture capture of Monte Carlo code I (MCI) in operation is shown in figure 6.15. It shows a point source of ^{137}Cs at the centre of a plane (x and y) and a 7.62x7.62 cm NaI(Tl) detector 0.1m above in the z-plane. Only a few of the path tracings are shown for clarity. An accumulated spectrum is shown within the panel to the lower right, before it has been processed with a resolution function.

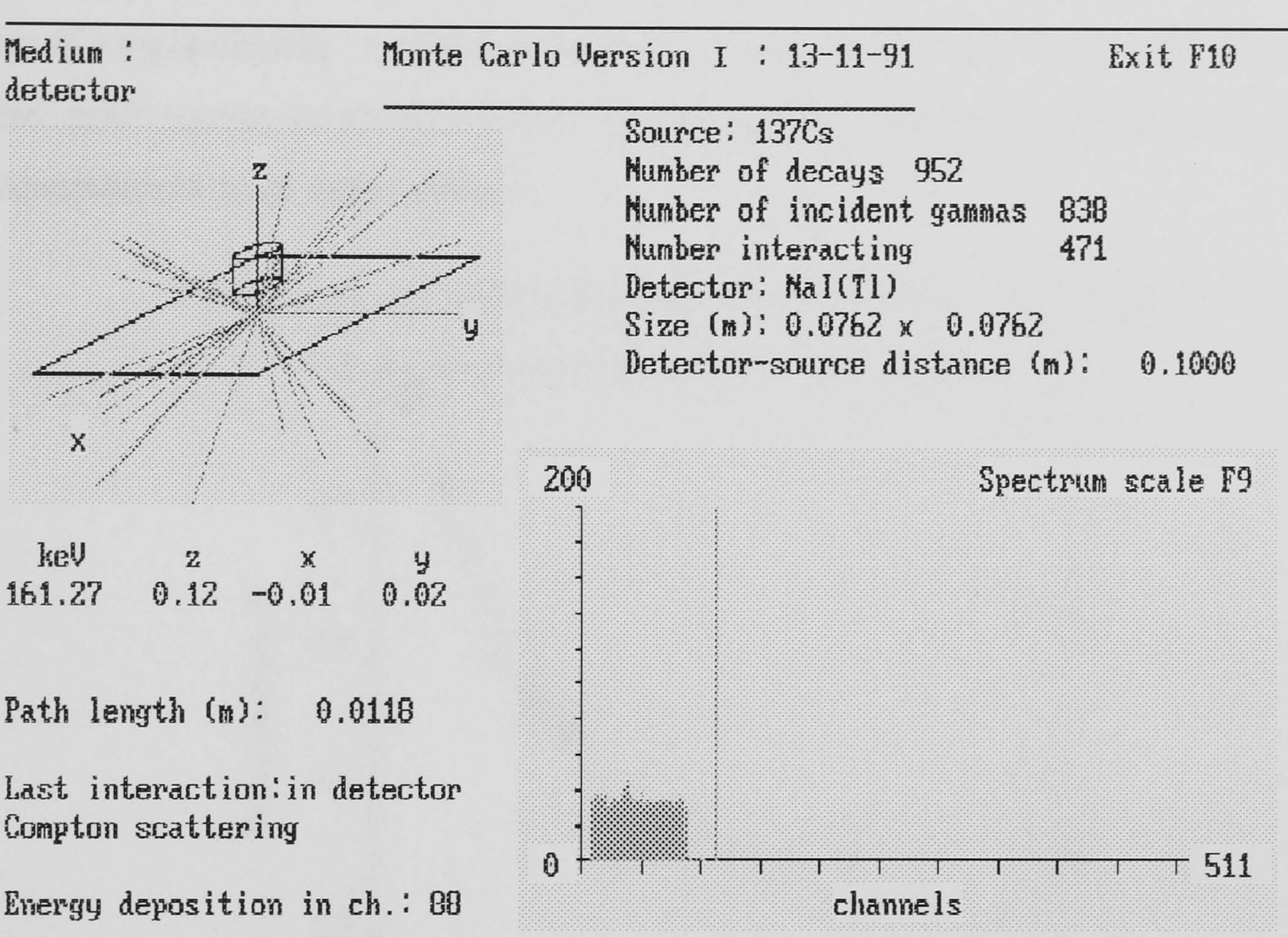

Figure 6.15 Monte Carlo code version I.

6.5.1 Validation

For the purposes of the following simulations it is assumed that the four crystal (total volume 16 litre) NaI(Tl) aerial survey detector behaves in the same manner as a single crystal of equal volume.

6.5.1.1 Detector Photofraction

The photofraction of a scintillation detector is a ratio of the peak to total counts and therefore an indicator of the relative full and partial absorption processes. It is primarily a function of detector size and γ-ray energy, although there is some source to detector distance dependency owing to different available interaction pathlengths within the solid angle presented to the detector from the source. For a point source at distances of greater than 0.5m, an approximately parallel beam of γ-rays is produced upon the front face of a right circular, cylindrical detector of diameter 7.62cm. Photofraction increases when point source-detector distances increase, up to a limiting value when parallel beam circumstances exist (*edge effects*).

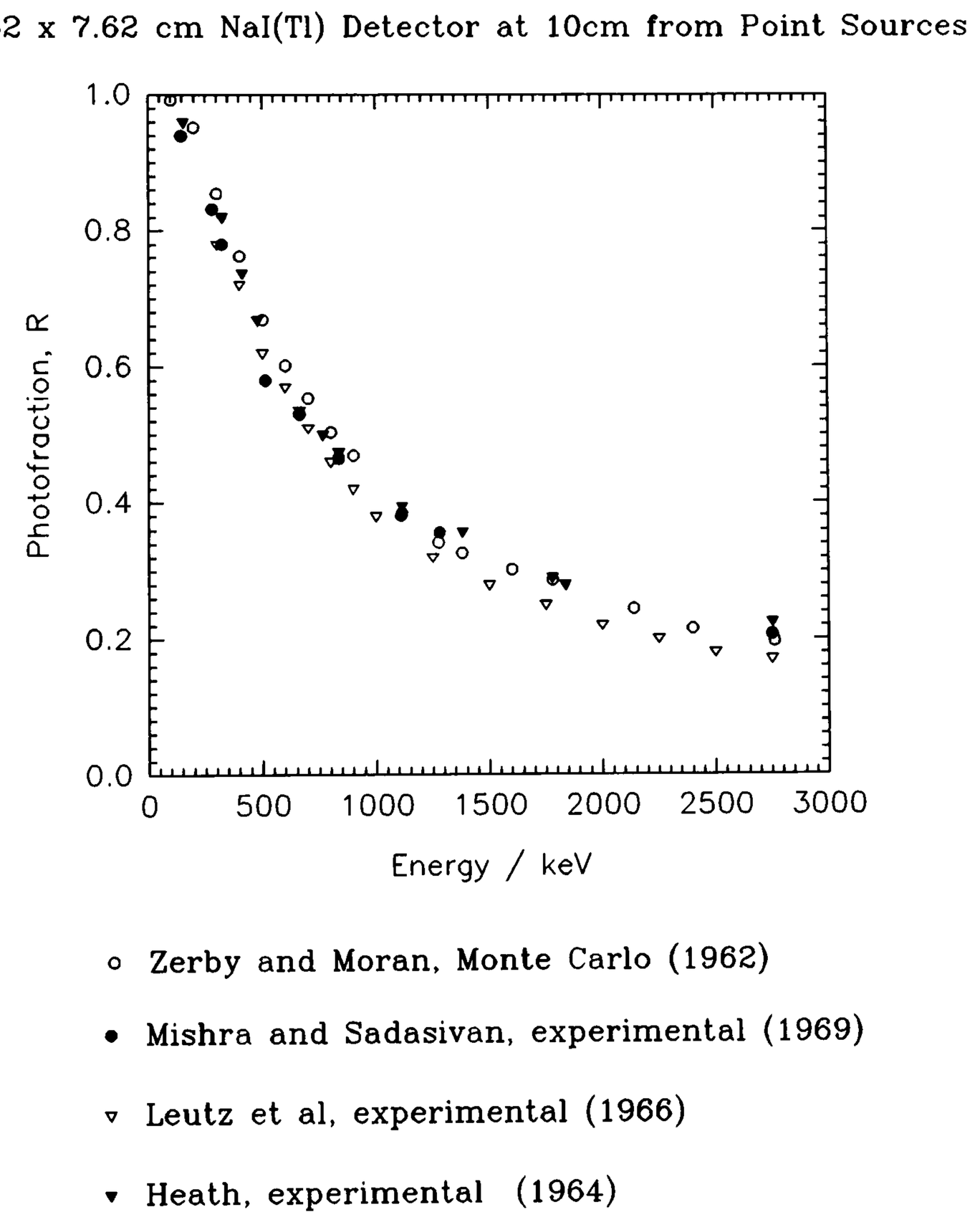

Figure 6.16 A comparison of photofraction variation from literature review.

Figure 6.16 shows a comparison of three experimental and single Monte Carlo

investigations of photofraction and γ-ray energy, at source detector distances of 10cm. The source is placed upon the central, cylindrical axis of a 7.62x7.62 cm NaI(Tl) detector.

Experimental measurements of photofraction are demanding and necessitate careful source preparations and large, empty rooms to minimise scattering effects. Even so, a backscatter peak may still persist owing to the close proximity of the photomultiplier tube and associated electronics. In such circumstances, an extrapolation of the Compton continuum across the region beneath the backscatter peak to zero bias channel is the usual method of subtracting the excess influences of backscatter peaks, x-rays, bremsstrahlung and beta particles (for the latter, good source encapsulation is the best method). It is also usual practice to include the pair escape peaks to the total intensity when present (Christaller, 1967). The accuracy of Monte Carlo calculations relies principally upon cross sectional data and treatment of interaction processes.

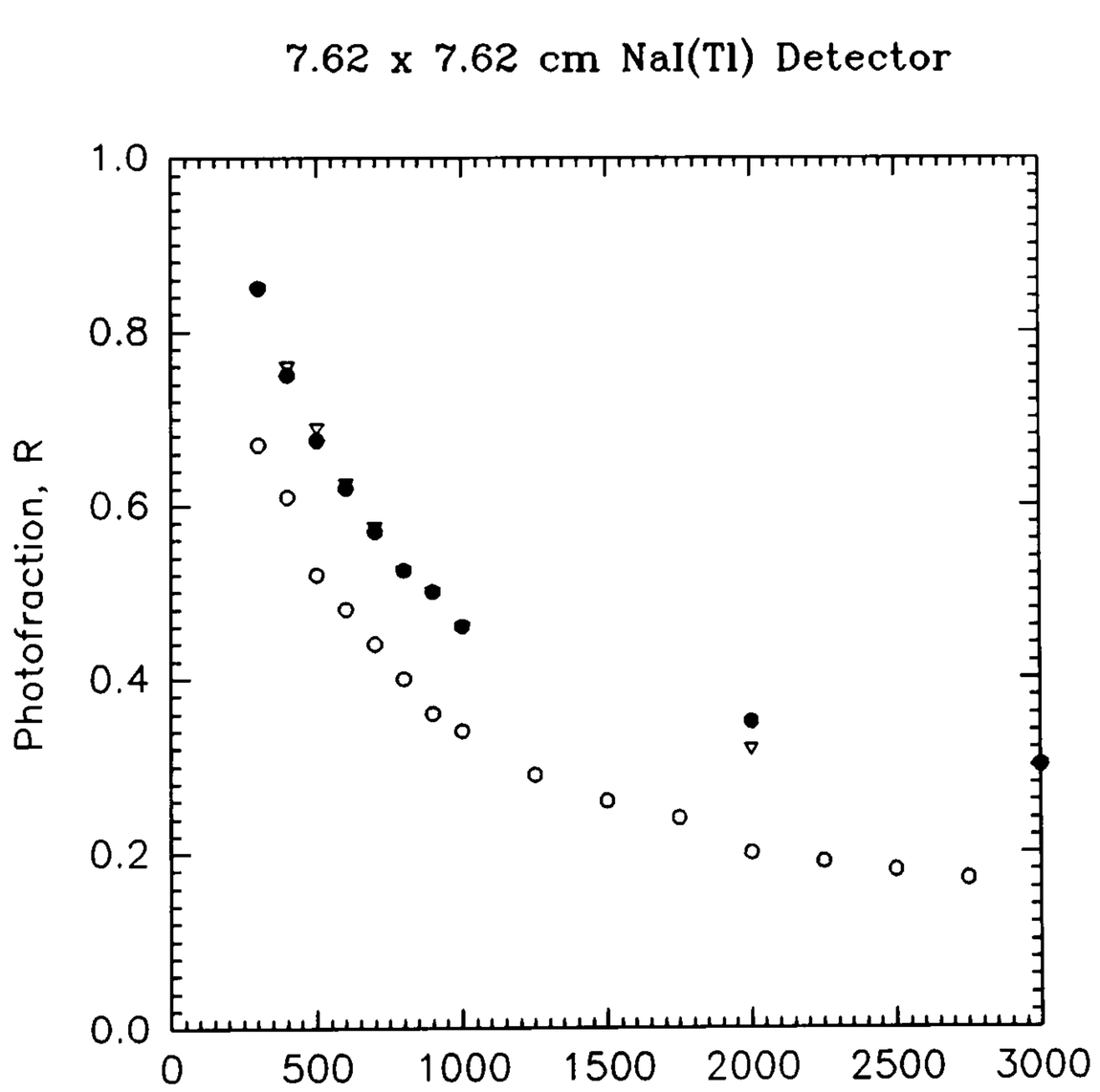

Figure 6.17 A comparison of photofraction data at extended distances.

Figure 6.17 shows a further comparison of photofraction at extended source detector distances. Weitkamp (1963) indicates little change in photofraction from 15 to 30cm source detector distance and is only slightly greater than that of figure 6.16 (at 10cm). Leutz *et al* (1966) show an experimental measurement taken at 50cm and is approximately 22% less than Weitkamp at 1000 keV. This may have been due to experimental difficulties. Bengtsson (1967) expresses a number of criticisms concerning evaluations of photofractions from different authors.

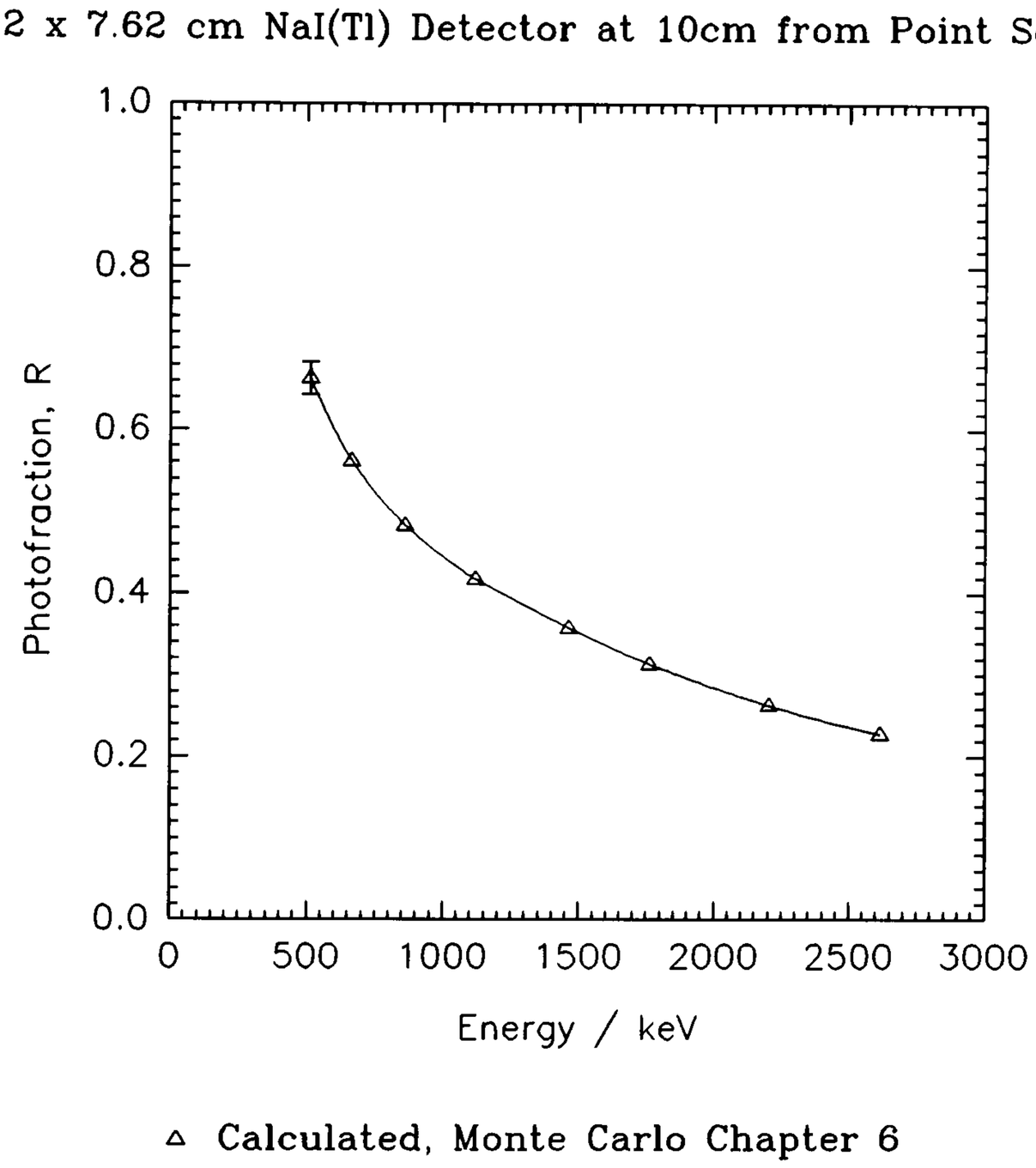

Figure 6.18 Monte Carlo calculated photofraction (Allyson).

Figure 6.18 shows photofraction determined using MCI, for point sources at 10cm from the front face of a 7.62x7.62 cm NaI(Tl) detector, without source or surrounding space scattering. Good agreement is seen in comparison with figure 6.16, thus validating MCI for this type of detector. Snyder (1967) reports that consideration of the escaping electrons and bremsstrahlung losses below 1.8 MeV has negligible effect on calculated photofraction. In general however, smaller values of photofraction are found in practice than by calculation and must be attributed to external scattering or background (Miller *et al*, 1957), the former frequently omitted from most Monte Carlo algorithms.

Cesana and Terrani (1989) have developed an empirical formula to calculate photofraction given volume of detector. Little published data has been found to compare photofractions of very large detectors, and so this formula and experimental measurements have been taken to establish the validity of photofractions of aerial survey detectors. Figure 6.19 shows data calculated using the Cesana and Terrani method. A photofraction of 0.69 occurs at 662 keV, for a 16 litre detector. Careful experimental measurements using this detector showed a photofraction of about 0.66 at the same energy, but this is probably underestimated owing to the presence of a strong backscatter peak (see fig. 6.21). Monte Carlo simulation of a 16 litre single crystal detector by MCI resulted in a photofraction of 0.79 at 662 keV. This is higher than expected and is attributed to the near absence of the packaging materials found in practice: each crystal is canned inside thin walled aluminium, with reflector and mechanically shock absorbing material, in addition to thermally insulating foam, hard plastic case and external aluminium frame.

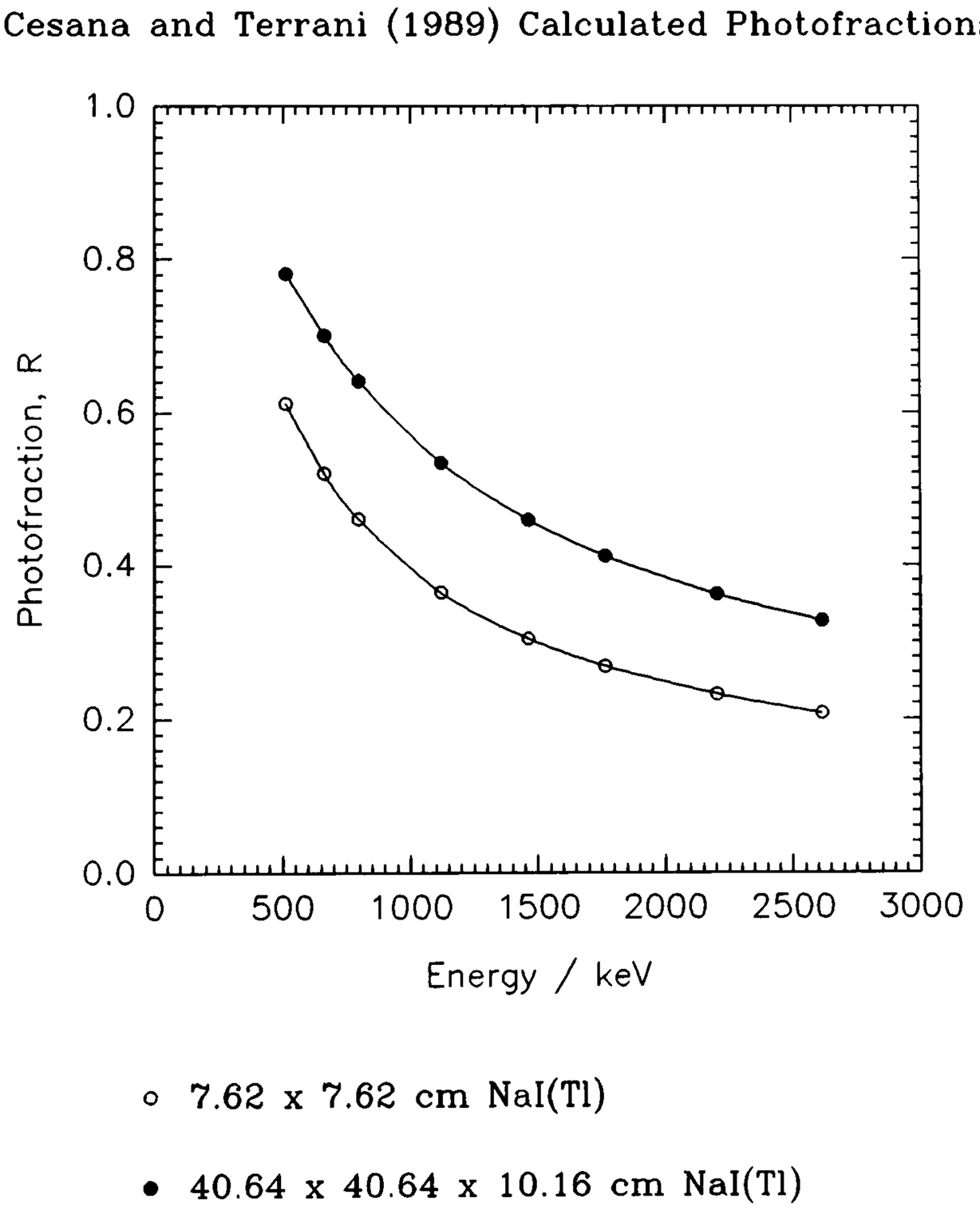

Figure 6.19 Empirical method by Cesana and Terrani (1989).

To improve the simulation for detector arrays it was decided to increase the aluminium representation of packaging materials used for small detectors from 0.0008 to 0.004m. This resulted in a photofraction of 0.74 at 662 keV (figure 6.20). Figure 6.21 shows the change in spectral shape as a result of additional scattering, predominantly in the forward direction: a filling of the valley between full energy peak and Compton edge occurs. The choice of aluminium thickness may still be conservative: Tsutsumi *et al* (1986) chose thicknesses of 0.01m and 0.0202m for the upper/lower and sides of a simulated detector respectively. This would have the effect of reducing photofraction further. The experimental measurement was made with a standard point reference source of ^{137}Cs (370kBq) held in air, 1m above the upper surface of the detector array. The detector was situated on a strong table, close to a plaster partition wall, and is likely to contribute to some scattering effects. The results have been simply normalised by adjustment of the relative peak heights.

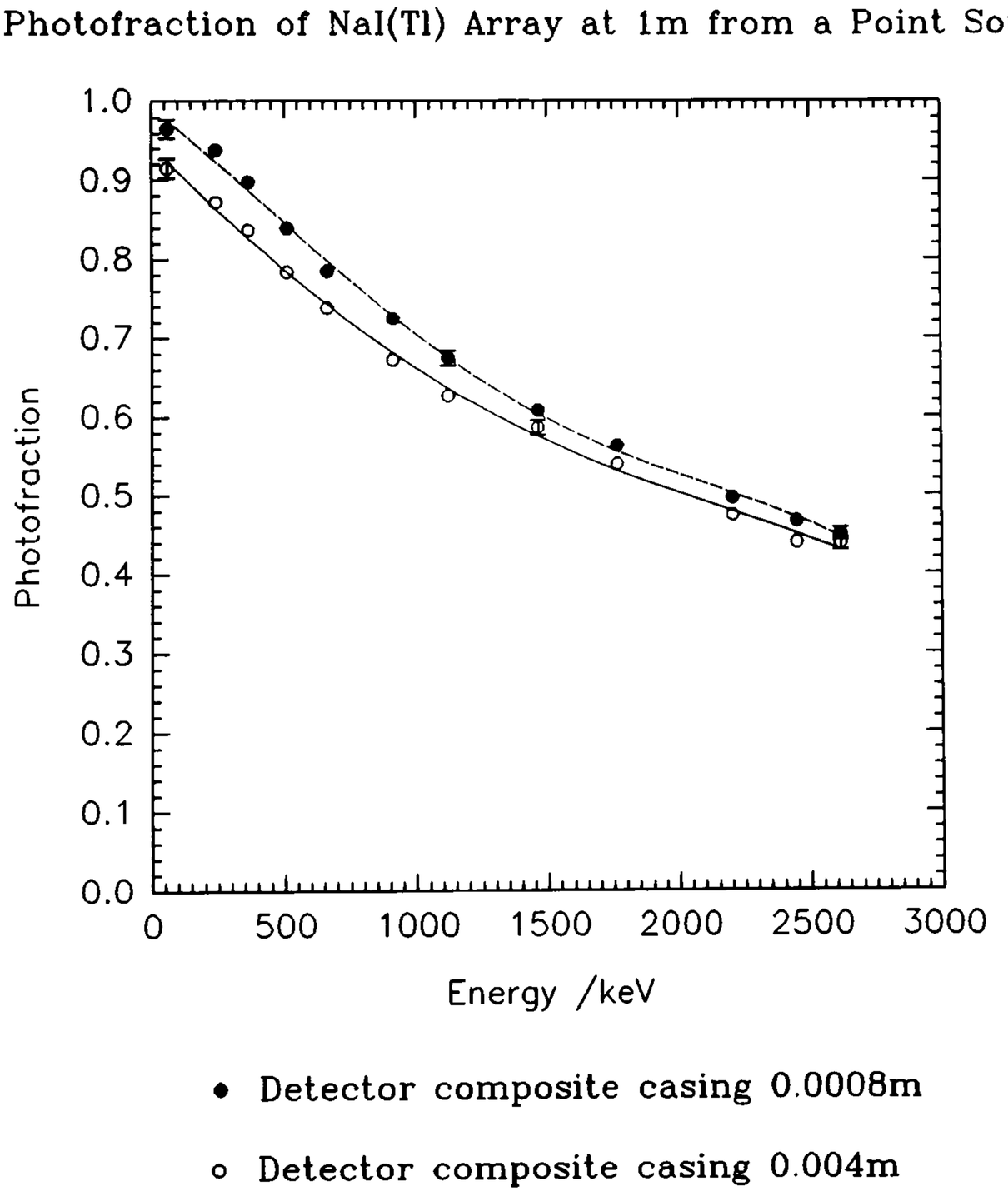

Figure 6.20 Photofraction of 40.64 x 40.64 x 10.16 cm NaI(Tl) detector and alternative housing thicknesses, by Monte Carlo methods (Allyson).

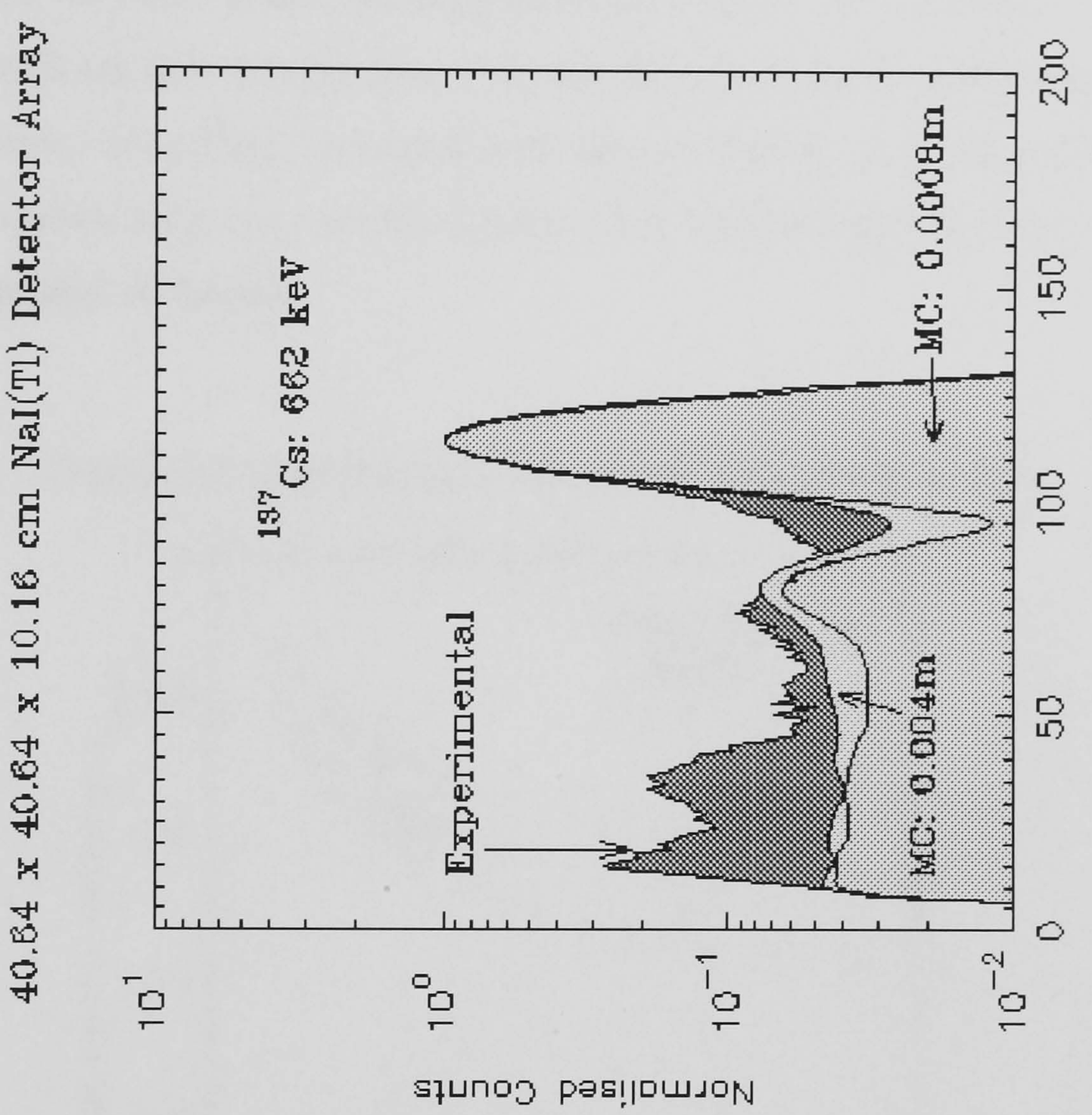

Figure 6.21 Experimental and Monte Carlo comparisons of ^{137}Cs spectra from 16 litre detector.

6.5.1.2 Detector Efficiencies

The total intrinsic efficiency $\varepsilon_{tot,int}$ calculated by Monte Carlo of a 7.62x7.62 cm NaI(Tl) detector, from point sources of various energies and distances, is shown in figure 6.22. A discrepancy between the results of Zerby & Moran (1962) and Grosswendt & Waibel (1976), for the same source detector distance is noted: the uncertainty of the latter is about $\pm 10\%$ and accounts for this. This may have been due to differences in interaction cross section, underlying assumptions or approximations. $\varepsilon_{tot,int}$ increases to a limiting value as a point source is removed further from the detector front face, until a parallel beam condition is reached.

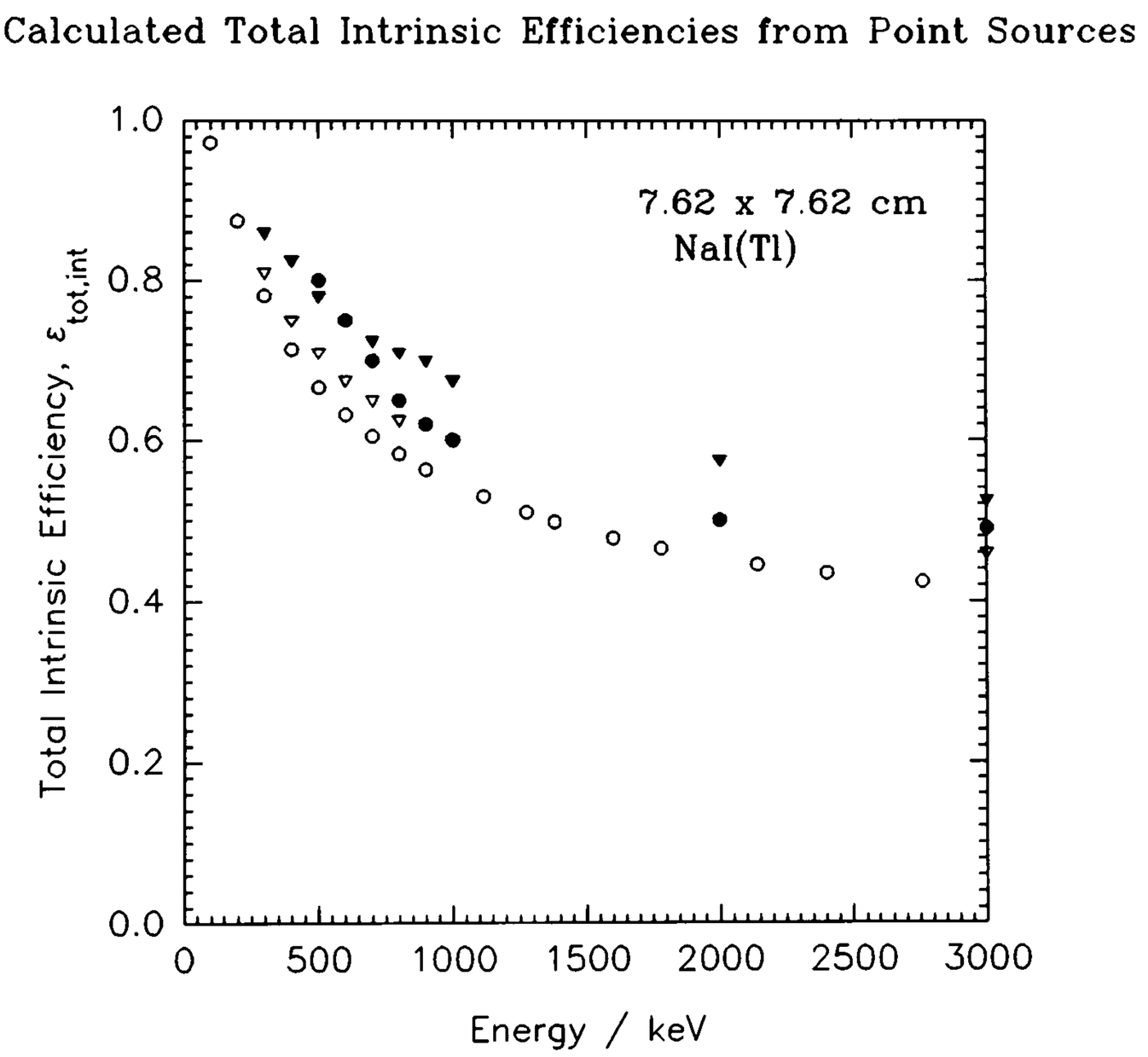

Figure 6.22 Total intrinsic efficiency as a function of γ-ray energy.

Figure 6.23 shows results from Monte Carlo code MCI in comparison with a solution of $\varepsilon_{tot,int}$ by an analytical method (Heath, 1964). The similarity between these two independent results is noted, and validates the simulation of efficiency for right cylindrical detectors. Jarczyk *et al* (1962), Chinaglia & Malvano (1966) and Green & Finn (1965) furnish values of full energy peak absolute efficiency or *photopeak efficiency* ($\varepsilon_{p,abs}$) for a wide range of NaI(Tl) detector sizes, energies and source-detector separations. Green and Finn also provide a summary of contemporary studies.

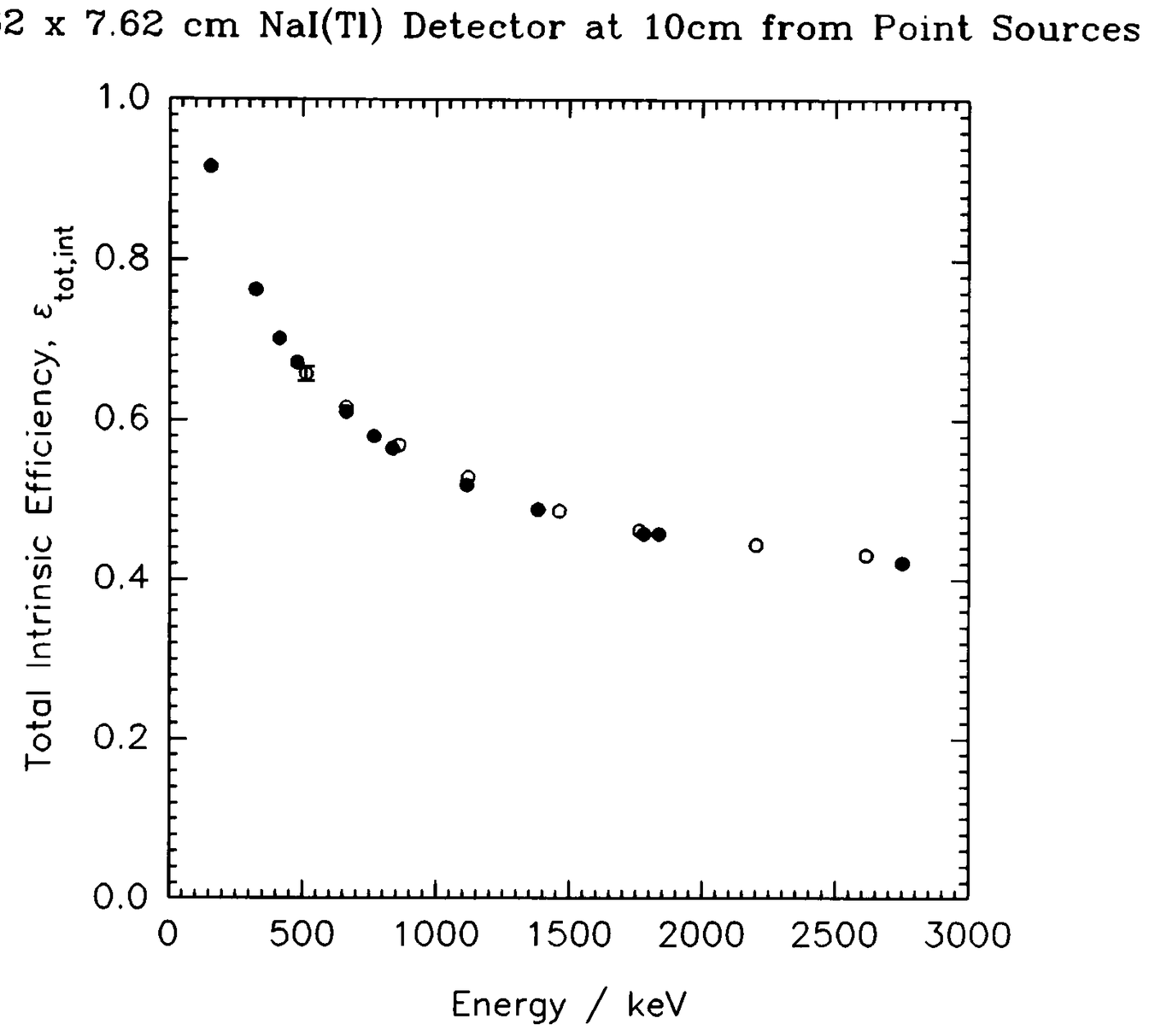

Figure 6.23 A comparison of calculated total intrinsic efficiency by Monte Carlo (Allyson) and analytical methods.

Finally, a comparison is made between an experimental measurement of peak intrinsic efficiency at 10cm using a number of small point sources, and that by Monte Carlo MCI (figure 6.24). Monte Carlo results lie between the $\pm 1\sigma$ experimental counting statistical error bars. At these distances, accurate measurement of the solid angle presented to the detector from the source is very important and may effect overall accuracy. It is estimated that this error is of the order of $\pm 2\%$. For peaks that are

incompletely resolved owing to nearby interferences, additional errors contribute to peak area estimates. The fitting of smooth gaussian functions through such data can improve accuracy over that of much simpler techniques (Carnahan, 1964). It is noted that at 1173 and 1333 keV (γ-ray energies of ^{60}Co), $\varepsilon_{p,int}$ is systematically less than expected and is probably subject to this type of error.

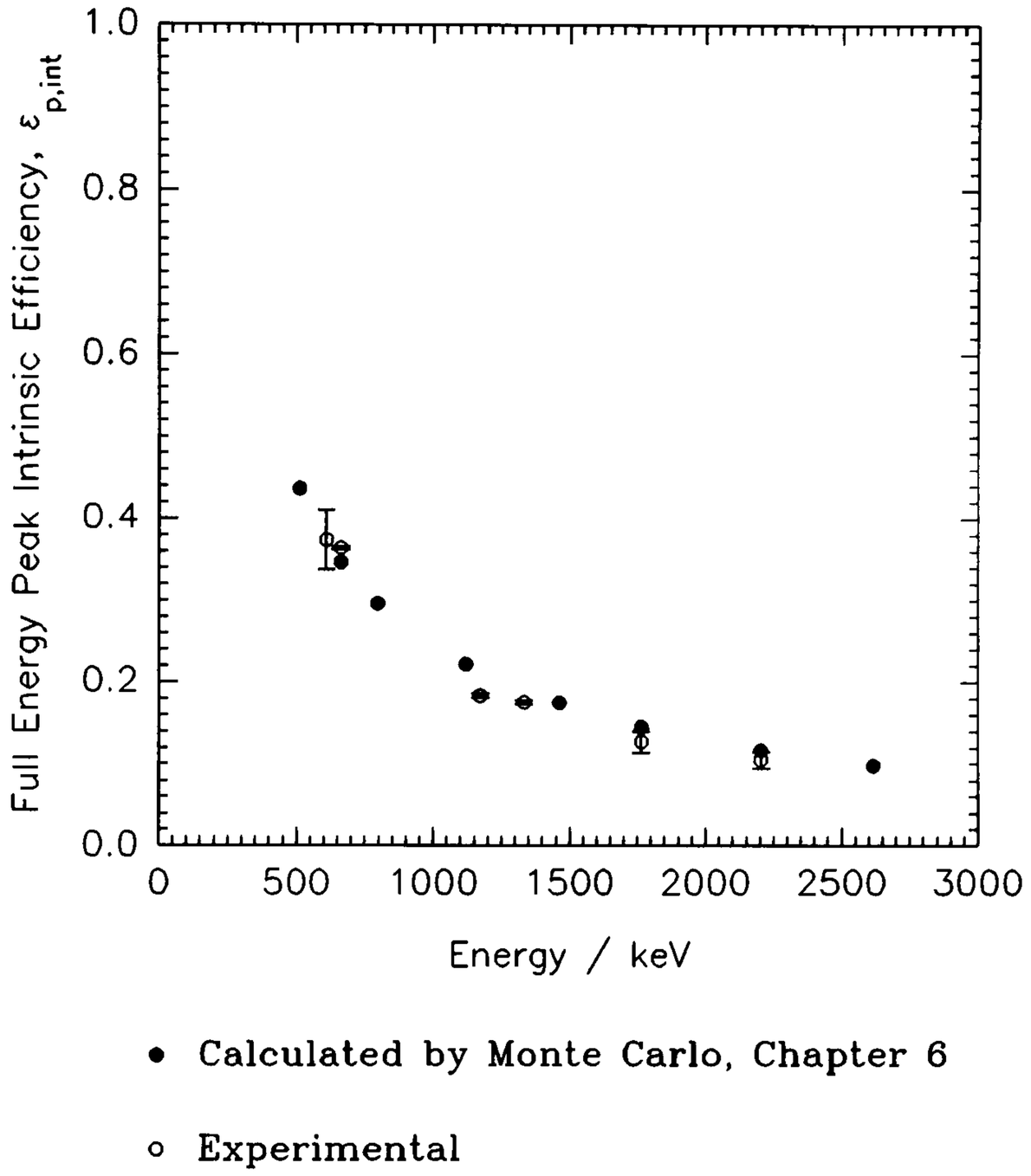

Figure 6.24 A comparison of Monte Carlo calculated and experimental intrinsic peak efficiency.

6.5.1.3 Detector Angular Characteristics

The directional characteristics or *directivity* of a detector, are important if the detector exhibits an asymmetrical response due to unusual shape or geometry of use. There are few published results (either theoretical or experimental) covering a wide range of detector sizes and γ-ray energies. Therefore, investigations were made of angular response using MCI. These results have been applied to the *field of view* calculations performed in chapter 5. A parallel, homogeneous beam of monoenergetic γ-rays that irradiates the whole of the scintillator has been used.

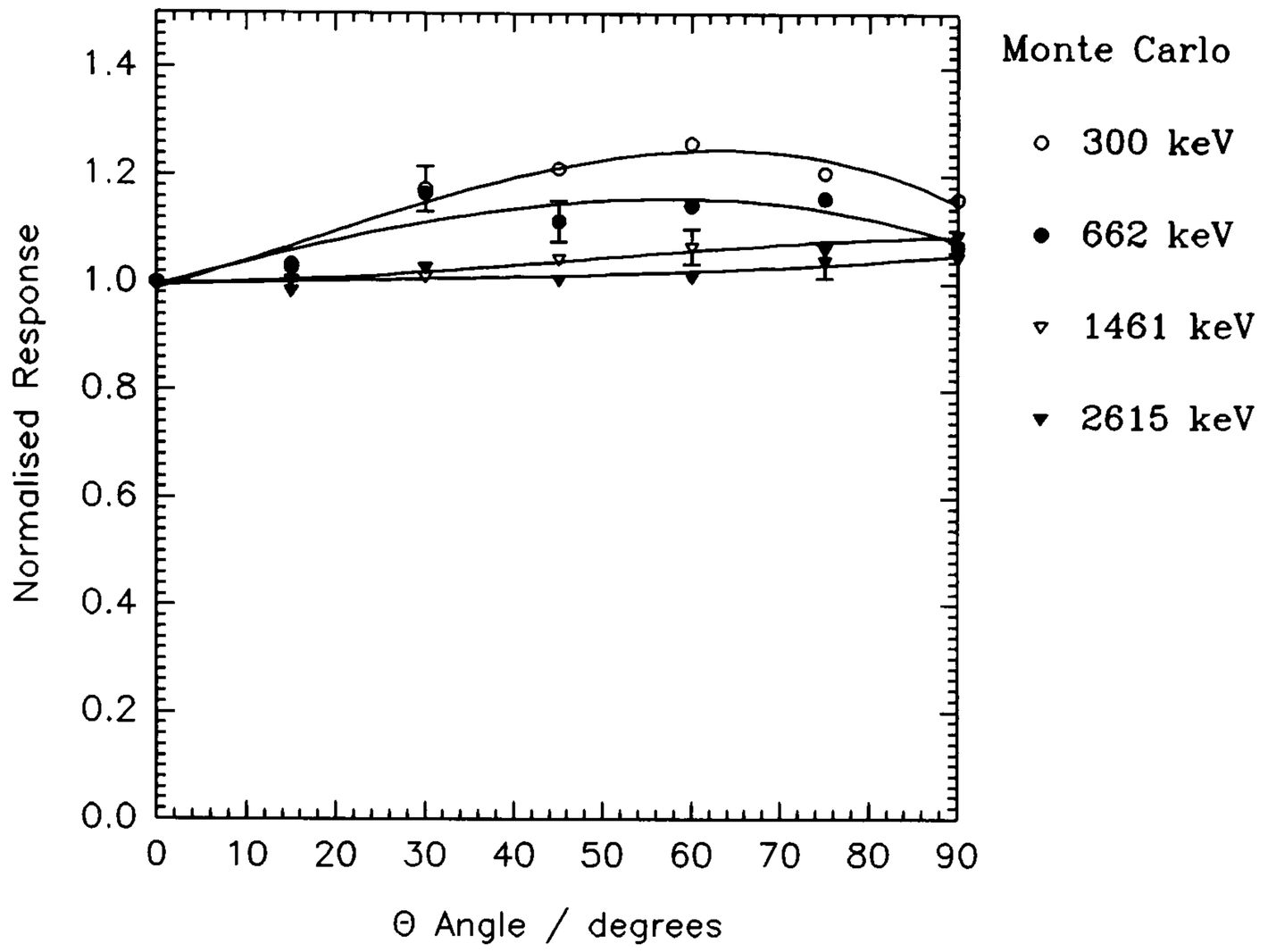

Figure 6.25 Angular characteristics of 7.62 x 7.62 cm NaI(Tl) detector determined by Monte Carlo method.

Figure 6.25 shows the estimated angular response of a 7.62x7.62 cm NaI(Tl) detector, from energies of 300, 662, 1462 and 2615 keV. These have been normalised to the $\Theta=0°$ direction, along the detector cylindrical axis. Response is symmetrical in the azimuthal, ϕ direction. Approximately $\pm 5\%$ random errors are associated with the Monte Carlo results. Petr *et al* (1971) have developed an analytical formula to calculate angular response of bare cylindrical detectors as shown in figure 5.3: it is expected that these results overestimate response owing to the absence of consideration of absorption from detector packaging materials when compared with MCI data. This also appears to be borne out when experimental comparisons are made using this type of detector and sources at distances of about 1m from the centre of the detector (figure 6.26). At low energies, directivity depends upon detector shape (height and radius for cylindrical detectors): at higher energies detector response becomes more isotropic regardless of shape.

Excellent agreement is seen with experimental results (Tsutsumi *et al*, 1986) in figure 6.27, for a 16 litre aerial survey detector along a common azimuthal direction.

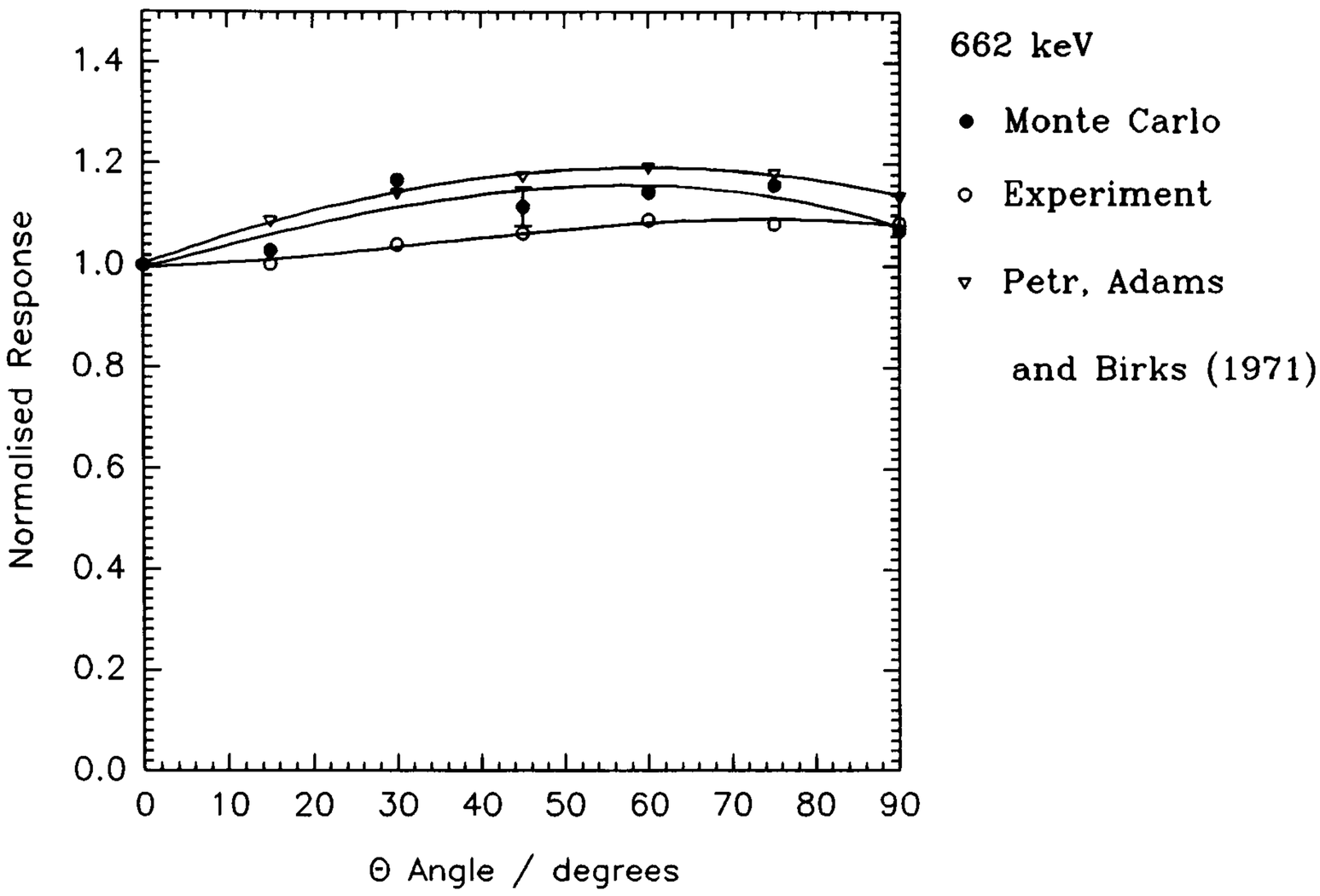

Figure 6.26 A comparison of Monte Carlo methods (Allyson), analytical solution and experimental angular characteristics to a broad parallel beam of 662 keV γ-rays.

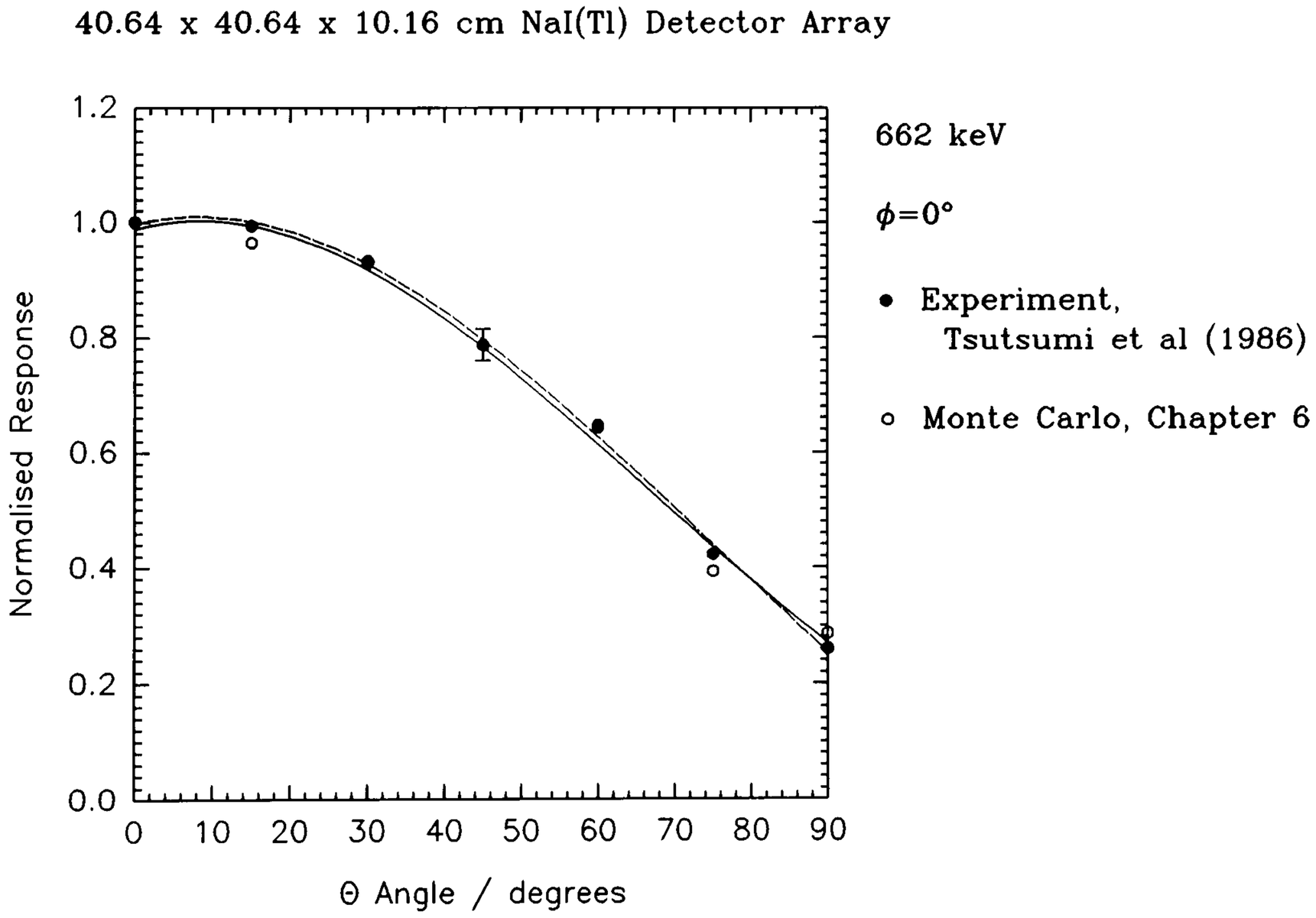

Figure 6.27 Angular characteristics of 16 litre aerial survey detector determined by Monte Carlo methods (Allyson) and experimental measurement.

The mean normalised response of a 16 litre detector, as is shown in figure 5.4, was constructed from figures 6.28-6.31 for energies 300, 662, 1462 and 2615 keV respectively.

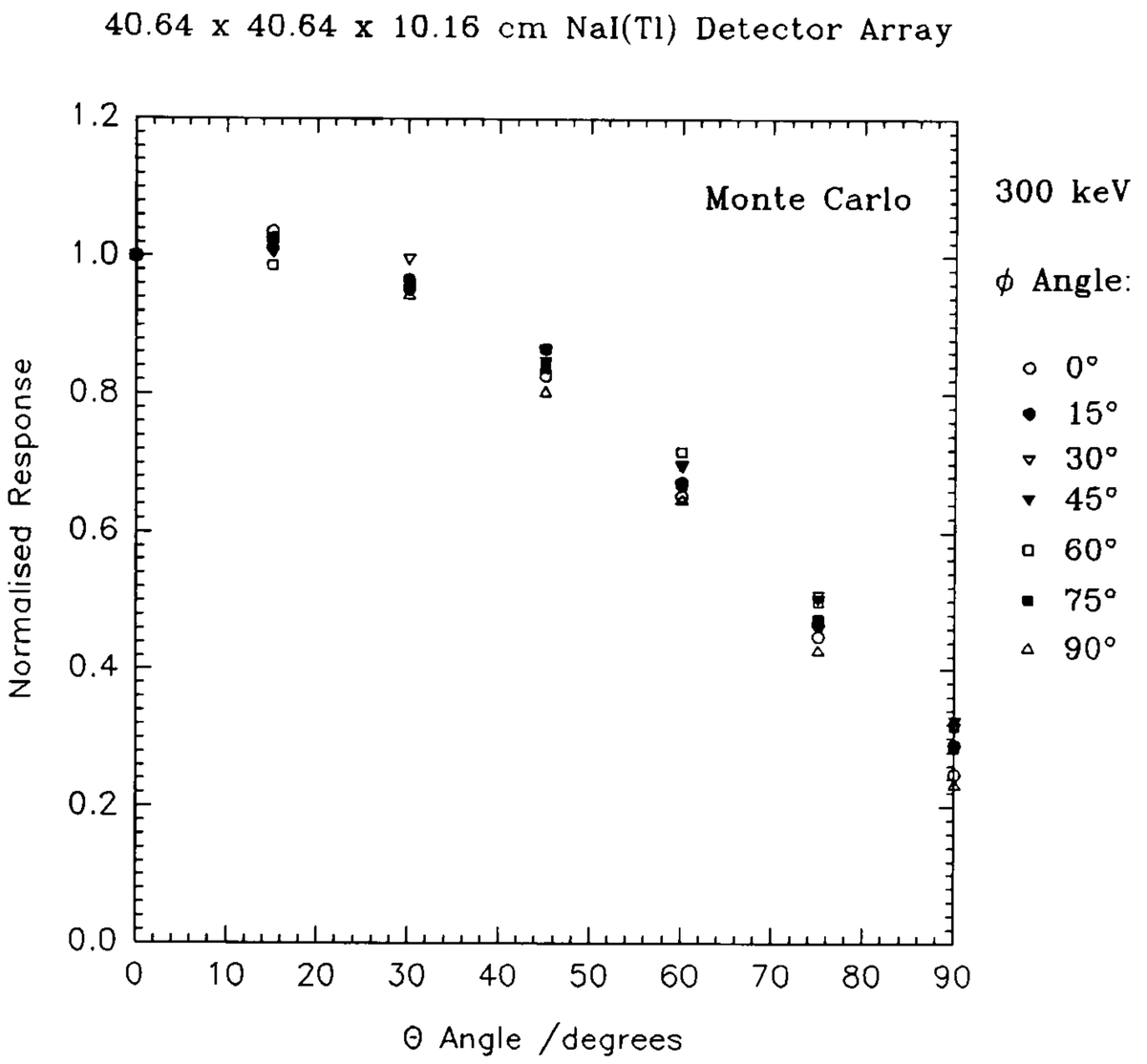

Figure 6.28 Angular characteristics of 16 litre detector to a broad parallel beam of 300 keV γ-rays, as a function of polar and azimuthal angles.

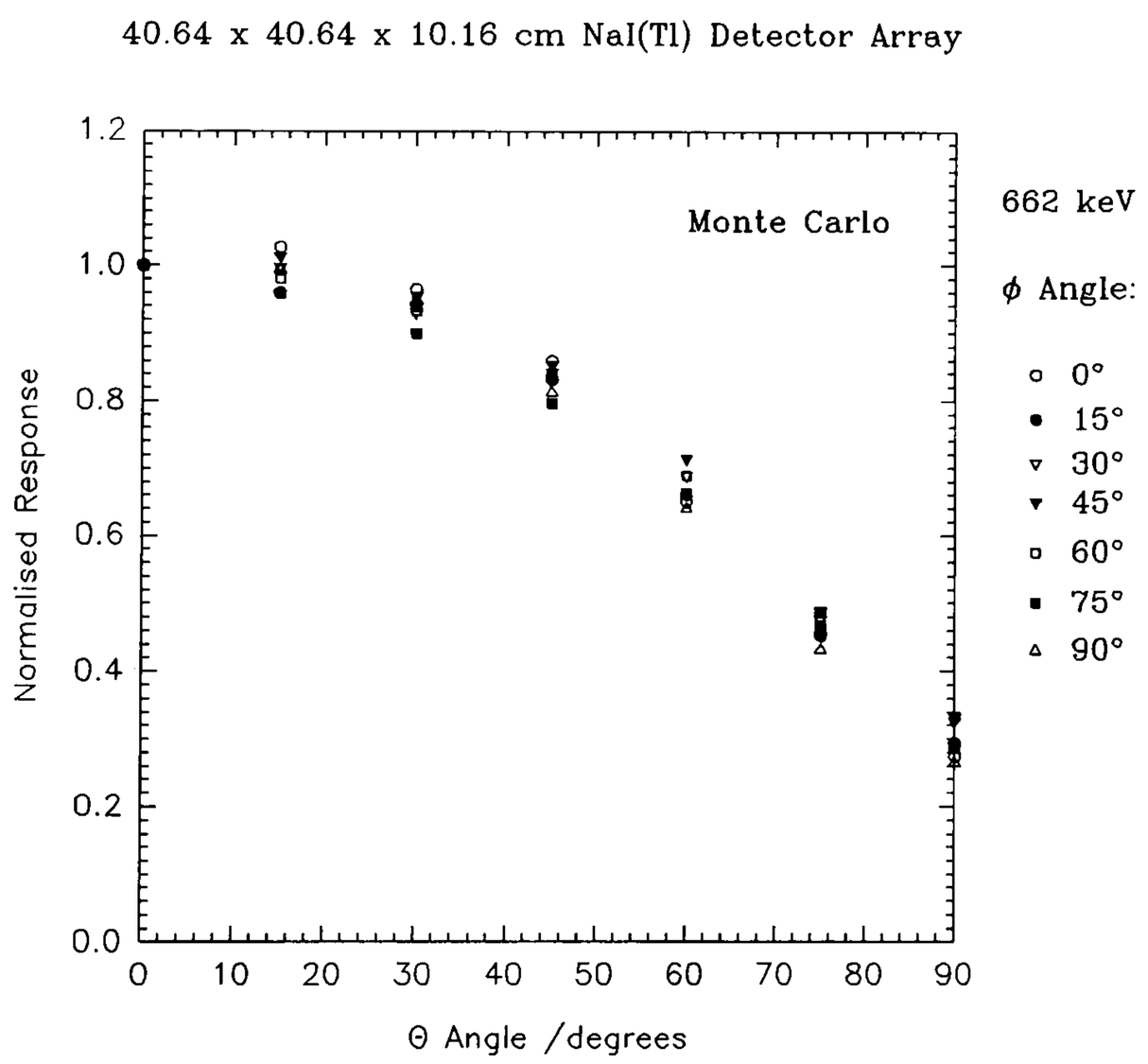

Figure 6.29 Angular characteristics of 16 litre detector to a broad parallel beam of 662 keV γ-rays, as a function of polar and azimuthal angles.

Taking account of the errors associated with these Monte Carlo results (about $\pm 5\%$), no significant variation of response is observed over the azimuthal angular direction: the detector may be regarded as having an effectively symmetrical response in this direction despite the rectangular shape.

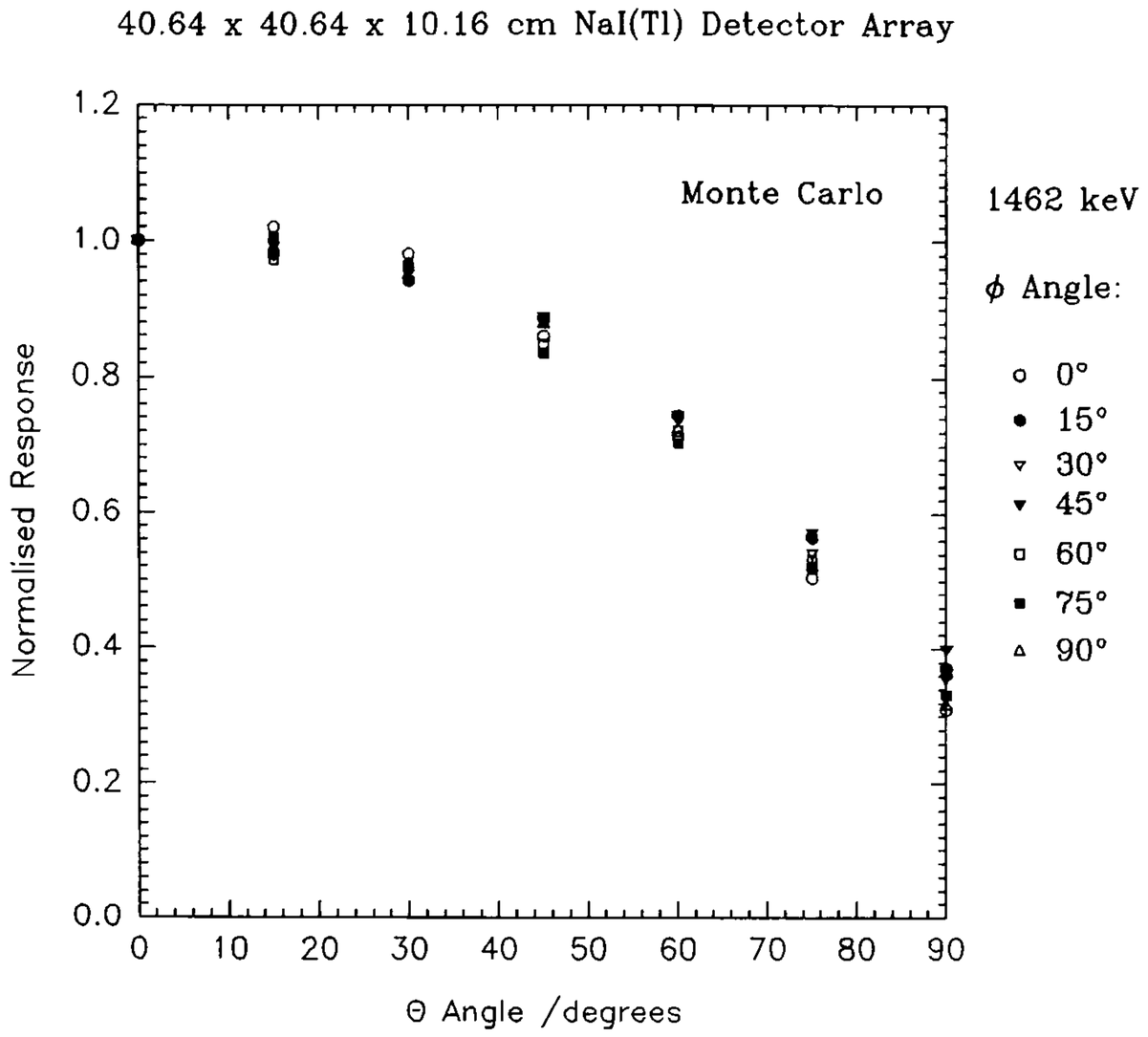

Figure 6.30 Angular characteristics of 16 litre detector to a broad parallel beam of 1462 keV γ-rays, as a function of polar and azimuthal angles.

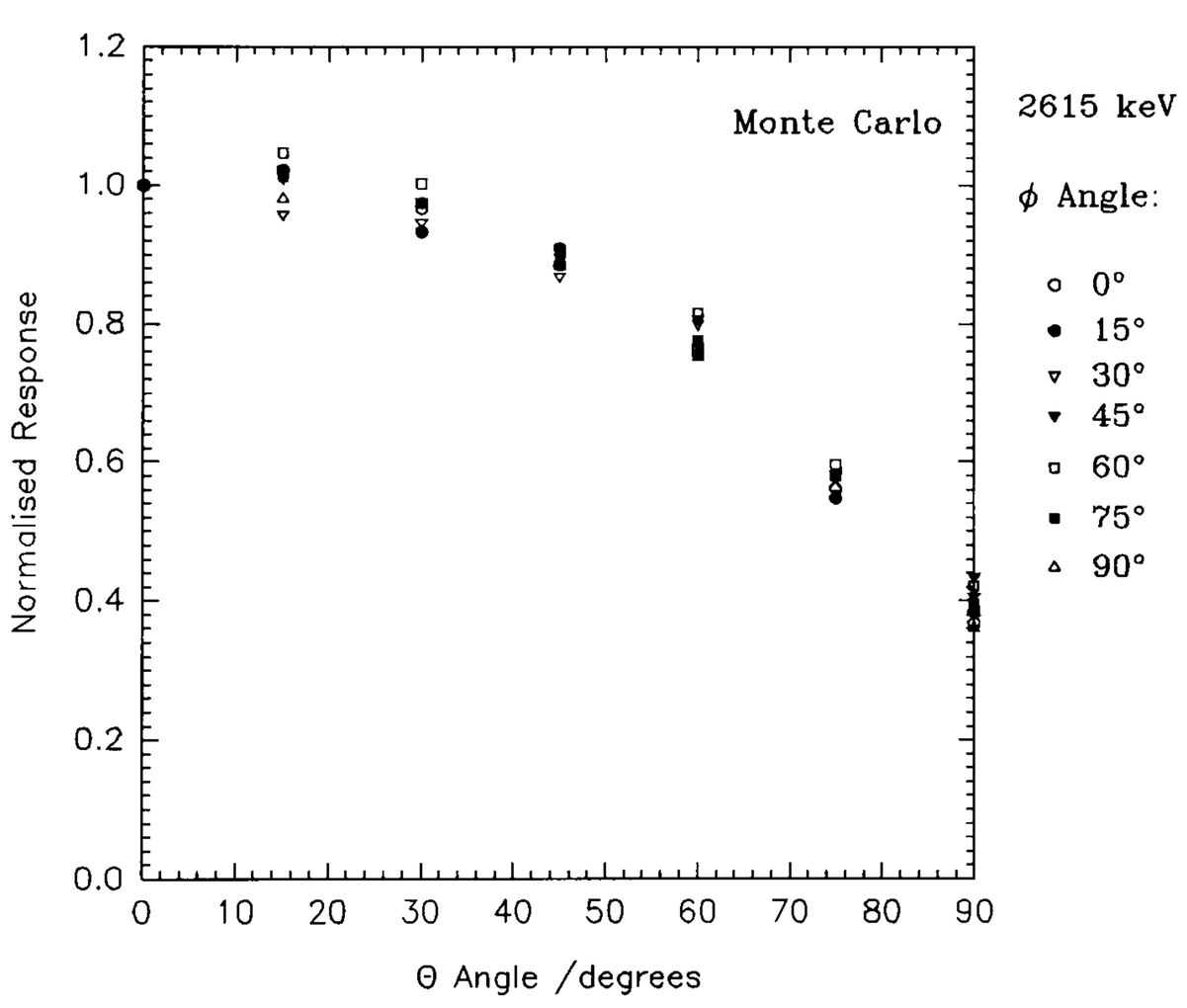

Figure 6.31 Angular characteristics of 16 litre detector to a broad parallel beam of 2615 keV γ-rays, as a function of polar and azimuthal angles.

Finally, the angular variation of photofraction has been investigated by using Monte Carlo code MCI. For a 7.62x7.62 cm NaI(Tl) detector, photofraction is independent of angular direction over the energy range of interest. A least squares line has been fitted to the data shown in figure 6.32.

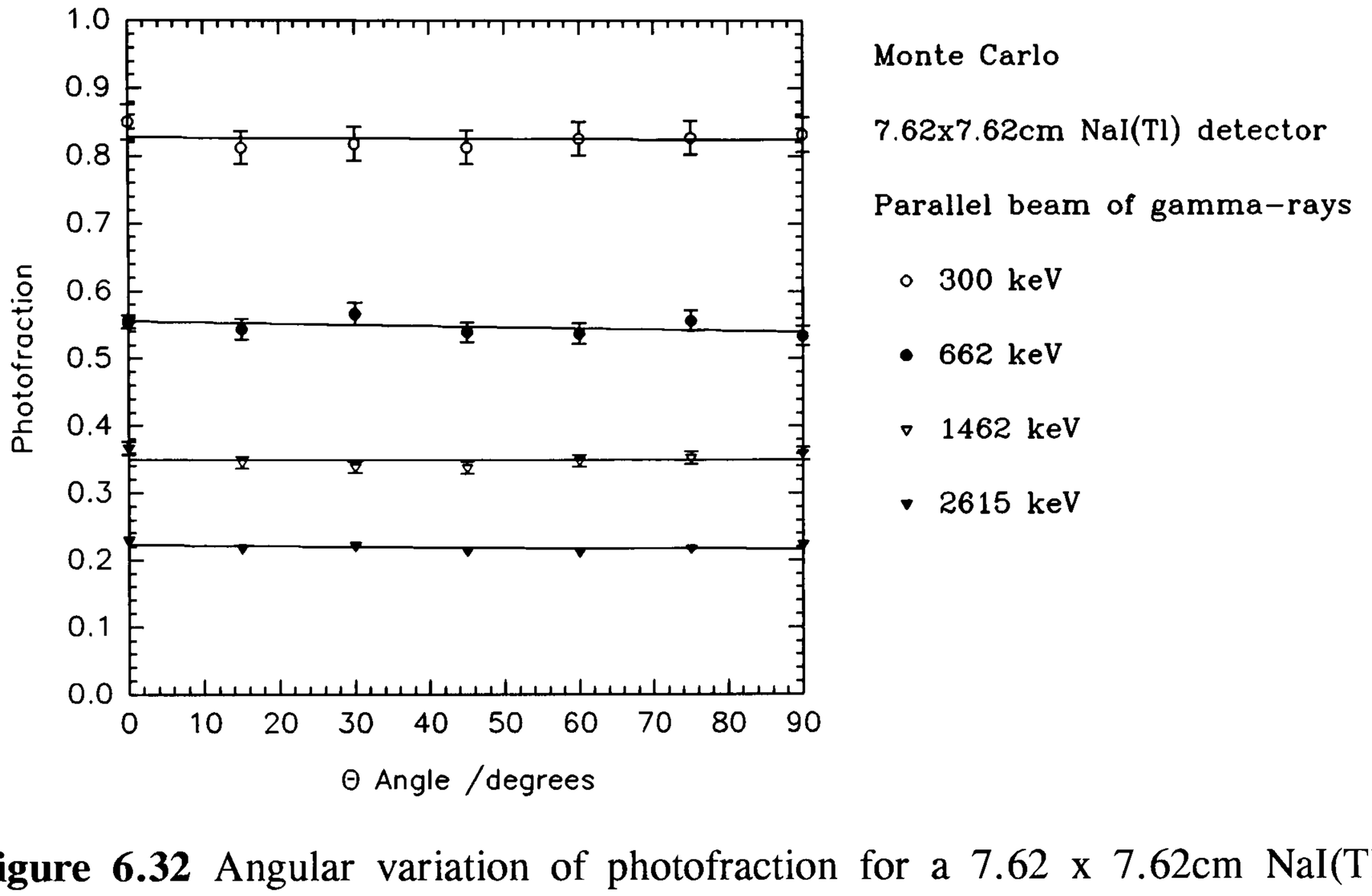

Figure 6.32 Angular variation of photofraction for a 7.62 x 7.62cm NaI(Tl) detector.

Angular dependence of photofraction is observed however for a 16 litre aerial survey detector, as shown in figures 6.33 & 6.34, although statistical precision is slightly worse. To an approximation this could be assumed slight.

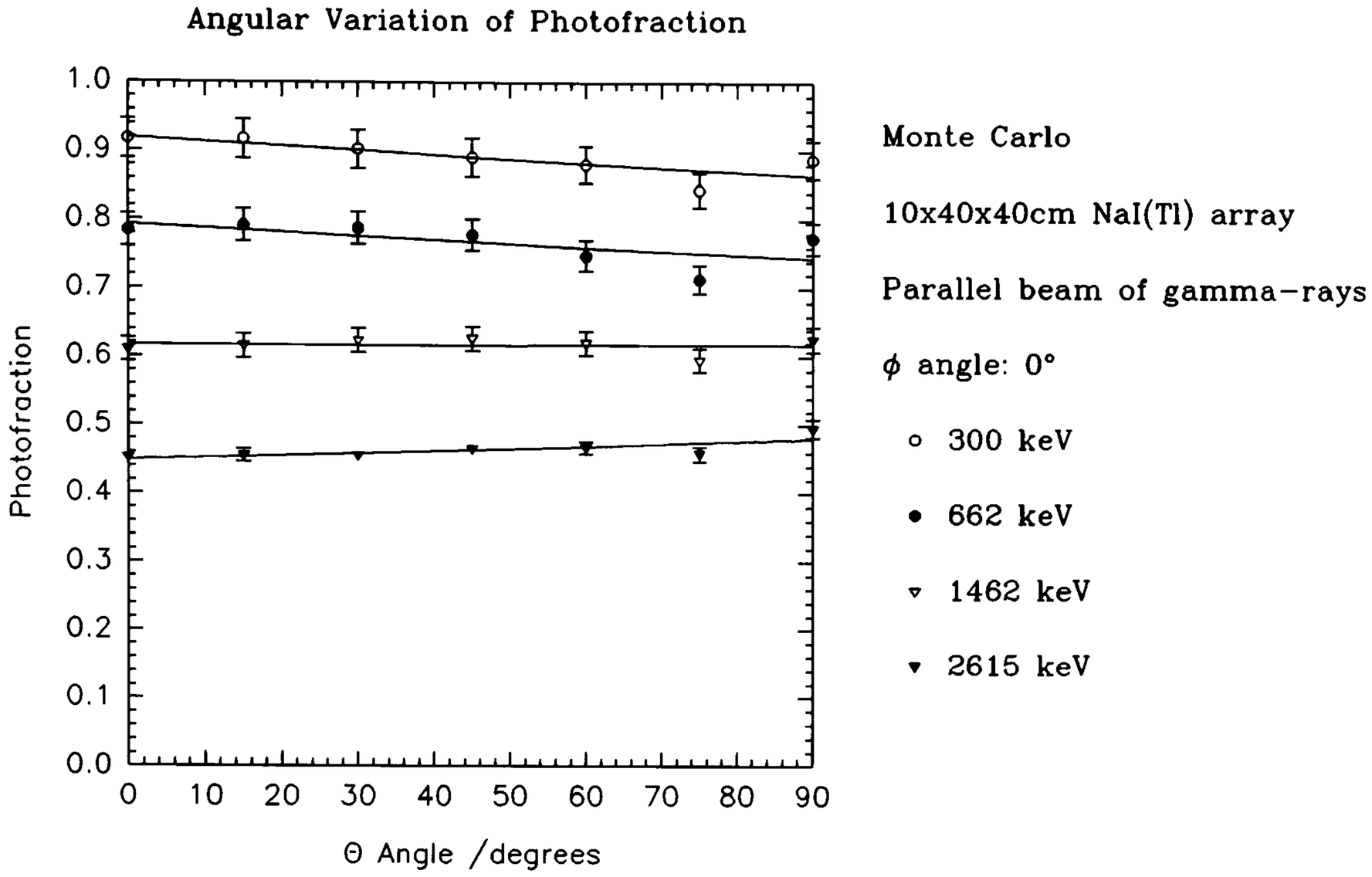

Figure 6.33 Angular variation of photofraction from a parallel source of γ-rays incident upon a single side of a 40.64 x 40.64 x 10.16cm NaI(Tl) detector array.

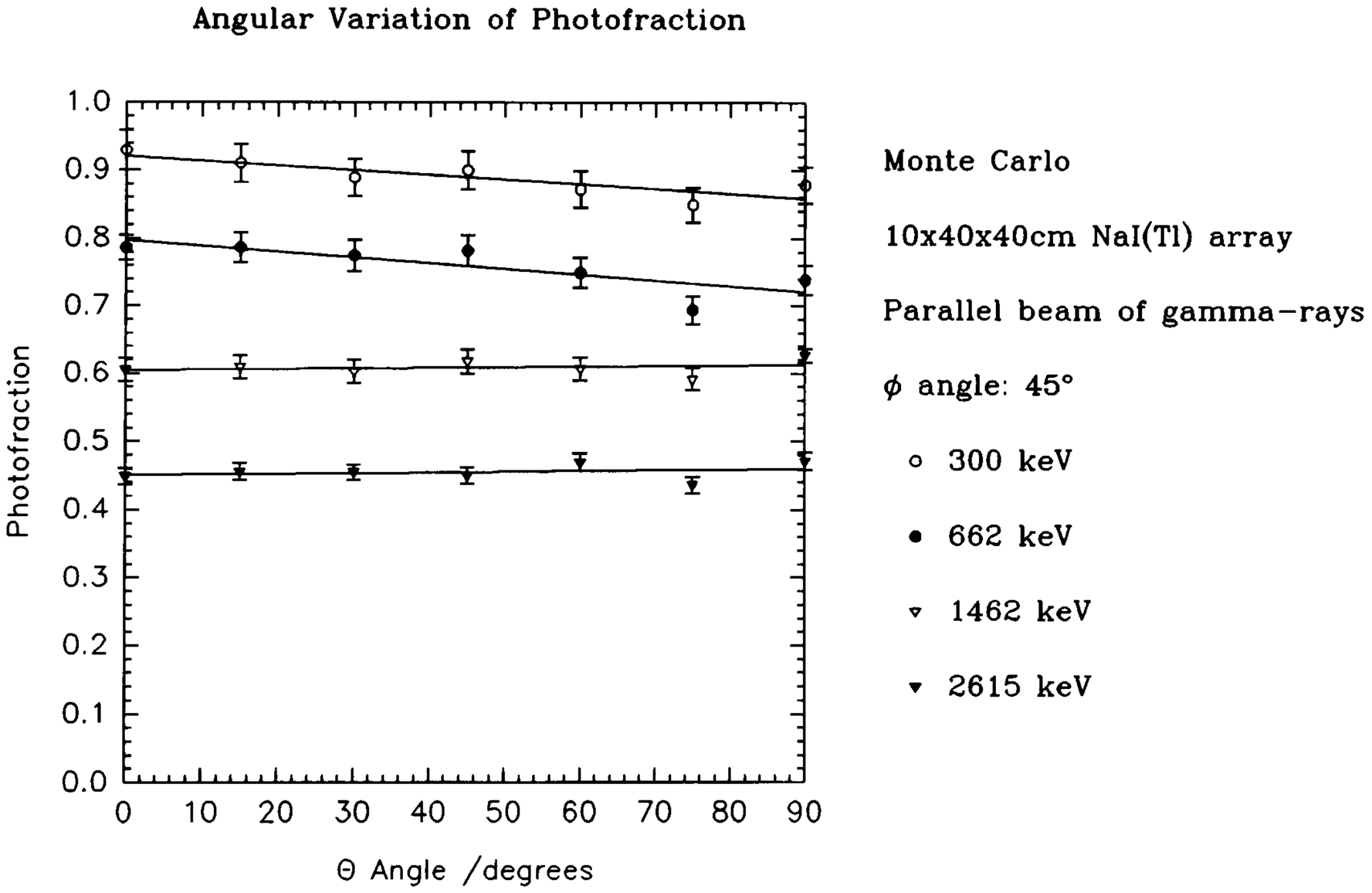

Figure 6.34 Angular variation of photofraction from a parallel source of γ-rays, incident upon two sides of a 40.64 x 40.64 x 10.16cm NaI(Tl) detector array.

6.5.2 Spectral Shape Comparisons

6.5.2.1 Simple Line Emissions

a). ^{137}Cs

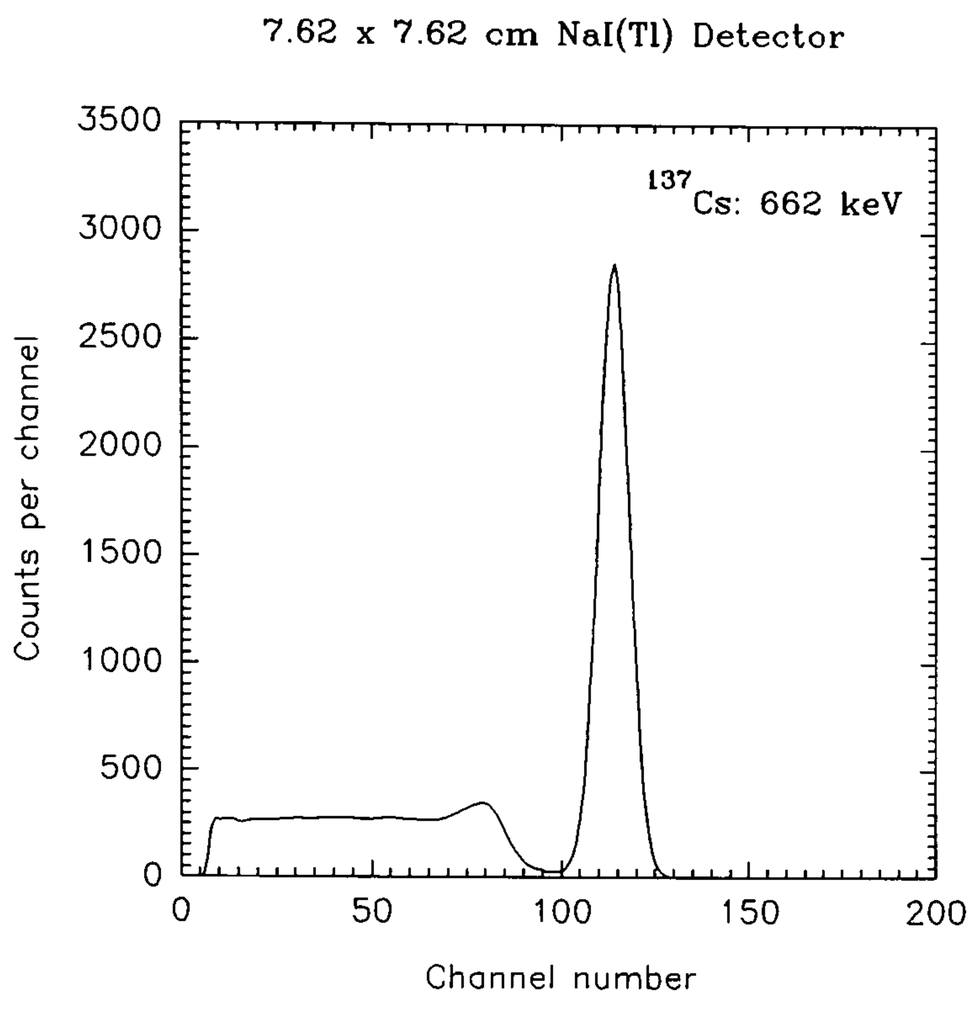

Figure 6.35 Monte Carlo derived ^{137}Cs spectrum 10cm from a point source and no peripheral scattering.

Figure 6.35 shows a Monte Carlo simulation of a point source of ^{137}Cs and 7.62x7.62 cm NaI(Tl) detector. The agreement with experimentally measured spectra can only be satisfactory if all scattering effects outside of the detector crystal are at the control of the experimenter and is very difficult to achieve. It has been noted that more realistic spectral simulations can be obtained by inclusion of detector canning materials.

The effect of the proximity of a photomultiplier tube has also been investigated. The PMT has a complicated structure, which is difficult to account for. A simple method has been used, shown by Nardi (1970), of extending the canning material by 5cm (aluminium); Saito and Moriuchi (1981, 1988) used 3cm and 5cm; Rogers (1982) 1cm. Beattie and Bryne (1974) simulated a PMT by using a thickness of glass. Figure 6.36 shows the backscatter peak occurring from the PMT, for a point source of ^{137}Cs 10cm from the front face of the detector. This contribution to the

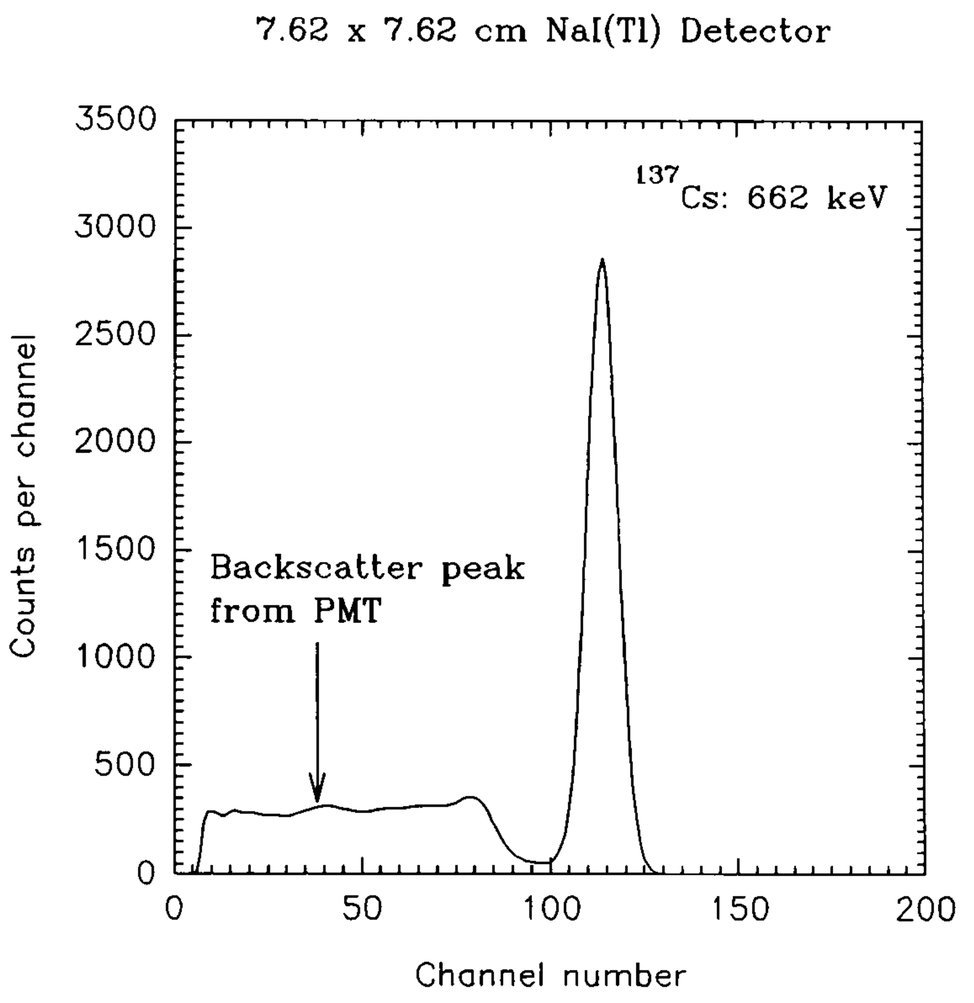

Figure 6.36 Simulation of ^{137}Cs and NaI(Tl) with photomultiplier tube.

Compton continuum is small owing to the high absorption probability for this thickness of NaI(Tl). Leutz *et al* (1966) experimentally observed a large backscatter peak that they attributed to the phototube, despite using a 10.16 x 10.16cm NaI(Tl) crystal. Backscattering from the source and surrounding materials is usually the most likely cause however and dominates the measured spectrum in the range of 180-250 keV in a normal laboratory environment (see figure 4.3).

b). ^{40}K

The simulation of a point source of ^{40}K is shown in figure 6.37. Again, for experimental sources one would expect to see scattering from within the source itself. This becomes even more intense within for example a calibration pad. The consequences of this are clear. It is most important to ensure the source scattering in the calibration spectrum is similar to that seen from a typical soil otherwise the stripping ratios will not be applicable and calibration be in error.

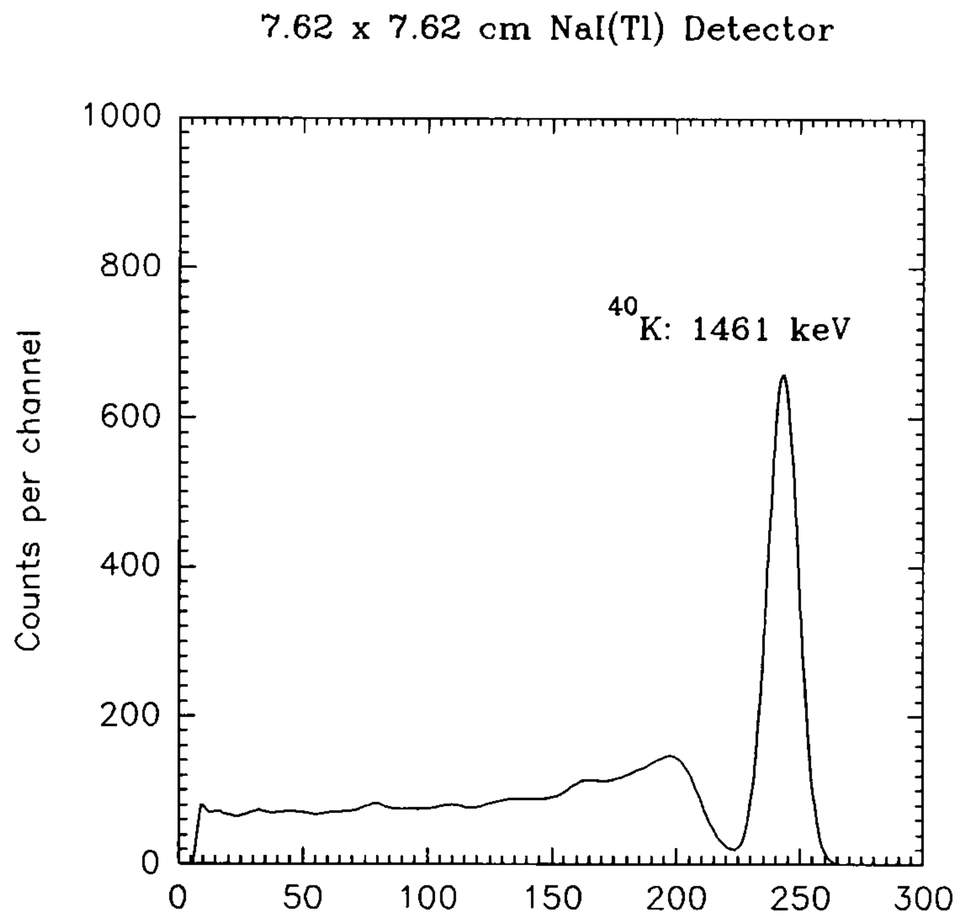

Figure 6.37 Monte Carlo derived ^{40}K spectrum, 10cm from a point source.

6.5.2.2 Complex Line Emission Spectra

In order to simulate spectra containing more than one source γ-ray energy, individual spectra are normalised and superposed according to their relative intensity. Each line is assumed to be emitted independently without angular correlation.

a). ^{134}Cs

A simulation of a point source of ^{134}Cs is shown in figure 6.38. Compare this with figure 4.4 and note the strong backscattered peak.

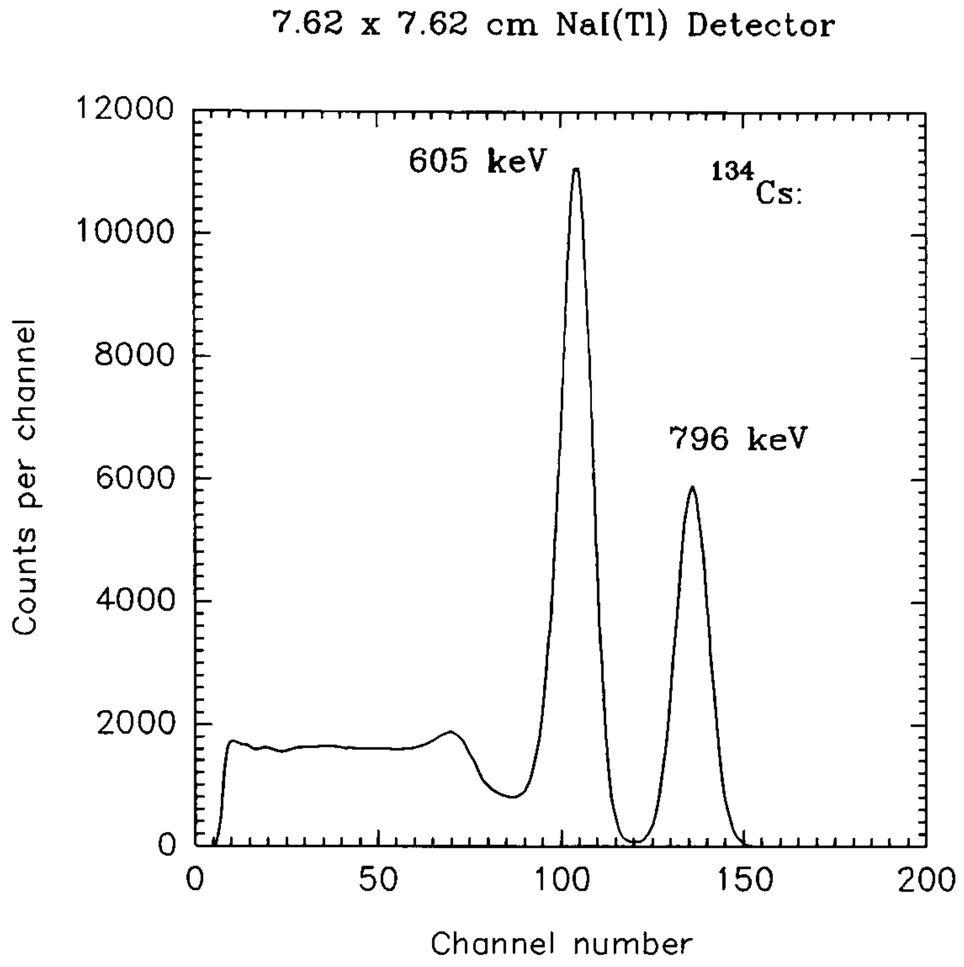

Figure 6.38 Monte Carlo calculated spectrum from a point source of ^{134}Cs, 10cm from a NaI(Tl) detector.

b). Uranium and Thorium Series

The uranium and thorium natural decay series comprise a great number of γ-rays as shown in figures 6.39 and 6.40. The most intense of these (greater than about 1%) and energetically greater than about 150 keV, have been simulated from a point source (table 6.1). If one compares figures 6.41 & 6.42 with figures 4.9 & 4.10 respectively, the effects of external detector scattering and source attenuation are again self evident in the spectral shape.

Table 6.1 Uranium and thorium decay series used for simple 7.62x7.62cm NaI(Tl) simulation (Lederer & Shirley, 1978).

^{238}U Series / keV	% Intensity	^{232}Th Series / keV	% Intensity
^{214}Bi:		**^{208}Tl:**	
609	46.10	277	2.47
768	5.00	511	7.85
806	1.253	583	31.13
934	3.256	763	0.597
1120	15.32	860	4.358
1155	1.725	2615	36.124
1238	6.056		
1281	1.505	**^{228}Ac:**	
1378	4.128	154	0.8024
1402	1.414	209	4.352
1408	2.524	270	3.645
1509	2.235	328	3.10
1730	3.035	338	11.968
1764	16.12	409	2.078
1847	2.144	463	4.678
2119	1.213	795	4.46
2204	5.08	911	27.2
2448	1.572	965	4.733
		969	16.4
^{214}Pb:		1588	3.522
242	7.68		
295	18.92	**^{212}Pb:**	
352	36.74	239	43.1
		300	3.27
		^{212}Bi:	
		727	6.32
		785	3.08
		1620	4.20

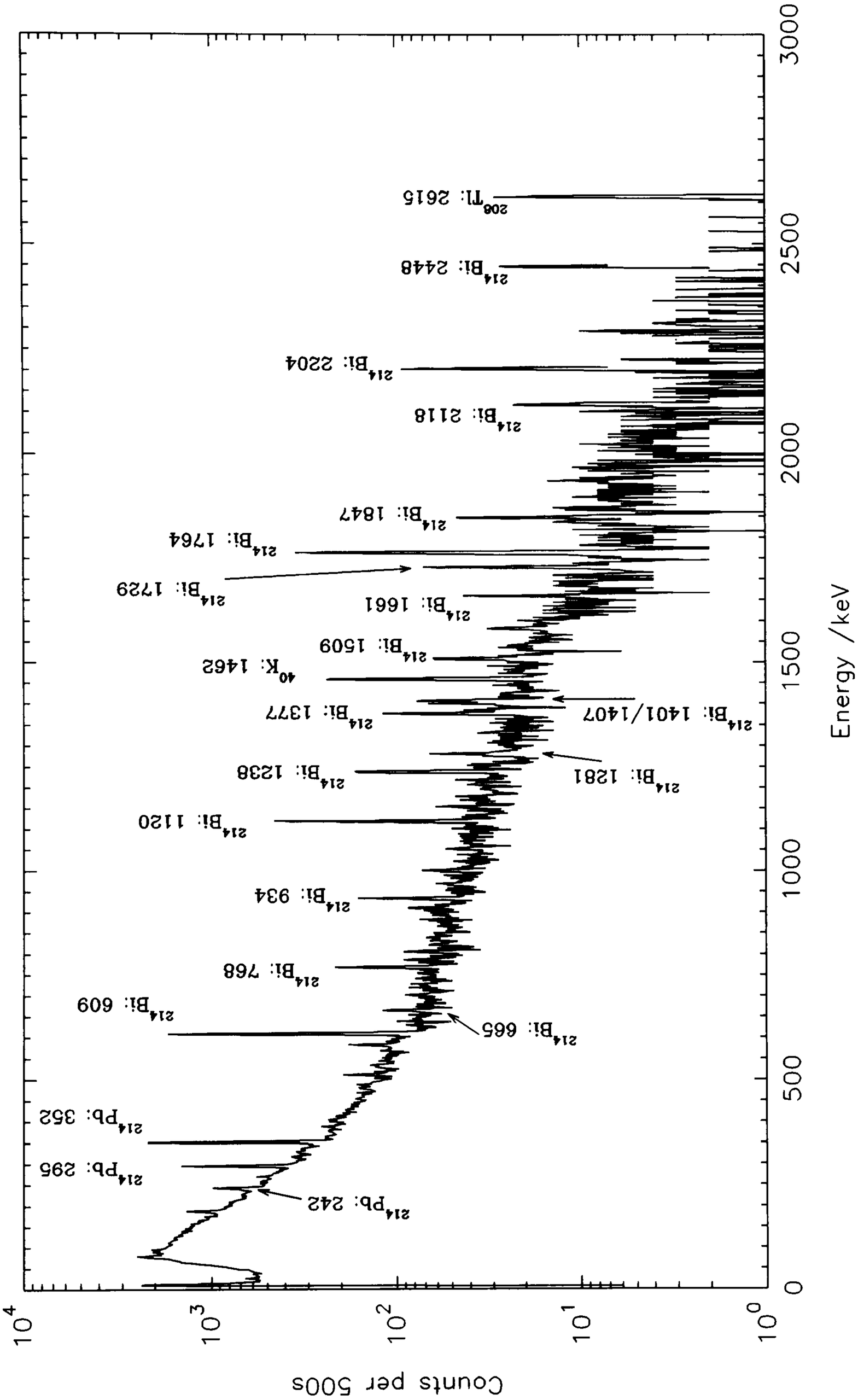

Figure 6.39 Uranium decay series, recorded from a calibration pad using a GMX semiconductor detector.

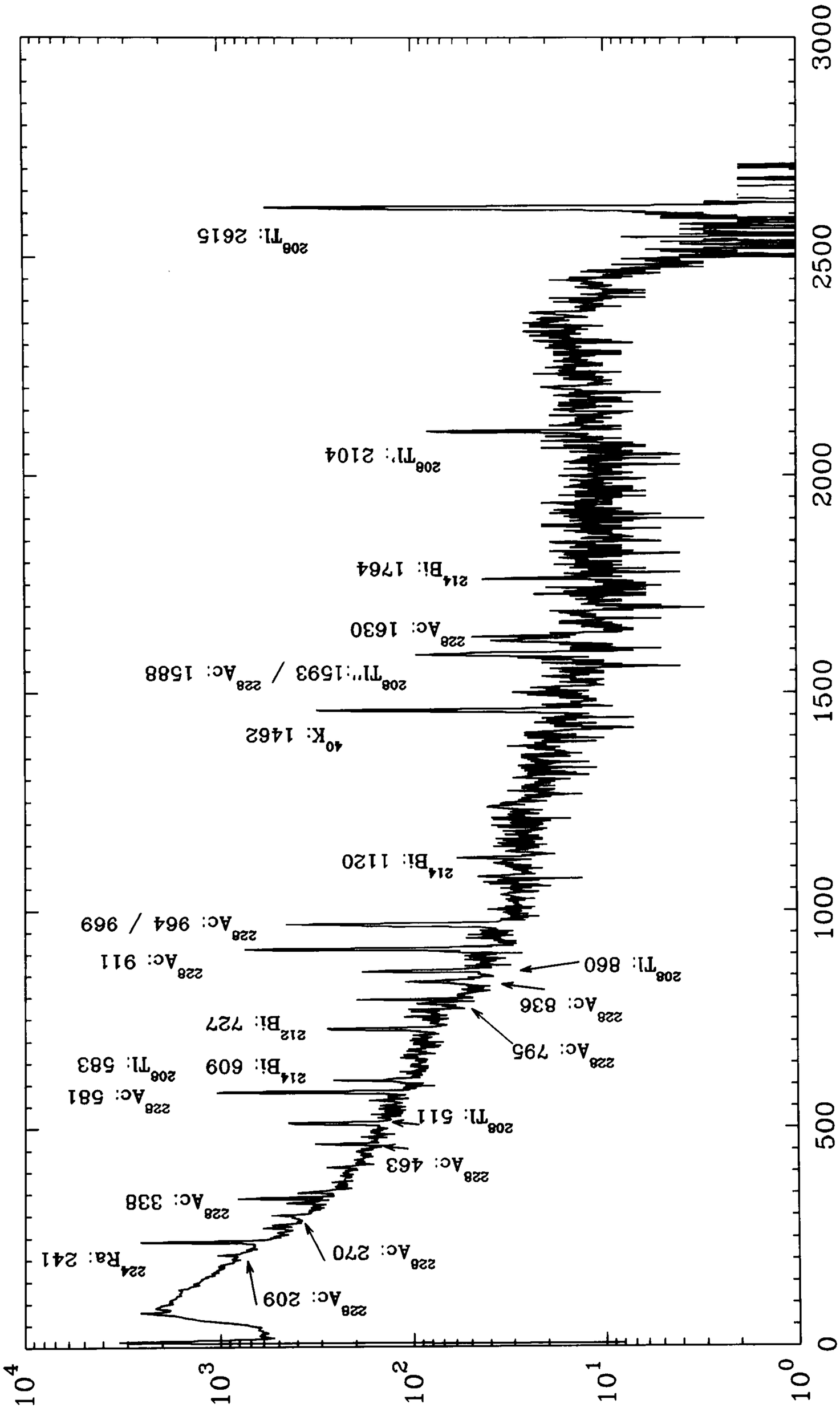

Figure 6.40 Thorium decay series, recorded from a calibration pad using a GMX semiconductor detector.

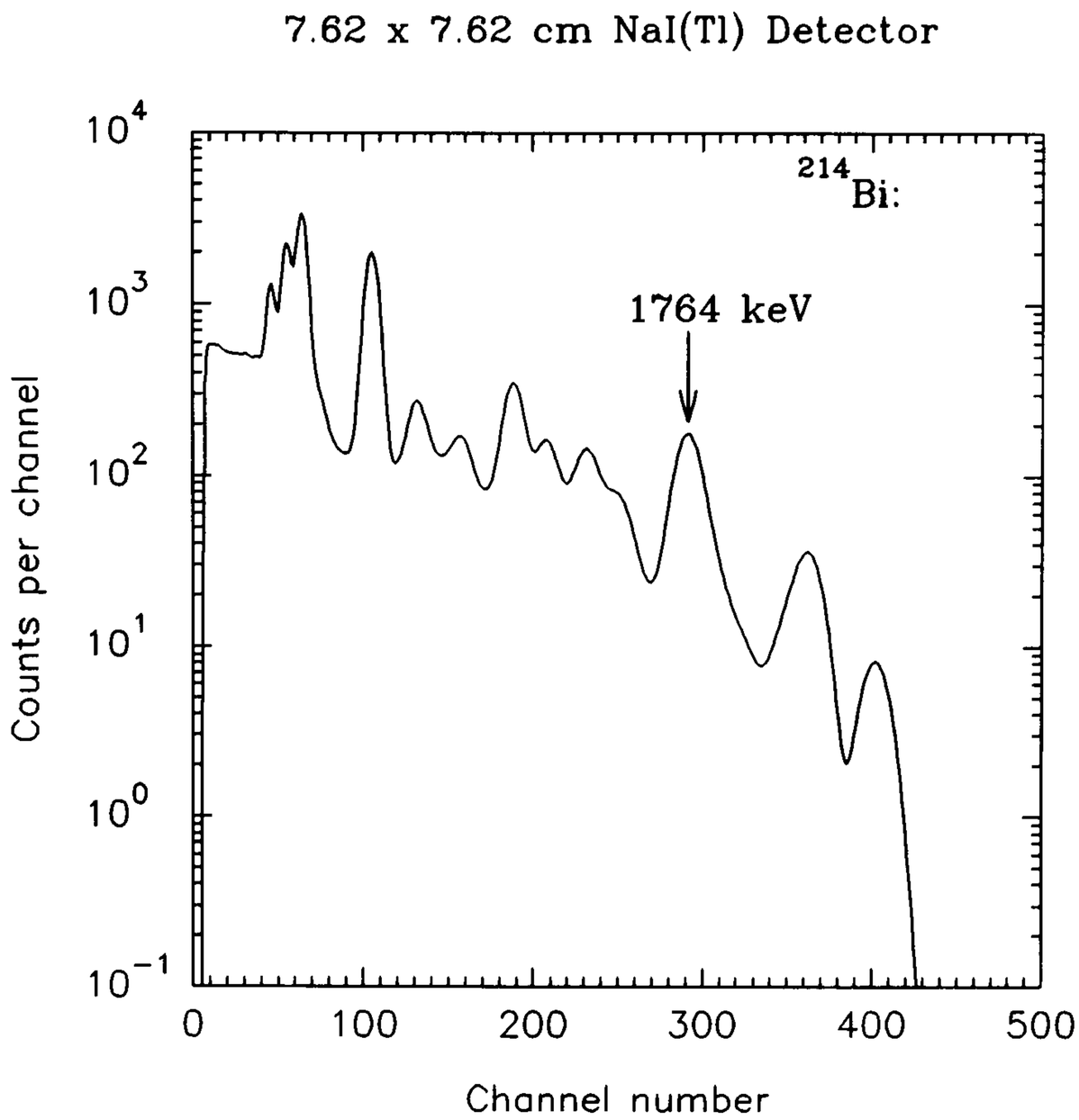

Figure 6.41 Monte Carlo derived spectrum of a point source uranium series, 10cm from NaI(Tl) detector.

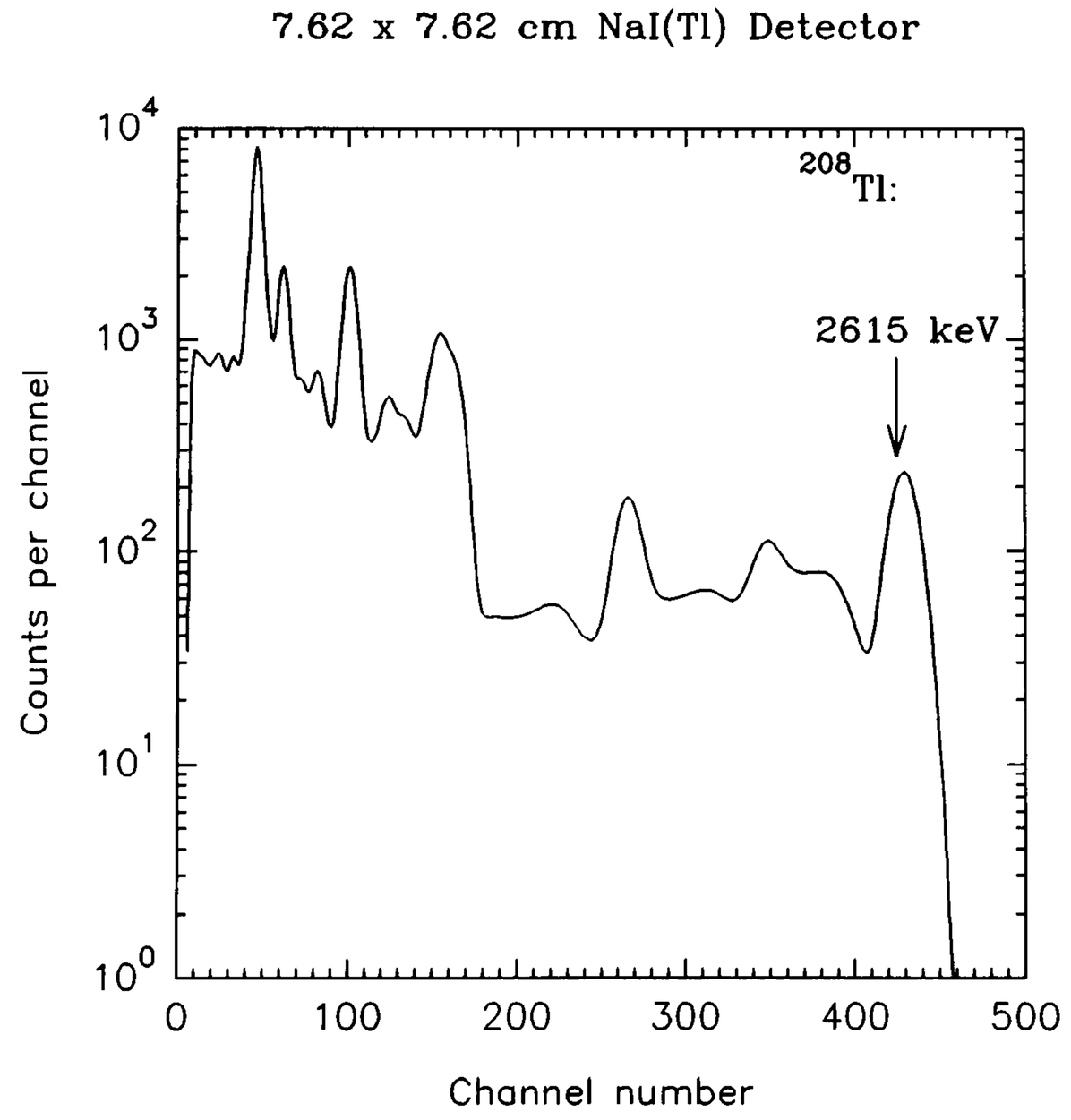

Figure 6.42 Monte Carlo derived spectrum of a point source thorium series, 10cm from NaI(Tl) detector.

6.5.3 Calculated Stripping Ratios for 7.62x7.62cm NaI(Tl) Detectors

From the simulations of point sources and 7.62x7.62 cm NaI(Tl) detectors made in this section, stripping ratios have been calculated for SURRC and IAEA windows (tables 6.2 & 6.3). The errors listed are for random counting statistics only. An additional error of approximately $\pm 5\%$ is required to account for cross-sectional data.

Table 6.2 Stripping ratios from 7.62x7.62 cm NaI(Tl), determined by Monte Carlo simulation of point sources and no peripheral scattering. SURRC windows.

	Spectral Windows				
	^{137}Cs	**^{134}Cs**	**^{40}K**	**^{214}Bi**	**^{208}Tl**
	95-130 ch.	**125-150 ch.**	**220-270 ch.**	**270-318 ch.**	**390-480 ch.**
^{137}Cs	1	0.0045 $\pm$0.0004	0.0	0.0	0.0
^{134}Cs	1.976 $\pm$0.016	1	0.0	0.0	0.0
^{40}K	0.271 $\pm$0.006	0.2167 $\pm$0.0050	1	0.0	0.0
^{214}Bi	5.852 $\pm$0.047	1.254 $\pm$0.009	1.079 $\pm$0.008	1	0.0403 $\pm$0.0005
^{208}Tl	5.053 $\pm$0.038	2.075 $\pm$0.016	0.661 $\pm$0.005	0.590 $\pm$0.005	1

A comparison of table 6.2 and table 4.4 shows the following differences. A residual contribution is observed in table 4.4 for the ^{40}K/^{134}Cs stripping ratio. Significant differences occur for the stripping ratios of ^{137}Cs/^{40}K (70.5% greater than calculated), ^{134}Cs/^{40}K (49.4% greater), ^{134}Cs/^{214}Bi (25% greater), ^{134}Cs/^{208}Tl (23.3% greater) and ^{40}K/^{208}Tl (41.7% greater), for the reasons previously given. For the other stripping ratios, they are close to or within estimated errors.

For completeness, table 6.3 shows calculated stripping ratios for IAEA windows. However, for field work at SURRC, the windows listed in table 6.2 have been used.

Table 6.3 Stripping ratios from 7.62x7.62 cm NaI(Tl), determined by Monte Carlo simulation of point sources and no peripheral scattering. IAEA windows.

	Spectral Windows				
	^{137}Cs	**^{134}Cs**	**^{40}K**	**^{214}Bi**	**^{208}Tl**
	95-130 ch.	**125-150 ch.**	**228-260 ch.**	**275-307 ch.**	**396-460 ch.**
^{137}Cs	1	0.0045 ±0.0004	0.0	0.0	0.0
^{134}Cs	1.976 ±0.016	1	0.0	0.0	0.0
^{40}K	0.277 ±0.006	0.2213 ±0.0051	1	0.0	0.0
^{214}Bi	6.537 ±0.055	1.400 ±0.011	0.886 ±0.007	1	0.0375 ±0.0005
^{208}Tl	5.389 ±0.041	2.213 ±0.017	0.333 ±0.004	0.385 ±0.004	1

6.6 Far Source-Detector Distances: Monte Carlo Code II

As a detector is moved away from a source, then its response or sensitivity decreases. A simulation by Monte Carlo methods naturally recreates this. A decrease in successful event histories (ie detected events) may cause an impractical increase in computation time and poor statistical precision. The analogue Monte Carlo code MCI, without the use of any variance reduction techniques, becomes hopelessly slow. However, a number of methods are discussed in the literature to improve the situation. These include rejection techniques; systematic sampling; survival probabilities; weighting schemes. Most of these are widely used in reactor physics and shielding investigations. The use of a finite *target* detector in this investigation is an additional problem.

An *Exponential Transform* is used in problems where the detector is far separated from the source and the radiation does not penetrate in sufficient intensity to reach the target (detector). The pathlength is artificially increased when its direction is towards the detector and decreased when its pathlength is in the reverse direction. The amount of stretching and shrinking is controlled, and correction weighting is used to account for this sampling scheme.

Splitting and Russian roulette are also used in deep penetration problems. A particle traversing a medium is split into identical species at defined boundaries points. Each is given a reduced weight to account for this scheme (Turner *et al*, 1985). The use of Russian roulette (a game of chance, with potentially lethal consequences) can make splitting more efficient by decreasing the number of less desirable histories and applying a survival probability when the particle is in less important regions.

Cramer *et al* (1986) have developed methods using a conceptually simple form of *angular biasing*. At each collision a spherical region is formed at the target destination, the solid angle of which defines a cone through which particles are allowed to scatter. A secondary (scattering) particle is created with direction chosen to be within the solid angle. By a series of weight adjustments, from that of the primary particle before collision by the product of solid angle and angular scattering probability, the efficient

transport of particles through even doubly bent radius ducts becomes practical.

A new method of biasing the direction of scattered γ-rays is to use a *learning* technique by which means the most favoured random numbers that lead to a detection event are preferentially used (Booth, 1986). As the method proceeds, the calculation selects from an ever increasingly well defined distribution of random numbers and becomes computational faster. Biasing in random number space requires only an analogue Monte Carlo code with a call to a subroutine that supplies biased random numbers, rather than in physical phase space.

The method of *Statistical Estimation* is one of the most effective variance reduction techniques in the Monte Carlo calculation of finite detector responses. This method was used to estimate fluence rates from contaminated nuclear weapons testing sites during the 1960's (French & Garrett, 1964), (Clark, 1967), but recently Mickael *et al* (1989) have developed this to include detector responses principally in the application of dual-spaced nuclear borehole well-logging tools.

6.7 Summary of Monte Carlo Code MCII

6.7.1 Statistical Estimation

The method of statistical estimation as defined by Mickael *et al* (1988), has been applied to the Monte Carlo code MCI to improve efficiency of the detector counting rate, particularly those of finite size and within large volume space. In place of counting particles that physically reach the detector, the total detection probability of those particles is estimated after each scattering interaction. Following this, the particle is allowed to scatter according to the Klein-Nishina law. If the particle scatters to the detector, no estimate is recorded because this estimate has already been accounted for. The total detector response is estimated by the sum of the individual detection estimates calculated over many particle histories.

The individual detection estimates following scattering events are evaluated as the product of three probabilities:

a). the probability that a particle is scattered within the solid angle subtended by the detector;

b). the probability that the scattered particle reaches the detector without interaction (owing to attenuation traversing through media);

c). the probability that the particle undergoes a detection event once inside the detector.

A numerical technique to determine the limiting angles subtended by finite detectors has been published recently. The scattering probability is calculated by integrating the transformation of the Klein-Nishina formula to the defined direction, over the limiting angles (Mickael *et al*, 1988). The second probability is easily calculated by existing code modules, by predicting the distances between element boundaries (ground space, detector can & crystal). The probability of not interacting has the form $e^{-\mu(l)x(l)}$ where μ is the linear attenuation coefficient and x the distance in medium l. The final probability is an inherent part of Monte Carlo code MCI and requires no further extension, other than the first collision in the detector is forced using a truncated exponential (Zerby, 1963).

At the start of a γ-ray history, each photon carries a weight=1. This weight is subsequently adjusted by forcing a Compton scatter interaction within the ground and air volume elements (weight=$\mu_{Compton}/\mu_{total}$), and by the above probability products. After each scattering event, the γ-ray is allowed to scatter normally, without biasing, and with a change in weight of $1-P_s$, where P_s is the calculated scattering probability. Mostly, P_s is so small that effectively no change in weight occurs. The photon has been allowed to scatter fifty times, whereupon the scattered γ-ray energy is very low (<20 keV approximately). Termination occurs either after fifty scatters, if the photon energy $<=10$ keV, or the photon leaves the field of interest completely.

Since the Mickael *et al* technique deals only with scattered γ-rays, a method of introducing those that enter the detector directly must be used. Therefore for each source emission, two γ-ray photons are produced. From the known, and random starting position (x,y,z), the fraction of the total solid angle to the detector is calculated. The first photon is sampled in such a way that the first interaction will not occur in the

detector, but as a Compton scattering event in the ground or surrounding air space. This photon is followed throughout its lifetime until it leaves the field of interest (beyond the 90% field of view, or to an altitude of 500m). Directly following this a second γ-ray photon is released from the same position and taken directly to the detector, but randomly sampled through the solid angle. For each source emission then, the correct proportion of peak and scattered events is estimated.

6.7.1.2 The Mickael, Gardner & Verghese (1988) Formulation

The Klein-Nishina probability distribution function is transformed into a preferred direction, making the evaluation of the limiting angles and integration much easier to perform. The KN formula is described by the general function $f(\mu,\phi)$ where μ is the cosine of the polar angle and ϕ is the azimuthal angle, along the direction of the original γ-ray before scattering. $\hat{f}(\nu,\rho)$ is the transformation of $f(\mu,\phi)$ with the cosine of the polar angle ν and azimuthal angle ρ along the direction of the target (detector).

$$\hat{f}(\nu,\rho)\ d\nu d\rho = f(\mu,\phi)\ d\mu d\phi \tag{6.44}$$

Since ϕ is uniformly distributed from 0 to 2π and $f(\mu,\phi)$ becomes a function of μ only:

$$\hat{f}(\nu,\rho)\ d\nu d\rho = \frac{1}{2\pi} f(\mu)\ d\mu d\phi \tag{6.45}$$

The relationship between the cosine of the polar angle μ to ν and ρ is:

$$\mu(\nu,\rho) = \nu\gamma + [(1-\gamma^2)(1-\nu^2)]^{1/2}\ \cos(\chi-\rho) \tag{6.46}$$

where γ is the cosine of the polar angle between the two directions and χ is the azimuthal angle between the two directions. Then:

$$\hat{f}(\nu,\rho)\,d\nu\,d\rho = \frac{1}{2\pi} f\,[\mu(\nu,\rho)]\ d\nu\,d\rho \tag{6.47}$$

since $[(d\mu.d\phi)/(d\nu.d\rho)]=1$

The KN probability distribution function (pdf) is given by:

$$f(\mu)\ d\mu\, d\phi\ = \left[\frac{K(\alpha)}{2\pi}\right] [\eta(\mu)+\eta^3(\mu)+(\mu^2-1)\,\eta^2(\mu)]\ d\mu\, d\phi \qquad (6.48)$$

where,

$\alpha = E_\gamma / m_0 c^2$, $\eta(\mu) = (1+\alpha-\alpha\mu)^{-1}$ and $K(\alpha)$ a normalisation constant given by

$$K^{-1}(\alpha)\ =\ \left[\frac{(\alpha^2-2\alpha-2)}{\alpha^3}\right]\ln(1+2\alpha)+\frac{2(\alpha^3+9\alpha^2+8\alpha+2)}{[\alpha^2(1+2\alpha)^2]}$$

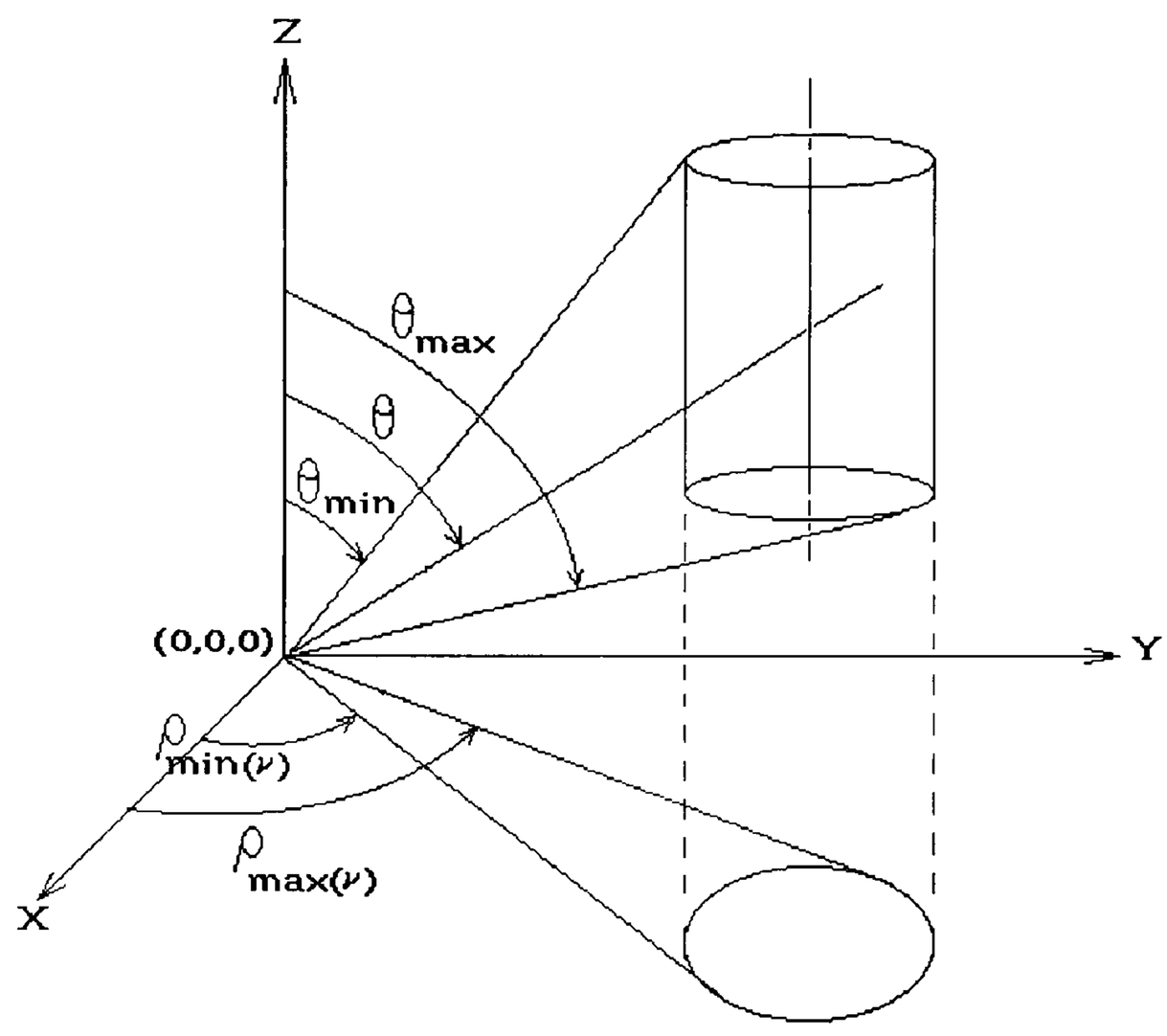

Figure 6.43 Limiting angles subtended by a right cylindrical detector.

The scattering point is defined to lie at the origin of new axes X, Y, Z and the limiting angles are measured from the direction that is parallel to the detector major axis.

Figure 6.43 shows the limiting angles that are evaluated by the procedures of Mickael *et al*. Note: $\theta = \cos^{-1}(\nu)$, $\theta_{min} = \cos^{-1}(\nu_{min})$ and $\theta_{max} = \cos^{-1}(\nu_{max})$.

The scattering probability to the detector is given by:

$$W_{\Omega} = \int_{\nu_{min}}^{\nu_{max}} \int_{\rho_{min}}^{\rho_{max}} \hat{f}\,(\nu,\rho)\; d\nu\, d\rho \qquad (6.49)$$

For cylindrical detectors, the scattering probability integral is divided into several integrands in each of which the limiting azimuthal angles are independent of the polar angles. Where this does not apply and the limiting azimuthal angles are dependent upon the polar angles, they are calculated using an average value of the polar angles between their limits. The recipe to evaluate this is given by Mickael *et al*, who also proposes an approximate method to enable an analytical solution to the integration. Since this holds only up to about 1000 keV, integrations have been carried out numerically in MCII.

Figure 6.44 shows a summary of the procedure of code MCII. Sequentially γ_2 is given preference first, then γ_1 follows.

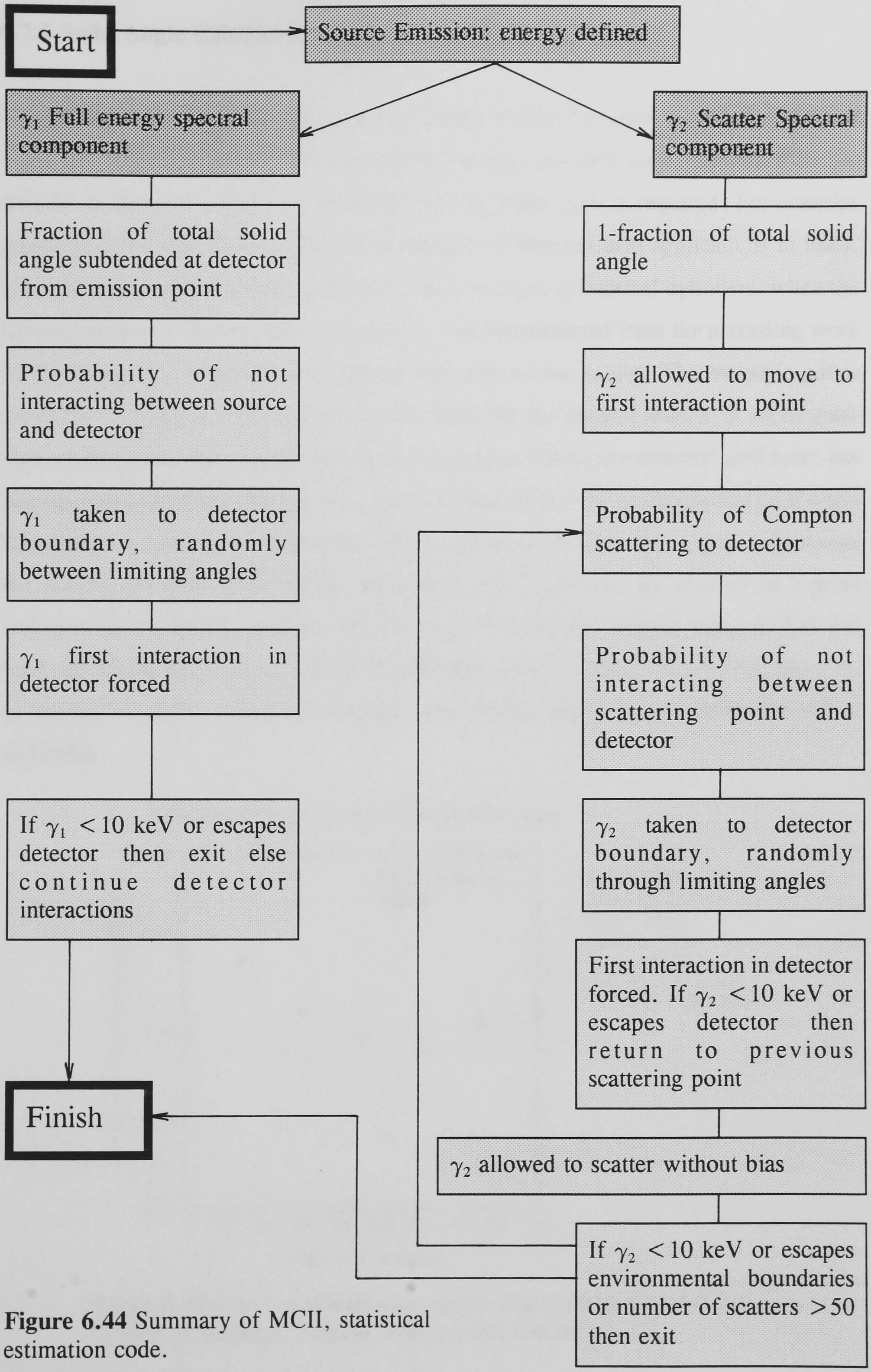

Figure 6.44 Summary of MCII, statistical estimation code.

6.7.2 Solid Angle Calculations

To combine a Monte Carlo simulation consisting of both Compton scattered γ-rays and those that directly enter the detector crystal through the solid angle subtended by the detector at the source position, an estimate of the solid angle is required. For complex geometries this calculation has been the subject of Monte Carlo applications in itself. However, the fractional solid angle subtended by right cylindrical cylinders, when the limiting angles to the boundaries are known, can be calculated from the preceding work by summing the integral of an isotropic pdf over all the angles. The isotropic pdf is given by $1/4\pi.d\mu d\phi$, transformed to $1/4\pi.dvd\rho$ for the limiting angles. A rectangular detector of equal sides, which includes the 16 litre aerial survey detector used here, has been approximated by reducing it to cylindrical geometry. The calculation of solid angle then becomes fast and without undue loss of accuracy. To test this, figure 6.45 shows the fraction of solid angle, $\Omega/4\pi$, subtended by a 7.62x7.62 cm detector at a point source twice the detector radius (7.62cm) away, as a function of polar angle θ. This has been calculated by Monte Carlo MCI (analogue code), Monte Carlo investigation by Green (1974) and by analytical function with limiting angles as defined by Mickael *et al* (1988).

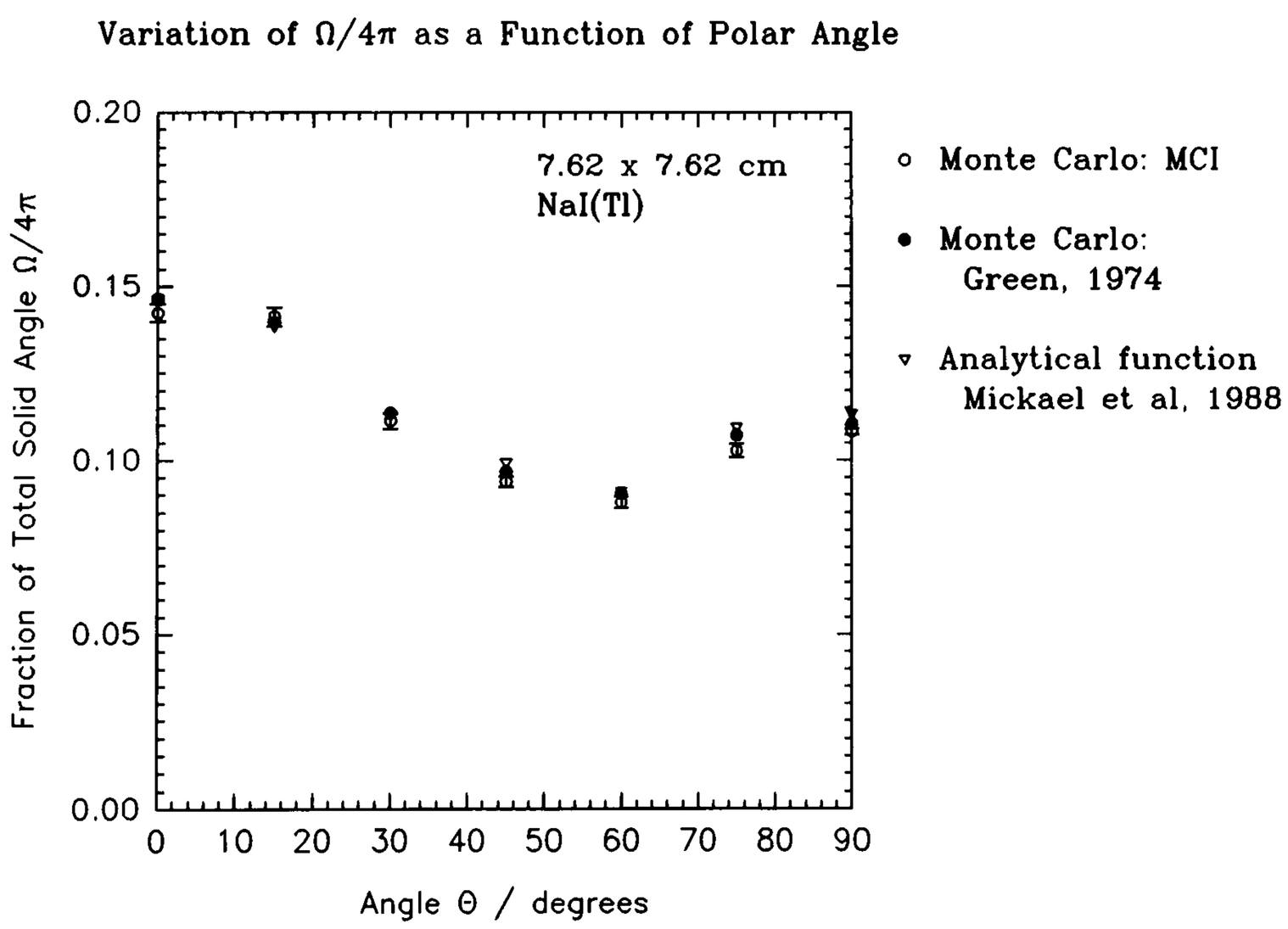

Figure 6.45 Fraction of total solid angle subtended by a 7.62x7.62 cm cylindrical detector, 7.62cm from a point source.

Good agreement amongst the data is seen, and within errors. In a similar manner, a comparison is shown in figure 6.46 of a truly rectangular detector of 10.16x40.64x40.64 cm dimensions (16 litre) and a cylindrical detector of radius that results in equal top/bottom surface areas as that of the former. The solid angle of the rectangular detector varies in accordance to whether one, two or three surfaces are visible from a point source (45.7cm distant) at any one time. The lines drawn through the data represent the extreme angular variation of solid angle with polar and azimuthal directions. The angular variation of the approximated rectangular detector is shown with triangular symbols. These data are seen to closely resemble that of a real rectangular detector except at polar angles 30-60°. Taking accuracy of the Monte Carlo solid angle estimates into account, even at these angles the approximation is reasonably valid.

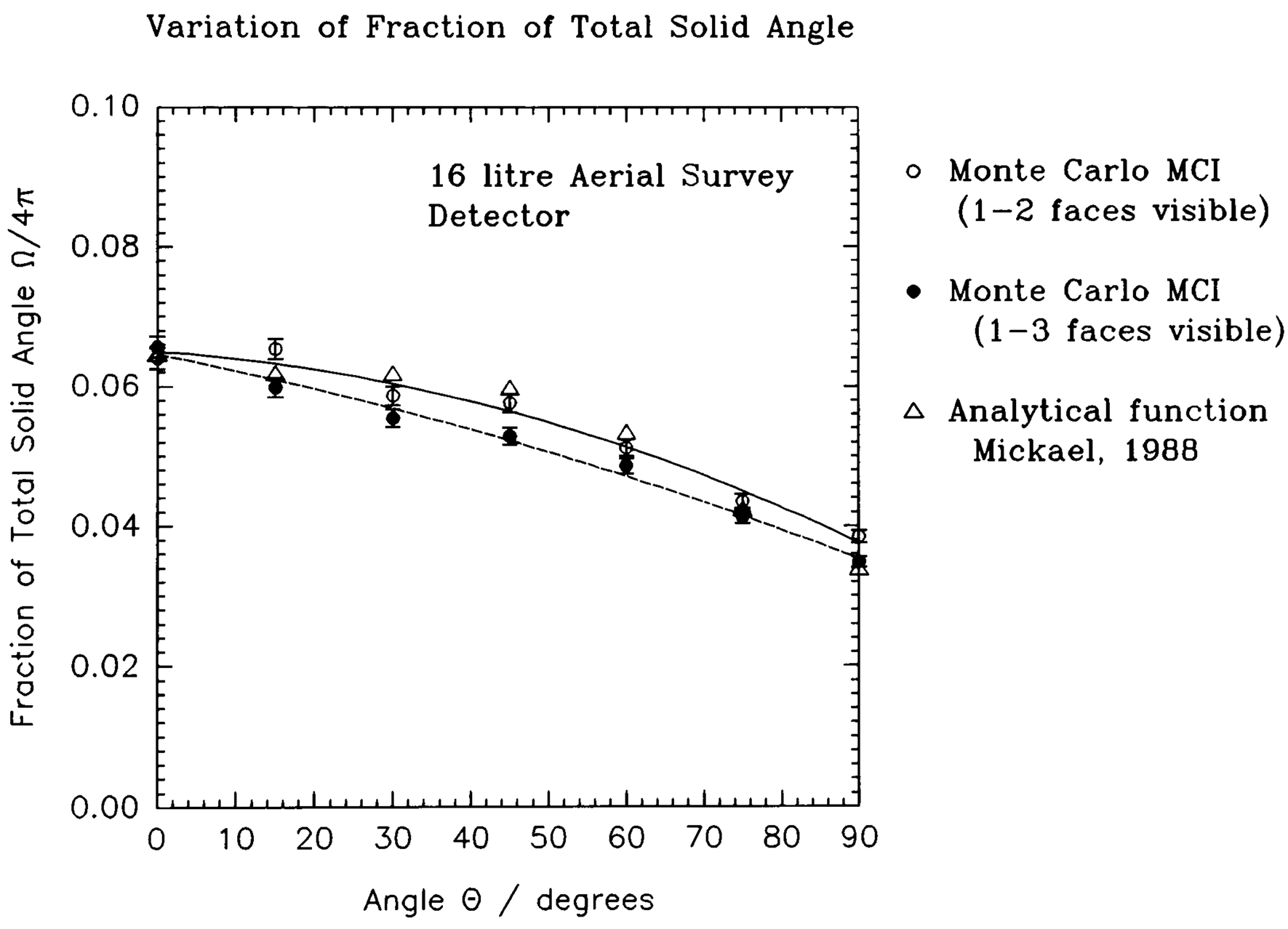

Figure 6.46 Fraction of total solid angle of rectangular and approximated rectangular detector.

It should be remembered that although such an approximation is made for the puposes of solid angle calculation, the angular characteristics of a rectangular detector have been retained.

6.7.3 Gamma-ray Emission Intensities of ^{238}U and ^{232}Th Natural Decay Series

In section 6.5.2.2, the complex schemes of ^{238}U and ^{232}Th were assembled from approximately 25 lines for each decay (emissions greater than 150 keV and 1% in intensity). In order to include a greater number of lower energy and less intense lines, data from Browne and Firestone (1986) were taken and sorted in order of preference. For the following investigations it was decided to include all emissions greater than 50 keV & 0.25% intensity for ^{238}U decay, and 50 keV & 0.50% for ^{232}Th decay. The lines chosen are shown in tables 6.4 and 6.5 respectively. In all, there are at least 600 γ-ray emissions for each decay of ^{238}U and ^{232}Th, the daughters of which are assumed to be in equilibrium. Figures 6.47 and 6.48 show the relative intensity of gamma rays emitted from ^{238}U and ^{232}Th respectively, as a function of emission energy. For the selection parameters given above and from figures 6.47 & 6.48, 96% and 95% of the total γ-ray emission has been considered respectively. For aerial survey detectors the inclusion of fewer low energy emissions may be permitted depending upon survey altitude and threshold limits.

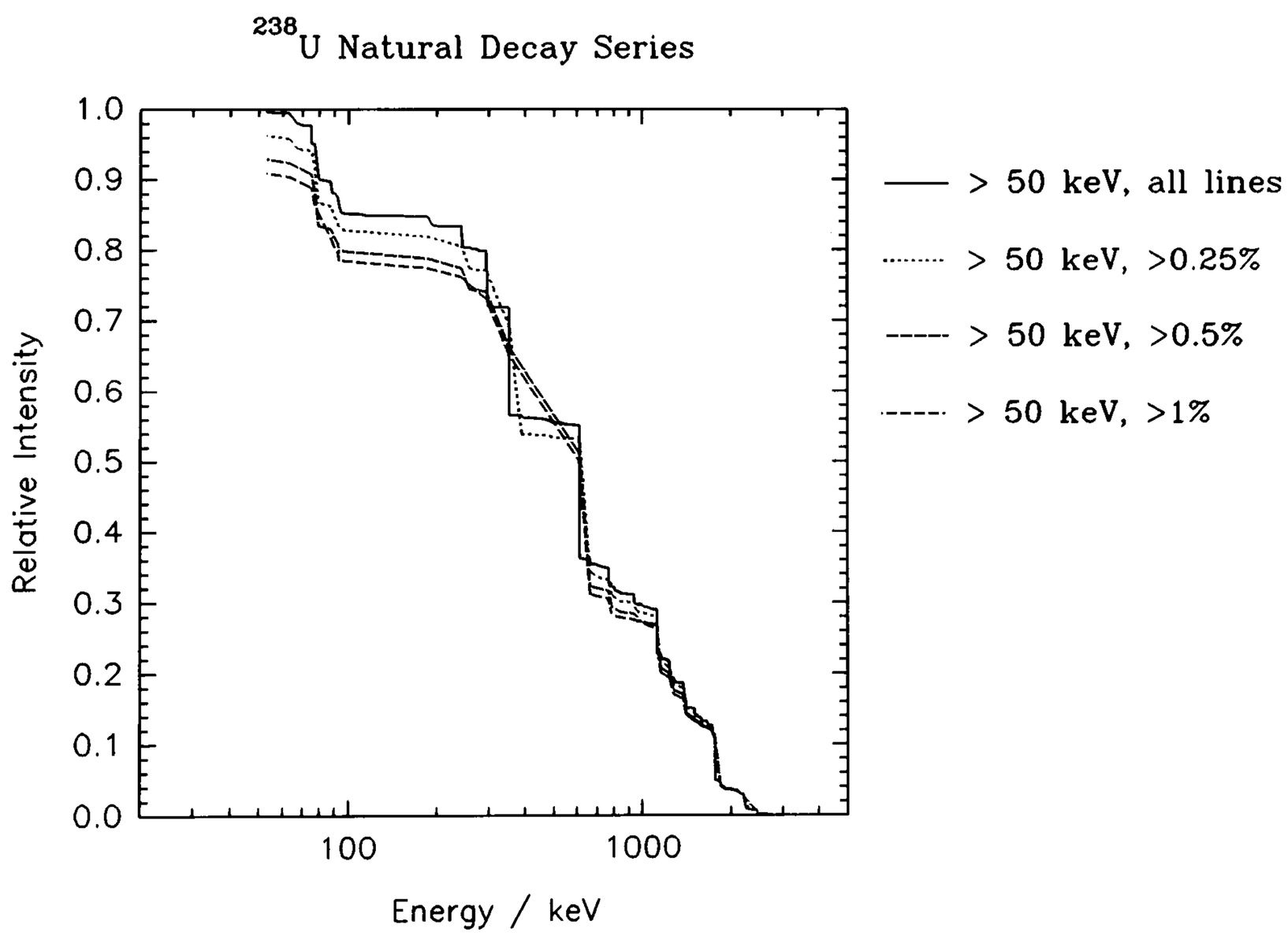

Figure 6.47

Table 6.4 Percentage Intensity of γ-ray Emission from ^{238}U, >50 keV and $>0.25\%$ (Browne & Firestone, 1986).

Energy / keV	% Intensity	Energy / keV	% Intensity	Energy / keV	% Intensity
53.172	1.0998	454.832	0.318	1207.674	0.46
63.288	3.8	480.32	0.3379	1238.107	5.92
67.6758	0.376	487.13	0.4389	1280.952	1.47
74.814	6.5187	580.06	0.3639	1377.659	4.02
76.858	0.58	609.311	46.1	1385.295	0.78
77.107	10.9978	665.442	1.56	1401.48	1.39
79.29	0.97	703.07	0.472	1407.97	2.48
83.787	0.292	719.856	0.403	1509.22	2.19
87.19	3.8792	768.35	4.88	1538.49	0.41
89.639	0.345	785.827	1.0898	1543.347	0.35
90.128	1.1498	786.42	0.31	1583.22	0.72
92.35	2.72	806.155	1.23	1594.78	0.265
92.78	2.69	838.999	0.5869	1599.3	0.334
186.11	3.28	934.039	3.16	1661.258	1.15
241.92	7.4585	964.07	0.383	1729.58	3.05
258.94	0.5499	1001	0.649	1764.49	15.9
274.56	0.3199	1051.95	0.315	1838.37	0.383
295.091	19.1962	1070.02	0.285	1847.41	2.12
351.87	37.0926	1120.273	15	2118.53	1.21
386.834	0.36	1133.65	0.255	2204.09	4.99
388.95	0.41	1155.183	1.69	2293.29	0.324
				2447.680	1.550

Table 6.5 Percentage Intensity of γ-ray Emission of ^{232}Th, >50 keV and $>0.5\%$ (Browne & Firestone, 1986).

Energy / keV	% Intensity	Energy / keV	% Intensity	Energy / keV	% Intensity
57.81	0.525	270.26	3.8	785.51	1.107
72.803	0.7212	277.28	2.2916	794.79	4.6
74.814	10.5	300.034	3.34	830.59	0.63
74.969	1.2132	328.07	3.5	835.6	1.71
77.107	17.7	338.42	12.4	840.44	0.94
84.26	1.21	340.94	0.52	860.3	4.044
87.19	6.27	409.62	2.2	904.29	0.89
89.955	3.4	463.1	4.6	911.16	29
90.128	1.86	510.606	7.2792	964.64	5.8
93.35	5.6	562.65	1.01	968.97	17.4
99.55	1.3	581.52	3	1078.69	0.535
105.362	2	583.022	28.982	1246.6	0.57
108.99	0.67	583.022	1.326	1459.19	1.06
115.122	0.591	677.07	0.9	1496	1.05
129.03	2.9	726.63	0.87	1501.44	0.58
153.89	0.84	727.25	6.65	1580.3	0.71
209.39	4.1	755.28	1.32	1588.2	3.6
216.24	0.8	763.06	0.5527	1620.66	1.51
238.578	43.6	772.28	1.09	1630.47	1.95
240.76	3.9	782.12	0.59	1638.1	0.54
				2614.35	33.6292
				2614.35	1.7238

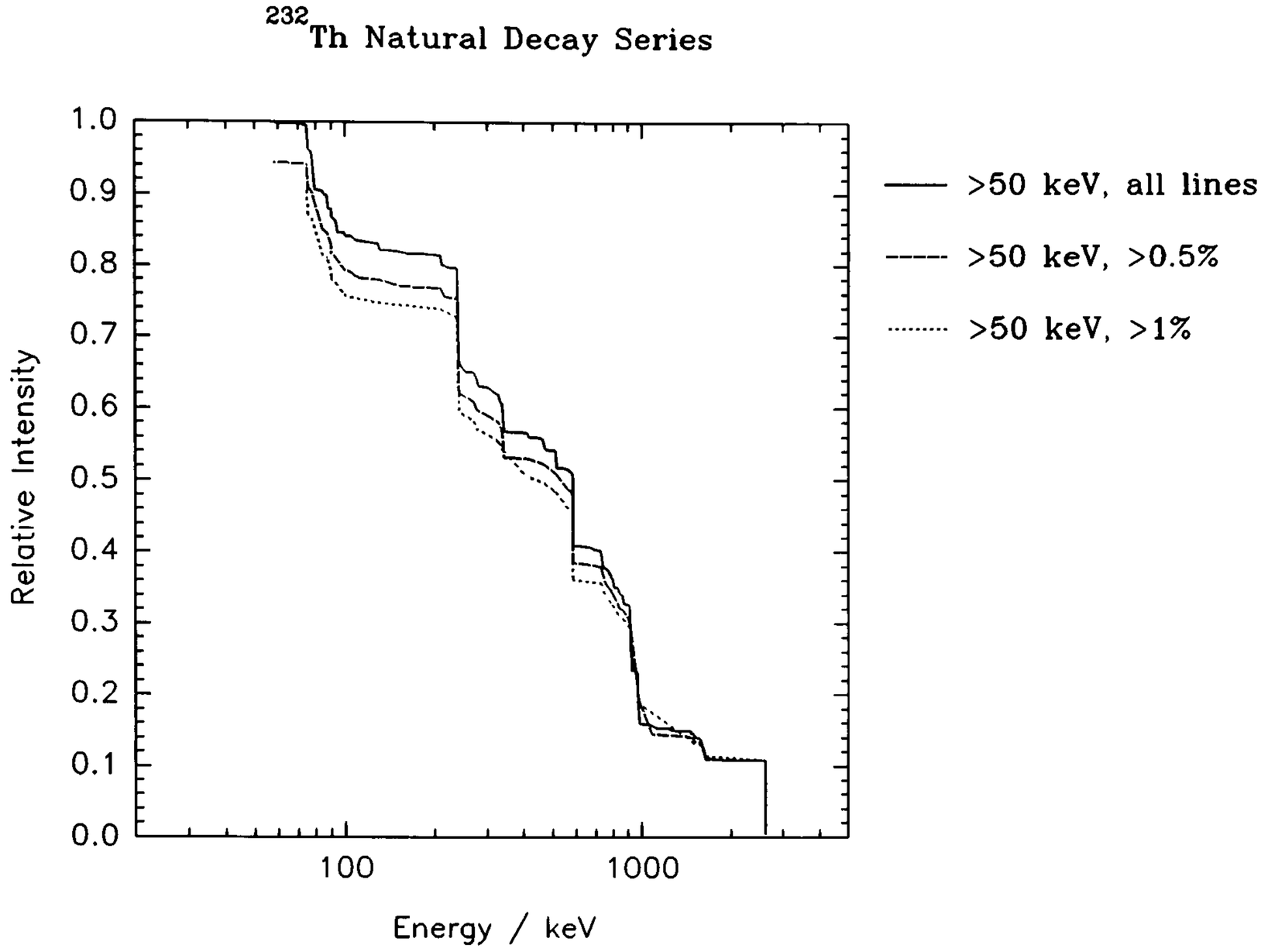

Figure 6.48

Browne and Firestone (1986) has been mostly used as a source of decay line intensities, for consistency as some variations do exist between authors. For ^{238}U decay series, most of the γ-ray emission lines are well known to an uncertainty of less than 1.7%. For the ^{232}Th decay series, the ^{208}Tl emission lines are known to <0.1%, ^{212}Bi less than 1.4% and ^{212}Pb less than 0.17%. However, ^{228}Ac is known to at best 14% uncertainty.

The natural concentration of ^{235}U is only 0.72%, and hence there is little contribution to the total gamma-ray emission of uranium and in line with other studies (IAEA, 1979) is not simulated here. There is little evidence that the simulated spectrum of ^{238}U departs significantly from a measured spectrum of natural uranium at the energies of interest here, for the well defined 7.62x7.62cm NaI(Tl) detector (this is despite the ratio of the specific activities of ^{235}U/^{238}U being 4.6%). More than 99% of the aerial dose rate produced by uranium is attributable to daughters of ^{238}U (Løvborg and Kirkegaard, 1975).

6.8 Results and Discussion II

6.8.1 Validation of Monte Carlo Code MCII

In order to test the efficiency and accuracy of the statistical estimation routines incorporated into MCII, a series of investigations have been carried out and comparisons made under identical experimental and analogue Monte Carlo (MCI) conditions. Although the extension to extreme source-detector separations cannot be compared with the analogue code, the testing at near geometries and with dense scattering media ought show similar characteristics with tenuous media (air) within large open volumes.

Figure 6.49 shows experimental, Monte Carlo MCI analogue and MCII statistical estimation code comparisons of peak intensity and backscattering that occurs from a point source of ^{137}Cs (662 keV), resting upon a surface of concrete (density: 2.23 gcm^{-3}). Source to detector distance is 20cm (to front face of detector). A residual background is noted in the net experimental spectrum, but is of low intensity. Qualitatively, the backscatter and full energy peaks from the Monte Carlo codes are represented well in comparison with experimental data. In the calculated response from MCI, the valley between full energy peak and Compton edge is slightly underestimated: this is also seen from MCII and appears deeper. For the latter, this is to be expected and is a shortcoming of this calculation. To increase efficiency of MCII, the first interaction in the detector is forced at the crystal boundary and not at the detector can: although attenuation of crystal housing is accounted for, forward scattering (and hence response in the valley) is not. For quantitative analysis between spectra, a Kolmogorov-Smirnov test has been used, a non-parametric test for determining the goodness of fit of a distribution, or comparing two distributions. With a large number of channel bins used here (to preserve energy resolution) the spectra have been regarded as continuous distributions. The test compares theoretical and observed data in the form of their cumulative relative frequencies. The absolute maximum deviation D between the cumulative frequencies defines the test statistic at a *level of significance*, α. Table 6.6 shows $D_{critical}$ and α for sample size n (Kennedy & Neville, 1986).

For the backscatter spectra, a K-S test between experimental and MCI data shows a value of $D=2.451x10^{-2}$, for a threshold channel of 10; between experiment and MCII data, $D=2.055x10^{-2}$.

Table 6.6 Critical statistic $D_{critical}$ for Kolmogorov-Smirnov test (Kennedy & Neville, 1986).

	Level of Significance, α		
Sample size, n	0.10	0.05	0.01
130	0.107	0.119	0.143
270	0.0742	0.083	0.0992
512	0.0539	0.060	0.07204

For a sample size $n=130$, $D_{critical}$ is much larger than D and thus, we cannot reject the null hypothesis (that both cumulative distributions are the same), ie. both spectra are statistically alike.

Kolmogorov-Smirnov tests have been applied to data shown in figures 6.50 and 6.51, which respectively show forward scattering from a point source of ^{137}Cs through a concrete slab of 5cm thickness and a complete simulation of the potassium concrete calibration pad, K-1. For the former, a value of $D=2.524x10^{-2}$ is obtained between experimental and MCI data; $D=4.093x10^{-2}$ between experimental and MCII data. Again, even at a 10% level of significance a statistically good overall fit is achieved despite differences particularly in the valley below the photopeak. The peak intensity determined from MCI code is approximately 5% greater than that of MCII and is attributable to a corresponding difference in estimation of solid angle.

For figure 6.51, the fit between experimental and MCI data, and experimental and MCII data yields $D=4.149x10^{-2}$ and $4.191x10^{-2}$ respectively, even at a low threshold channel of 10. Observation of the spectra shows differences in the peak valley and low energy scattering region (below channel 50, equivalent to energy 265 keV) with respect to the experimental spectrum.

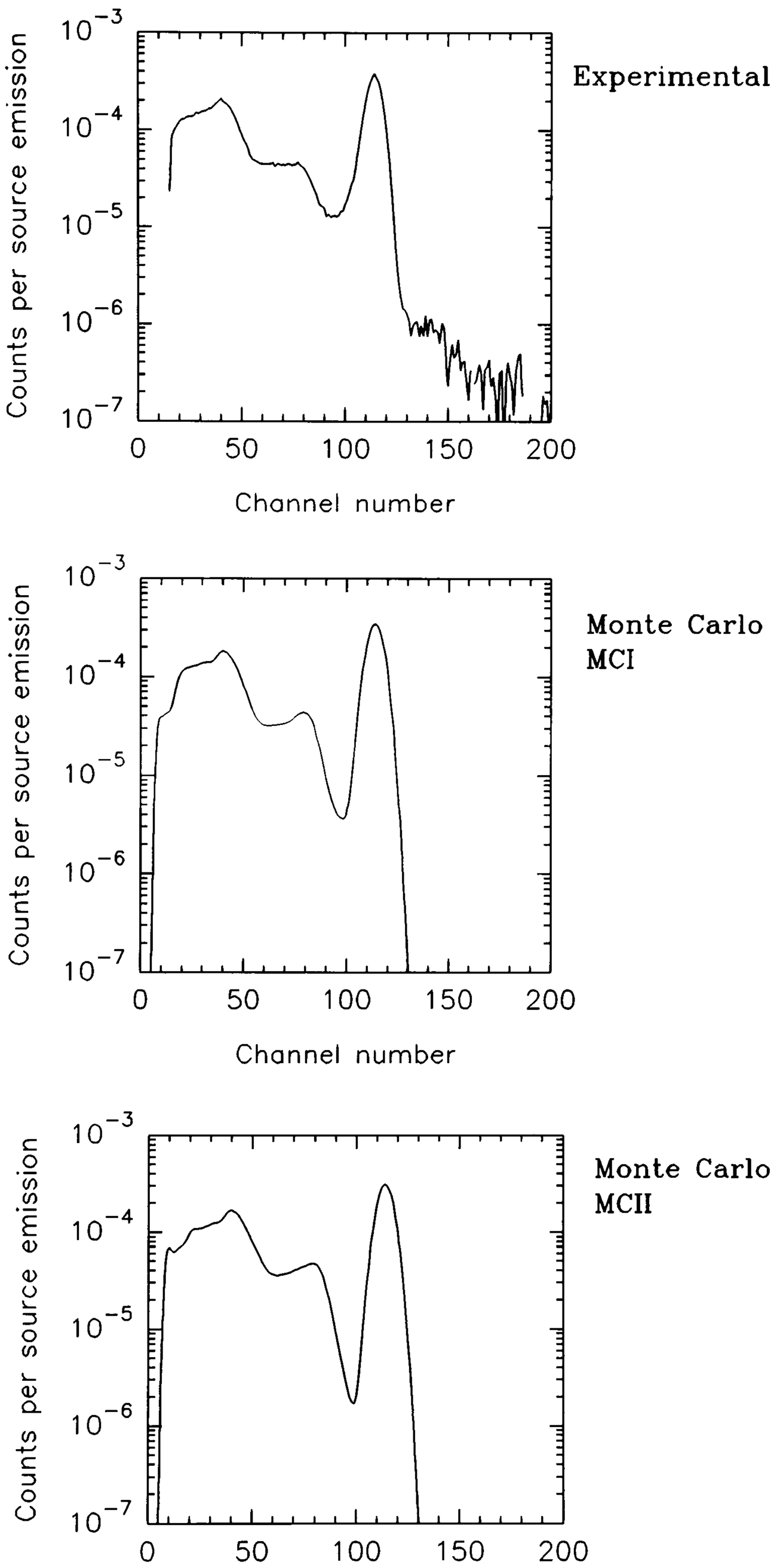

Figure 6.49 Backscatter and full energy peak from ^{137}Cs: 662 keV. 7.62x7.62 cm NaI(Tl) detector.

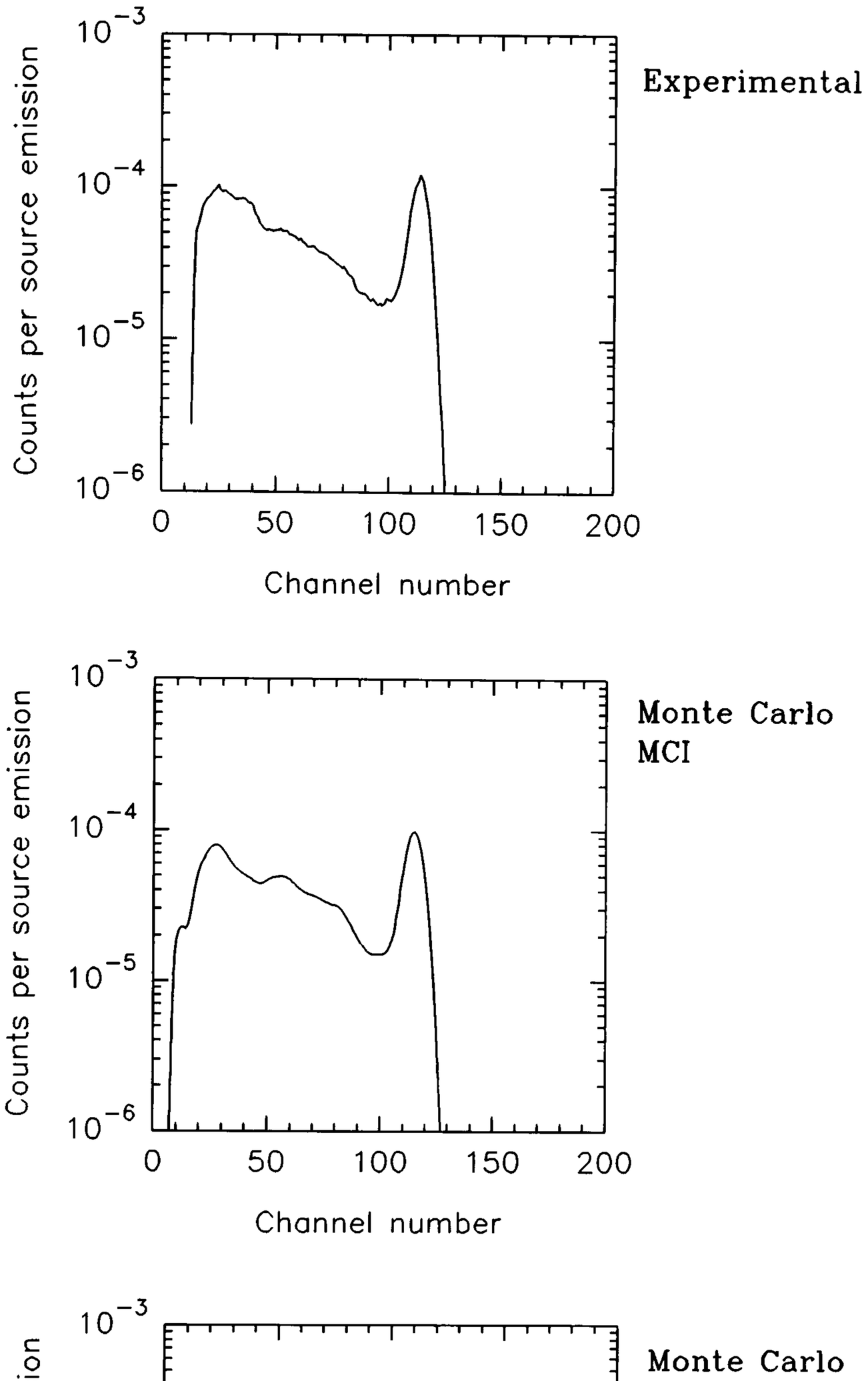

Figure 6.50 Predominantly forward scattering of ^{137}Cs 662 keV γ-rays through a concrete paving slab. 7.62x7.62 cm NaI(Tl) detector.

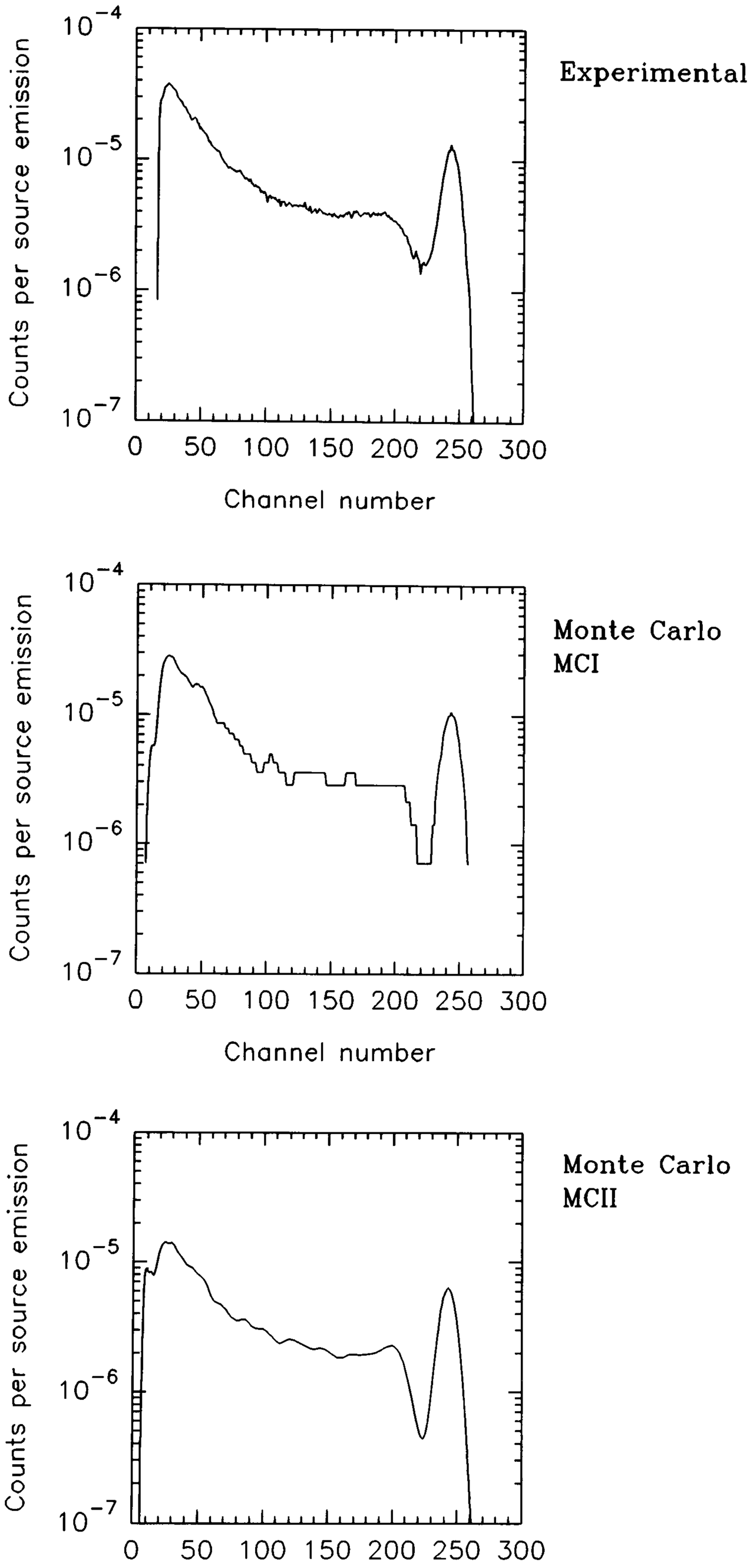

Figure 6.51 Comparisons between experimental, Monte Carlo MCI and MCII simulations of potassium concrete calibration pad K-1. 7.62x7.62 cm NaI(Tl) detector.

One should be aware that the spectrum produced from MCI analogue code in figure 6.51, is for 2.5×10^6 source γ-ray emissions and yet relatively few events have been detected (note discontinuous nature of spectrum). The spectrum produced from MCII has been for 22521 source γ-ray emissions and is equivalent to having recorded approximately 10 times the events from the data of MCI, owing to each source γ-ray contributing to the spectrum in a statistically weighted sense.

An additional verification of MCII may be obtained from the field of view calculations of Chapter 5 (at a corresponding circle of investigation radius). Comparisons of count rates per source γ-ray emission for surface and depth profiles, calculated as in Chapter 5, show that MCII predicts a response generally 6-13% less. This is consistent with the differences in field of view sampling, in solid angle calculation by Monte Carlo code MCI, as noted previously, with additional components probably arising from accuracy of cross-sectional data and weighting schemes made in MCII. Field of view of Monte Carlo calculations were limited to approximately 66-88% in order to keep the sampling within practical bounds. Table 6.7 shows a comparison of estimated count-rate per kBq m^{-2} for ^{137}Cs, calculated by numerical methods of Chapter 5 and by Monte Carlo MCII.

Table 6.7 A comparison of ^{137}Cs cps per kBq m^{-2} surface deposition, between numerical (Chapter 5, Allyson) and Monte Carlo methods (Allyson).

Height / m	**cps per kBq m^{-2} at 662 keV**	
	Numerical (Allyson)	**Monte Carlo MCII (Allyson)**
1 (7.62x7.62 cm NaI(Tl) detector)	4.52 (100% field of view)	2.253 (66%) 3.43 (projected 100%)
100 (16 litre NaI(Tl) detector array)	9.90 (100%)	8.93 (88%) 10.07 (projected 100%)

6.8.2 Simulation of other Radionuclides

The multiple γ-ray emissions of complex decay schemes have been simulated and normalised to a scale of counts per source decay, for convenience. Figures 6.52 and 6.53 show the expected spectra from ^{238}U and ^{232}Th, calculated by MCII. Kolmogorov-Smirnov tests of these in comparison with measurements shown in figures 4.9 and 4.10, indicate values of $D=4.032\text{x}10^{-2}$ and $D=4.738\text{x}10^{-2}$ respectively, for a channel threshold of 23 (100 keV). For thresholds below this, the goodness of fit becomes progressively worse. By contrast, the results shown in figures 6.41 & 6.42 for point sources and no peripheral scattering have corresponding values of $D=0.3262$ & $D=0.292$ respectively, that would be just acceptable for $\alpha=0.10$, at a channel threshold of 160 (947 keV) and 250 (1505 keV).

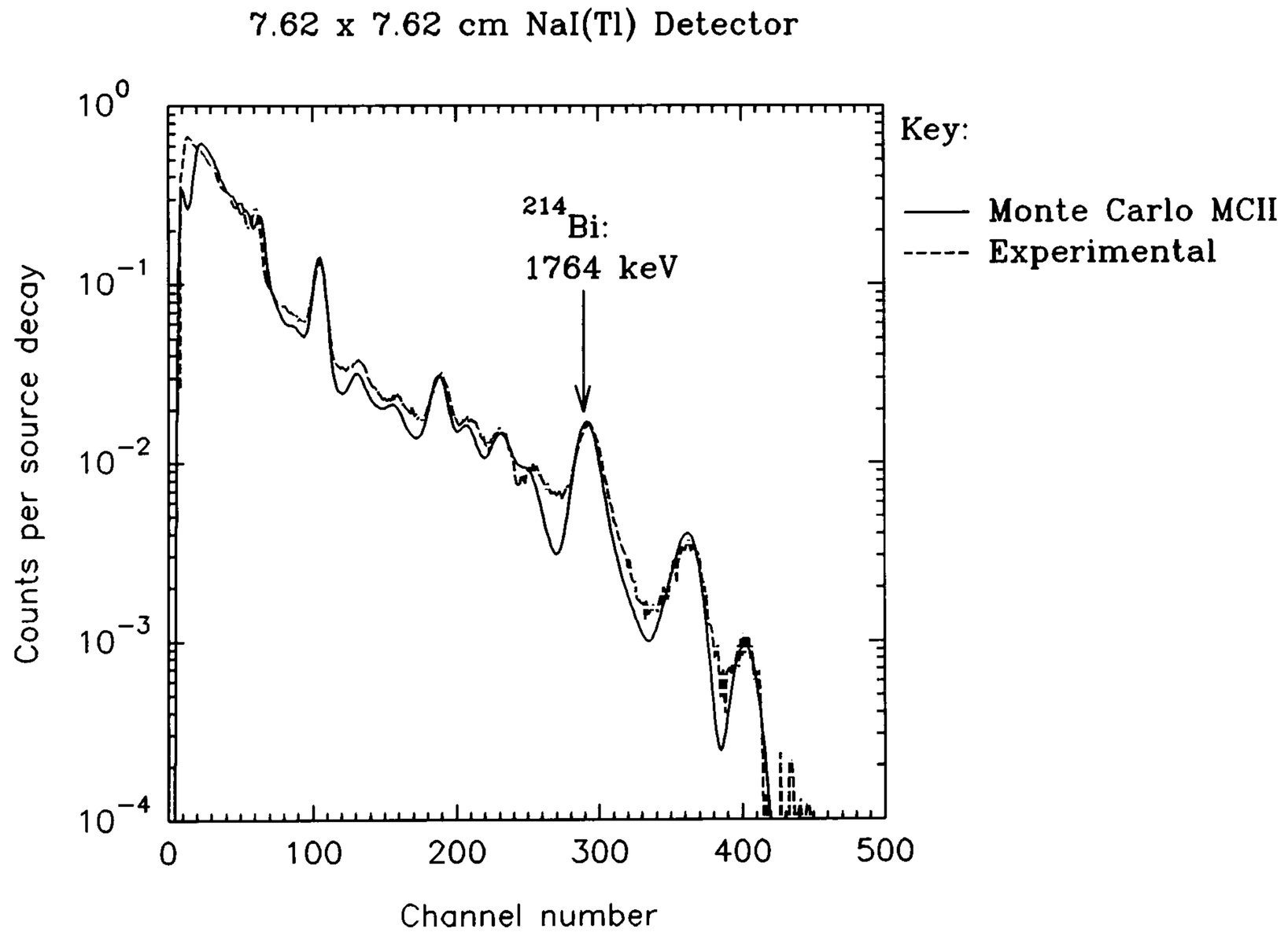

Figure 6.52 Monte Carlo MCII and experimental comparison of ^{238}U spectra, using a 7.62x7.62cm NaI(Tl) detector. Both are from a concrete pad of activity.

It is noted that clear agreement is seen in the case of the uranium spectra. The goodness of fit between calculated and experimentally measured thorium spectra is discussed further in section 6.8.6.

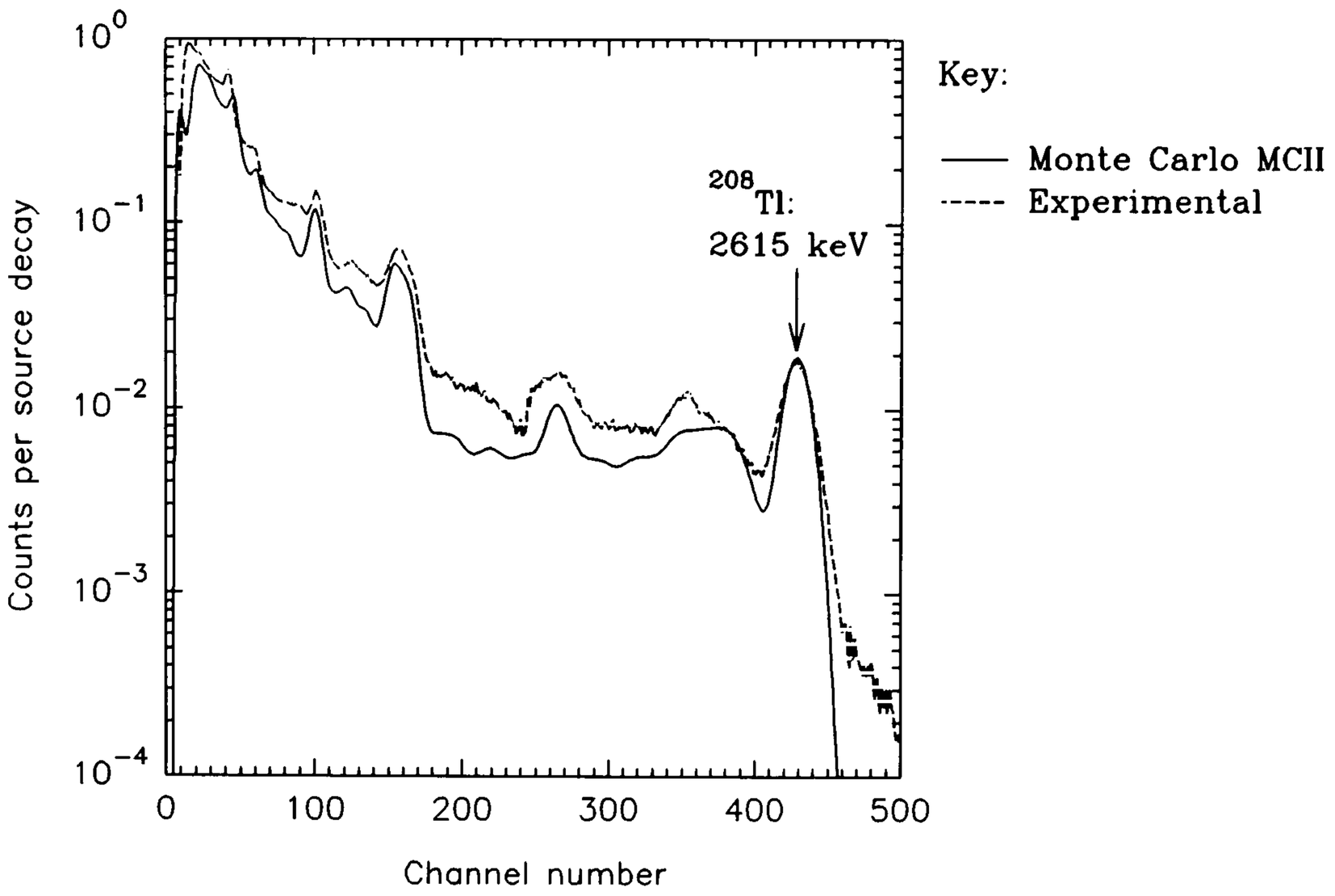

Figure 6.53 Monte Carlo MCII and experimental comparison of ^{232}Th spectra, using a 7.62x7.62cm NaI(Tl) detector, from a concrete pad of activity.

6.8.3 Calculated Stripping Ratios for 7.62x7.62cm NaI(Tl) Detectors

Stripping ratios have been calculated from simulated concrete calibration pads containing potassium, uranium (^{238}U) and thorium (^{232}Th), using MCII. This enabled direct comparisons to be made with experimental measurements using the SURRC calibration pad facility (for potassium see fig. 6.51). In addition the stripping ratios predicted from sources of ^{131}I, ^{137}Cs and ^{134}Cs have been calculated. For ^{131}I, a surface source has been assumed across a concrete calibration pad, as above. For ^{137}Cs and ^{134}Cs, a depth profile of linear depth distribution constant α=0.11 cm^{-1} (relaxation mass per area: 14.5 gcm^{-2}) has been assumed. Table 6.8 shows stripping ratios for SURRC windows, table 6.9 for IAEA recommended windows. An energy window of 55-77 channels has been chosen to encompass the 364.5 keV ^{131}I full energy peak.

Løvborg (1982) has measured the stripping ratios α,ß and γ from six different pad facilities in five countries, using a 7.62x7.62cm NaI(Tl) detector. These are, for comparison purposes, α: 0.597$\pm$0.024; ß: 0.512$\pm$0.026; γ: 0.765$\pm$0.023.

Table 6.8 Stripping ratios for 7.62x7.62 cm NaI(Tl), determined by Monte Carlo MCII simulations of concrete calibration pads. SURRC windows.

	Spectral Windows					
	^{131}I 55-77 ch.	^{137}Cs 95-130 ch.	^{134}Cs 125-150 ch.	^{40}K 220-270 ch.	^{214}Bi 270-318 ch.	^{208}Tl 390-480 ch.
^{131}I	1	0.05382 ±0.00318	0.0	0.0	0.0	0.0
^{137}Cs	0.6734 ±0.0125	1	0.00389 ±0.0007	0.0	0.0	0.0
^{134}Cs	1.9345 ±0.1096	2.0503 ±0.1151	1	0.0	0.0	0.0
^{40}K	1.0758 ±0.029	0.9077 ±0.0275	0.5542 ±0.0194	1	0.0	0.0
^{214}Bi	9.6576 ±0.9155	5.501 ±0.538	1.6671 ±0.1897	1.1906 ±0.1451	1	0.0470 ±0.0197
^{208}Tl	6.5857 ±0.6612	4.469 ±0.462	1.8109 ±0.2102	0.7027 ±0.1019	0.5614 ±0.0870	1

Table 6.9 Stripping ratios for 7.62x7.62 cm NaI(Tl), determined by Monte Carlo MCII simulations of concrete calibration pads. IAEA windows.

	Spectral Windows					
	^{131}I 55-77 ch.	^{137}Cs 95-130 ch.	^{134}Cs 125-150 ch.	^{40}K 228-260 ch.	^{214}Bi 275-307 ch.	^{208}Tl 396-460 ch.
^{131}I	1	0.05382 ±0.00318	0.0	0.0	0.0	0.0
^{137}Cs	0.6734 ±0.0125	1	0.00389 ±0.0007	0.0	0.0	0.0
^{134}Cs	1.9345 ±0.1096	2.0503 ±0.1151	1	0.0	0.0	0.0
^{40}K	1.1199 ±0.032	0.9449 ±0.0289	0.5769 ±0.0203	1	0.0	0.0
^{214}Bi	10.999 ±1.107	6.2649 ±0.6482	1.8987 ±0.2254	0.9787 ±0.1335	1	0.0444 ±0.0204
^{208}Tl	7.0437 ±0.7282	4.779 ±0.508	1.9369 ±0.2298	0.4347 ±0.1397	0.3868 ±0.0708	1

In comparison with tables 6.2 and 6.3 (simulation of point sources and no peripheral scattering), simulation of calibration pads by MCII is more satisfactory and this is reflected in the stripping ratios, which are more representative of the experimentally derived factors.

6.8.4 Spectral Response and Depth Profiles

Shown in figure 6.54 are results from MCII, for a plane and exponentially distributed source of ^{137}Cs through a matrix of soil with Beck composition (density 1.6 gcm^{-3}).

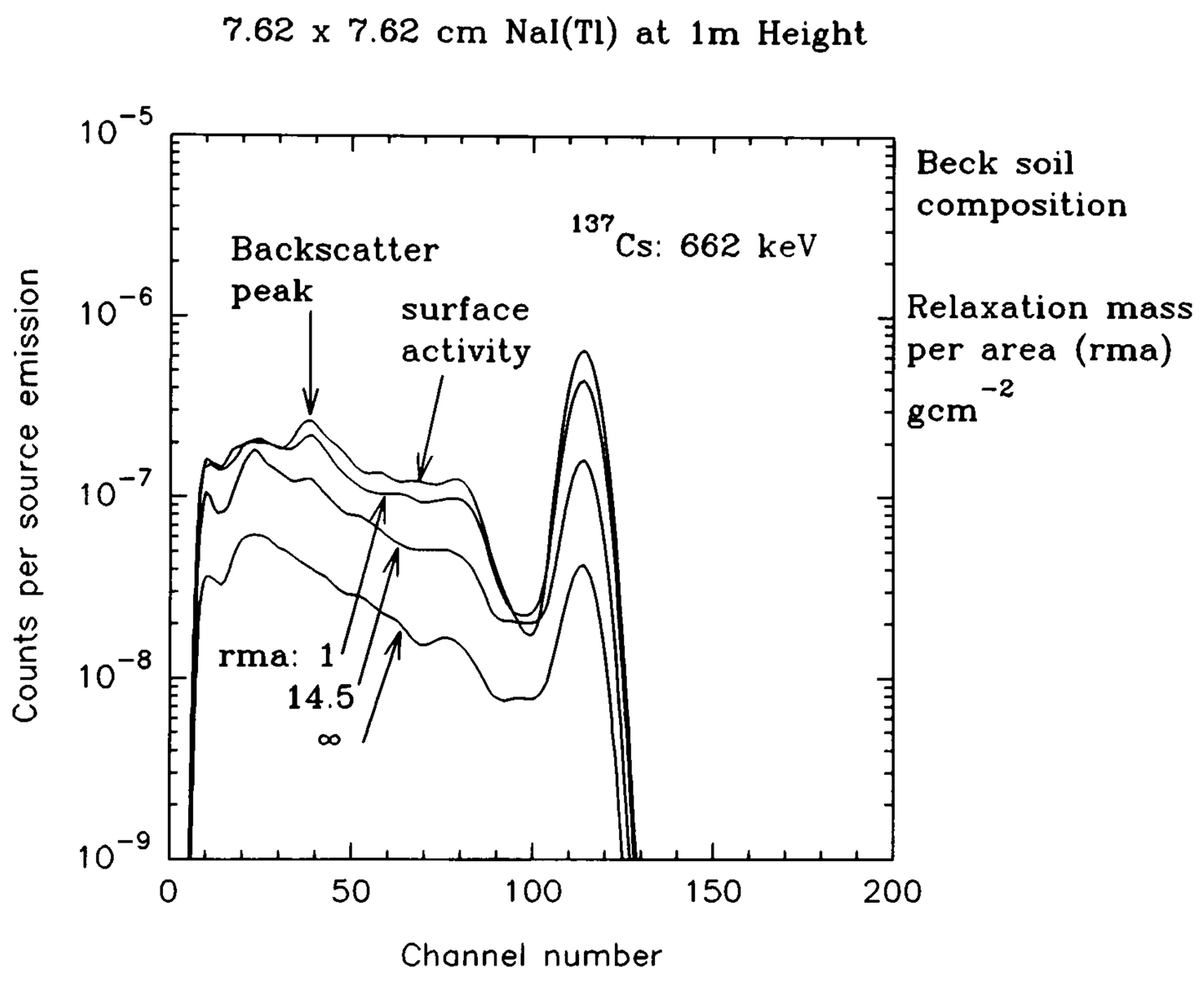

Figure 6.54 Response to ^{137}Cs activity distributed on and through Beck soil matrix of density 1.6 gcm^{-3}.

The absolute intensities of the full energy peak and Compton continuum are noted to decrease with increasing source depth. The relative intensities of peak-to-Compton continuum decreases with depth, since the proportion of scattering increases.

The spectral shape information provided by figure 6.54 can potentially provide useful estimates of depth profile exponential constants, if such a distribution can be assumed (see Chapter 5.3.5.4). The ratio of counts in the full energy peak/valley provide a sensitive measure of mean depth (the inverse of α) up to about 10cm in Beck soil

(ρ_{soil}=1.6 gcm^{-3}), corresponding to a relaxation mass per area of 16 gcm^{-2}. Beyond these limits, the ratio becomes relatively invariant with depth (fig. 6.55). A linear function (solid line) with the log(mean depth) may be applied over the useful range, although a quadratic function (dotted line) makes the better fit. The ^{137}Cs peak is defined by a window 575-761 keV; the valley by 526-569 keV.

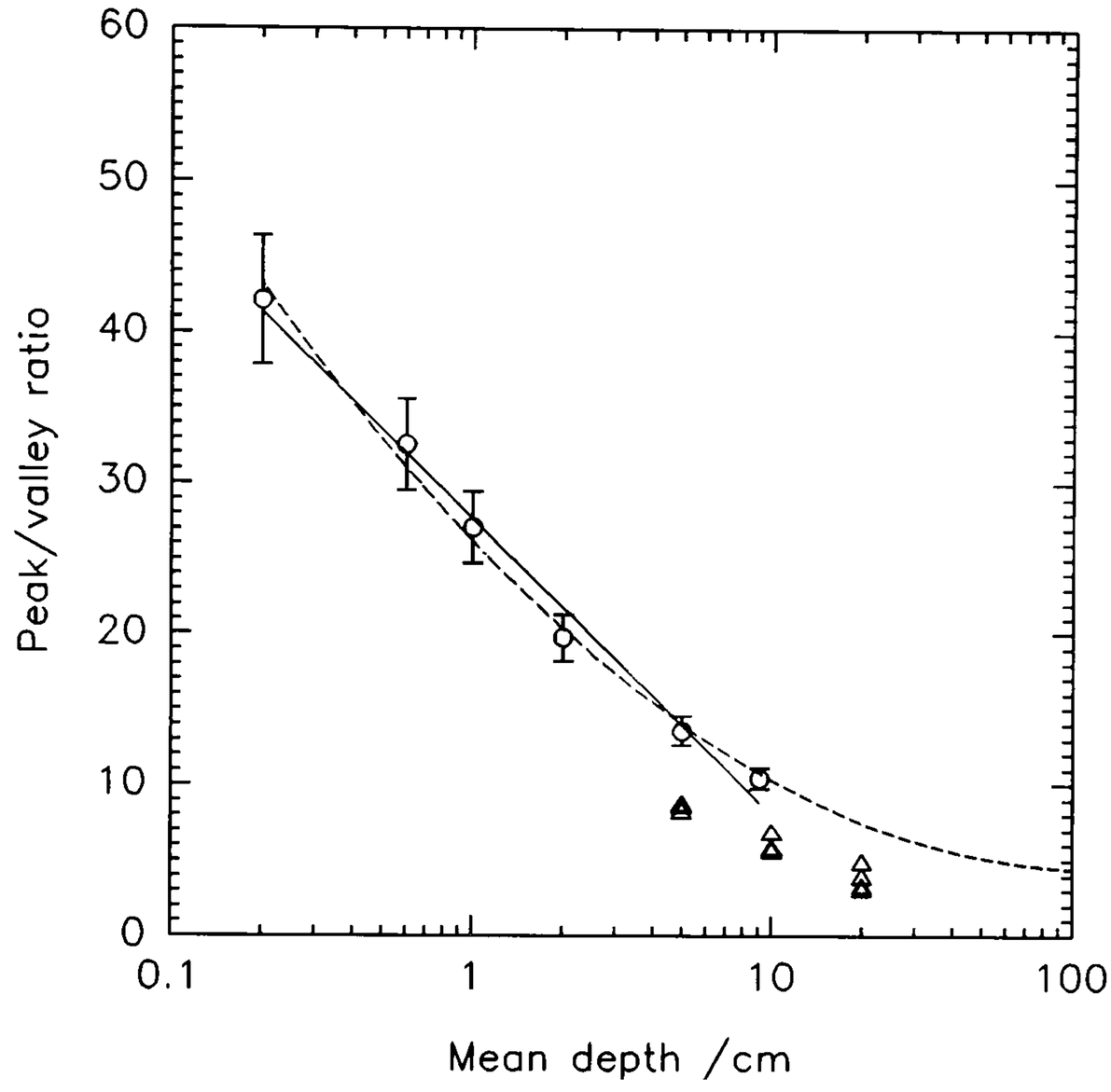

Figure 6.55 Ratio of counts in peak/valley for ^{137}Cs distributed through Beck soil matrix.

The few triangular data-points of figure 6.55, represent Gaussian distributed activity with peak activity at depths 5cm, 10cm and 20cm and σ=4, 5, 6 and 7. Although further work is necessary, some cursory observations may be made. To rely solely on the ratio of peak/valley counts to provide information of activity distribution may mislead: a deep exponentially distributed activity (> 10cm mean depth) appears with the same ratio as Gaussian distributed activity. A second parameter to describe an activity distribution may be required. Further spectral analysis may yield this. The practical use of this is limited by the presence of background interferences.

6.8.5 Aerial Survey Detector

The spectral response of a 16 litre aerial survey NaI(Tl) detector has been simulated, primarily to investigate anthropogenic radionuclides (^{131}I, ^{134}Cs & ^{137}Cs) hitherto not dealt with so completely previously, and secondary potassium (^{40}K), uranium (^{238}U) and thorium (^{232}Th). The naturals have been used as basis upon which comparisons can easily be made with known experimental data. It has been assumed that the anthropogenics are distributed as a planar source and the naturals as a uniformly distributed source with depth.

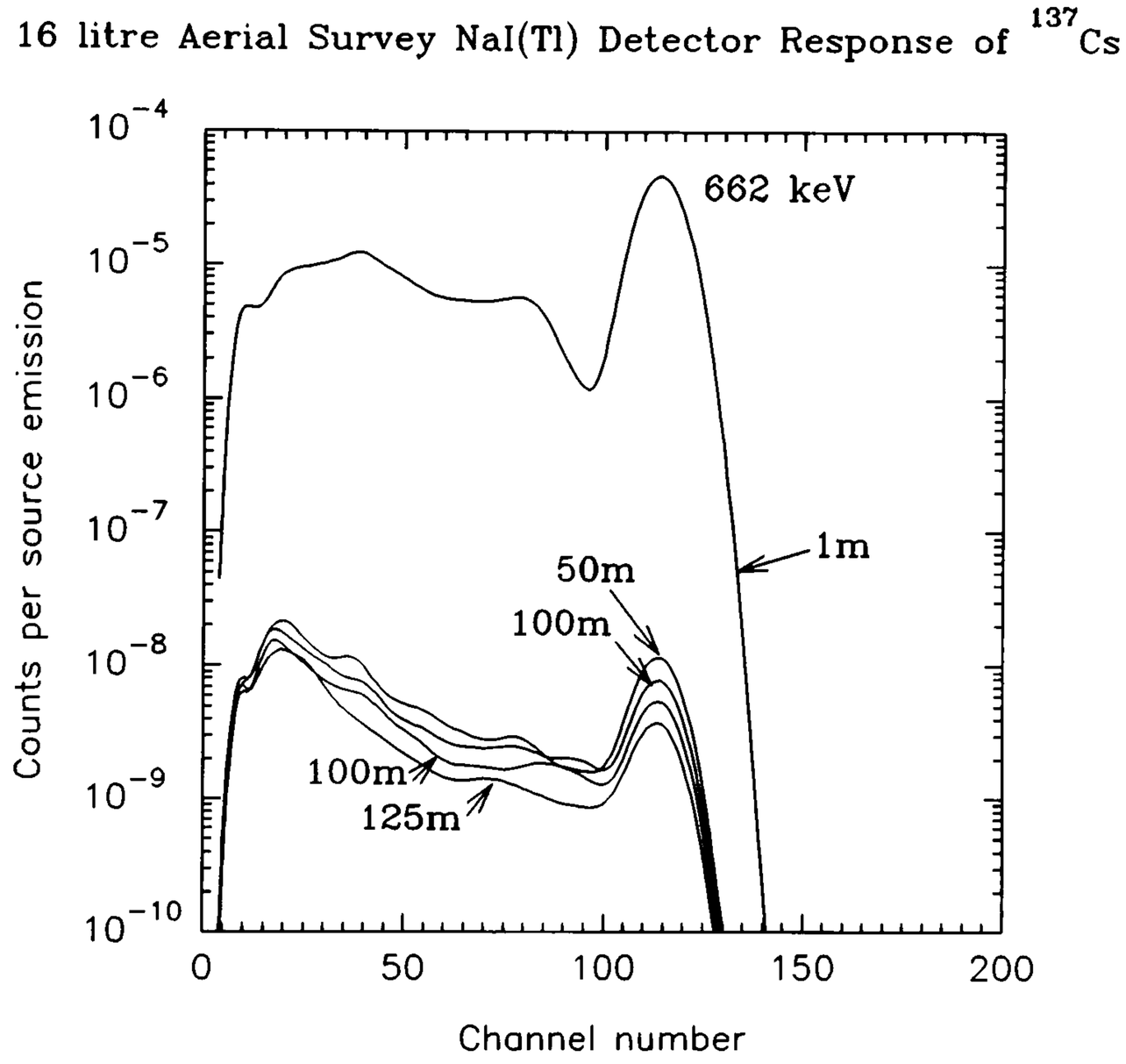

Figure 6.56 The effect of increasing altitude on spectral shape of a plane ^{137}Cs source.

The full energy peak and Compton scatter components of ^{137}Cs are seen to be attenuated with increasing height in figure 6.56. In addition, the relative proportion of scatter to total response increases with height owing to the combined effects of attenuation and air scattering. In all the spectral responses, the backscatter peak at about channel 40 becomes less of a prominent feature as altitude increases. The scattered part of a recorded spectrum includes a constant fraction owing to the partial energy deposition within the detector itself. The ratio of scattered to total components from the detector

alone is (1-photofraction).

The effect of distributing activity through a depth profile, on the spectral shape above, is of course the same as increasing the effective height of the air column. The scatter/total response increases further, although not as quickly as that of air scattering alone over the first 1-50m height (table 6.10). For example, at 100m altitude, an increase in the effective mean source depth from the surface to 9cm (rma=14.5 gcm^{-2}, ρ_{soil}=1.6 gcm^{-3}) results in an increase of scattered/total from 83.5% to 87.6%. From 1m to 100m, the scattered/total ratio increases from 49.3% to 83.5% respectively for a surface source.

Table 6.10 Total and scattered components of ^{137}Cs as a surface planar and exponentially distributed source.

	^{137}Cs and Aerial Survey (16l) Detector Response		
Source distribution	**Scattered counts per source emission >25keV**	**Total counts per source emission**	**Scattered fraction of total**
1m: Surface	$6.049x10^{-4}$	$1.228x10^{-3}$	49.3%
50m :Surface	$6.464x10^{-7}$	$8.164x10^{-7}$	79.2%
75m: Surface	$5.499x10^{-7}$	$6.702x10^{-7}$	82.1%
100m: Surface	$4.339x10^{-7}$	$5.196x10^{-7}$	83.5%
125m: Surface	$3.623x10^{-7}$	$4.217x10^{-7}$	85.9%
100m: rma=1 gcm^{-2}	$4.543x10^{-7}$	$5.288x10^{-7}$	85.9%
100m: rma=14.5 gcm^{-2}	$2.693x10^{-7}$	$3.073x10^{-7}$	87.6%
100m: Uniform	$1.466x10^{-7}$	$1.659x10^{-7}$	88.4%

rma=relaxation mass per area

The radionuclides of ^{134}Cs and ^{131}I have been similarly studied. Their spectral response

are seen in figures 6.57 & 6.58 respectively. A surface area of 10x10m (100 m^2) was chosen for 1m height calculations: 400x400m ($160x10^3$ m^2) for >1m height.

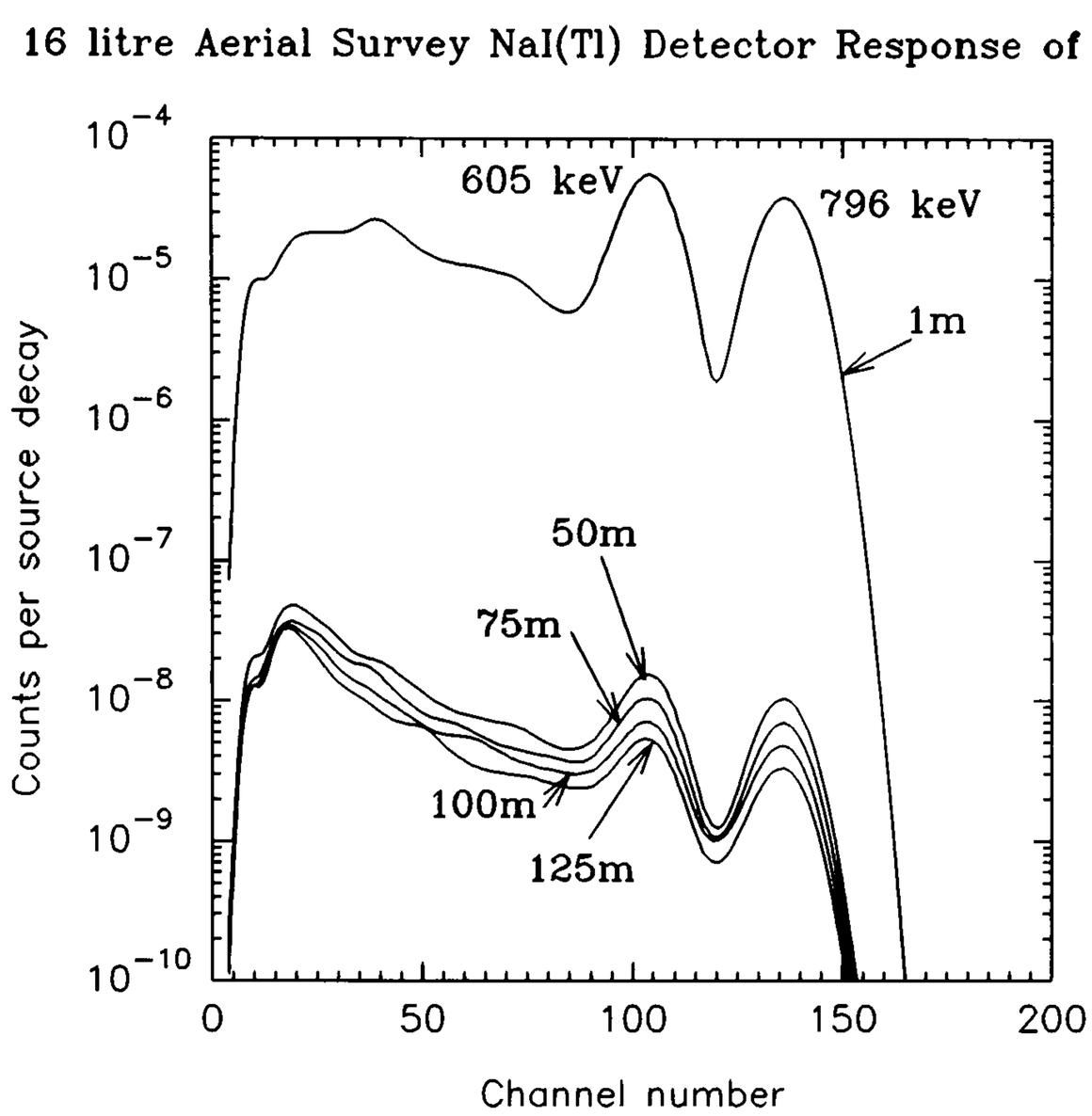

Figure 6.57 The effect of increasing altitude on spectral response of a plane ^{134}Cs source.

Table 6.11 Total and scattered components of ^{134}Cs distributed as a surface planar source.

	^{134}Cs and Aerial Survey (16l) Detector Response		
Source distribution	**Scattered counts per source emission >25 keV**	**Total counts per source emission**	**Scattered fraction of total**
1m: Surface	$1.208x10^{-3}$	$2.623x10^{-3}$	46.1%
50m: Surface	$1.407x10^{-6}$	$1.837x10^{-6}$	76.6%
75m: Surface	$1.091x10^{-6}$	$1.391x10^{-6}$	78.4%
100m: Surface	$9.210x10^{-7}$	$1.137x10^{-6}$	80.9%
125m: Surface	$7.899x10^{-7}$	$9.486x10^{-7}$	83.3%

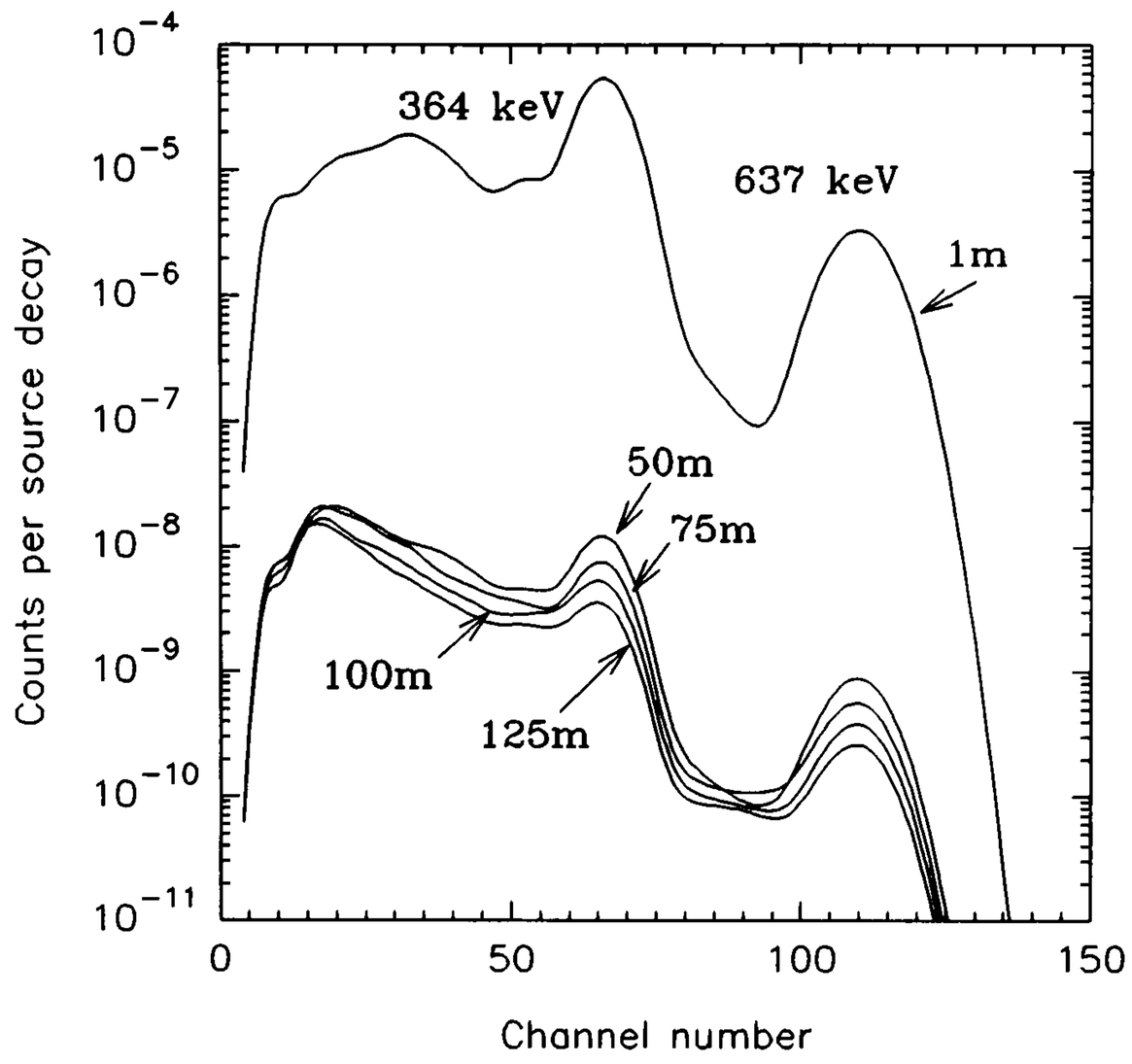

Figure 6.58 The effect of altitude on spectral response of a plane surface source of ^{131}I.

Table 6.12 Total and scattered components of ^{131}I distributed as a surface planar source.

	^{131}I and Aerial Survey (16l) Detector Response		
Source distribution	**Scattered counts per source emission >25 keV**	**Total counts per source emission**	**Scattered fraction of total**
1m: Surface	5.462×10^{-4}	1.175×10^{-3}	46.5%
50m: Surface	5.177×10^{-7}	6.775×10^{-7}	76.4%
75m: Surface	4.748×10^{-7}	5.772×10^{-7}	82.2%
100m: Surface	3.635×10^{-7}	4.392×10^{-7}	82.8%
125m: Surface	3.132×10^{-7}	3.655×10^{-7}	85.7%

6.8.6 Calculated Stripping Ratios of Aerial Survey Detector

Estimates of the variation of stripping ratios over extended source distances, and the use of an aerial survey 16 litre NaI(Tl) detector have been calculated. The soil matrix used has been of Beck composition. Studies have also included responses to different depth profiles of ^{137}Cs. Tables 6.15-6.24 show stripping ratios for SURRC and IAEA windows as defined previously. Figures 6.61-6.67 show graphically the stripping ratio variation with altitude. This is seen to be both positive and negative. Direct comparison may be made with corresponding figures 4.27-4.33. In summary, the trends and rates of change with altitude are mostly within error estimates of the experimentally derived stripping ratios of Chapter 4, but the errors are large. The absolute values show some differences, of up to 37% less than practically measured. Direct comparison with spectra measured across the concrete calibration pads is instructive, but certain allowances have to be made.

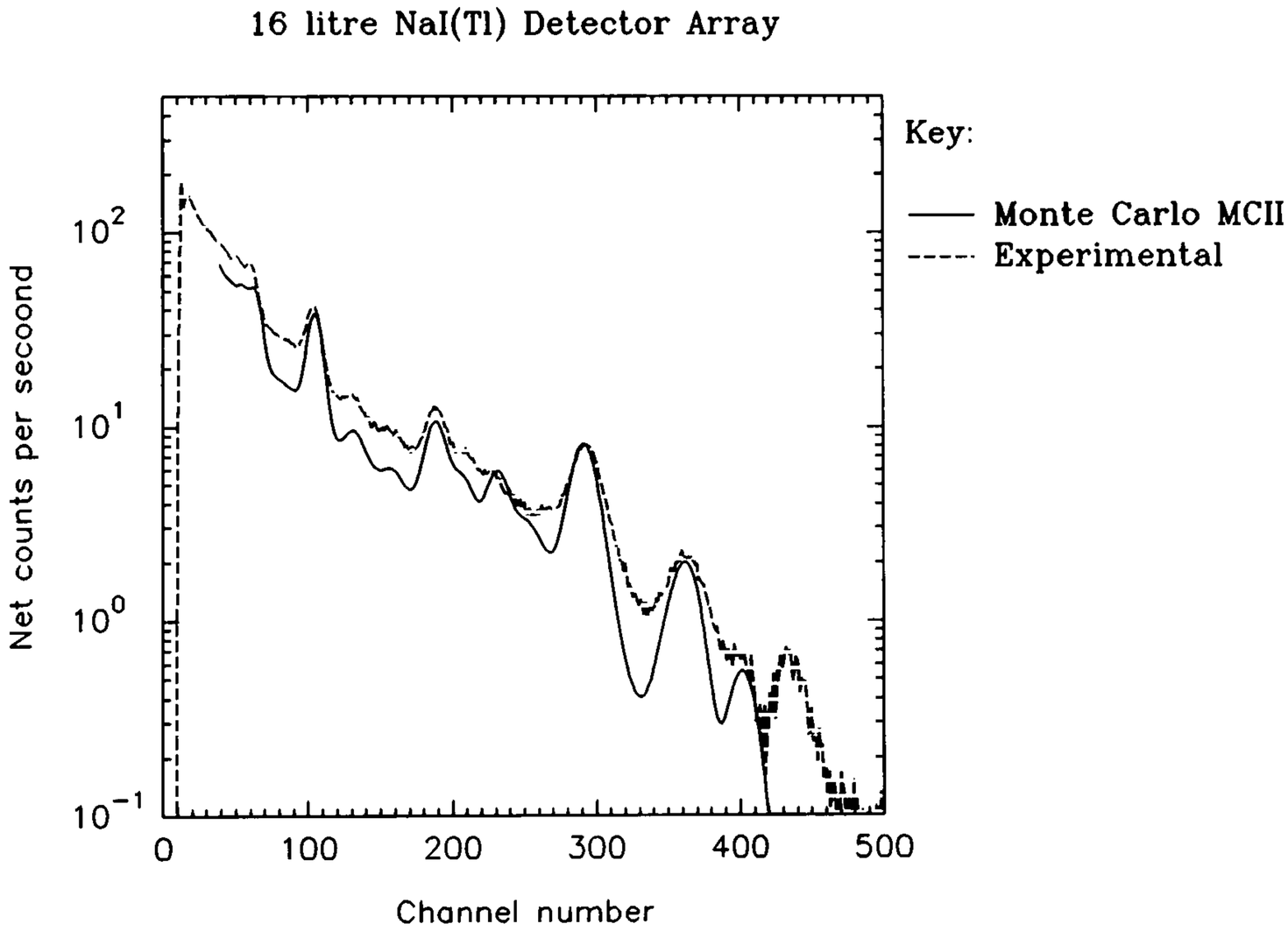

Figure 6.59 Monte Carlo MCII and experimental comparison of ^{238}U spectra, using a 16 litre NaI(Tl) detector array at 1m height, from a matrix of Beck soil and concrete pad respectively.

Underestimation of scattering between full energy peaks has arisen from probably a too conservative thickness of detector housing material. The experimental spectra probably show contributions from scattering not originating from the calibration pads alone. The

spectral comparison of uranium using a 7.62x7.62cm NaI(Tl) is so close that there seems little reason in principle to expect any difference in the thorium spectrum. Løvborg *et al* (1972) noted deviations between simulation of 7.62x7.62cm NaI(Tl) detectors above uranium and thorium doped concrete calibration pads, but assumed the differences to be in the omission of escape peaks in the Monte Carlo code.

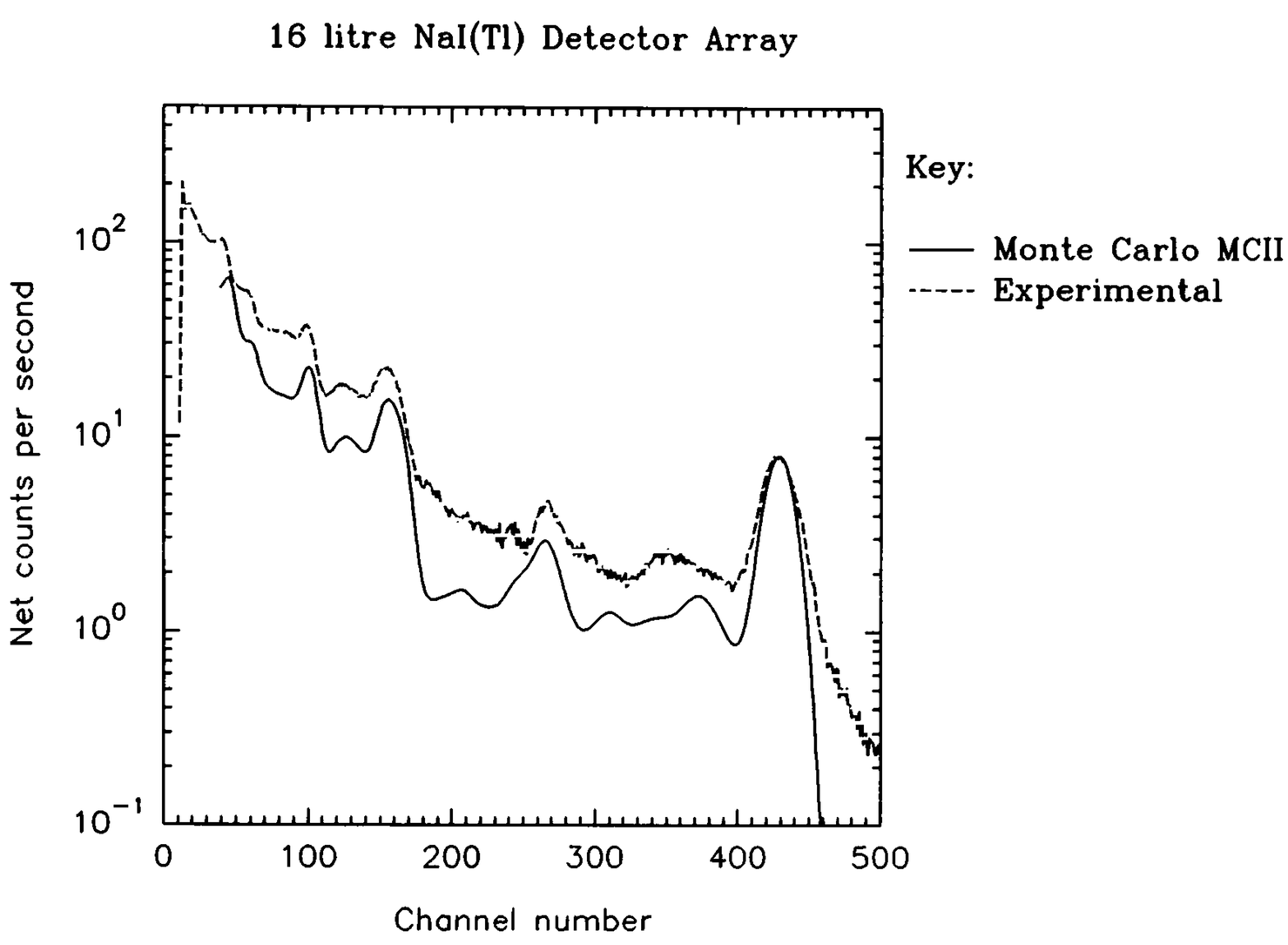

Figure 6.60 Monte Carlo and experimental comparison of ^{232}Th spectra, using a 16 litre NaI(Tl) detector array at 1m height, from a matrix of Beck soil and concrete pad respectively.

The full energy peak of ^{208}Tl (2615 keV, 429 channel) appears suppressed in the experimental spectrum with respect to the scattering and escape peak components. If thorium exhibited some non-uniformity of concentration in the top subsurface layers of the pad, this could explain this occurrence.

Close scrutiny of the experimental spectra shows residual contributions from thorium in the uranium spectra and potassium in the thorium spectra. The use of the blank pad, to provide a background measurement, may lead to difficulties if the doped and blank pads are located within slightly different radiation environments. Each calibration pad is situated between thick blank concrete blocks, to eliminate *cross-talk*. It is likely that these provide potential scattering media from the calibration pads to detector, and increase Compton scattering contributions to the measured spectra. The values of α, ß

and γ determined by MCII are listed below for IAEA windows.

$$\alpha = (0.0003329 \pm 0.0001895)z + (0.1835 \pm 0.0127) \quad (6.50)$$

$$\beta = (0.0005108 \pm 0.000438)z + (0.2907 \pm 0.0295) \quad (6.51)$$

$$\gamma = (0.0004011 \pm 0.0002856)z + (0.7290 \pm 0.0192) \quad (6.52)$$

The proportion of ^{137}Cs entering into the higher, and slightly overlapping, energy window of ^{134}Cs remains constant over a change in altitude up to 125m. Comparison with figure 4.27 shows good agreement, although some fall-off is observed experimentally. Stripping ratios that exhibit some variation with altitude are summarised in table 6.13, with comparisons with corresponding experimental results of Chapter 4.

Table 6.13 Stripping ratio variation with altitude: SURRC windows.

Stripping Ratio	**Monte Carlo MCII (Allyson)**		**Experimental (Chapter 4, Allyson)**	
	Slope /m	**Intercept**	**Slope /m**	**Intercept**
$^{137}Cs/^{40}K$	(1.737 ± 0.163) x10^{-3}	0.3447 ± 0.0129	(3.129 ± 0.143) x10^{-3}	0.459 ± 0.0106
$^{134}Cs/^{40}K$	(9.222 ± 1.305) x10^{-4}	0.2230 ± 0.0103	(1.591 ± 0.090) x10^{-3}	0.278 ± 0.007
$^{137}Cs/^{214}Bi$	$-(3.931 \pm 1.575)$ x10^{-3}	3.245 ± 0.106	(4.234 ± 1.300) x10^{-4}	3.474 ± 0.009
$^{134}Cs/^{214}Bi$	(1.096 ± 0.323) x10^{-3}	0.966 ± 0.0217	(1.779 ± 0.088) x10^{-3}	1.282 ± 0.006
$^{40}K/^{214}Bi$	(5.846 ± 3.553) x10^{-4}	0.919 ± 0.0239	(8.684 ± 0.597) x10^{-4}	0.902 ± 0.004
$^{137}Cs/^{208}Tl$	$-(1.041 \pm 1.175)$ x10^{-3}	2.179 ± 0.079	$-(2.372 \pm 17.7)$ x10^{-5}	2.862 ± 0.013
$^{134}Cs/^{208}Tl$	$-(4.879 \pm 4.740)$ x10^{-4}	1.137 ± 0.032	$-(8.599 \pm 1.206)$ x10^{-4}	1.603 ± 0.009
$^{40}K/^{208}Tl$	(7.670 ± 7.228) x10^{-4}	0.468 ± 0.048	(6.253 ± 0.824) x10^{-4}	0.614 ± 0.006
$^{214}Bi/^{208}Tl$	(4.792 ± 3.843) x10^{-4}	0.288 ± 0.025	(8.111 ± 0.415) x10^{-4}	0.433 ± 0.003

From table 6.13, the absolute values (at 0m) of stripping ratios are less than their respective experimentally derived estimates by up to 34%. That of $^{40}K/^{214}Bi$ provides good agreement. The rate of change with altitude is generally within the uncertainties of calculation, with the exception of $^{137}Cs/^{40}K$ and $^{134}Cs/^{40}K$ (44% & 42% less, each).

Table 6.14 shows the stripping ratio variation with altitude, using IAEA windows. Similar inspection shows differences, that in this instance are slightly worse by a few more percent. Absolute values (at 0m) are less and vary by up to 42%. The rate of change with altitude shows some agreement (errors considered) with the exception of $^{137}Cs/^{40}K$, $^{134}Cs/^{40}K$ and $^{134}Cs/^{214}Bi$ (less by 46.6%, 43.7% and 41.3% respectively).

Table 6.14 Stripping ratio variation with altitude: IAEA windows.

Stripping Ratio	**Monte Carlo MCII (Allyson)**		**Experimental (Chapter 4, Allyson)**	
	Slope /m	**Intercept**	**Slope /m**	**Intercept**
$^{137}Cs/^{40}K$	$(1.963 \pm 0.171) \times 10^{-3}$	0.3628 ± 0.0135	$(3.676 \pm 0.168) \times 10^{-3}$	0.509 ± 0.012
$^{134}Cs/^{40}K$	$(1.051 \pm 0.139) \times 10^{-3}$	0.2349 ± 0.0110	$(1.868 \pm 0.097) \times 10^{-3}$	0.309 ± 0.007
$^{137}Cs/^{214}Bi$	$-(4.123 \pm 1.945) \times 10^{-3}$	3.714 ± 0.131	$(9.202 \pm 1.336) \times 10^{-4}$	4.309 ± 0.009
$^{134}Cs/^{214}Bi$	$(1.408 \pm 0.369) \times 10^{-3}$	1.105 ± 0.0248	$(2.399 \pm 0.081) \times 10^{-3}$	1.589 ± 0.006
$^{40}K/^{214}Bi$	$(4.011 \pm 2.856) \times 10^{-4}$	0.729 ± 0.0192	$(7.868 \pm 0.875) \times 10^{-4}$	0.711 ± 0.006
$^{137}Cs/^{208}Tl$	$-(9.25 \pm 10.95) \times 10^{-4}$	2.239 ± 0.074	$-(2.229 \pm 1.753) \times 10^{-4}$	3.090 ± 0.013
$^{134}Cs/^{208}Tl$	$-(4.169 \pm 4.549) \times 10^{-4}$	1.168 ± 0.031	$-(1.005 \pm 0.120) \times 10^{-3}$	1.729 ± 0.009
$^{40}K/^{208}Tl$	$(5.108 \pm 4.380) \times 10^{-4}$	0.291 ± 0.0295	$(4.271 \pm 0.567) \times 10^{-4}$	0.392 ± 0.004
$^{214}Bi/^{208}Tl$	$(3.329 \pm 1.895) \times 10^{-4}$	0.184 ± 0.0128	$(5.958 \pm 0.400) \times 10^{-4}$	0.317 ± 0.003

Table 6.15 Stripping ratios for 16 litre NaI(Tl) aerial survey detector at 1m, determined by Monte Carlo MCII simulations. SURRC windows.

	Spectral Windows					
	^{131}I 55-77 ch.	^{137}Cs 95-130 ch.	^{134}Cs 125-150 ch.	^{40}K 220-270 ch.	^{214}Bi 270-318 ch.	^{208}Tl 390-480 ch.
^{131}I	1	0.0759 ±0.002	0.0	0.0	0.0	0.0
^{137}Cs	0.20653 ±0.00396	1	0.02204 ±0.00119	0.0	0.0	0.0
^{134}Cs	0.49135 ±0.01373	1.6095 ±0.0328	1	0.0	0.0	0.0
^{40}K	0.41769 ±0.00834	0.3290 ±0.0072	0.2148 ±0.0055	1	0.0	0.0
^{214}Bi	4.2137 ±0.283	3.287 ±0.224	0.9724 ±0.083	0.9346 ±0.0792	1	0.0574 ±0.0142
^{208}Tl	2.511 ±0.179	2.189 ±0.159	1.151 ±0.095	0.4582 ±0.0484	0.3037 ±0.0369	1

Table 6.16 Stripping ratios for 16 litre NaI(Tl) aerial survey detector at 1m, determined by Monte Carlo MCII simulations. IAEA windows.

	Spectral Windows					
	^{131}I 55-77 ch.	^{137}Cs 95-130 ch.	^{134}Cs 125-150 ch.	^{40}K 228-260 ch.	^{214}Bi 275-307 ch.	^{208}Tl 396-460 ch.
^{131}I	1	0.0759 ±0.002	0.0	0.0	0.0	0.0
^{137}Cs	0.2065 ±0.0039	1	0.0220 ±0.0012	0.0	0.0	0.0
^{134}Cs	0.4914 ±0.0137	1.6095 ±0.0328	1	0.0	0.0	0.0
^{40}K	0.4429 ±0.0089	0.3489 ±0.0077	0.2278 ±0.0059	1	0.0	0.0
^{214}Bi	4.831 ±0.342	3.768 ±0.270	1.1147 ±0.0986	0.7408 ±0.0716	1	0.0533 ±0.0146
^{208}Tl	2.5794± 0.1863	2.249 ±0.165	1.1826 ±0.0982	0.287 ±0.037	0.1918 ±0.0285	1

Table 6.17 Stripping ratios for 16 litre NaI(Tl) aerial survey detector at 50m, determined by Monte Carlo MCII simulations. SURRC windows.

	Spectral Windows					
	^{131}I 55-77 ch.	^{137}Cs 95-130 ch.	^{134}Cs 125-150 ch.	^{40}K 220-270 ch.	^{214}Bi 270-318 ch.	^{208}Tl 390-480 ch.
^{131}I	1	0.0823 ±0.0038	0.0	0.0	0.0	0.0
^{137}Cs	0.4469 ±0.0099	1	0.0192 ±0.0017	0.0	0.0	0.0
^{134}Cs	1.1312 ±0.0410	1.7412 ±0.0576	1	0.0	0.0	0.0
^{40}K	0.6291 ±0.0142	0.4576 ±0.0115	0.2868 ±0.0085	1	0.0	0.0
^{214}Bi	4.1176 ±0.2358	3.0155 ±0.1775	0.9988 ±0.0721	0.9283 ±0.0671	1	0.0634 ±0.0127
^{208}Tl	2.6969 ±0.1651	2.1552 ±0.1362	1.1005 ±0.0795	0.5554 ±0.0473	0.2937 ±0.0313	1

Table 6.18 Stripping ratios for 16 litre NaI(Tl) aerial survey detector at 50m, determined by Monte Carlo MCII simulations. IAEA windows.

	Spectral Windows					
	^{131}I 55-77 ch.	^{137}Cs 95-130 ch.	^{134}Cs 125-150 ch.	^{40}K 228-260 ch.	^{214}Bi 275-307 ch.	^{208}Tl 396-460 ch.
^{131}I	1	0.0823 ±0.0038	0.0	0.0	0.0	0.0
^{137}Cs	0.4469 ±0.0099	1	0.0192 ±0.0017	0.0	0.0	0.0
^{134}Cs	1.1312 ±0.0409	1.7412 ±0.0576	1	0.0	0.0	0.0
^{40}K	0.6669 ±0.0152	0.4851 ±0.0123	0.3039 ±0.0091	1	0.0	0.0
^{214}Bi	4.7286 ±0.2855	3.4629 ±0.2143	1.1470 ±0.0856	0.7334 ±0.0607	1	0.0588 ±0.0131
^{208}Tl	2.7753 ±0.1716	2.2179 ±0.1414	1.1325 ±0.0824	0.3419 ±0.0349	0.1879 ±0.0243	1

Table 6.19 Stripping ratios for 16 litre NaI(Tl) aerial survey detector at 75m, determined by Monte Carlo MCII simulations. SURRC windows.

	Spectral Windows					
	^{131}I 55-77 ch.	^{137}Cs 95-130 ch.	^{134}Cs 125-150 ch.	^{40}K 220-270 ch.	^{214}Bi 270-318 ch.	^{208}Tl 390-480 ch.
^{131}I	1	0.0867 ±0.0036	0.0	0.0	0.0	0.0
^{137}Cs	0.5005 ±0.0119	1	0.0182 ±0.0019	0.0	0.0	0.0
^{134}Cs	1.2554 ±0.0501	1.8054 ±0.0373	1	0.0	0.0	0.0
^{40}K	0.6382 ±0.0153	0.4478 ±0.0121	0.2798 ±0.0089	1	0.0	0.0
^{214}Bi	4.0245 ±0.2355	2.8364 ±0.1709	1.0719 ±0.0775	0.9479 ±0.0696	1	0.05914 ±0.0127
^{208}Tl	2.7407 ±0.1612	2.0002 ±0.1233	1.0672 ±0.0751	0.4725 ±0.0409	0.3042 ±0.0307	1

Table 6.20 Stripping ratios for 16 litre NaI(Tl) aerial survey detector at 75m, determined by Monte Carlo MCII simulations. IAEA windows.

	Spectral Windows					
	^{131}I 55-77 ch.	^{137}Cs 95-130 ch.	^{134}Cs 125-150 ch.	^{40}K 228-260 ch.	^{214}Bi 275-307 ch.	^{208}Tl 396-460 ch.
^{131}I	1	0.0867 ±0.0036	0.0	0.0	0.0	0.0
^{137}Cs	0.5005 ±0.0119	1	0.0182 ±0.0019	0.0	0.0	0.0
^{134}Cs	1.2552 ±0.0501	1.8054 ±0.0373	1	0.0	0.0	0.0
^{40}K	0.6815 ±0.0166	0.4781 ±0.013	0.2987 ±0.0096	1	0.0	0.0
^{214}Bi	4.6346 ±0.2862	3.2663 ±0.2071	1.2344 ±0.0925	0.7457 ±0.0628	1	0.0549 ±0.0131
^{208}Tl	2.8423 ±0.1693	2.0759 ±0.1294	1.1068 ±0.0786	0.2943 ±0.0309	0.2017 ±0.0244	1

Table 6.21 Stripping ratios for 16 litre NaI(Tl) aerial survey detector at 100m, determined by Monte Carlo MCII simulations. SURRC windows.

	Spectral Windows					
	^{131}I 55-77 ch.	^{137}Cs 95-130 ch.	^{134}Cs 125-150 ch.	^{40}K 220-270 ch.	^{214}Bi 270-318 ch.	^{208}Tl 390-480 ch.
^{131}I	1	0.0779 ±0.0032	0.0	0.0	0.0	0.0
^{137}Cs	0.5027 ±0.0119	1	0.0176 ±0.0018	0.0	0.0	0.0
^{134}Cs	1.5175 ±0.0555	1.8209 ±0.0643	1	0.0	0.0	0.0
^{40}K	0.6775 ±0.0164	0.5175 ±0.0137	0.3165 ±0.0099	1	0.0	0.0
^{214}Bi	4.9246 ±0.306	2.954 ±0.193	1.069 ±0.083	1.000 ±0.078	1	0.0607 ±0.0133
^{208}Tl	2.7193 ±0.1632	2.136 ±0.133	1.119 ±0.079	0.5611 ±0.0458	0.361 ±0.034	1

Table 6.22 Stripping ratios for 16 litre NaI(Tl) aerial survey detector at 100m, determined by Monte Carlo MCII simulations. IAEA windows.

	Spectral Windows					
	^{131}I 55-77 ch.	^{137}Cs 95-130 ch.	^{134}Cs 125-150 ch.	^{40}K 228-260 ch.	^{214}Bi 275-307 ch.	^{208}Tl 396-460 ch.
^{131}I	1	0.0779 ±0.0032	0.0	0.0	0.0	0.0
^{137}Cs	0.5027 ±0.0119	1	0.0176 ±0.0018	0.0	0.0	0.0
^{134}Cs	1.5175 ±0.0555	1.8209 ±0.0643	1	0.0	0.0	0.0
^{40}K	0.7359 ±0.0182	0.5621 ±0.0150	0.3438 ±0.0109	1	0.0	0.0
^{214}Bi	5.715 ±0.377	3.428 ±0.237	1.242 ±0.100	0.787 ±0.070	1	0.057 ±0.013
^{208}Tl	2.806 ±0.170	2.204 ±0.138	1.156 ±0.082	0.355 ±0.035	0.228 ±0.026	1

Table 6.23 Stripping ratios for 16 litre NaI(Tl) aerial survey detector at 125m, determined by Monte Carlo MCII simulations. SURRC windows.

	Spectral Windows					
	^{131}I 55-77 ch.	^{137}Cs 95-130 ch.	^{134}Cs 125-150 ch.	^{40}K 220-270 ch.	^{214}Bi 270-318 ch.	^{208}Tl 390-480 ch.
^{131}I	1	0.0798 ±0.0035	0.0	0.0	0.0	0.0
^{137}Cs	0.5583 ±0.0137	1	0.0168 ±0.0019	0.0	0.0	0.0
^{134}Cs	1.5914 ±0.0594	1.9550 ±0.0702	1	0.0	0.0	0.0
^{40}K	0.7154 ±0.0132	0.5603 ±0.0111	0.3216 ±0.0078	1	0.0	0.0

Table 6.24 Stripping ratios for 16 litre NaI(Tl) aerial survey detector at 125m, determined by Monte Carlo MCII simulations. IAEA windows.

	Spectral Windows					
	^{131}I 55-77 ch.	^{137}Cs 95-130 ch.	^{134}Cs 125-150 ch.	^{40}K 228-260 ch.	^{214}Bi 275-307 ch.	^{208}Tl 396-460 ch.
^{131}I	1	0.0798 ±0.0035	0.0	0.0	0.0	0.0
^{137}Cs	0.5583 ±0.0137	1	0.0168 ±0.0019	0.0	0.0	0.0
^{134}Cs	1.5914 ±0.0594	1.9550 ±0.0702	1	0.0	0.0	0.0
^{40}K	0.7737 ±0.0146	0.6059 ±0.0123	0.3478 ±0.0085	1	0.0	0.0

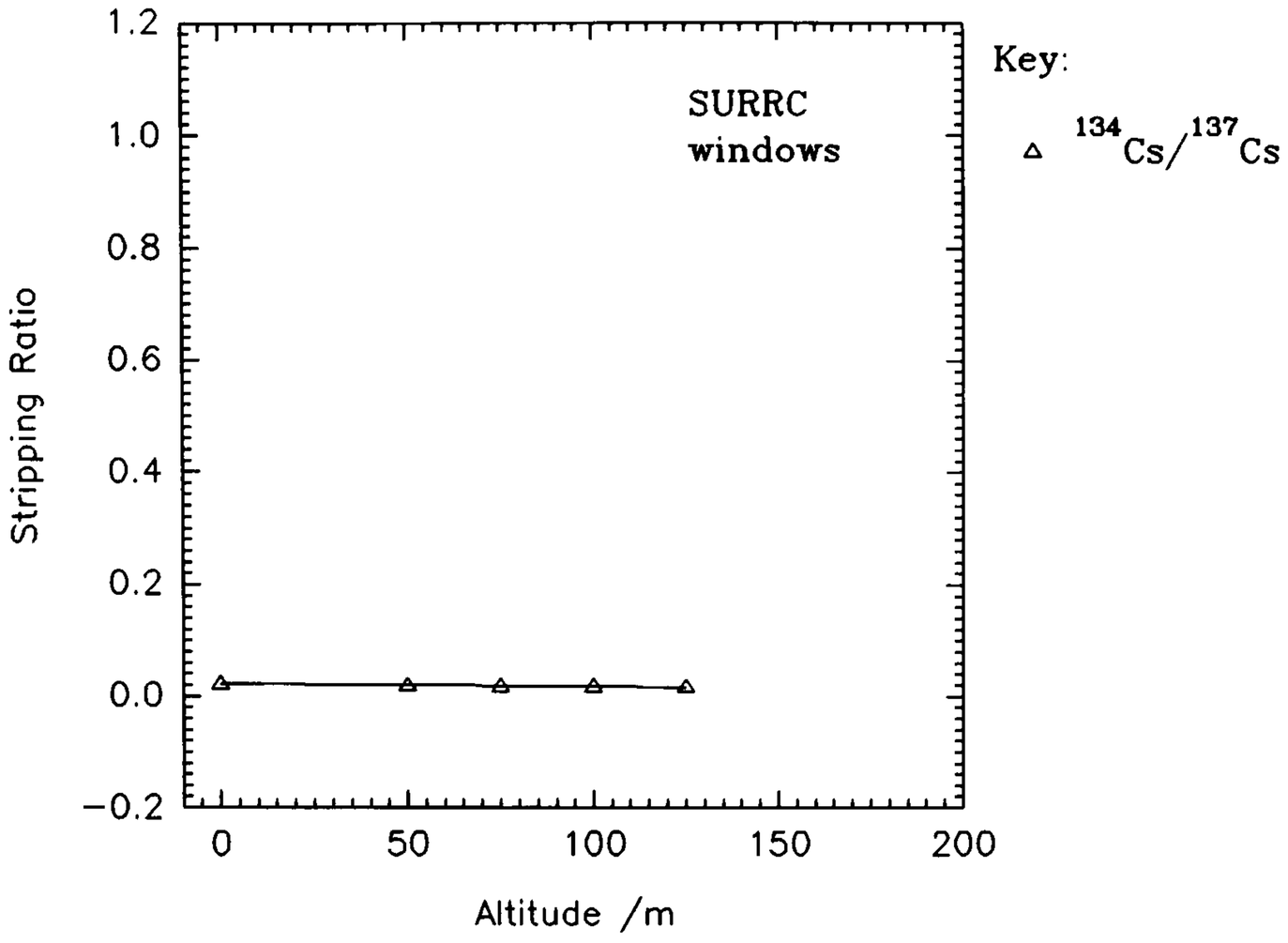

Figure 6.61 Stripping ratios of ^{137}Cs into ^{134}Cs, for SURRC windows.

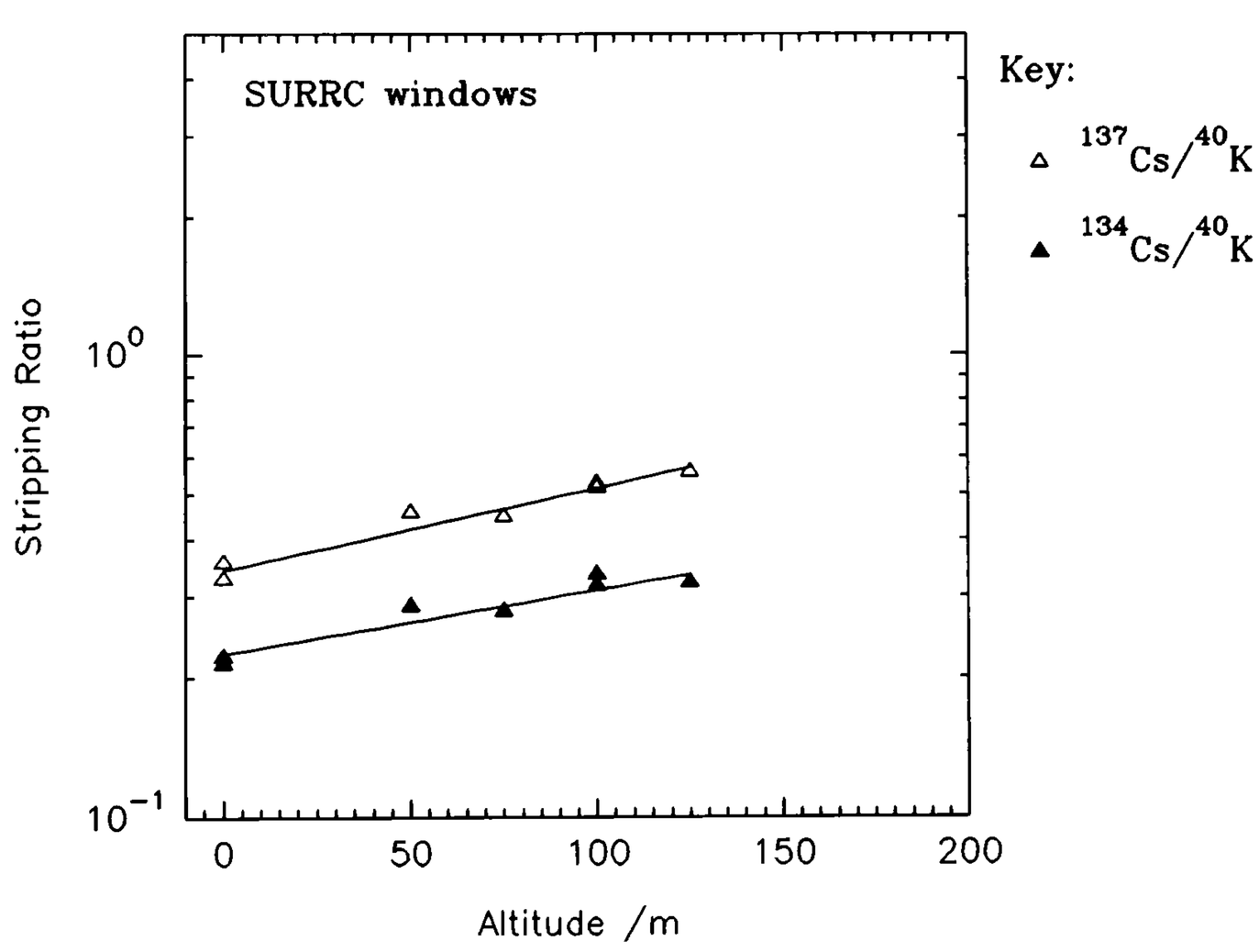

Figure 6.62 Stripping ratios of ^{40}K into ^{137}Cs and ^{134}Cs, for SURRC windows.

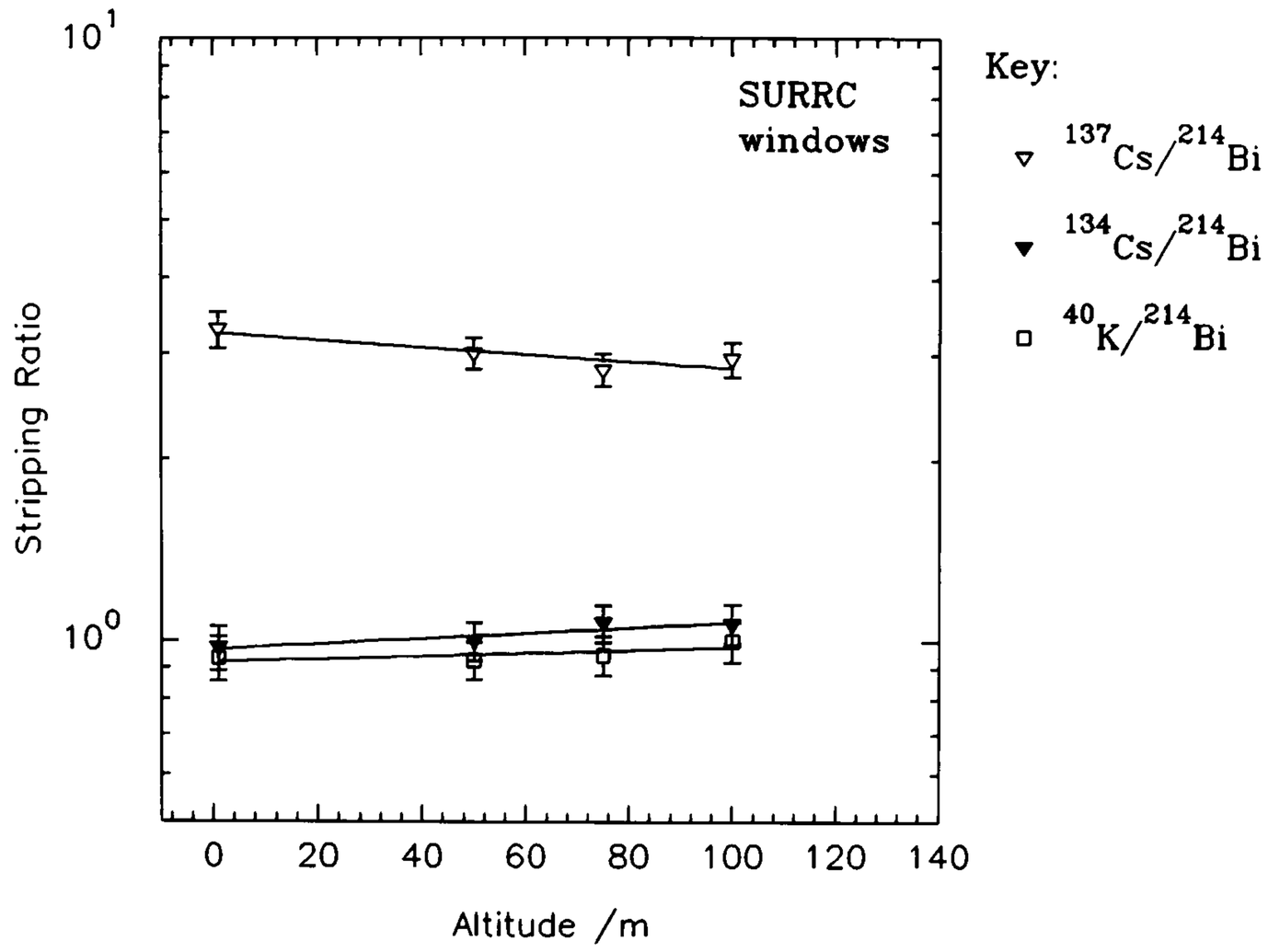

Figure 6.63 Stripping ratios of ^{214}Bi into ^{137}Cs, ^{134}Cs and ^{40}K, for SURRC windows.

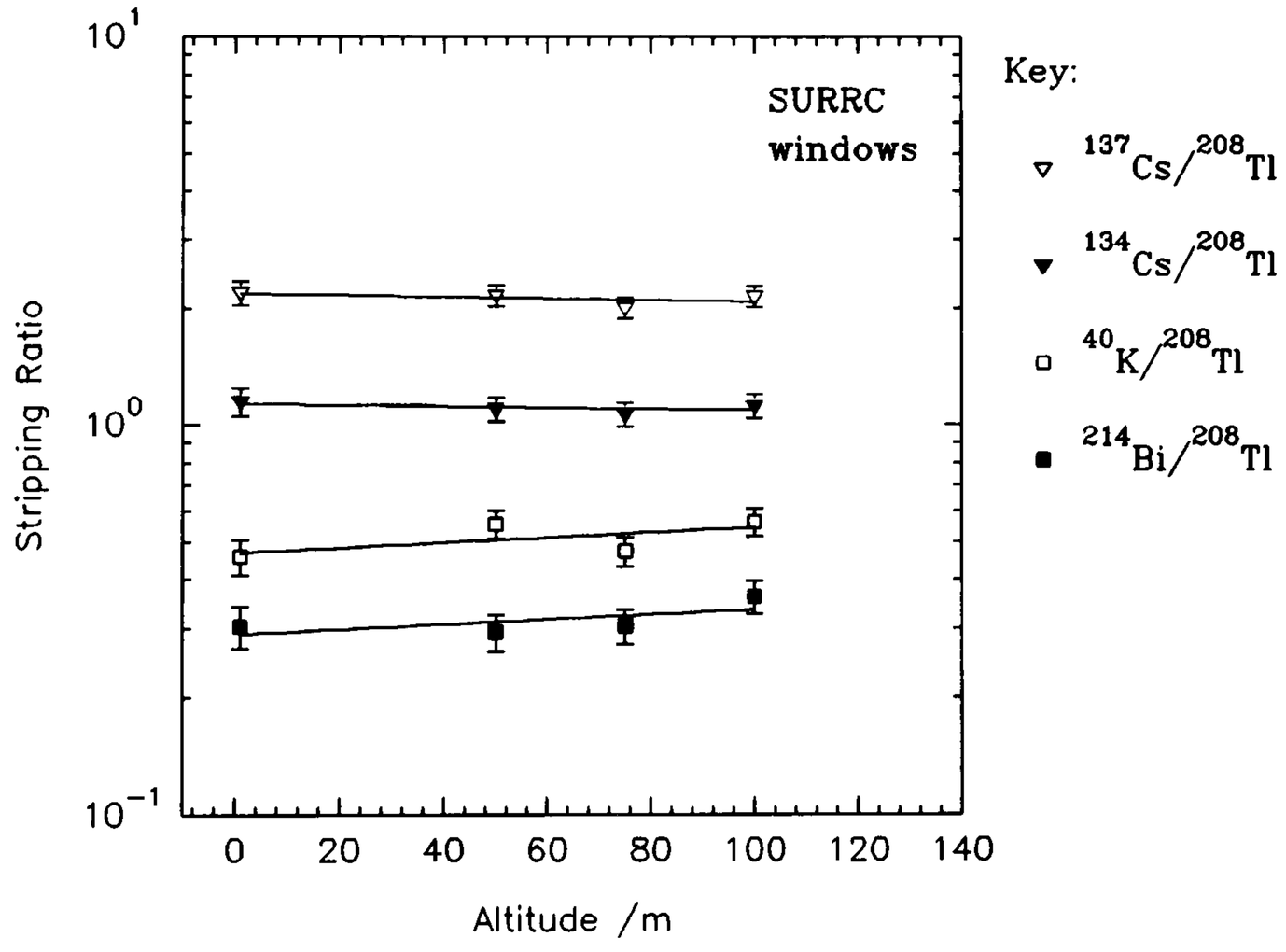

Figure 6.64 Stripping ratios of ^{208}Tl, into ^{137}Cs, ^{134}Cs, ^{40}K and ^{214}Bi, for SURRC windows.

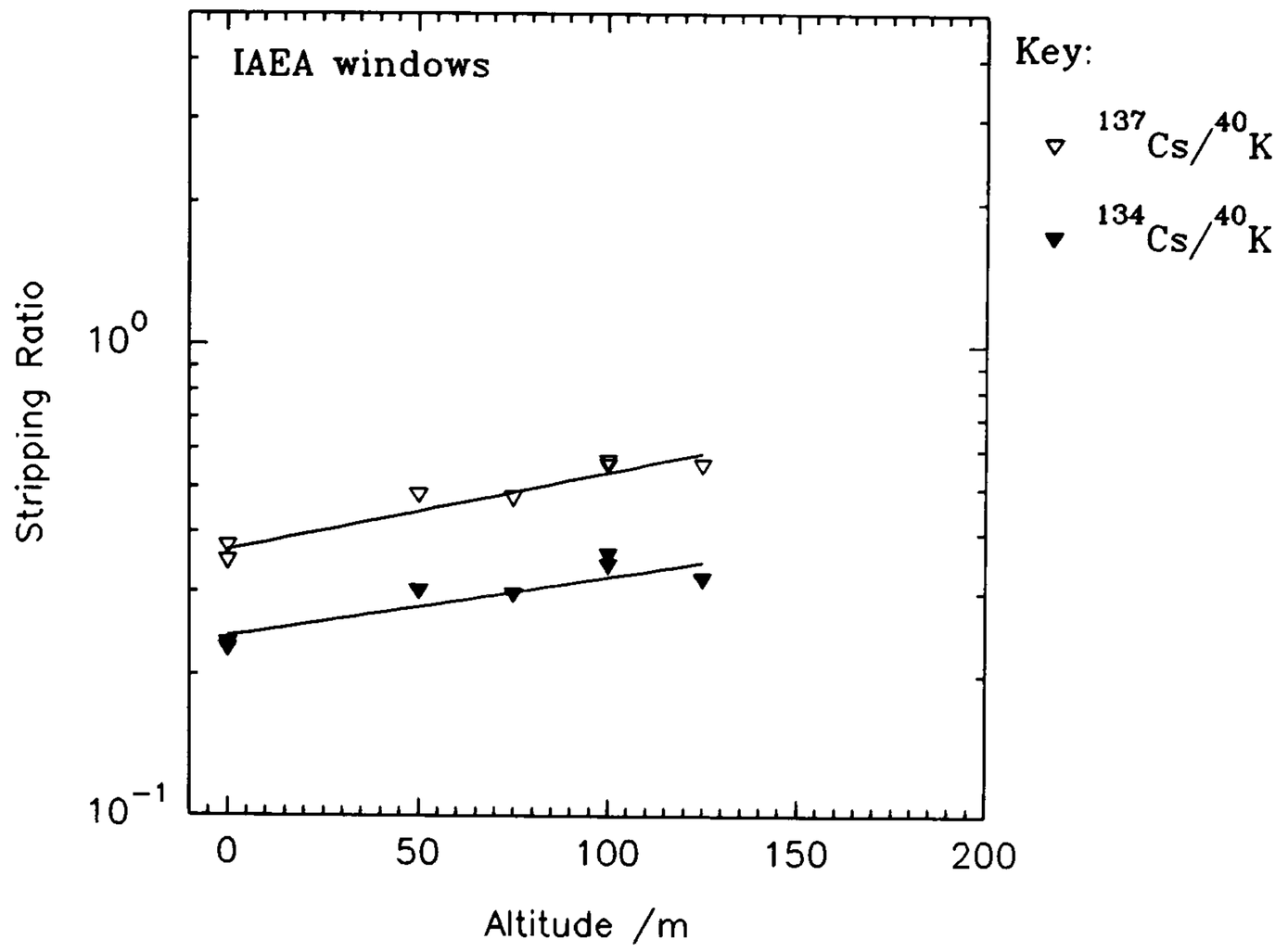

Figure 6.65 Stripping ratios of ^{40}K into ^{137}Cs and ^{134}Cs, for IAEA windows.

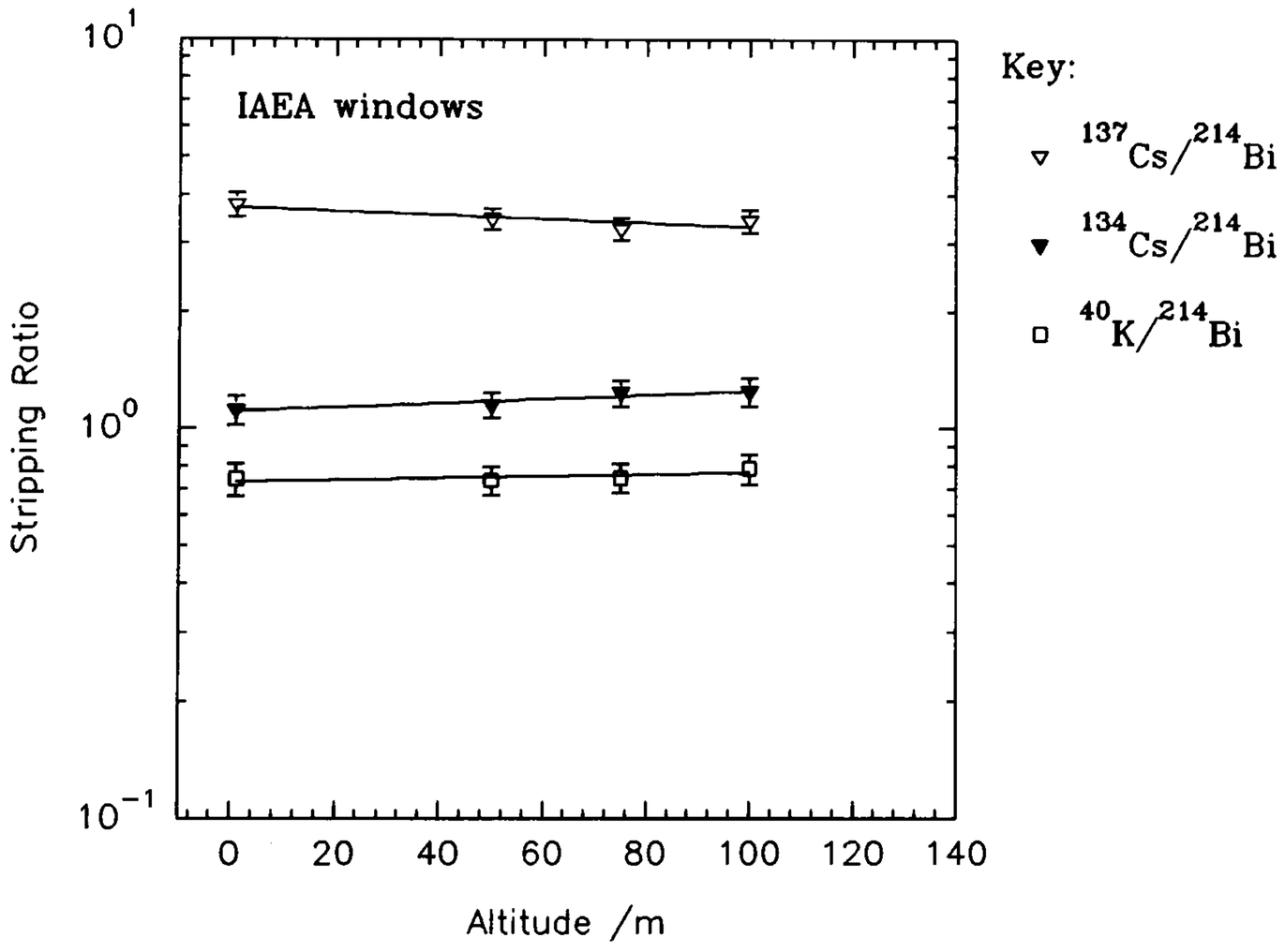

Figure 6.66 Stripping ratios of ^{214}Bi, into ^{137}Cs, ^{134}Cs and ^{40}K, for IAEA windows.

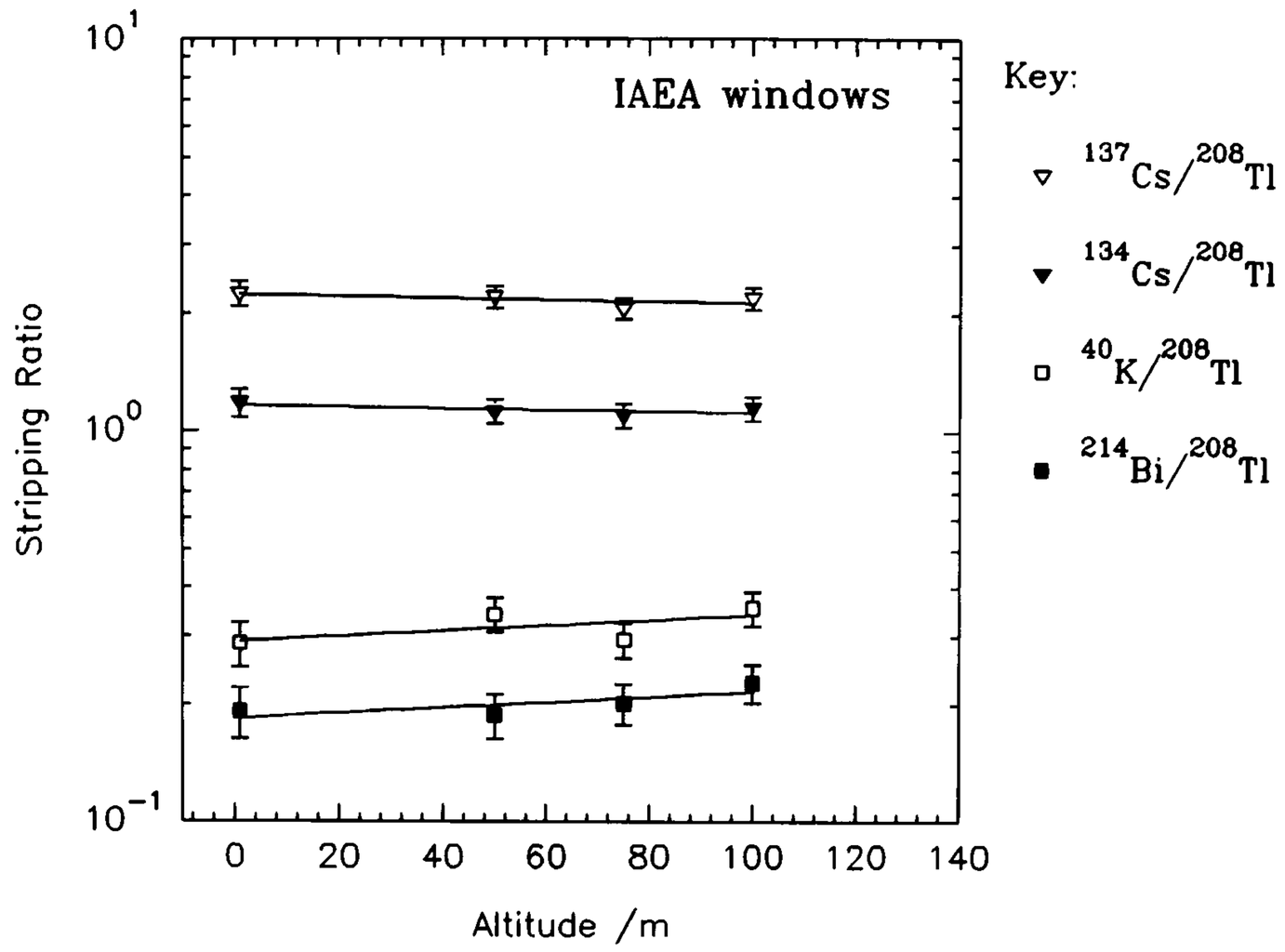

Figure 6.67 Stripping ratios of ^{208}Tl into ^{137}Cs, ^{134}Cs, ^{40}K and ^{214}Bi, for IAEA windows.

6.8.6.1 Treatment of Errors

The uncertainties derived from Monte Carlo MCII results, have been calculated from the total frequency distribution accumulated from summing the separate detection probabilities during the course of the entire source emission histories for a given geometry. The fraction of the total frequency distribution within a defined energy window, weighted in accordance with emission intensity for multi-radionuclides or lines, times the number of overall historical events gives an estimate of the number of counts expected (expected frequency). Poisson statistics applied to these random counting events furnishes the uncertainties in the normal manner. For errors associated with the calculations of solid angle and scattering probabilities, it is assumed that these are systematic and constant. Errors of approximately 5% have been attributed to these.

In the implementation of such a highly complicated code, it is essential that each piece can be broken down and tested individually, to reveal programming *bugs*. The overall scheme was also tested and compared with reference data. It remains a possibility that conflicts may arise in unusual combinations of parameters, not usually encountered

during testing. Whilst every effort has been made to minimise programming errors, certain features became apparent during very long runs. It was not clear whether this was as a result of a programming conflict or an inherent problem associated with the weighting scheme not previously witnessed with other applications. Occasionally, ($<0.01\%$ of all events on average) a weight was attached to a scattered γ-ray of many orders of magnitude different from the average received in a given source-detector geometry and source energy. This occurred only at aerial survey altitudes. At these detector heights, the field of view as we have seen is many hundreds of metres and a source emission occurs at a random position (x,y,z) within the ground or surface matrix. A detector placed within an air space, above this ground matrix, will record an estimate of the average fluence-rate for this geometry. It may be that, if a γ-ray scatters very close to the detector, an unusually high weight is attached. Given that the air volume space is very large (80×10^6 m^3), then this would not occur very often and may account for this phenomenon. This problem did not occur at 1m detector heights. This problem remained unresolved and it was decided to replace weights that were clearly wrong with average values from adjacent energy bins (the data were smoothed).

6.8.7 Spectral Stripping of Aerial Survey Data

The practical implications of using stripping ratios derived by alternative methods and applied to real aerial survey data will become more apparent with some examples. For many calibration sites identified by SURRC, especially those near estuarine environments of the Irish Sea in SW Scotland, the most predominant radionuclide is ^{137}Cs. For example, the Caerlaverock calibration site, near Dumfries, is a low lying salt water marsh (merse). Its location, prevalent geochemistry and sea inundation are such that radiocaesium discharged from the BNF plc reprocessing plant at Sellafield accumulates in the sediments: mean ^{137}Cs 74 kBq m^{-2} (Sanderson *et al*, 1992). The local Caerlaverock bedrock contains only relatively small amounts of ^{214}Bi and ^{208}Tl (mean: 3.87 and 1.74 kBq m^{-2}, respectively), although ^{40}K is abundant (mean: 136 kBq m^{-2}), (Sanderson *et al*, 1992). A helicopter survey conducted by SURRC on behalf of the Scottish Office during 1993 (Sanderson *et al*, 1993b) used a number of sites, including Caerlaverock, for calibration purposes. The 16 litre NaI(Tl) spectrometer response at different altitudes is shown in figures 6.68-6.72, for ^{137}Cs, ^{134}Cs, ^{40}K, ^{214}Bi and ^{208}Tl respectively. These are essentially in-situ measurements with the aircraft at the hover.

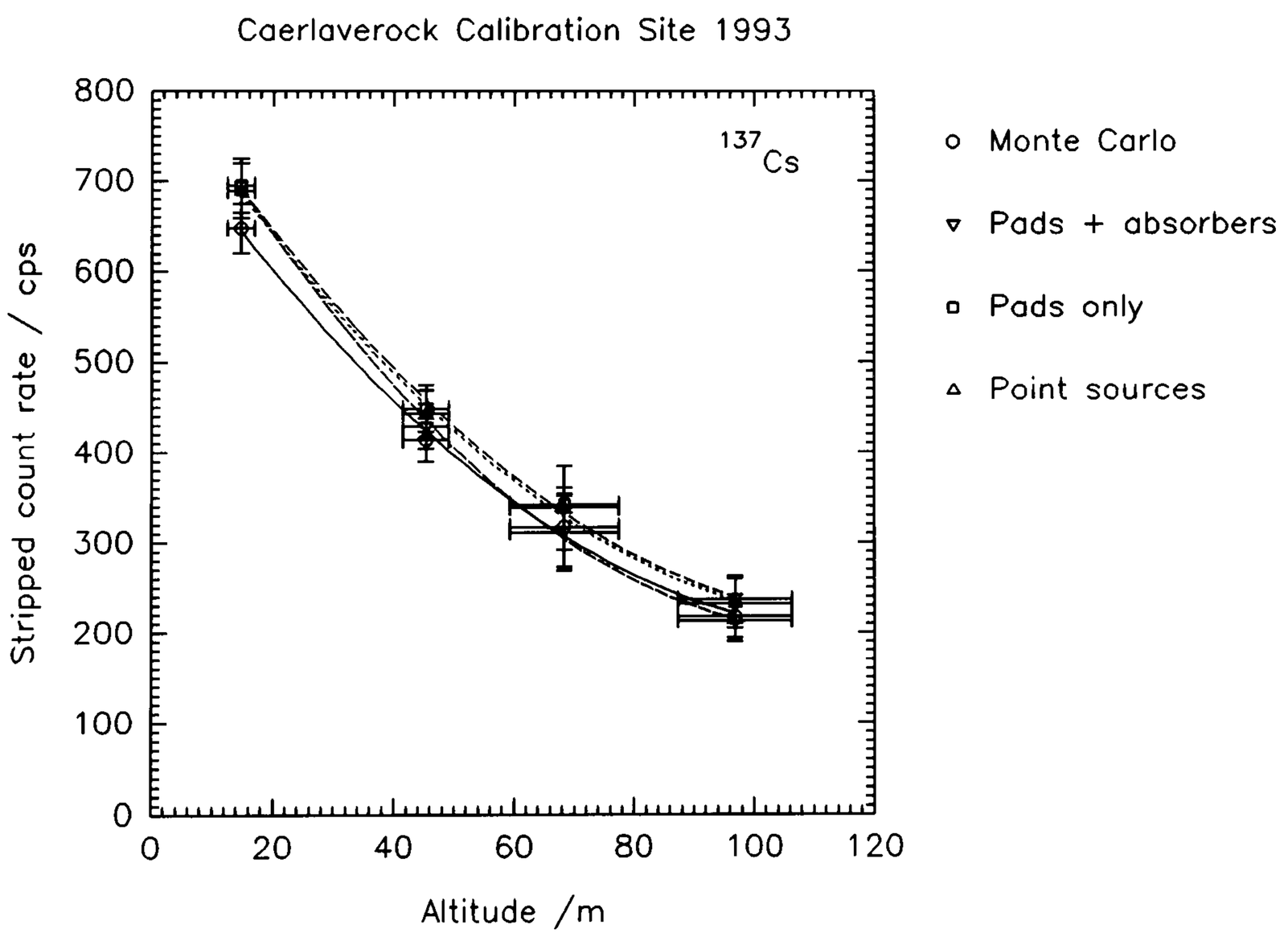

Figure 6.68 ^{137}Cs stripped count rates at helicopter hover heights.

The errors have been calculated from consecutive data taken at each constant hover station. At 14.7±2.2m altitude, the mean of ten data (n=10) was formed; at 45.3±3.8m, n=8; at 68.3±9.1m, n=16 and 96.1±9.5m, n=10.

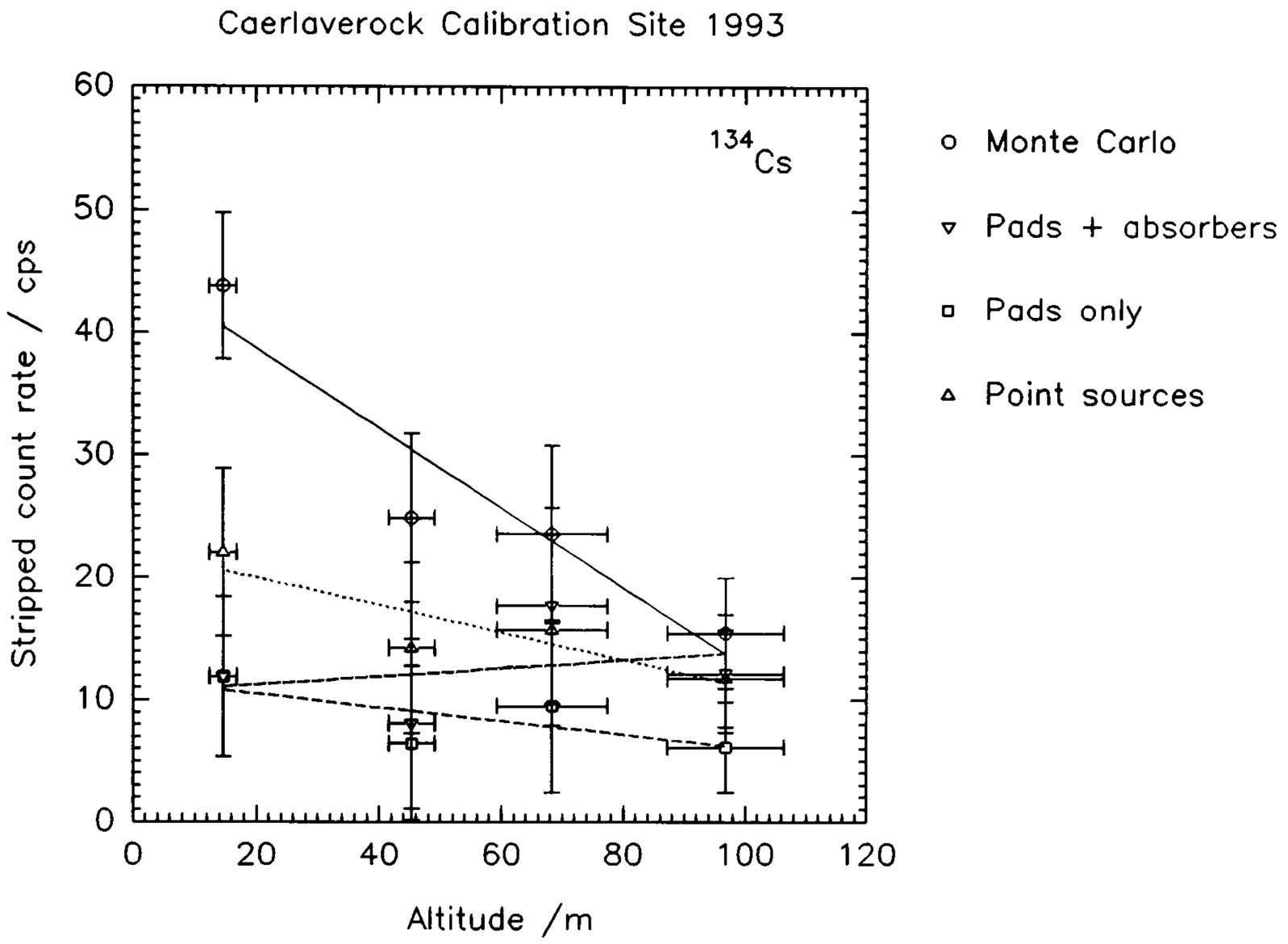

Figure 6.69 ^{134}Cs stripped count rates at helicopter hover heights.

These data have been processed from net count rates (background corrected) using Monte Carlo calculated and experimentally derived stripping ratios. For the latter, the concrete calibration pads (doped with concentrated amounts of potassium, uranium and thorium) and a plane source of ^{137}Cs were employed, with and without perspex absorbers (acting as height correction media). In addition, a comparison was made with laboratory point sources (except ^{134}Cs). For ^{134}Cs, no geometrically realistic source was available and therefore a small bottle containing a solution of this radioisotope was presented to the detector. The ^{137}Cs plane source and ^{134}Cs solution were placed inside an empty pad cell from which measurements were taken: they are therefore described (not quite correctly) as "pads" and "pads + absorbers".

In the presence of low concentrations of uranium and thorium, the differently derived

stripping ratios provide quite similar true count rates for ^{137}Cs and within single standard deviations. Height dependency of the stripped count rate is not a significant factor in this data, since the fractional interferences from higher energy windows contribute little due to the low concentrations of the naturals. The low levels of ^{134}Cs and ^{214}Bi are reflected in higher uncertainties and systematic variations (mainly at very low heights) using the different stripping models (fig. 6.69 and 6.71 respectively). It is interesting to note that for ^{134}Cs and ^{214}Bi at $\approx$100m altitudes, all stripped count rates converge to approximately the same value. Figure 6.70 shows the strong presence of ^{40}K effectively negating the relative contributions from uranium and thorium. For ^{208}Tl, only uranium has some influence as an interference at 2615 keV. As a result, all stripping models produce similar true count rates.

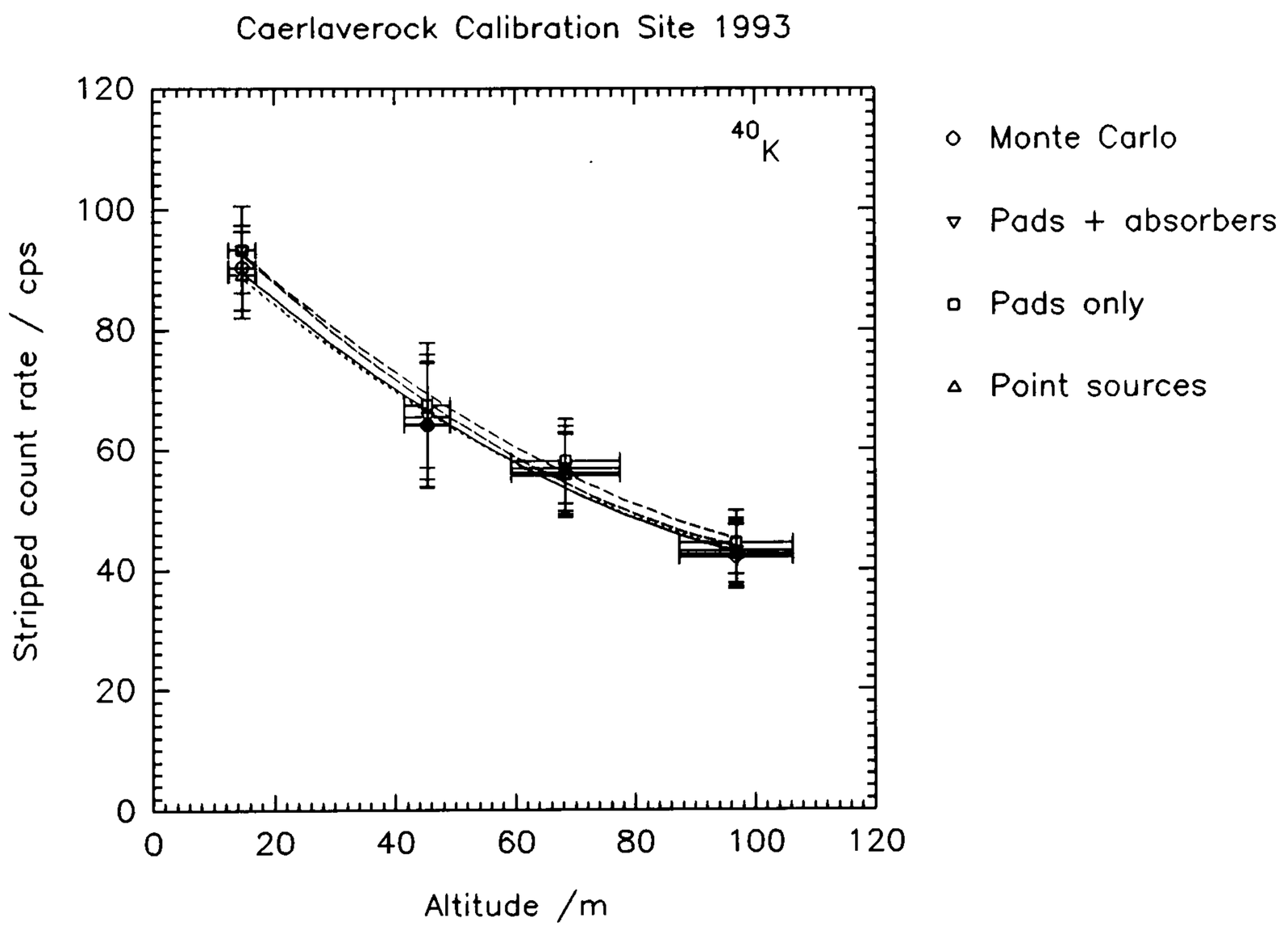

Figure 6.70 ^{40}K stripped count rates at helicopter hover heights.

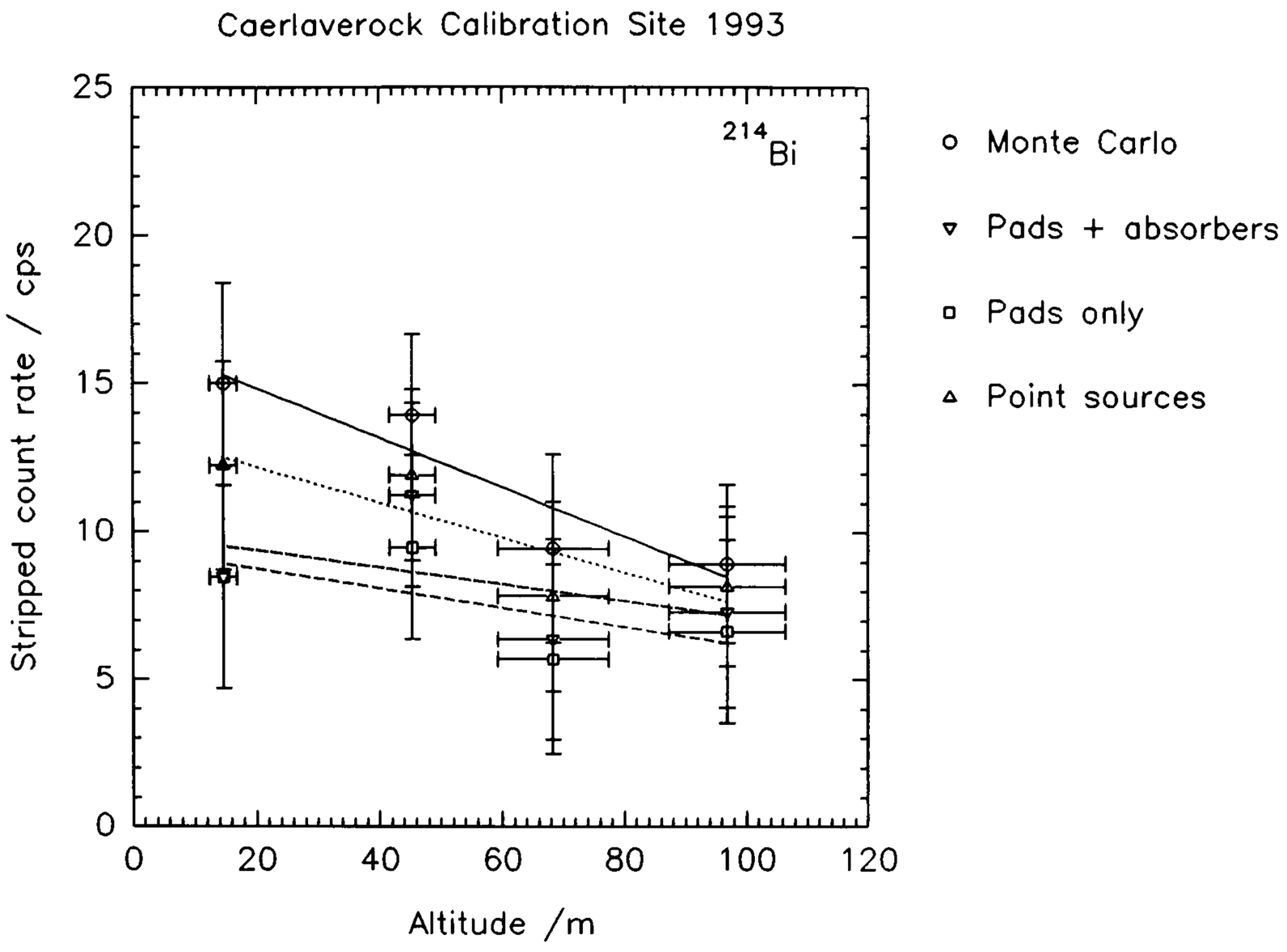

Figure 6.71 ^{214}Bi stripped count rates at helicopter hover heights.

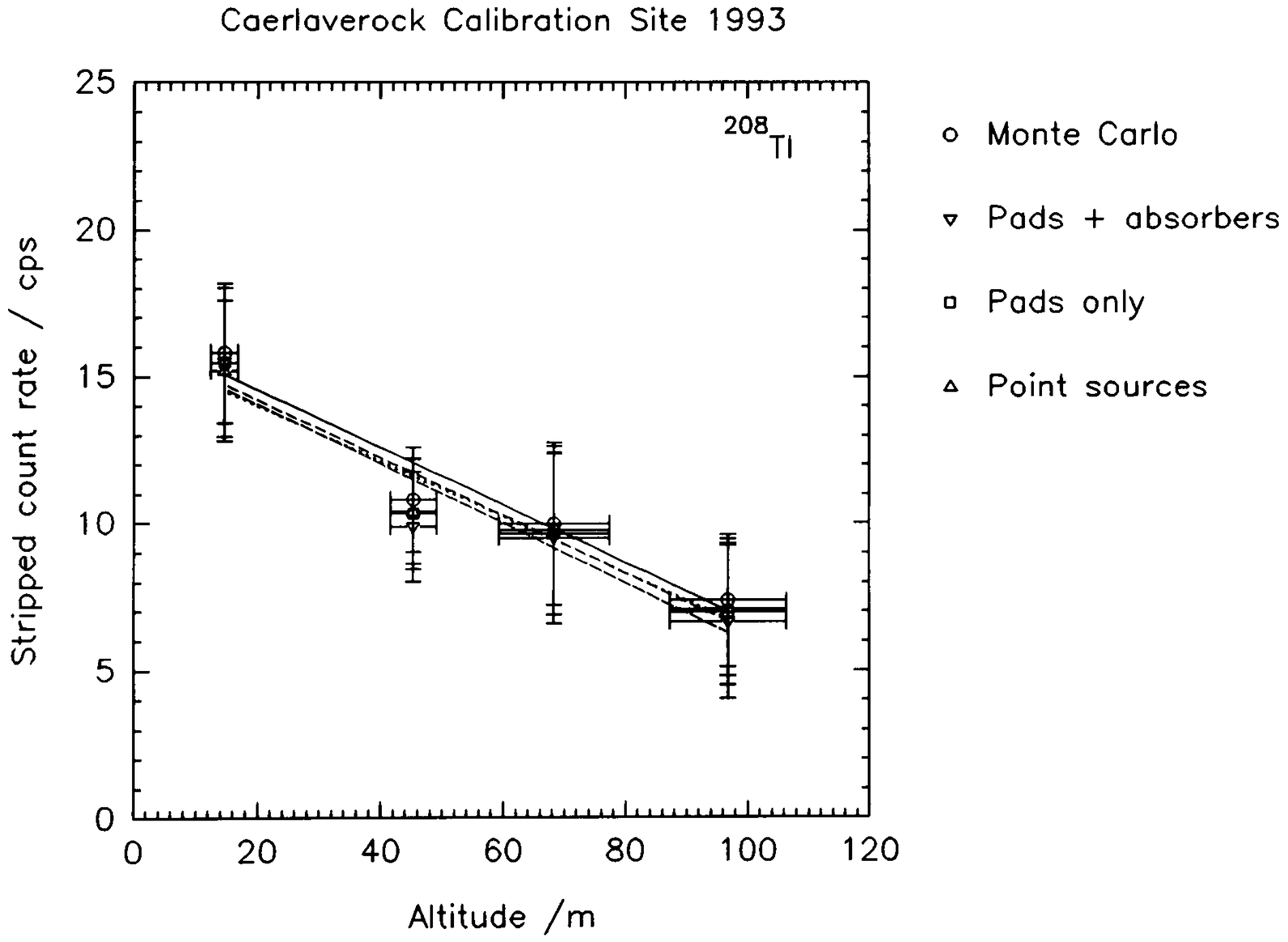

Figure 6.72 ^{208}Tl stripped count rates at helicopter hover heights.

Expected stripped count rates, as a function of altitude, have been calculated from the estimated radionuclide inventories at the Caerlaverock merse calibration site. Samples of soil were taken across the site in an expanding hexagon pattern, developed by Tyler (1994) to relate detector field of view with ground sampling strategies. Laboratory analysis of the soil cores revealed ^{137}Cs in high concentrations and distributed to form a pronounced sub-surface maximum 10-15cm below the surface. The non-exponential depth profile observed, is an indication of the complex transportation, deposition and re-distribution mechanisms that occur in such environments.

Figure 6.73 shows the calculated response from a 16 litre aerial survey detector, based upon the analytical/numerical methods developed in Chapter 5 and the estimated radionuclide inventories at the Caerlaverock site determined by laboratory high resolution gamma-spectrometry. The mean inventories within a 30cm depth core for ^{137}Cs, ^{134}Cs, ^{40}K, ^{214}Bi and ^{208}Tl are respectively: 73.7 ± 19.3, 0.89 ± 0.07, 135.7 ± 8.9, 3.87 ± 0.32 and 1.74 ± 0.12 kBq m^{-2}. For ^{137}Cs and ^{134}Cs a surface source has been assumed since no adequate depth distribution function was available. The calculated stripped cps is therefore known to be overestimated for ^{137}Cs. The calculated response from ^{134}Cs is compatible with the stripped cps from the different stripping models, and suggests a surface deposition, but has not been confirmed from core analysis. It is not known if this radionuclide is distributed in a similar manner to ^{137}Cs.

For the natural radionuclides, a uniform depth distribution is assumed and detector response at various altitudes has been calculated. It is interesting to note that the predicted response from ^{40}K, ^{214}Bi and ^{208}Tl is much less than that measured at the calibration site. It is possible that in such a dynamic region, the natural radionuclides exhibit complex deposition patterns also, and hence the discrepency.

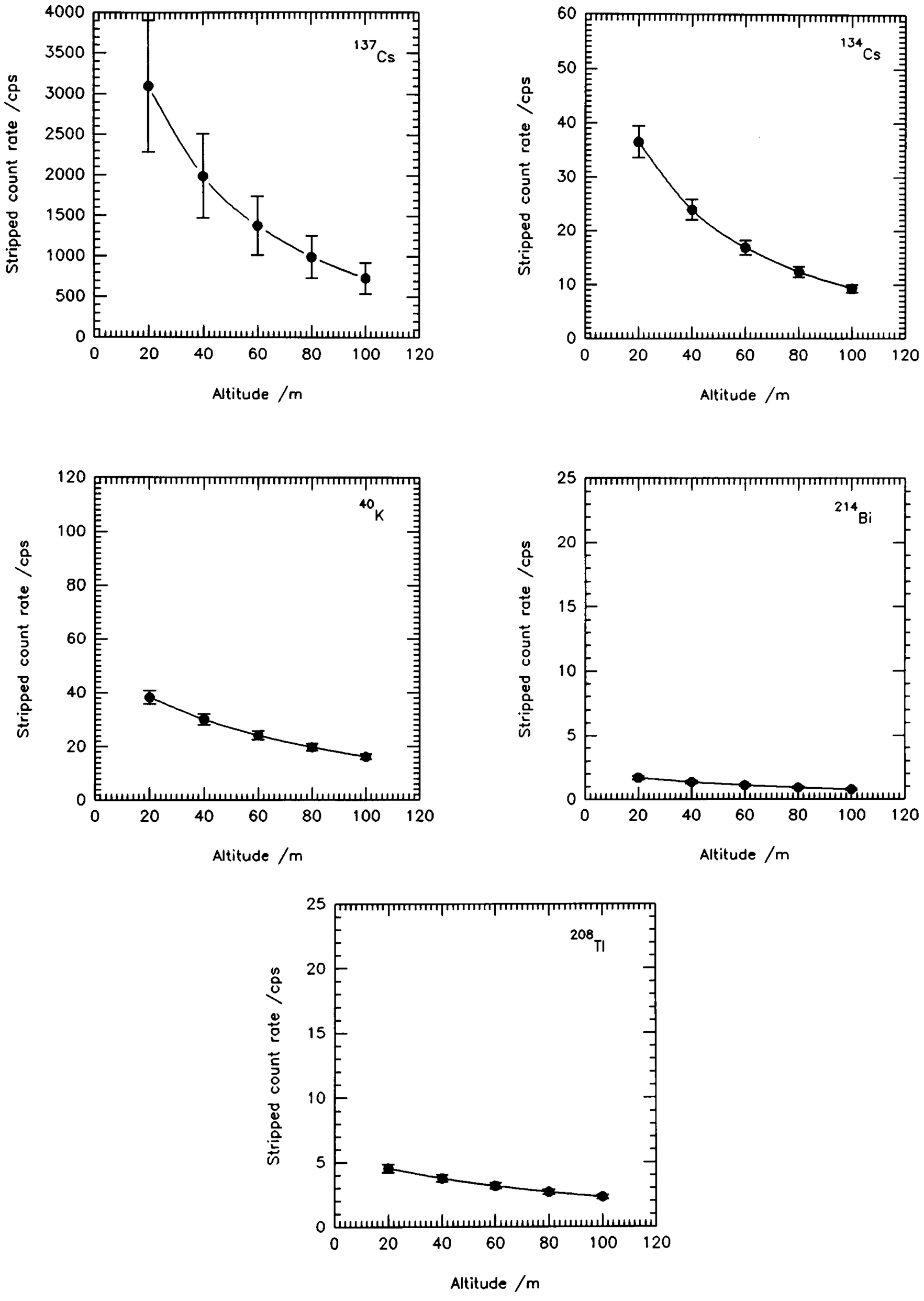

Figure 6.73 Calculated response of aerial survey detector at Caerlaverock site from estimated inventories.

The effect that elevated levels of uranium and thorium might have on the residual stripped count rates in the radiocaesium windows, in low ^{137}Cs and ^{134}Cs environments will now be discussed. A region within Dumfries and Galloway, near the BNF plc operated Chapelcross nuclear power station, is approximately at weapons testing fallout levels of $<2kBq\ m^{-2}$. Chernobyl derived radiocaesium may be found further west and north. The natural radioelements are more significant in this region however: ^{40}K varies across this region 60-210 $kBq\ m^{-2}$ (143-500 $Bq\ kg^{-1}$); ^{214}Bi, 1.6-5.6 $kBq\ m^{-2}$ (3.8-13.3 $Bq\ kg^{-1}$); ^{208}Tl, 1.2-5.6 $kBq\ m^{-2}$ (2.86-13.4 $Bq\ kg^{-1}$). A west-east flight transect flown across this region has been analysed to take net count rates through to stripped, true count rates using the stripping ratios discussed. This flight was made at 120kph ground speed and 68.0±7.1m mean altitude. Where applicable, 75m altitude dependent stripping ratios have therefore been used. The systematic differences relative to Monte Carlo derived stripping ratios are shown in figures 6.74, 6.75, 6.77, 6.78 and 6.79.

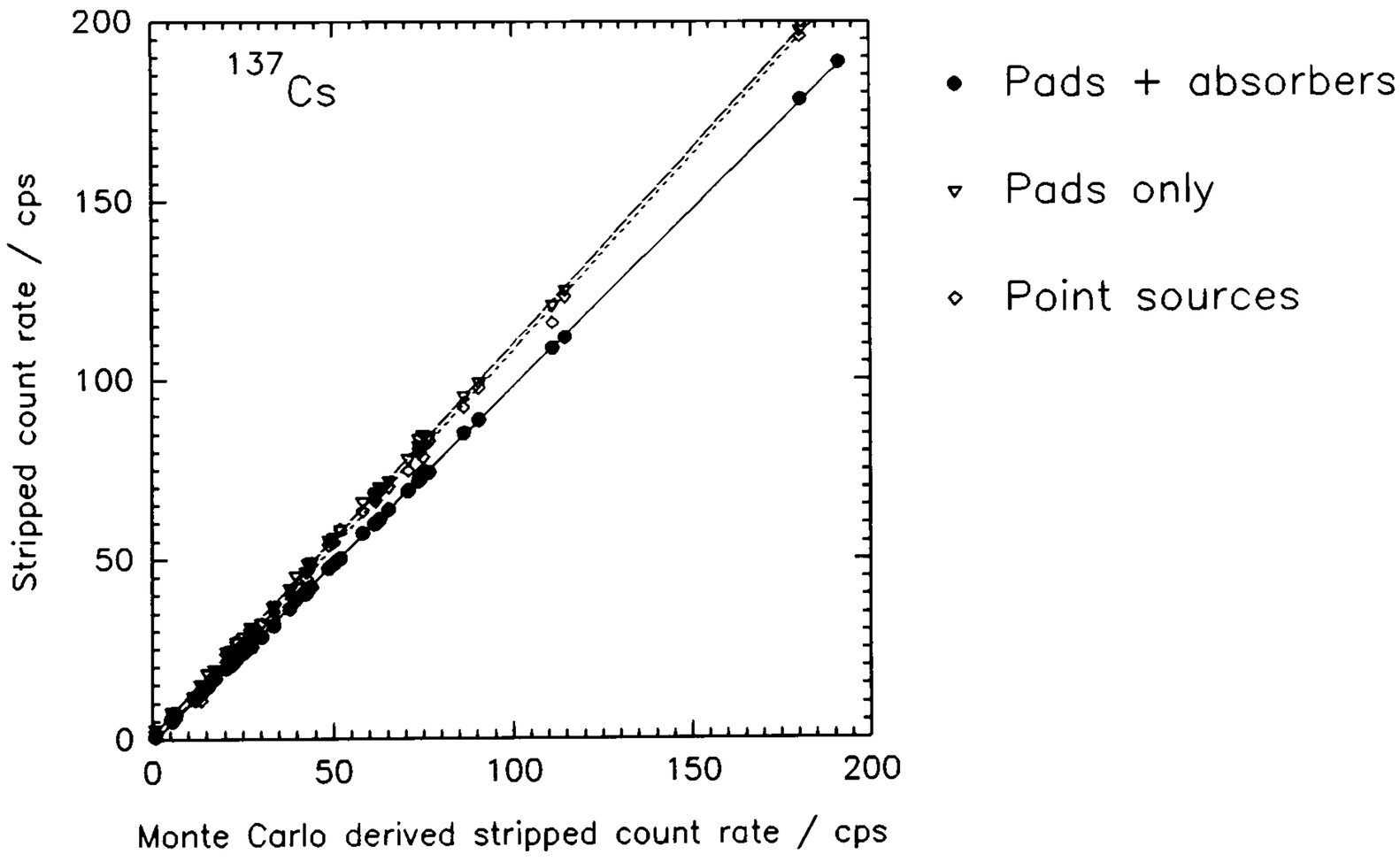

Figure 6.74 Comparison between methods of stripping for ^{137}Cs.

For ^{137}Cs (fig. 6.74), the slopes of the best fit regression lines for stripped count rates obtained from i). pads and absorbers, ii). pads only and iii). point sources show differences of -1.4%, +8.9% and +9.2% respectively, with respect to those derived by Monte Carlo calculation (slope=1.0). If Monte Carlo stripping ratios are used to obtain a true count rate of 100 cps, the alternative methods yield 98.6, 108.9 and 109.2 cps. Differences of this sort will become statistically apparent for long counting periods

(eg. greater than >5s in low ^{137}Cs environments).

Figure 6.75 shows systematic differences for ^{134}Cs at the ordinate intercept (zero x-axis). All the experimental methods utilized for this radionuclide are limited geometrically and may account for some differences. At the intercept, residual count rates are observed for i). -2.8, ii). +0.9 and iii). +3.7 cps. We have noted that Monte Carlo stripping ratios derived here, although showing similar trends with altitude compared with experimental simulations, are systematically less in magnitude. A deficiency of count rate in i). is expected then and observed. The stripping ratios derived from iii). are significantly less then 75m altitude Monte Carlo estimates since no account is made of spectral shape variation with altitude, and indeed these results confirm excess count rates. The extra scattered component from the calibration pads results in greater stripping ratios then iii)., and not dissimilar (by chance) to those determined by Monte Carlo at 75m survey height, which in turn results in less difference between the two methods. It is ^{40}K that mostly drives stripping ratio variation with altitude for ^{134}Cs and ^{137}Cs (^{214}Bi and ^{208}Tl are less sensitive to ^{40}K). The differences of the slopes to that of the reference for ^{134}Cs are i). -12.7%, ii). -15.9% and iii). -1.79% respectively.

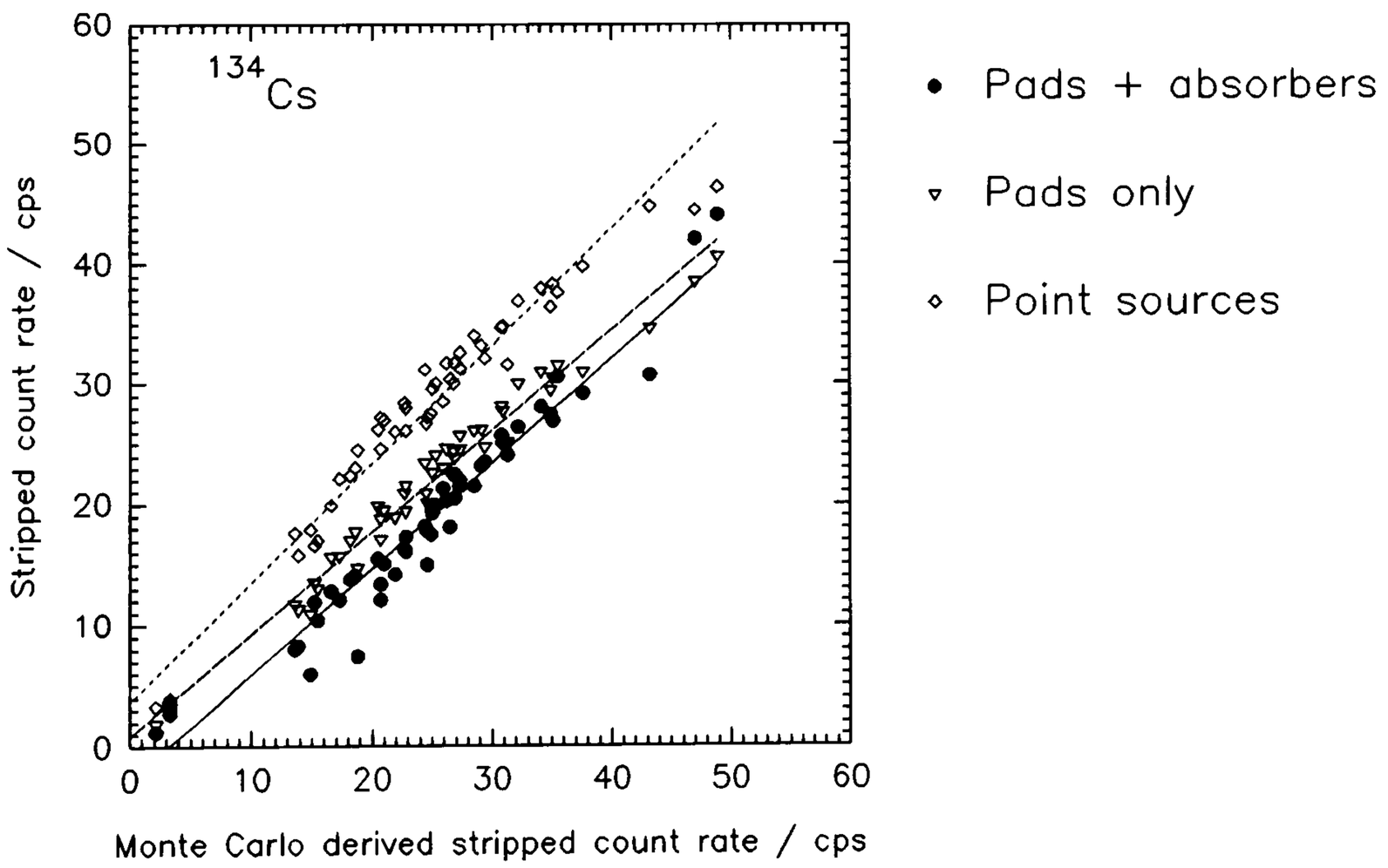

Figure 6.75 Comparison between methods of stripping for ^{134}Cs.

The same data are shown as a histogram in figure 6.76. The residual stripped count rates of ^{134}Cs are shown when stripped by using ratios determined by a). Monte Carlo Method, b). pads+absorbers, c). pads only and d). point sources. The means of the data, and the standard error of the means are respectively (for number of observations, n=50): a). 24.6±1.5, b). 18.9±1.3, c).21.6±1.2, d). 27.9±1.5.

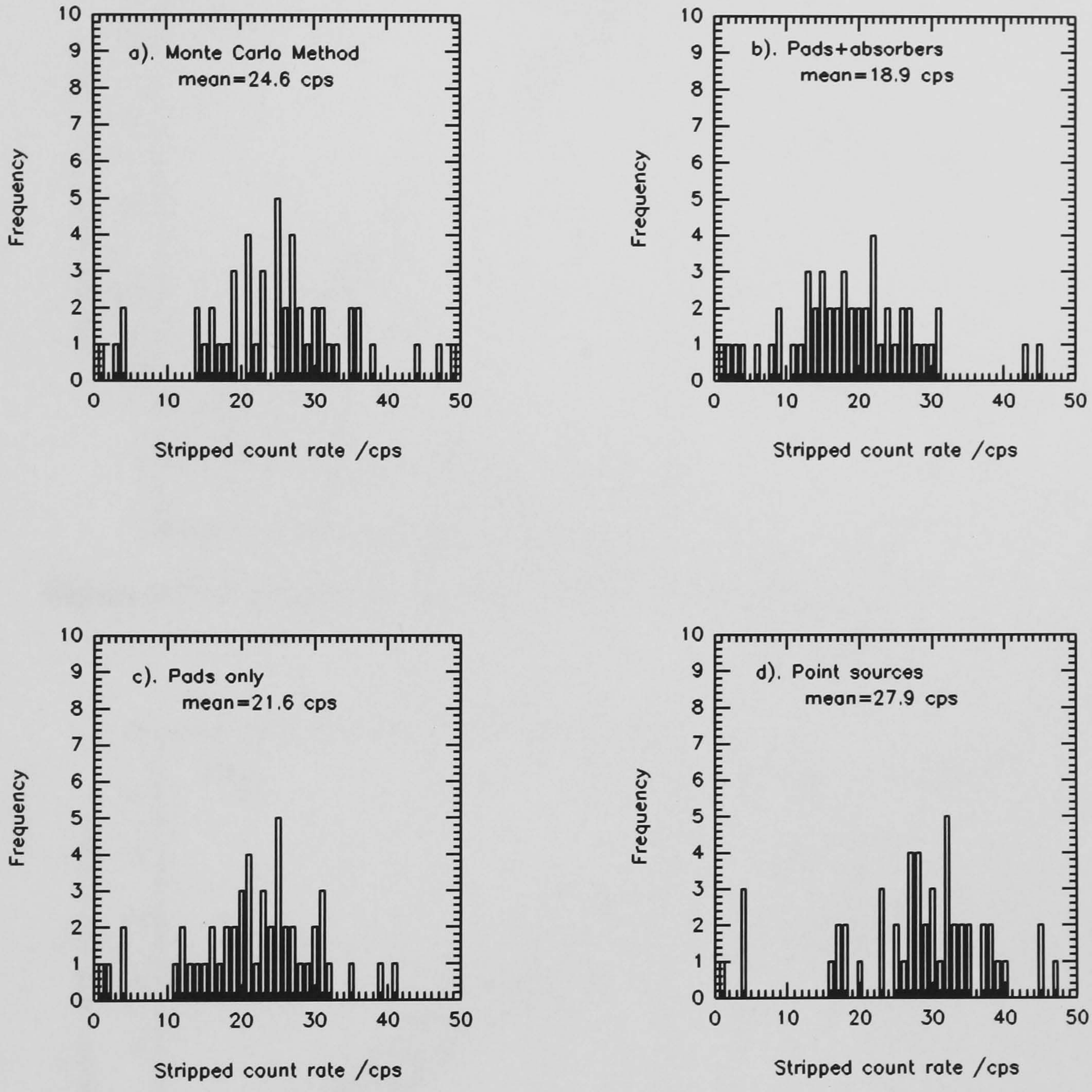

Figure 6.76 Histogram of residual ^{134}Cs levels, taken in a low caesium environment.

Point sources leave the highest residuals in the ^{134}Cs window, owing to underestimating the contribution from Compton scattering. Next comes the Monte Carlo method, pads only and the method that leaves the lowest residuals is the pads+absorbers. On this analysis, one may favour the use of pads+absorbers as the preferred method of obtaining the least residual count rates in the ^{134}Cs window.

Figures 6.77 and 6.79 show relative comparisons for ^{40}K and ^{208}Tl. All methods are equally valid and lead to almost identical stripped count rates. For ^{40}K, the slopes of i). and ii). differ by +1.3% and +2.03%, whilst iii). is -0.4%. For ^{208}Tl, all slopes are less than 1.0 (-1.96%, -1.88% and -1.63% different).

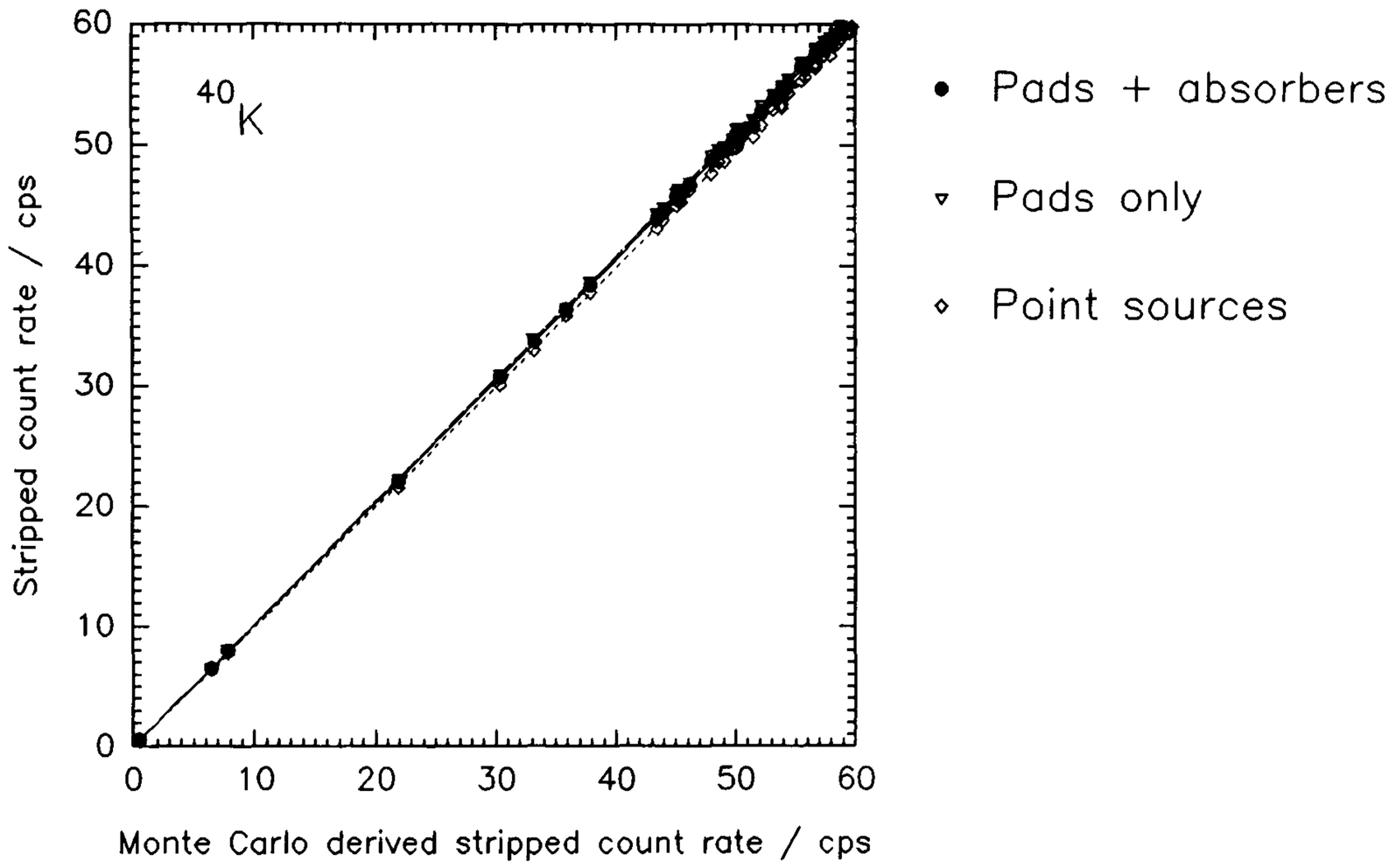

Figure 6.77 Comparison between methods of stripping for ^{40}K.

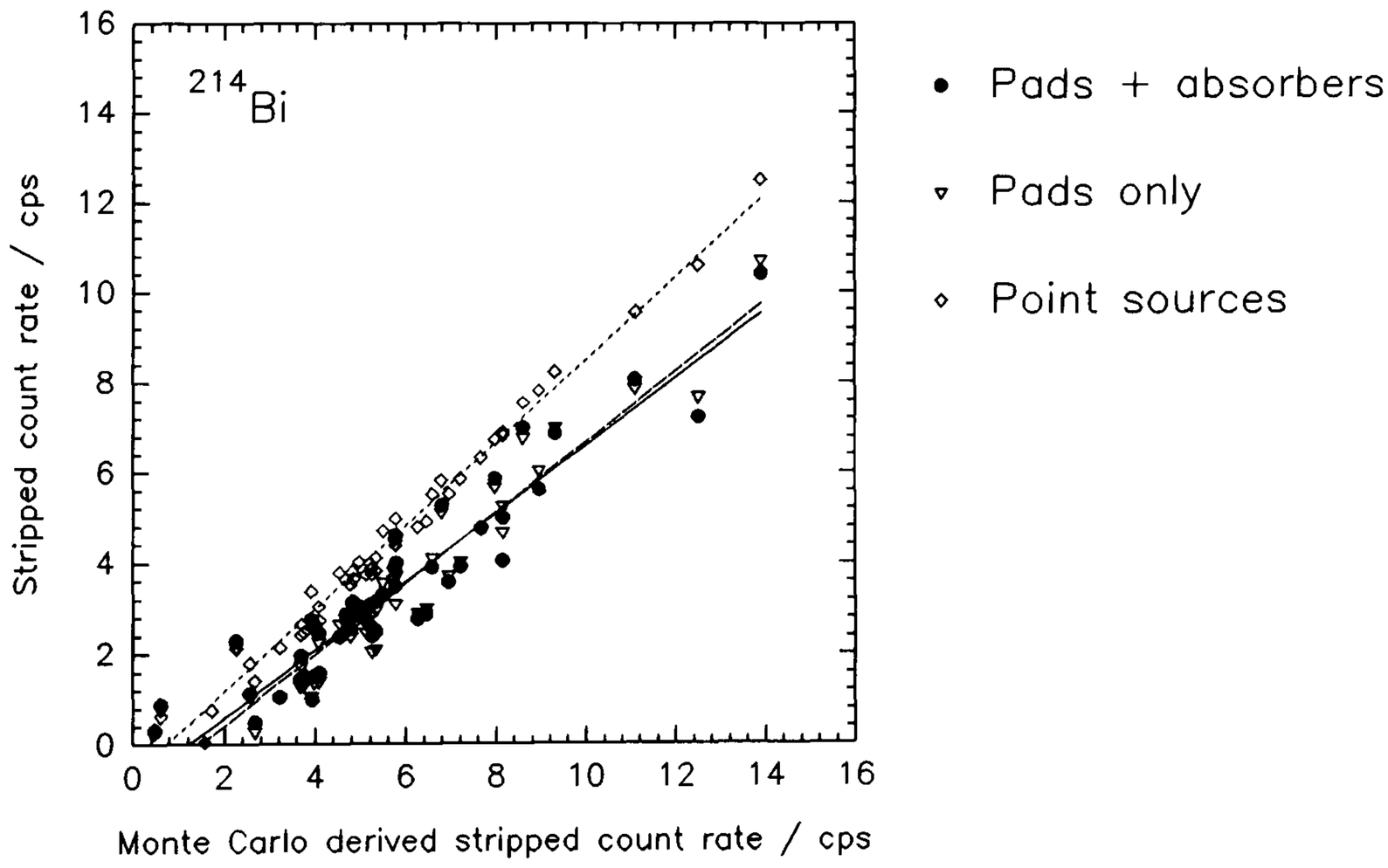

Figure 6.78 Comparison between methods of stripping for ^{214}Bi.

For ^{214}Bi, shown in figure 6.78, there are small deficiencies of count rates at the zero x-axis (-0.9, -1.1 and -0.7 cps). The three alternative methods of deriving stripping

ratios also lead to underestimates at high ^{214}Bi levels relative to Monte Carlo calculations owing to the slopes of the regression lines being more significantly different to Monte Carlo (-24.9%, -21.8% and -8.4%). This is due to the stripping ratios of ^{208}Tl being underestimated by Monte Carlo, resulting in excess stripped count rates in the ^{214}Bi window.

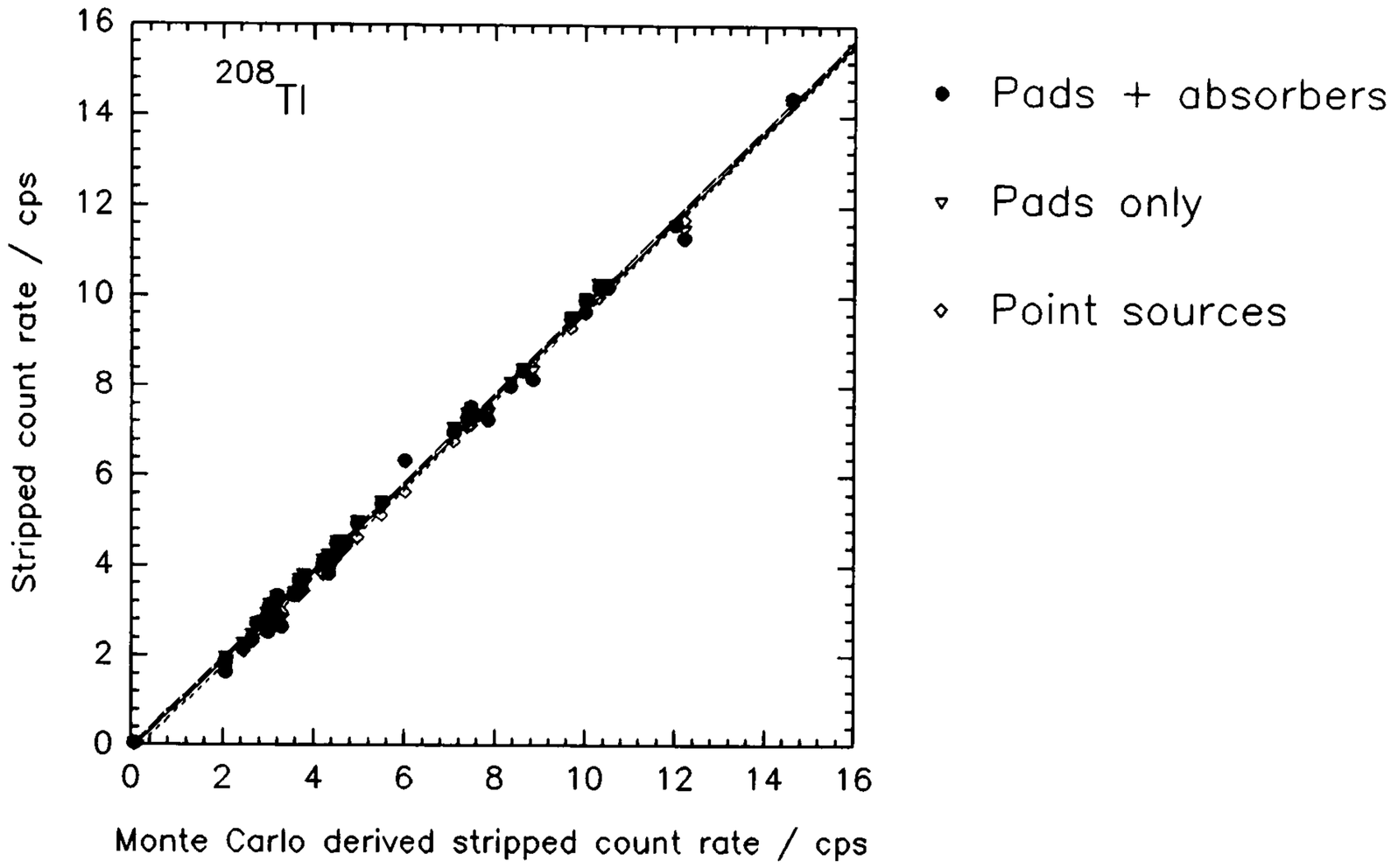

Figure 6.79 Comparison between methods of stripping for ^{208}Tl.

6.8.8 Total Spectral Deconvolution

For rapid quantification of environmental radioelement concentrations, the use of energy windows surrounding the full energy peaks of interest and a knowledge of relative interferences in the form of stripping ratios is the most appropriate method to apply. Full spectral deconvolution has the additional advantage of increasing the precision of measurement however. This can only be satisfactorily performed if all radioelement components are identifiable and standard reference spectra are available that have been recorded under identical measurement (or simulated) conditions (geometry, detector bias, energy calibration, etc). In order to enable radioelement concentrations to be determined, the concentrations of the standard data set must also be known.

By fitting standard spectra to an unknown composite spectrum, usually by the method

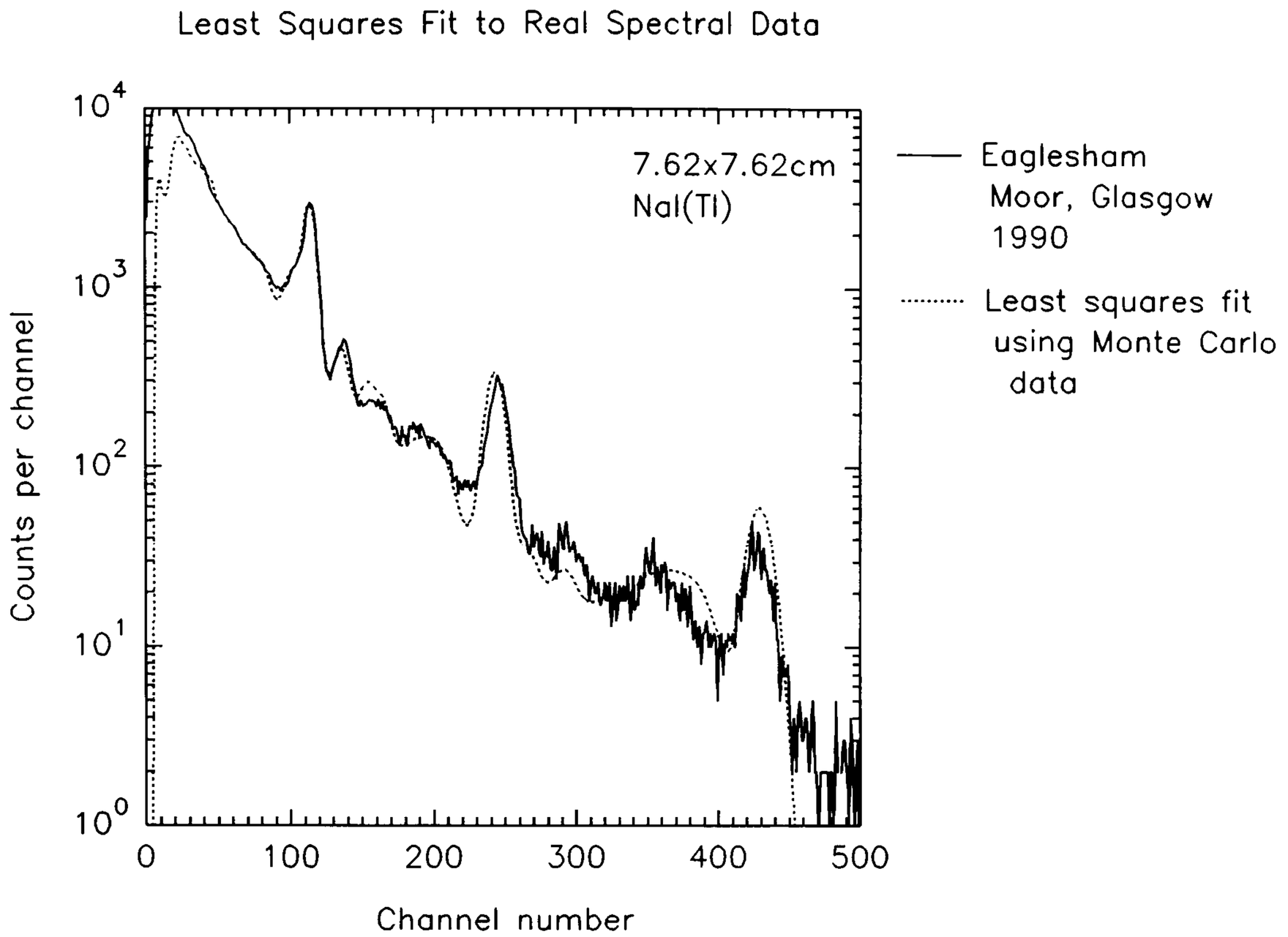

Figure 6.80 Least squares fit of Monte Carlo derived spectra to Eaglesham Moor (Glasgow, 1990) ground based measurement.

of least squares, the coefficients of the linear simultaneous equations and their variances can be found (Salmon, 1961). These represent ratios of unknown/standard concentrations. These methods have been applied to data recorded in-situ at Eaglesham Moor, near Glasgow, during 1990. This is an area of open countryside contaminated from Chernobyl fallout. Figure 6.80 shows a spectral measurement taken using a 7.62x7.62cm NaI(Tl) detector and a least squares composite fit of Monte Carlo (code MCII) derived spectra. Generally good agreement is seen around regions of most prominence. The method can be alternatively presented, as in figure 6.81, by the way of successive deconvolution from high to low energies. Figure 6.81a shows the same data as figure 6.80, minus ^{208}Tl (fig. 6.81b), minus ^{214}Bi (fig. 6.81c), ^{40}K (fig. 6.81d) and finally minus ^{134}Cs (fig.6.81e). Stripping methods of this sort are inherently less precise at lower energies because of successive subtraction and may lead to the appearance of artificial features, even peaks. Care must be taken in the interpretation following multiple deconvolution. It is important that prior to deconvolution, any spectral drifts are corrected for that may lead to errors in the fitting procedure.

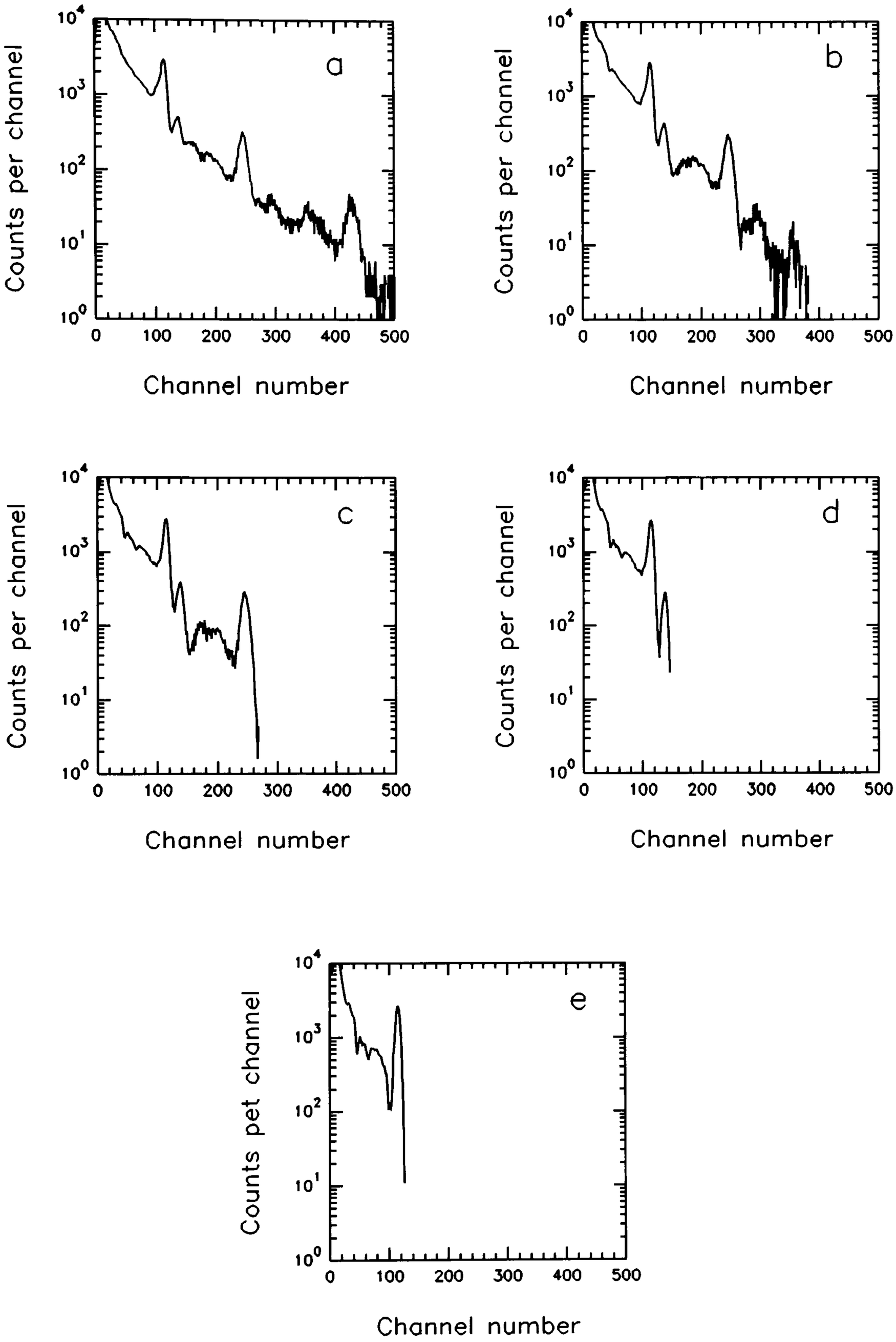

Figure 6.81 Successive stripping from high to low energies.

6.8.9 Optimisation of Aerial Survey Detector

The development of many aerial survey detector systems has arisen from the experiences of geophysical applications. The prospecting of uranium for example is usually based upon the measurement of ^{214}Bi at 1764 keV. Although alternative energies of this daughter product exist, this is the most favourable in terms of emission intensity and being relatively free from interferences. For high energy γ-rays, a minimum thickness of scintillant is necessary for effective detection probability. However, at lower energies a thinner crystal may be as practical in some circumstances. The γ-ray study of fission and activation products, released during nuclear discharges or accidents is mostly below 800 keV (table 6.25): a thickness of NaI(Tl) could be as effective in their measurement without penalty of excessive weight or the equivalent difference in volume could be utilised elsewhere providing a larger surface area and hence a more sensitive system for a given total volume.

Table 6.25 Fission and neutron activation products (Lederer & Shirley, 1978).

Radionuclide	**γ-Ray Energy / keV**	**Half-life**
^{241}Am	59.5	432a
^{132}Te	49.7, 228	3.3d
^{131}I	364	8.04d
^{103}Ru	497	39.4d
^{137}Cs	662	30.2a
^{95}Zr	757	64d
^{95}Nb	766	35d
^{134}Cs	795	2.06a
^{58}Co	811	70.8d
^{54}Mn	838	312d
^{60}Co	1172, 1333	5.27a

An investigation has been carried out to determine the inherent peak and Compton sensitivities, of detectors with constant surface area and various thicknesses of NaI(Tl) scintillant. In the absence of interfering backgrounds, backscatter peaks and peripheral

scattering, this investigation is pertinently accomplished by Monte Carlo methods.

A detector housing material of 0.8mm has been used and will vary between actual detectors. The surface area of detector is 40.64x40.64cm (1652 cm^2).

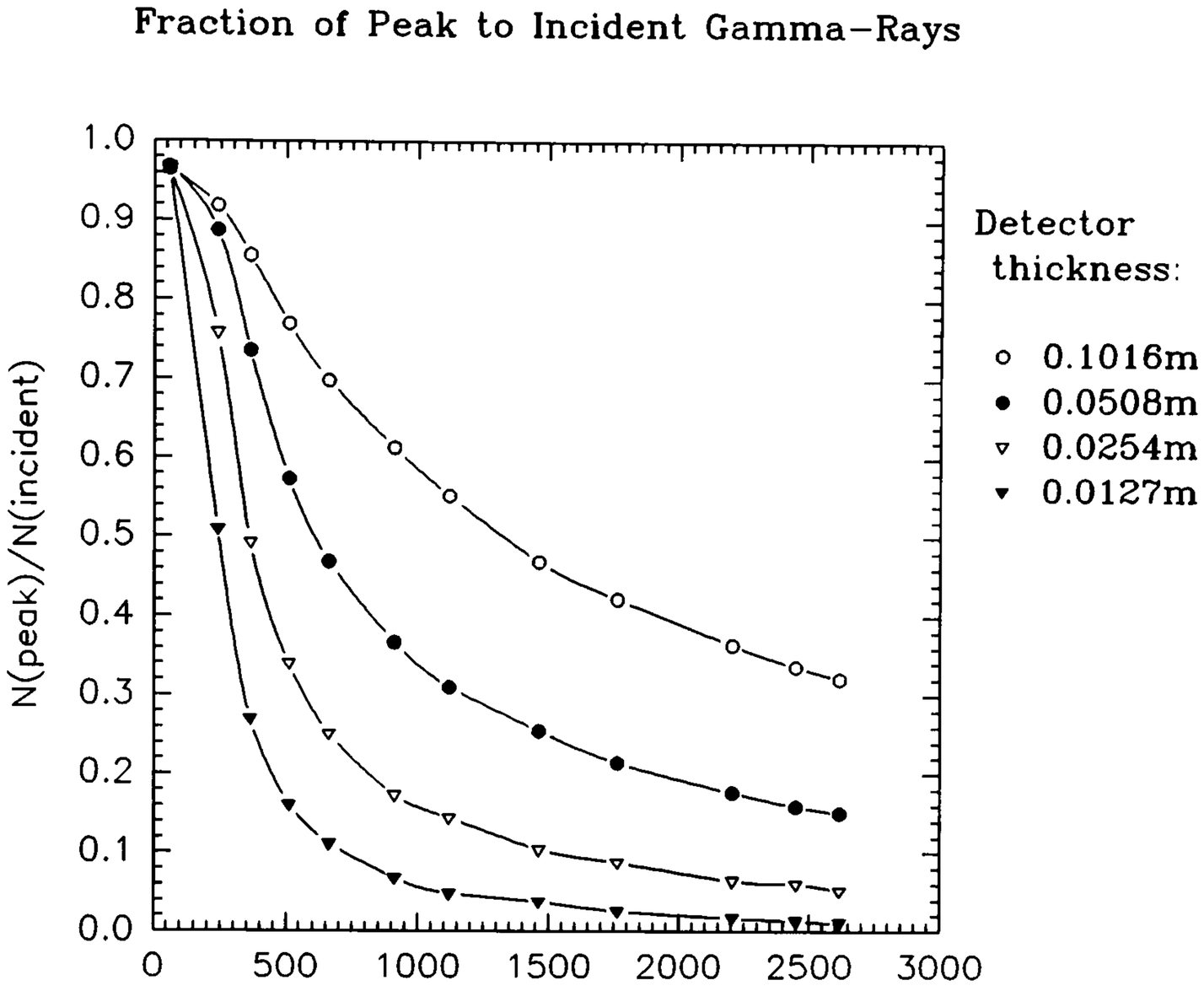

Figure 6.82

Figure 6.82 shows full energy peak response per incident γ-ray. For comparison purposes, a thickness of 10.16cm of scintillant has also been included. For this thickness, the probability of obtaining a peak count varies from 78% at 500 keV, 66% at 800 keV and 32% at 2615 keV. At 300 keV and less, it is better than 90%. The following curves shown in figure 6.82 indicate the change with progressively thinner scintillants. From thicknesses of 2.54cm to 1.27cm, the peak response becomes increasingly constant (approximately) above energies of 1200 keV and 900 keV respectively. Below these energies, the change in response becomes rapid especially below 500 keV. For 364 keV, a ^{131}I energy, a thickness of 1.27cm yields a peak response of 40%. The choice of thickness would depend upon the acceptable counting rate (efficiency), and therefore counting period, statistical precision and possibly ground spatial resolution required.

Although, over 96% of a 59 keV γ-ray (^{241}Am) occurs in the full energy peak regardless of scintillant thickness, the discrimination of such an energy may not be easy if the Compton continuum upon which a peak appears is large. Figure 6.83 shows the partial absorptive properties owing to Compton scattering, that occur per incident γ-ray. For a 10.16cm thickness, this fraction gradually increases with energy. It is interesting to note that for other, thinner thicknesses this fraction remains constant from about 600 keV. Again above this energy, the thinner the scintillant, the smaller the proportion of counts appearing in a continuum. At certain energies a chosen thickness can produce greater partial energy deposition than 10.16cm. A 1.27cm thickness provides the least Compton fraction above energies of 700 keV, but below this, is worse by almost a factor of two at 300 keV.

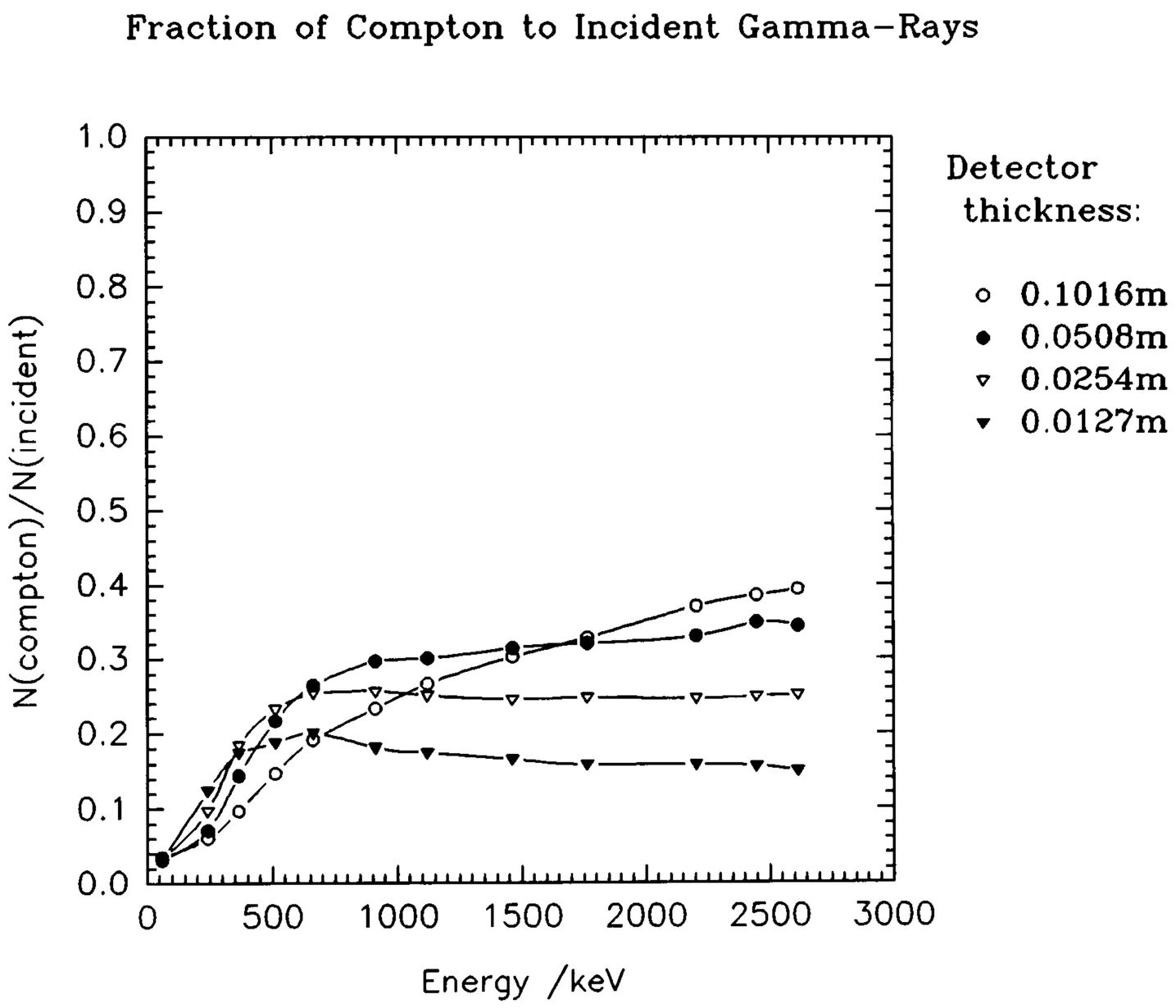

Figure 6.83

At about 800 keV, the fraction of Compton counts for a thickness of 10.16cm is equal to that of 1.27cm. However, the fraction of peak counts drops from 66% to 10% (a reduction by a factor of 7.5). In the presence of high energy γ-rays (2615 keV for example) the Compton continuum could be reduced by a factor of 2.7 (40% to 15%) by using this thinner detector. Even so, the advantage gained is really negated by poor peak response due to the greater transmission factor. In this context, the only

advantages in using a system of thinner dimensions than 10.16cm is at very low energies, probably for ^{241}Am. There would be little loss of peak counts and in the presence of high energy γ-rays, the Compton contribution would be minimised. For a detector of 16 litres total volume, 8 separate detectors of thickness 1.27cm and equal surface area could be used without significant weight difference (additional photomultiplier tubes will add some). Eight detectors spread across a thin floor pan could provide a sensitive detection system for ^{241}Am. Sharma *et al* (1972) calculated by Monte Carlo, the response of very thin NaI(Tl) detectors (1-3mm) over an energy range 10-100 keV. Energy resolution is poor; 30-40% at 60 keV. In the presence of comparable concentrations of low energy natural emitters, clear identification and measurement is difficult (^{231}Th: 58.6, 63.0, 74.8 keV; ^{232}Th: 63.3 keV; ^{234}Th: 62.9, 63.3 keV). Additional difficulties arise owing to the strong attenuation of γ-rays by soils that is greatly influenced by chemical composition (5.3.5.4). Joshi (1989) describes methods of determining ^{241}Am in-situ by the use of planar Ge(Li) detectors. The relatively recent advent of high efficiency semiconductor detectors offer the most promising hope for low energy aerial counting systems.

6.8.10 Semiconductor Detectors

The Monte Carlo simulation of semiconductor detectors is a relatively straightforward modification and alteration of the existing code for NaI(Tl) detectors. The attenuation coefficients of germanium or silicon are available in Storm and Israel (1970). Figure 6.84 shows the linear attenuation coefficients of germanium for the processes involved in the γ-ray energy range of interest. Comparison with those of NaI(Tl), figure 6.8, reveals greater absorptive properties of germanium at energies of less than 40 keV. The absolute peak efficiency of a large high purity GMX detector now is around at least 50% that of NaI(Tl), measured at 1333 keV and 25cm source-detector distance. This opens up opportunities that have hitherto have been practical only to scintillation detectors where measurement times have necessitated to be short for environmental monitoring. The particular advantage of semiconductor detectors is that complex radionuclide γ-ray decay lines can be recorded unambiguously.

Trials have been conducted using Monte Carlo codes MCI and MCII, with germanium cross sections shown in figure 6.84. The range of electrons and positrons in germanium is different to that of NaI(Tl) and has been treated in the same manner, but using different parameters used by Mukoyama (1976). The presence of the central inert core of a semiconductor detector effectively reduces the geometrical volume of the cylinder to an annulus comprising the *active volume*. For proper simulation, the detector annulus must be used, unless the inert core is small compared to the overall dimensions. The exact dimensions of the active volume are often much less well known than those of scintillation crystals owing to the diffuse nature of the boundaries.

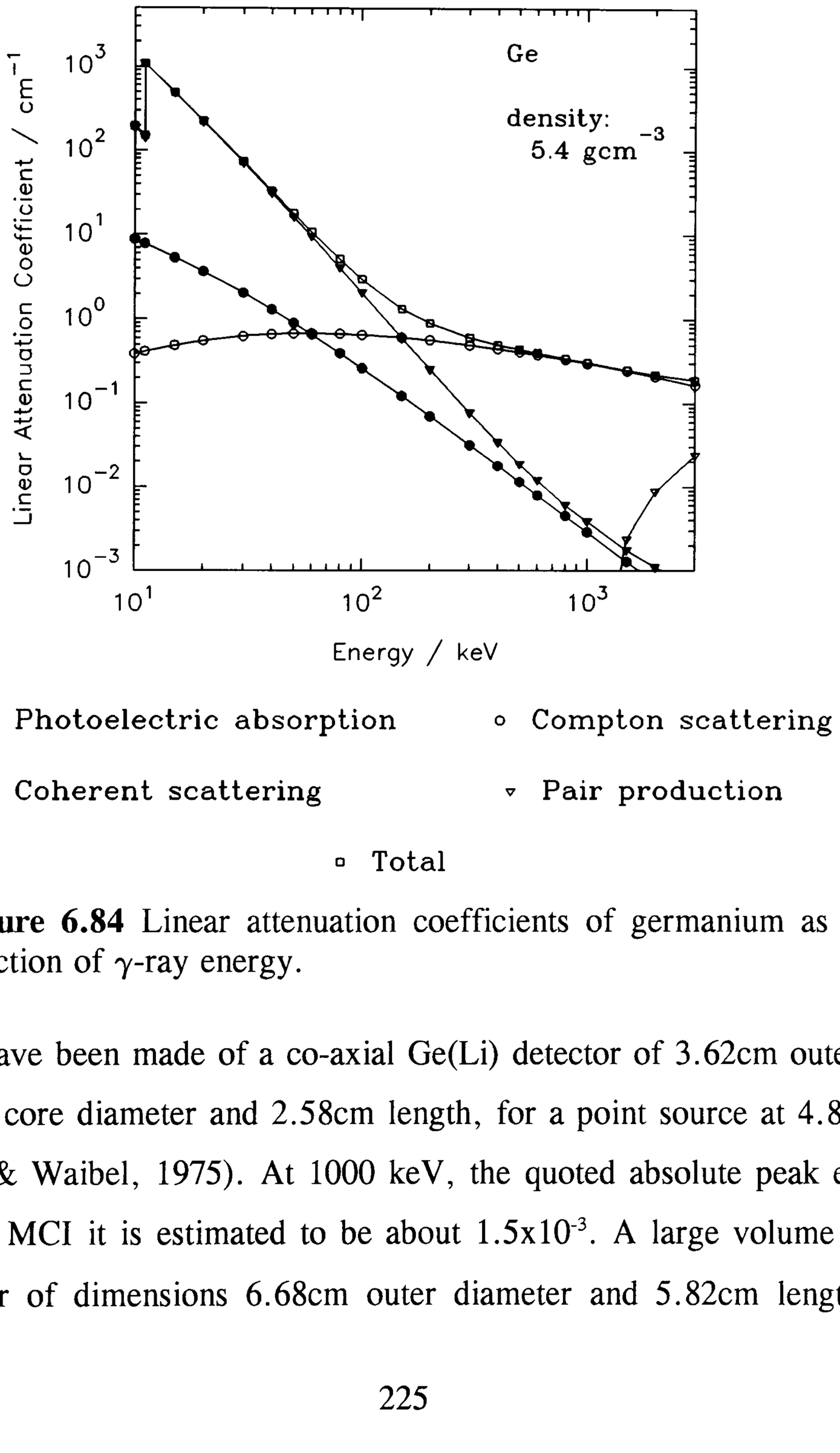

Figure 6.84 Linear attenuation coefficients of germanium as a function of γ-ray energy.

Simulations have been made of a co-axial Ge(Li) detector of 3.62cm outer diameter, 0.62cm inner core diameter and 2.58cm length, for a point source at 4.83cm distant (Grosswendt & Waibel, 1975). At 1000 keV, the quoted absolute peak efficiency is 1.35×10^{-3}: by MCI it is estimated to be about 1.5×10^{-3}. A large volume high purity GMX detector of dimensions 6.68cm outer diameter and 5.82cm length has been

simulated with an assumed inner core diameter of 1cm. This yields an absolute peak efficiency of $8x10^{-4}$ compared with $6.36x10^{-4}$ as determined by EG & G. A 26 cm^3 co-axial Ge(Li) detector has been simulated by Rogers (1982), who reports that calculated peak efficiencies are 20% greater than measured, if the dead regions of the detector are neglected (detector cylindrical surface, detector jacket). The author quotes that it is "..virtually impossible to do a reliable calculation of the absolute efficiency of a Ge(Li) detector unless the counters inert layers can be accurately specified".

To illustrate how powerful an analytical tool a large volume GMX HP detector can be, a few trials have been applied to the problem of buried radionuclide sources. The potential to identify radionuclide distribution profiles in-situ is as we have seen, an important consideration in order to estimate fluence rates and radiobiological consequences. Figure 6.85 has been calculated using Monte Carlo code MCII and clearly shows the change in spectral shape as a function of burial depth. The upper figure shows a source of ^{137}Cs activity distributed as a plane across a soil of Beck composition. Note the absence of forward scattering immediately below the full energy peak. The middle figure shows the expected change in spectral shape from a deep exponential source profile of activity. The valley beneath the peak is significantly different from the planar source. In addition, the back-scatter peak (channel 40) is suppressed and the low energy Compton continuum is more pronounced. The lower figure shows activity dispersed uniformly through a depth of 0.4m. The peak intensity is reduced and the valley contains further contributions. Although the same processes occur and may be measurable using scintillation detectors, the details are difficult to observe (figure 6.54). More importantly, in the presence of multi-radionuclide decays, the ratio of peak-to-valley as a measure of source dispersion can be clearly identified without interference.

There are many references concerning the simulation of semiconductor detectors using Monte Carlo methods. Amongst those which are equally useful in the applicability to scintillation detectors are Grosswendt & Wabel (1975), Meixner (1974), Gaggero (1971), Lal & Iyengar (1970) and Aubin *et al* (1969).

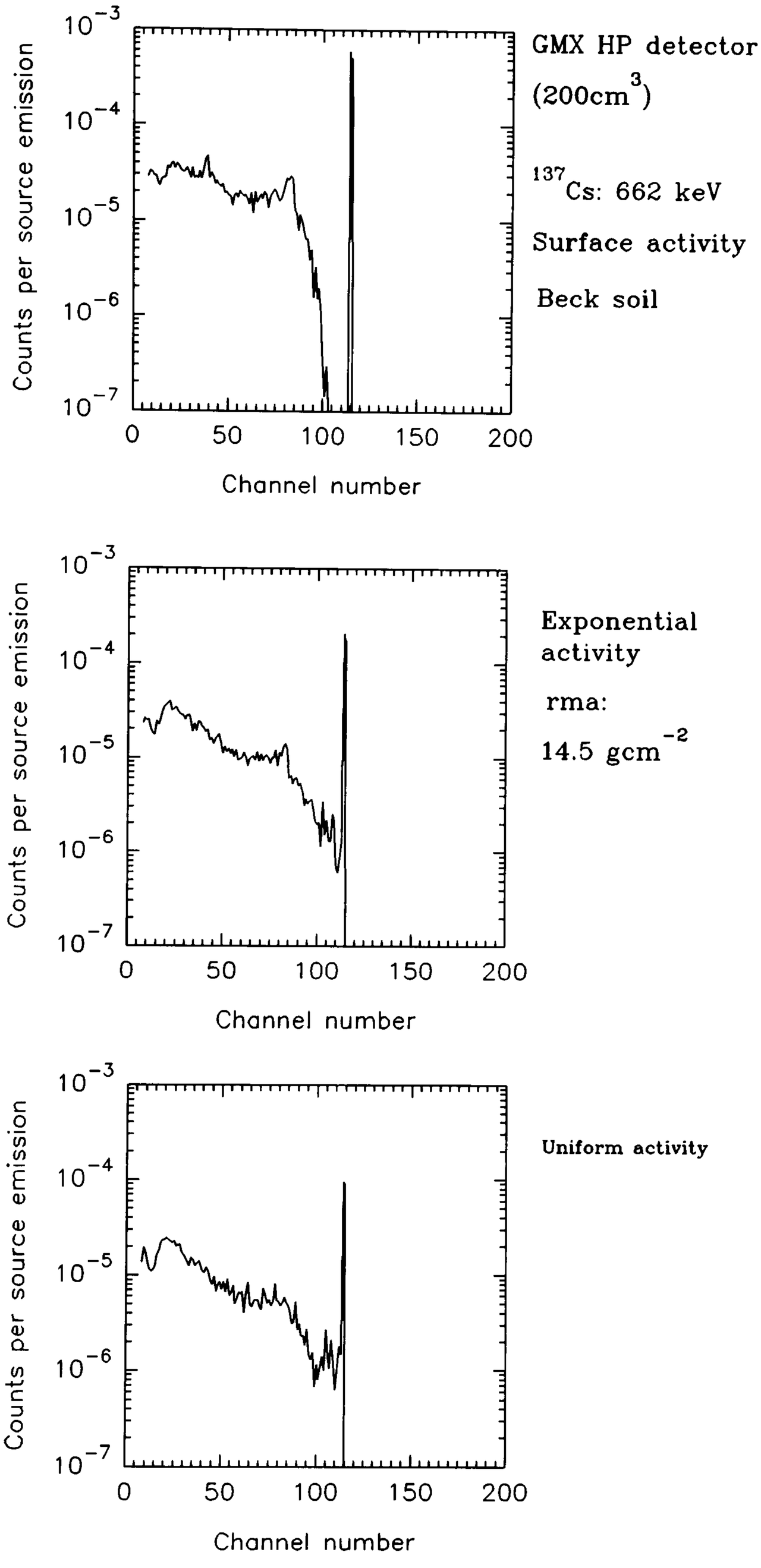

Figure 6.85 Simulation using Monte Carlo MCII, of a GMX HP semiconductor detector of active volume 200cm^3 and 50% relative efficiency.

6.9 Application of Monte Carlo Simulations to Deconvolution of ^{234m}Pa and ^{228}Ac

Depleted uranium (deficient in ^{235}U) has characteristic γ-ray emissions, the most prominent at 1001 keV, which can lead to it's unequivocal identification. The production of depleted uranium is usually by separation of ^{235}U in a diffusion plant or irradiation of natural uranium in a reactor. Since depleted uranium will not be in equilibrium with its daughters, the measured γ-ray spectrum will show more prominence to ^{234m}Pa then normally encountered from equilibrated uranium owing to its faster rate of growth. ^{234m}Pa is present in the decay series of ^{238}U, supported by ^{234}Th. The potential measurement of ^{234m}Pa was investigated at SURRC prior to the British Nuclear Fuels funded aerial survey of Springfields fuel fabrication facility and surrounding Ribble Estuary (Sanderson *et al*, 1993a), by analysis of the spectral response of the survey detector from depleted uranium. During the processing of the Springfields data and the mapping of ^{234m}Pa, it became clear that an excess count-rate occurred in the ^{234m}Pa channel window owing to an unforeseen interference.

Calibration of ^{234m}Pa to equivalent concentration levels was not possible owing to insufficient ground based measurements or theoretical studies and therefore only height corrected stripped count rates were displayed. Following a careful visual inspection of the full spectral measurements, ^{234m}Pa was positively identified at Springfields despite flights made around the perimeter of the plant or at a regulation 500 ft over the site. A second observation was seen near the riverbank in Preston (BNF has documented this source during past discharges). In the Ribble estuary, a low intensity peak was observed corresponding in energy to about 930 keV, below that of ^{234m}Pa (1001 keV).

It was postulated that an excess ^{228}Ac, owing to disequilibrium with respect to the parent ^{232}Th radioisotope, was seen in those regions therefore. Three gamma-ray emission lines of ^{228}Ac occur at 911, 964 and 969 keV. The resolution of the detector is such that a single broad peak is formed by the superimposition of these lines. Figure 6.86 shows the summation of four spectra, two near Springfields and two near Preston, to accentuate the ^{234m}Pa peak. Likewise, figure 6.87 shows the accumulation of ten spectra to show the broad ^{228}Ac peak (this peak is nevertheless low in intensity).

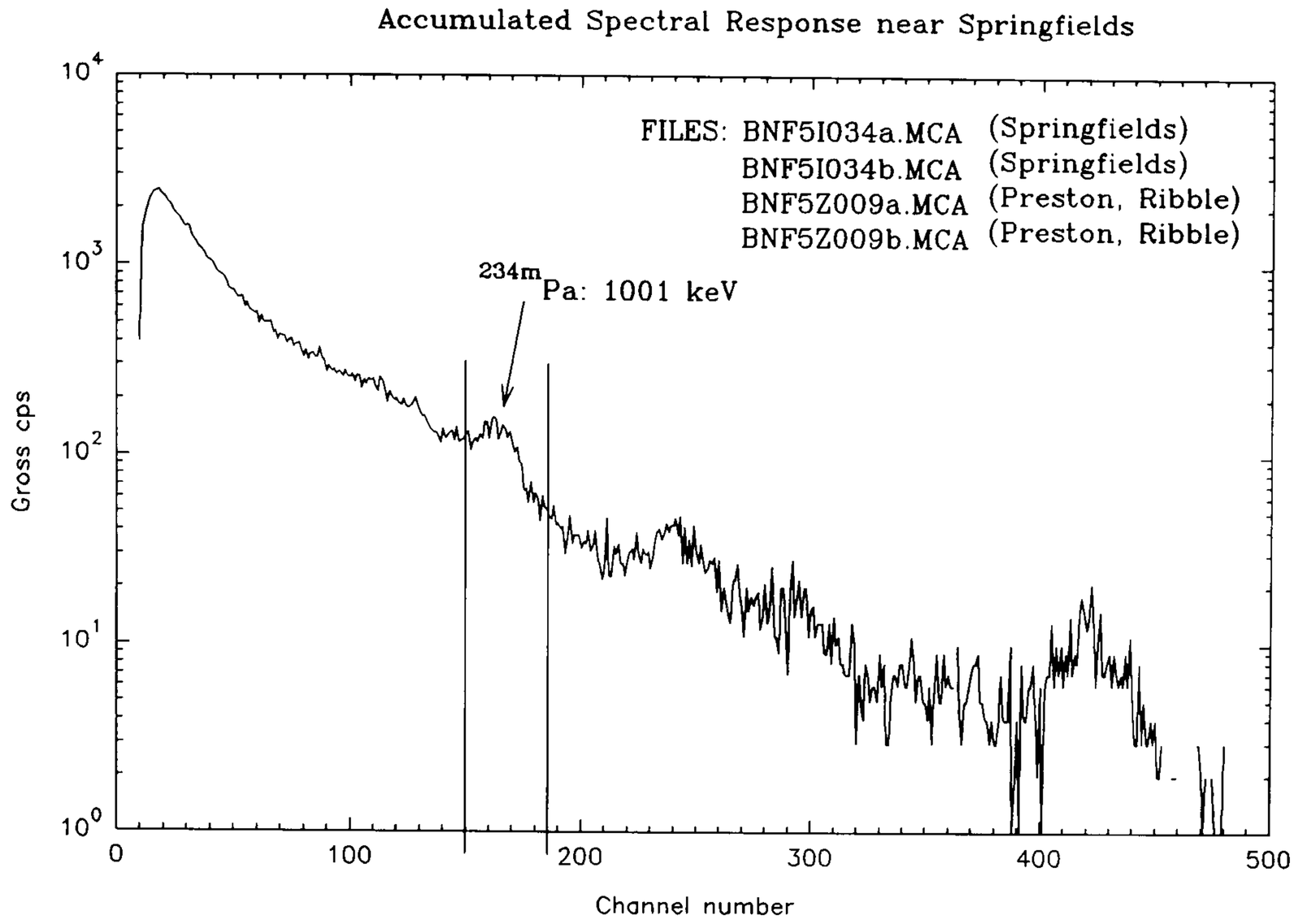

Figure 6.86 ^{234m}Pa Accumulated Spectra.

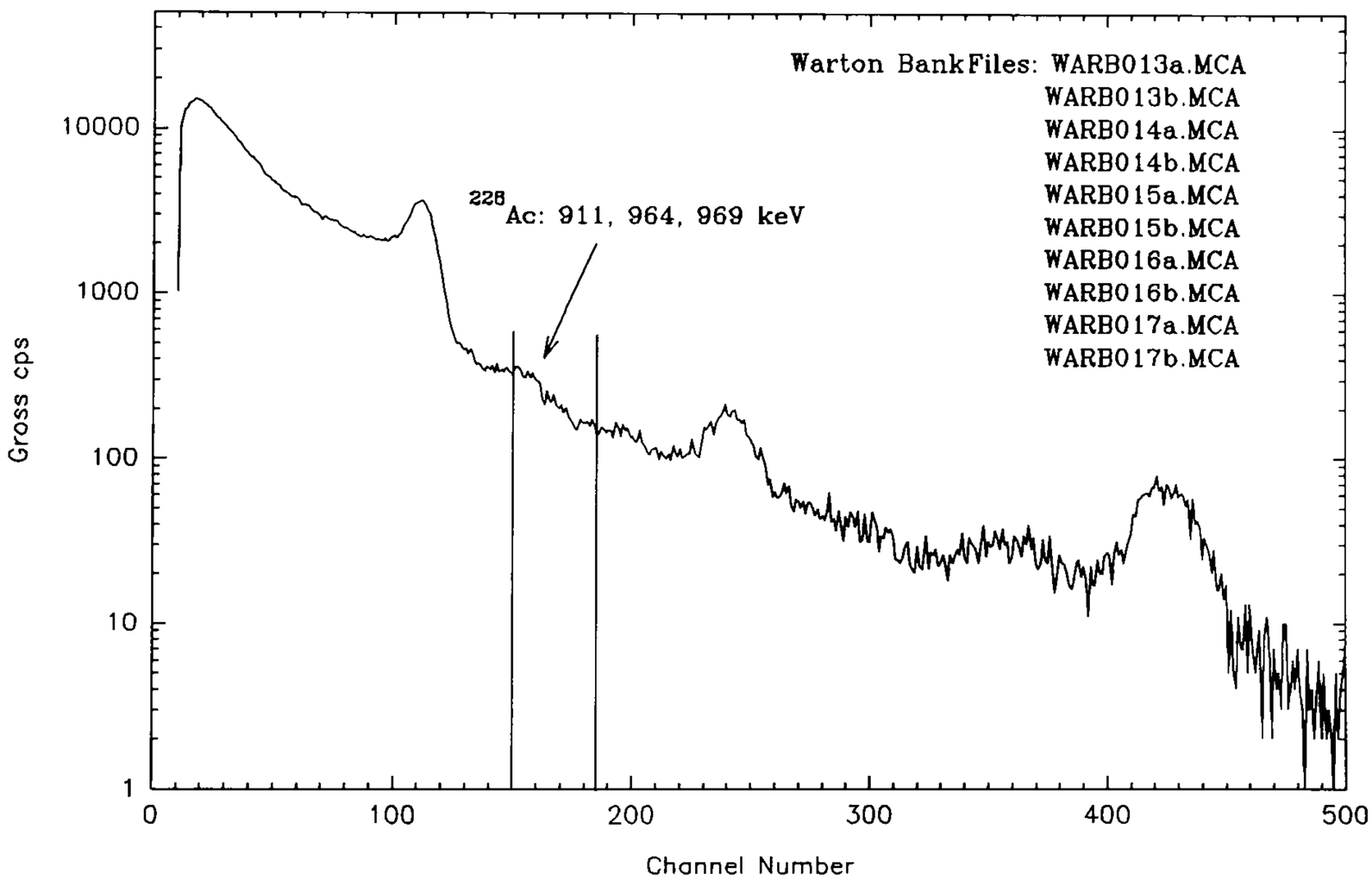

Figure 6.87 ^{228}Ac Accumulated Spectra.

Attempts were made to separate the ^{234m}Pa/^{228}Ac pair, using an extension of standard SURRC data processing procedures. This was particulary difficult owing to the almost overlapping nature of the observed peaks. Excessive overlapping of spectral windows is undesirable, therefore two narrow and adjacent windows (140-160ch, 160-180ch)

were tentatively chosen instead of the single 150-185 channel window as used during the survey. It must be noted that each peak contributes to some extent into its neighbouring window. A 6x6 stripping matrix was formed using experimental and Monte Carlo based results. Since an experimental gamma-ray measurement of a pure source of ^{228}Ac was not available, an estimation of its spectrum was calculated at aerial survey heights and with full simulation of the detector package (figure 6.88).

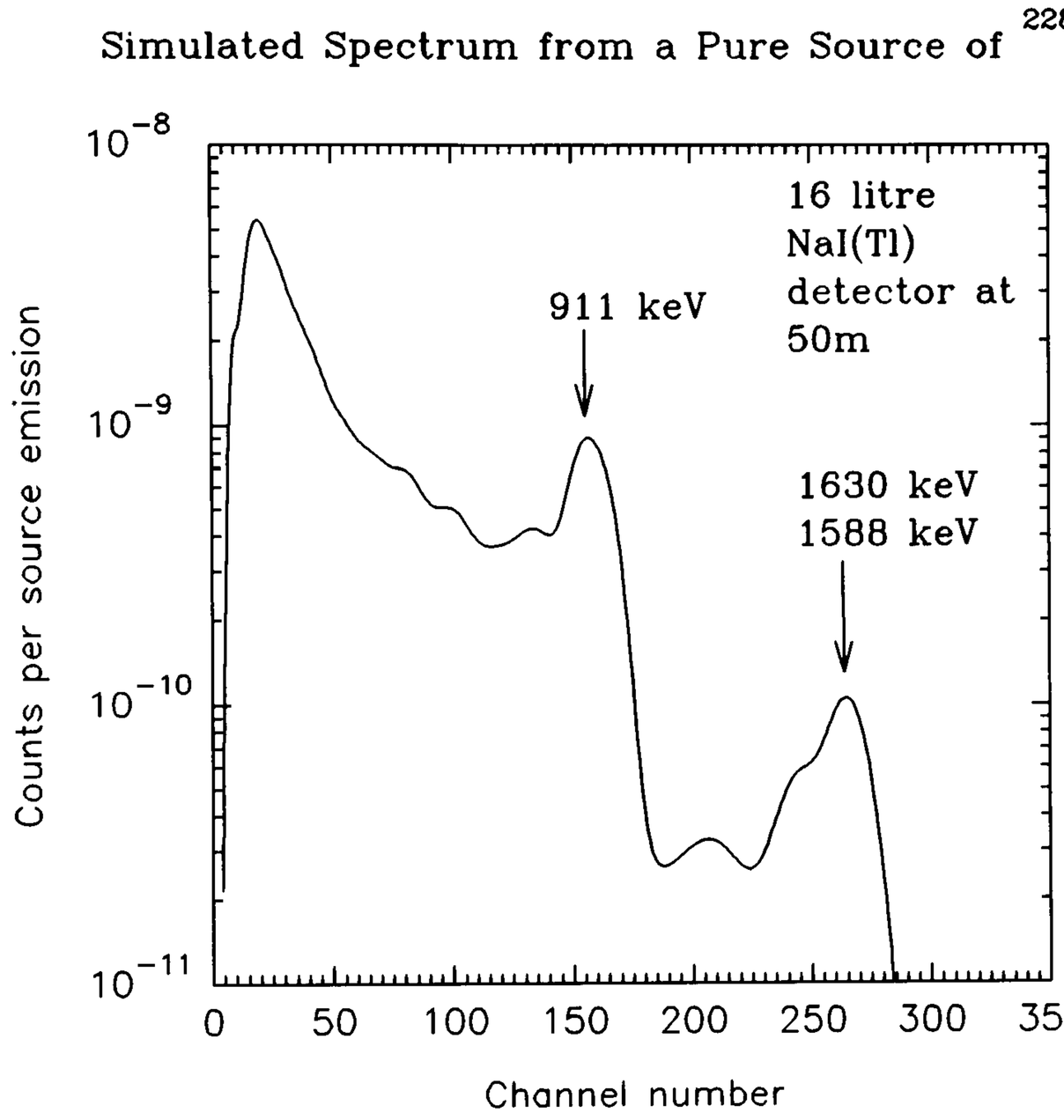

Figure 6.88 Estimate of pure ^{228}Ac spectrum at 50m altitude.

Upon reintegrating the entire data-set, and producing new summary, net and stripped count-rates, the full survey area was remapped. Comparison with the previous preliminary stripped count-rates showed near identical results for ^{137}Cs, ^{40}K, ^{214}Bi and ^{208}Tl. Analysis of ^{234m}Pa and ^{228}Ac stripped data showed a correlation between the two, likely caused by inadequate separation due to overlapping peaks and poor deconvolution. However, the probable interpretation from this advanced processing provided a reasonable indication of the distribution of the two radioisotopes: ^{234m}Pa was clearly seen at Springfields and at the upper reaches of the Ribble: ^{228}Ac was estimated to be in regions of the salt marsh and Springfields. Other spuriously high estimates, particularly of ^{234m}Pa in the more inland regions, could only be explained in terms of

processing limitations.

This is a significant development in the application of aerial survey to the studies of a dynamic source, ^{234m}Pa. Owing to the limitations of detector energy resolution, the presence of ^{228}Ac prevented a clear interpretation. Aerial survey remains the only practical and cost effective means of extensive mapping of such dynamic sources. The technique is rapid, crossing all geographical barriers and enables time series measurements to be made.

In a second demonstration of the use of these techniques to identify and locate ^{234m}Pa, an aerial survey conducted on behalf of The Scottish Office included a Ministry of Defence gunnery range near Dundrennan, in SW Scotland (Sanderson *et al*, 1993b). Depleted uranium has many uses including a heavy metal component of military projectiles. The survey was able to confirm that exposure to harmful γ-ray radiation was not significant in that signals observed across the range were of similar magnitude to those found naturally elsewhere. No excess signals were identified, but future specifically designed surveys (ie. lower altitude) may reveal spatially small concentrations of activity.

6.10 Chapter Summary

In this chapter, the principles of Monte Carlo methods have been applied to the comprehensive simulation, of in-situ and aerial survey detectors, and the γ-ray fluences resulting from a variety of radionuclides distributions. The entire system lends itself to direct comparison with real measurements and as an aid where complex field variables aren't completely known or are difficult to find for controlled experiments. The simulation of right cylindrical detectors of 7.62x7.62 cm NaI(Tl) has been accomplished satisfactorily, to the energies of interest here. The modelling of larger, scintillation arrays has been demonstrated successfully, although it is thought that the equivalent thickness of the housing materials has been chosen too conservatively. This may have contributed to the photofraction being systematically overestimated by around 12%. It is interesting to note that the estimated photofraction of a single prismatic detector is

well in keeping with experimental measurements. It is possible that the summing of four prismatic detectors may not increase the photofraction as significantly as predicted by simulation of a single equal volume detector: the summed output from a four prismatic detector array exhibits the photofraction characteristics of a single crystal. It is also noted that Monte Carlo estimates of count rates per activity deposition are systematically 6-13% less than those obtained by the numerical methods of Chapter 5. This may be due to having restricted the deposition extent to a non-infinite source.

The Compton scatter component of spectral measurements has been fully simulated, within the detector and arising from the near and far environments. In conjunction with the primary, full energy component, stripping ratios of ^{137}Cs, ^{134}Cs, ^{131}I, ^{40}K, ^{214}Bi and ^{208}Tl have been calculated for the first time for a 16 litre NaI(Tl) aerial survey detector, with respect to their defined energy windows. Comparison with evaluations from experimental methods show differences that may be attributable to the limitations of both approaches. Stripping ratios can have positive and negative altitude dependency.

Optimisation trials for scintillation detector thickness, specifically for a post-nuclear accident scenario, have been attempted. The results show that little overall advantage may be witnessed in choosing slimmer detectors as a preference over standard prismatic types. It may beneficial to use less sensitive, semiconductor detector types in high count rate contexts expected to be present in such situations and these certainly aid interpretation of complex decay schemes. Simulation of semiconductor detectors has been demonstrated with some examples.

Finally, an example of the application of Monte Carlo results has been presented by the deconvolution of ^{234m}Pa and ^{228}Ac, from within a complex marine environment. The actual presence of these radionuclides, at the locations identified, has been confirmed by ground sampling teams. This is a clear demonstration of how powerful a tool Monte Carlo methods are in the study of a wide range of interesting phenomena.

7. Conclusions

The preceding chapters have introduced and investigated a range of factors influencing the relationship between in-situ and aerial survey scintillation detector responses and ground level radionuclide depositions (calibrations). Calibrations differ depending upon how radionuclides are dispersed in the environment and the type of detectors employed. Problems associated with operational procedures (multi-detector arrays, gain shifts, resolution effects), data processing and methodologies (allowances for altitude dependencies of stripping ratios) have been considered. This chapter draws together all these points and discusses the findings under the four main headings described at the outset.

7.1 Operational Investigations of Detector Use

The analysis of spectral information has been developed by quantifying peak energy deposition (in the form of count rates) and relating it through a calibration procedure to estimated radionuclide concentration. The effects of detector drifts and collective shifts have to be corrected prior to processing. The selection criteria for regions of interest surrounding peaks must be based upon detector resolution and for multi-crystal array systems it may be necessary to allow a greater tolerance to account for spectral broadening and small gain drifts. As a result of drifts, either under- or over-estimates of true window count rates may occur.

The stripping of net spectral data can be extended to many radionuclides, providing that pure reference spectral shapes can be determined. Whereas for geological mapping a great deal of attention has been paid to the construction of calibration pads from which stripping ratios can be determined, there are few examples of the extension of such facilities to environmental nuclides. It is possible to supplement calibration pads for natural sources by additional laboratory scale facilities: initial SURRC surveys used pure reference materials such as point sources, or pure radiochemical solutions. However, the use of point sources cannot be recommended owing to the absence of realistic scattering conditions that are encountered in practice. Doped sheets of activity

used in conjunction with absorbers offers a means of extending calibrations to other radionuclides.

For a 16 litre aerial survey array consisting of four prismatic NaI(Tl) crystals and collectively coupled, drifts between individual units can lead to worsening energy resolution. It has been found that variation of stripping ratios with resolution for SURRC windows remains relatively small over the range 8.5 (the minimum, inherent resolution) to 13%. Provided that these limits can be adhered to, a single suite of stripping ratios will suffice for deconvolution purposes.

Stripping ratios also show some variation with changes in overall (collective) detector gain shift. It is recommended from investigations completed here, that gain shifts of greater than $\pm 1\%$ cannot be tolerated and will introduce significant errors into the deconvolution process, if stripping ratios are determined under such circumstances. For multi-detector systems, collective gain shifts also lead to the addition or loss of counts from regions of interest, but once again, a single set of stripping ratios is sufficiently robust to enable survey data to be deconvoluted successfully. In practice it is easily viable to maintain better than $\pm 1\%$ gain stability and in any case it would be possible to recover data showing large collective gain shifts during post-processing, with appropriate energy calibration and re-integration procedures, at the expense of rapid quantification.

7.2 Experiments to Determine Stripping Ratio Altitude Dependency

The altitude dependence of stripping ratios has implications mainly for aerial survey calibrations. However, the same effects are observed from radionuclide depositions that are buried deep within subsurface strata. We have noted that stripping ratios must be ideally determined from a source configuration that closely resembles the source to be measured. For aerial survey spectrometers, this is not easy to achieve, again for the reasons of source homogeneity and availability. The use of doped calibration pads, with interspersed absorbers goes some way towards simulating on a small scale the air-path scattering, and in the absence of any other method, corrections of this sort are

acceptable, but not ideal. This is because experimental simulations of ground-air interfaces, between sources and detectors are limited to an artificial scattering geometry which is not necessarily encountered in full scale field conditions. Also, anthropogenic sources may show a vertical profile with depth including sub-surface maxima or pronounced burial: these are not available as convenient, well characterised, calibration facilities.

Spectral behaviour of calibration pads can be modified by the addition of absorbers to simulate air path lengths, low activity soil overburden and water, between source and detector. The use of such absorbers is recommended to minimise under-stripping of ^{137}Cs and ^{134}Cs, especially from ^{40}K at aerial survey heights. The consequences of under-stripping ^{134}Cs additionally feeds through to ^{137}Cs and may result in over-stripping relative to ^{134}Cs (the overall effect on ^{137}Cs is difficult to quantify and some self compensation could occur in some circumstances). Absorber composition has been found to be important below 150 keV. Perspex and wood have similar mass attenuation coefficients to that of air, Beck soil and water. The former is chemically well defined, and has uniform thickness and density. The calibration facility based on Grasty (1980b) and Dickson (1981) has been extended and enhanced by the use of perspex absorbers, each representing 9.6 metres equivalent standard air. The absorbers can be placed between source and detector, or above the detector, or both (but not perfectly). In this way experiments have been devised to simulate source-detector path lengths comparable with air path lengths found at aerial survey heights. The altitude dependence of stripping ratios can be determined with the use of absorbers, but the results are constrained in the absence of *skyshine* and proper geometrical considerations (scaling detector dimensions and height). However, trends observed in these measurements show a linearly increasing dependence with altitude for ^{40}K into ^{137}Cs and ^{134}Cs windows. The rate of change of stripping ratios with altitude is small and, for some, constant (for ^{214}Bi and ^{208}Tl into the lower energy windows). This is the overall effect resulting from attenuation of photopeaks and increasing Compton scattering that both occur with increasing altitude, in the set windows. Monte Carlo simulations of pure spectral responses appear to be the only means of overcoming the limitations of experimental stripping ratios.

7.3 Detector Sensitivities by Semi-analytical and Numerical Methods

It is possible to calculate fluence rates from decay emissions of radionuclides, and to predict the count rates observed per unit activity concentration for detectors whose energy and angular efficiencies have been determined with laboratory sources or theoretical means. Such analytical and numerical methods can be readily developed to determine detector sensitivities for a wide range of anthropogenic sources.

Numerical integration of analytical transport equations in combination with measured or Monte Carlo derived detector responses can yield sensitivity estimates for short lived environmental radionuclides which would be difficult to determine solely by experimental methods. The integration of analytical expressions can also be used to estimate detector fields of view. The angular response of the detector is also an important aspect in this, especially for non-spherical detector geometries. For commonly used prismatic NaI(Tl) arrays, the effect of angular response is to narrow the field of view with respect to that of a spherical detector at the same height. The angular response has been determined using Monte Carlo methods over full polar and azimuthal directions, and is energy dependent. For rectangular detectors, a small variation is observed around the azimuthal direction, increasing towards the corners, but may be neglected for simplification purposes. Photofraction is found to be relatively invariant with angular direction.

A range of source depth profiles has been considered and the corresponding fluence-rates and count-rates determined that can be used to predict likely counting statistics and measurement times required for a given radionuclide. The conventional assumption of exponential burial profile for aged fallout is not justified on many sites however, and therefore it may be necessary to extend the equations normally used. Nevertheless, calibration factors derived for ^{137}Cs, show very good comparison to those determined by experimental methods when depth assumptions are correctly applied.

7.4 Detector Responses by Monte Carlo Methods

Monte Carlo methods have been applied to the study of γ-ray transport from the environment to cylindrical and prismatic scintillation and semiconductor detectors. A full simulation using relatively new techniques, shows how calibration factors, stripping ratios and spectral shape characteristics can be reproduced in detail. A specific purpose code was developed to enable incorporation of all relevant details and optimise efficiency.

The successful full spectral responses of small hand held (eg. 7.62x7.62 cm) NaI(Tl) detectors have been used as a basis of code validation. Comparisons are made with published experimental and theoretical data, and this author's own work. This has been an important element and has given some indication that direct comparison with experimental findings must be treated with care. The spectral responses from simulations of concrete calibration pads (uniformly doped with potassium, uranium and thorium) have shown good agreement in terms of shape fitting for small detectors, less so for multi-detector arrays. These discrepancies may be explained by experimental limitations (false geometry, background interferences, near source scattering) and model assumptions. For the latter, a four crystal prismatic array was assumed to behave in the same way as an equivalent single volume, in order to simplify the simulation. This would seem reasonable, considering that the cross-sectional area of each crystal is large compared with mean interaction pathlength. The calculated angular response of such a detector bears this assumption out, but considers only full energy deposition. When scattering contributions are considered, the estimated photofraction is higher than expected by about 12%. Errors of up to 5% can be attributable to cross sections used in the Monte Carlo technique. The calculated photofraction of a single prismatic crystal compares favourably with experimental measurements. The collective combined signal from four detectors appears to reproduce the photofraction from an individual, single unit (not four) despite the fact that experimental measurements of photofraction are notoriously difficult to acquire (detectors placed in "scatter free" environments, suspended sources). Although some attempt has been made to include the scattering and attenuating properties of detector housings and photomultiplier units, a complete

simulation of all materials is difficult to achieve. A compromise has been sought by using an *effective thickness* of aluminium to represent many composite materials found in practice (thermal insulation, heating elements, electronics, mechanical shock insulation, etc). In addition, external, tubular bracing and aircraft structures add their own contributions, and have been neglected. The chosen effective thickness may have been too conservative: an additional thickness would reduce photofraction estimates, but may disguise the underlying problem of the single crystal assumption. Further work is necessary to absolutely confirm these indications.

Calculated stripping ratios for the 16 litre detector array show generally an underestimation and this is likely to be a further result of overestimating photofraction. The altitude dependency of stripping ratios has been studied for a 16 litre NaI(Tl) at aerial survey heights and for a wide variety of radionuclides. There exist some differences between those derived by measurement in small scale experiments and those calculated by simulation. The rate of change with altitude is comparable with, if not quite as strong as, that seen in small scale experiments incorporating absorbers, and systematic differences in magnitude are significant (although the associated errors are large). Direct comparison with calculated values should be considered carefully however. As a result, excess stripped count rates are formed compared with absorber experiments, but not as excessive as using point sources alone (these cannot now be recommended). The ^{40}K stripping ratios derived solely using calibration pads (without perspex absorbers, ie. at ground level) are similar to Monte Carlo estimates at approximately 75m altitude, for a 16 litre detector array. Stripping ratio variations of ^{214}Bi and ^{208}Tl into ^{137}Cs and ^{134}Cs windows are shown to be relatively mild with altitude, owing to a fortuitous compensation that has hitherto not been obvious or recognised. There are circumstances (radionuclides of high concentration and little relative interference) when the method of deriving stripping ratios becomes irrelevant in obtaining certain true window count rates. For instance, the altitude dependence of stripping ratios doesn't matter in areas of high natural potassium and high ^{137}Cs deposition. The effects of stripping on ^{208}Tl (at 2615 keV) are small because of low interference from other radionuclides. At the present time, the choice of selecting a particular suite of stripping ratios and accepting their derivation method is one of

experimental preference first and then in the absence of any other information, theoretically based methods. The experimental method of pads+absorbers to describe altitude dependency of stripping ratios appears to give the least residual stripped count rates in the defined ^{134}Cs window, in environments of high natural and low radiocaesium concentrations. This will be so until closer comparisons can be obtained by improvements in Monte Carlo based methods (and indeed better experimentally based simulations). It must also be noted that it still remains unclear if the observed differences between experimental and Monte Carlo derived spectra are attributable to the scattering geometries of the former not fully representing the true condition.

The simulation of short lived radionuclides has enabled stripping ratios to be calculated, which can be applied to large detectors at survey altitudes. Having a precalibration before nuclear accidents is desirable for rapid quantification. A demonstration of separating ^{234m}Pa from ^{228}Ac, by employing a simulated pure spectrum of ^{228}Ac, has enabled the mapping of both components in a marine estuarine environment for the first time (Sanderson *et al*, 1993a, 1993b) and could be extended in principle to more radionuclides.

The filling of the valley between peak and Compton edge (as a result of forward scattering) and intensity of Compton continuum relative to the full energy peak, may provide some indication of depth profile. The ratio of peak/valley counts may be helpful in definition of simple exponential profiles, but certain conditions can lead to ambiguity. This is also seen in semiconductor detector simulations. This, relatively new consideration, may enable the proper selection of calibration factors to be made from in-situ field measurements.

The optimisation of detector size and geometries has been investigated by Monte Carlo methods. For low energy emitting, complex decay scheme radionuclides (released after a nuclear accident for example), there be may fewer advantages with smaller, thinner detectors than larger detectors developed for geological uses. The fewer Compton events occurring through a thinner scintillant and the expected reduction in Compton derived background is correspondingly met by fewer full energy recorded events.

Table 7.1 Thesis Summary

Investigation	Previous Finding	Thesis Finding	Recommendation	Future Proposals
Operational:				
Effects of resolution on stripping ratios	Unknown	Determined for naturals and man-made sources	Use up to maximum of 13%, at 662 keV	Investigate for other radionuclides
Effects of gain shifts on stripping ratios	Unknown	Determined for naturals and man-made sources	Single set of stripping ratios required for ±1% change in gain	Investigate for other radionuclides
Calibration:				
Detector angular responses	Available mostly for cylindrical detectors	Determined for large, rectangular prismatic aerial survey detector	Required for field of views and calibrations	Other aerial survey detectors: 8 litre (2 detector package)
Fields of view	For the natural radionuclides only. Little angular response considered	Determined for lower energy, man-made radionuclides	Use for survey designs	Extend to other energies and aerial survey detector packages
Effects of topography	Limited	Can influence spectral readings in extreme cases	Measurements to be taken away from crests or valley sides	Corrections to be applied to spectral data
Photofraction of large survey arrays	Unknown	Overestimation. Independent of angular response	Requires further investigation	Possible use of split model detectors and other housing thicknesses
Altitude dependency of stripping ratios (experimental)	For the naturals, by small scale experiments or flight trials on certain sites	Reproduction for natural radionuclides. Use of perspex for air equivalent medium	Complete coverage of detector required to ensure that all scattering angles are covered.	Possible larger facilities necessary. Remains to be confirmed that no small scale geometrical limitations exist
Altitude dependency of stripping ratios (Monte Carlo)	Limited. None for man-made sources	Full simulation of natural and man-made sources	Model assumptions require further investigation	Further refinement before full acceptance
Study of depth profiles	Limited	Use of spectral characteristics to find distribution parameters	More sophisticated Monte Carlo codes with x-ray emission lines needed	Further investigations required
Optimisation of aerial survey detectors for environmental use	Limited	Thinner detectors may not offer significant enhancement of spectral data	Thinner detectors to spread over wider area. Lighter systems are advantageous	Further investigations necessary
Deconvolution of ^{234m}Pa	Unknown	Search for depleted uranium shells and separation from ^{228}Ac in marine environment	Careful selection of windows. Good resolution requirements necessary	Principles to be applied to more radionuclides

"To reach completion is to return to one's starting point", Colette (1954).

Bibliography

Attix, F.H. (1986). *Introduction to Radiological Physics and Radiation Dosimetry*. John Wiley.

Aubin, G., Barrette, J., Lamoureux, G., Monaro, P. (1969). Calculated Relative Efficiency for Coaxial and Planar Ge(Li) Detectors.

Avignone, F., Jeffreys, J.A. (1981). Empirical Polynomials for Computing Gamma-ray Cross-Sections and Coefficients in Ge and NaI(Tl). *Nucl. Inst. and Methods*, **179**, 159-162.

Aviv, R. and Vulkan, V. (1983). Calibration of Airborne Gamma-ray Survey over Israel. *Israel Atomic Energy Comm. Report Z.D.* **58/82**.

Beam, G.B., Wielopolski, L., Gardner, R.P., Verghese, K. (1978). Monte Carlo Calculation of Efficiencies of Right-Circular Cylindrical NaI Detectors for Arbitrarily Located Point Sources. *Nucl. Inst. and Methods*, **154**, 501-508.

Beattie, R.J.D., Byrne, J. (1974). A Monte Carlo Program for Evaluating the Response of a Scintillation Counter to Monoenergetic Gamma-rays. *Nucl. Inst. and Methods*, **104**, 163-168.

Beck, H.L., Planque, G. (1968). The Radiation Field in Air due to Distributed Gamma-ray Sources in the Ground. *HASL-195, USEAC.*

Beck, H.L., Decampo, J., Gogolak, C. (1972). In-situ Ge(Li) and NaI(Tl) Gamma-ray Spectrometry. *HASL-258.*

Beck, H.L. (1972). The Physics of Environmental Gamma Radiation Fields. Proceedings on the 2nd Int. Symposium on the Natural Radiation of the Environment.

The Natural Environment. *CONF-720805-P2/P1*, **1-2**.

Beck, H.L. (1977). Symposium Proceedings of Aerial Techniques for Environmental Monitoring (1977). *Nevada Section, American Nuclear Soc.*, Aladdin Hotel, Las Vegas, Nevada, March 7-11. **ISBN 0-89448-104-5**.

Belluscio, M., Leo, R. de, Pantaleo, A., Vox, A. (1974). Efficiencies and Response Functions of NaI(Tl) Crystals for Gamma-rays from Thick Disk Sources. *Nucl. Inst. and Methods*, **118**, 553-563.

Bengtsson, G. (1967). Peak to Total Ratios for NaI(Tl) Crystals. *Nucl. Inst. and Methods*, **46**, 356-358.

Bennett, B.G., Beck, H.L. (1967). Legendre, Tschebyscheff and Half-range Legendre Polynomial Solutions of the Gamma-ray Transport Equation in Infinite Homogeneous and Two Media Plane Geometry. *Oak Ridge National Laboratory Report* , **HASL-185**.

Berger, M.J., Doggett, J. (1956). Response Function of NaI(Tl) Scintillation Counters. *The Rev. Sci. Inst.*, **27**(5).

Berger, M.J., Seltzer, S.M. (1972). Response Functions for NaI Scintillation Detectors. *Nucl. Inst. and Methods*, **104**, 317-332.

Booth, T.E. (1986). A Monte Carlo Learning/Biasing Experiment with Intelligent Random Numbers. *Nucl. Sci. and Eng.*, **92**, 465-481.

Bristow, Q. (1978). The Application of Airborne Gamma-ray Spectrometry in the Search for Radioactive Debris from Russian Satellite COSMOS 954 (Operation "Morning Light"). *Geol. Survey of Canada, Current Research Part B*, **78-1B**, 151-162.

Bristow, Q. (1979). A Gamma-ray Spectrometry System for Airborne Geological Research. *Geological Survey Commission of Canada, Current Research Part C*, **79-1C**.

Bristow, Q. (1983). Airborne Gamma-ray Spectrometry in Uranium Exploration: Principles and Current Practice. *Int. J. Appl. Rad.*, **34**(1), 199-229.

Brown, R.T. (1975). Differential Cross-sections for Coherent Photon Scattering by Elements Z=2 to Z=26. *Atomic Data and Nuclear Data Tables*, **15**, 111-139.

Browne, E., Firestone, R.B. (1986). *Tables of Radioactive Isotopes*. John Wiley.

Burcham, W.E. (1979). *Elements of Nuclear Physics*. Longman.

Burson, Z.G., French, R.L. (1970). Simulating Energy and Angle Distributions Above Infinite Plane Sources. *Health Physics*, **18**, 507.

Burson, Z.G. (1974). Airborne Surveys of Terrestrial Gamma Radiation in Environmental Research. *IEEE Transactions on Nuclear Science*, **NS-21**(1).

Capponi, M., Massa, I., Piccinini, M. (1983). Monte Carlo Simulated Detector Responses to Gamma Radiations Coming from Extended Sources. *Nucl. Inst. and Methods*, **217**, 465-471.

Carnahan, C.L. (1964). A method for the Analysis of Complex Peaks Occurring in Gamma-ray Pulse Height Distributions. *Nucl. Inst. and Methods*, **30**, 165-183.

Carter, L.L. Cashwell, E.D. (1975). Particle Transport Simulation with the Monte Carlo Method. *U.S. Energy Res. Develop. Admin., Washington.*

Cesana, A., Terrani, M. (1989). An Empirical Method for Peak to Total Ratio Computation of a Gamma-ray Detector. *Nucl. Inst. and Methods*, **A281**, 172-175.

Chinaglia, B., Malvano, R. (1966). Efficiency Calibration of 3x3" NaI(Tl) Crystals. *Nucl. Inst. and Methods*, **45**, 125-132.

Christaller, G. (1967). Experimental Peak to Total Ratios of a 4x4" NaI(Tl) Crystal. *Nucl. Inst. and Methods*, **50**, 173-176.

Clark, M.J., Smith, F.B. (1988). Wet and Dry Deposition of Chernobyl Releases. *Nature*, **332**(17), 245-249.

Clark, A.B., Duval, J.S., Adams, J.A. (1972). Computer Simulation of an Airborne Gamma-ray Spectrometer. *J. Geophy. Res.*, **77**(17).

Clarke, E.T. (1967). Gamma-ray Scattering Near an Air-ground Interface. *Nucl. Sci. and Eng.*, **27**, 394-402.

Compton, A.H., Allison, S.K. (1935). *X-rays in Theory and Experiment*, 2nd edn.

Coppola, M., Reiniger, P. (1974). Influence of the Chemical Composition on the Gamma-ray Attenuation by Soils. *Soil Science*, **117**(6).

Cramer, S.N., Gonnord, J., Hendricks, J.S. (1986). Monte Carlo Techniques for Analyzing Deep Penetration Problems. *Nucl. Sci. and Eng.*, **92**, 280-288.

Crossley, D.J., Reid, A.B. (1982). Inversion of Gamma-ray Data for Element Abundances. *Geophysics*, **47**(1), 117-126.

Crouthamel, C.E. (1970). *Applied Gamma-ray Spectrometry*, 2nd edn.

Currie, L.A. (1968). Limits for Qualitative Detection and Quantitative Determination: Application to Radiochemistry. *Anal. Chemistry*, **40**(3).

Deal, L.J., Doyle, J.F., Burson, Z.G., Boyns, P.K. (1972). Locating the Lost Athena Missile in Mexico by the Aerial Radiological Measuring (ARMS). *Health Physics*, **23**, 95-98.

Desbarats, A.J., Killeen, P.G. (1990). A Least-Squares Inversion Approach to Stripping in Gamma-ray Spectral Logging. *Nucl. Geophysics*, **4**(3), 343-352.

Dickson, B.H., Bailey, R.C., Grasty, R.L. (1981). Utilizing Multi-channel Airborne Gamma-ray Spectra. *Can. J. Earth Sci.*, **18**, 1793-1801.

Duval, J.S., Cook, B., Adams, J.A.S. (1971). Circle of Investigation of an Airborne Gamma-ray Spectrometer. *J. Geophy. Res.*, **76**(35), 8466-8470.

Feimster, E.L. (1979). An Aerial Radiological Survey of U.S. Department of Energy Sites in Ames, Iowa. *EGG-1183-1686.*

French, R.L., Garrett, C.W. (1964). Gamma-ray Energy and Angular Distributions Near the Air-ground Interface from Plane Fallout and Point ^{60}Co Sources. *Radiation Research Associates Inc.,* Report **RRA-M42**.

French, R.L. (1965). Gamma-ray Energy and Angular Distributions above Fallout. *Health Physics*, **11**, 369.

French, R.L. (1968). On the Buried Source Model for Computing Ground Roughness Effects. *Health Physics*, **14**, 331.

Gaggero, G. (1971). Monte Carlo Calculations for the Photofractions and Energy Loss Spectra of Ge(Li) Semiconductor Detectors. *Nucl. Inst. and Methods*, **94**, 481-492.

Giannini, M., Oliva, P.R., Ramorino, M.C. (1970). Monte Carlo Calculation of the Energy Loss Spectra for Gamma-rays in Cylindrical NaI(Tl) Crystals. *Nucl. Inst. and Methods*, **81**, 104-108.

Gorrod, M.J., Coe, M.J., Yearworth, M. (1989). Parallel Processing of Monte Carlo Simulations using a Transputer Array. *Nucl. Inst. and Methods*, **A281**, 156-161.

Govindaraju, K. (1989). *Geostandards Newsletter*. The International Working Group: Analytical Standards of Mineralisation, Ores and Rocks, July 1989. ISSN 0150-5505.

Grasty, R.L. (1975). Uranium Measurement by Airborne Gamma-ray Spectrometry. *Geophysics*, **40**(3).

Grasty, R.L. (1976a). The Field of View of Gamma-ray Detectors: A Discussion. *Geological Survey of Canada, Report of Activities Part B*, 76-1B.

Grasty, R.L. (1976b). A Calibration Procedure for an Airborne Gamma-ray Spectrometer. *Geological Survey of Canada*, **76-16**.

Grasty, R.L., Kosanke, K.L., Foote, R.S. (1979). Fields of View of Airborne Gamma-ray Detectors. *Geophysics*, **44**(8), 1447-1457.

Grasty, R.L. (1980a). *The Search for COSMOS 954*. Search Theory and Applications, Plenum Press Co.

Grasty, R.L. (1980b). Skyshine and the Calibration of Ground Gamma-ray Spectrometers. *Geological Survey of Canada*, *Current Research Part A*, **80-1A**.

Grasty, R.L. (1982). Utilizing Experimentally Derived Multi-channel Gamma-ray Spectra for the Analysis of Airborne Data. *Proc. symp. Uranium Explor. Methods (Rev. of Nuclear Energy Agency/ IAEA, Paris)*.

Grasty, R.L., Glynn, J.E., Grant, J.A. (1985). The Analysis of Multi-channel Airborne Gamma-ray Spectra. *Geophysics*, **50**(12), 2611-2620.

Grasty, R.L. (1987). The Design, Construction and Application of Airborne Gamma-ray Spectrometer Pads: Thailand. *Geological Survey of Canada*, **87-10**.

Grasty, R.L., Holman, P.B., Blanchard, Y.B. (1991). Transportable Calibration Pads

for Ground and Airborne Gamma-ray Spectrometers. *Geological Survey of Canada*, **90-23.**

Green, R.M., Finn, R.J. (1965). Photopeak Efficiencies of NaI(Tl) Crystals. *Nucl Inst. and Methods*, **34**, 72-76.

Green, M.V. (1974). The Solid Angle Subtended by a Solid Right, Circular Cylinder as seen from a Point Source in Space. *Nucl. Inst. and Methods*, **117**, 409-412.

Grodstein, G.W. (1957). X-Ray Attenuation Coefficients from 10keV to 100MeV. *National Bureau of Standards Circular*, **583**.

Grosswendt, B., Waibel, E. (1975). Determination of Detector Efficiencies for Gamma-ray Energies up to 12 MeV (Part II). *Nucl. Inst. and Methods*, **131**, 143-156.

Grosswendt, B., Waibel, E. (1976). Monte Carlo Calculation of the Intrinsic Gamma-ray Efficiencies of Cylindrical NaI(Tl) Detectors. *Nucl. Inst. and Methods*, **133**, 25-28.

Heath, R.L. (1964). *Scintillation Spectrometry: Gamma-ray Spectrum Catalogue*, 2nd edn, **1-2**, IDO-16880-1, Phillips Petroleum Co., USAEC.

Heath, R.L. (1966). Computer Techniques for the Analysis of Gamma-ray Spectra Obtained with NaI and Lithium-ion Drifted Ge Detectors. *Nucl. Inst. and Methods*, **43**, 209-229.

Helfer, I.K., Miller, K.M. (1988). Calibration Factors for Ge Detectors Used for Field Spectrometry. *Health Physics*, **55**(1), 15-29.

Hilton, L.K. (1979). Mallinckrodt Nuclear Marylands Heights Facility: An Aerial Radiological Survey of the Surrounding Area. *EG & G*, **EGG-1183-1721**.

Hofstadter, R. (1949). The Detection of Gamma-Rays with Thallium Activated Sodium

Iodide Crystals. *Physical Review*, **75**(5), 796-797.

Hubbell, J.H. (1977). Photon Mass Attenuation and Mass Energy Absorption Coefficients for H, C, N, O, Ar and Seven Mixtures from 0.1 keV to 20 MeV. *Radiation Research*, **70**, 58-81.

Hubbell, J.H. (1982). Photon Mass Attenuation and Energy Absorption Coefficients from 1 keV to 20 MeV. Int. J. Appl. Rad. Isotopes, **33**.

Huddleston, C.M. (1965). Ground Roughness Effects on the Energy and Angular Distribution of Gamma Radiation from Fallout. *Health Physics*, **11**, 537.

IAEA Technical Report Series. (1976). Radiometric Reporting Methods and Calibration in Uranium Exploration. *IAEA Report*, **174**.

IAEA Technical Report Series. (1979). Gamma-ray Surveys in Uranium Exploration, *IAEA Report*, **186**.

IAEA Technical Report Series. (1990). The Use of Gamma-ray Data to Define the Natural Radiation Environment. *IAEA Report*, **IAEA-TECDOC-566**.

IAEA Technical Report Series (1991). Airborne Gamma-ray Spectrometer Surveying. *IAEA Report*, **IAEA-TECDOC-323**.

ICRU Report (1972). Measurement of Low-Level Radioactivity. Report number **22**, June 1972.

ICRU Report (1993). In-situ Gamma-ray Spectrometry in the Environment. Draft Committee Report, March 1993.

International Civil Aviation Organization, ICAO (1964). *Manual of the ICAO Standard Atmosphere*, U.S. Government Printing Office, Washington D.C.

Jarczyk, L., Knoepfel, H., Lang, J., Muller, R., Wolfli, W. (1962). Photopeak Efficiency and Response Function of Various NaI(Tl) and CsI(Tl) Crystals in the Energy Range up to 11 MeV. *Nucl. Inst. and Methods*, **17**, 310-320.

Jones, D.G., Miller, J.M., Roberts, P.D. (1984). The Distribution of ^{137}Cs in Surface Intertidal Sediments from the Solway Firth. *Marine Pollution Bulletin*, **15**(5), 187-194.

Joshi, S.R. (1989). Determination of ^{241}Am in Sediments by Direct Counting of Low-Energy Photons. *Appl. Rad. Isotope (Int. J. Rad. Appl. Inst. Part A)*, **40**(8), 691-699.

Kahn, H. (1950). Random Sampling Techniques in Neutron Attenuation Problems (I and II). *Nucleonics*, **May**.

Kennedy, J.B., Neville, A.M. (1986). *Basic Statistical Methods for Engineers and Scientists*, 3rd edn, Harper and Row.

Killeen, P.G., Carmichael, C.M. (1970). Gamma-ray Spectrometer Calibration for Field Analysis of Thorium, Uranium and Potassium. *Can. J. Earth Sci.*, **7**, 1093.

Kirkegaard, P., Løvborg, L. (1974). Computer Modelling of Terrestrial Gamma-radiation Fields. *Danish Atomic Energy Commission*, RISØ Report **303**.

Kirkegaard, P., Løvborg, L. (1980). Transport of Terrestrial Gamma-radiation in Plane Semi-Infinite Geometry. *J. Computational Physics*, **36**, 20-34.

Knasel, T.M. (1970). Accurate Calculations of Radiation Lengths. *Nucl. Inst. and Methods*, **83**, 217-220.

Kosanke, K.L., Koch, C.D. (1978). An Aerial Radiometric Data Modelling Program. *IEEE Transactions on Nuclear Science*, **NS-25**(1).

Lal, B., Iyengar, K.V.K. (1970). Monte Carlo Calculations of Gamma-ray Response

Characteristics of Cylindrical Ge(Li) Detectors. *Nucl. Inst. and Methods*, **79**, 19-28.

Lapp, R.E., Andrews, H.L. (1972). *Nuclear Radiation Physics*, 4th Ed. Pitman & Sons Ltd.

Lederer, C.M., Shirley, V.S. (1978). *Table of Isotopes*, 7th Ed. Lawrence Berkely Laboratory, University of California, Berkely. John Wiley & Sons.

Leutz, H., Schultz, G. & Van Gelderen, L. (1966). Peak to Total Ratios for NaI(Tl) Crystals. *Nucl. Inst. and Methods*, **40**, 257-260.

Lister, B.A.J. (1963). The Use of Helicopters for Emergency District Survey after an Accidental Release of Radioactive Material. *Health Physics*, **9**, 309.

Løvborg, L., Wollenberg, H., Sørensen, P., Hansen, J. (1971). Field Determination of Uranium and Thorium by Gamma-ray Spectrometry, Exemplified by Measurements in the Ilimaussaq, Alkaline Intrusion, South Greenland. *Economic Geology*, **66**(3).

Løvborg, L., Kirkegaard, Rose-Hansen, J. (1972). Quantitative Interpretation of the Gamma-ray Spectra from Geologic Formations. Proceedings on the 2nd Int. Symposium on the Natural Radiation of the Environment. The Natural Environment. *CONF-720805-P2/P1*, **1-2**.

Løvborg, L., Kirkegaard, P. (1974). Response of 3x3" NaI(Tl) Detectors to Terrestrial Gamma-radiation. *Nucl. Inst. and Methods*, **121**, 239-251.

Løvborg, L., Kirkegaard, P. (1975). Numerical Evaluation of the Natural Gamma-radiation Field at Aerial Survey Heights. *Danish Atomic Energy Commission Research Est.*, RISØ Report **317**.

Løvborg, L., Kirkegaard, P., Christiansen, E.M. (1976). Design of NaI(Tl) scintillation Detectors for Use in Gamma-ray Surveys of Geological Sources. *IAEA-SM-208/21*.

Løvborg, L., Grasty, R.L., Kirkegaard, P. (1977). Symposium Proceedings of Aerial Techniques for Environmental Monitoring (1977). *Nevada Section, American Nuclear Soc.*, Aladdin Hotel, Las Vegas, Nevada, March 7-11. **ISBN 0-89448-104-5**.

Løvborg, L., Bøtter-Jensen, L., Kirkegaard, P. (1978). Experiences with Concrete Calibration Sources for Radiometric Field Instruments. *Geophysics*, **43**(3), 543-549.

Løvborg, L. (1982). Error Analysis of Calibration and Field Trials with Spectrometers and Counters. *Symposium on Uranium Exploration Methods*. OECD Nuclear Energy Agency in Collaboration with IAEA, Paris, 1-4th June.

Løvborg, L., Mose, E. (1987). Counting Statistics in Radioelement Assaying with a Portable Spectrometer. *Geophysics*, **52**(4), 555-563.

Markevich, N., Gertner, I. (1989). Comparison Among Methods for Calculating FWHM. *Nucl. Inst. and Methods*, **A283**, 72-77.

Meixner, C.H. (1974). A Monte Carlo Program for the Calculation of Gamma-ray Spectra for Germanium Detectors. *Nucl. Inst. and Methods*, **119**, 521-526.

Mellander, H. (1989). Airborne Gamma Spectrometric Measurements of the Fallout over Sweden after the Nuclear Reactor Accident at Chernobyl, USSR. *Swedish Geological Co., Airborne Dept.*, **IAEA/NENF/NM-89-1**.

Mickael, M., Gardner, R.P., Verghese, K. (1988). An Improved Method for Estimating Particle Scattering Probabilities to Finite Detectors for Monte Carlo Simulation. *Nucl. Sci. and Eng.*, **99**, 251-266.

Mickael, M.W., Gardner, R.P., Verghese, K. (1989). A New Approach for Monte Carlo Simulation of Dual-Spaced Neutron Porosity Log Responses. Trans. Am. Nuc. Soc.

Miller, W.F., Reynolds, J., Snow, J.W. (1957). Efficiencies and Photofractions for NaI(Tl) Crystals. *The Rev. Sci. Inst.*, **28**(9).

Mishra, U.C., Sadasivan, S. (1969). Experimental Peak to Total Ratios for a Few NaI(Tl) Crystal Sizes. *Nucl. Inst. and Methods*, **69**, 330-334.

Mudahar, G.S., Sahota, H.S. (1988). Effective Atomic Number Studies in Different Soils for Total Photon Interaction in the Energy Region 10-5000 keV, *Int. J. Rad. Appl. Inst. (Appl. Rad. Iso.)*, **39**(12).

Mudahar, G.S., Modi, S., Singh, M. (1991). Total and Partial Attenuation Coefficients of Soil as a Function of Chemical Composition. *Int. J. Rad. Appl. Inst.*, **42**(1).

Mukoyama, T. (1976). Range of Electrons and Positrons. *Nucl. Inst. and Methods*, **134**, 125-127.

Nardi, E. (1970). A Note on Monte Carlo Calculations in NaI Crystals. *Nucl. Inst. and Methods*, **83**, 331-332.

Paatero, P. (1964). Drift: A Drift Correcting Computer Subroutine for Nuclear Spectroscopy. *Nucl. Inst. and Methods*, **31**, 360.

Petr, I., Adams, A., Birks, J.B. (1971). Directional Characteristics of Cylindrical Scintillators. *Nucl. Inst. and Methods*, **95**, 253-257.

Pitkin, J.A., Duval, J.S. (1980). Design Parameters for Aerial Gamma-ray Surveys. *Geophysics*, **45**(9), 1427-1439.

Raeside, D.E. (1974). An Introduction to Monte Carlo Methods. *AJP*, **42**.

Raghuwanshi, S.S., Bhaumik, B.K. (1989). Estimation of Stripping Ratios at Survey Height in Airborne Gamma-ray Spectrometry. *Nucl. Geophysics (Int. J. Rad. Appl.*

Inst. Part E), **3**(2), 113-118.

Rangelov, R., Hetu, R., Grant, J.A., Grasty, R.L. (1990). Monitoring Man-made Radiation by Airborne Gamma-ray Spectrometry (Bulgaria). *Geological Survey of Canada*.

Richardson, K.A. (1981). High Sensitivity Airborne Radiometric Surveying Over Tropical and Rain Forest Areas. *IAEA-AG-162/04*.

Rogers, D.W.O. (1982). More Realistic Monte Carlo Calculations of Photon Detector Response Functions. *Nucl. Inst. and Methods*, **199**, 531-548.

Rybacek, K., Jacob, P., Meckbach, R. (1991). In-situ Determination of Deposited Radionuclide Activities: Improvement of the Method by Deriving Depth Distributions from the Measured Photon Spectra. Submitted for publication in *Health Physics* (Sept.).

Saito, K., Moriuchi, S. (1981). Monte Carlo Calculation of Accurate Response Functions for a NaI(Tl) Detector for Gamma-rays. *Nucl. Inst. and Methods*, **185**, 299-308.

Saito, K., Moriuchi, S. (1985). Development of a Monte Carlo Code for the Calculation of Gamma-ray Transport in the Natural Environment. *Radiation Protection Dosimetry*, **12**(1), 21-28.

Saito, K., Moriuchi, S. (1988). Data Catalogue of Gamma-ray Response Functions for NaI(Tl) Scintillation Detectors by Monte Carlo. *Japanese Atomic Energy Research Est.*, JAERI-**1306**.

Saito, K. (1991). External Doses Due to Terrestrial Gamma-rays on the Snow Cover. *Radiation Protection Dosimetry*, **35**(1), 31-39.

Salmon, L. (1961). Analysis of Gamma-ray Scintillation Spectra by the Method of Least

Squares. *Nucl Inst. and Methods*, **14**, 193-199.

Salomon, M. (1978). Comparisons of Reflectors Used in Scintillation Counters. *Nucl. Inst. and Methods*, **153**, 289-290.

Sanderson, D.C.W., Scott, E.M., Baxter, M.S., Preston, T. (1988a). A Feasibility Study of Airborne Radiometric Survey for UK Fallout. *SURRC Report*.

Sanderson, D.C.W., East, B.W., Robertson, I., Scott, E.M. (1988b). The Uses of Aerial Radiometrics in the Search for a lost ^{137}Cs Source. *SURRC Report*.

Sanderson, D.C.W., Scott, E.M. (1988c). Aerial Radiometric Survey in West Cumbria. *MAFF Project N611*.

Sanderson, D.C.W., Baxter, M.S., Scott, E.M. (1989). The Use and Potential of Radiometrics for Monitoring Environmental Radioactivity. *COGER, Lancaster Conference*.

Sanderson, D.C.W., Scott, E.M., Baxter, M.S. (1990a). Use of Airborne Measurements for Monitoring Environmental Radioactive Contamination. *IAEA SM-306/138*, **1**.

Sanderson, D.C.W., Allyson, J.D., Martin, E., Tyler, A.N., Scott, E.M. (1990b). An Airborne Gamma-ray Survey of Three Ayrshire Districts. *SURRC Report*.

Sanderson, D.C.W., Allyson, J.D., Cairns, K.J., MacDonald, P.A. (1990c). A Brief Aerial Survey in the Vicinity of Sellafield Reprocessing Plant in September 1990. *SURRC Report*.

Sanderson, D.C.W., Allyson, J.D. (1991). An Aerial Gamma-ray Search for a Missing ^{137}Cs Source in the Niger Delta. *SURRC Report*.

Sanderson, D.C.W., Tyler, A.N., Cairns, K.J. (1991). Radiometric Flight Trials in the Forth Estuary. *SURRC Report*.

Sanderson, D.C.W., Allyson, J.D., Tyler, A.N., (1992). An Aerial Survey of Chapelcross and its Surroundings in February 1992. *SURRC Report*.

Sanderson, D.C.W., Allyson, J.D., Tyler, A.N., Murphy, S. (1993a). An Aerial Gamma Ray Survey of Springfields Fuel and Ribble Estuary in September 1992. *SURRC Report*.

Sanderson, D.C.W., Allyson, J.D., Tyler, A.N., Ni Rian, S., Murphy, S. (1993b). An Airborne Gamma-Ray Survey of Parts of SW Scotland in February 1993. *SURRC Report*.

Sanderson, D.C.W., Allyson, J.D., Tyler, A.N., Scott, E.M. (1993c). Environmental Applications of Airborne Gamma Spectrometry. *Technical Committee Meeting on the Use of Uranium Exploration Data and Techniques in Environmental Studies, Vienna, Austria. 9-12 November 1993.*

Sanderson, D.C.W., Allyson, J.D., Tyler, A.N. (1993d). Rapid Quantification and Mapping of Radiometric Data for Anthropogenic and Technically Enhanced Natural Nuclides. *Technical Committee Meeting on the Use of Uranium Exploration Data and Techniques in Environmental Studies, Vienna, Austria. 9-12 November 1993.*

Sanderson, D.C.W., Scott, E.M., Baxter, M.S., Martin, E., Ni Rian, S. (1993e). The Use of Aerial Radiometrics for Epidemiological Studies of Leukaemia. *SURRC Report*.

Schaarsshimidt, A., Keller, H.J. (1969). Calculation of Efficiency and Cross-Section of Cylindrical Scintillators in Axisymmetrical Gamma-ray Fields. *Nucl. Inst. and Methods*, **72**, 82.

Shafroth, S.M. (1967). *Scintillation Spectroscopy of Gamma-Ray Radiation*, **1**. Gordan

& Breach Science Publishers.

Sharma, R.C., Garg, S.P., Somasundaram, S. (1972). Monte Carlo Calculations for Thin NaI(Tl) Crystals at Energies Below 100 keV. *Nucl. Inst. and Methods*, **101**, 413-422.

Shreider, Y. A. (1966). *The Monte Carlo Method*, Pergamon Press.

Snyder, B.J., Knoll, G.F. (1966). Calculated Gamma-ray Photofractions for Well Type Scintillation Detectors. *Nucl. Inst. and Methods*, **40**, 261-266.

Snyder, B.J. (1967). Comparison of Calculated and Experimental Scintillation Crystal Photofractions. *Nucl. Inst. and Methods*, **46**, 173-176.

Storm, E., Israel, H.I. (1970). Photon Cross-Sections from 1keV to 100MeV for Elements Z=1 to Z=100. *Nuclear Data Tables*, **A7**, 565-681.

SURRC Report (1992). Allyson, J.D., Tyler, A.N., Sanderson, D.C.W. (1992). *Mass Attenuation Coefficients of Soils*. Internal SURRC report, May 1992.

Tsutsumi, M., Saito, K., Sakamoto, R., Nagaoka, T., Moriuchi, S. (1986). Developments of Aerial Gamma Radiation Survey I, Measuring Instruments of Gamma Radiation, Position Data and Data Processing Method. *JAERI-M*, **86-072**.

Turner, J.E., Wright, H.A., Hamm, R.N. (1985). A Monte Carlo Primer for Health Physicists. *Health Physics*, **48**(6), 717-733.

Tyler, A.N. (1994). *Environmental Influences of Gamma-Ray Spectrometry*. Phd Thesis. University of Glasgow.

U.S. Standard Atmosphere (1976). National Oceanic and Atmospheric Administration, National Aeronautics & Space Administration, USAF. *NOAA-S/T* 76-1562.

Verghese, K., Gardner, R.P. (1990). A Generalized Approach to Designing Specific Purpose Monte Carlo Programs: A Powerful Simulation Tool for Radiation Applications. *Nucl. Inst. and Methods*, **A299**, 1-9.

Weitkamp, C. (1963). Monte Carlo Calculation of Photofractions and Intrinsic Efficiencies of Cylindrical NaI(Tl) Scintillation Detectors. *Nucl. Inst. and Methods*, **23**, 13-18.

Williams, D., Cambray, R.S. & Maskell, S.C. (1957). An airborne radiometric survey of the Windscale area, Oct 19-22, 1957. *UKAEA Research Group Report*, **AERE-R-2890**.

Williams, D., Cambray, R.S. (1960). Environmental Survey from Air. *UKAEA Research Group Report*, **AERE-R-2954**.

Wilson, R.R. (1951). The Range and Straggling of High Energy Electrons. *Physical Review*, **84**(1).

Xiangbao, L., Yangzhong, X. (1992). Relationship Between ^{131}I Ground Surface Contamination Activity and Gamma Spectra Above Ground. *Health Physics*, **62**(4).

Zerby, C.D., Moran, H.S. (1962). Calculation of the Pulse Height Response of NaI(Tl) Scintillation Counters. *Oak Ridge National Laboratory, Neutron Physics Division*, USAEC **ORNL-3169.**

Zerby, C.D. (1963). A Monte Carlo Calculation of the Response of Gamma-ray Scintillation Counters. *Methods of Computational Physics*, **1**.

Zombori, P., Andrási, A., Németh, I. (to be published). A New Method for the Distribution of Radionuclide Distribution in Soil by In-situ Gamma-ray Spectrometry. *Inst. for Atomic Energy Research*, Hungary. Awaiting submission.

Appendix A

Definitions of Efficiency

a). Geometrical Efficiency: ε_G

For a point source, this is the fraction of the total radiation that is incident on the crystal face, ie. the fraction of the solid angle Ω that the crystal subtends at the source to the total solid angle (4π).

b). Total Intrinsic Efficiency: $\varepsilon_{tot,int}$

The fraction of the monoenergetic isotropic radiation incident on the crystal face that interacts to produce a scintillation event. A wealth of data has been accumulated for the intrinsic efficiency of various right cylindrical NaI(Tl) crystals and may be found by the following means. The probability of a photon traversing a path x, in a crystal of height h, with no interaction is $e^{-\mu x}$. Thus $(1-e^{-\mu x})$ is the interaction probability: μ is the total absorption coefficient per unit length. For a parallel beam normally incident on the front face of a crystal x=h and therefore $\varepsilon_{tot,int}=(1-e^{-\mu h})$. For a point source (unless it is far away) $\varepsilon_{tot,int}$ must be calculated by integrating over all possible path lengths of the crystal dimensions.

c). Total Absolute Efficiency:

$$\varepsilon_{tot,abs} = \varepsilon_{tot,int}\varepsilon_G \qquad (A.1)$$

d). Full Energy Peak Intrinsic Efficiency:

$$\varepsilon_{p,int} = \varepsilon_{tot,int} R \qquad (A.2)$$

R is the *photofraction* or *peak-to-total ratio*, which is the ratio of the area beneath the full energy peak to the area beneath the total spectrum of a monoenergetic photon. It is the probability of a detected γ-ray being recorded in the full energy peak of a spectrum.

e). Full Energy Peak Absolute Efficiency:

$$\varepsilon_{p,abs} = \varepsilon_{tot,int} \varepsilon_G R \qquad (A.3)$$

Small variations in detector resolution do not usually affect the full energy peak efficiency. It must be remembered however that the full energy peak represents events that have occurred in a single interaction (eg. photoelectric) and by multiple coincident interactions (within the time resolution of the detector).

Appendix B

Table B.1 Variation of stripping ratios with an air equivalent medium.

		Stripping Ratios of ^{137}Cs: SURRC Windows			
Sheet No.	**^{137}Cs**	**^{134}Cs**	**^{40}K**	**^{214}Bi**	**^{208}Tl**
0	1	0.0541 ±0.0002	0.002 ±0.002	0.0029 ±0.0009	-0.0007 ±0.0009
1	1	0.0488	-0.009	0.0011	-0.0028
2	1	0.0448	-0.018	-0.0010	-0.0026
3	1	0.0403	-0.033	-0.0019	-0.0061
4	1	0.0396	-0.046	-0.0049	-0.0061
5	1	0.0337	-0.067	-0.0062	-0.0091
6	1	0.0219	-0.085	-0.0080	-0.0136
7	1	0.0366	-0.093	-0.0085	-0.0141
8	1	0.0088	-0.140	-0.0146	-0.0196
9	1	-0.0324	-0.203	-0.019	-0.023
10	1	-0.0300	-0.232	-0.026	-0.032
11	1	-0.06	-0.31	-0.04	-0.038
12	1	-0.12	-0.41	-0.05	-0.049
13	1	-0.19	-0.55	-0.06	-0.066
14	1	-0.26	-0.68	-0.09	-0.087
15	1	-0.34	-0.88	-0.11	-0.11
16	1	-0.50	-1.24	-0.15	-0.15
17	1	-0.68	-1.64	-0.19	-0.19
18	1	-1.09	-2.47	-0.35	-0.32
19	1	-2.03	-4.43	-0.58	-0.57
20	1	-14.36 ±6.62	-29.9 ±13.7	-3.99 ±1.84	-3.73 ±1.75

Table B.2 Variation of stripping ratios with an air equivalent medium.

	Stripping Ratios of ^{40}K: SURRC Windows				
Sheet No.	**^{137}Cs**	**^{134}Cs**	**^{40}K**	**^{214}Bi**	**^{208}Tl**
0	0.460 ±0.008	0.278 ±0.006	1	0.027 ±0.003	-0.004 ±0.002
1	0.501	0.303	1	0.028	-0.006
2	0.511	0.301	1	0.025	-0.005
3	0.550	0.328	1	0.032	-0.001
4	0.589	0.343	1	0.025	-0.011
5	0.630	0.364	1	0.019	-0.001
6	0.637	0.368	1	0.021	-0.021
7					
8	0.691	0.383	1	0.023	-0.013
9	0.705	0.405	1	0.029	-0.019
10	0.715	0.410	1	0.020	-0.009
11	0.790	0.454	1	0.027	-0.029
12	0.849	0.457	1	0.029	-0.023
13	0.871	0.502	1	0.028	-0.017
14	0.926	0.546	1	0.012	-0.030
15	0.924	0.527	1	0.013	-0.021
16	0.881	0.521	1	0.041	-0.039
17	0.995	0.558	1	0.042	-0.016
18	0.858	0.531	1	0.040	-0.017
19	1.050	0.586	1	0.024	-0.028
20	0.941 ±0.067	0.567 ±0.044	1	-0.023 ±0.020	-0.163 ±0.018

Figure B.3 Variation of stripping ratios with an air equivalent medium.

Stripping Ratios of ^{214}Bi: SURRC Windows

Sheet No.	^{137}Cs	^{134}Cs	^{40}K	^{214}Bi	^{208}Tl
0	3.486 ±0.014	1.269 ±0.006	0.903 ±0.006	1	0.142 ±0.002
1	3.488	1.304	0.901	1	0.149
2	3.489	1.320	0.923	1	0.151
3	3.492	1.333	0.919	1	0.154
4	3.486	1.354	0.939	1	0.157
5	3.493	1.368	0.964	1	0.158
6	3.490	1.388	0.949	1	0.159
7	3.478	1.400	0.952	1	0.166
8	3.497	1.410	0.959	1	0.167
9	3.479	1.415	0.975	1	0.157
10	3.496	1.447	0.987	1	0.174
11	3.516	1.459	0.985	1	0.178
12	3.544	1.490	1.015	1	0.181
13	3.564	1.530	1.011	1	0.164
14	3.698	1.654	1.127	1	0.186
15	3.897	1.773	1.326	1	0.200
16	3.750	1.682	1.135	1	0.192
17	3.752	1.706	1.136	1	0.211
18	3.846	1.800	1.260	1	0.214
19	3.786	1.704	1.158	1	0.220
20	3.619 ±0.038	1.637 ±0.020	0.773 ±0.016	1	0.188 ±0.007

Table B.4 Variation of stripping ratios with an air equivalent medium.

	Stripping Ratios of ^{208}Tl: SURRC Windows				
Sheet No.	**^{137}Cs**	**^{134}Cs**	**^{40}K**	**^{214}Bi**	**^{208}Tl**
0	2.821 ±0.013	1.574 ±0.008	0.600 ±0.006	0.440 ±0.003	1
1	2.821	1.571	0.600	0.442	1
2	2.884	1.615	0.634	0.442	1
3	2.892	1.600	0.635	0.455	1
4	2.879	1.586	0.642	0.466	1
5	2.871	1.568	0.652	0.461	1
6	2.870	1.546	0.652	0.476	1
7	2.871	1.545	0.656	0.486	1
8	2.893	1.550	0.663	0.498	1
9	2.871	1.527	0.686	0.500	1
10	2.849	1.512	0.681	0.505	1
11	2.848	1.512	0.690	0.518	1
12	2.825	1.501	0.670	0.529	1
13	2.853	1.482	0.670	0.544	1
14	2.832	1.501	0.670	0.530	1
15	2.853	1.512	0.693	0.557	1
16	2.821	1.452	0.699	0.562	1
17	2.814	1.474	0.727	0.562	1
18	2.833	1.467	0.734	0.584	1
19	2.759	1.437	0.719	0.588	1
20	2.924 ±0.023	1.513 ±0.017	0.746 ±0.013	0.627 ±0.009	1

Table B.5 Variation of stripping ratios with an air equivalent medium.

Stripping Ratios of ^{137}Cs: IAEA Windows					
Sheet No.	**^{137}Cs**	**^{134}Cs**	**^{40}K**	**^{214}Bi**	**^{208}Tl**
0	1	0.054 ±0.002	-0.001 ±0.002	0.0020 ±0.0008	-0.0009 ±0.0008
1	1	0.049	-0.010	0.0003	-0.0028
2	1	0.045	-0.019	-0.001	-0.0028
3	1	0.040	-0.030	-0.0004	-0.0057
4	1	0.040	-0.044	-0.003	-0.0058
5	1	0.034	-0.06	-0.005	-0.0082
6	1	0.022	-0.08	-0.006	-0.0127
7	1	0.037	-0.09	-0.007	-0.013
8	1	0.009	-0.12	-0.011	-0.018
9	1	-0.032	-0.15	-0.01	-0.02
10	1	-0.03	-0.19	-0.02	-0.03
11	1	-0.06	-0.25	-0.03	-0.04
12	1	-0.1	-0.3	-0.04	-0.04
13	1	-0.2	-0.4	-0.05	-0.06
14	1	-0.2	-0.5	-0.06	-0.08
15	1	-0.3	-0.7	-0.09	-0.10
16	1	-0.5	-0.9	-0.12	-0.14
17	1	-0.7	-1.2	-0.14	-0.18
18	1	-1.1	-1.9	-0.26	-0.30
19	1	-2.0	-3.4	-0.44	-0.54
20	1	-14.4 ±6.6	-22.8 ±10.5	-2.9 ±1.4	-3.4 ±1.6

Table B.6 Variation of stripping ratios with an air equivalent medium.

	Stripping Ratios of ^{40}K: IAEA Windows				
Sheet No.	**^{137}Cs**	**^{134}Cs**	**^{40}K**	**^{214}Bi**	**^{208}Tl**
0	0.511 ±0.009	0.309 ±0.006	1	0.018 ±0.003	-0.006 ±0.002
1	0.557	0.337	1	0.022	-0.007
2	0.570	0.336	1	0.020	-0.007
3	0.615	0.367	1	0.022	-0.004
4	0.663	0.386	1	0.021	-0.013
5	0.710	0.410	1	0.017	-0.011
6	0.718	0.415	1	0.015	-0.022
7					
8	0.785	0.435	1	0.025	-0.015
9	0.798	0.459	1	0.025	-0.023
10	0.811	0.465	1	0.018	-0.010
11	0.892	0.512	1	0.020	-0.034
12	0.968	0.521	1	0.03	-0.024
13	0.994	0.57	1	0.03	-0.02
14	1.066	0.63	1	0.02	0.08
15	1.072	0.61	1	0.02	-0.02
16	1.01	0.60	1	0.04	-0.04
17	1.14	0.64	1	0.04	-0.02
18	0.97	0.60	1	0.04	-0.02
19	1.20	0.67	1	0.03	-0.03
20	1.098 ±0.08	0.66 ±0.05	1	-0.004 ±0.02	-0.19 ±0.02

Table B.7 Variation of stripping ratios with an air equivalent medium.

	Stripping Ratios of ^{214}Bi: IAEA Windows				
Sheet No.	**^{137}Cs**	**^{134}Cs**	**^{40}K**	**^{214}Bi**	**^{208}Tl**
0	4.31 ±0.02	1.570 ±0.008	0.703 ±0.006	1	0.144 ±0.003
1	4.33	1.618	0.704	1	0.152
2	4.33	1.638	0.728	1	0.154
3	4.35	1.660	0.730	1	0.159
4	4.34	1.686	0.743	1	0.162
5	4.35	1.703	0.771	1	0.166
6	4.35	1.731	0.756	1	0.167
7	4.35	1.750	0.766	1	0.175
8	4.36	1.760	0.765	1	0.176
9	4.39	1.784	0.785	1	0.166
10	4.39	1.819	0.795	1	0.186
11	4.44	1.84	0.79	1	0.191
12	4.45	1.87	0.82	1	0.195
13	4.40	1.90	0.78	1	0.170
14	4.59	2.05	0.83	1	0.201
15	4.89	2.23	0.90	1	0.217
16	4.64	2.08	0.84	1	0.207
17	4.66	2.12	0.84	1	0.230
18	4.76	2.23	0.90	1	0.233
19	4.72	2.12	0.88	1	0.238
20	4.51 ±0.05	2.04 ±0.03	0.40 ±0.02	1	0.202 ±0.008

Table B.8 Variation of stripping ratios with an air equivalent medium.

	Stripping Ratios of ^{208}Tl: IAEA Windows				
Sheet No.	**^{137}Cs**	**^{134}Cs**	**^{40}K**	**^{214}Bi**	**^{208}Tl**
0	3.05 ±0.01	1.704 ±0.009	0.386 ±0.005	0.323 ±0.003	1
1	3.05	1.698	0.384	0.325	1
2	3.11	1.74	0.402	0.324	1
3	3.11	1.72	0.407	0.336	1
4	3.09	1.70	0.41	0.340	1
5	3.09	1.69	0.42	0.336	1
6	3.09	1.66	0.42	0.348	1
7	3.09	1.66	0.42	0.354	1
8	3.11	1.67	0.42	0.367	1
9	3.08	1.64	0.44	0.361	1
10	3.06	1.62	0.44	0.370	1
11	3.06	1.63	0.45	0.385	1
12	3.03	1.61	0.43	0.387	1
13	3.05	1.59	0.43	0.400	1
14	3.04	1.61	0.43	0.393	1
15	3.06	1.62	0.45	0.419	1
16	3.02	1.56	0.44	0.416	1
17	3.01	1.58	0.47	0.417	1
18	3.04	1.57	0.48	0.436	1
19	2.96	1.54	0.46	0.442	1
20	3.14 ±0.03	1.63 ±0.02	0.47 ±0.01	0.467 ±0.008	1

Appendix C

Table C.1 The uranium ^{238}U series. Radioactive nuclides occurring between Z=81-92 are known as the (4n+2) series (where n is an integer) because each member has a mass number (4n+2).

Atomic Number Z	Name		Half-life	Principal Radiation
92	Uranium	^{238}U (UI)	$4.5x10^{9}a$	α
90	Thorium	^{234}Th (UXI)	24.1d	β^-
91	Protoactinium	^{234m}Pa (UXII)	1.16m	β^-
92	Uranium	^{234}U (UII)	$2.5x10^{5}a$	α
90	Thorium	^{230}Th (I_o)	$8.0x10^{4}a$	α
88	Radium	^{226}Ra	1602a	α
86	Radon	^{222}Rn	3.82d	α
84	Polonium	^{218}Po (RaA)	3.05m	α
82	Lead	^{214}Pb (RaB)	26.8m	β^-,γ
83	Bismuth	^{214}Bi (RaC)	19.7m	β^-,γ
84	Polonium	^{214}Po (RaC′)	160μs	α
81	Thallium	^{210}Tl (RaC″)	1.5m	β^-
82	Lead	^{210}Pb (RaD)	21a	β^-
83	Bismuth	^{210}Bi (RaE)	5d	β^-
84	Polonium	^{210}Po	138d	α
82	Lead	^{206}Pb	stable	

Table C.2 Thorium series (4n).

Atomic Number Z	Name		Half-life	Principal Radiation
90	Thorium	^{232}Th	1.4×10^{10}a	α
88	Radium	^{228}Ra (MsI)	6.7a	β^-
89	Actinium	^{228}Ac (MsII)	6.13h	β^-, γ
90	Thorium	^{228}Th	1.91a	α
88	Radium	^{224}Ra (ThX)	3.64d	α
86	Radon	^{220}Rn (Thoron)	55s	α
84	Polonium	^{216}Po (Th-A)	0.16s	α
82	Lead	^{212}Pb (Th-B)	10.6h	β^-, γ
83	Bismuth	^{212}Bi (Th-C)	60.6h	α (36%) β^-, γ (64%)
84	Polonium	^{212}Po (Th-C′)	300ns	α
81	Thallium	^{208}Tl (Th-C″)	3.1m	β^-, γ
82	Lead	^{208}Pb	stable	

Table C.3 Actinium (^{235}U) series (4n+3).

Atomic Number Z	Name		Half-life	Principal Radiation
92	Uranium	^{235}U (AcU)	7.1×10^8a	α
90	Thorium	^{231}Th (UY)	25.5h	β^-
91	Protoactinium	^{231}Pa (Pa)	3.2×10^4a	α
89	Actinium	^{227}Ac (Ac)	21.6a	β^-
90	Thorium	^{227}Th (RdAc)	18.2d	α
88	Radium	^{223}Ra (AcX)	11.4d	α
86	Radon	^{219}Rn (An)	4s	α
84	Polonium	^{215}Po (AcA)	1.78ms	α
82	Lead	^{211}Pb (AcB)	36.1m	β^-
83	Bismuth	^{211}Bi (AcC)	2.15m	α
81	Thallium	^{207}Tl (AcC″)	4.79m	β^-
82	Lead	^{207}Pb (AcD)	stable	

Appendix D

Transformations and Conversions

The calculated estimates of fluence rates and count rates, given per Bq kg^{-1} and kBq m^{-2} can be converted to other concentration terms by the use of the following transformations.

Table D.1 Transformation parameters.

Parameter:	**Equivalent Parameter:**
1 disintegration/s	1 Becquerel (Bq)
1 Curie	$3.7x10^{10}$ Bq
1 mCi kg^{-1}	37000 Bq g^{-1}
1 mCi km^{-2}	37 Bq m^{-2}
1 γ s^{-1} cm^{-2} (Flux) per γ s^{-1} cm^{-2} (emitted by source)	1 γ s^{-1} m^{-2} (Fluence rate) per γ s^{-1} m^{-2} (emitted by source)
1 γ s^{-1} cm^{-2} (Flux) per γ s^{-1} cm^{-2} (emitted by source)	1.ß γ s-1 m-2 (Fluence rate) per Bq m^{-2} (activity of source) ß=decay branching ratio
1 γ s^{-1} cm^{-2} (Flux) per γ s^{-1} g^{-1} (emitted by source)	10 γ s^{-1} m^{-2} (Fluence rate) per γ s^{-1} kg^{-1} (emitted by source)

Note. Fluence rate has superseded flux as the conventional unit.

Transforming Between Concentration Parameters

a). Specific Activity

The specific activity of any radionuclide can be determined from first principles by the use of the following formula:

$$Specfic\ Activity = \frac{\lambda N_A I_{ab}}{A} \qquad Bq\,g^{-1} \tag{D.1}$$

where, λ-decay constant

N_A = Avogadro's Number

I_{ab} = Isotopic Abundance

A = Atomic Weight

The specific gamma ray activity, for a given decay and gamma ray emission line is

$$Specific\ \gamma\text{-}Activity = Specific\ Activity . \beta \qquad \gamma s^{-1} g^{-1} \qquad \text{(D.2)}$$

where, ß = branching ratio of the gamma emission line

The specific activity of ^{40}K (of total potassium) is 30.7272 Bq g^{-1}. The specific gamma activity is 3.278 γ s^{-1} g^{-1}.

The specific activity of ^{238}U is 1.229×10^4 Bq g^{-1} of total uranium. The corresponding specific gamma activity of ^{214}Bi (1764 keV) is 1.955×10^3 γ s^{-1} g^{-1}.

The specific activity of ^{232}Th is 4.104×10^3 Bq g^{-1} of total thorium. The specific gamma activity of ^{208}Tl (2615 keV) is 1.482×10^3 γ s^{-1} g^{-1} (36% of the ^{232}Th decay chain is via ^{208}Tl).

b). Percentage Concentrations

In order to convert x% concentration into γ cm^{-2} s^{-1}, for a given altitude, the following may be used:

$$x\%\ conc. \rightarrow [Fl.rate\ per\ Bq\,kg^{-1}] \frac{[Specific\ \gamma\ Activity . 10^3]}{[\beta . 10^{-2}]}$$

$$.[x.10^{-2}] . 10^{-4} \qquad \gamma\, cm^{-2} s^{-1} \qquad \text{(D.3)}$$

where ß (number of γ-rays emitted per decay) and x are in percentages.
For x% potassium, the γ cm^{-2} s^{-1} of ^{40}K at 1461 keV (β=10.67%) is

$$[Fl.rate\ per\ Bq\,kg^{-1}]\ 0.0307216\ x \tag{D.4}$$

Similarly,

$$x\%\ conc. \rightarrow [cps\ per\ Bq\,kg^{-1}]\ \frac{[Specific\,\gamma\,Activity.10^{3}]}{[\beta.10^{-2}]}$$

$$.[x.10^{-2}]\quad cps \tag{D.5}$$

Again for x% of potassium, the estimated count rate (cps) is

$$[cps\ per\ Bq\,kg^{-1}]\ 307.216\ x \tag{D.6}$$

c). PPM Concentrations

In order to convert x ppm concentration into γ cm^{-2} s^{-1}, for a given altitude, the following may be used:

$$x\ ppm\ conc. \rightarrow [Fl.rate\ per\ Bq\,kg^{-1}]\frac{[Specific\,\gamma\,Activity.10^{3}]}{[\beta.10^{-2}]}$$

$$.[x.10^{-6}].10^{-4}\quad \gamma\,cm^{-2}s^{-1} \tag{D.7}$$

For x ppm uranium, the γ cm^{-2} s^{-1} of ^{214}Bi at 1764 keV (β=15.9%) is

$$[Fl.rate\ per\ Bq\,kg^{-1}]\ 0.0012296\ x \tag{D.8}$$

For x ppm thorium, the γ cm^{-2} s^{-1} of ^{208}Tl at 2615 keV (β=99.79%) is

$$[Fl.rate\ per\ Bq\,kg^{-1}]\ 0.00014851\ x \tag{D.9}$$

And,

$$x\ ppm\ conc. \rightarrow [cps\ per\ Bq\,kg^{-1}]\ \frac{[Specific\,\gamma\,Activity.10^{3}]}{[\beta.10^{-2}]}$$

$$.[x.10^{-6}] \quad cps \tag{D.10}$$

For x ppm of uranium, the estimated count rate (cps) is

$$[cps\ per\ Bq\,kg^{-1}]\ 12.296\ x \tag{D.11}$$

For x ppm of thorium, the estimated count rate (cps) is

$$[cps\ per\ Bq\,kg^{-1}]\ 1.4851\ x \tag{D.12}$$

Note. These conversions are only valid for sources that are effectively infinite in plane extension (in terms of photon transport), and evenly distributed with depth.